THREE DIMENSIONAL COMPUTATIONAL FLUID DYNAMICS MODELS OF POLLUTANT TRANSPORT IN A DEEP OPEN PIT MINE UNDER ARCTIC AIR INVERSION AND MITIGATION MEASURES

By

Kumar Vaibhav Raj

RECOMMENDED:

Dr. Rajive Ganguli

Dr. Michael G. Nelson

Dr. G. Javier Fochesatto

Dr. Sukumar Bandopadhyay
Advisory Committee Chair

Dr. Rajive Ganguli
Chair, Department of Mining and Geological Engineering

APPROVED:

Dr. Doug Goering
Dean, College of Engineering & Mines

Dr. John C. Eichelberger
Dean of the Graduate School

24 April 2015
Date

THREE DIMENSIONAL COMPUTATIONAL FLUID DYNAMICS MODELS OF POLLUTANT TRANSPORT IN A DEEP OPEN PIT MINE UNDER ARCTIC AIR INVERSION AND MITIGATION MEASURES

A

THESIS

Presented to the Faculty

of the University of Alaska Fairbanks

in Partial Fulfillment of the Requirements

for the Degree of

DOCTOR OF PHILOSOPHY

By

Kumar Vaibhav Raj, M.S.

Fairbanks, Alaska

May 2015

Abstract

As open pit mines continues to grow deeper and productivity continues to increase, the management of air pollution can become challenging. One of the challenges, common during winter in deep open pit mines operating in the Arctic, is the occurrence of atmospheric inversion. In itself, inversion is not hazardous. However, due to the emission of gases and particulates during the mining process, the air within the pit can be severely contaminated, rather quickly, leading to serious health and safety consequences. The problem is complex and any solution approach will require a good understanding of the interaction of the aerodynamic movement of air, the air inversion process, the meteorology, the pollutant sources, and the application of mechanical ventilators in open pit mines. Scientific literatures related to open pit mine ventilation, particularly with respect to air inversion, are practically non-existent in the English literature. This is perhaps the first account of a three dimensional computational fluid dynamics (CFD) model of pollutant transport in an actual open pit mine under an Arctic air inversion.

Advanced technology has made computers faster and more powerful, which allows computational fluid dynamics (CFD) procedures to be applied to many air flow problems. Thus, a CFD approach can be used to understand the transport of contaminant in the pit during inversion by using several turbulence models. An array of data is required to develop CFD models for open pit mine ventilation. The meteorological conditions within deep open pit mines are significantly affected by temperature and roughness conditions, which ultimately generate complex dispersion phenomena including separation of air flow and its recirculation. For the application of CFD, various data such as pollutants concentrations, temperature, velocity, pit contours, equipment locations, and radiation (shortwave and longwave) were collected from the selected open pit mine and the weather stations located nearby. Analysis of the weather data showed that inversions are due to elevated inversions in the selected open pit mine.

Because an exact flow situation in open pit mines is not known a-priori, open pit air flow simulation and pollution transport are often highly sensitive to the type of flow model employed. It is therefore necessary to investigate various turbulent models to identify the appropriate model that will simulate the flow phenomena with reasonable accuracy and predict the contaminant distributions within the pit. Dispersion models differ in their assumptions and structures as well as in the algorithm used and as a result, predictions vary from model to model. Furthermore, it is

also important to investigate the behavior of a CFD model when simulating complex phenomena, such as the transport and distribution of contaminants in an open pit mine under an Arctic air inversion. The simulation of an enhanced period of turbulence in the stable boundary layer (SBL) is of particular interest because traditional air pollution dispersion models cannot explicitly treat intermittent turbulence events, and yet the SBL is often the worst-case scenario in open pit pollution transport.

Realizable κ-ε and Large Eddy Simulation (Lesieur et al.) models were used for understanding flow of gaseous contaminants. The 2010 pit configuration was used to develop models for understanding the gaseous transport under air inversion. During an inversion, turbulence is dominant at the bottom of the pit, while in the middle portion of the pit turbulence is intermittent and flow over the upper portion of the pit is mostly laminar. The realizable κ-ε model tends to over-predict the contaminant concentration, whereas, the LES model under-predicts the level of pollutant concentrations.

Validation of the developed model was performed using the 2013 pit configuration. Despite the complex synoptic situations, the different meteorological input data and the fast changing conditions, the simulation results from the validation model were in good agreement regarding the dispersion of pollutants and other turbulent variables. Pollutant concentration values in the selected locations showed differences, but remained within the same order of magnitude in most cases.

Removal of the harmful pollutants from the pit is significantly important for the health and safety of the mine workers. The mitigation models were developed for both the 2010 and the 2013 pit configurations. Several remedial measures such as the use of mechanical ventilators in forcing and exhaust mode, push-pull ventilation and a novel approach of using cloud cover were considered. Mitigation efforts employing mechanical means were unsuccessful in removing or diluting the contaminants to a safe level. The novel approach of using cloud cover over an open pit mine showed promise. With this approach, the model showed that the inversion could be lifted and pit could be cleared of all pollutants.

This thesis is dedicated to my parents,
Shanti and Gopal Mandal.

For their endless love, support, encouragements, patience and hearty blessings.

Table of Contents

List of Figures

Page

List of Tables

Page

Acknowledgments

This research was supported by the National Institute for Occupational Safety and Health (NIOSH), and Dr. Sukumar Bandopadhyay served as the principal investigator for the project. I would like to express my deep sense of gratitude and indebtedness to Dr. Sukumar Bandopadhyay for suggesting the problem for this research. Without his encouragements, patience and the guidance this study would not have been completed. I wish to thank the support of our industrial partner for sharing the operational and meteorological data, access to the mine, and in-kind financial support in setting up the instruments at the mine. Assistance of the technical support team of ANSYS is also gratefully acknowledged.

I would also like to thank the members of the graduate advisory committee: Dr. Rajive Ganguli, and Dr. Michael Nelson for their support. I especially like to thank Dr. Javier Fochesatto, a member of the graduate advisory committee, for his valuable suggestions during this research. Special thanks to Dr. R. V. Ramani, Professor Emeritus, The Pennsylvania State University and Christopher Pritchard, Technical Project Officer for this project, for their support, advice, and encouragements.

I would also take this opportunity to thank my fellow graduate students, Abhishek Choudhary and Will Collingwood for their valuable suggestions and constructive criticisms in this research. I would like to thank Sontu Mandal, Ipshita Majhi, Ashish Agrawal, Santosh Panda, Rijo Simon, Bindu Gadamsetty and all my friends for their constant support and encouragements.

Chapter 1 Introduction

1.1 Background

The Arctic region contains vast mineral resources. Mining of these resources is a major activity in the Arctic regions of several countries, particularly the United States. With the advancement of open pit mining technology, the depth to which minerals can be profitably mined has increased, resulting in deeper pits than ever before. This increase in depth has several inherent challenges for mining operations. One of the challenges for deep open pit mining in a cold climate is atmospheric air inversion. Air inversion, a meteorological phenomenon, occurs mainly due to negative net radiation balance at the Earth surface. In this condition, the temperature of the air mass at the pit bottom cools more rapidly than the air mass above it, leading to the creation of a positive upward temperature gradient in the open pit. By itself, inversion is not hazardous. However, due to the presence and emission of gases and particulates during the mining process, the air within the pit can be severely and sometimes quickly contaminated, leading to serious health and safety consequences. In order to maintain and enhance the health and safety of the mine workers, effective measures are necessary to both minimize pollutant emissions and adequately ventilate the pit to dilute, disperse, and remove toxic pollutants (Bandopadhyay and Izaxon 2005).

Extreme cases of unsafe respirable atmospheres have been associated with air inversions in both large urban areas such as Los Angeles, California; Mexico City, Mexico; Sao Paulo, Brazil; Santiago, Chile; Mumbai, India; Beijing, China; and Tehran, Iran, and in smaller cities like Oslo, Norway; Salt Lake City, Utah; and Boise, Idaho. In Fairbanks, Alaska, low-level inversion occurs more than 95% of the time during winter (Wendler and Nicpon 1975). During a severe inversion, trapped air pollutants form a brownish haze which can cause respiratory problems. The Great Smog, one of the most serious examples of such an inversion, occurred in London in 1952 and is blamed for thousands of deaths (Wilkins 1954; Kotin and Falk 1955).

In extreme climatic conditions, deep open pit mines tend to trap pollutants at pit bottom due to air inversions. Keeping open pits adequately ventilated is a considerable challenge for the mining community. Mine operators in cold regions are very familiar with this problem, the severity of which can be judged from Figure 1.1 and Figure 1.2. The top portion of the figures shows

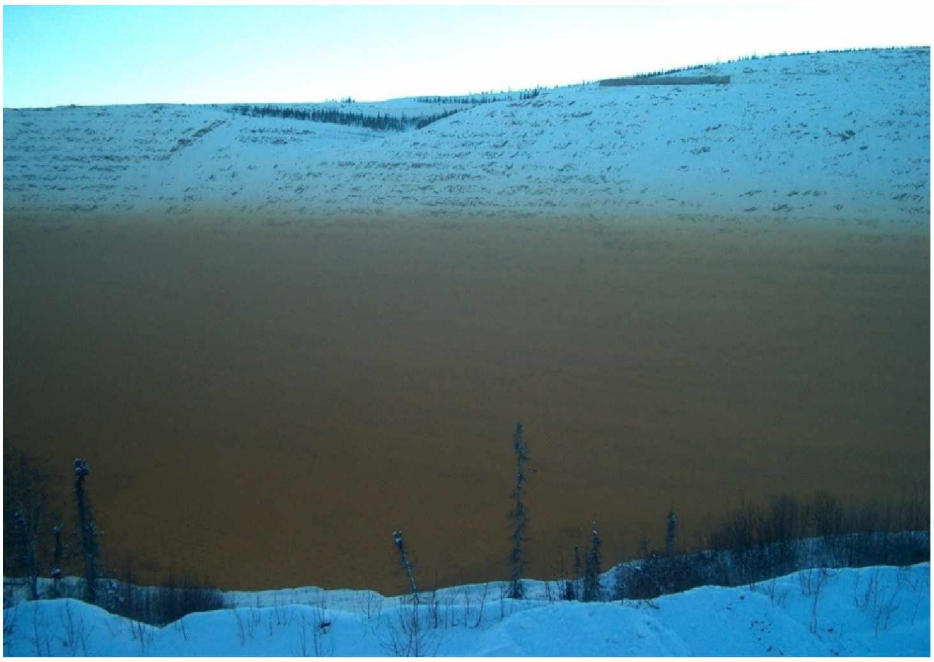

Figure 1.1: Typical Air Inversion at an Open Pit Mine, View 1.

Figure 1.2: Typical Air Inversion at an Open Pit Mine, View 2.

clear sky and snow covered benches. The brown haze, containing various contaminants accumulated over time in the pit under the air inversion, can be seen in the bottom portion of the figures. Several Arctic or sub-Arctic mines have reported air inversions, including the Kinross Fort Knox (Fairbanks) and Teck Cominco Red Dog mines in Alaska, the BHP Billiton Ekati mine

in Canada, the Boliden Aitek mine in Sweden, and the Mirni and Udachini diamond open pit mines in Russia. Even Rio Tinto's Bingham Canyon pit in Utah has reported local air inversions from time to time (Whiteman and Hoch 2014).

Minimizing the effects of air inversions has been recognized as an important aspect of healthy and safe mining conditions. Natural ventilation is one of the preferred means to deal with pollutants in open pit mines (Peng and Lu 1995). The wind flow pattern in open pit mines is generally of the recirculatory type under neutral atmospheric conditions. Under neutral atmospheric conditions inversion is not present. However, during a clear day, incoming solar radiation heats up the pit surface, breaking the thermal stratification and driving out pollutants via local mixing and thermal buoyancy. Even with the thermal convection due to solar heating of the surface, most space in a deep open pit is not exposed to the solar radiation, resulting in recirculation zones; therefore the conditions for natural ventilation are far from ideal. Increased wind speed entering the pit is useful for the dilution and dispersion of air pollutants. Even in ideal natural convection conditions, there may be an accumulation of pollutants at the bottom of a pit, thus necessitating artificial remedial measures. Frequent air inversions exacerbate this naturally occurring phenomenon. Furthermore, the benches and overall pit slope generally impede natural ventilation in an open pit. Thus, a detailed examination of the cause-effect relationship between the forcings causing inversions and resulting pollution leading to a predictive model for air inversion in Arctic open pit mines is necessary.

1.2 Problem Statement

The accumulation of pollutants poses a serious threat to the health and safety of the miners present in an open pit mine during an inversion. To understand and analyze air inversions, it is necessary to understand the process by which such inversions and consequent accumulation of pollutants takes place. Since pollution in a mine is anthropogenic and often emitted from a mobile source, any proposed solution must include consideration of these factors.

Natural ventilation cycles exist in open pit mines and have traditionally been the primary mode of dilution and elimination of pollutants in such mines. Natural ventilation in an open pit originates from the windward side of the pit and flows into the pit as a turbulent stream (Figure 1.3). The turbulent flow has two effects on the concentrations of the pollutants. First, it re-circulates and

redistributes the concentrations of the pollutants already existing within the pit. Second, it may introduce pollutants into the pit that did not originate there.

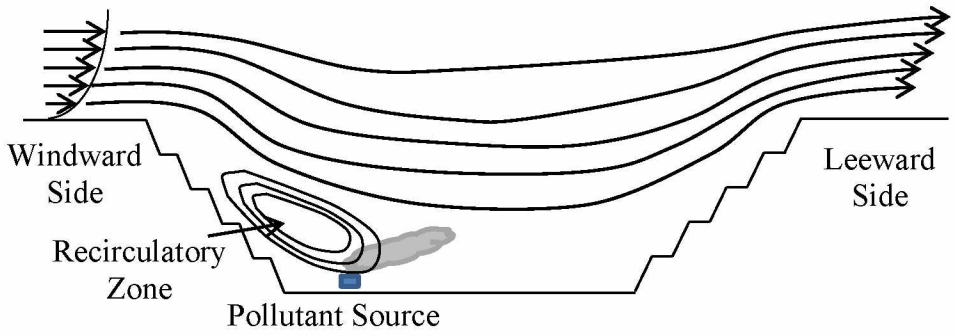

Figure 1.3: Illustration of Wind Flow in an Open Pit Mine.

Atmospheric air inversion results from the radiative cooling of the Earth surface in the absence of solar radiation as well as advection of cold air front near the Earth surface and advection of warm air over the cold air pool. The presence of warmer air above a colder air mass disrupts the vertical movement of air, thus making the atmosphere stable. Event of inversion has been associated with low wind speed, clear sky and night time situation (Wendler and Nicpon 1975). One of the important goals of this research is to understand turbulent transport within the inversion layer. Two main types of turbulent transport are observed in the atmosphere: wind shear driven mechanical turbulence and thermal turbulence due to convection. However, the mechanical turbulence is dominated by the thermal turbulence during an inversion due to the lower wind speed. As the inversion layer starts to build up, the mechanical turbulence dies out due to several thermal layers which behave as a cap for the pollutants, impeding their escape into the atmosphere. In deep open pit mines, equipment running continuously during an inversion also enhances the accumulation of pollutants in the pit.

To solve the problem of air inversion in Arctic open pit mines, the air flow in an open pit mine must first be examined. The air flow through the mine profile has several demarcated zones. Recognition of these zones can help not only model the flow of air and advective contaminants in the open pit, but also allows estimation of the final concentration profile in a steady state situation.

Ventilation design for open pit mines requires knowledge of the quantity of pollutants that are liberated into the pit by various stationary and mobile sources. The most important criteria in the total balance of pollutants in open pit mines are the stationary point sources, i.e., drilling rigs, excavators, loading machines and moving sources, such as trucks. The distribution of pollutants from these sources in an open pit mine is directly related to the aerodynamics of the airflows in the open pit. Evaluation of the atmospheric conditions in an open pit mine requires determination of the concentration of pollutants. Therefore, it is necessary to calculate the intensity of the continuous point sources of pollutants and the frequencies and magnitudes of the dissipation of pollutants from the sources located at various aerodynamic zones in the pit.

When considering neutral atmospheric conditions, flow separation hampers natural ventilation of pollutants released from various mobile and stationary sources. Flow separation takes place at the leading edge of the pit and creates a re-circulatory zone in the open pit. Flow separation because of the fractioning of the kinetic energy leads to the loss of energy at the point of separation and an insufficient amount of energy to transport pollutants in the pit (Chang 1970).

Over the past two decades, numerous meteorological and tracer experiments have been conducted to investigate the dispersive characteristics of valley atmospheres (Allwine et al. 1997). These and other studies have led to the identification and more complete understanding of key physical processes governing dispersion in valleys. The important physical processes include up and down valley wind speeds, turbulent diffusion, convective boundary layer growth, temperature inversion descent, nocturnal temperature inversion breakup, tributary flows, cross-valley circulations, and interaction with above-ridge top winds (Whiteman 1980). Studies on the flow and dispersion of diesel exhaust in underground airways, from point and moving sources, have also been conducted by Bandopadhyay and Ramani (1983,1984,1985,1988). However, while application of these models is limited—because the geometry and air flow characteristics of open pit mines are much different from those in underground mines—the findings are still relevant to the study of the mine ventilation conditions in an open pit mine.

In an open pit mine, the upward heat flux also develops a convective boundary layer (CBL) over the pit surface, but, in contrast, the heated pit slopes cause the warm air parcels to flow up-slope due to thermal buoyancy. These up-slope flows remove mass from the base of the temperature inversion, resulting in a general subsiding motion over the center of the open pit

(Allwine et al. 1997). The CBL growth and descent of the inversion are both functions of sensible heat flux, atmospheric pressure, air density, radiative flux, pit potential temperature lapse rate at sunrise, and the synoptic-thermodynamic conditions above the pit.

In the past three decades, the development of computational fluid dynamics (CFD) has made it possible to better understand pollutant flow in open pit mines. CFD can be used to predict air flow and pollutant distribution. The majority of these CFD programs are based on Navier-Stokes (N-S) equations, the energy equation, the mass conversion, and transport equations for turbulent viscosity and its scale. CFD models provide a pattern of air flow, distribution of pollutant concentration, and temperature within an open pit. CFD modeling has been widely used in atmospheric pollution studies in urban areas. However, none of those models or studies has addressed ventilation design for deep, open pit mines in general and especially in Arctic or sub-Arctic conditions. The phenomenon of buoyancy driven flow in an open pit is an important issue of mass and energy transport between the incoming air and the stringent air mass under Arctic inversion. Very few CFD studies of air flow in open pit mines have been reported for the Arctic region, especially using the Large Eddy Simulation (Lesieur et al.).

1.3 Scope of this Research

There are three methods generally used to study the air flow distribution and contaminant transport in open pit mines: empirical models, experimental measurements, and computational fluid dynamics (CFD). Most researchers use scale model measurements and empirical models to study the pollutant distribution driven by convection and diffusion only. Although these models are simple, they cannot account for the highly transient and complicated behavior of the ABL, interaction with solar radiation, and pit geometry of open pit mines. Therefore, full-scale experimental investigation is critically important. Nevertheless, due to the extensive size of an open pit mine, experimental measurements are expensive in terms of time and cost, and are therefore deemed impractical.

CFD is an alternative approach to study the complex natural phenomena of Arctic inversion. Any solution to the problem of air inversion and removal of pollutants will require an extensive understanding of the interaction of the aerodynamic movement of air, air inversion, meteorology, pollutant source, transport phenomena, and fan applications in open pit mines. The CFD modeling

effort proposed here is: to develop and solve the coupled conservation equations of mass, momentum, and energy with appropriate initial and boundary equations.

Most airflows of interest are turbulent flows characterized by velocity fluctuations with turbulent eddies distributed within the flow structure (as opposed to laminar stratified flow). Mathematically, the ability to accurately model and resolve these turbulent fluctuations with the bulk airflow pattern during computer simulation ultimately determines the accuracy of the overall numerical simulation.

In this study, the CFD work is performed using an academic research version of the fluid dynamics software package ANSYS-CFD to import and mesh open pit geometry and model contaminant transport under an Arctic air inversion. ANSYS-CFD uses finite volume method (FVM) based code for fluid flow simulation. Meshing is one of the most critical steps in getting good simulation results. For importing and meshing, ANSYS ICEM-CFD is used. Meshing is a step to discretize a continuous domain into discrete grid points; however, due to the complexity of the model domain mesh may not be of desired mesh quality for better model convergence and reasonable simulation outcomes. Once a good quality mesh is obtained, it is brought into the model solver ANSYS-FLUENT for turbulent modeling.

The fluctuations in the velocity of turbulent airflow mix transported quantities such as momentum, energy, and pollutant concentrations, and cause them to fluctuate as well. Since these fluctuations can be of small scale and high frequency, they are too computationally expensive to simulate directly in open pit ventilation calculation. Instead, the instantaneous governing equations can be time averaged, ensemble averaged, or otherwise manipulated to remove small scale fluctuations, resulting in a modified set of equations that are computationally less expensive to solve. The important issue of CFD, however, is the equations used to capture the turbulent behavior of flow. With change in the geometry and aspect ratio of the model domain flow behavior also change. Because an exact flow situation in open pit mines is not known a-priori, and open pit air flow simulation and pollution transport are often highly sensitive to the type of flow model employed, therefore, requires a range of turbulent models of varying complexity and accuracy. It is therefore very important to select the suitable turbulent models for CFD in order to get a better understanding of the air flow patterns and turbulent characteristics of the air in open pit mines.

Turbulence is an eddying motion that exists at higher Reynolds numbers. Turbulence has a wide spectrum of eddy sizes with a corresponding spectrum of fluctuation frequencies. The large eddies have sizes of the same magnitude as the flow domain, have low frequencies, and are affected by the flow conditions at the boundaries and the mean flow.

The Reynolds-Averaged Navier-Stokes (RANS) equations represent transport equations for the mean flow quantities only, with all scales of turbulence being modeled. The RANS approach is generally adopted for practical engineering calculations and uses models such as κ-ε and its variants.

Unlike Reynolds averaging, which relies on ensemble-averaging in its mathematical formulations and calculates mean flow characteristics, LES models divide the overall flow structure into large and small scale motions. The large scale motions are directly calculated, while the small scale motions are modeled.

LES provides the solution for time-dependent and three-dimensional flows. In LES, the large scale turbulence is not modeled, and only eddies smaller than the mesh size need to be represented by a so-called sub-grid scale model. Therefore, it is important that the grids are fine enough to describe the small eddies. The mean flow quantities predicted from transient calculations need sufficient time to obtain a steady averaged solution. Thus, the LES contains the time-dependent evolution of eddies in three dimensions.

ANSYS-FLUENT has a number of turbulent models built-in, but the choice of turbulent model is problem-specific. However, these turbulence models falls in two categories, namely, Reynolds Averaged Navier-Stokes (RANS) based models and Scale Resolving Simulation (SRS) models. Once the turbulent model of interest is selected for the modeling of pollutant transport under inversion the next step is to validate the model. In this research, we use κ-ε and LES turbulent models for CFD, then compare the results with the measured data. This will be done in order to compare these two different turbulent modeling approaches.

While the methodology developed in this research will be useful in any open pit mine ventilation situation, the scope of this research is limited to a discussion of pollutant flow in deep open pit mines under Arctic inversion. Specifically, the following tasks will be undertaken: (a) investigate the air inversion process in open pit mines; (b) identify and categorize the factors influencing air inversion and air pollution; (c) review literature and develop appropriate CFD

models to study the air inversion problem in active open pit mines; (d) collect data from operating open pit mines in Alaska and validate the model; (e) test κ-ε from RANS based models and Large Eddy Simulation (Lesieur et al.) from SRS based models to simulate the atmospheric air inversions in Arctic deep open pit mines; (f) analyze alternative ventilation planning schemes for mitigating pollution in open pit mines under inversion; and (g) synthesize the results of the research into a set of recommendations.

1.4 Organization of the Thesis

Research will be presented in several chapters. The problem of contaminant transport in open pit mines under Arctic inversion is specific to the Arctic and sub-Arctic regions.

Chapter 2- Atmospheric Boundary Layer: Atmospheric air inversion, in general, is a common feature in the Arctic during the winter months, and a considerable amount of research has been conducted to understand the phenomenon of air inversion. This chapter presents a comprehensive review of the literatures related to ABL, the formation of inversion layer, and topics related to meteorological phenomena affecting inversion

Chapter 3- Literature Review: Published scientific literature on open pit mine ventilation, particularly with respect to air inversion, is practically non-existent in English literature. However, researchers at the Kola Mining Institute in the Murmansk region of Russia and the Yakutsk Mining Institute of the North at the Soviet Academy of Sciences have done considerable amounts of work on open pit mine ventilation. This chapter presents a review of published research available in the Russian language, collected from these research institutes and other sources.

Chapter 4- Characterization of the Variables and Data Collection: The meteorological inputs needed to determine contaminant concentration are wind speed and direction of airflow. The wind speed and direction observations at one height are used to determine the main forcing flow outside the pit. Data will be collected from an operating mine regarding the number of stationary equipment in place (e.g. shovels, generators, drills), the number of moving equipment (e.g. dozers, graders, trucks), their locations, and their operation status, i.e., ready hours, delay hours, and stand by hours. Data will also be collected on moving sources (such as trucks) from shift reports and status reports to develop the duty cycles of the trucks so that reasonable exhaust pollution loading information can be developed for model application. This chapter presents information collected during the data gathering and the CFD model building phases such as: (a) mean diurnal wind

velocity (mean values for each month); (b) number of calm days, their distribution both daily and monthly, the mean and maximum duration of calm weather; (c) number of foggy days according to the months and their duration (mean and maximum); (d) mean monthly humidity of the atmospheric air (for the warm period of the year); (e) duration of the period with freezing soil temperatures (below 0°C); (f) mean monthly air temperature with absolute maxima and minima; (g) sources of air pollution and volume and rate of contaminants for each point source; (h) air inversion frequencies and durations; and (i) air quality values during air inversions, and required standards that need to be met are presented.

Chapter 5- Preprocessing of Data for CFD Model Development: Modeling turbulent flow in open pit mines requires preprocessing of data. The actual open pit mine geometry adds considerable inherent complexity to the problem. This chapter presents a detailed discussion on the various challenges with regard to geometry and meshing encountered during modeling.

Chapter 6- Modeling of Gaseous Contaminant Transport and Diffusion under Conditions of Air Inversion: This chapter presents modeling of contaminant transport under air inversion using the model developed in the previous chapter.

Chapter 7- Model Validation: Sufficiently validated, the CFD model becomes an important design tool. The models developed in Chapters 6 and 7 will be validated using data from an operating mine in Alaska. This chapter presents the validation results.

Chapter 8- Mitigation Measures for Removal or Reduction of Pollutants from the Selected Open Pit Mine: In order to mitigate the pollution problem, several remedial measures would be considered. The layer of air closest to the ground requires energy to restart the convective cycle and dissipate the pollutants. This energy can be imparted to it either kinetically or thermally. A kinetic solution would entail placing a fan in the mine pit or at the top of the pit, thus resulting in dilution ventilation. A truck mounted fan-duct system is ideal for such an operation. A thermal solution would entail adding heat to the air, creating a chimney effect. Other technically implementable solutions will be developed and evaluated, such as cascade ventilation, where ventilators are positioned so as to form an air corridor, the horizontal unit supplies the air and, hence, the contaminants to the operating zone of the vertical unit, which removes them from the pit. The CFD model will be modified to represent an existing open pit mine including single point, multi-point, and moving sources. This chapter presents the results of the various mitigation efforts.

Chapter 9- Summary and Conclusions: This chapter presents a summary and conclusions of the research and future scope of the work.

Chapter 2 Stable Boundary Layer in Open Pit Mines

Deep open pits tend to trap pollutants at the pit bottom due to air inversions and presents a considerable challenge for the mining community in adequately ventilating the pit. An inversion layer can be described as the thermal stratification between atmospheric layers that attenuates the vertical movement of trapped pollutants. Most of the pollutants are within the atmospheric boundary layer of an open pit mine. Therefore, a clear understanding of the ABL of an open pit mine is required to mitigate the pollutants within the pit.

The concept of the boundary layer was first developed by Ludwig Prandtl (1904). Prandtl demonstrated that the flow over a solid surface could be split into two regions: an inner boundary layer where the viscous force is dominant, and an outer layer where the viscosity can be neglected. Prandtl boundary layer theory has been effectively applied in understanding the flow on flat plate, and other types of bodies.

In the Prandtl flat plate boundary layer theory, the Earth is considered as a spherical body, continuously rotating on its own axis, and a huge mass of air is enclosing it. The circulation of air over the Earth's surface and the diurnal cycles of solar radiation allow the distinction of an air layer close to the earth surface. This layer of air is characterized by varying scales of motion in time and space, called the atmospheric boundary layer (ABL). The height of this boundary layer ranges from hundreds of meters to a few kilometers. Stull (1988) defines "**the boundary layer as that part of the troposphere that is directly influenced by the presence of the earth's surface, and responds to surface forcings with a timescale of about an hour or less (p. 2).**" Surface forcings that are considered include frictional drag, evaporation and transpiration, heat transfer, pollutant emission, and terrain induced flow modification. Within the depth of the boundary layer, the transport of momentum, heat, and pollutants is carried out due to turbulence. Thus, turbulence is one of the important mechanisms dominating the transport processes in the atmospheric boundary layer.

The Atmospheric Boundary Layer (ABL) is the turbulent atmospheric layer adjacent to the Earth's surface that is directly affected by diurnal cycles at the surface. Thus, the ABL is a turbulent layer that is characterized by irregular eddies. The length scale of turbulence in the atmosphere ranges from a millimeter to thousands of meters (Stull 1988; Garratt 1994). The

turbulent eddy motions are generated by two mechanisms: wind shear and buoyancy. When a flow travels over a rough surfaces such as trees, buildings and terrain, cause the wind to develop shear turbulence and influences the temperature or any scalar field. Buoyancy on the other hand leads to the formation and rise of thermals.

In Figure 2.1 the effects of diurnal cycles on the boundary layer structure over land surfaces in high pressure regions are presented. As it can be seen, the boundary layer structure has three major components: (1) a mixed layer, (2) a residual layer, and (3) a stable boundary layer.

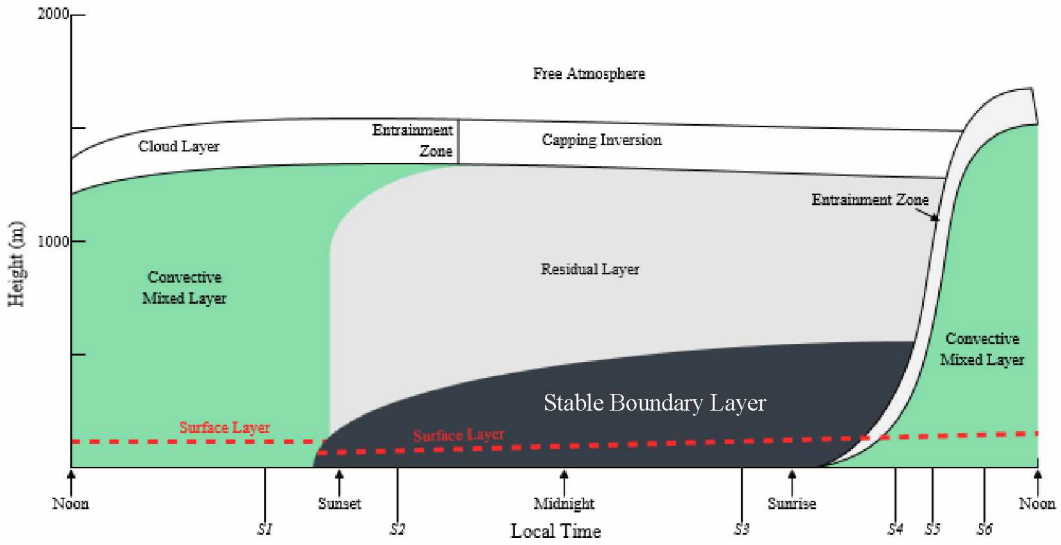

Figure 2.1: The Boundary Layer in High Pressure Region over Land (Stull 1988).

A mixed layer evolves after the sunrise, mainly driven by convection. It is also called convective boundary layer (CBL). In the absence of clouds, the ground surface is heated by the incoming solar radiation. This causes the thermals to rise up, developing a turbulent motion in the atmosphere. The turbulent mixes the heat, momentum, moisture, and pollutants in the vertical direction. While at the same time, the atmospheric flow is in constant contact with the surface, and develops turbulence to maintain the progression of the ABL diurnal cycle.

In the absence of any cold air advection, the thermals generated during the day in fair weather conditions tend to cease just before the sunset. This allows the turbulence to decay in the formerly well-mixed layer (Sorbjan 1989). This new layer formed is called the residual layer. The residual layer attains near-neutral stability under non-advective conditions (Fochesatto et al. 2001a,b).

After the sunset, and as the night approaches, the surface heat fluxes is negative (surface cooling). Thus the bottom portion of the residual layer in contact with the ground is transformed into a stable boundary layer (SBL). The stable boundary layer prevails at night, but can also develop during the daytime in Arctic and sub-Arctic regions due to the lack of adequate sunlight during the winter months. The SBL is characterized by statically stable air where the vertical stability suppresses the surface turbulence. The SBL formed during the night time, sometime referred to as the nocturnal boundary layer.

The SBL, can also be developed by warm air advection over a cooler surface (Mayfield and Fochesatto 2012). In majority of the high pressure situations, temperature inversions are observed. Various studies have been conducted on the temperature inversion in Fairbanks, Alaska (Wendler 1969; Wendler and Jayaweera 1972) and more recently Fochesatto and others (2013), Mayfield and Fochesatto (2012) and Malingowski and others (2014). Understanding the physics of the stable boundary layer is relevant to air flow and pollutant transport in deep open pit mines. Since under SBL, due to it suppressed vertical motion, pollutants generated in an open pit mine primarily spreads in the horizontal direction and does not leave the open pit.

Strong stable boundary layers can be found in high latitudes in the winters when the air in the surface layer is confined to a cold-closed basin. The local and areal radiative forcing dominates the formation and breakup of the inversion, whereas, advection is limited by the geometry of the area. In these conditions, the flow in the cold pool is susceptible to developing strong stratified inversion layers.

2.1 Processes Affecting the SBL

Several forces such as the radiation, the conduction, the turbulence, the subsidence, the advection and the local terrain configurations affect the formation and destruction of the SBL (Stull 1988). Among these forces, radiation plays a critical role both in the formation and destruction of the SBL. Conduction acts within few millimeters above the ground. It has a very low magnitude elsewhere in the boundary layer, and can be neglected. For the purpose of modeling of pollutant transport in open pit mines, some of these forcings can be neglected depending upon the specific environmental conditions.

2.1.1 Radiation

In the absence of solar radiation and advective flows, the net radiation is dominated by long-wave radiation (Stull 1988) which introduces the radiative cooling. There are generally four types of energy fluxes at an ideal surface: (1) the net radiation to and from surface, (2) the sensible (direct), (3) latent (indirect) heat fluxes to and from atmosphere, and (4) the heat flux into or out of the sub-medium (Arya 2001). The net radiation is the sum total of the incoming and out-going shortwave and longwave radiation. For a flat surface, the net radiation is illustrated in Figure 2.2, where SW ↓ is the down-welling shortwave radiation; SW ↑ is the up-welling shortwave radiation; LW ↓ is the down-welling longwave radiation; and LW ↑ is the up-welling longwave radiation. The net radiation (R_N) is given as:

$$R_N = SW\downarrow - SW\uparrow + LW\downarrow - LW\uparrow \qquad (2.1)$$

During the day in fair-weather conditions, the down-welling solar radiation is dominant. The surface gains energy from the solar heating, resulting in a net positive radiation. On the other hand, at night, in the absence of solar heating, the longwave radiation going out of the surface is prevalent, resulting in surface cooling, and net negative radiation. Due to the surface cooling a positive upward temperature profile near the ground is developed. Therefore, during the night, the longwave radiation balance plays a key role in determining the structure of the SBL.

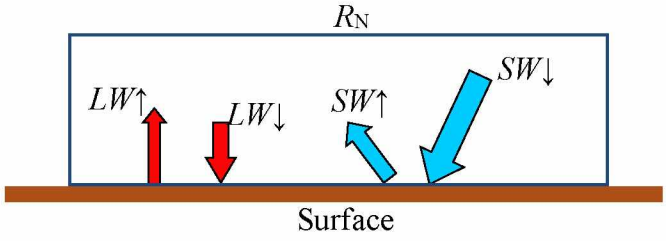

Figure 2.2: An Illustration of Net Radiation Fluxes.

As can be seen in Figure 2.2, if pressure gradient forces can be neglected the incoming solar radiation is the major external surface forcing. Whereas, the sensible, latent, and ground heat fluxes are the response on and near the surface. It is, therefore, the net radiation is always in balance with these fluxes, and expressed as:

$$R_N = H_S + H_L + H_G \qquad (2.2)$$

Where, the terms H_S and H_L are the sensible and latent heat fluxes to and from the atmosphere, and the term H_G is the ground heat flux into or out of the sub-mediums.

The sensible heat flux is the result of temperature difference between the surface and the air above it. During the day, the sensible heat flux is directed away from the surface. During the night time, however, the fluxes are towards the surface and therefore, the flux is negative.

Molecular sub-layer is defined as the first few millimeters of the air layer. In this layer, conduction and molecular diffusion are the dominant forcing. Above the molecular sub-layer, turbulent processes combined with advection or convection is the primary mode of heat exchange. Evaporation or condensation or more generally, evapotranspiration at the surface results in the latent heat flux exchange. The moisture content in the sub-medium determines the magnitude of the latent heat flux into or out of a sub-medium. At times, the latent heat flux can also be represented by phase change, i.e., from ice to water and water to water vapor and vice versa. A small value of latent heat flux is observed in Arctic and sub-Arctic locations, such as Fairbanks during the mid-winter when the air is very dry (Wendler and Jayaweera 1972; Fochesatto et al. 2013).

The ground heat flux into or out of a sub-medium is due to the exchange of heat through the ground. During the day in fair weather condition, the ground surface is heated by solar heating and the heat exchange into the ground is primarily due to conduction. During the night time and in the absence of solar radiation, the fluxes are directed out of the ground. Figure 2.3 shows a typical energy balance at the ground surface during the day and the night time. The heat loss due to the out-going radiation is balanced by the sensible and latent heat fluxes.

Figure 2.3 (a) shows a typical day time scenario of energy balance, where the net radiation, R_N, is of the highest magnitude and pointing towards the ground surface. However, the actual magnitudes of the various fluxes depend on several factors such as the medium type and its characteristics (moisture content, texture, vegetation, etc.), the season, the time of day, the weather conditions, and the geographical location. Figure 2.3(b) shows a typical night time scenario of energy balance.

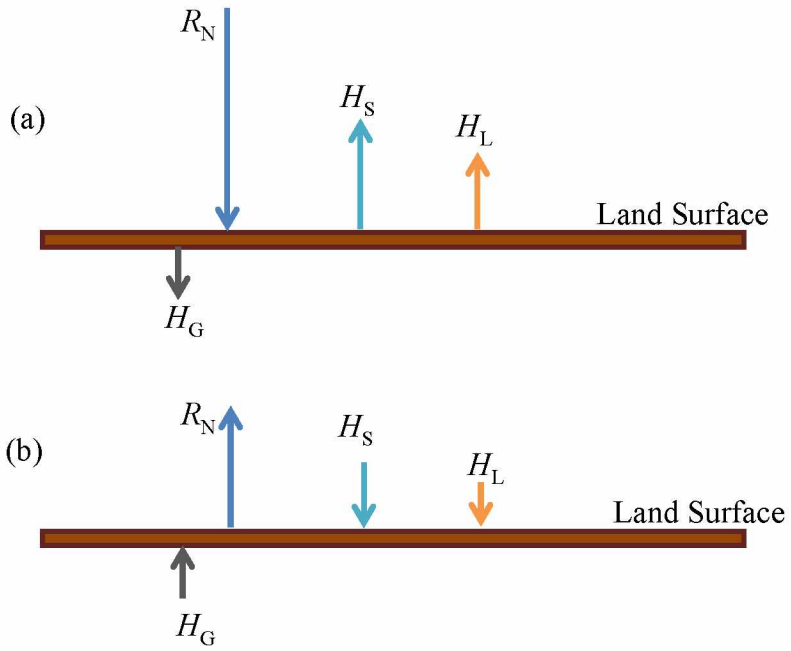

Figure 2.3: A Typical Energy Balance during (a) Day-time (b) Night-time.

2.1.2 SBL formation due to Subsidence and Advection

Formation of SBL is mainly attributed to the negative radiation balance. Subsidence and advection of warm air aloft, however, can also lead to the development of a SBL. Under a high pressure situation, and in the absence of warm air advection an upper layer subsidence causes warming of the upper layer of the ABL (Bowling et al. 1968; Carlson and Stull 1986).

As previously stated, SBL is also formed due to the advection of warm air over a cooler surface. During winters, the advection of warm air over a surface-based inversion leads to the continuation of an existing inversion (Bradley et al. 1992).

2.2 Atmospheric Temperature Inversions in Arctic and Sub-Arctic Region

As discussed previously, during the day, the ground surface is heated and the air mass rises as a result of solar heating. This results in a negative vertical temperature gradient as a function of elevation. Figure 2.4(a) shows the vertical temperature profile of air at Fairbanks International Airport (FAI) in mid-summer under fair weather conditions. It can be seen from the figure that the air temperature decreases with altitude.

On the other hand, under high pressure situation and at night time, due to the radiative cooling of the Earth surface leads to the lower air temperatures near the surface than at higher altitude, thus, forming a stable boundary layer. The Earth's surface cools rapidly due to the radiative loss and the thermal properties of the surface. The lowest layers of the atmosphere cool more rapidly than the upper layers due to the cooling of the Earth's surface. Thus, a negative temperature gradient is established with its base on the surface (Figure 2.4(b)).

Three distinct physical processes mainly govern the evolution and the structure of SBL: turbulence, radiative cooling, and the interaction of the SBL with the underlying sub-medium. Besides advection and thermodynamic processes, additional features such as katabatic flows, density currents, and downward transport of residual-layer turbulence also contribute to the formation of the SBL. One of the following three archetypes may occur, depending on the relative importance of radiation and turbulence: (1) fully turbulent, (2) intermittently turbulent and (3) radiative SBL. A stable boundary layer includes both intermittent and radiative archetypes.

In a weakly stratified boundary layer, the turbulence occurs continuously due to stronger wind and/or weaker surface cooling. Whereas, in the case of a strong SBL, turbulence is weak and intermittent with small fluctuations (Mahrt 1998). A strong or very stable regime of boundary layers occurs under clear skies due to a large surface cooling rate and generally, a lower mean wind velocity.

Surface-based inversion (SBI) is a common phenomenon during the winters in the Arctic and sub-Arctic regions (Wendler and Jayaweera 1972; Wendler and Nicpon 1975). A typical winter temperature profile is presented in Figure 2.4(b). The winters, in the Arctic and sub-Arctic regions under high pressure situation create a favorable condition for inversions. Under such a condition, the stagnant air layers in contact with the ice and snow covered surfaces are cooled by the infrared radiation loss (Garratt and Brost 1981). The inversion with its base at the surface is known as surface-based inversion (Bowling 1986).

The balance of various energy fluxes can be used to explain the change in surface temperature and development of inversions near the surface. Wendler and Jayaweera (1972) showed that a decrease in cloudiness leads to a decrease in the surface temperature. The cooling rate in Fairbanks was observed to be more than 1°C per hour during the first 10 hours. They explained this is solely based on the negative radiation balance. Since during winter time in Fairbanks, the incoming

shortwave radiation is negligible, where the surface energy balance is dominated by the net negative radiation.

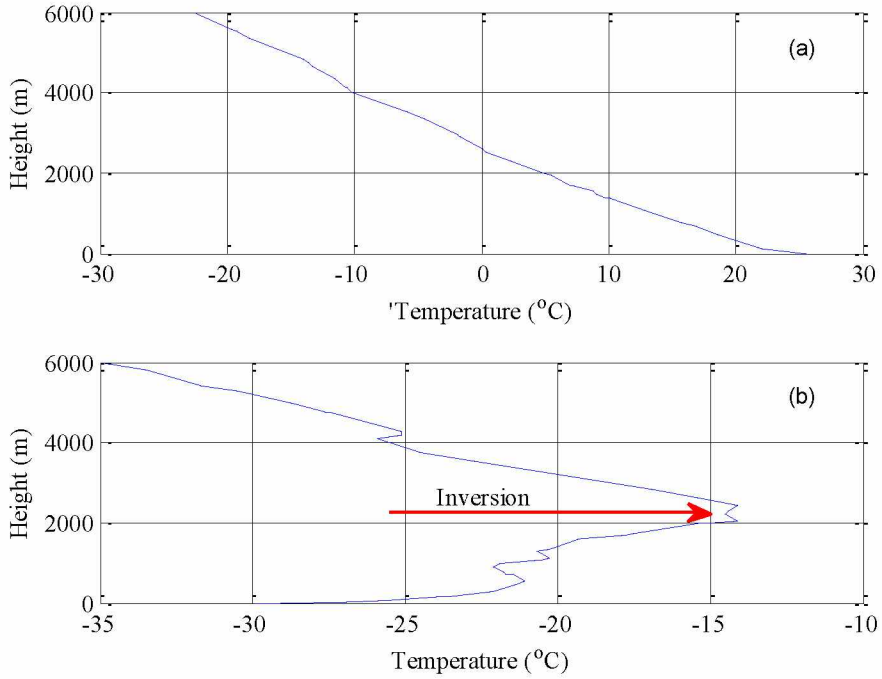

Figure 2.4: Typical Vertical Temperature Profile at Fairbanks International Airport under Fair-Weather Condition on a (a) Mid-Summer and (b) Mid-Winter Day. (http://weather.uwyo.edu/upperair/sounding.html)

Fog can prevail over large areas for a long time in Arctic regions. Wendler (1969) also discussed ice fog which occurs during the winter months when the temperature tends to be below -35°C. When the surface cooling is strong, the air becomes saturated. A radiation fog starts to form over a certain layer where the dew point temperature reaches the actual air layer temperature. The fog onset also rigorously modifies the radiative transport within the boundary layer, and consequently the energy balance. The long-wave emission to space occurs at the top of the fog layer, which consequently cools rapidly. This rapid cooling destabilizes the fog layer, and the fog layer starts mixing. During ice fog conditions, the inversion is weakened and adiabatic conditions are found within the ice fog layer. The final temperature profile follows the saturated-adiabatic lapse rate, with the surface relatively warmer than the overlying atmosphere., during which the upper boundary of the ice fog loses most of the energy due to the negative radiation balance.

Wendler and Nicpon (1975) characterized the inversions in Fairbanks, Alaska on a statistical basis. Using the hourly data from March 1967 to February 1968, they defined the occurrence of an inversion as higher temperatures at 200 m than at one meter above the ground surface. It was reported that, during the winter, statistically, an inversion occurred more than 95% of the time and more than 50% of the time for the whole study period. A more recent study comparing the radiosonde data from 1957 to 2004 was collected for the winter surface temperature inversions in Fairbanks by Hartmann and Wendler (2005). They characterized the surface temperature inversion in terms of temperature difference (ΔT) with altitude, pressure difference (ΔP), inversion depth (Δz), and by the ratio of the terms $\Delta T/\Delta z$. They reported a decrease of 212 m in the mean inversion depth (height) over the years (Figure 2.5). They also associated the surface wind direction with the events of surface inversion and no surface inversion, as shown in Figure 2.6. The southerly winds are associated with both the inversion and no inversion conditions. No inversion events during southerly winds indicate that the advection of warmer and moist air accompanied by an increase in cloudiness restrains the formation of any surface-based inversion.

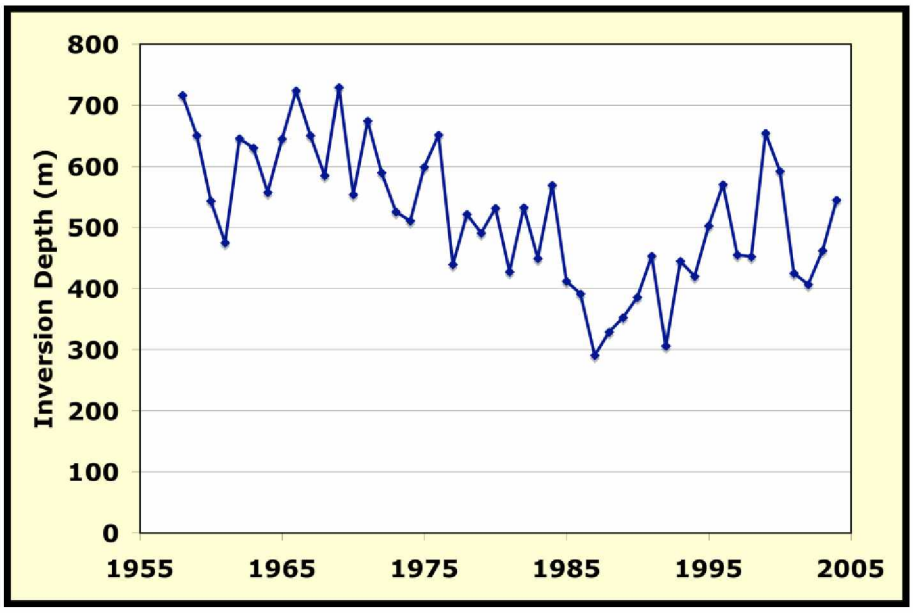

Figure 2.5: Time Series of the Mean Winter Surface-based Inversion Depth (Hartmann and Wendler 2005).

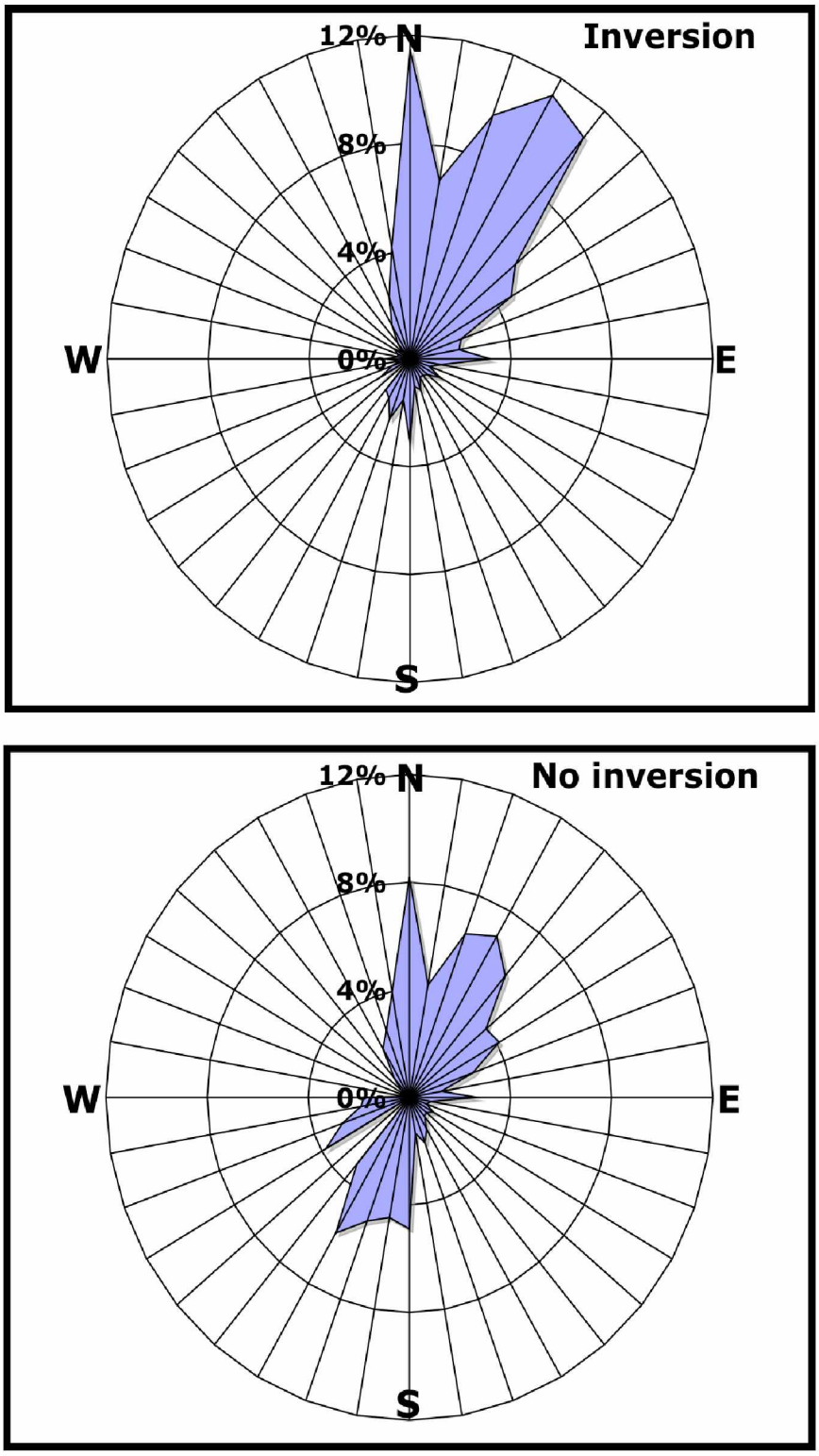

Figure 2.6: Frequency Distribution of Surface Winds for Surface Inversion and No Surface Inversion Cases (Hartmann and Wendler 2005).

The air inversions, depending on their mode of development, height, and the processes that caused them, can be classified as surface-based and elevated inversions. A surface-based inversion (SBI) is an inversion with its base at the surface, whereas, an inversion developed over a surface-based inversion is called an elevated inversion (EI). Air inversions can either be surface-based, elevated, or both at the same time in the atmosphere depending on the meso-scale and micro-scale meteorology.

In the Arctic, apart from the surface-based inversion, another type of inversion has also been observed at higher elevations (Mayfield and Fochesatto 2012). Depending upon synoptic conditions, the flow above the surface-based inversion may also develop elevated inversions. The elevated inversions are discontinuities in air density that occur between the surface-based inversion and the free troposphere, mainly as a function of specific synoptic large-scale flow. Known mechanisms (Mayfield and Fochesatto 2012) that give rise to elevated inversions in the atmospheric boundary layer flow are (1) warm-air advection flows or frontal inversions and (2) anti-cyclonic or subsidence inversions.

The warm air advection occurs when synoptic warm air flows over a stagnant low-level ABL flow or when warm air flows over large bodies of cold water. Elevated inversions during the anti-cyclone occur due to the subsidence of dry air which warms up the atmospheric layer above the surface-based inversion.

An example of a surface-based inversion along with an elevated inversion at FIA is presented in Figure 2.7. The data were collected on 12 UTC (Coordinated Universal Time) January 1st 2014. 12 UTC is 3:00 AM in Alaska Standard Time (Whiteman and Hoch) on January 1st 2014. The data at the Fairbanks International Airport are the radiosonde observational data taken every 0000 and 1200 UTC. The 0000 UTC represents 3:00 PM AST a day before and 1200 UTC is 3:00 AM AST on the same day. Figure 2.7 shows the base of an inversion starting at 0 m, i.e., the ground surface, making the first inversion, a surface-based inversion and another inversion starting to build up at around 1000 m above ground level (Monin and *,*I*,*Aglom). The inversion starting around 1000 m elevation is the base of the inversion known as the elevated inversion. A detailed discussion on various inversion layers in the Fairbanks area is presented by Mayfield and Fochesatto (2012).

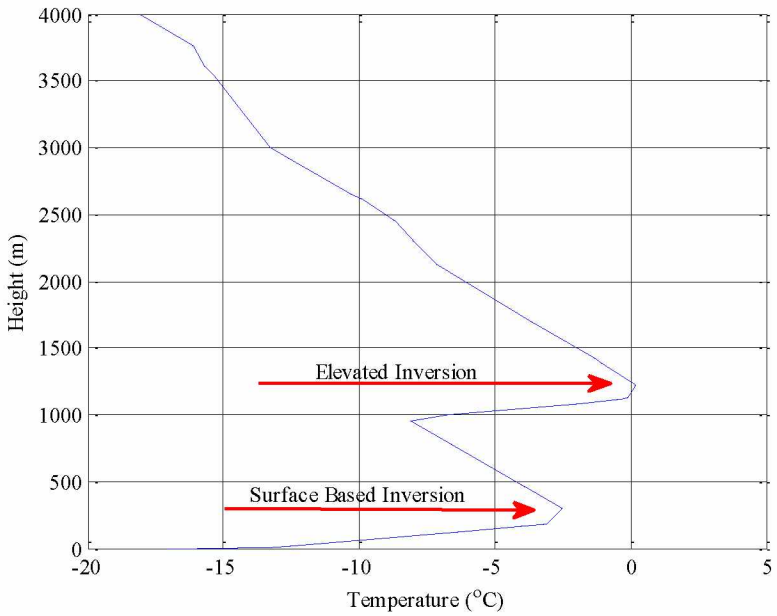

Figure 2.7: An Example of a Temperature Profile with Multiple Inversion Layers. May be use arrows to indicate the EI and SBI.

2.3 SBL of Open pit Mines

Open pit mines geometry is very much similar to mountain valleys in smaller scale with all sides closed. In order to understand the formation of SBL in open pit mines, a SBL of valley flow is presented here. Flows in mountain valleys are constrained due to the topographic configurations. Formation of inversions in the mountain valleys are attributed to the net negative radiation as well as in some cases subsidence and warm air advection. Several studies have been published on the SBL of valleys (Wendler and Jayaweera 1972; Wendler and Nicpon 1975; Whiteman 1980,1982).

Events of air inversion has been reported in various open pit mines in Arctic and sub-Arctic region. Several open pit mines such as, Kinross Fort Knox (Fairbanks) and Teck Cominco Red Dog mines in Alaska, BHP Billiton Ekati mine in Canada, Boliden Aitek mine in Sweden, and the Mirni and Udachini diamond open pit mines in Russia. Even Rio Tinto's Bingham Canyon mine in Utah has reported local air inversions from time to time (Whiteman and Hoch 2014). To illustrate the SBL regimes in Bingham Canyon Mine vertical structures of the temperature profile is presented in Figure 2.8.

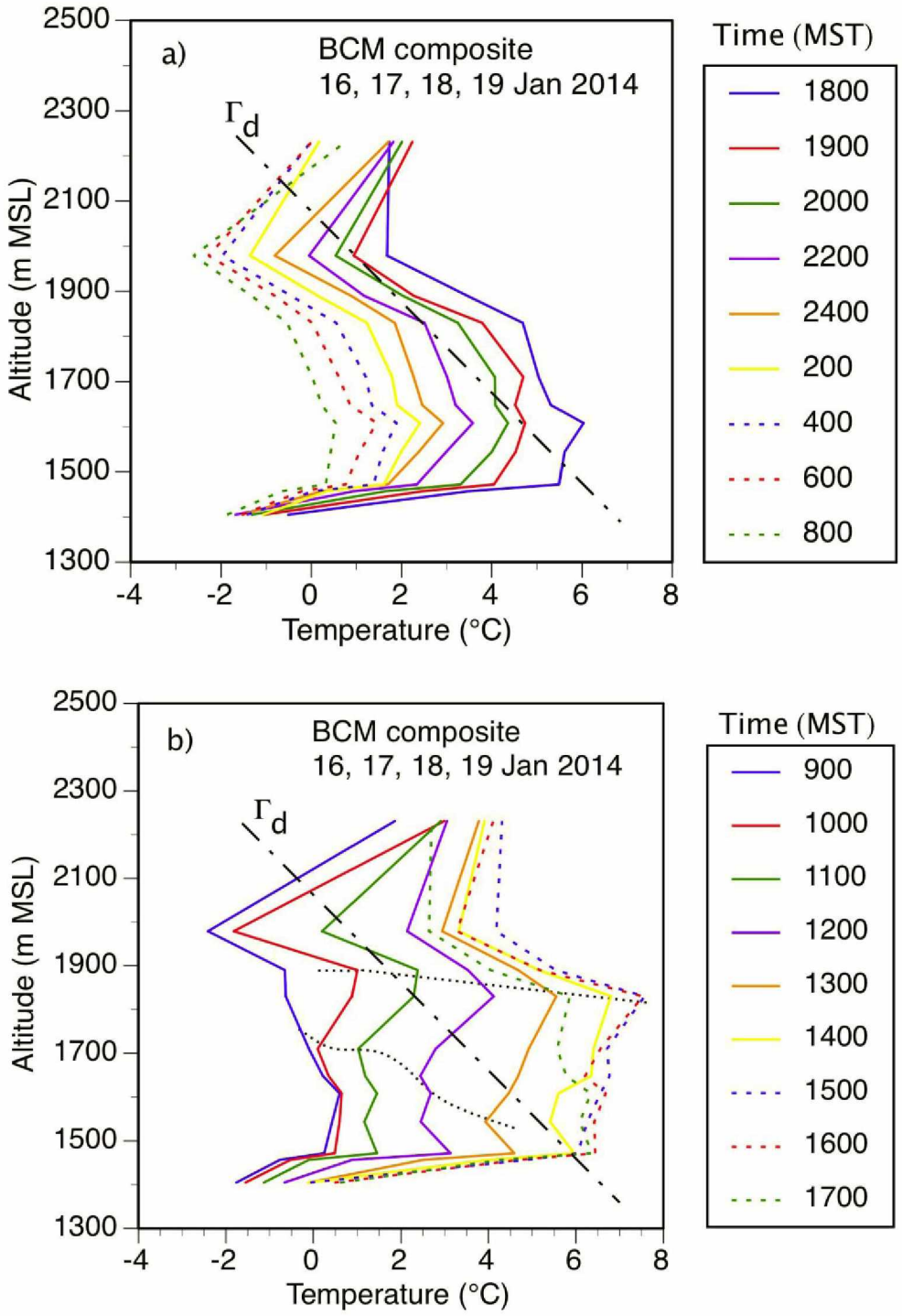

Figure 2.8: Vertical Temperature Profile at Bingham Canyon Mine, Salt Lake City, Utah (Whiteman and Hoch 2014).

Figure 2.8 shows a strong inversion at the lower level of the pit. This inversion is mainly due to the infrared cooling of the pit surface after the sunset. Apart from the surface-based inversion

at the pit bottom, an elevated inversion can also be observed at higher elevation. The elevated inversion may have been formed due to the relatively faster cooling of the air mass near the Bingham pass and advection of the cold air mass. During the daytime after solar radiation hits the pit walls, the stable stratification is weakened at the Bingham Canyon Mine.

In the Arctic and sub-Arctic region, during the winter months under high pressure system, the open pit mine surfaces start to cool continuously due to the radiative cooling (i.e., longwave radiation losses). The turbulent intensity is suppressed by the thermal stratification (buoyancy suppression). Therefore, only the mechanical wind shear remains a source of turbulence. The atmospheric boundary layer (ABL), consequently becomes stably stratified and sometimes strongly-stratified. In Arctic regions, the ABL is dominated by stably stratified layers during a large part of the winter months. The occurrence of inversion at an open pit mine depends on the location. In the following section, the inversions at a selected mine is discussed.

Analysis of the collected inversion data indicates that the inversions at the selected open pit mine is not consistent with the inversions in the Fairbanks area. The inconsistency in the frequency of inversions thus required further analysis.

The Fairbanks International Airport (FAI) data are from a radiosonde which included temperature, pressure, dew point temperature, relative humidity, wind velocity and other variables at different elevations. Analysis of the collected temperature data indicates that SBI is common in Fairbanks area. On the other hand, the temperature data at the selected open pit suggests that the SBI is not a common occurrence. There is, however, a direct qualitative correlation between the elevated inversions in the Fairbanks area and the inversions at the selected open pit. The selected open pit mine is located at a higher elevation than the Fairbanks area. For example, the FIA is at an elevation of 132 m, whereas the selected open pit has an elevation of 600 m (Figure 2.9). The difference in elevation is significant since the selected mine is above the vertical extent of the surface-based inversion generally found in the Fairbanks area.

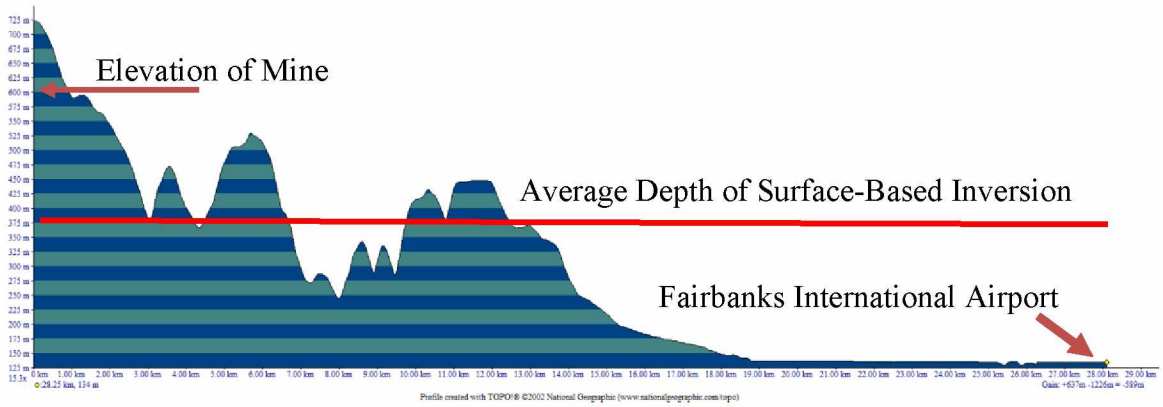

Figure 2.9: Elevation Profile of the Local Topography from FAI to the Selected Mine.

There is a strong correlation between the inversions and the correlation can be established from the frequency of inversions during the same time period at both locations. To establish a correlation, a period of six months over the winters of 2013-2014 was selected. A number of inversions were observed at the selected open pit mine during 3rd through 6th December 2013 and 31st December 2013 through 2nd January 2014. For the same duration, the vertical temperature profiles at the Fairbanks International Airport are presented in Figure 2.10-Figure 2.12. These figures, indicate surface-based inversions in the Fairbanks area. During the same time frame there were multiple instances of elevated inversions (Figure 2.10-Figure 2.12). It can be seen from these figures that, during the night time, there is a very strong surface-based inversion, whereas the elevated inversion is more prevalent during the evenings. On December 4th, 2013 at 0000 UTC, a surface-based and elevated inversion is observed and continued to persist over the next twelve hours. It can be noted that surface-based inversion led to a colder temperature. Whereas, elevated inversions occur at warmer temperatures. Elevated inversion can be seen around the 1000 m level in most cases. At the same time, there can be multiple layers of elevated inversions in the atmosphere. For the next couple of days multiple layers of elevated inversion were observed in the atmosphere which is likely caused by the synoptic forcing or warm air advection.

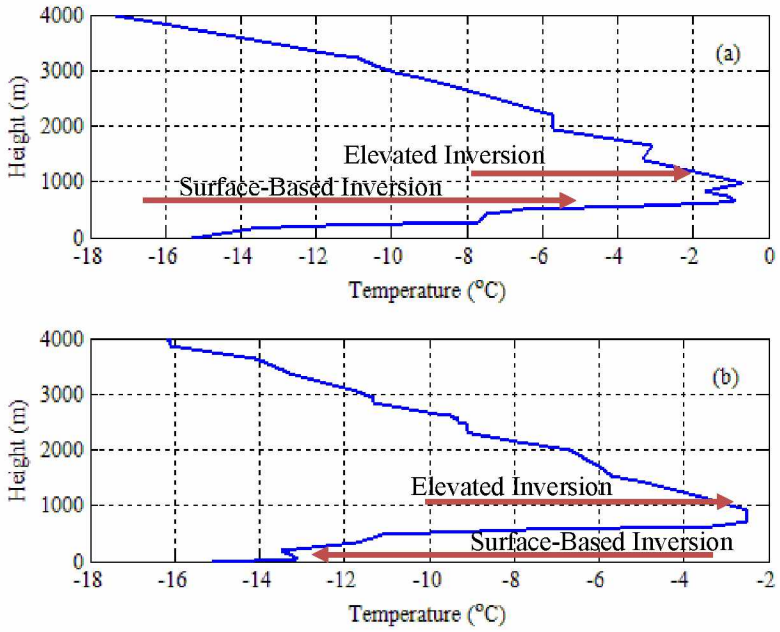

Figure 2.10: Temperature Profile from FIA at (a) 0000 and (b) 1200 UTC December 4th 2013.

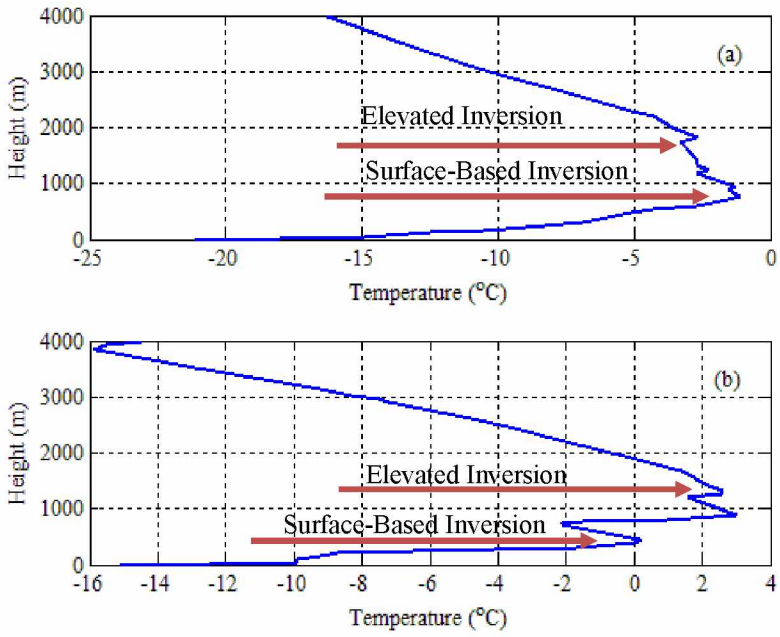

Figure 2.11: Temperature Profile from FIA at (a) 0000 and (b) 1200 UTC December 5th 2013.

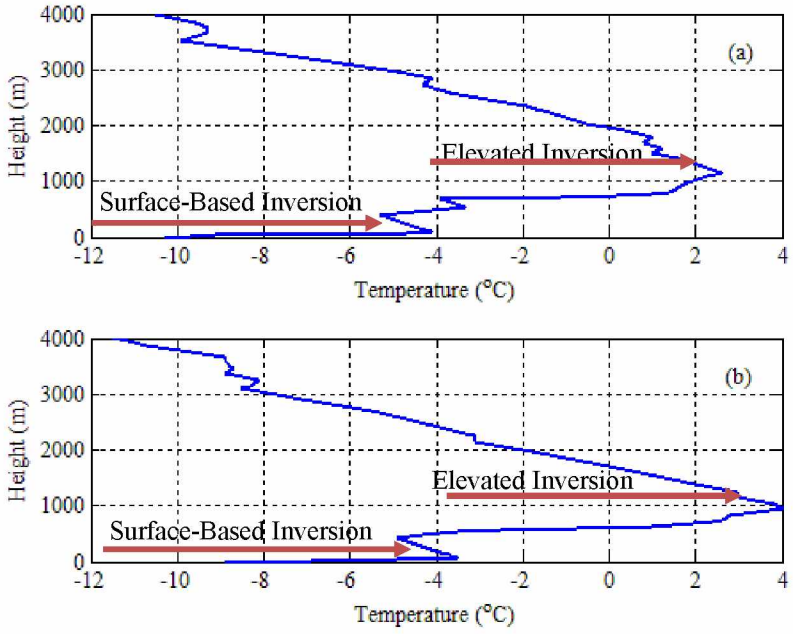

Figure 2.12: Temperature Profile from FIA at (a) 0000 and (b) 1200 UTC December 6th 2013.

In another instance, during December 31st, 2013 to January 2nd, 2014, there were inversions at the selected open pit mine as well as elevated inversions in the Fairbanks area. Figure 2.13-Figure 2.15 are the temperature profiles during the December 31st, 2013 to January 2nd, 2014 period. It is clearly seen from the figures that during the 3 days there were elevated inversions in the Fairbanks area as well as at the mine. Thus, it can be said that inversion at the selected open pit mine is mainly due to the elevated inversion and not influenced by the frequently occurring surface-based inversions in the Fairbanks area. It is also clear that, the altitude and the local topography of the selected open pit play an important role in the frequency of inversions.

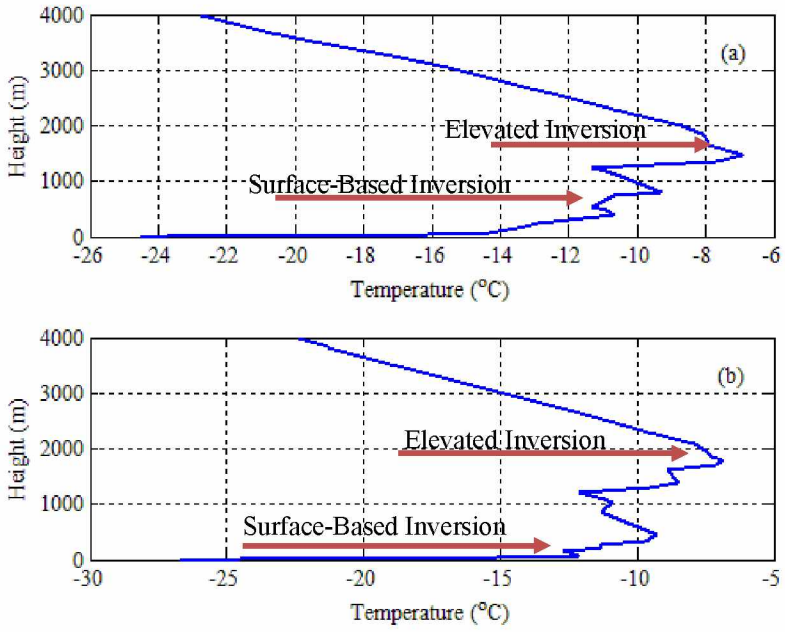

Figure 2.13: Temperature Profile from FIA at (a) 0000 and (b) 1200 UTC December 31st 2013.

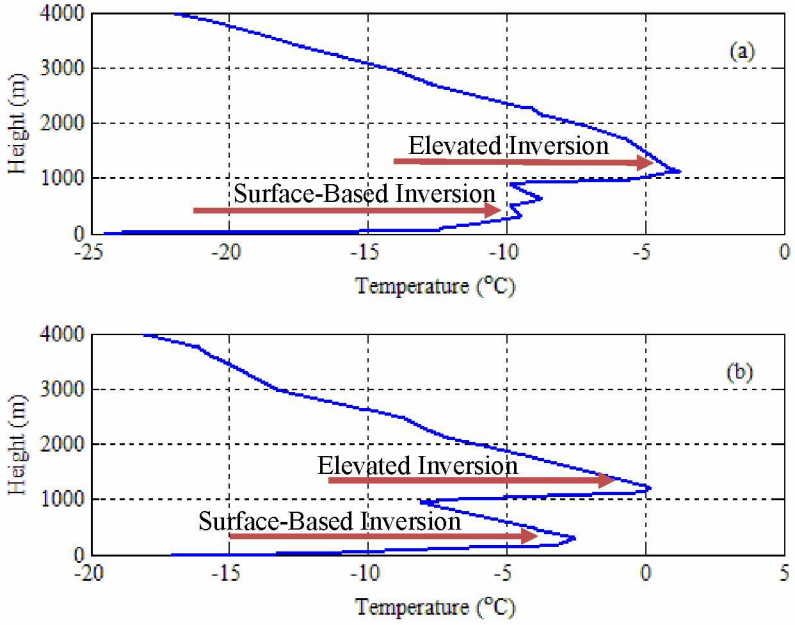

Figure 2.14: Temperature Profile from FIA at (a) 0000 and (b) 1200 UTC January 1st 2014.

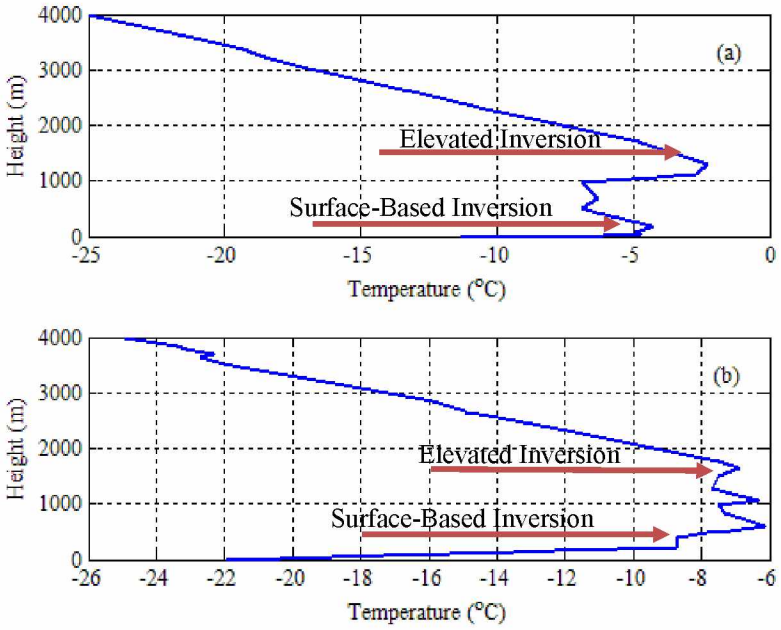

Figure 2.15: Temperature Profile from FIA at (a) 0000 and (b) 1200 UTC January 2nd 2014

Stable boundary layer is formed generally due to the net negative radiation during the night time. In the Arctic and sub-Arctic region, such a night time situation prevalent during the winters creating favorable condition for the formation of a SBL. SBL is not always formed due to surface-based inversions near the ground but could also occur at higher elevation above the SBI as elevated inversions. Elevated inversions can be caused by warm air advection or subsidence.

The occurrence of inversions at the selected open pit mine is primarily the effect of elevated inversions in the Fairbanks area. The local topography and location of the mine plays an important role in understanding the occurrence of inversions at the open pit mine.

Chapter 3 Literature Review and Previous Modeling Approaches

Published accounts of open pit mine ventilation, particularly with respect to air inversion, are practically non-existent in English literature. Researchers at the Kola Mining Institute, Murmansk region of Russia, and Yakutsk Mining Institute of the North, Soviet Academy of Sciences, have done some research in open pit mine ventilation. Published research from these research institutes, mostly available in Russian, has been collected and translated into English. The following sections contain a brief review of available literature describing air inversions as related to open pit mines. The literature cited in this chapter focuses on the phenomenon of temperature inversions in the atmosphere, the movement and quality of air in open pit mines as related to air inversions, and possible remediation measures that have previously been attempted in Russia.

3.1 Previous Modeling Approaches

Meteorological and tracer experiments have been conducted to investigate the dispersive characteristics of valley atmospheres (Allwine et al. 1997). These and other studies have led to the identification and more complete understanding of key physical processes governing dispersion of pollutants in valleys. The important physical processes include up and down valley wind speeds, up and down slope winds, turbulent diffusion, convective boundary layer growth, temperature inversion decent, nocturnal temperature inversion breakup, tributary flows, cross-valley circulations, and interaction with above-ridge top winds. Studies on the flow and dispersion of diesel exhaust in underground airways, from point and moving sources, have also been conducted by Bandopadhyay and Ramani (1983,1984,1985,1988). However, while application of these models is limited—because the geometry of and airflow characteristics in open pit mines are much different than those in underground mines—the findings are still relevant to the study of the mine ventilation conditions in an open pit mine.

In an open pit mine, the upward heat flux also develops a convective boundary layer (CBL) over the pit surfaces, but, in contrast, the heated pit slopes cause warmed air parcels to flow up-slope. These up-slope flows remove pollutants from the base of the temperature inversion and maintain the mass continuity, which results in a general circulatory vertical movement over the center of the open pit (Allwine et al. 1997). The CBL growth and descent of the inversion are both

functions of sensible heat flux, atmospheric pressure, air density, solar flux, pit potential temperature lapse rate at sunrise, and the warm-air advection rate above the pit.

The subject of natural airflow in open pit mines has been under study for some time, particularly in the former Soviet Union (USSR). Researchers have worked on the mechanism of wind flow, along with a study of the factors that influence such flow. Some of these studies are described below.

Vershinin (1976) compared the effectiveness of two schemes for ventilation of open pits, using either upward or downward air motion to remove contaminants. Vershinin's work is notable as an early, physical model of open pit ventilation. He assumed a contaminant level of 5 to 6 times greater than the permissible level and calculated the time required for the contaminant level to reach the permissible level, given an initial flow pattern of a given velocity and diameter. The source of the assumed flow is not specified, but Vershinin briefly mentions the use of artificial heating devices, turboprops, and turbojets for such purposes.

Vershinin states that, all other things being equal, the upward ventilation scheme is preferable because the pit sides will be swept by pure air, with the contaminated air being removed by flow up the center of the pit. Vershinin's solution for both cases is based on the basic equation of discontinuity, in which the rate of descent of the boundary between the contaminated and uncontaminated zones, ω, is given by

$$\omega = \int_F \frac{\rho u dF}{\rho_n S_q} \qquad (1)$$

Where:

F = cross-sectional area of the current,

$\tilde{n}$ = density of the air,

u = rate of airflow within the current at a given level z,

$\tilde{n}_n$ = air density in area around the current at cross-section F, and

S_q = cross-sectional area of the pit at level z.

When the current is isothermic and the temperature gradient in the pit is adiabatic, the expression is simplified to

$$\omega = Kz/S_q, \qquad (2)$$

Where:

K is a proportionality constant, defined by Abramovich as

$K \approx 0.31(W_0 d_0 \cos\alpha)$, where

Q_0 = initial flow rate of the current, and

d_0 = initial diameter of the current.

From these equations, Vershinin derived solutions for $\tau\uparrow$, the ventilation time required with upward airflow, and $\tau\downarrow$, the time required with downward airflow. The integrated equations are solved by computer for two simple truncated cones, one with a wall slope of 14°20', the other with a wall slope of 35°25'. A table is prepared showing the relative efficiencies of the two ventilations schemes for pit (cone) volumes ranging from 100×10^6 and 600×10^6 m^3 and contamination volumes ranging from 50×10^6 and 550×10^6 m^3. In general, when the volume of the contaminated zone is relatively small, upward motion cleared the pits faster, but the results are far from clear.

This model has two serious shortcomings. First, no field data is presented to verify the model. Second, the model assumes that current is isothermic and the temperature gradient in the pit is adiabatic. The latter shortcoming is particularly acute for the present study, which seeks to analyze situations (inversions) where the temperature gradient is specifically non-adiabatic.

An early study by Aloyan and others (1982) describes the use of a three-dimensional, non-stationary numerical model for open pit ventilation. The primary challenge in this study is adapting the standard method to micro-scale atmospheric processes, which required accurately accounting for the surface relief. This goal is accomplished by describing the surface (the open pit) using a grid of rectangles, which could be altered to achieve the desired configuration and accuracy. The following problems are solved with this model:

1. Simulation of the winds in a quarry under various thermal conditions (stable, unstable, and equilibrium stratifications) and examination of the effects of an external wind on the temperature inversion in a quarry.
2. Estimation of the time interval for ventilation of a quarry with constantly acting pollution sources and after instantaneous large-scale rock blasting, the study of the time dependence of the ventilation in the presence of various factors (temperature stratification, external wind, geometrical parameters of quarry, and source output).
3. Determination of maximum quarry depth from the viewpoint of ventilation.

4. Simulation of air motion in the quarry due to the temperature inhomogeneity at the surface, with estimation of the effects of solar radiation and the diurnal temperature variation on the ventilation.
5. Dependence of the ventilation processes on the absorbing properties of the surface for various pollutants.
6. Examination of the scope for artificial ventilation under various meteorological situations and various locations of the sources and sinks.

The authors showed the results for natural ventilation of a typical quarry in northern latitudes with characteristic dimensions R (radius) = 600 m and H (depth) = 300 m (Figure 3.1). The figure shows the concentration of pollutants in the pit after three, six, and nine hours. The figure shows reasonable results.

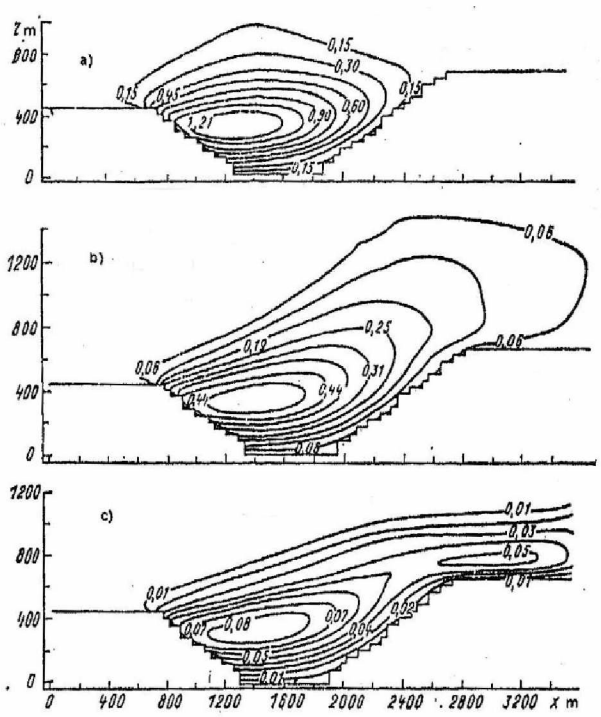

Figure 3.1: Lines of Equal Concentration for a Pollutant in a Propagating Aerosol Cloud in a Quarry, at 3-hour Intervals (Aloyan et al. 1982).

Measurements are made in the Saam and Olenegora pits in the Kola Peninsula, and there is "...good qualitative agreement between the calculated distributions and actual measurements." However, the actual data is not presented.

Baklanov (1984) constructed a model similar to that described by Aloyan and others (1982), with the goal of solving the following problems:

1. Propagation of an initially specified cloud or impurities in a pit over time.
2. Atmospheric contamination with local or point contamination sources acting steadily or temporarily.
3. Estimating the time interval of ventilation with a specified discharge for the cases of natural or artificial pit ventilation.
4. Studying the propagation of impurities as a function of the absorbing properties of the surface and the interaction between the impurities.
5. Estimating the background contamination of the atmosphere and immediate surroundings with the release of a gas/dust cloud from open pits.
6. Suppression and neutralization of the extraneous impurity cloud using chemical reagents and moisture jets.

Baklanov's results for propagation of an aerosol cloud are almost identical to those of Aloyan. He also considered emanation of impurities from a point source, and diffusion of impurities in under stagnant conditions. Again, field measurements are made, and "...sufficiently good agreement" is found between those measurements and the model results. Also again, no data to support the study are presented.

In 1986, Baklanov established a thermodynamic model of the dynamics of open pit ventilation systems. The model can simulate the diurnal change that takes place during the differential solar heating of the surface during the day and the release of this energy during the evening. In the 1986 model, the volume of the pit is interpreted as a system where the kinetic energy of a directed movement of the air is lost to forces of friction (mainly turbulent friction). For the air movement in the pit to be maintained naturally, external energy sources are necessary to supplement the reserve of kinetic energy. These include factors such as the energy of background currents and the influx of solar energy. With regard the energy flux through the surface of the region under study the main factors forming the natural ventilation of pits are said to be the flows of kinetic and

thermal energy of background processes through the boundary with the outer air mass and the thermal energy flux through the ground surface.

The heat flux from the pit surface into the atmosphere is in many cases (especially in the absence of winds) is defined as the main source forming the microclimate and the atmospheric circulations in the pit. It is affected by several factors and is determined by the radiative and thermal balance on the discontinuity surface between the atmosphere and the ground. The hydro-meteorological regime of the pit atmosphere, therefore, is described in combination with the energy exchange of the ground and the atmosphere. The mathematical models describing the dynamics and the atmosphere in the pits are combined with the system for calculating the thermal and radiative balance on the surface and the model for the thermal regime of the ground. The problem of microclimate in the pit has been reduced to a description of the energy interactions in the "atmosphere-surface-ground" system. The integral identity and the energy balance equation are thus written for the entire "atmosphere/surface/ground" system. Belousov (1995) noted that because the air above the pit cools slower than the air above the ground at the same altitude, there is a resultant horizontal flow of air toward the pit. He also noted that the air above the pit in such cases would rise, due to the standard adiabatic process, to a maximum height of:

$$H = \Delta t_h / (\gamma_a - \gamma) \qquad (3)$$

Where

H is the maximum height air above the pit top can rise (m),

Δt_h is the horizontal temperature difference (degrees),

γ_a is the adiabatic vertical temperature gradient (degrees/m), and

γ is the actual vertical temperature gradient (degrees/m).

This rise in the air could result in the removal and mixing of pollutants from the pit, provided the pollutants generated at the pit bottom reach the top layers of the air in the pit. In very cold climates, the movement of pollutants from the bottom to the top of the pit is severely restricted due to lack of energy in the bottom layers and possible inversion caps in place. Belousov noted that it has been observed that the surface flow at the very top of the pit is coupled with flow from the surface adjacent to the mine, while the air mass at the bottom of the pit is decoupled from the airflow at the top of the pit. Such decoupling and lack of energy in the bottom layers of the air in the pit will actively hinder removal of pollutants from the bottom of the pit, which is where most

of the pollutants are generated. This finding underlies the need for an artificial ventilation schemes to introduce fresh air into and remove pollutants from the lower reaches of the mine.

In earlier papers, Belousov (1985,1989) noted that the ventilation of open pit mines is affected by the relief of the surface near of the mine over which the wind flows before it approaches the pit, as well as the geometric properties of the pit itself. The model scale chosen in the study is 1:1,000. The study also used "air walls," which the author defined as a system of vanes or wings on the windward side of the model pit that are used to direct the natural flow of wind toward the pit-bottom. The author found that the removal of pollutants from the bottom of the mine is aided by the placement of air walls. Such removal is also aided by the removal of ordinary iste dumps from the leeward side of the mine because such dumps increase the effective depth of the pit, decreasing the reach of either the turbulent of the laminar flow zones into the mine. The author has also reported a close agreement with observed results of velocity profiles in mines. However, the incident air velocity in the model that is used to solve the problem is much greater in magnitude that can be reasonably supported. The model scale being 1:1,000, the air velocity used for solving the problem is roughly the same as the observed velocities in actual mines. It would be more reasonable to scale down the velocities used to numbers more representative of the scale in which the model is placed. In addition, the author predefined the expansion angle of the air jet entering the mine (primarily based on the wings placed on the windward side of the flow) to $\alpha = 15°$. This behavior is schematically described in Figure 3.2.

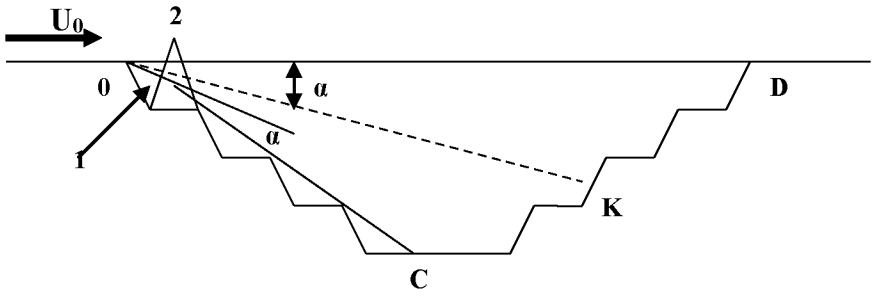

Figure 3.2: The Angle of Expansion of an Air Jet in an Open-pit Mine (Belousov 1989)

In Figure 3.2, α is the opening angle of the free plane (expansion of the jet), set at 15°; *1* indicates the position of the shield (wing); *2* indicates the position of the mast on to which the shield is attached.; U_0 is the incident velocity of wind across the pit in m/s.

In the 1990 paper, Belousov regarded the presence of the vanes as an aid to the natural circulation occurring in mines. He stated that in the absence of the vanes or shields, the air entering the pit with a velocity U_0 would directly ventilate the volume of the pit marked *0KD0* on the cross section in Figure 3.2 . The section *0CK0* would be ventilated by recirculation. With the presence of the vanes, however, the lower boundary *0K* is moved downward, and converges with *0C*, thus ventilating almost the entire pit.

There are several problems with this approach. As described before, there is hardly any crosswind registered when capping inversions are in place, or in extremely cold weather, even without a capping inversion. This fact negates the possibility that such natural winds may be marshaled to aid in removal of pollutants. Setting of the angle α at 15° may also be erroneous.

In a 1995 study, Belousov analyzed the conditions under which surface breezes would induce circulation in an open pit. Such breezes result from temperature differentials, which lead to heat and mass transfer, and horizontal temperature and pressure differentials, ultimately resulting in airflow toward the lower-pressure sections. The flow velocities, depending on the magnitude of the pressure drop and the scale of the surfaces of the sections, may be as great as several meters per second.

The probability of a breeze is determined by radiation and circulation factors. The natural conditions under which breezes will develop are clear or slightly cloudy weather, little or no baric wind, a generally stable state of the atmosphere in the particular district, and the presence of sufficiently large horizontal differentials of air density, determined mainly by the air temperature. The stability of a breeze will depend on the rate of heating of the air mass of the low flow to a certain temperature in the region of the relatively warm section; with an inadequate rate, the circulation may either die out or pulsate.

The difference in radiation conditions between the pit itself and the adjacent territory is responsible for the existence of significant horizontal differences of temperature. For example, many years of data from atmospheric probes at the Sibai mine have shown that a temperature difference as great as 7°C may exist between the air above the center of the pit at the surface level and on a meteorological platform at a level of 2 m located 100 m from the pit. With above-freezing temperatures at night and in the morning, the density gradient is usually directed toward the pit. The magnitude of the gradient decreases toward midday, and the direction of the gradient changes.

During the cold period of the year, the gradient is very nearly zero. This behavior indicates that a breeze between an open pit and the adjacent territory is most likely to be observed in the warm part of the year, when the amplitude of the diurnal variation of air temperature and the difference in radiation conditions are at their greatest.

Belousov calculated the minimum temperature differential, between the air above the pit and the adjacent air mass, required to generate a stable, recirculating breeze. For above-pit temperatures (T_p) ranging from 233 to 313 °K, and actual temperature gradient (γ) from 0 to – 0.04 °K /m, these differentials varied from 2.33 to 6.33 °K, increasing with increasing T_p and decreasing γ. The magnitude of this temperature differential is also affected by the ratio of pit depth to pit radius, and the ratio of the distance through which the air mass or breeze over the pit will pass when heated sufficiently to create a convective rise to the pit radius.

Peng and Lu (1995) constructed a 1:1,000 scale model of a surface mine located in southern China. Their study focused on the movement and circulation of wind in deep open pit mines. An important part of their work consisted of conducting experiments to verify the claim made by Belousov and others that the angle α is approximately 15°. They reported a wide variation of the angle, from 6° to 32°, and observed that the angle is not only influenced by the topography surrounding the mine, but that it is also related linearly to the pit depth. They reported the relation to be:

$$\alpha = -1.234 + 0.0172H \qquad (4)$$

Where:

α is the angle of expansion of the jet (degrees), and

H is the height or depth of the pit in (m).

Peng and Lu concluded that most of the pit would be ventilated by recirculation under natural ventilation conditions. To augment natural ventilation and recirculation, they used natural ventilation guides in the form of trumpet-shaped air walls or vanes, to simulate the Venturi effect. They reported that the recirculation area in the deeper regions of the pit disappeared with the introduction of the vanes. This mitigation technique, however, had the same drawback described previously: In the absence of a crosswind, there is no possibility of natural circulation to aid in removal of pollution.

When the concept of the angle α is examined thoroughly, two significant problems can be noted. Firstly, the reach of the vane or wing system to influence the angle expansion may have been overestimated. All of the models described in the literature so far have been scaled-down models. The problem with this approach lies in the nature of the interaction between the wind and the model environment. Turbulent or laminar airflow, when injected into a model space, would be influenced by the dimensions of that space. In a scaled-down model, the airflow would be shaped by a much smaller space in all three dimensions, thus restricting its movement and creating more turbulence, but on a smaller scale. While this situation might be claimed to reflect actual conditions in mines, there are two significant problems.

First, many of the models used natural or near natural wind velocities as an input. This approach creates a huge disparity in scales between the velocity and the volume on which it would work. Thus, the eddies and the recirculation zones that are formed in the models are grossly over-scaled. When an eddy is observed in the model, its location, approximate dimensions, and area of influence are noted, and then scaled up according to the model scale. Thus, the resultant (scaled-up) eddy would be very large and would likely never form under natural conditions.

Additionally, when a scaled-down model is used, there is very little or no control over the timescale on which processes take place in the model. For example, if a small source of gaseous pollutant is placed at a location in the model, the gas emitted from it will diffuse according to the diffusivity constant, which can be expressed dimensionally as $[L^2/T]$, where L is length and T is duration. This ratio indicates that the gas, whether or not carried by convection, will travel at roughly the same rate in a model that it would in the natural environment, with minor adjustments for temperature, pressure and concentration gradient. The resultant concentration profile in the model would not be realistic in that case.

The second significant problem with the application of the angle α lies in the nature of the resistance that inflowing air faces once it enters the pit. A detailed examination of the concept of α in the literature, along with the diagrammatic representations of the same, suggests that it is assumed that the inflowing air would have a momentum sufficiently large to displace the existing air in the pit with little compression of the inflowing air. The inflowing air would thus be able to flow wherever its momentum directed, without interference. This appears not to be the case in reality. The air toward the bottom of the pit is cooler, therefore denser, and contains pollutants in

both gaseous and particulate form, so it has a high inertia. If the inflowing wind does not have a sufficient velocity or mass, it is quite possible that the inflow will be compressed and, on meeting a more massive and denser body of air, the path of its momentum will deflect. Such deflection, coupled with turbulent mixing, will induce the formation of recirculation or eddy zones in the upper reaches of the pit (where the inflow wind meets the in-situ air). These turbulences will destroy the linear motion of the inflow wind assumed in the formulation of the angle α, mixing the sharply delineated boundary layers, and invalidating the angle as an indicator of ventilation.

Peng and others (1995) presented a series of wind tunnel tests conducted on a scaled open pit mine. The geometry of this model is complex. It is based on an actual open pit mine located in southern China. As in other studies, a recirculatory wind profile is observed in the pit bottom. This recirculation increased with increasing pit depth. The 'wind expansion angle' that separates the recirculatory region from the region of uniform flow is found to vary between 6° and 32° Smoke concentration (here used to simulate the concentration of irrespirable gases and harmful dusts) increased with increasing recirculation in the pit. Finally, the application of vanes to guide the wind into the bottom of the pit is found to be an effective means of ventilating the pit.

Plank et al. (1971) presented another wind tunnel test of an open pit mine. In this particular situation, an open pit coal mine in an inverted position is modeled. Accumulation of harmful gases related to spontaneous combustion of coal and shale is of particular concern in this situation, especially under conditions of atmospheric inversion. In the wind tunnel, conditions of atmospheric inversion are simulated by capping the open pit with a false roof and creating temperature variations using resistance heaters, using a 1:600 scale model of a typical open-pit coal mine. The study focused on the dispersion pattern occurring in the presence of clearly-defined and stable stratified zones in the atmosphere above the mine. The scale model is placed on the roof of the Monash Environmental Wind Tunnel. Vertically and horizontally spaced heating elements are placed upwind of the model, so air flowing in the wind tunnel would pass over the heating elements resulting in differential heating and the resultant stratification sought in the modeling effort. The scaling of the flow is achieved by considering the Froude number for the scaled down mine and adjusting the gravitational component of the Froude number for temperature due to heating. The behavior and movement of contaminants in the pit by is studied by placing visible contaminant sources in the pit. The penetration of flow into the pit is found to be a function

of Froude number and the magnitude of the inversion. The "...general behavior of the flow is found to agree with previous atmospheric experience, salt-water drag tank models, linear perturbation analysis, and computational-fluid-dynamics models."

This approach can generate a multitude of problems. The stratification achieved by preheating the air before it reaches the mine pit, presumably generates the stratified layers, while the air at the pit bottom, unaffected by the heat remains cooler. The heated air is then swept past the model pit by momentum imparted by the fan in the wind tunnel, which, with limited mingling with the air at the pit bottom, preserves the stratification. However, the momentum, otherwise expressed as the velocity head of the fan would have to unrealistically high for the scaled down model (even with the Froude number adjustment), to achieve this. Thus the stratification in the model may not reflect actual conditions, and the actual boundary layers between the dynamic and static layers of the wind-flow may not correspond to those predicted by the model. Additionally, the scenario modeled seems unrealistic: it seems unlikely that a flow of such warm air with high lateral velocity would enter the stable atmosphere of a mine pit during the night. The Froude number adjustment would be difficult to make in this case.

The Froude number depends on the hydraulic length of the system, which in this case would amount to the mine profile. As posited by the investigators, the full length of the mine profile is not in use by the flowing air as in does not affect the lower reaches of the pit. This fact, coupled with the observation that the boundary layer between the static and the dynamic layer of air is spatially variable, would indicate that the effective length for the Froude number would be significantly variable, and thus very difficult to evaluate.

Moreover, the placing of the scaled down model in an inverted position on the roof of the wind tunnel may cause additional problems. After heating, the airflow is pushed by momentum on to the mine pit. Of course, warm air tends to rise. When on top of the pit, even with the momentum impetus, the air will tend to rise. In the present case, this rise will take it into the pit, rather than out of it, as is naturally valid. This behavior will destabilize the inverted layer that the experimental setup attempted to create. Contaminant transport would also be affected by this phenomenon. In the contaminant distribution contours shown in the investigation, it is clear that contaminants from sources placed on the downwind slope of the mine display a tendency to expand into the mine.

This expansion would only happen if the prevalent convection currents are forcing the flow of the contaminants towards the bottom of the pit.

(Fomin 1996) conducted a thorough investigation of the nature of convective flow in deep open pit mines. The mathematical model generated during his investigation took into account various factors that affect the flow of air and contaminants in a mine in the absence of a forced convective system. Because a forced convective system could also include inflow of air into the mine by atmospheric convective processes, Fomin assumed that there is no airflow near the mine, and that only convection from the heated walls of the pit could impart energy and therefore velocity to the wind. In the model, the contaminants (O_2, N_2, and CO_2) are injected into the pit uniformly from the sides and the bottom of the pit. This injection also carries heat into the model, as exhaust gases are hot. Fomin defines the Grashof number (for heat) as follows:

$$Gr_q = \frac{g\beta q h^4}{\lambda \upsilon^2} \qquad (5)$$

Where:

g = acceleration due to gravity,

β = volumetric expansion coefficient,

q = heat flow due to exhaust gas,

h = depth of the pit,

λ = coefficient of thermal conductivity of air, and

ν=– kinematic viscosity coefficient of air.

He also defines the Grashof number for mass balance as follows:

$$Gr_R = \frac{gR_i h^4}{\rho D \upsilon^2} \qquad (6)$$

g = acceleration due to gravity,

R_i = rate of mass injection of a particular gas (i varies from 1 = 4 for the four contaminants,

h = depth of the pit,

ρ = density of the composite gas (assumed to be constant),

D = Diffusivity constant of the contaminant gas in air, and

ν = kinematic viscosity coefficient of air.

The Grashof number is a measure of the ratio of the buoyant forces to the viscous forces in a natural convection situation. In this case, however, the investigator set the depth (h) of the model to 500 and 600 m. This means that the buoyant force experienced by any quantum of air will always be the same as if it was at the bottom of the pit. The buoyant force will decrease as the air moves up (considering an adiabatic and mass-impermeable boundary around the quantum of gas in question). Therefore, the ratio of the buoyant force in the Grashof number is exaggerated, and will result in dramatic upward convective velocities. This behavior is probably the reason why the model results show a veritable chimney effect at the center of the model.

The boundary conditions and the initial conditions used by Fomin (1996) are standard and often used. He considered the pit walls to be impermeable to mass or momentum and the pit top and sides to be open boundaries. This assumption allowed for (convection permitting) a quasi-laminar flow state in the model and greatly simplified the flow patterns. Fomin observed that the air seemed to roll down the sides of the hot walls of the pit before being taken upwards at the center of the pit by upward convective flows. He explained that while it could naturally be expected for the hot injected gas to rise immediately, after a certain time, the convected heat would be conveyed beyond the horizon of the mine and a stable convection current established. This would create the vertical convective column that draws all air from the vicinity along the contour. He used several temperature gradients upward from the floor of the mine, so that the temperature on the vertical axis increased with height, which effectively established an inversion cap on the system. This setup, along with a fixed pit-bottom temperature, ensures that the convective column is established and stable. The force of convection upwards, however, is not only controlled by the heat injection, but also by the momentum balance of the buoyant air, which is exaggerated.

3.2 Solution Approaches

Shi and others (2000) noted that that local air quality is closely related to the ABL in complex terrain. They pointed out that many numerical ABL models have been utilized to study meso-scale or micro-scale systems over complex terrain, such as land-sea breezes, mountain-valley and river valley winds. Special micro-scale terrains, such as open-pit mines, have not attracted much attention.

Shi and associates constructed a high-resolution, non-hydrostatic, three-dimensional ABL model. They considered the characteristic features of an open-pit mine, which is only 2 km by 2

km wide and more than 100 m deep. Physical processes such as shortwave radiation of the sun and its uneven distribution on the ground, longwave radiation of earth-atmosphere systems, sensible and latent heat fluxes and heat flowing into the substrate of the earth, are involved in the model. Using this model ABL structures over this kind of micro-scale concave terrain (an open-pit mine) are fully studied.

The results showed that the most important characteristics of the stationary ABL are the recirculation, which has a closed structure and high turbulent kinetic energy. This structure of the stationary ABL is consistent with the results of wind-tunnel experiments conducted earlier. The depth of the pit, the slope angle of the pit wall, the incident airflow velocity, and the indicating shear of the initial velocity profile all influenced the structure of the ABL greatly. It is found that thermal forcing and mechanical forcing are equally important mechanisms in the evolution of the ABL.

Some difficulties in the simulation arose from the complex forcing mechanisms that induce turbulence at night. In addition, there are some difficulties in deciding how to choose the parameters for the closure model. Nonetheless, the results are considered relatively significant and useful for the forecasting and control of the local air quality in open-pit mines. The numerical results showed that strong turbulence exists in the pits of the type modeled, possibly caused by the interaction between the non-linear and diffusion terms in the governing equations. It is thought that the local topography of the terrain also had an effect on the turbulence.

Sharan and Modani (2006) developed an analytical model for estimating the crosswind concentration of a pollutant released from an elevated source. The analytical model developed by the authors is logically superior to the existing Gaussian model developed by Doran and Horst (1985), for two reasons. First, the authors use a power-law function to estimate wind speed, which tends to increase with height. Existing models assume that wind speed is constant with height. Second, the mathematical model developed by the authors calculates eddy diffusivity as a function of downwind distance from the source. Existing models assume that eddy diffusivity is constant. The authors go on to compare their model to actual data collected at three different sites. For two of the three sites, the model formulated by the authors performs as well as or better than existing models. For the third site, the model did not perform as well as existing Gaussian models.

Lowndes and others (1994) proposed that optimal modeling of open pit emissions might be more accurately achieved by the use of a multi-scale, predictive modeling approach. They suggested using computational fluid dynamics (CFD) methods, for high resolution near source dispersion, and conventional Gaussian based methods for far field dispersion modeling. They presented a numerically-based flow and dispersion analysis of a typical open pit using CFD in conjunction with a conventional Gaussian, plume-based methods. Typical operating emissions and meteorological conditions are obtained from long-term data records collected at a large operating quarry extraction operation in the UK. Emissions are modeled using a Lagrangian framework within conventional ABL profiles expressed as functions of turbulence and velocity parameters under assumed neutral conditions. Results are presented in terms of the impact of site topography on in pit retention as compared to the Gaussian based method.

In the paper, Lowndes and associates summarized a series of recent CFD studies on fugitive dust conducted by a team of researchers from the University of Nottingham, UK. These studies are validated using field meteorological and dust deposition data collected at a large limestone quarry in the UK. All studies are validated with field data.

The terrain immediately surrounding the quarry is undulating farm grazing land. The in-pit topography is characterized by a complex series of interconnected ramps, vertical faces and working benches. Detailed site elevation survey data at 4-m grid spacing are used to delineate the detailed topography of the working pit and surrounding terrain. These data are used to construct the surface topography of the model domain within the Gambit pre-processor model used by the commercial FLUENT software, which in turn is used to construct the flow and dust dispersion simulations. The size of the total model domain constructed is approximately 4 km $\times$ 4 km. The model could be rotated to allow for the ease of simulation of the direction of the simulated ABL to represent the mean average wind speed and direction. The rectangular domain mesh is divided into four primary flow boundaries, a background flow inlet and outlet and two boundary walls to define the flow across the quarry opening.

For the dust, four particle sizes 2.5, 10, 30, and 75 μm, at mass fractions of 0.05, 0.45, 0.3, and 0.2 respectively, are used to simulate fugitive dust emission sources within the quarry. The quantities of dust released from each individual or collection of fugitive dust emission events modeled (bench blasting, loading, truck haulage, etc.) are calculated using the emission factors

defined by the US EPA AP-42 fugitive dust emission models. Detailed analyses are made of the influence of pit topography, and factors influencing in-pit dispersion and deposition of dust.

Lowndes and associates suggest that a number of recent research studies have concluded that the use of the US EPA AP-42 dust emission models for large open pit and quarry operations, together with conventional Gaussian plume dispersion models, can produce over-predictions of off-site emission and deposition. They go on to state that these studies have also concluded that the EPA methods are unable to replicate the true nature of the in-pit fugitive dust emissions, dispersion and deposition. They suggested that the use of an appropriate, three-dimensional, field-validated computational model might allow for improved simulation of these events, which could allow the mine operator to predict the occurrence of in pit reduced visibility.

The authors then suggest the development of a three component modeling approach:

1. Improved dust emission models to represent more accurately the emission characteristics of stationary and mobile in pit fugitive dust sources.
2. More complex three-dimensional computational fluid dynamic models, for more accurate prediction of the influence of the in-pit microclimate on the dispersion and deposition of fugitive dust within the pit.
3. A method for determination of an area emission factor for dust through a defined area across the mine opening, and the transference of the determined areal dust emission to the background atmospheric boundary layer, with the resultant far-field, downwind dust dispersion to be solved by a conventional, Gaussian-plume dispersion model.

The research presented by Shi Yong et al. (2000) is of particular interest for this project. In this study, the authors used non-hydrostatic equations to develop a numerical model for an open pit mine with dimensions of approximately 2 km $\times$ 2 km $\times$ 295 m in depth. Upon running the models, the authors observed a pronounced recirculation in the center of the pit. This recirculation is validated by wind tunnel experiments. After creating additional models, the authors discovered that the magnitude of this recirculation increased with increasing pit depth, slope angle, and initial wind velocity. The shear of the initial wind velocity also influenced the recirculation. One weak area of this study is that the authors have not validated their numerical models with real world observations of conditions in an actual open pit mine.

Aloyan and others (1982) proposed a novel scheme to solve the flow of air into a mining pit. The scheme of equations solved took into account not only the mass and momentum balance equations that would be solved in the normal course of such a solution, but also external planetary parameters like the Coriolis force. The effects of temperature and the resulting stratification of the air above the pit, the effects of pressure, and the contours of the pit are also taken into account, as are external sources of heat flow into the system, whether artificial or natural, such as solar radiation. Pollutant sources are placed in the model to account for the generation or inflow of pollutants in the model. The system of equations is then solved using a novel technique called the use of "fictitious" regions in the model space. In this technique, the irregular topography of the actual mine could be approximated as a set of rectangular parallelepipeds. The mass and momentum equations could then be re-specified for the new boundaries that are generated. The regions of the mine that are compliments to the parallelepiped are then simply continuations of the same boundary and domain conditions as the approximated rectangle.

This system brings forth a generalized model that can theoretically be applied to any mine topography and thus is very flexible. The numerical experiments provide an interesting correlation among the feasible depth of an open pit mine that can be ventilated, the behavior of contaminants under different thermal conditions, and an estimate of the time it would take to ventilate the pit after a major pollutant dispersion event (such as a blast).

Very few data are presented from the experimental results. The results that are presented indicate that the escape of pollutants from the pit is directly proportional to the velocity of the influent air. However, at high influent velocities, the lower regions of the pit will be affected by turbulence, and the contaminants would be subject to remixing with the local air, thus altering their concentrations and possibly chemistry. This turbulent zone mixing should be clearly visible in contaminant contours. The data presented, however, show no sign of turbulent mixing, even with high velocities of 16 m/s, and contours drawn indicate laminar, stratified flow. The same lack of turbulent mixing is observed in the work of Baklanov (1984).

3.3 Proposed Remediation Measures

There have been several approaches to ventilation of open pit mines in Soviet Russia. Baklanov and Rigina (1993) presented their research into the application of cascade ventilation to the dilution of contaminants in large, open pit mines. A number of open pit ventilation

configurations are simulated using numerical models. Most of the models are executed under conditions of atmospheric inversion with no wind. In this study, pits ranging from 420 to 750 m in depth, with ventilation configurations ranging from two to seven individual fans, are simulated. The only cascade ventilation system that is effectively able to remove contaminants from the pit is a system of seven units applied to a pit of 450 m in depth. The power consumption for this scenario is 3.4×10^5 kW. The authors of the study concluded that cascade ventilation is not an effective means of ventilating open pits. No specific details are given as to the construction of the numerical models used in this study or the assumptions made in applying the cascading ventilation systems to the models.

Belousov (1989) discussed how improved ventilation in open pit mines could be achieved by the installation of "aerodynamic foils" (wings) on the windward sides of open pits. The author conducted 210 wind tunnel tests with a 1:1,000 scale model of an open pit coupled with an aerodynamic foil. Mathematical relationships are developed from the wind tunnel tests that relate the required geometrical parameters of the wing to wind speed and the dimensions of the open pit. The author suggested that additional benefits could be realized by combining aerodynamic foils with combinations of fans and pipes located in the pit. The author claimed, "when wings are installed with optimal parameters, virtually the entire pit is ventilated by direct flow." The effectiveness of this technique requires, of course, that a constant wind of suitable velocity is flowing over the open pit.

In an example where the method is employed to create rarefaction on the windward side for an open pit in a plain land terrain with a pit 1,000 m long and 250 m deep, with a wall slope of 30°, the minimum critical wind velocity required for effective air exchange without accumulation of toxic impurities is 2.8 m/sec. To intensify the ventilation requirements, a perforated pipeline 200 m long is installed along the windward side of the pit. According to the model, the total quantity of air to be pumped out is 105 m^3/sec. This flow rate of pumping is achieved by connecting to the pipeline centrifugal fans, installed beneath it on the slope every 20 m. The air from the fans is ejected through flat sleeves with an output cross section of 0.5 m $\times$ 6 m along the slope. According to the model, this method would double the air exchange efficacy.

In general, the model showed that, in pits where the ratio of depth to length (or radius) and the pit wall angle are large, the efficacy of ventilation by air pumping on the windward side could be

increased by a factor of 3 to 4. Controlling the boundary layer of the wind stream makes it possible to improve the environmental conditions in an open pit.

Belousov (1995) also discussed yet another approach to ventilation of an open pit mine, and examined the ventilation of open pits due to thermodynamic processes, such as temperature differences. This form of air exchange is referred to as "breeze circulation." In open pit mines, breeze circulation tends to develop naturally in warm months when there is a temperature gradient between the center and the edges of the pit. In cold months, this temperature gradient trends towards zero, and breeze circulation typically is not present.

The author developed mathematical relationships for the development of stable breeze circulation based upon thermodynamic first principles. Relationships are developed for both circular and elongated pits. The magnitude of breeze circulation is greater in elongated pits for the same initial conditions than for circular pits. The relationships developed show that stable breeze circulation can develop when a temperature gradient of 5 to 10°C is present. The efficiency of this circulation can be improved by creating turbulence in the flow by the installation of air vanes above the pit.

Chapter 4 Data Collection

Ventilation design for open pit mines requires the knowledge of the quantity of the pollutants that are liberated into the pit by various dust and gas sources. The most important items in the total balance of pollutants in open pit mines are the stationary point sources (drilling rigs, excavators, loading machines) and moving sources (such as the trucks). The spreading of admixtures from these sources in an open pit mine is directly related to the aerodynamics of the airflows in the open pit space. Evaluation of the atmospheric conditions in an open pit mine requires a determination of the concentration of injurious mixtures. The problem is complex and any solution approach would require a good understanding of the interaction of the aerodynamic movement of air, air inversion process, meteorology, pollutant sources, and application of air movers in open pit mines. An array of data is required to create and validate open pit mine ventilation numerical models. The meteorological conditions within the deep open pit mine are significantly affected by temperature (stability) and roughness conditions, which ultimately generate complex dispersion phenomenon including separation of atmospheric boundary layer and recirculation.

The meteorological inputs needed to determine the contaminant concentration are the wind speed and direction as a function of time at one height, the nocturnal temperature inversion characteristics at sunrise, the heating rate of the pit atmosphere after sunrise, and the turbulent eddy diffusivities as function of atmospheric stability. The wind speed and direction observations at one height will be used to determine the advection term.

Among others, the following information need be collected during the data gathering and CFD model building phases: (a) Mean diurnal wind velocity (mean values for each month); (b) Number of calm days, their distribution both daily and monthly, the mean and maximum duration of clam weather; (c) Number of foggy days according to the months and their duration (mean and maximum); (d) Mean monthly humidity of the atmospheric air (for the warm period of the year); (e) Duration of the period with freezing soil temperature (below 0 deg. C); (f) Mean monthly air temperature with absolute maxima and minima; (g) Sources of air pollution, volume and rate of contaminants for each point source; (h) Air inversion frequencies and durations ; (i) Air quality values during air inversions, and required standards that need to be met.

Data are needed from an operating open pit mine regarding the number of stationary equipment in place (shovels , generators, drills, for example), and number of moving equipment (dozers, graders, trucks, for example), their locations, and status of operation (ready hours, delay hours, and stand by hours). Data is also needed on moving sources (such as trucks) from shift reports and status reports to develop the duty cycles of the trucks so that reasonable pollution loading information can be developed for model application. Engine make, model, specification, numbers and types of equipment in the pit, diesel exhaust information from pre-test, if available for diesel operated equipment in the pit. Topographic parameters including the slope angle (α) and the azimuth (β), and the solar azimuth B on the distribution of solar radiation on the ground, the mine depth, the angle of the terrain, the initial air velocity and its vertical shear, air quality data (air samples) at various open pit benches. Particularly, concentrations of NO_X, CO and DPM, and dust at various working or active benches. Pit geometry (depth, slope angles, bottom width, bottom length, elevation of various benches, widths of working benches), and in electronic format (Auto-cad files, for example)a and Digital pictures of the pit, (f) air inversion frequencies and durations; (g) air quality values during air inversions, and required standards that need to be met.

Meteorological data is compiled from the Cleary Summit Weather Station (Figure 4.1), which is located approximately 7.7 kilometers from the mine site. Operational data is collected from an operating mine. This data includes the number of stationary equipment in place (shovels, generators, drills, etc.), number of moving equipment (dozers, graders, trucks, etc.), the location of the equipment, and the status of operation (ready hours, delay hours, and stand by hours). Data is also collected on moving sources (such as trucks) from shift reports and status reports to develop the duty cycles of the trucks so that reasonable pollution loading information could be developed for model application.

To validate the models, it is necessary to collect air quality data at various open pit benches. Concentrations of NO_X and CO at various working or active benches during inversions is collected. Figure 4.2 to Figure 4.8 provides a representative sample of the data collected during the research. Various data collected during the research are also presented in Appendix I.

Figure 4.1: Weather Station Located near the Selected Open Pit Mine.

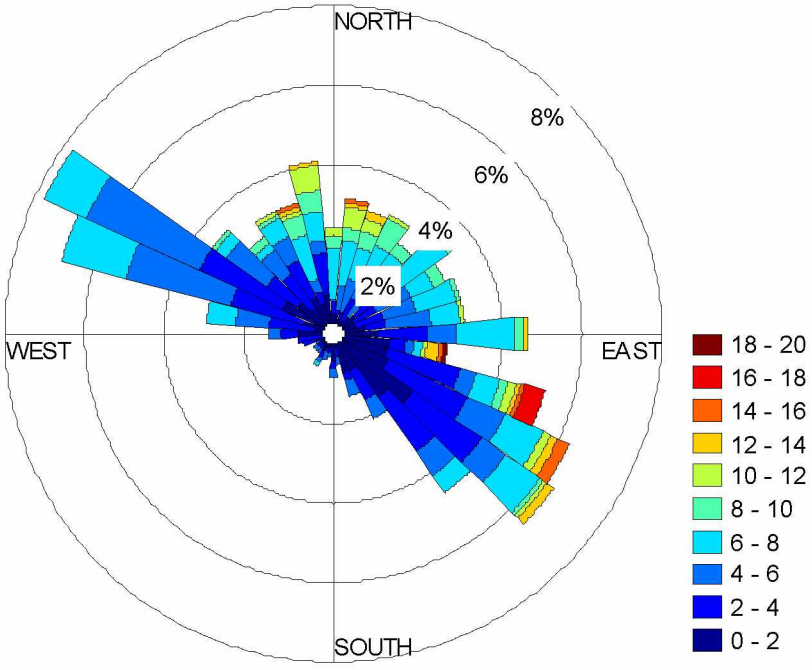

Figure 4.2: Wind Rose Diagram of Wind Direction and Maximum Wind Speed for October 2009.

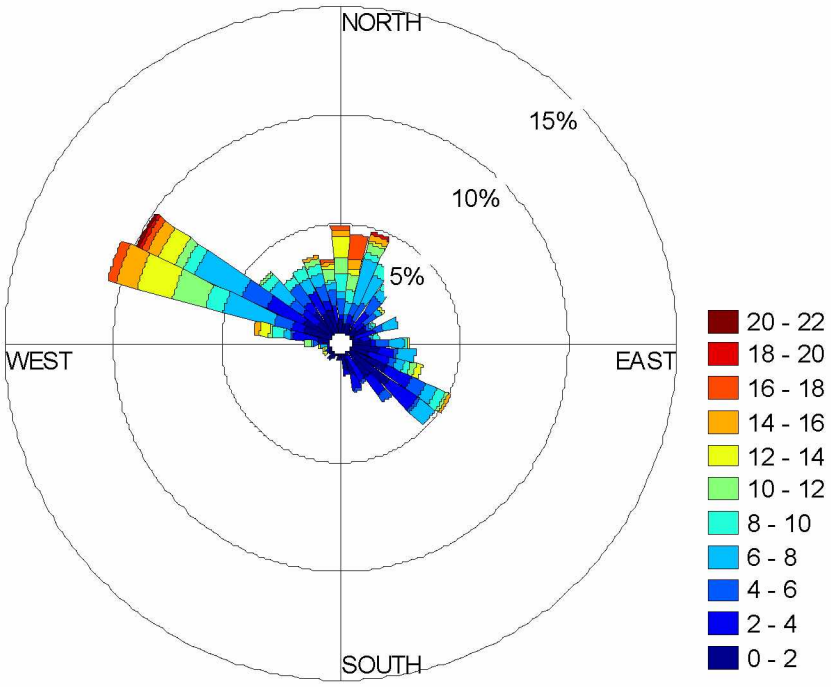

Figure 4.3: Wind Rose Diagram of Wind Direction and Maximum Wind Speed for November 2009.

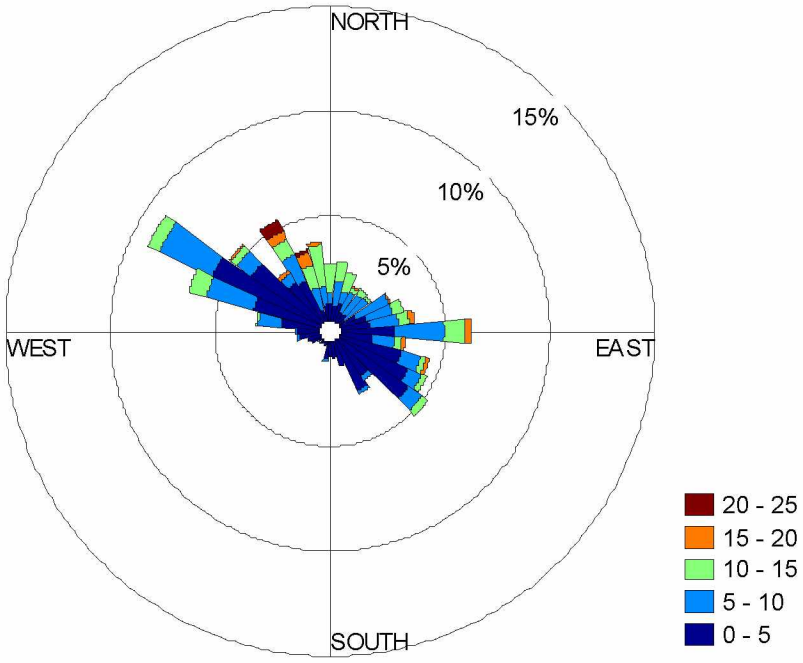

Figure 4.4: Wind Rose Diagram of Wind Direction and Maximum Wind Speed for December 2009.

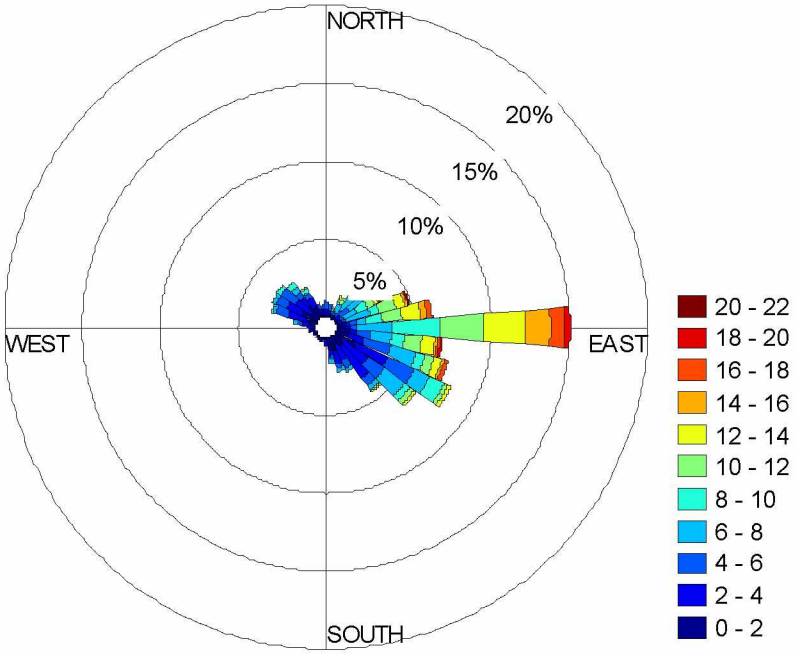

Figure 4.5: Wind Rose Diagram of Wind Direction and Maximum Wind Speed for January 2010.

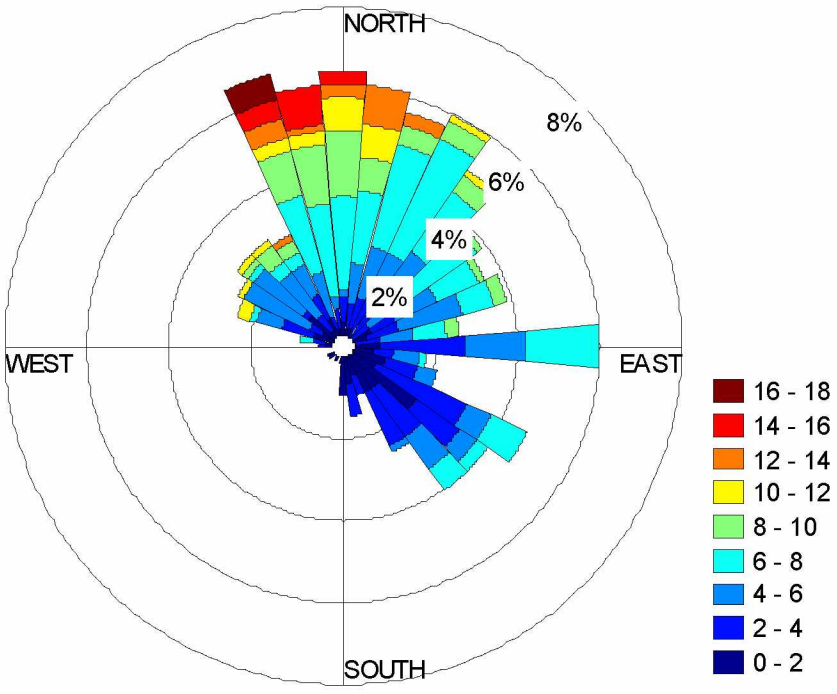

Figure 4.6: Wind Rose Diagram of Wind Direction and Maximum Wind Speed for February 2010.

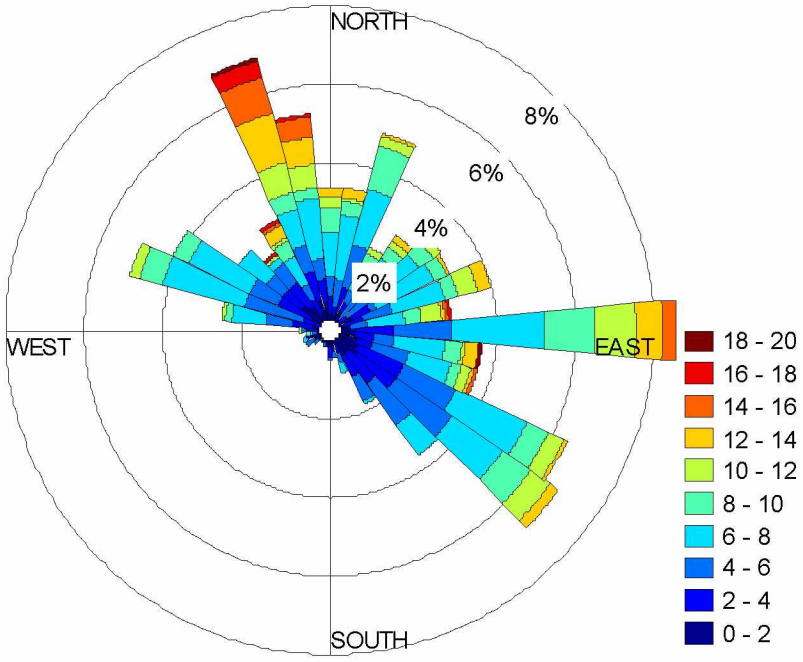

Figure 4.7: Wind Rose Diagram of Wind Direction and Maximum Wind Speed for March 2010.

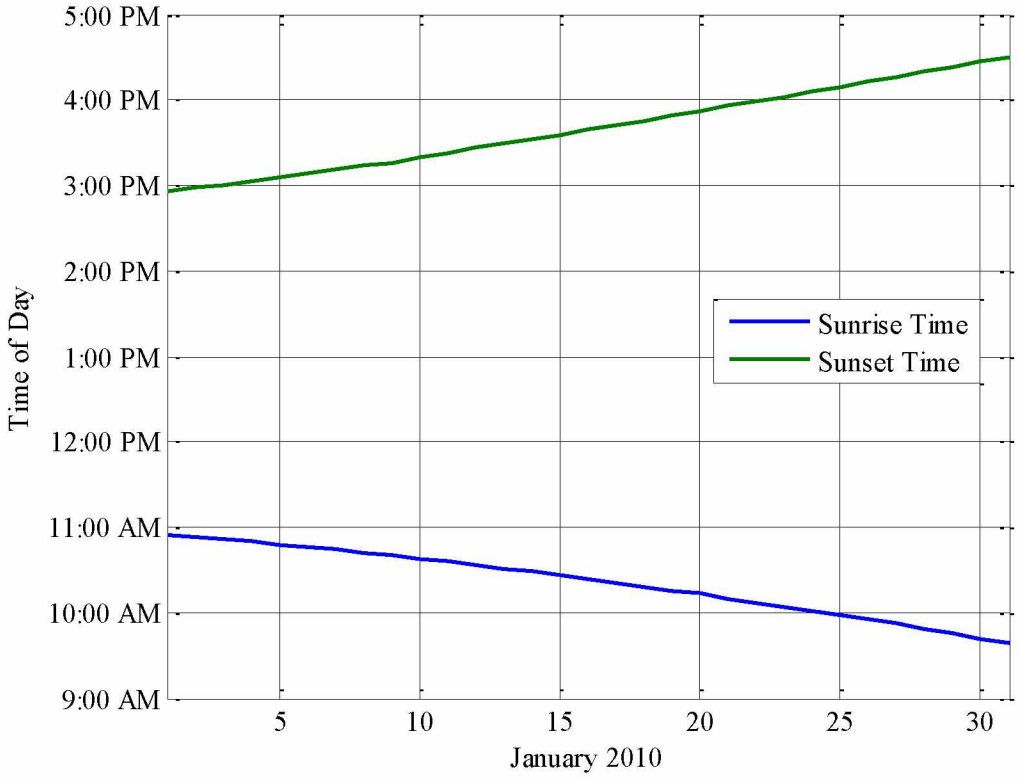

Figure 4.8: Sunrise and Sunset Times (January 2010).

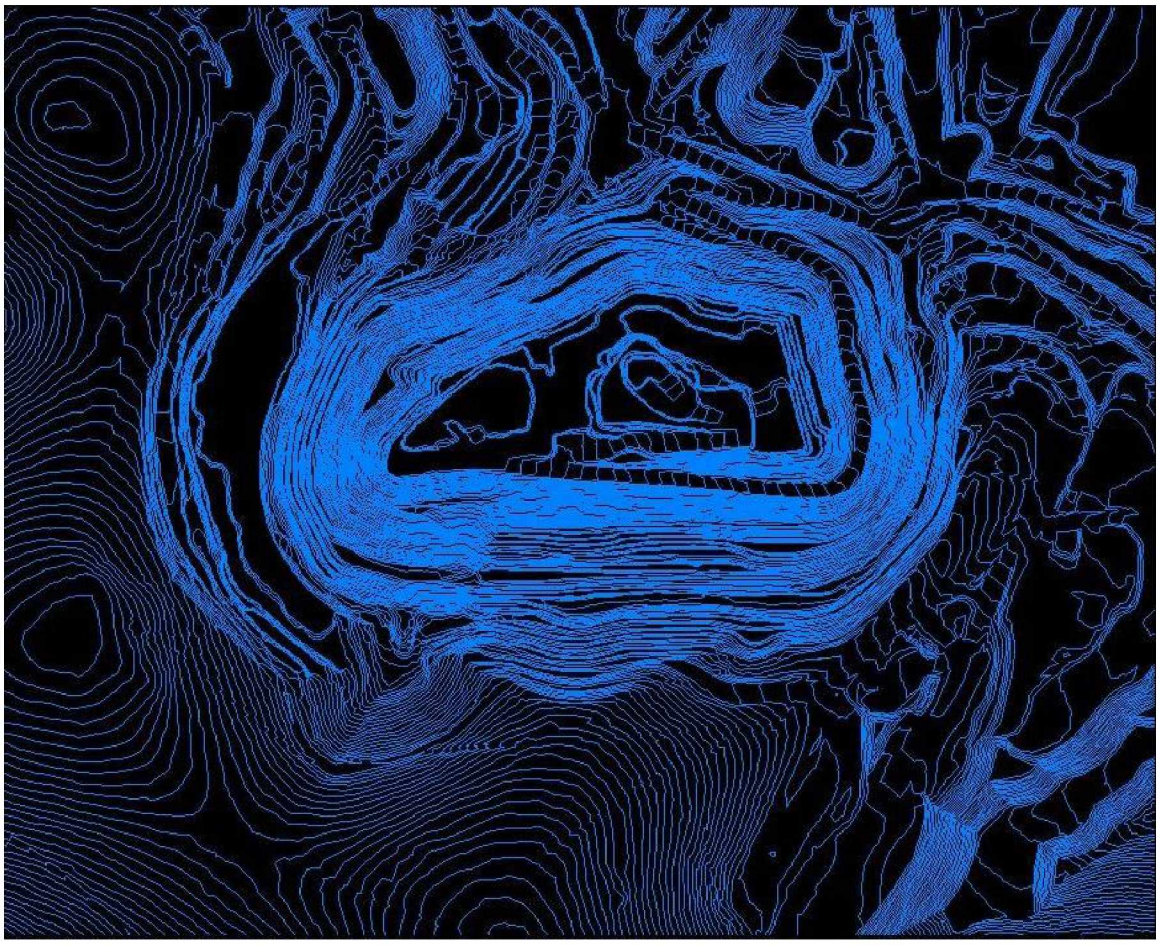

Figure 4.9: Contour Lines for the 2010 Pit Configuration.

4.1 Instrument Setup at the Mine for Temperature, Longwave and Shortwave Radiation Data

In order to have a significant model outcome, actual radiation data from the selected open pit mine is needed and for that purpose, two set of instruments are installed at the selected open pit mine. A schematic of the instrument setup at the selected open pit mine is given in Figure 4.10. Two set of instruments containing radiometer, NR01 and 109 temperature probes are installed in the pit and at the pit rim. The radiometers will provide us with the short-wave and long-wave radiation data for the pit bottom and the pit rim. Three temperature probes at varying heights of 1.5 (5 ft.), 3.6 (12 ft.) and 10 (35 ft.) meter are installed at pit bottom to obtain temperature profile in the vertical direction. Similarly, two temperature probes at the height of 1.5 (5 ft.) and 3.6 (12 ft.) meter are installed at the pit rim. One of the objectives of this research is to have a

better understanding of the temperature inversion within the pit. The radiation and temperature data at the pit rim will provide an understanding of the existing thermal conditions.

Figure 4.11 and Figure 4.12 shows the instrument setup at the pit bottom.

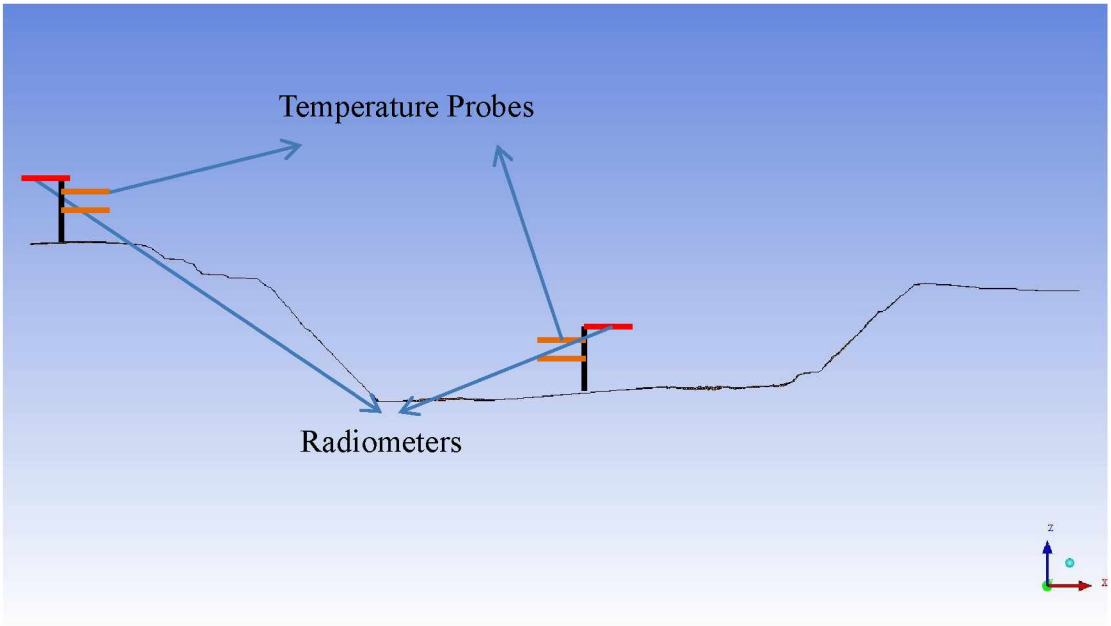

Figure 4.10: Schematic for the Instrumentation in the Mine.

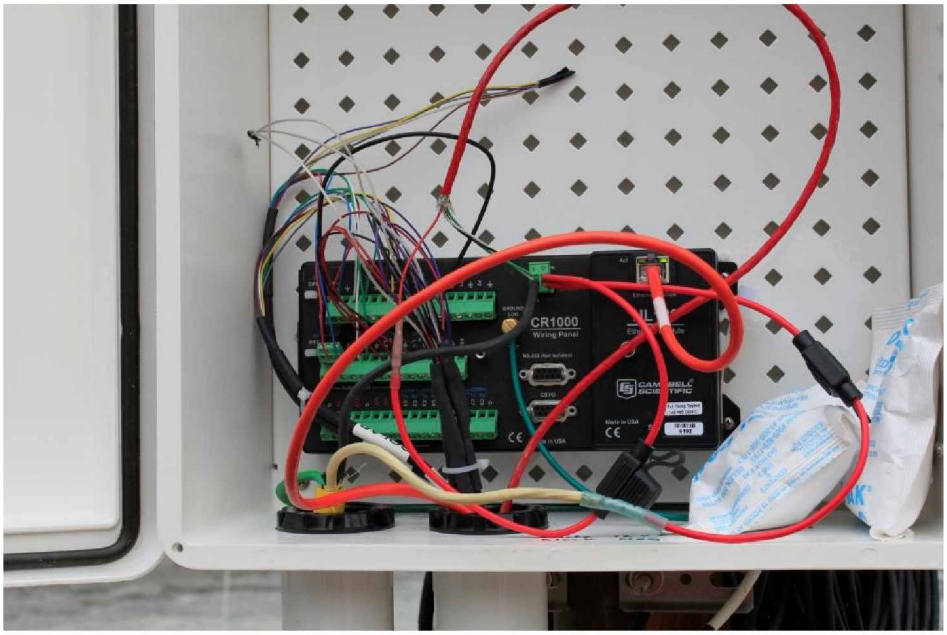

Figure 4.11: Data Logger at Pit Bottom.

Figure 4.12: Ten Meter Tower with Temperature Probes and Radiometer at the Pit Bottom.

4.1.1 Radiation and Temperature Data Collected from the Mine

The instruments installed at the partner mine during September 2013 are in operation and has provided a better understanding of the thermal regime of the mine air. The data collected from the mine is one of a kind and has helped in improving the model prediction results. The radiative flux data, shortwave and longwave radiation, gives the insight about the effect of radiative flux on the vertical temperature profile at the pit. The instruments are collecting throughout the time period and storing data for every twenty four hour time period at mid-night.

The data presented here in graphical form (Figure 4.13 through Figure 4.36) are for a selected twenty four hour time period of different radiative fluxes (shortwave and longwave), net radiative flux and temperature data at different elevations. The data are collected as average of every ten minute time period. Figure 4.13 presents four different radiative fluxes; shortwave upwelling (SR01Up_Avg), shortwave down-welling (SR01Dn_Avg), longwave upwelling (IR01Up_Avg) and longwave down-welling (IR01Dn_Avg) for the pit bottom station recorded on September 22nd 2013. It can be seen from the figure that the incoming shortwave radiation starts to increase around 7:30 AM and keeps on increasing but at some point in time, sudden changes can be observed. This

is due to presence of the cloud cover over the pit; as the cloud passes over the radiometer, a sudden decline in the incoming shortwave radiation is observed and at the same time, a rise in the longwave radiation can be observed. Figure 4.14 shows the net radiative flux, i.e., the summation of all the incoming and outgoing shortwave and longwave radiations. For convention, incoming radiation is treated as positive and outgoing as negative. From the figure, it can be seen that the net radiation is negative during the night time. It is due to the force of surface cooling net radiation, which is as low as negative 60 W/m^2. During the night time, however, a rise in the net radiation around 2:00 AM can be observed, which remains almost constant at negative 15 W/m^2. This, too, might be due to the presence of cloud over the mine.

An increase in the net radiation is observed after the sun rise and keeps on increasing until a cloud passes over the radiometer. The decrease in the net radiation is observed after the sun set.

Figure 4.15 shows the vertical temperature profiles at three different elevations; 1.5 (5 ft.), 3.6 (12 ft.) and 10 (35 ft.) meter denoted as T109_1_C_Avg, T109_2_C_Avg, and T109_3_C_Avg respectively. The temperatures given are in degree Celsius, taken as average of ten minute time interval. From the figure, it can be seen that temperature decreases with increasing elevation and the temperature profile corresponds to the radiation input. With net radiation around negative 50 W/m^2, a decrease in the temperature is observed. With increase in net radiation, the expected change in the temperature is also observed. During the day time, the temperature increases with the increase in net radiation. Figure 4.16 to Figure 4.18 are the plots on the same day from the data collected at the station location at the pit rim. Similar trends follow in the pit rim data as to the pit bottom data.

Figure 4.19-Figure 4.24 are the data plots for October 25th, Figure 4.25-Figure 4.30 are for November 23rd and Figure 4.31-Figure 4.36 are from December 23rd 2013 data.

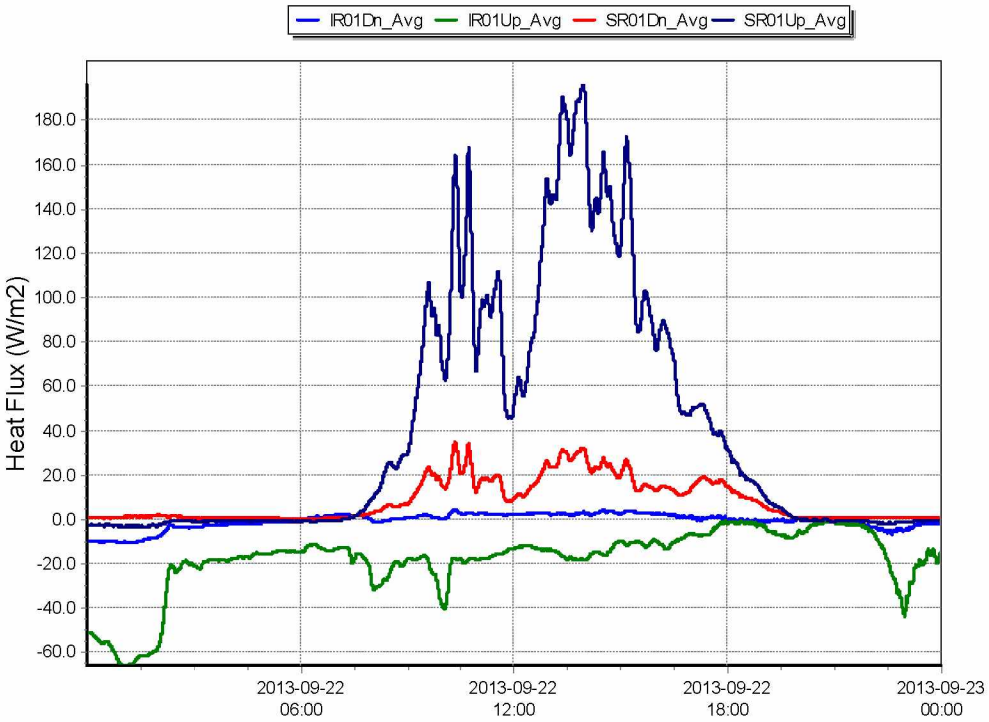

Figure 4.13: Radiative Flux Data from the Tower at the Pit Bottom on September 22nd 2013.

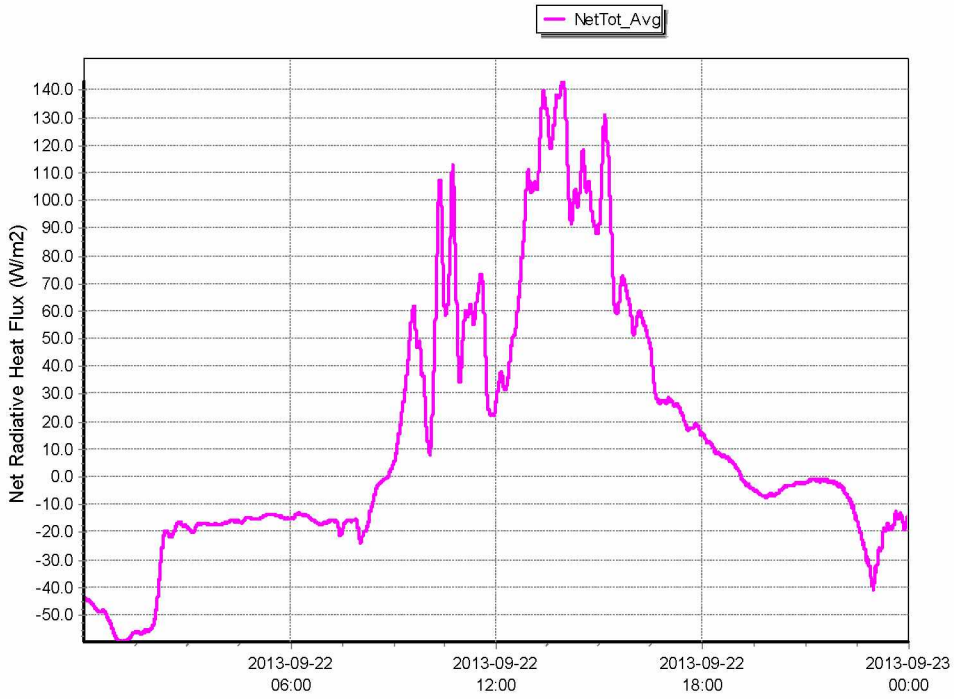

Figure 4.14: Net Radiative Flux Data from the Tower at the Pit Bottom on September 22nd 2013.

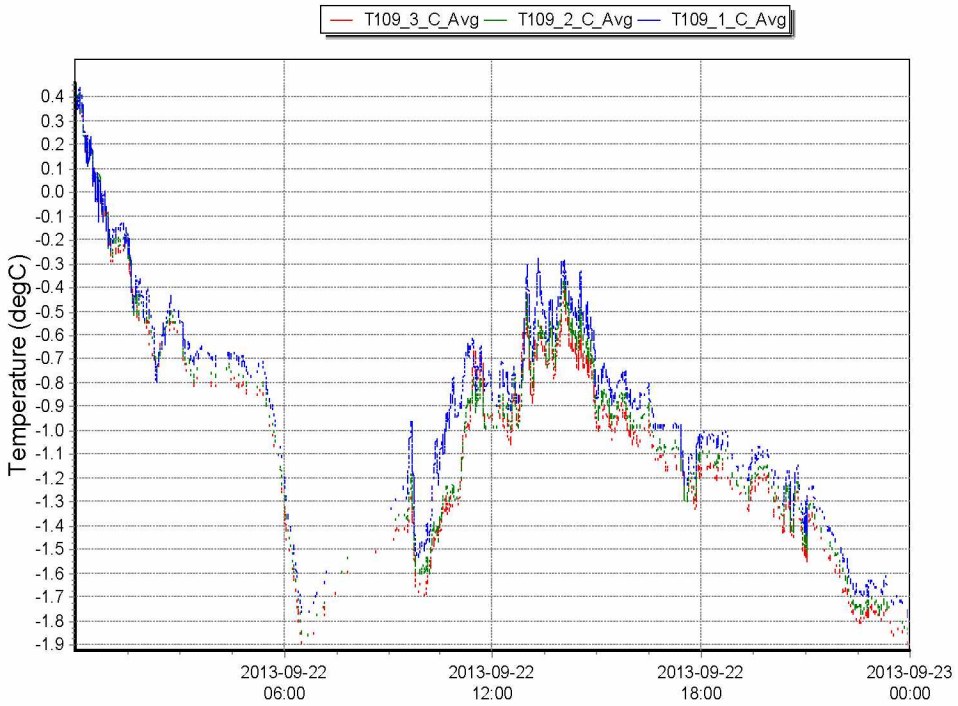

Figure 4.15: Temperature Data from the Tower at the Pit Bottom on September 22nd 2013.

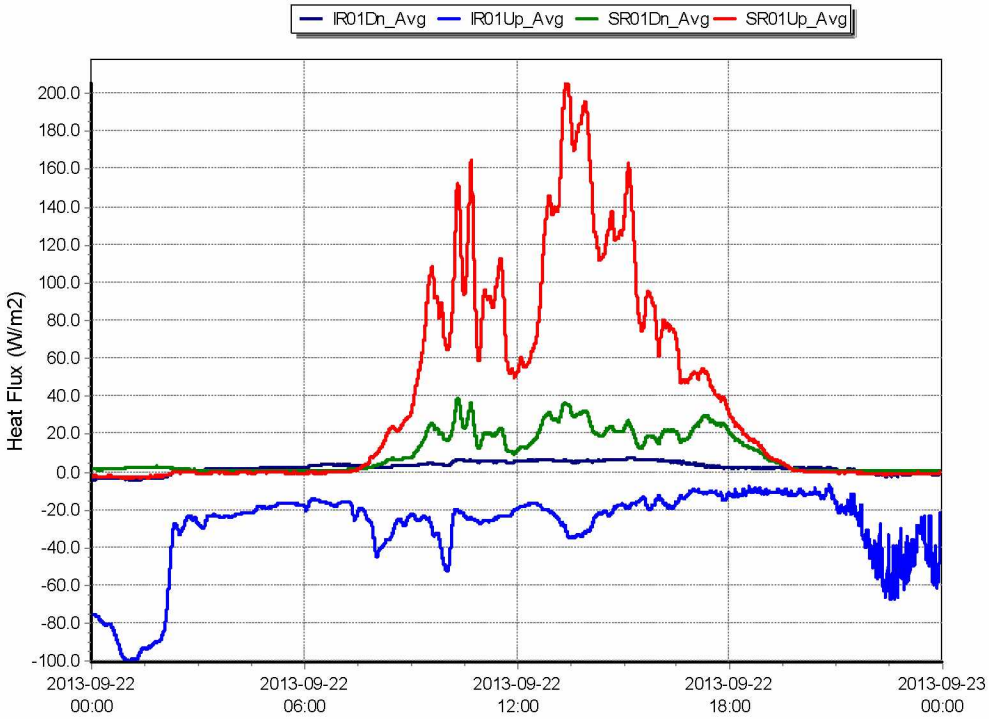

Figure 4.16: Radiative Flux Data from the Tower at the Pit Rim on September 22nd 2013.

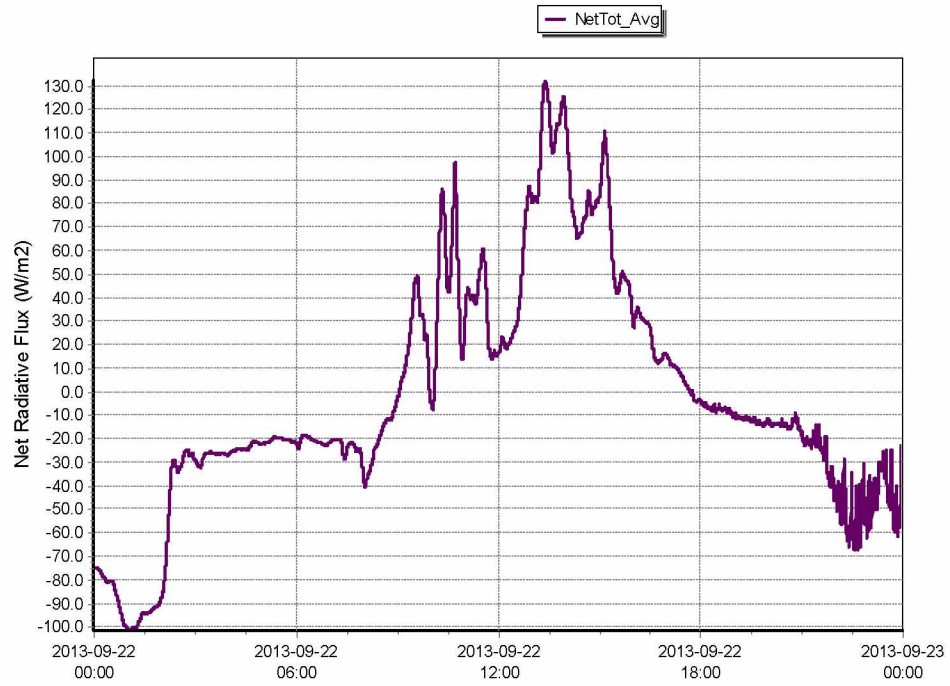

Figure 4.17: Net Radiative Flux Data from the Tower at the Pit Rim on September 22nd 2013.

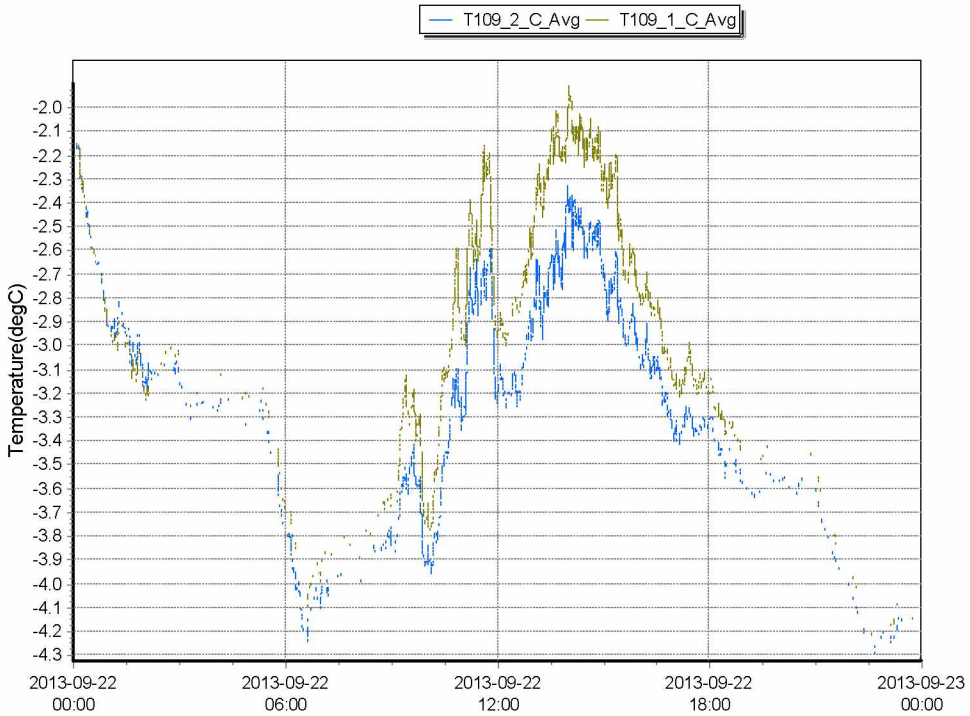

Figure 4.18: Temperature Data from the Tower at the Pit Rim on September 22nd 2013.

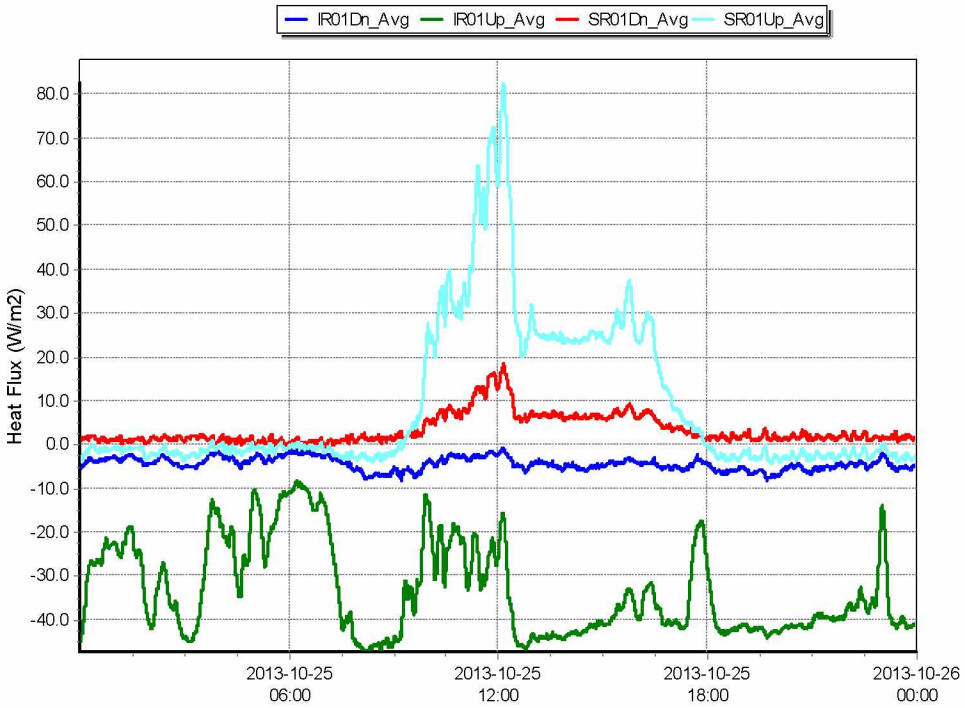

Figure 4.19: Heat Flux Data from the Tower at the Pit Bottom on October 25th 2013.

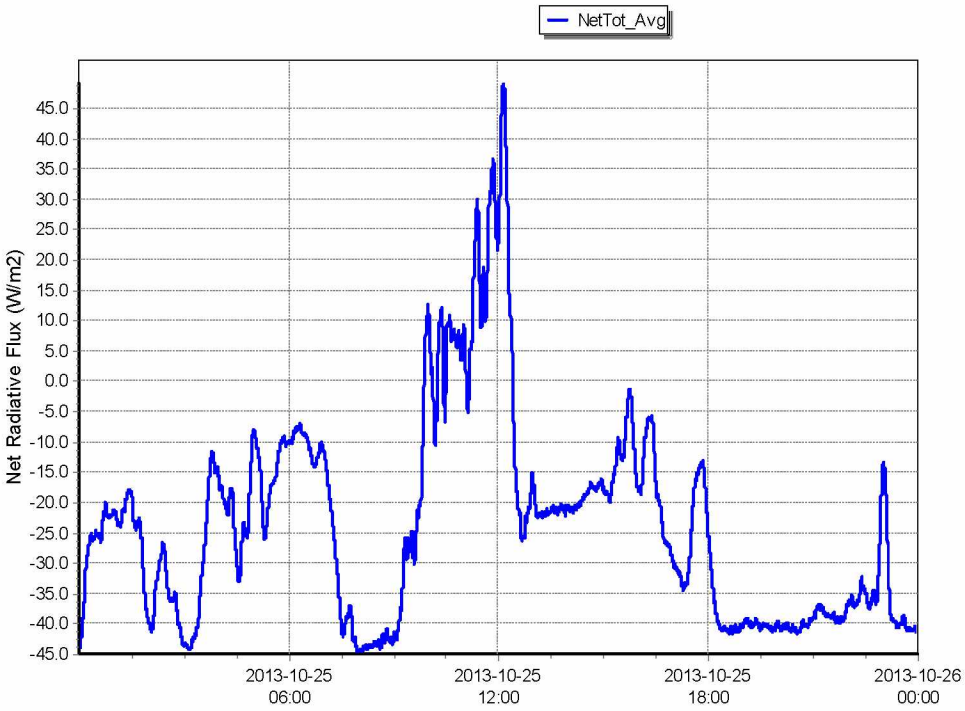

Figure 4.20: Net Radiative Flux Data from the Tower at the Pit Bottom on October 25th 2013.

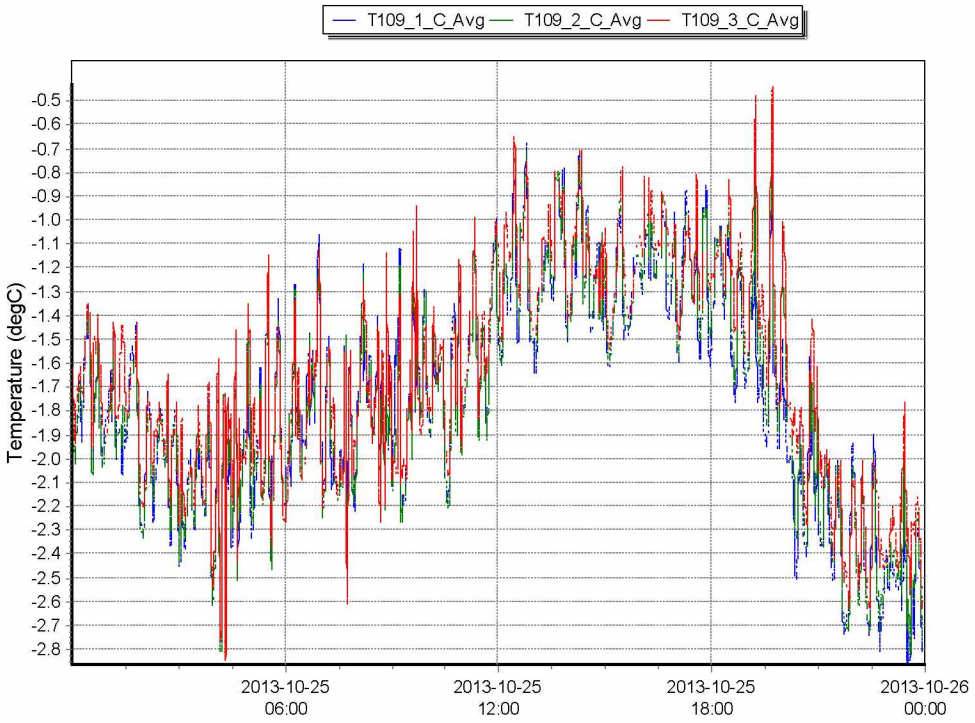

Figure 4.21: Temperature Data from the Tower at the Pit Bottom on October 25th 2013.

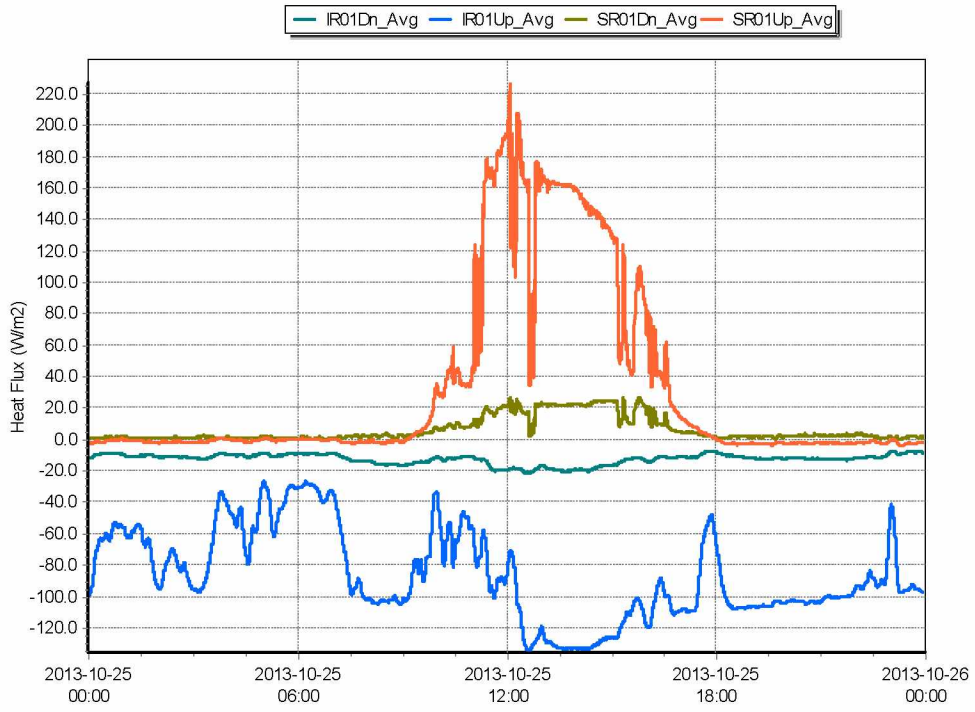

Figure 4.22: Heat Flux Data from the Tower at the Pit Rim on October 25th 2013.

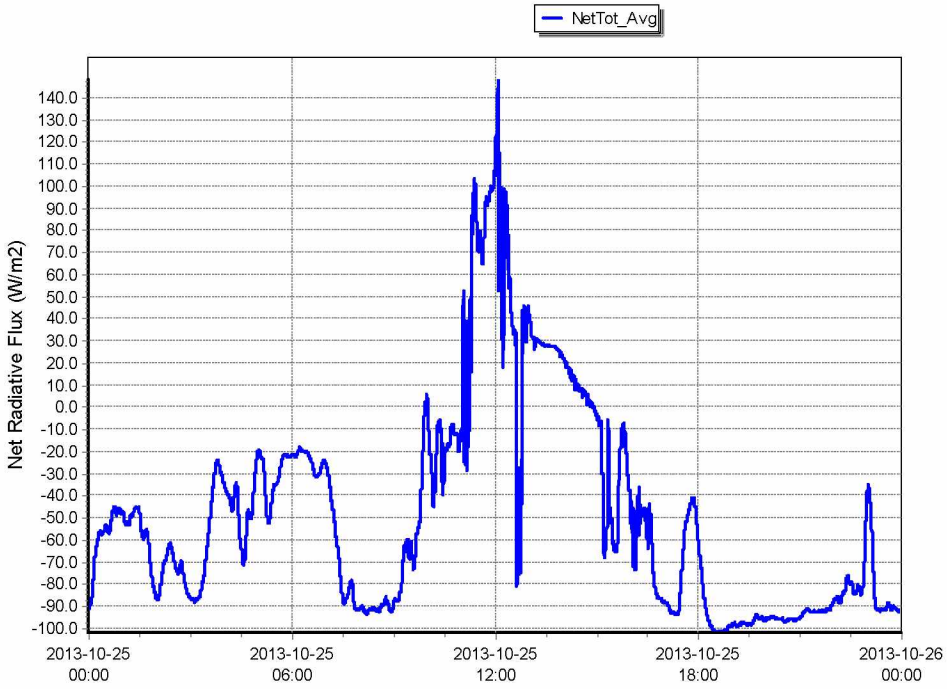

Figure 4.23: Heat Flux Data from the Tower at the Pit Rim on October 25th 2013.

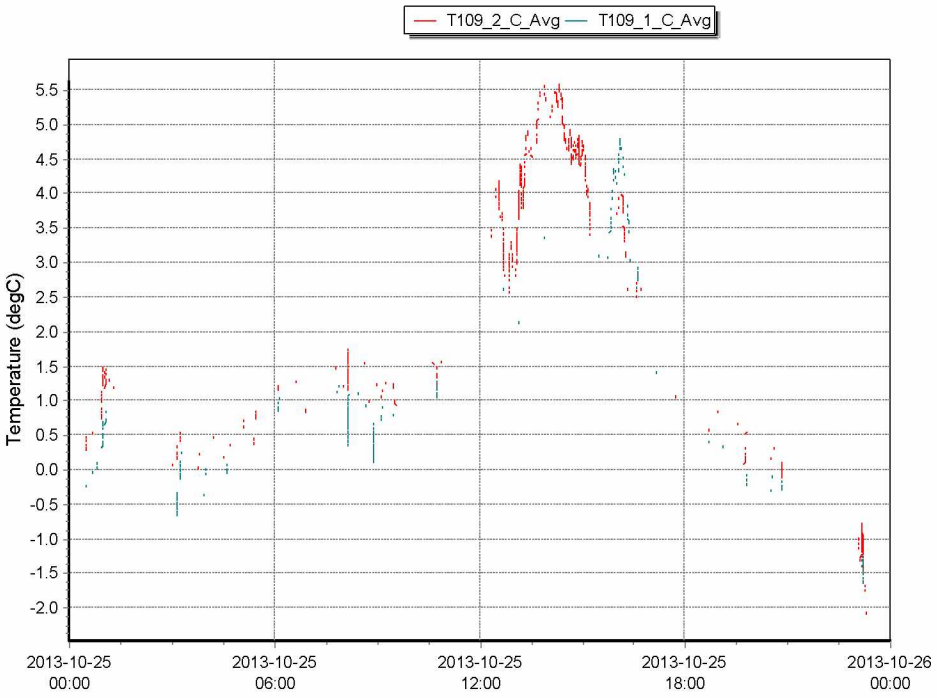

Figure 4.24: Temperature Data from the Tower at the Pit Rim on October 25th 2013.

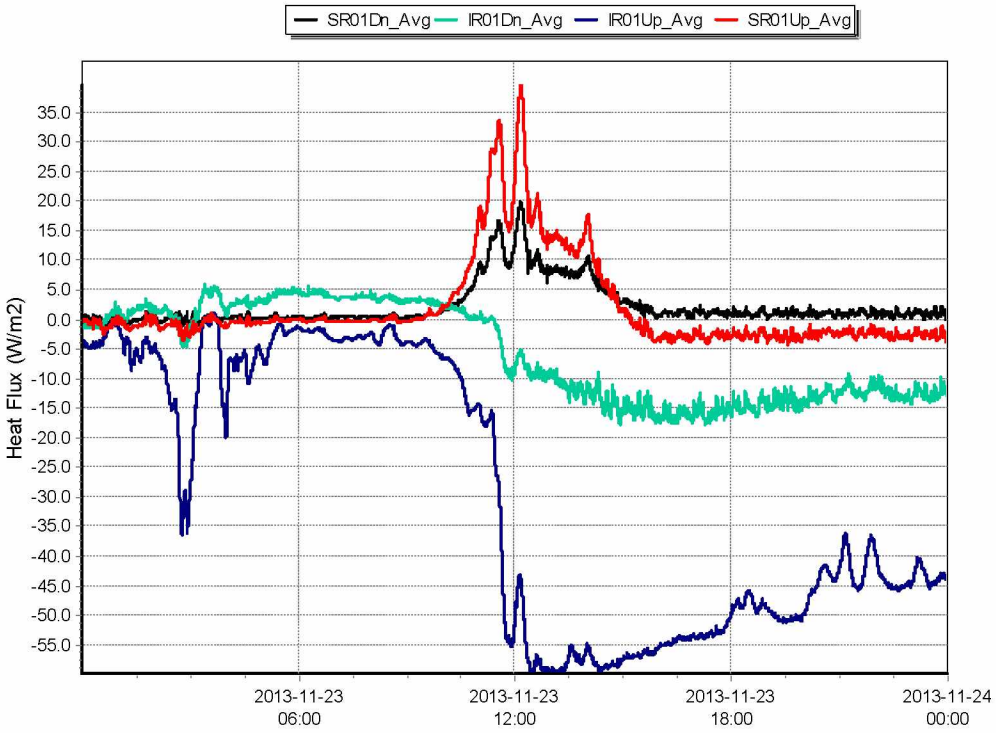

Figure 4.25: Heat Flux Data from the Tower at the Pit Bottom on November 23rd 2013.

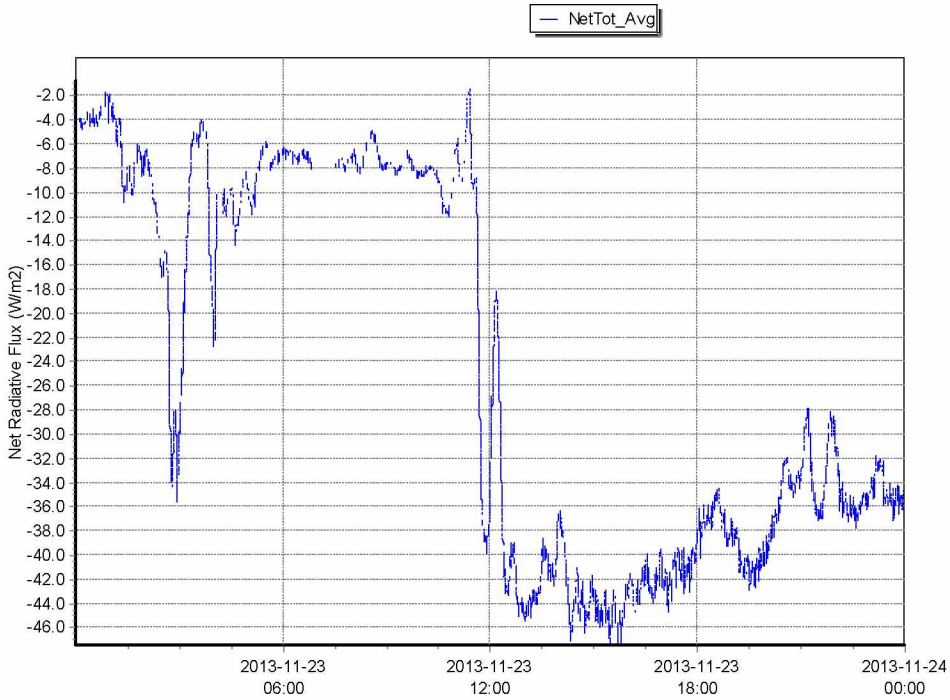

Figure 4.26: Net Radiative Flux Data from the Tower at the Pit Bottom on November 23rd 2013.

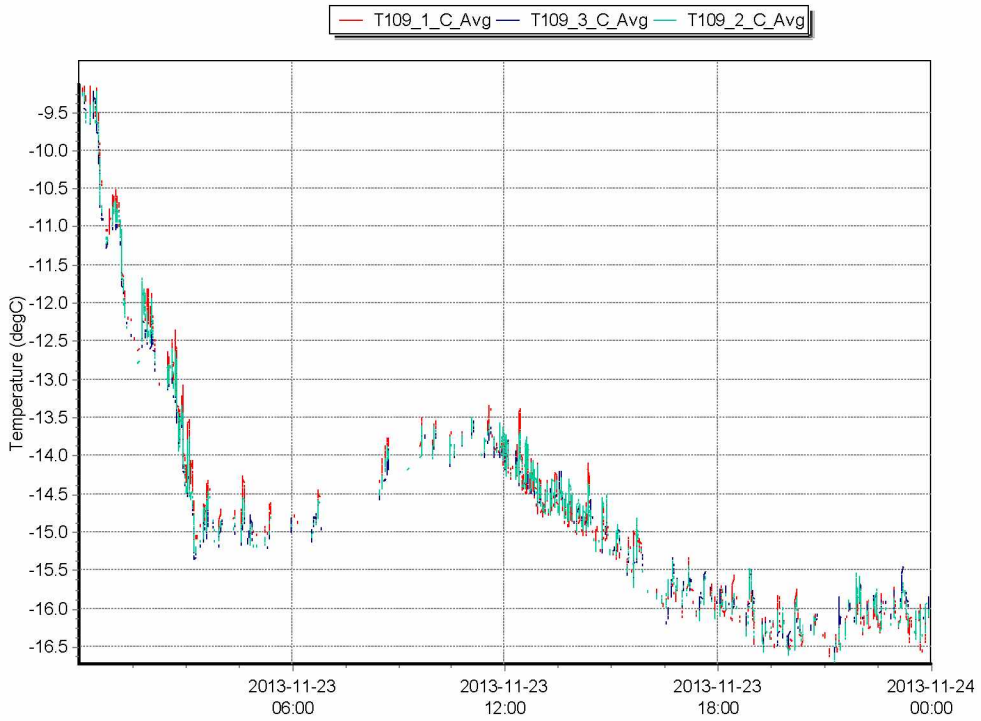

Figure 4.27: Temperature Data from the Tower at the Pit Bottom on November 23rd 2013.

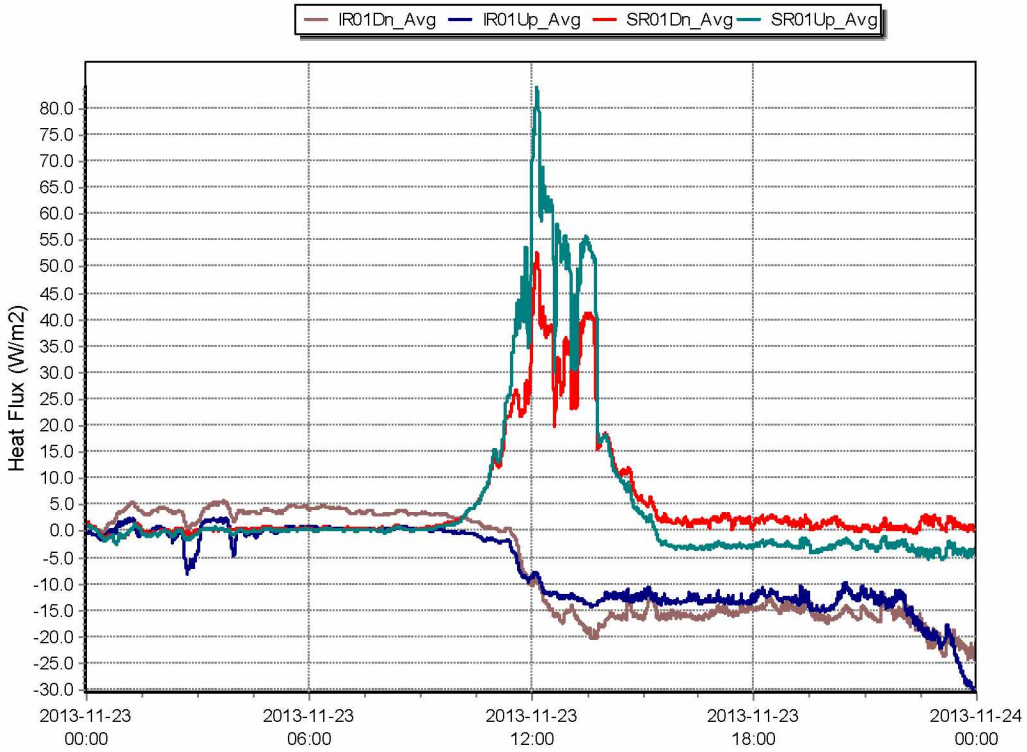

Figure 4.28: Heat Flux Data from the Tower at the Pit Rim on November 23rd 2013.

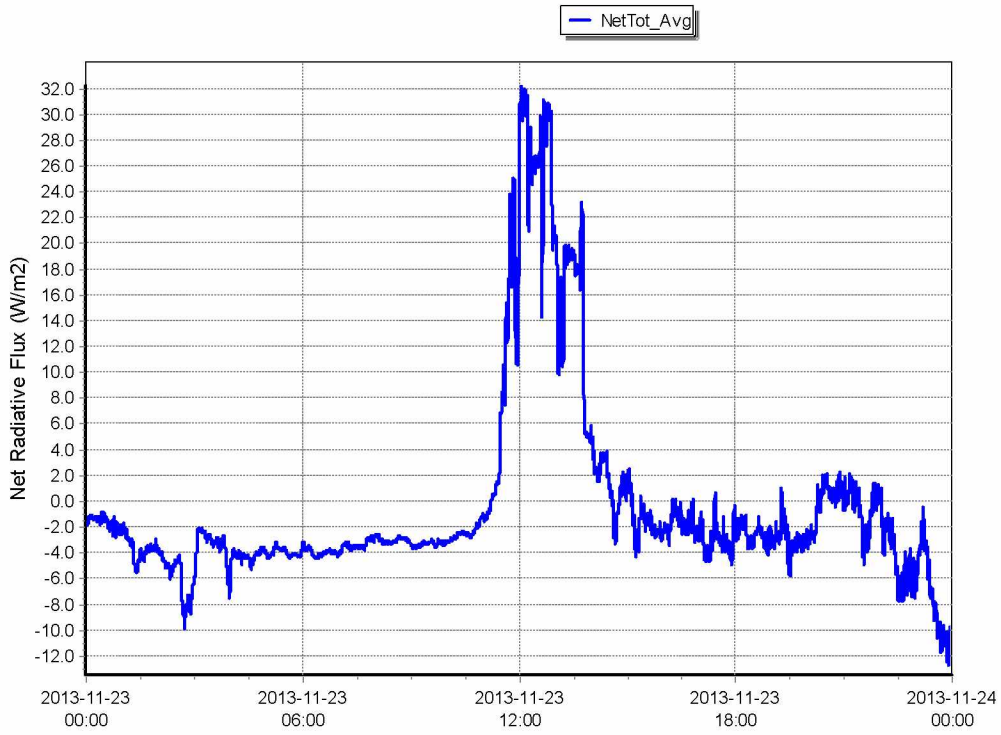

Figure 4.29: Net Radiative Flux Data from the Tower at the Pit Rim on November 23rd 2013.

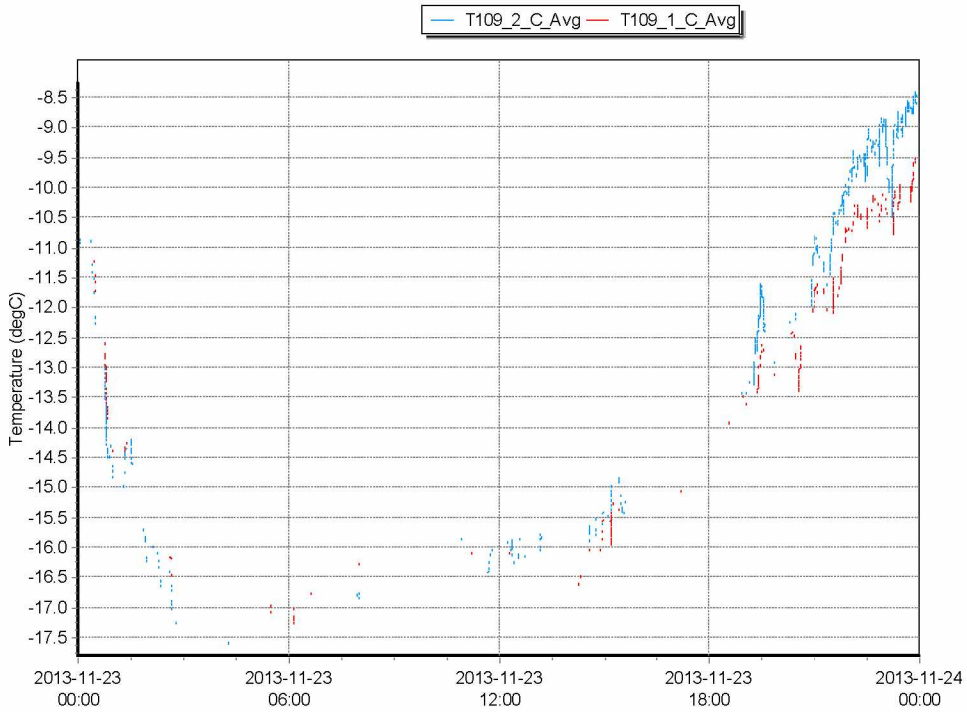

Figure 4.30: Temperature Data from the Tower at the Pit Rim on November 23rd 2013.

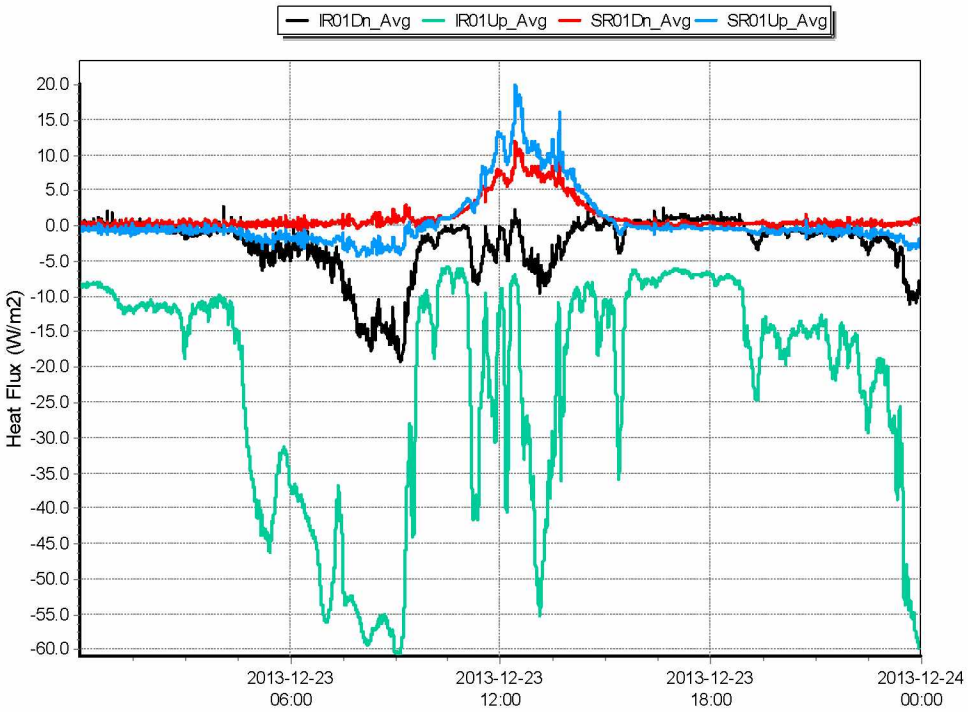

Figure 4.31: Heat Flux Data from the Tower at the Pit Bottom on December 23rd 2013.

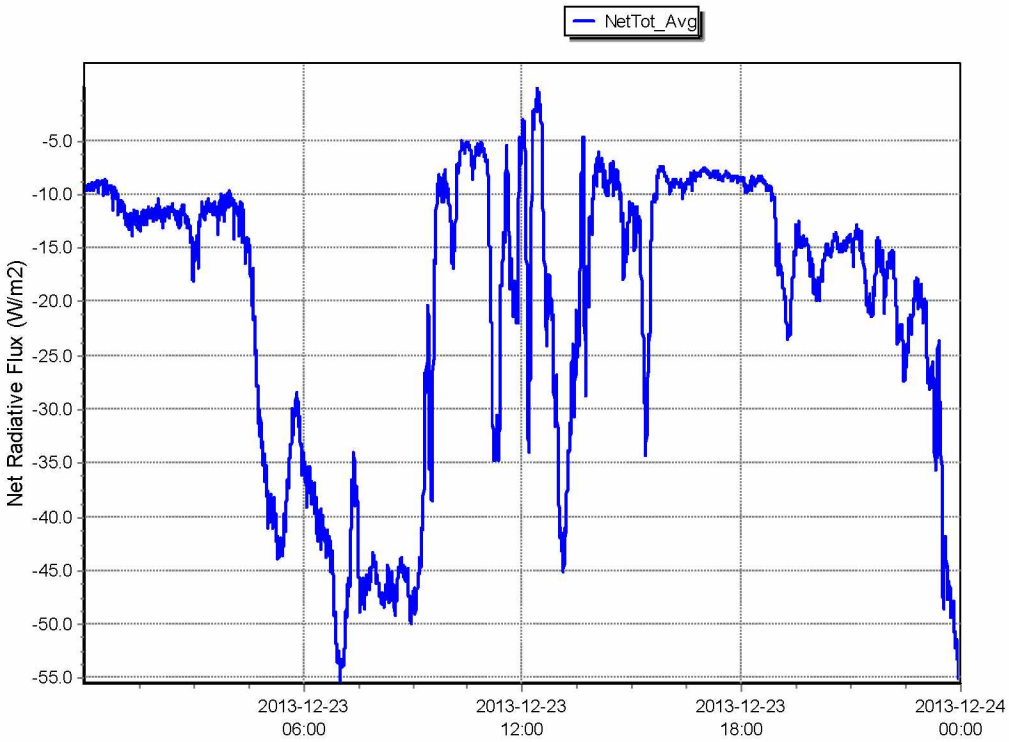

Figure 4.32: Net Radiative Flux Data from the Tower at the Pit Bottom on December 23rd 2013.

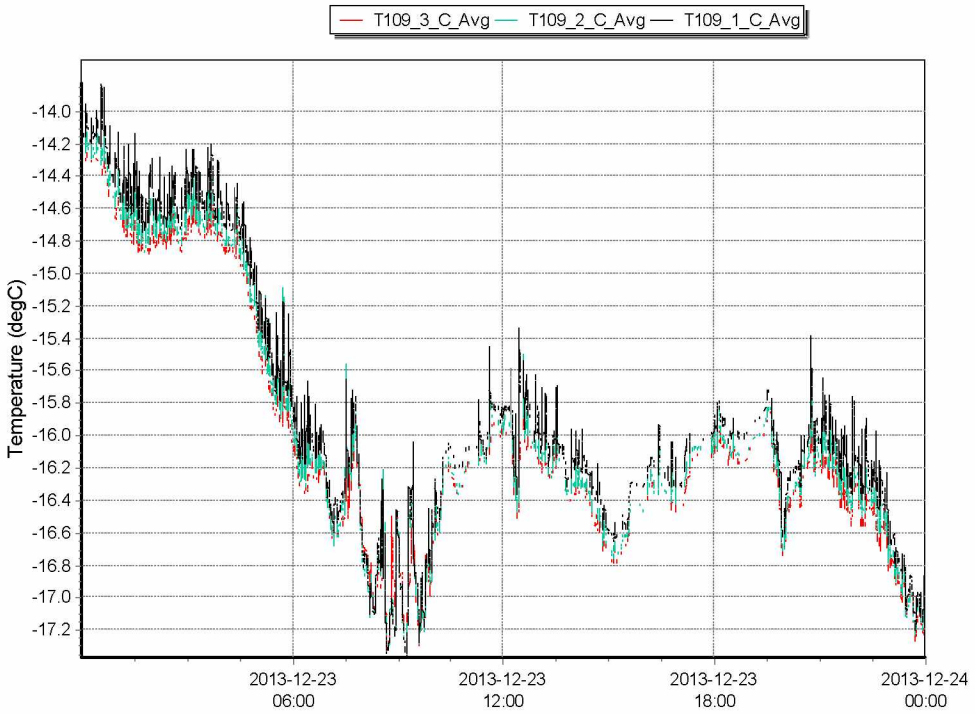

Figure 4.33: Temperature Data from the Tower at the Pit Bottom on December 23rd 2013.

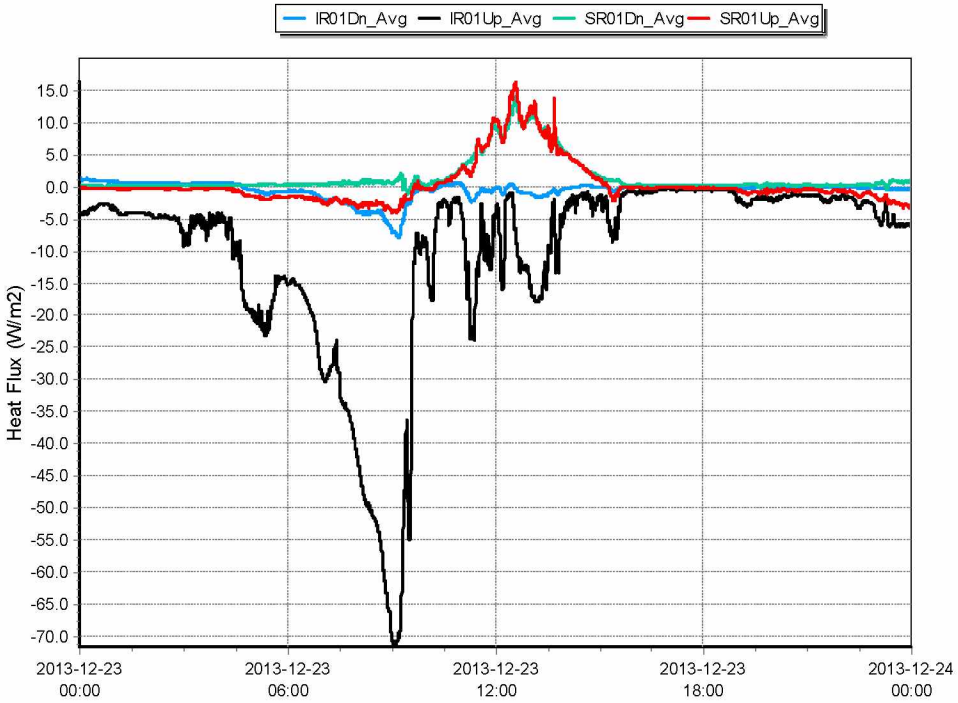

Figure 4.34: Heat Flux Data from the Tower at the Pit Rim on December 23rd 2013.

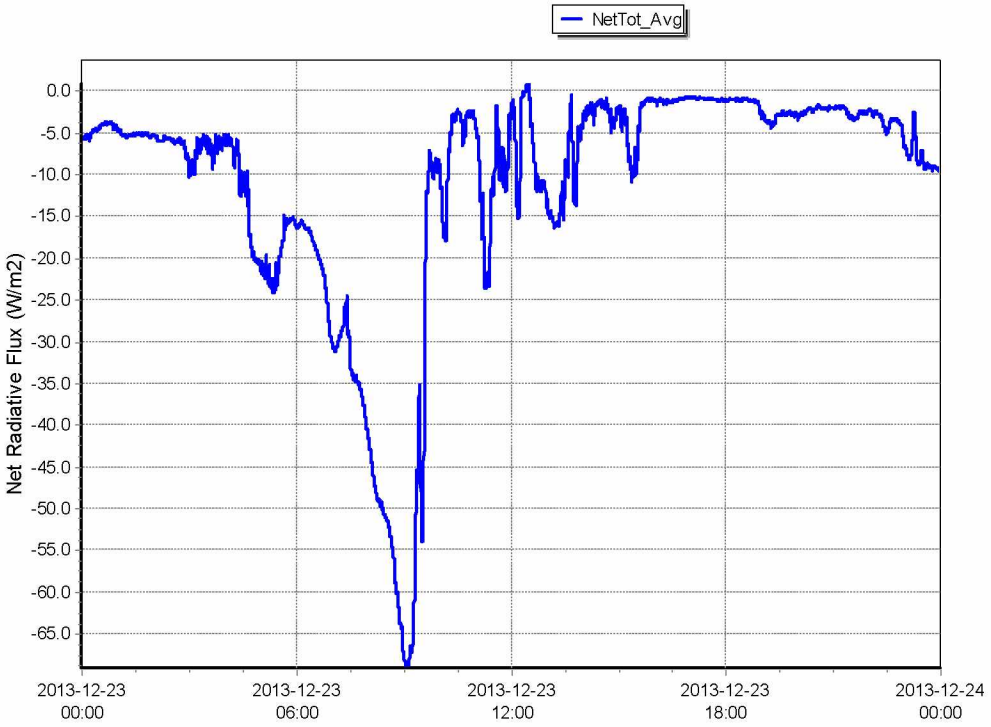

Figure 4.35: Heat Flux Data from the Tower at the Pit Rim on December 23rd 2013.

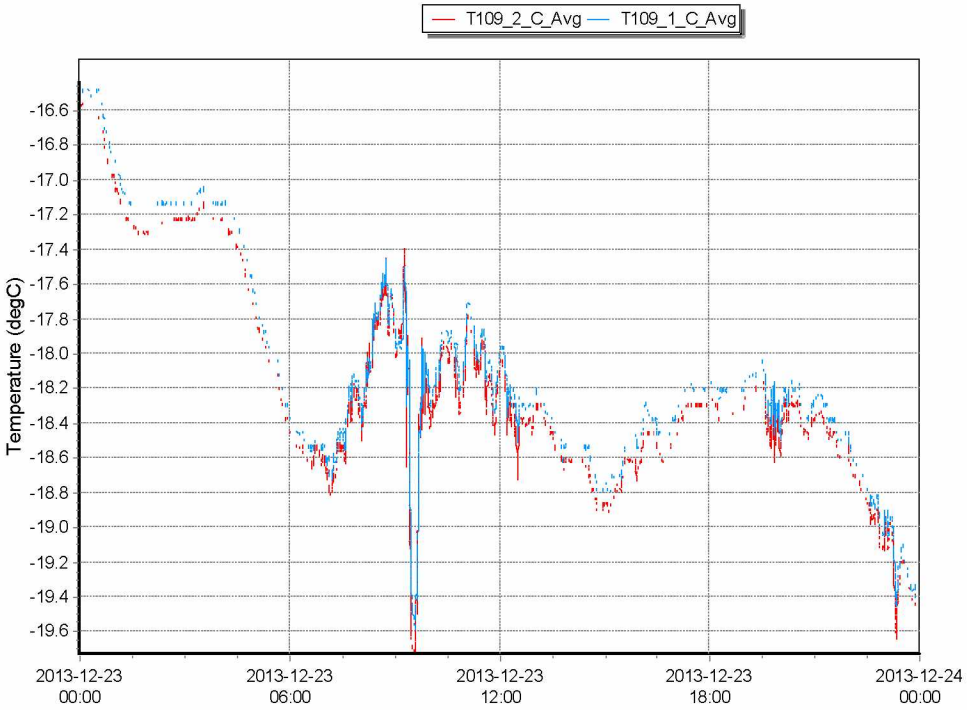

Figure 4.36: Temperature Data from the Tower at the Pit Rim on December 23rd 2013.

4.2 Data Needed for Modeling & Validation

A. The meteorological inputs needed to determine the contaminant concentration are the wind speed and direction as a function of time at one height, the nocturnal temperature inversion characteristics at sunrise, the heating rate of the pit atmosphere after sunrise, and the turbulent eddy diffusivities as function of atmospheric stability. The wind speed and direction observations at one height will be used to determine the advection term. Among others, the following information need be collected during the data gathering and CFD model building phases: (a) Mean diurnal wind velocity (mean values for each month); (b) Number of clam days, their distribution both daily and monthly, the mean and maximum duration of clam weather; (c) Number of foggy days according to the months and their duration (Mean and Maximum); (d) Mean monthly humidity of the atmospheric air (for the warm period of the year); (e) Duration of the period with freezing soil temperature (below 0°C); (f) Mean monthly air temperature with absolute maxima and minima; (g) Sources of air pollution, volume and rate of contaminants for each point source; (h) Air inversion frequencies and durations; (i) Air Quality values during air inversions, and required standards that need to be met.

B. Data are needed from an operating open pit mine regarding the number of stationary equipment in place (shovels , generators, drills, for example), and number of moving equipment (dozers, graders, trucks, for example), their locations, and status of operation (ready hours, delay hours, and stand by hours). Data will also be collected on moving sources (such as trucks) from shift reports and status reports to develop the duty cycles of the trucks so that reasonable pollution loading information can be developed for model application.

C. Engine make, model, specification of equipment, numbers & types of equipment in the pit, diesel exhaust information from pre-test, if available for diesel powered equipment in the pit.

D. Topographic parameters including the slope angle (α) and the azimuth (β), and the solar azimuth B on the distribution of solar radiation on the ground, the mine depth, the angle of the terrain, the initial air velocity and its vertical shear

E. Air quality data (air samples) at various open pit benches. Particularly, concentrations of NO_X, CO and DPM, and dust at various working or active benches.

F. Pit geometry (Depth, slope angles, bottom width, bottom length, elevation of various benches, widths of working benches), and in electronic format (Auto-cad files, for example)

G. Digital pictures of the pit.

4.2.1 Data Collected

Inversions are prevalent during the months of November through February. Therefore, the data required for this study are from the 2009-11 inversion events and the corresponding pit geometry.

1. Solar Exposure Data

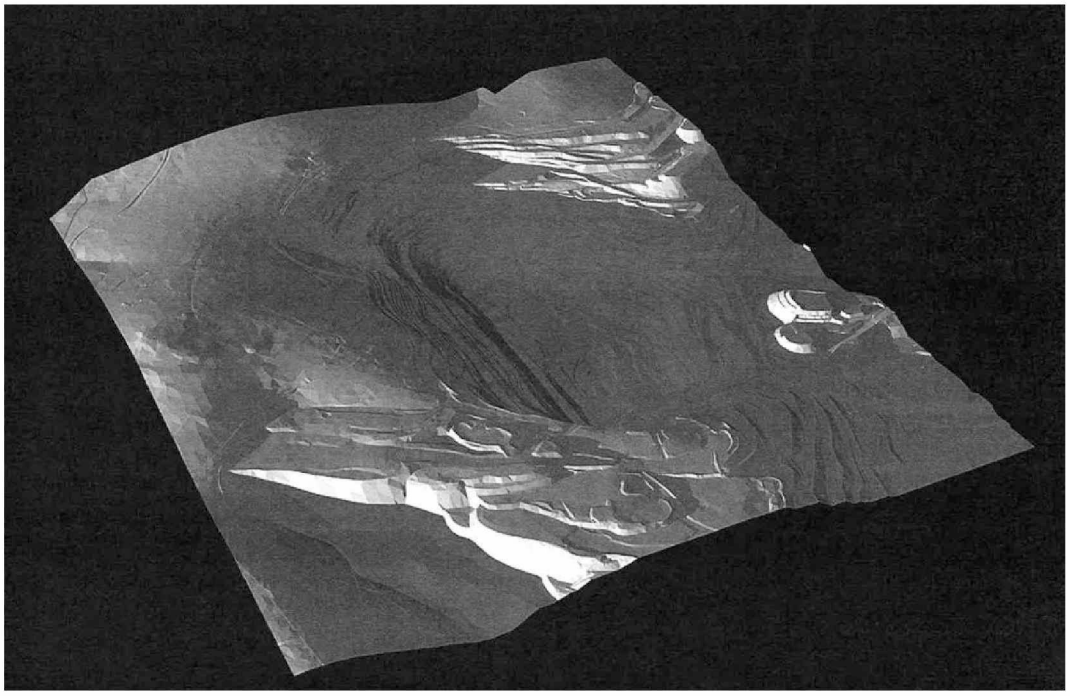

Figure 4.37: Solar Exposure on the Pit in the Month of November.

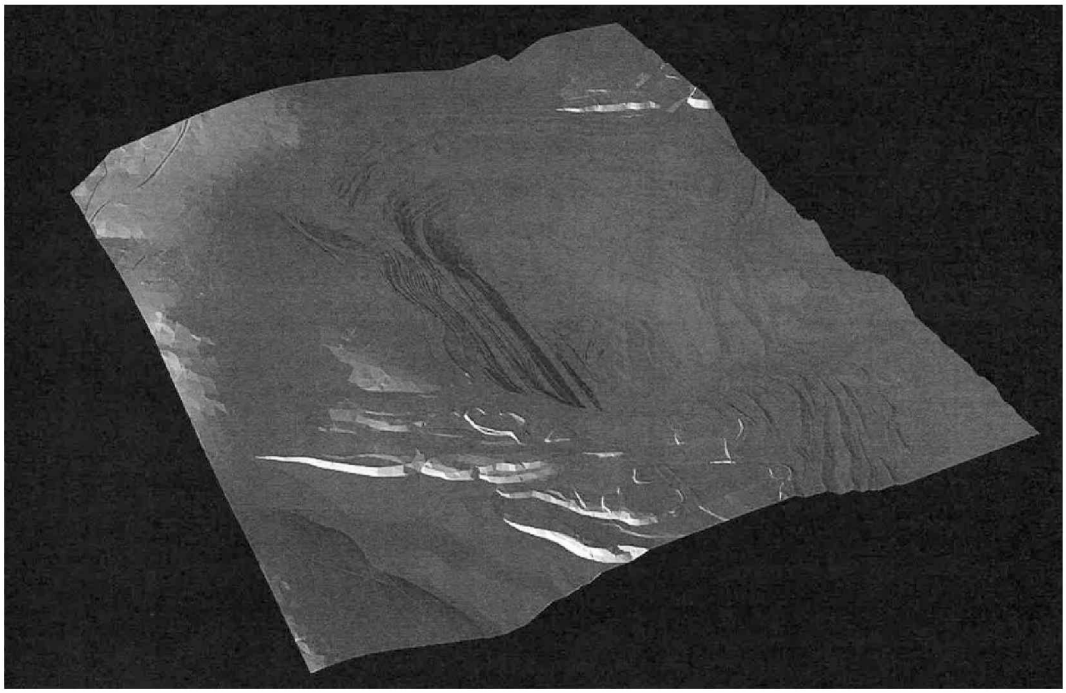

Figure 4.38: Solar Exposure on the Pit in the Month of December.

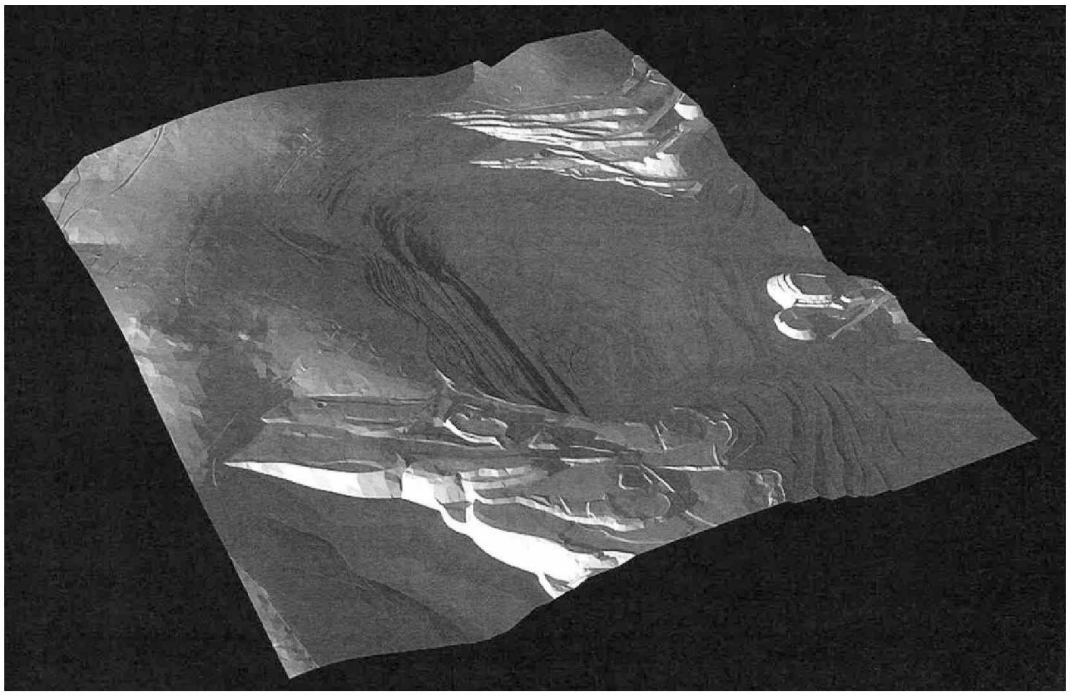

Figure 4.39: Solar Exposure on the Pit in the Month of January.

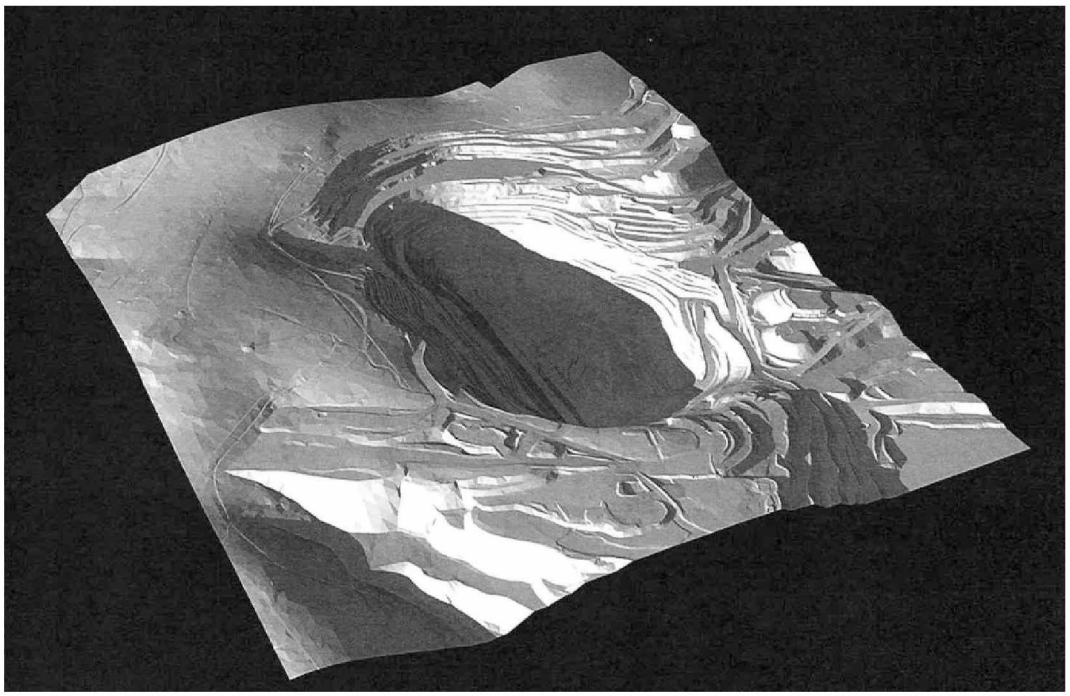

Figure 4.40: Solar Exposure on the Pit in the Month of February.

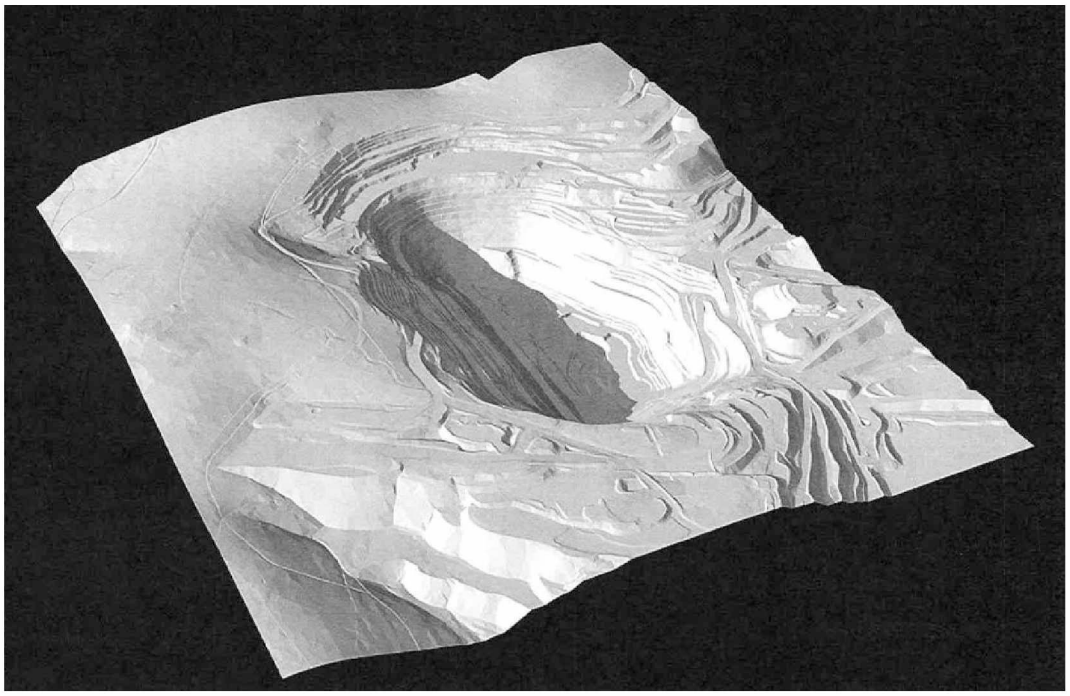

Figure 4.41: Solar Exposure on the Pit in the Month of March.

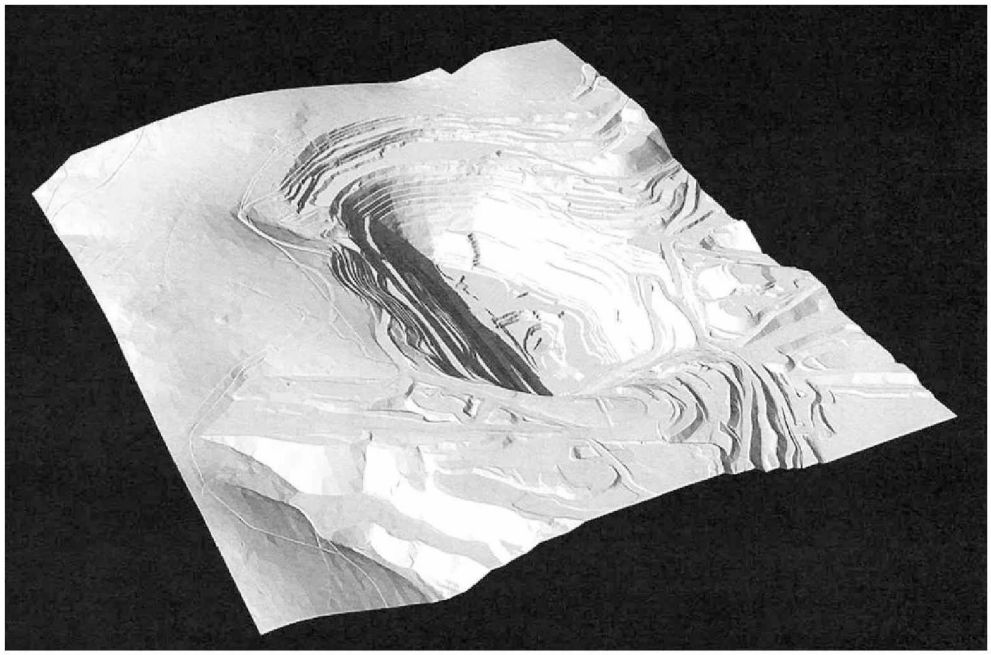

Figure 4.42: Solar Exposure on the Pit in the Month of April.

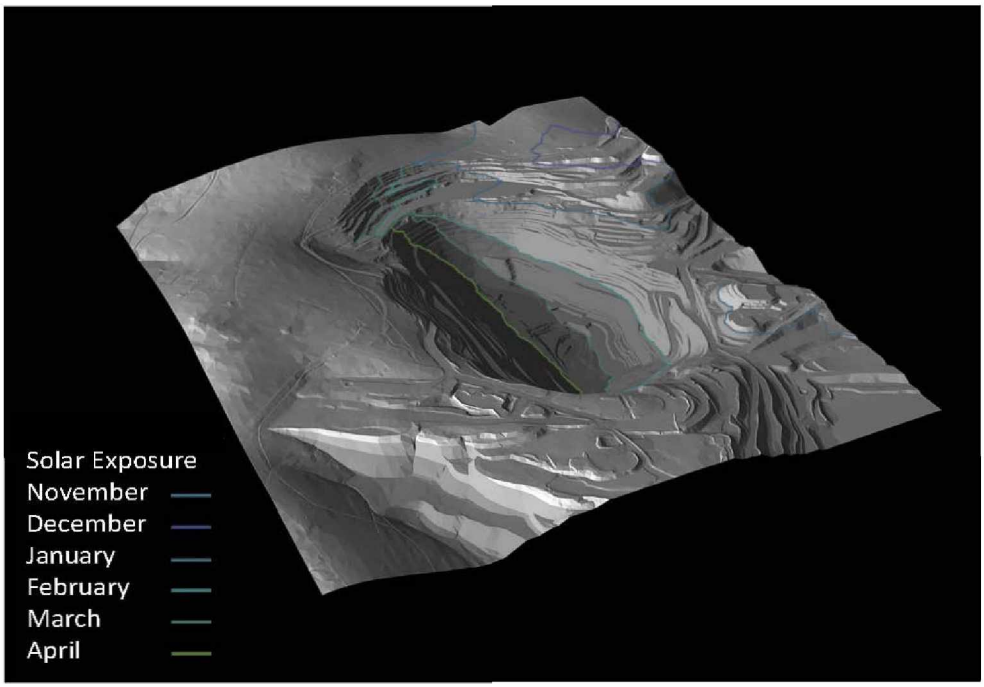

Figure 4.43: Comparison of Solar Exposure on the Pit from the Month of November to April.

2. Air Inversion Frequency

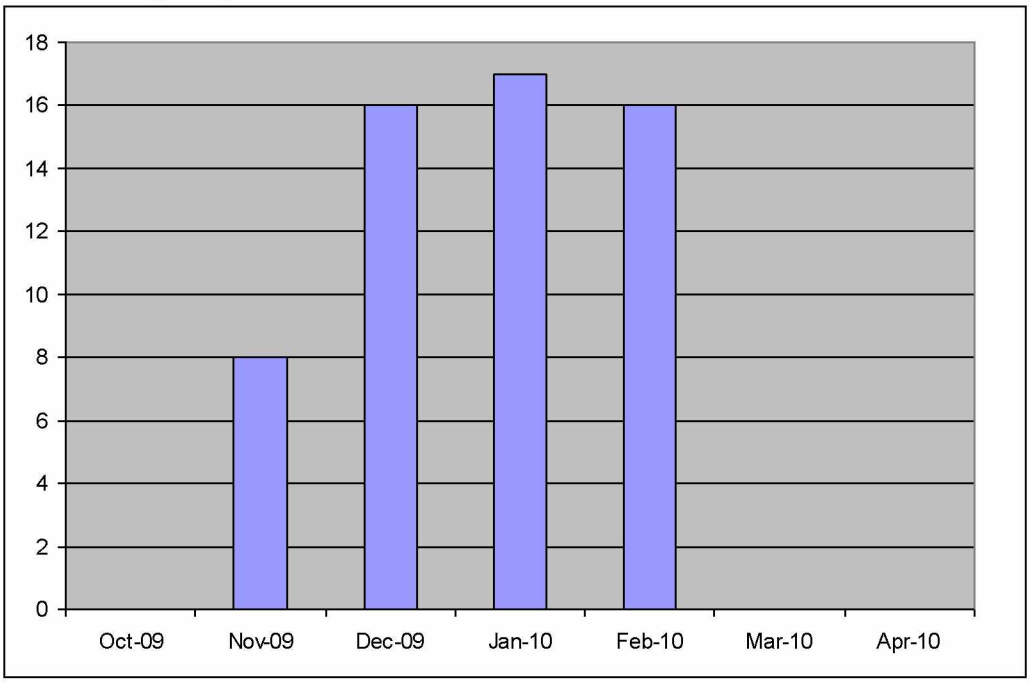

Figure 4.44: Air Inversion Frequency from October 2009 to March 2010.

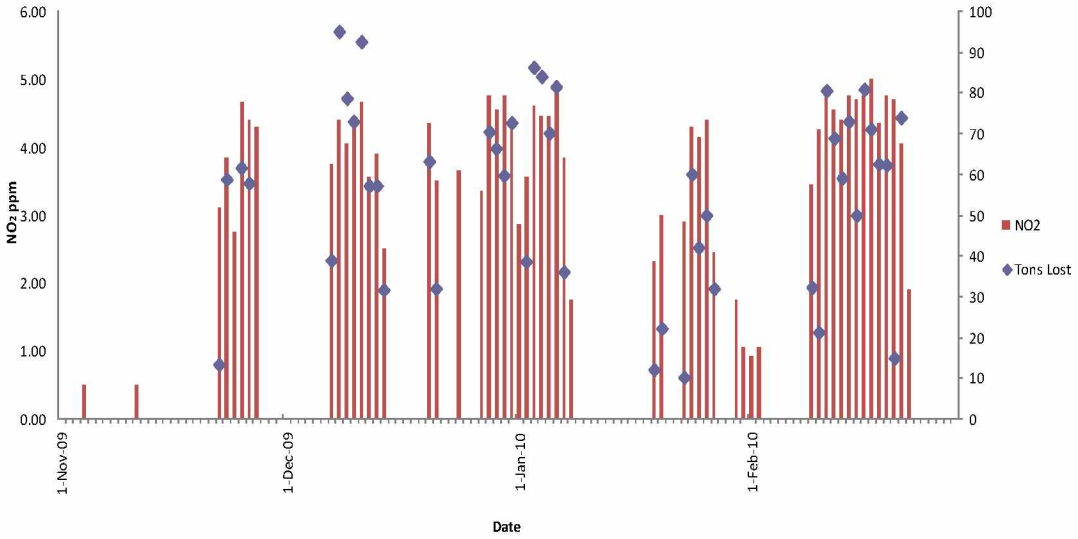

Figure 4.45: Air Quality and Tonnage Lost during Air Inversions from November 2009 to February 2010.

The data presented are used for modeling pollutant transport in the selected open pit mine. The modeling efforts, the validation of the model and mitigation efforts are presented in the subsequent chapters.

Chapter 5 Model Development

In the past three decades, the development of computational fluid dynamics (CFD) has made it possible to better understand pollutant flow in open pit mines. The majority of these CFD program are based on the Navier-Stokes (N-S) equations, the energy equation, the mass conversion, and the transport equations. CFD models provide a pattern of air flow, distribution of pollutant concentration, and temperature within an open pit. CFD modeling has been widely used in atmospheric pollution studies in urban areas. However, none of these models or studies has addressed ventilation design for deep, open pit mines in general or in Arctic or sub-Arctic conditions in particular. The phenomenon of buoyancy driven flow in an open pit is an important issue of mass and energy transport between the incoming air and the stagnant air mass under Arctic inversion.

There are three methods generally used to study air flow distribution and contaminant transport in open pit mines: empirical models, experimental measurements, and computational fluid dynamics (CFD). Most researchers use scale model measurements and empirical models to study the pollutant distribution driven by convection and diffusion only. Although these models are simple, they cannot account for the highly transient and complicated behavior of the air flow in Arctic and sub-Arctic conditions, interaction with solar radiation, and pit geometry of open pit mines. Therefore, a full-scale experimental investigation is critically important. Nevertheless, due to the extensive size of an open pit mine, experimental measurements are expensive in terms of time and cost; therefore, deemed impractical.

CFD is an alternative approach to studying the complex natural phenomena of Arctic inversion. Any solution will require an extensive understanding of the interaction of air movement, air inversion, meteorology, pollutant source, transport phenomena, and fan applications in open pit mines. The CFD modeling effort presented in this chapter is to develop and solve the coupled conservation equations of mass, momentum, and energy with appropriate initial and boundary conditions. Figure 5.1 shows the generic flow chart for the steps involved in CFD simulation.

Even with a simple geometry, CFD modeling of an open pit mine is complex and challenging. The complexity of the problem increases manifold when the actual topography of an open pit is considered. This complexity is due to the unstructured geometry of an open pit, with numerous sharp features. These features result in a poor-quality mesh during domain discretization. Apart

from the complex geometry of an actual pit, a good-quality mesh is essential for solution convergence. Selection of appropriate boundary conditions that reflect the actual physical phenomena of air inversions in open pit mines is important and provides for better model convergence.

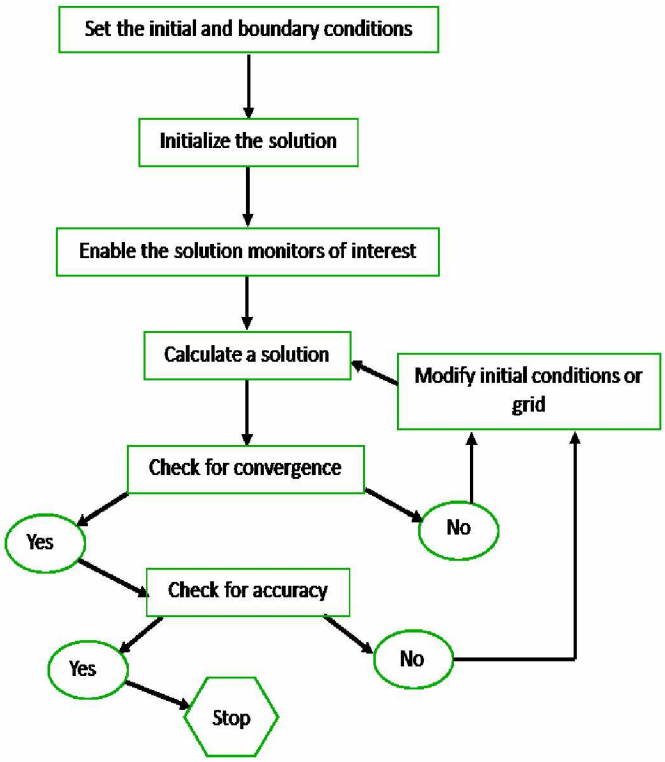

Figure 5.1: Generic Flow Chart for CFD Modeling.

Selection of an appropriate turbulence model is another important criterion for the accuracy and convergence of any fluid flow model. Many of the commercial CFD packages available are designed and tested on specific problems related to specific application, such as wing design in aerodynamics, flow around supersonic projectiles, and ventilation design in buildings, among other. A considerable amount of published literature is available on the application of CFD to these topics (Yakhot et al. 1992; Bardina et al. 1997). Air flow in an open pit mine, especially under an Arctic inversion, is very different. The air flow in open pit mines is often stratified, i.e., an inversion layer forms in the absence of solar radiation. This phenomenon falls in the category of boundary layer meteorology (Stull 1988).

The challenges of modeling air flow and pollutant transport in open pits are many and are related to geometry, meshing, boundary conditions, and most importantly, turbulent model

parameterization. The following section presents various challenges in modeling the transport process in an open pit mine under an Arctic air inversion and some of the approaches used to address these challenges in modeling with ANSYS-CFD.

To develop a CFD model of air flow and pollutant dispersion, an actual, deep open pit mine is selected. Due to its location and surrounding topography, the mine often experiences Arctic air inversions during the winter months. The open pit is around 1880 m (6170 feet) wide in the East-West direction, 1219 m (4000 feet) wide in the North-South direction, and approximately 365 m (1200 feet) deep. The surface topography of the selected mine (Figure 5.2) is complex, unstructured, and irregular.

Figure 5.2: Picture of the Open pit Mine under Study.

5.1 Geometry

The first step in CFD modeling is to define an appropriate model/domain geometry. A model geometry is created using any of the available CAD packages, such as AutoCAD, Solid Work, or ProE. In the present study, an open pit geometry in the form of a CAD file in *.dwg format is available. It is important to note that this geometry file is different from other commonly used file formats. The pit geometry is a surface consisting of groups of connected polygons (typically triangles, as shown in Figure 5.3). These types of geometries are termed faceted geometries.

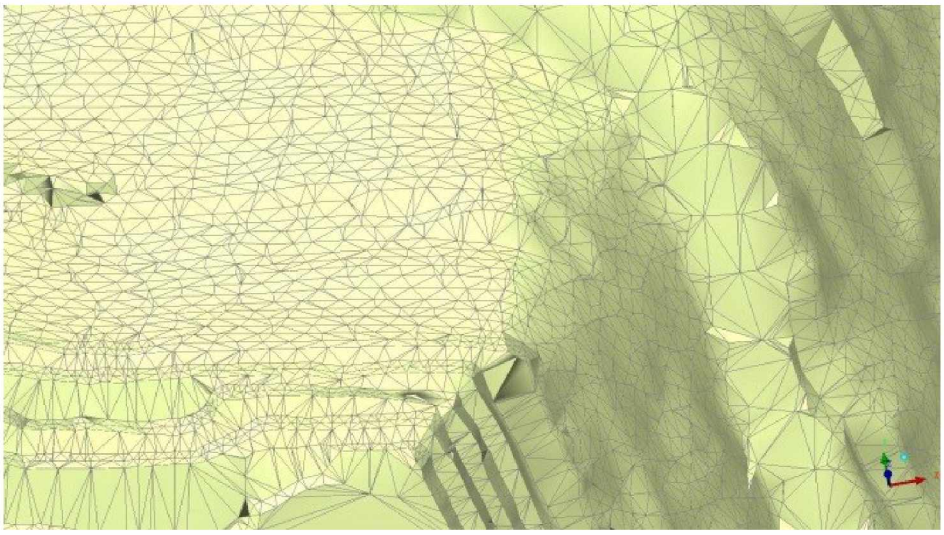

Figure 5.3: Faceted Geometry of the Pit Surface.

The major challenge is related to importing the geometry into the meshing platform. Initially, ANSYS DesignModeler is selected for importing the geometry into the ANSYS CFD package. The available version of ANSYS DesignModeler is not designed for this type of geometry. Attempts to convert the geometry to other file formats such as *.step and *.iges and to import it to ANSYS-CFD are unsuccessful. Because the AutoCAD *.dwg format is not the best format to use, conversion of the *.dwg file format to *.ParaSolid or *.STL is attempted. This is unsuccessful because the conversion is not supported in the case of faceted geometries.

The ANSYS ICEM-CFD meshing package is used successfully to import the geometry to the meshing platform. The model domain, however, is still incomplete due to the unspecified volume (fluid) region, and the software is not able to address this. As a result, it is decided to export the pit geometry into a mine design program such as Vulcan, and a solid model is created to enclose the volume region (Figure 5.4). Once the side and top wall enclosing the fluid domain are defined, the geometry file is imported into the meshing platform.

5.2 Meshing

Meshing is one of the most challenging issues in any CFD modeling. Discretization of a continuous model domain into control volumes of varying size takes an ample amount of time for complex geometries. Prior to discussing the significant steps necessary to address an open pit geometry, a summary of the meshing capabilities of the ANSYS ICEM-CFD is presented here. Meshing is the process of dividing a model domain into discrete surfaces, or volumes. During a CFD analysis, the fundamental equations are solved for each mesh element in the model domain.

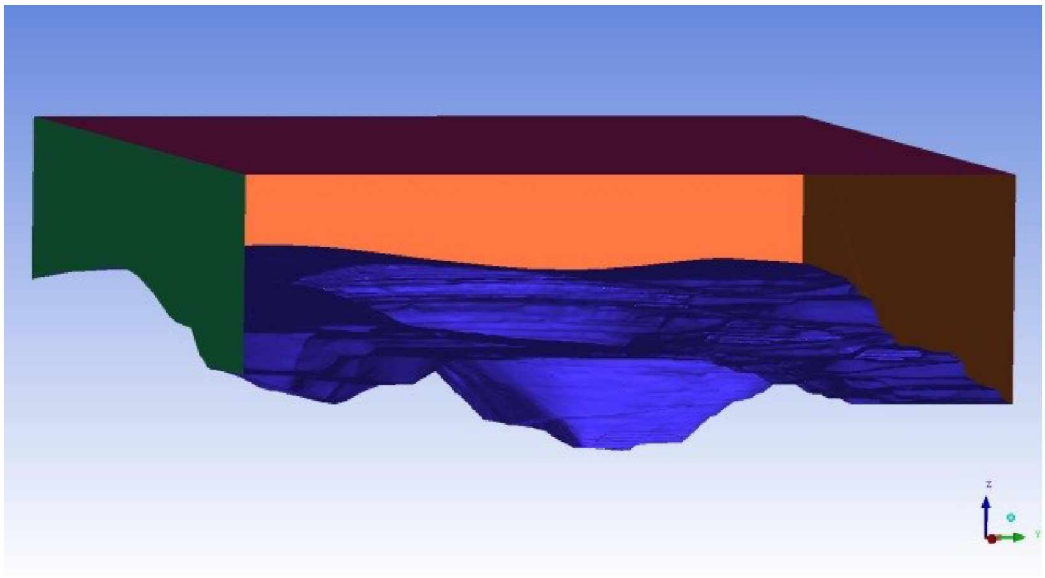

Figure 5.4: 3-D Pit Geometry with Side and Top Walls to Enclose a Fluid Domain.

A good-quality mesh is essential to a good-quality CFD analysis. For model convergence, it is important to refine the mesh in areas where large flow gradients are present. A variety of meshing styles are available in commercial CFD programs. For a 2-D geometry, four possible mesh configurations are available: 1) quadrilateral dominant, 2) all triangles, 3) uniform quad/tri, and 4) uniform quad, whereas for a 3-D geometry, four possible mesh types are available: 1) tetrahedron, 2) hexahedron, 3) pyramid, and 4) prism. The mesh complexity of a model domain depends largely on the geometry of the domain. If the geometry is smooth, using a structured hexahedral mesh produces better results. If the geometry is unstructured and irregular with sharp edges, a tetrahedral mesh may be required. As an alternative to using a single mesh configuration, a combination of various mesh configurations can also be selected. Generally, pyramids are formed where tetrahedral and hexahedral mesh cells converge. Prism meshes are formed when a tetrahedral mesh is extruded. Examples of various mesh elements are shown in Figure 5.5-Figure 5.10. The quality of the mesh is as important for convergence as the quantity (i.e., the number of elements). The selection of mesh type influences the quality of the resulting mesh for varying domain geometries. A poor-quality mesh can result in numerical diffusion in the model. Numerical diffusion, in this situation, refers to increasingly erroneous calculations of the variable with increasing simulation time.

Figure 5.5: 2-D Quadrilateral Element in ANSYS ICEM-CFD.

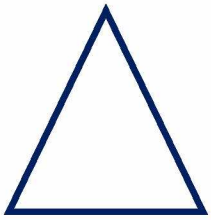

Figure 5.6: 2-D Triangular Element in ANSYS ICEM-CFD.

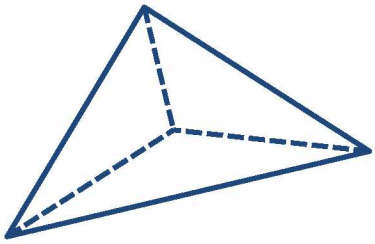

Figure 5.7: Tetrahedral Mesh Element in ANSYS ICEM-CFD.

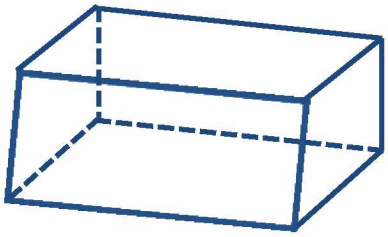

Figure 5.8: Hexahedral Mesh Element in ANSYS ICEM-CFD.

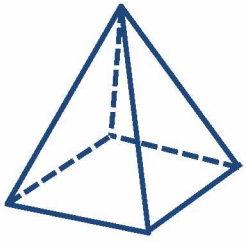

Figure 5.9: Pyramidal Mesh Element in ANSYS ICEM-CFD.

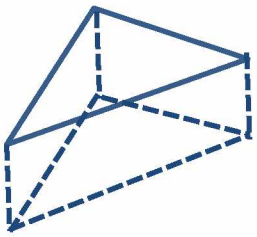

Figure 5.10: Prismatic Mesh Element in ANSYS ICEM-CFD.

Open pit mine geometries are typically asymmetrical and have numerous sharp edges and curves of varying sizes (Figure 5.11). These edges and curves tend to lead to poor-quality meshes.

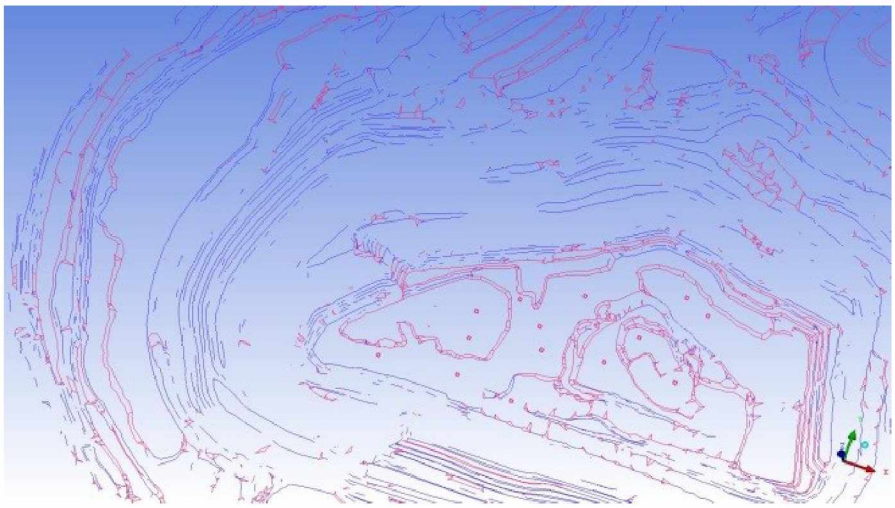

Figure 5.11: Various Curves and Edges Associated with the Surface Geometry of the Pit.

Most meshing problems arises from the geometry. The model geometry is a combination of points, curves and surfaces, and when these features are sufficiently close, the mesh algorithm will try to respect these features. The resulting mesh will be constrained to have nodes and edges sufficiently close to degrade the quality. In addition, if there is a cluster of points sufficiently close, the mesh will project nodes at these points, and in that case, the quality degrades. In these cases, a small compromise in the geometry may lead to a high-quality mesh. The sizing of the mesh in areas with tight geometries can also be helpful. An open pit mine geometry is really a very large domain, and computational resources are always a constraint. It is important not to lose any geometric feature by keeping the geometry as it is. An alternative approach is adopted, and the unnecessary curves and points that form tight angles are removed from the geometry so that the meshing module does not try to follow all of the curves in the geometry. To eliminate these curves and points, they are usually filtered out on the basis of a tolerance value. The tolerance value defines the surface-to-surface proximity. Filtering the geometry leads to removal of curves

and points less than the tolerance value, while higher tolerance curves are maintained. To capture the geometric features essential for CFD modeling, it is essential that not all of the curves and points are removed from consideration. Figure 5.12 and Figure 5.13 shows two different scenarios for the same pit geometry, where one (Figure 5.12) has the curves filtered out using a low tolerance value and the other has the curves filtered out with a high tolerance value. Curves and points can also be filtered out using an angle. In this case, curves and points will be maintained only if the angle is greater than the given input angle. Meshing is affected by both the curves and the points present in the geometry. In patch-dependent meshing, nodes are projected onto the points present in the geometry. The points that are close to each other tend to deteriorate the quality of mesh (Figure 5.14).

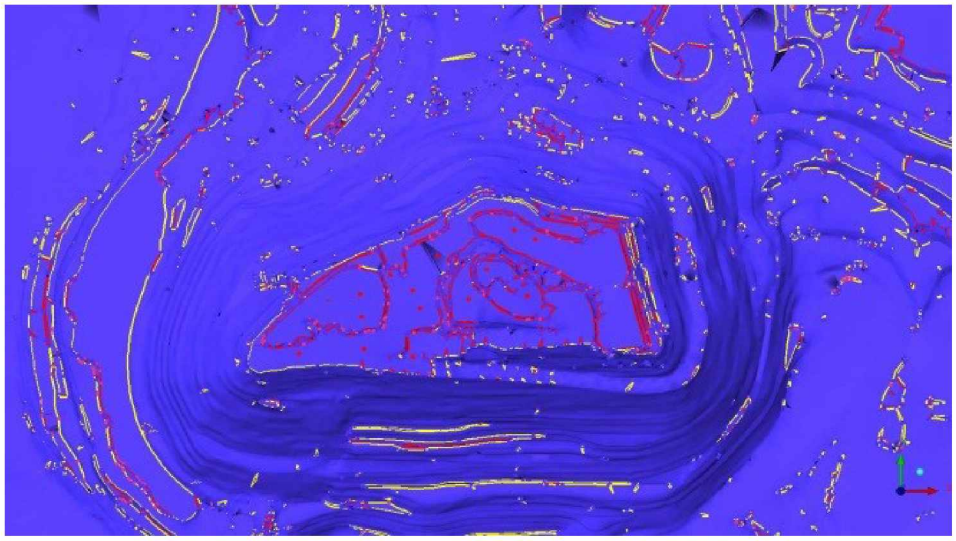

Figure 5.12: Filtered-Out Curves with a Low Tolerance Value.

ICEM CFD uses mesh quality as the quality parameter by which the mesh elements are assessed, although other quality parameters such as the skewness and the aspect ratio are also available. Creating a perfect mesh element for a rough geometry is impossible; a good-quality mesh can be generated, to a certain extent, and a low-quality mesh can be repaired or edited using a mesh editor. A more detailed overview of mesh editing follows.

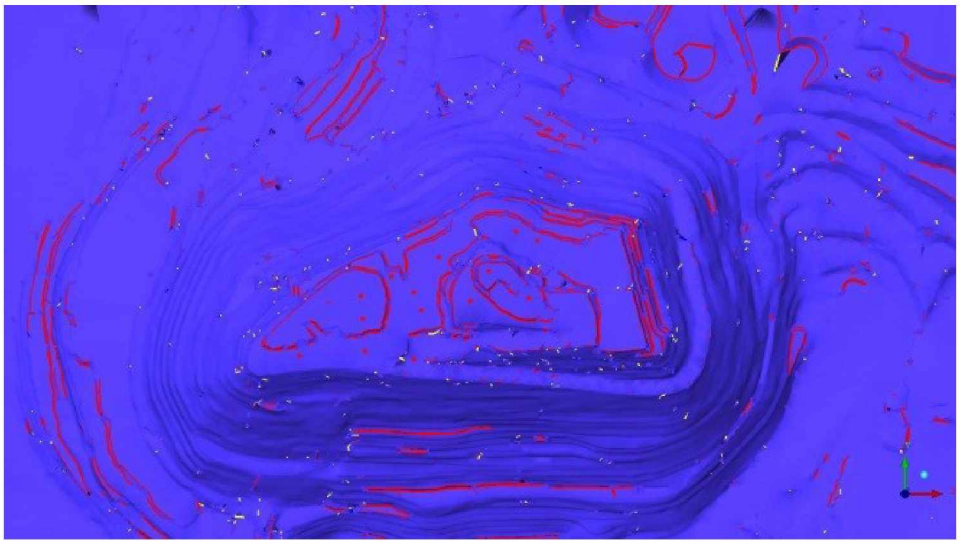

Figure 5.13: Filtered-Out Curves with a High Tolerance Value.

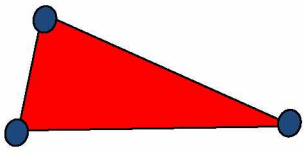

Figure 5.14: Skewed Cell as a Result of Points Close Together.

In the initial phase of this study, a 32-bit computer with 3 GB of RAM is used to create the mesh elements for the model domain. Whenever the mesh module is used to generate the mesh elements, the computer system crashed. This problem occurred because of the memory limitations of the 32-bit computer. A 32-bit computer can handle memory needs up to 4 GB, whereas the RAM needed for the mesh elements is in excess of 4 GB. Therefore, it is important to note that the external geometry, the extent, and the size of the model domain must be considered in assessing the required amount of computational power.

In meshing the open pit mine geometry, it is important to divide the model geometry into several sub-domains after the curves and points are extracted (Figure 5.15) from the model geometry.

The sub-domains are used to define the boundary conditions during the simulation run. For the model geometry presented here, six sub-domains, FA, NORTH, SOUTH, EAST, WEST, and PIT, are created. Figure 5.16 shows the various sub-domains of the model geometry. The coordinate system that is used in the model is similar to that used in surveying, i.e., north as the Y-axis, east as the X-axis, and elevation as the Z-axis. All the sub-domains representing the

directions are in their respective directions, whereas FA, which represents the free atmosphere above the boundary layer of the pit, is at the top of the geometry, and the PIT boundary represents the open-pit surface.

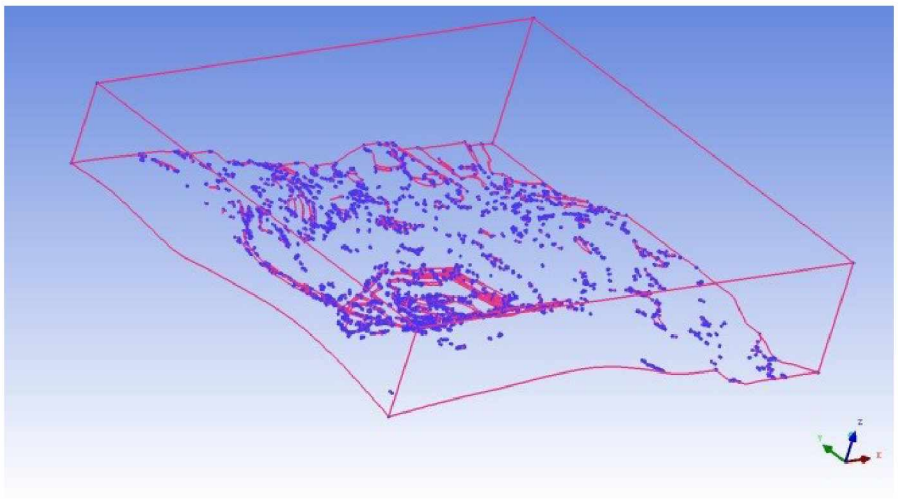

Figure 5.15: Extracted Curves and Points of the Model Geometry.

Creation of sub-domains ensures appropriate setup of the boundary conditions. Creating sub-domains is followed by setting proper meshing parameters. Meshing parameters such as the scale factor, the maximum element size, curvature-based refinements, etc., are defined. Setting these parameters ensures that the mesh elements created are of the desired quantity and quality within the computational constraints (RAM memory). Too many elements will exhaust all the memory and lead to crashing of the computer or slower processing of the solvers (FLUENT, CFX, etc.). On the other hand, a very low number of elements will not give the desired simulation results. The global scale factor value affects the number of elements generated in the model domain. This value is usually set to 1.2; however, it can be adjusted if required. The maximum element size is the value that fixes the maximum size of the mesh in the model. The maximum mesh size is, in fact, the product of the global scale factor and the maximum element size. For example, if the scale factor is 1.2 and the maximum element size is 100, then the maximum mesh size is 120. Another parameter that needs to be considered in setting the mesh parameters is the "ignore size." The value of this parameter should not be less than the tolerance value used in extracting the curves in the geometry. Setting this value lower than the tolerance value will create holes in the surface mesh. In addition to the above parameters, there are several other parameters that require attention.

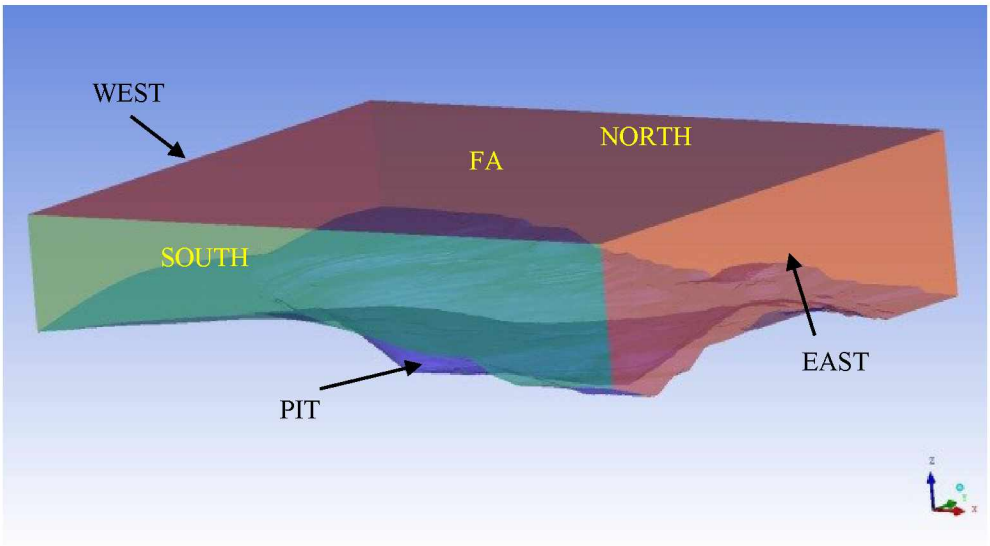

Figure 5.16: Various Sub-Domains of Model Geometry.

Specifying the mesh type and the method are equally important in generating the type of mesh elements (triangular, quadrilateral, tetrahedral, hexahedral, etc.). If an open pit mine geometry is unstructured and asymmetrical, then a tetrahedral mesh is appropriate. A hexahedral mesh, on the other hand, will be of low quality if applied to open pit mine geometry and is more appropriate for a structured geometry. In terms of the mesh method, for surface meshing, the patch-dependent mesh method is selected to respect the line and point elements of the geometry, while the Octree method is selected for meshing the volume domain. In ICEM-CFD, various methods for surface meshing, such as patch-dependent, patch-independent, autoblocking, and shrinkwrap are available. In the shrinkwrap method, larger features, gaps, and holes can be ignored, whereas autoblocking performs well when the surface is smooth. The patch-independent method is good for rough geometry, ignoring small features gaps and holes. In this study, patch-dependent surface meshing is opted to ensure that the meshing algorithm respects the geometrical features so that a more realistic representation of the open pit geometry is generated. Octree meshing starts with a cube enclosing the entire model domain, where all the elements are of a given maximum element size. The cube is then subdivided into smaller sub-cubes to accommodate the curvature of the geometry. Meshing of the model geometry is an iterative process. The Octree method does not need to begin with any existing surface mesh because a surface mesh is created in the process. In contrast, volume mesh modules such as the Delaunay and advancing front methods require an initial surface mesh. One of the reasons to use the Delaunay or advancing front methods is to generate more uniform mesh growth. The Delaunay method not only generates uniform mesh growth but also

improves model convergence during simulation. The Octree method does not produce uniform meshes; thus, during model simulation, divergence is encountered. Figure 5.17-Figure 5.19 shows the various sections of the mesh generated by Octree method.

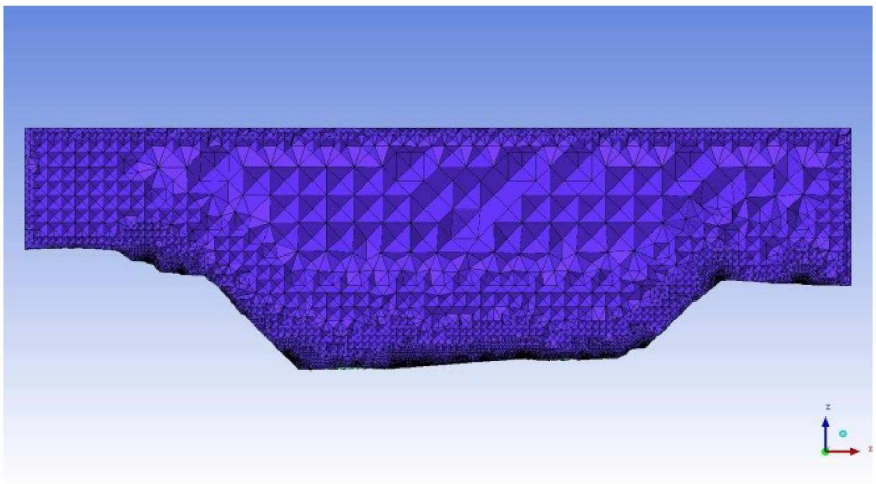

Figure 5.17: East-West Section of the Created Volume Mesh of the Open Pit.

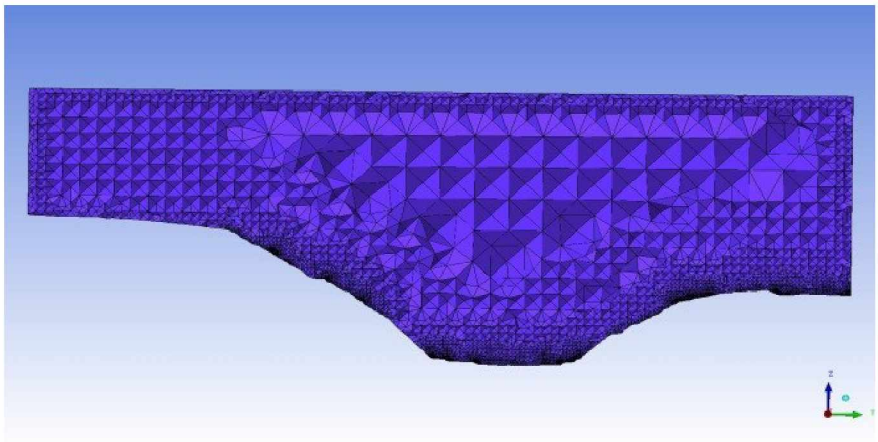

Figure 5.18: North-South Section of the Created Volume Mesh of the Open Pit.

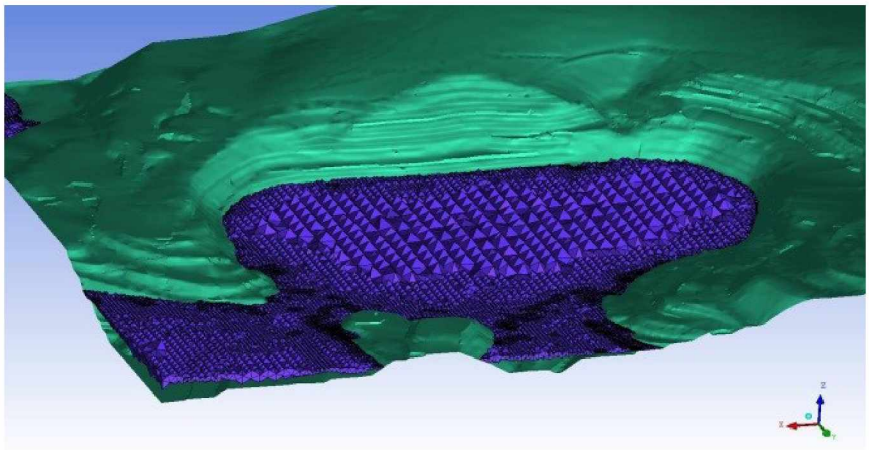

Figure 5.19: Horizontal Section of the Created Volume Mesh of the Open Pit.

Before it can be used directly by the solver, the mesh needs to undergo checks for problems, errors and, most importantly, a quality check. Errors such as duplicate elements, uncovered faces, missing internal faces, etc., and problems such as multiple edges, single edges, unconnected vertices, etc., must be checked. If any errors or problems exist, they need to be corrected. Once these errors and problems are fixed, a quality diagnosis of the mesh elements is performed. Several mesh quality criteria, such as "quality," "aspect ratio," "skewness," and "min angle" are available to assess the quality of the mesh elements. In this study, the "quality" criterion is used to assess mesh quality (Figure 5.20).

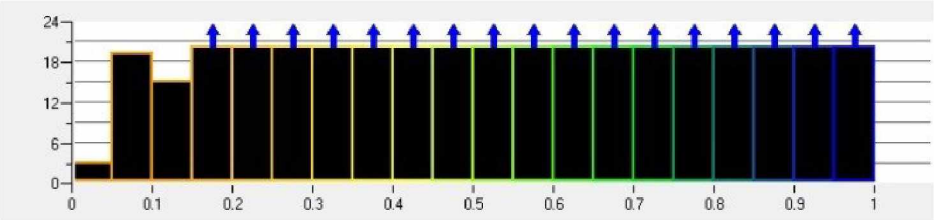

Figure 5.20: Quality Histogram of the Created Mesh before Editing.

Meshes contain elements of high quality (i.e., 1) and low quality (near 0). To obtain a reasonable simulation outcome, mesh elements of good quality are necessary. The actual open pit mine geometry under consideration has many sharp features. It is therefore impossible to generate a high-quality mesh near the pit walls. A mesh editor module is a useful tool for addressing such issues. A function in the mesh editor helps to automatically improve the mesh quality. In the case of geometry with very sharp features, this function does not perform well. There are several functions in the mesh editor that can be used to improve the mesh quality manually. Moving and merging nodes helps significantly in improving the quality of a mesh. If two nodes are so close that it lowers the mesh quality, then merging the two nodes leads to the deletion of that cell. If nodes are moved farther apart, the mesh quality (aspect ratio) is improved without deleting any cells. It is advisable to keep the quality above 0.9 to ensure convergence of the simulation model. In a 2-D geometry, it is relatively easy to modify the nodes, whereas in a 3-D mesh it becomes difficult to correct the mesh quality if the number of poor-quality elements is large. Thus, it is a good practice to delete the volume mesh and work only on the surface mesh. Because the created surface mesh is patch-dependent, it respects the lines and the points while the mesh is generated. Because the geometry is rough, with several close sharp curves, leads to a poor-quality mesh. Once the surface mesh quality is improved, the volume mesh is created using the surface mesh.

The volume mesh can be created using the Delaunay method or the advancing front method. In the present study, the Delaunay method is used to generate the volume mesh (Figure 5.21). Once again, the mesh is checked for errors and problems, and a quality check is conducted.

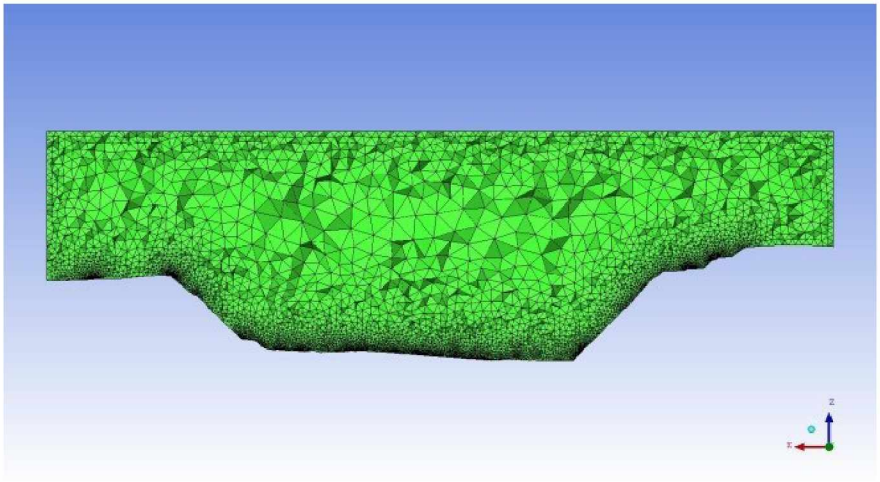

Figure 5.21: Volume Mesh Created using Delaunay Method.

The quality histogram of the created mesh is presented in Figure 5.22. It can be observed from the figure that the quality of the mesh is above 0.15. Before exporting the mesh to a format suitable for the solver, the boundary conditions are set for the different sub-domains. The mesh is then exported in a format suitable for the solver module. For this study, ANSYS-FLUENT is used.

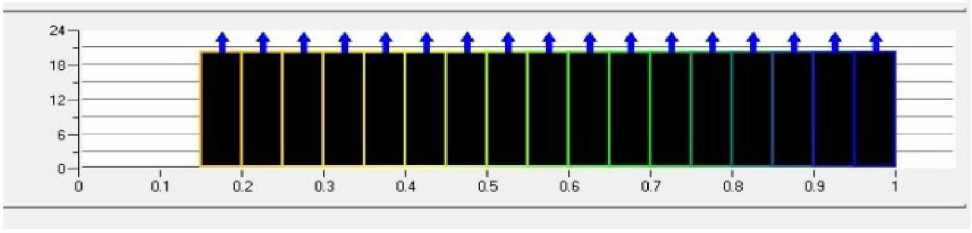

Figure 5.22: Quality Histogram of the Created Mesh after Editing.

5.2.1 Mesh Conversion in FLUENT

A good-quality mesh does not eliminate all of the issues related to modeling. Importing the mesh into the solver platform initiates a new set of problems and challenges. Some of these challenges are related to the large number of mesh elements, the selection of an appropriate turbulence model that can simulate the physics of the problem, and the selection of appropriate boundary conditions. Practical approaches to addressing some of these challenges are discussed in the following section.

For the problem domain under consideration, the number of elements created for the open pit mine geometry is extremely large, and the number of cells generated is approximately 8 million, which requires significant computational resources. To minimize the computational resources and time required to solve the problem, the tetrahedral mesh elements are converted to polyhedral elements. Conversion to a polyhedral mesh significantly reduces the number of cells and, at the same time, improves the mesh quality (ANSYS 2011f). The converted mesh, however, cannot be adapted or further converted. Figure 5.23 shows the polyhedral mesh after conversion. Changes in the polyhedral mesh can be observed in comparison to the tetrahedral mesh (Figure 19). The number of cells is reduced by approximately 21%.

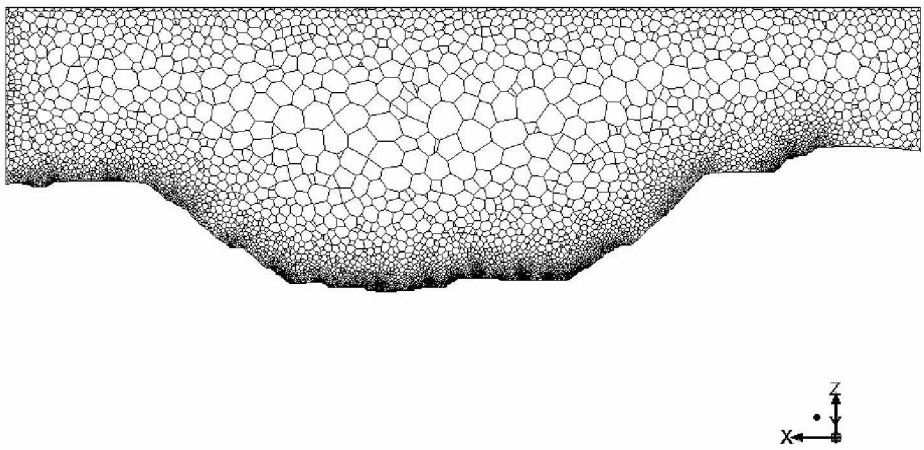

Figure 5.23: Polyhedral Mesh after Conversion in FLUENT.

A good-quality and appropriately sized mesh is required to obtain good results from a CFD simulation. Any strategy for CFD modeling starts with the geometry. Usually, if the geometry is simple, then meshing is not a problem. In the case of a highly unstructured and irregular geometry, as described in this study, a considerable amount of time and a significant effort are required to generate a good-quality mesh. Instead of depending on automatic meshing processes, it is preferable to manually edit the mesh to achieve the desired quality.

Appropriate boundary conditions and a good-quality mesh do not ensure model convergence. Airflow models often feature many complex nonlinear terms that are designed to resolve a very specific problem in the problem domain. The side effects of such terms in complex flows are often not sufficiently considered. To ensure that the model runs and produces meaningful output, several

model settings need to be monitored, such as the pressure–velocity coupling method, the under-relaxation factor, and the solution limits because many of these settings are meant for small-scale flow such as pipe flow and wing bodies. One such setting that helped in achieving convergence in this open pit mine analysis is increasing the maximum turbulence viscosity ratio from 10000 to 1e+10.

After a quality mesh is generated it is exported to a format readable by ANSYS-FLUENT solver with appropriate boundary term assignment. In FLUENT, the "Species Transport" model is switched on with no chemical reaction or combustion in addition to a realizable κ-ε model for turbulence.

Chapter 6 Turbulent Models for Pollutant Transport in Open Pit Mines under the Stable Boundary Layer

Modeling contaminant transport under Arctic air inversions is an important step for assessing the pollutants concentrations within an open pit mine. The airflow in open pit mines can be considered to be in an unbounded volume of a large scale and does not strictly follow the principles of pipe flow. The airflow problems in actual open pit mines are far more complex. Computational fluid dynamics (CFD) models provide detailed information about the airflow pattern and air velocity distribution, temperature, and pollutant concentration within the enclosed domain of an open pit. The atmospheric boundary layer flow over rough terrain, such as an open pit mine, is classified as entirely rough because the roughness elements are so large that the laminar sub-layer is mostly eliminated. This is, however, the case for airflow in the upstream and downstream portion of the computational model domain, but not necessarily for the airflow over the explicitly modeled surfaces with small-scale roughness in the central part of an open pit domain.

There is no known application of CFD in the three-dimensional modeling of airflow in large open pit mines located in the Arctic region. However, two equation turbulence closure formulation of Kappa-Epsilon (κ-ε) model, and Large Eddy Simulation (Lesieur et al.), have been used to solve stable boundary layer (SBL) problems in atmospheric sciences. Because an exact flow situation in open pit mines is not known a priori, it is necessary to investigate various turbulent models to identify the model that would simulate flow phenomena and predict contaminant distributions within the pit with reasonable accuracy. Dispersion models differ in their assumptions and structures as well as in the algorithm used; as a result, the simulated predictions vary from model to model. Furthermore, it is also important to investigate the performance of a CFD model when simulating complex phenomena such as the transport and distribution of contaminants in an open pit mine under an Arctic air inversion. The simulation of an enhanced period of turbulence in SBL is of particular interest because traditional air pollution dispersion models cannot explicitly treat such intermittent events, and yet the SBL is often the worst-case scenario in open pit pollution transport.

The majority of the CFD models are based on the solutions of the Navier-Strokes equations, the energy equation, the mass and concentration equations as well as transport equations for turbulent viscosity and its scale in a well-defined domain. In this study, the CFD simulation is

performed by using an academic research version of fluid dynamics software package ANSYS-CFD, which is a finite volume (FVM) based code for fluid flow simulation, importing and meshing the open pit geometry and modeling contaminant transport under Arctic air inversion. Most of the turbulence models available in ANSYS-FLUENT are based on Reynolds averaging of the turbulent quantities using the Reynolds-averaged Navier-Stokes (RANS) equations. The RANS equations are formulated in terms of the time-averaged flow field (velocity, pressure, density and temperature). This averaging concept for the Navier-Stokes (N-S) equations significantly reduces the complexity of simulating turbulent flow. This simplification, however, results in the additional Reynolds stress tensor that appears in the RANS equation as a result of the nonlinear terms of the underlying N-S equations (Versteeg and Malalasekera 1995).

Two equation κ-ε model is one of most widely used turbulence model for simulating industrial flow problems such as wing-body, pipe flow etc. Apart from the solution to the industrial flow problem the κ-ε model has found wide acceptability in atmospheric science (Richards and Hoxey 1993; Blocken et al. 2007). The κ-ε model provides quick solution to many flow problems with reasonable accuracy at relatively low computational cost. However, the κ-ε model is incapable of capturing the internally induced fluctuations of the flow field on which the transport of pollutant depends (Menter 2012). Therefore, to account for turbulent mixing, other turbulent models need to be examined.

In recent years, with advancement in computation power LES is becoming an attractive alternative to the flow problems where the κ-ε models lack accuracy. LES has been widely used in simulating the ABL structure (Kosović and Curry 2000; Basu and Porté-Agel 2006). LES resolves the fluctuations of flow variables, which are shown to vary significantly over time thus capturing the transient mixing. The simulated wind fields can then be used to study transport and dispersion under a variety of atmospheric conditions. Therefore, a LES modeling of the open pit mine is also studied.

This chapter presents CFD modeling of pollutant transport in a deep open pit mine under a stable boundary layer (SBL) using both the κ-ε and LES turbulent models. The primary objective of this chapter is to test turbulence models using identical input conditions, model constants, and similar geometry. In addition, the pollutant concentrations in the 2010 pit are compared with the measured data. This is done to compare the two different turbulent models. One other purpose of

using both turbulent models is to investigate inter-model variability. It is hypothesized that simultaneous uses of the two models, as well as, adjusting the parameterization based on the measured data, can largely improve pollutant dispersion simulations and will provide valuable information. In the following, CFD modeling with both RANS κ–ε and LES turbulent models is presented.

6.1 RANS Based Models

In Reynolds averaging, the solution variables in the instantaneous (exact) Navier-Stokes equations are decomposed into mean (ensemble-averaged or time-averaged) and fluctuating components. For any given flow property, the variable φ can be expressed as

$$\varphi = \bar{\varphi} + \varphi' \tag{6.1}$$

where, $\bar{\varphi}$ is the mean and φ' is the fluctuating components. For the velocity components:

$$u_i = \bar{u}_i + u_i' \tag{6.2}$$

where, $\bar{u}_i$ and u_i' are the mean and fluctuating velocity components, respectively (i = 1, 2, 3).

Substitution of the Reynolds averaged variables in the instantaneous continuity and momentum equations of the Navier-Stokes (N-S) equations results in the following:

$$\frac{\partial \rho}{\partial t} + \frac{\partial}{\partial x_j}(\rho u_i) = 0 \tag{6.3}$$

$$\frac{\partial}{\partial t}(\rho u_i) + \frac{\partial}{\partial x_j}(\rho u_i u_j) = \frac{\partial p}{\partial x_i} + \frac{\partial}{\partial x_j}\left[u\left(\frac{\partial u_i}{\partial x_j} + \frac{\partial u_j}{\partial x_i} - \frac{2}{3}\delta_{ij}\frac{\partial u_l}{\partial x_d}\right)\right] + \frac{\partial}{\partial x_j}\left(-\rho\overline{u_i' u_j'}\right) \tag{6.4}$$

Equations (6.3 and 6.4) are called Reynolds-averaged Navier-Stokes (RANS) equations. There are, however, some additional terms, $-\rho\overline{u_i' u_j'}$ in Equation 6.4, due to the effects of turbulence. These additional terms are referred to as the Reynolds stress tensor, and often lead to another problem known as the closure problem. The RANS equations have more unknowns in the four equations, and in order to solve the equations, the Reynolds stress tensor must be modeled.

A number of RANS based turbulence models such as the Spalart-Allmaras, the κ-ε, kappa-omega (κ-ω), etc., are available in ANSYS-FLUENT. These models use their own unique formulations for resolving the turbulence and closing the set of equations. Based on its proven applicability in wide range of problems, the two equation κ-ε model is often selected (Menter 2010). There are three variations of the two equation κ-ε model namely: the Standard κ-ε model

(Launder and Spalding 1974), the RNG κ-ε model (Orszag et al. 1993), and the realizable κ-ε model (Shih et al. 1995). These three models have similar forms and include transport equations for turbulent kinetic energy (κ) and turbulent dissipation rate (ε). The differences among the models are primarily due to

- the method used to calculate the turbulent viscosity
- the turbulent Prandtl numbers governing the turbulent diffusion of κ and ε, and
- the generation and destruction terms in the ε equation.

Since, the RANS-based model offers accurate and fast solutions at a relatively low computational cost, the realizable κ-ε model is selected for modeling the air flow and pollutants transport in open pit mines under Arctic inversions. The realizable κ-ε model is suitable of modeling the flows with strong streamline curvature, vortices, and rotation (ANSYS 2011a).

As the temperature inversion starts to build up in an open pit, thermal turbulence dominates the mechanical turbulence. As a result, the air mass within the open pit cools very rapidly. The air mass within the open pit becomes denser than the warmer air pool above it. To simulate this specific condition, the effect of buoyancy on turbulence must be considered. To account for the change in density, the incompressible ideal gas law is applied. This implies that density is a function of temperature alone and the pressure is assumed to be constant.

$$\rho = \frac{p_{op}}{\frac{R}{M_W}T} \tag{6.5}$$

where,

R = the universal gas constant,

M_W = the molecular weight of the gas in gram (g),

p_{op} = the operating pressure in Pascal (Pa), and

T = the air temperature in Kelvin (K).

In the present research, different modules of the ANSYS-CFD package have been used as the pre-processor, solver and post-processor. Chapter 5 discusses different aspects of geometry and mesh creation. Once the pre-processing is done and a good quality mesh is obtained, the selection of an appropriate turbulence model, boundary and initial conditions is critical in producing a

reasonable prediction. The solver program in the ANSYS-CFD is ANSYS-FLUENT which contains various turbulence models. Most of these models are based on Reynolds averaging of the turbulent quantities, accomplished using the Reynolds-averaged Navier-Stokes (RANS) equations. The RANS equations are formulated in terms of the time-averaged flow field (velocity, pressure, density and temperature). This averaging concept for the Navier-Stokes (N-S) equations significantly reduces the complexity of simulating turbulent flow (Menter et al. 2006).

6.2 Scale Resolving Simulation

Scale-resolving simulation (SRS) is another simulation approach used to solve turbulence problems. SRS methods such as scale-adaptive simulation (SAS), detached eddy simulation (DES), and LES have been used for various flow problems (Menter 2012). The scale-adaptive simulation model (SAS) is based on the introduction of the von Kármán length scale (L_{VK}) into the turbulent model. L_{VK} allows the model to adjust to the resolved structures of the simulation and automatically reduces the eddy viscosity.

Typically, the κ-ε method results in a "steady state" solution to an averaged version of the flow equations, while LES results in a transient solution to the actual Navier-Strokes equations. Because real turbulent flow situations are inherently transient, LES methods could have an advantage in modeling turbulent flow.

LES is based on the concept of filtering the Navier-Stokes equations over a finite spatial domain (typically the control volume) and by resolving only those portions of the turbulence larger than the filter width. Turbulence structures smaller than the filter width are subsequently modeled, typically by a simple Eddy Viscosity model (Menter 2012). The filtering operation is defined with the following equations:

$$\bar{\phi} = \int_{-\infty}^{\infty} \phi(\vec{x}')G(\vec{x} - \vec{x}')\, d\vec{x} \tag{6.6}$$

$$\int_{-\infty}^{\infty} G(\vec{x} - \vec{x}')\, d\vec{x}' = 1 \tag{6.7}$$

where G is the spatial filter. Filtering the Navier-Stokes equations results in the following form (density fluctuations neglected):

$$\frac{\partial \rho \overline{u_i}}{\partial t} + \frac{\partial \rho \overline{u}_j \overline{u_i}}{\partial x_j} = -\frac{\partial p}{\partial x_i} + \frac{\partial}{\partial x_j}\left(2\mu_t \bar{S}_{ij} + \tau_{ij}\right) \tag{6.8}$$

The equations feature an additional stress term due to the filtering operation:

$$\tau_{ij} = \rho\bar{u}_i\bar{u}_j - \rho\overline{u_i u_j} \tag{6.9}$$

where τ_{ij} is the sub-grid scale stress tensor responsible for the momentum exchanges between the sub-grid and the filtered scales.

6.2.1 Sub-Grid Scale Models

The sub-grid scale (SGS) turbulence models in ANSYS-FLUENT employ the Boussinesq hypothesis (Lesieur et al. 2005), and the sub-grid scale turbulent stresses are computed using the following equation:

$$\tau_{ij} - \frac{1}{3}\tau_{kk}\delta_{ij} = -2\mu_t\bar{S}_{ij} \tag{6.10}$$

where μ_t is the sub-grid scale turbulent viscosity.

The isotropic part of the sub-grid scale stress τ_{kk} is not modeled, but added to the filtered static pressure term. $\bar{S}_{ij}$ is the rate of the strain tensor for the resolved scale defined by the following equation:

$$\bar{S}_{ij} = \frac{1}{2}\left(\frac{\partial\bar{u}_i}{\partial x_j} + \frac{\partial\bar{u}_j}{\partial x_i}\right) \tag{6.11}$$

ANSYS-FLUENT offers a number of sub-grid scale models under LES, such as, the Smagorinsky–Lilly model, the Wall-Adaptive Local Eddy model (Monti et al. 2002), the Algebraic-Wall Modeled LES (WMLES) and the kinetic energy transport model.

The WALE and the WMLES sub-grid scale models are used where the innermost part of the wall boundary layer is modeled by applying the RANS model and then a LES model for the main part or the filtered part of the boundary layer. The basic difference between these sub-grid scale models is the manner in which their eddy-viscosities are modeled. In the WALE model, the eddy-viscosity is modeled by the following equation:

$$\mu_t = \rho L_S^2 \frac{\left(S_{ij}^d S_{ij}^d\right)^{3/2}}{\left(\bar{S}_{ij}\bar{S}_{ij}\right)^{5/2} + \left(S_{ij}^d S_{ij}^d\right)^{5/4}} \tag{6.12}$$

where L_S is the mixing length for sub-grid scales. L_S and S_{ij}^d in the WALE model are defined, by the following equations:

$$L_s = \min\left(kd, C_w V^{1/3}\right) \tag{6.13}$$

$$S_{ij}^{d} = \frac{1}{2}\left(\bar{g}_{ij}^{2} + \bar{g}_{ji}^{2}\right) - \frac{1}{3}\delta_{ij}\bar{g}_{kk}^{2}, \bar{g}_{ij} = \frac{\partial \overline{u_i}}{\partial x_j} \qquad (6.14)$$

where k is the von Kármán constant, d is the distance to the closest wall, and C_w is the WALE constant. A C_w value of 0.325 provided satisfactory results for a wide range of flow problems. The term $V^{1/3}$ represents the local grid scale (ANSYS 2011a).

One of the advantages of the WALE model is that the return of zero turbulent viscosity for laminar shear flows allows the model to correctly treat the laminar zones in the model domain.

Conversely, in the WMLES sub-grid scale model, the RANS portion of the model is only activated in the inner part of the logarithmic layer, and the remainder of the boundary layer is simulated using a modified LES formulation. The WMLES model combines a mixing length model, a modified Smagorinsky model, and the wall-damping function of Piomelli. The eddy viscosity is calculated with the use of a hybrid length scale:

$$\mu_t = \lim\left[(kd_w)^2, \left(\mathrm{C_{S_{mag}}}\,\Delta\right)^2\right] \cdot s \cdot \left\{1 - \exp\left[-\left(y^+/_{25}\right)^3\right]\right\} \qquad (6.15)$$

where d_w is the wall distance, S is the strain rate, $k = 0.41$ and $C_{Smag} = 0.2$ are constants, and y^+ is the normal to the wall inner scaling (ANSYS 2011a).

The LES model is based on a modified grid scale to account for grid anisotropies in wall-modeled flows:

$$\Delta = \min\left(\max(C_w.d_w;\ C_w.h_{max},\ h_{wn});\ h_{max}\right) \qquad (6.16)$$

where h_{max} is the maximum edge length of the cell, h_{wn} is the wall-normal grid spacing, and C_w (0.15) is a constant. Detailed descriptions of these sub-grid scale models can be found elsewhere (Nicoud and Ducros 1999; Shur et al. 2008). The choice of the sub-grid scale model is also based on how the two models formulate the different mechanical and thermal structures in the atmosphere at different time horizons.

6.3 Modeling of Stable Boundary Layer

Modeling the stable boundary layer (SBL) is difficult due to the intermittency in the turbulence. The intermittent nature of turbulent in the SBL makes the modeling challenging and difficult. Moreover, the turbulence length scale is smaller due to the buoyancy suppression and only mechanical turbulence prevails near the inversion layer. On the other hand, as the cooling rate

increases the effect of buoyancy dominates the lower level of the atmosphere. In order to capture the small scale turbulence a finer grid resolution is needed, thus increasing the computational cost exponentially. The stable boundary layer was first modeled using the LES by Mason and Derbyshire (1990), followed by several other researchers (Andrén 1995; Saiki et al. 2000; Basu and Porté-Agel 2006). Much of the modeling efforts are, however, related to contaminant transport in the atmosphere. LES is becoming widely accepted by the atmospheric sciences community as a powerful numerical modeling approach compared with experimental observations. Due to the sub-grid scale (SGS) models of the LES, reproduction of the characteristics of moderately and strongly stable boundary layers could not be successfully implemented (Basu and Porté-Agel 2006). Large eddies are suppressed by static stabilities, leaving only the smaller eddies that cannot be resolved by a LES model. With recent advances in computational power and memory, it is now possible to have much finer grids to resolve much smaller eddies by LES.

During neutral conditions, smaller eddies dominate near the surface, while larger eddies are more important aloft. These large eddies are often elongated in the direction of the shear vector (Mason and Thomson 1987). The LES model has been widely used for modeling atmospheric flows (Moeng 1984). LES-based CFD simulation for open pit air flow, however, has not been conducted. CFD computer models can be used to understand the ABL/SBL structure over an open pit mine.

In a CFD simulation, the flow properties of mean wind speed and turbulent quantities that are applied at the inlet plane of the computational domain are generally fully developed, equilibrium profiles. These profiles are approximate representations of the roughness characteristics of the part of the upstream terrain that is not included in the computational domain. The turbulence in open pits under neutral conditions is mostly due to a shear effect. Any turbulence that is generated in the stable boundary layer can be either by the mechanical turbulence or due to negative buoyancy. However, the generation of both the source of turbulence is space and time dependent. Mechanical turbulence due to wind shear is dominant at the start of the formation of SBL which dies out with increase in cooling rate and stratification where buoyancy prevails. The mechanical wind shear is prevalent at top of the inversion layer whereas in the middle portion turbulence is mainly intermittent as the turbulence due to both mechanical shear and thermal buoyancy. The interplay between buoyancy and shear effects weakens the turbulence intensity in the middle portion. Thermal buoyancy is dominant at the bottom portion of the SBL where cooling rate is

highest due to radiative cooling. This phenomenon is more clearly observed in a stable boundary layer than the neutral and convective boundary layers (Stull 1988). A stable boundary layer is thus somewhat shallower and characterized by small scale eddies. A higher accuracy in predicting the pollutant distribution can be obtained if these eddies are modeled based on their length scales.

6.4 Simulation of Pollutant Transport in Open Pit Mines under Arctic Inversion

Under Arctic inversion, turbulence due to thermal buoyancy is dominant at the bottom of the open pit.

Figure 6.1 demonstrates that the length scale for the larger eddies are significantly larger than that of the smaller eddies present in the thermally stratified layers.

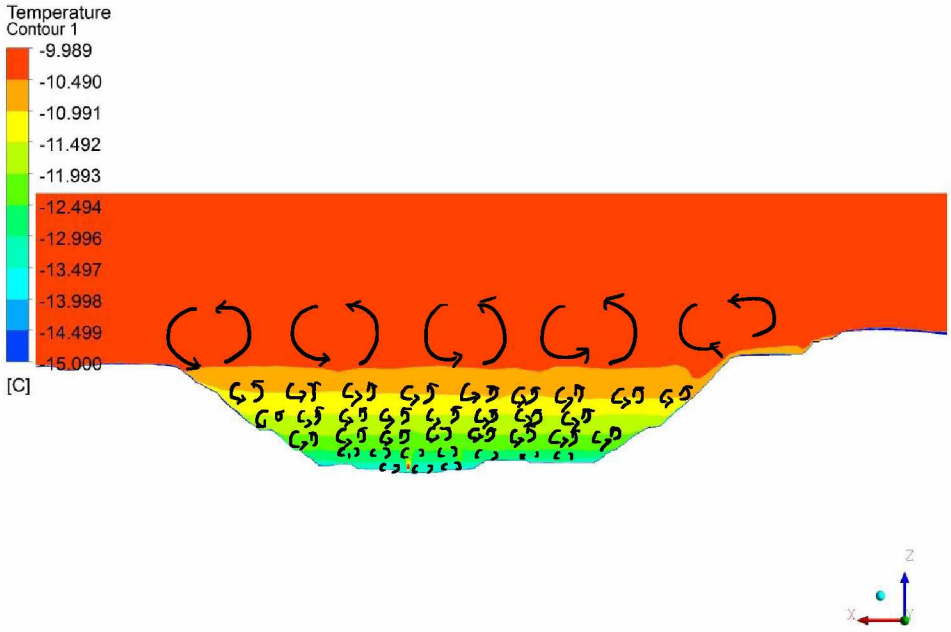

Figure 6.1: Eddies of Different Length Scale (Raj and Bandopadhyay 2014).

6.4.1 Geometry of the Selected Open Pit

The 2010 pit configuration selected for simulation modeling is 1,880 m (6,170 ft.) wide in the East-West direction, 1,219 m (4,000 ft.) wide in the North-South direction, and approximately 366 m (1,200 ft.) deep. Detailed discussions on meshing the pit and model domain are presented in Chapter 5.

6.4.2 Boundary Conditions

The specified boundary conditions for the simulations are provided in Table 6.1. At the east boundary of the model domain, an inlet velocity and temperature are specified. Because there is no specific information available for the western part of the model domain, an outflow boundary condition is prescribed, and a value of one (1) is used, thus ensuring the conservation of mass. The south, north and free atmosphere (FA) in the model domain are considered wall boundaries and zero heat flux boundaries, i.e., there is no heat exchange between the wall and the air mass across the model boundaries. Finally, the pit boundary is considered as a wall boundary with a prescribed negative heat flux magnitude of 16 W/m^2 (Wendler and Jayaweera 1972). This negative heat flux accounts for the net radiation balance at night which is supported by the radiation data collected at the mine site presented in Chapter 3.

Table 6.1: Boundary Specifications at Various Segments of the Model Domain.

Boundary Part	Boundary Type	Boundary Condition Specifications
East	Velocity Inlet	Inlet velocity: 1 m/s (3.28 ft./s)
		Thermal Condition: -10°C (14°F)
		Turbulent Intensity: 5%
		Viscosity Ratio: 5
West	Outflow	1
South	Wall	Thermal Condition: 0 W/m^2
North	Wall	Thermal Condition: 0 W/m^2
FA	Wall	Thermal Condition: 0 W/m^2
Pit	Wall	Thermal Condition: -16 W/m^2

6.4.3 Pollutant Sources in an Open Pit Mine

The modeling of contaminant transports in an open pit mine requires the introduction of source terms. This can be done either by selecting a volume cell in ANSYS-FLUENT or by revisiting the geometry and creating the geometry that represents the contaminant sources. For this research, the second option is selected and geometries are created to represent the contaminant sources. The contaminant sources in the open pit are drill machines and shovels. The trucks are pulled out of the pit at the time of inversion and, therefore, they are not specifically modeled. There are altogether 9 pieces of operating equipment at various locations in the pit, six of which represents

the drill machines and other three are shovels. The machines run continuously, even when the pit is under an inversion. Since, it is not possible to represent the exact dimensions of the drill machines or the shovels; these are idealized to cubes of dimension 6 m (20 ft.). One of the faces is termed as the exhaust and the others as machine body (Figure 6.2). These faces serve as the heat source, since almost 60% of the fuel energy goes to generate waste heat. The specific location of these pollutant sources is based on the data obtained from the mine's management.

Figure 6.3 and Figure 6.4 show the respective locations of the pollutant sources in the pit. The pit-modified geometry resulting from the addition of the contaminant sources is subjected to the re-meshing process. Inclusion of the pollutant sources leads to more complexity in the simulation domain; therefore, the mesh created of the model domain must be of high quality. To avoid numerical diffusion or divergence during a simulation run, the mesh quality of the model domain must exceed a value of 0.9 or better.

Once the pit geometry is modified by adding the contaminant sources, the modified geometry is subjected to the meshing process. Inclusion of the pollutant sources leads to more complexity in the simulation domain. It is therefore the mesh created of the model domain must be of high quality. In ANSYS-FLUENT best quality is defined as zero whereas worst is 1. In order to avoid numerical diffusion or divergence during a simulation run, the mesh quality of the model domain must be less than the value of 0.9.

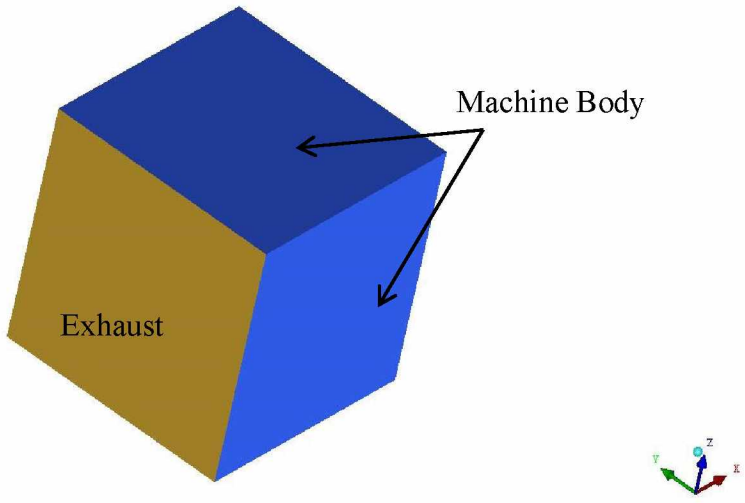

Figure 6.2: Equipment as a Cube to be used in the Model.

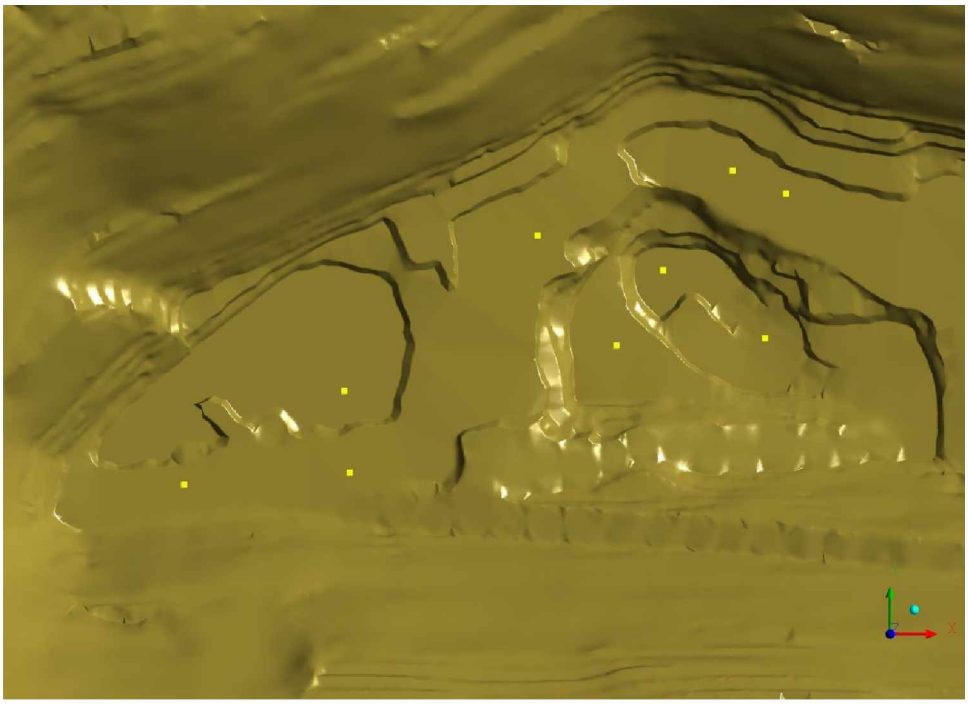

Figure 6.3: Pollutant sources placed at different Location in the pit.

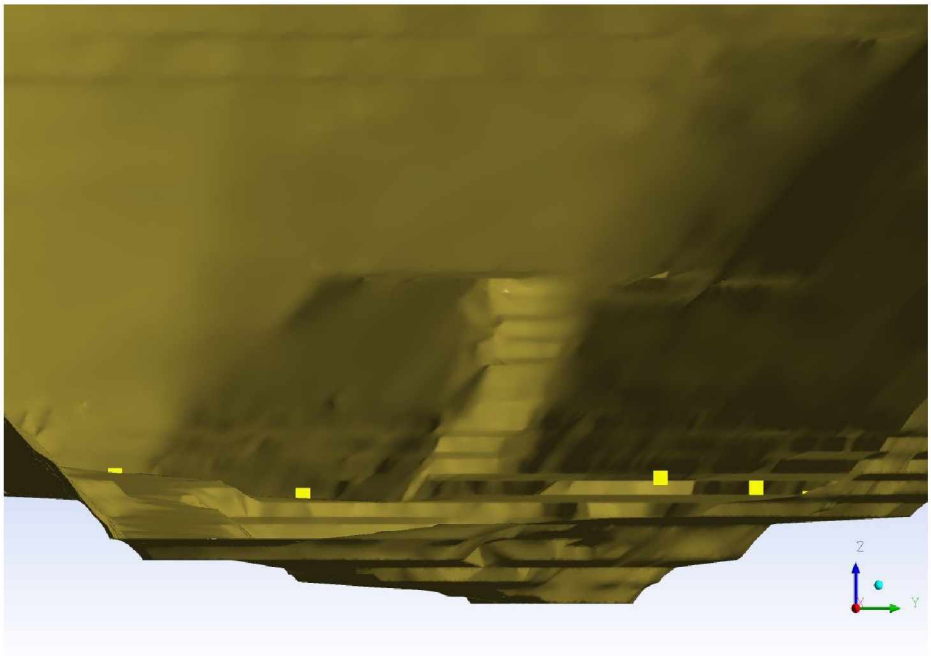

Figure 6.4: Sectional View of Pollutant Sources Placed at Different Location in the Pit.

6.5 Modeling of Contaminant Transport under SBL using Realizable κ-ε Model

6.5.1 Time Stepping

Because an atmospheric inversion is not a steady state phenomenon, the transient approach is required to model the inversion. Two different approaches can be used for time stepping in a transient model. In the first approach, a constant time step is used throughout the model run. In the second approach, adaptive time stepping, the optimal time step size for convergence and computational efficiency is automatically selected.

An adaptive time step scheme is adopted for the time domain. The time step is determined by the Courant–Friedrich–Levy (CFL) criterion (ANSYS 2011a). Using the adaptive approach, a small time step is used for the initial iterations where the flow remains unsteady. At the initial stage of the simulation, the time-steps are as low as 0.001 second, but as the simulation progresses, the time-steps increased to a maximum of 30 seconds. However, the time-steps are not fixed to a single value rather varying from 1 to 15 seconds for model convergence.

The atmospheric inversion is a micro-meteorological phenomena occurring for few hours to few days. Simulation of an enhanced period of turbulence in the SBL is important. For this reason, the simulation is run for 16 hours' time period using the time-adaptive method for automatically modifying the time intervals. The simulation is run for 16 hours to include the diurnal cycle of the short day span and the longer night time in the Arctic. The initial simulation clock resembles 4:00 PM of the first day and ends at 8:00 AM the following day.

6.5.2 Simulation Results

Results are presented along the vertical section taken in the East-West direction shown in Figure 6.5. Another view of the vertical section can be found in Figure 6.6. Velocity and NO_2 concentration contours are plotted on the vertical section plan. Temperature, turbulent kinetic energy (TKE), and turbulent intensity (TI) are plotted at seven different locations along elevation of the pit (Figure 6.7). Six locations are within the pit, whereas, the seventh is at the pit rim.

The temperature profiles along Line 5 at various times are presented in Figure 6.8. From Figure 6.8, it is seen that the inversion develops over time. The contours of the wind velocity are presented in Figure 6.9 through Figure 6.12. Analysis of the velocity profiles indicates that the air velocity within the pit decreases with strength of inversion.

The contours of NO_2 concentrations (in parts per million, ppm) are presented in Figure 6.13 through Figure 6.16. With growing strength of inversion within the open pit, the concentration of the pollutant also increases. The contours of NO and CO concentrations are presented in Appendix II.

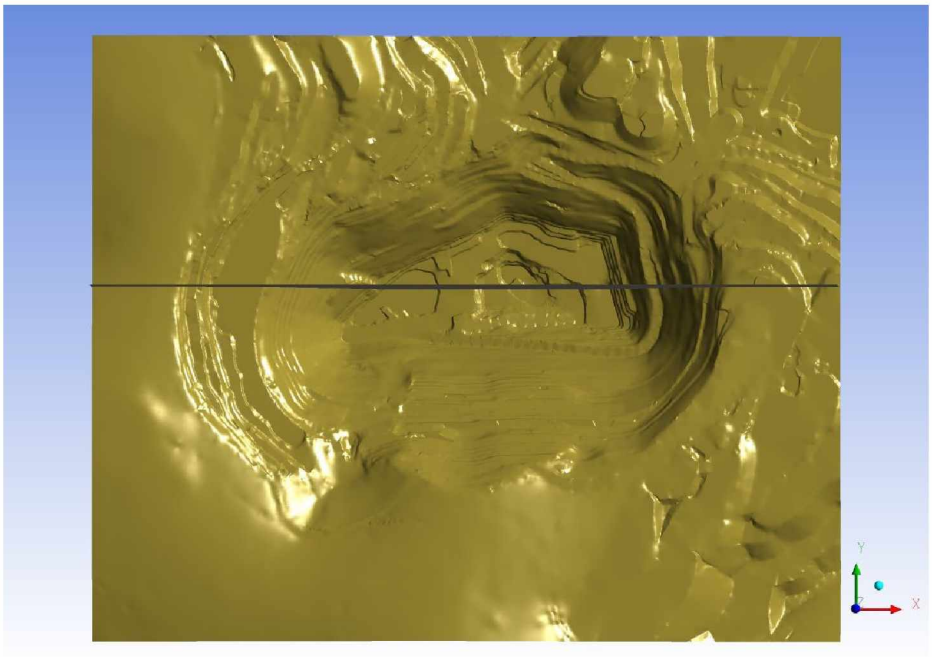

Figure 6.5: A View of Vertical Section in East-West direction.

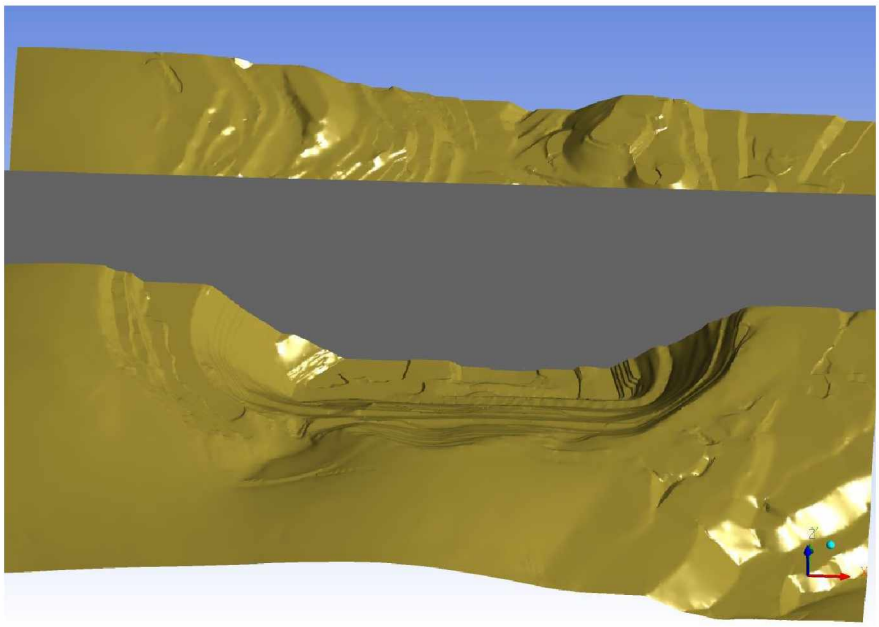

Figure 6.6: A View of the Vertical Section in East-West direction.

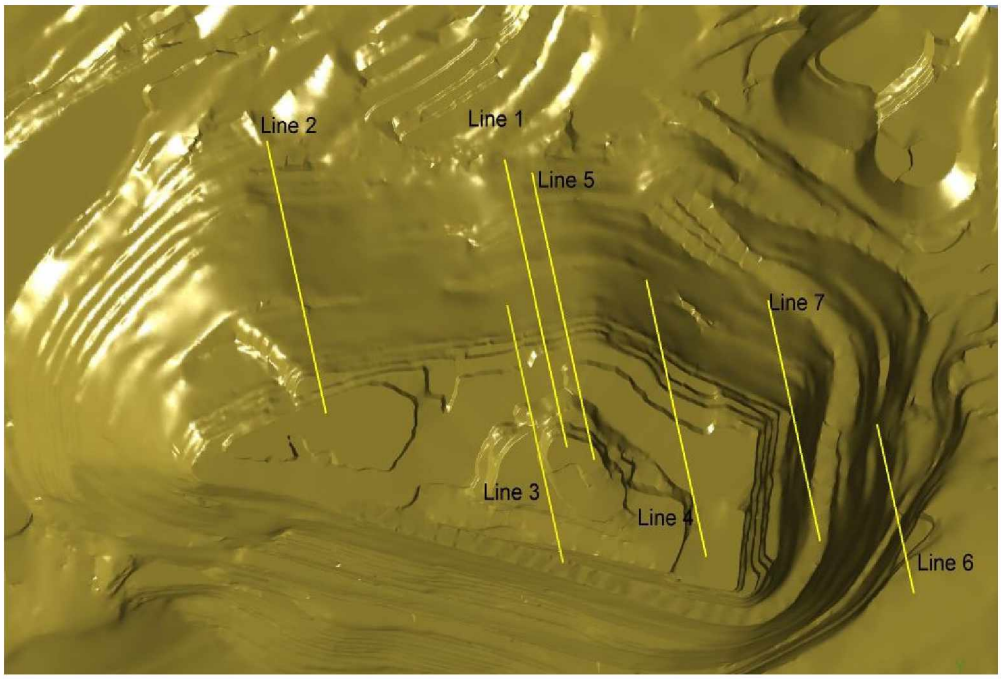

Figure 6.7: Different Lines for Plotting Simulation Results.

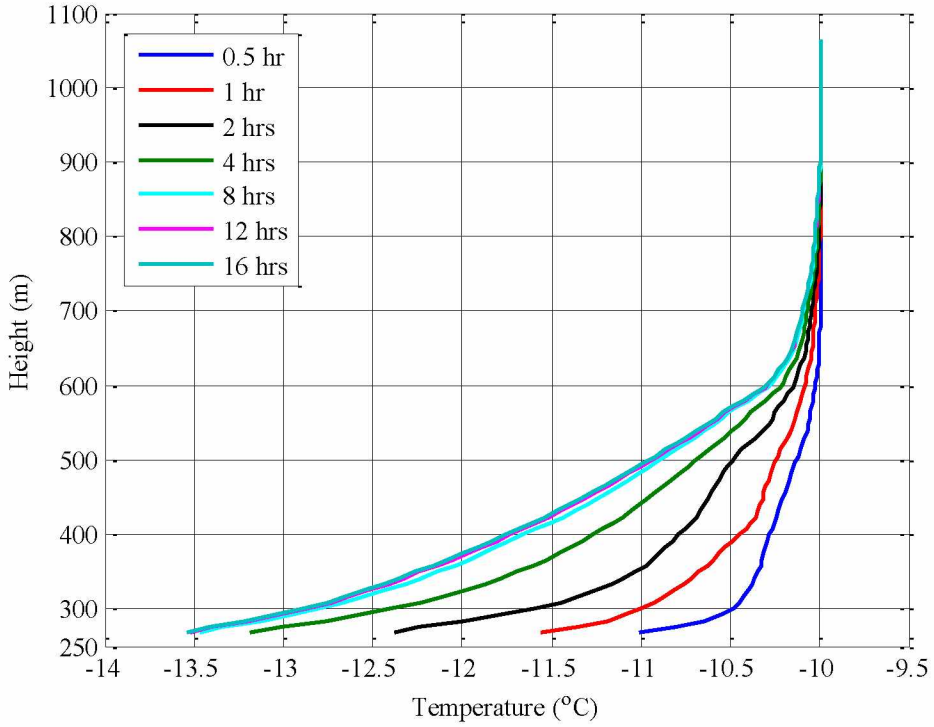

Figure 6.8: Temperature Profiles along Line 5 at Various Time Intervals.

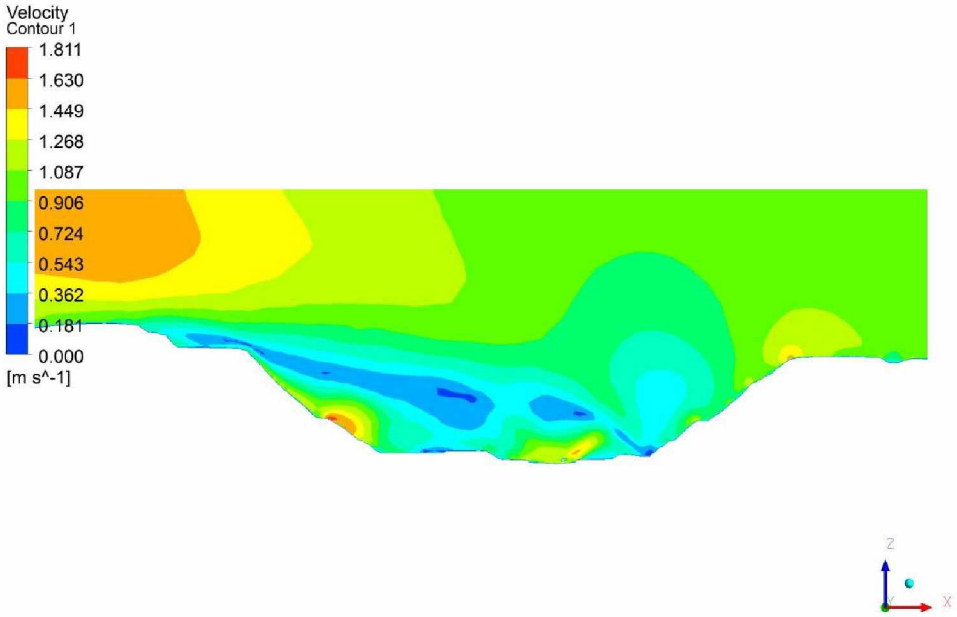

Figure 6.9: Velocity Profile at Time Step (t ≈0.5 hr.).

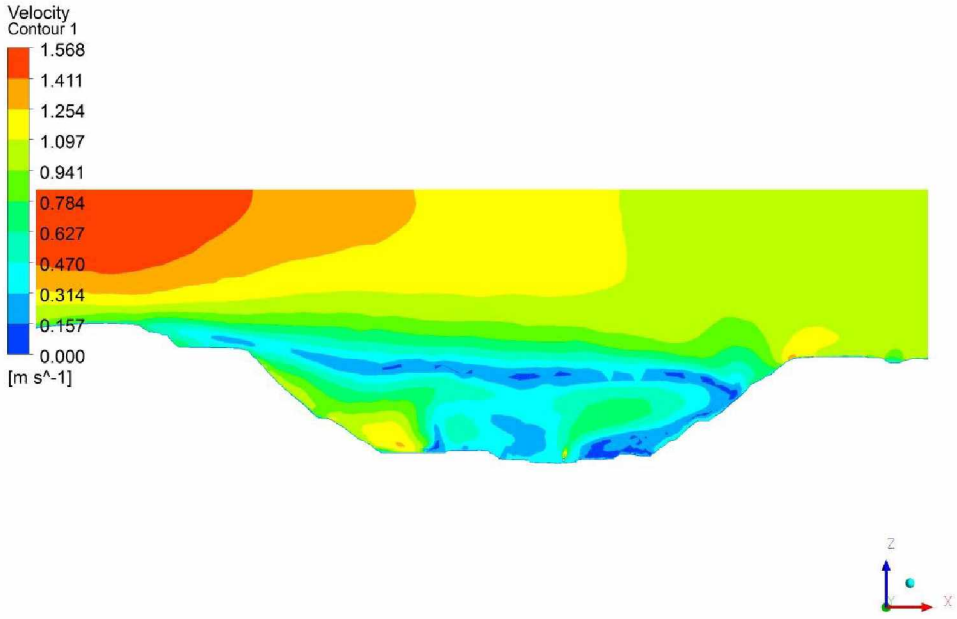

Figure 6.10 : Velocity Profile at Time Step (t ≈ 1 hr.).

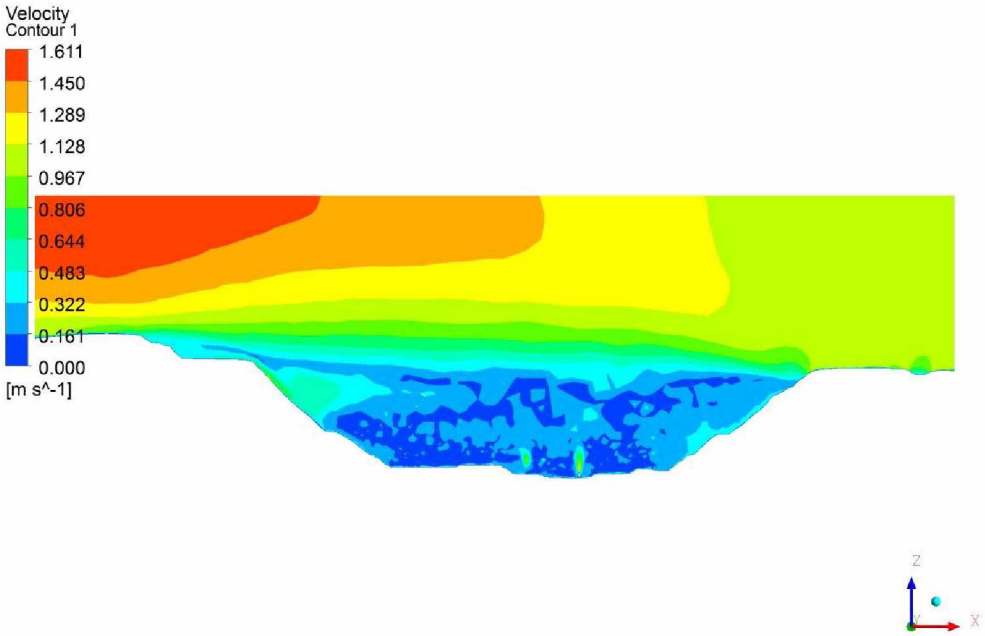

Figure 6.11: Velocity Profile at Time Step (t ≈ 4 hrs.).

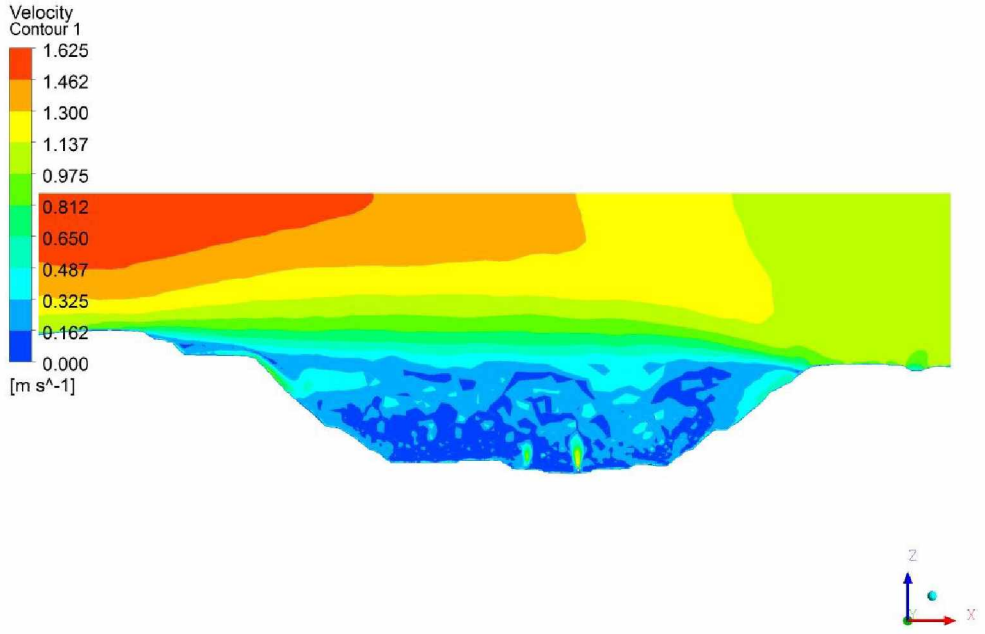

Figure 6.12: Velocity Profile at Time Step (t ≈ 16 hrs.).

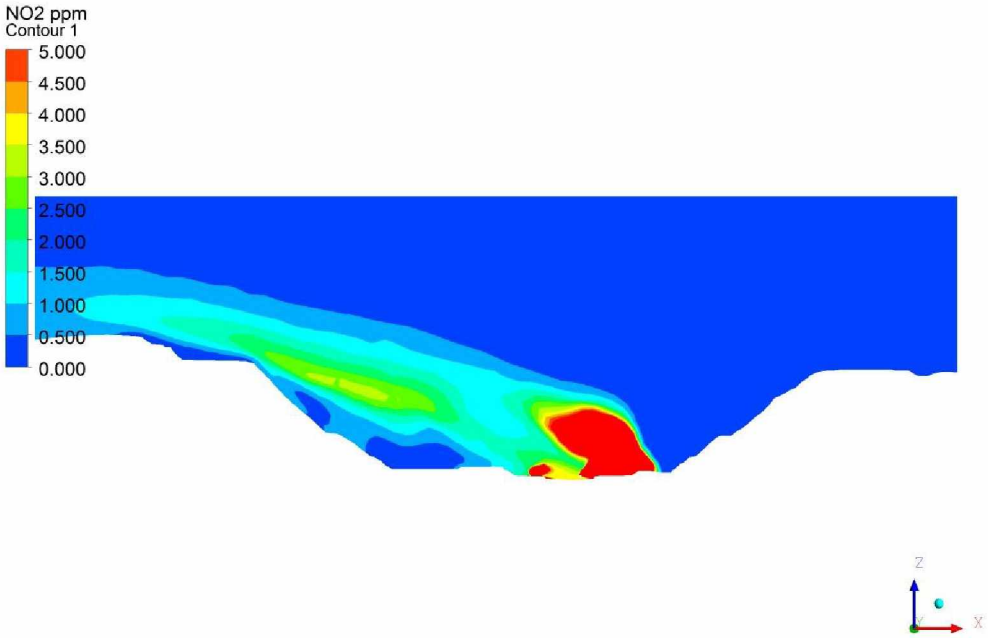

Figure 6.13: Concentration of NO_2 (in ppm) at Time Step (t ≈ 0.5 hr.).

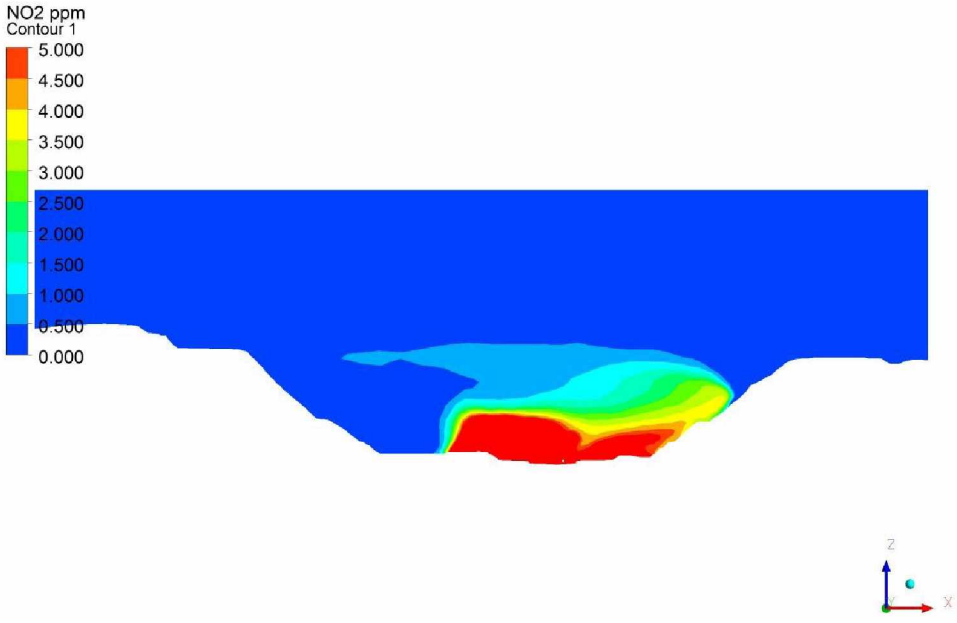

Figure 6.14: Concentration of NO_2 (in ppm) at Time Step (t ≈ 1 hr.).

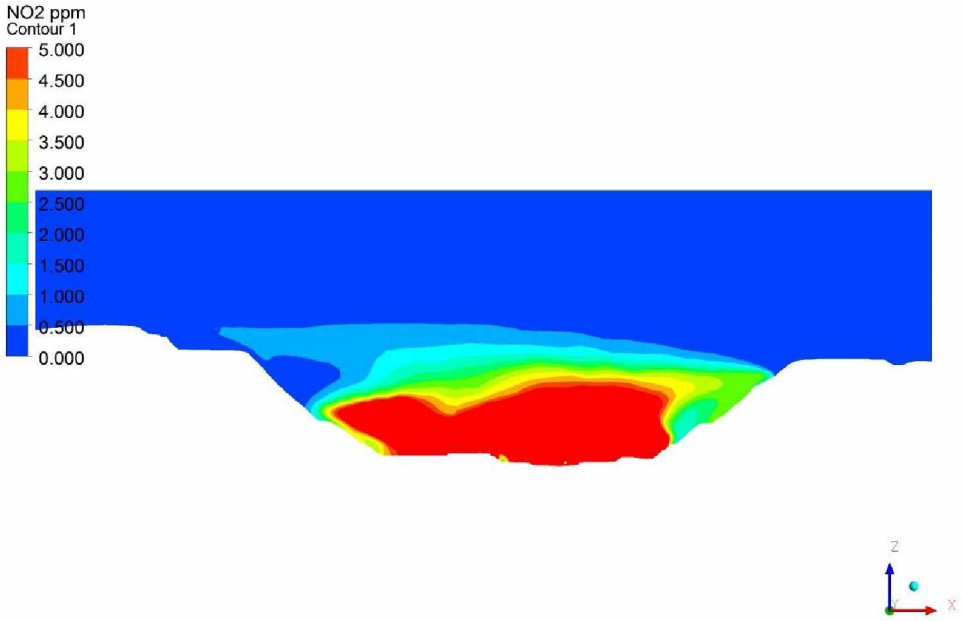

Figure 6.15: Concentration of NO_2 (in ppm) at Time Step ($t \approx 4$ hrs.).

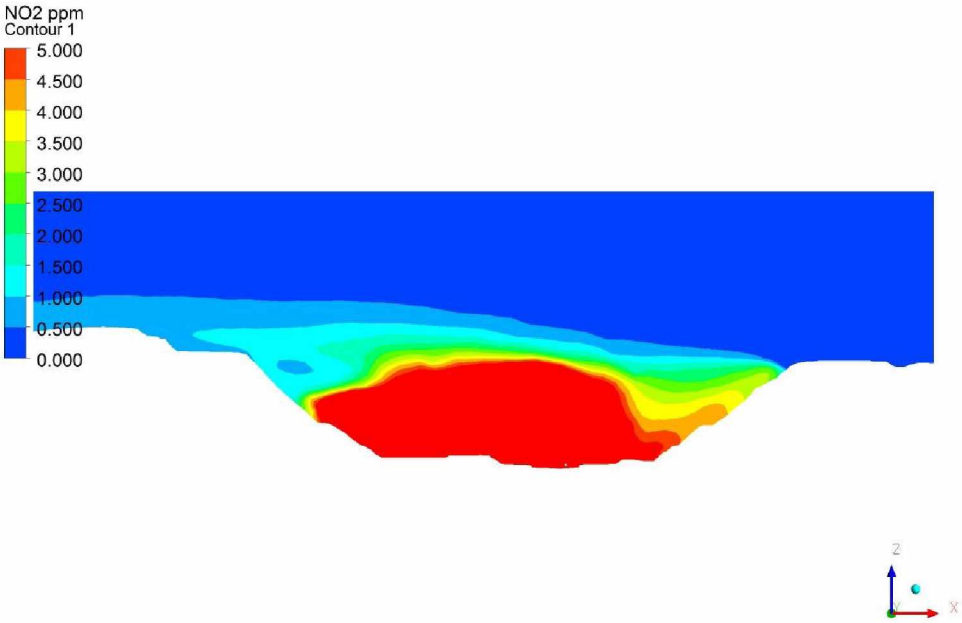

Figure 6.16: Concentration of NO_2 (in ppm) at Time Step ($t \approx 16$ hrs.).

Once the simulation is initialized and the simulation time advances, the change in the domain can be seen in Figure 6.8 after 30 minutes of simulation. The changes in the domain is, however,

not significant in terms of pollution concentration and strength of inversion. In the velocity profile (Figure 6.9), some recirculatory zones can be seen and at the same time, these recirculatory zones match with the flow of pollutant (NO_2). No retention of pollutant is seen in the pit bottom. Since, no inversion has yet developed; the air mass from the East boundary of the pit (inlet boundary) reaches the leading edge of the pit, where it expands. At this point, the flow is separated into two parts, one, which goes over the pit and another goes into the pit. The air mass flowing within the pit has lower energy and further energy loss results when the air comes in contact with the pit wall. As a result, the velocity decreases within the pit. The resulting wall-shear stress plays an important role in creating the recirculatory zones within the pit. According to the classical theory of flow separation, the point where flow separation occurs, the wall-shear stress is zero, or in other words, the viscous force vanishes (Chang 1970).

After one hour of simulation, the temperature profile (Figure 6.8) starts to build up in the pit. From the velocity profile (Figure 6.10), it is observed that the large recirculatory zones in the pit vanished and the smaller eddies are generated. Thus, it can be said that the change in the thermal regime in the pit affects the eddy characteristics of within the pit. One can also infer from the velocity profile that there is variation in the velocities within the pit. With inversion getting stronger and the air density at the pit bottom starts to increase, thus, the air layer at the bottom starts to develop a different flow regime than the layers above. The effect of the increased inversion strength is exhibited as decreasing air movement followed by increased accumulation of contaminants. Corresponding concentration profile (Figure 6.14) of the NO_2 shows some visible accumulation in the region where thermal regime is changed.

The temperature profile (Figure 6.8) after four hours of simulation shows significant change in thermal regime within the pit and the development of inversion layers is now evident. From the figure, it can be seen that the change in thermal regime covers the entire pit. This change prevails due to the negative heat flux at the pit walls. The ground surface is losing heat due to which the air masses just above the surface get cooled rapidly than the air masses above it. Thus, the change in thermal regime within the pit is observed. Corresponding to the temperature change, the density of the air mass also changes according to the incompressible ideal gas law where the density is only function of the temperature, assuming the pressure is constant. The change in density is directly reflected in the velocity profile (Figure 6.11). There is a significant change in the velocity profile within the pit. With the growth in strength of inversion and change in air density, the

velocity of air within the pit significantly decreases. As the lighter air mass coming from the inlet boundary hits the denser air mass within the pit, the air mass velocity at the point of contact also changes. This is due to the fact that the air mass coming from the inlet has lower density and when it hits the air mass of high density over the pit, it acts as a large flat plate with flat plate surface density slightly higher than the air mass, thus, one can see the thin flow of varying velocity over the denser air masses (Figure 6.11). Also due to the wind shear there is very little change in the air velocity of the denser air mass. From Figure 6.11, it can be seen that there is two distinct zones of flow velocities, one just above the dense air mass and one within the dense air mass in the pit.

There are two equipment near the section plan from where the results are taken. The heat coming out of the equipment changes the thermal regime in its surroundings, thus, causes the changes in the velocity profile within the open pit. This results in a high velocity zone within the pit.

The concentration profile of NO_2 is clearly visible in the pit (Figure 6.15). The entire open pit is covered with high concentrations of NO_2, and it is far above the threshold limit value (TLV) for NO_2.

It is evident that with time, the strength of inversion increases and the air mass within the pit becomes much denser and heavier. The change in temperature and density directly impacts the flow regime within the pit. The air mass within the pit has very low velocity. There is very little impact of the inlet air velocity on the dense mass within the pit. This results in accumulation of pollutants within the pit. Thus, it can be said that with the increase in strength of inversion at the pit bottom the accumulation of the contaminants within the pit also increases.

6.5.3 Turbulence Results from the Simulation

The developed RANS model can be used to understand the ABL/SBL structures over an open pit mine and to characterize the nature of turbulence which would explain the recirculatory nature of the airflow in the pit. The turbulent kinetic energy (TKE) in boundary layer is an important determination of turbulent mixing and dispersion. The increase in wind shear and TKE leads to enhanced dispersion. It is also important to have several turbulence variables/quantities from the simulation; however, there is no data available on measured turbulence values at the selected mine. Apart from the TI and TKE, Richardson number (Ri) is calculated and plotted at different time intervals along the vertical lines at those seven locations.

Line 6 (Figure 6.7) which is located at the pit rim, at an elevation around 600 m (1950 ft.), is outside of the inversion layer. It can be observed that the TKE is very low near the surface and diminishes with increasing altitude (Figure 6.17). The TKE and TI (Figure 6.18) values are also the same for all the simulated time periods. This phenomenon is due to the effect of wind driven shear with a constant wind velocity coming from the inlet boundary.

Figure 6.20 through Figure 6.22 show the TKE and the TI profiles along the Line 1 and Line 5 which are located in the pit. Since, the other lines within the open pit show almost similar characteristics, Line 1 and 5 are selected for the analysis. Line 1 and 5 originate from the lowest elevation level in the pit. Line 1, however, is located near an operating equipment. The magnitudes of turbulent intensity along Line 1 and 5 increase at an approximate height of 530 m (1750 ft.) level. This rise in the turbulent intensity is also reflected in the turbulent kinetic energy, and follows the same trend. The sudden rise in the magnitude of turbulent intensity and turbulent kinetic energy is mainly due to the negative thermal buoyancy. At the pit bottom, due to the negative radiation balance, the surface is getting colder and air mass above making it denser and settles down, thus, creating turbulence. Negative buoyancy as experienced by eddies under stable stratification serves as an important sink for the TKE. However, the propagation of turbulence does not reach enough height and is thus dissipated. The increase in the magnitude with altitude and reaching a peak value approximately at 530 m (1750 ft.) level is a result of the turbulence due to mechanical shear.

Under stable conditions, in the absence of buoyant turbulence production, wind shear is the only mechanism creating turbulence. The turbulence generated at around 530 m (1750 ft.) level is mainly due to the mechanical shear driven by wind. The air mass within the pit is denser and stagnant, when stuck by an incoming air mass from the inlet boundary which less dense creates wind shear at the surface of contact, thus, creating a mechanical turbulence.

Among the selected lines, Line 1 is very close to one of the equipment in the pit. Its proximity to the equipment is reflected on the temperature profile (Figure 6.23). From Figure 6.23, it is evident that at some selected elevation, the temperature is higher than the inflow temperature at the inlet boundary. Whereas, Figure 6.8 is the vertical distribution of temperature as a function of height shows a gradual decrease in temperature at the bottom of the pit for Line 5.

An important dimensionless number, namely the Richardson number (Ri), is also plotted along the selected lines. The Richardson number is the ratio of the buoyant production or loss term to mechanical shear production/loss term which are represented in ANSYS-FLUENT as:

$$G_k = \mu_t S^2 \tag{6.17}$$

$$G_b = -g_i \frac{\mu_t}{\rho Pr_t} \frac{\partial \rho}{\partial x_i} \tag{6.18}$$

where, the G_k is the TKE production due to the mechanical wind shear, the variable term S, is the strain rate tensor, g is the acceleration due to gravity, the term μ_t is the turbulent viscosity and the term Pr_t, is the turbulent Prandtl number taken as 0.85 (ANSYS 2011a).

The respective data for calculating the buoyant and the shear production/loss term are extracted from the model simulation results and plotted along the selected lines. The Richardson number is important in defining the turbulent regimes within the stable boundary layer and determining its dynamic stability (Stull 1988). There is a critical value (0.2) of Richardson number, below which the laminar flow becomes turbulent. Also, if the Richardson number is above 1, the turbulent flow becomes laminar. The flow encounters intermittent turbulence if the Richardson number value is between 0.2 to 1. The Richardson number plots from two selected lines (Line 1 and Line 5) are presented in Figure 6.25 and Figure 6.26 for further analysis.

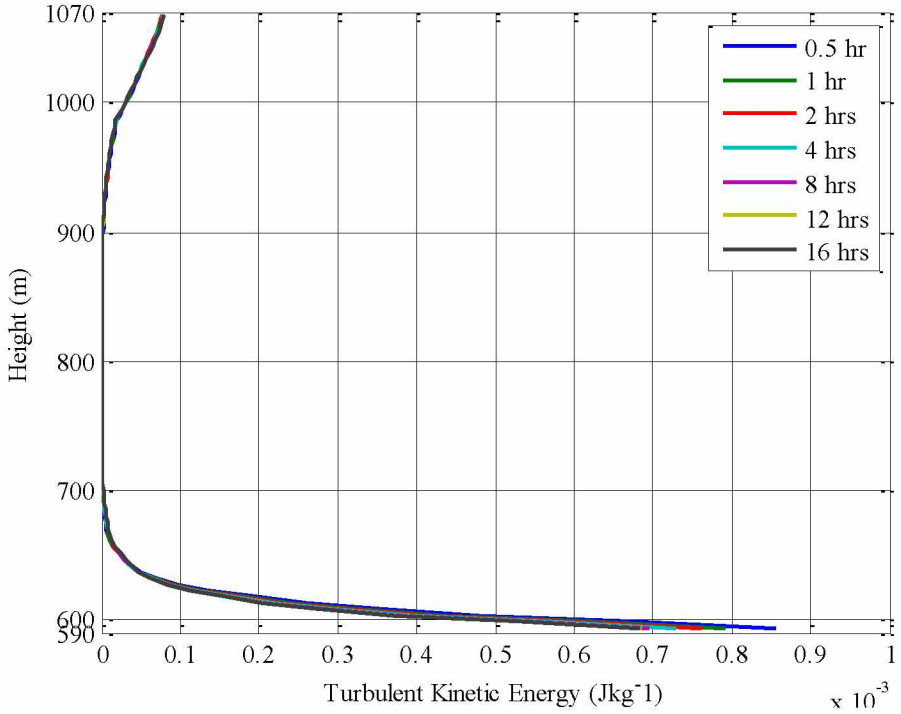

Figure 6.17: Turbulent Kinetic Energy (J/kg) along Line 6 at Various Time Intervals.

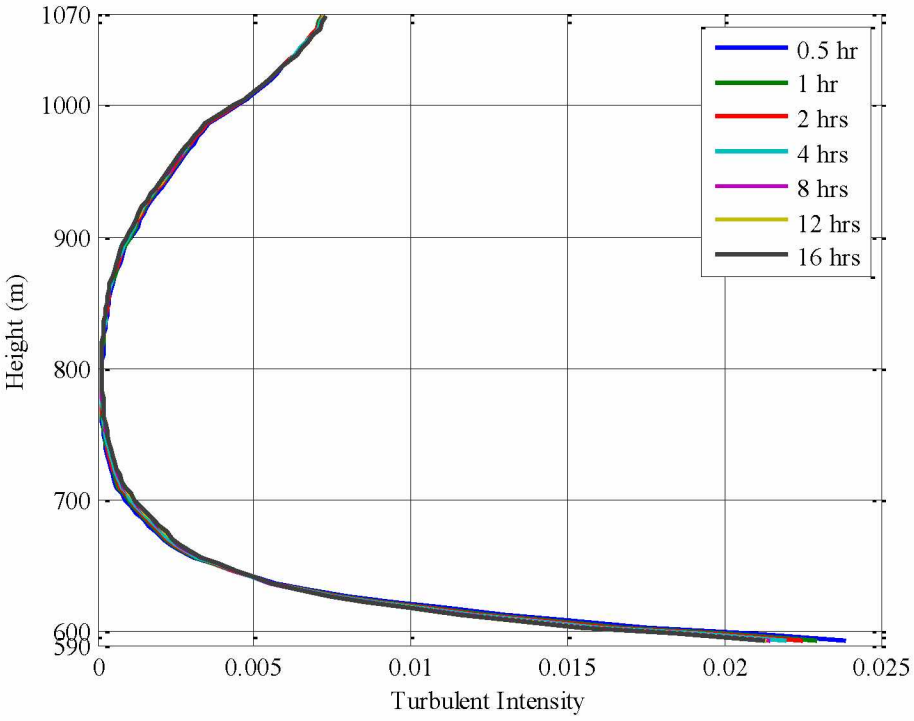

Figure 6.18: Turbulent Intensity along Line 6 at Various Time Intervals.

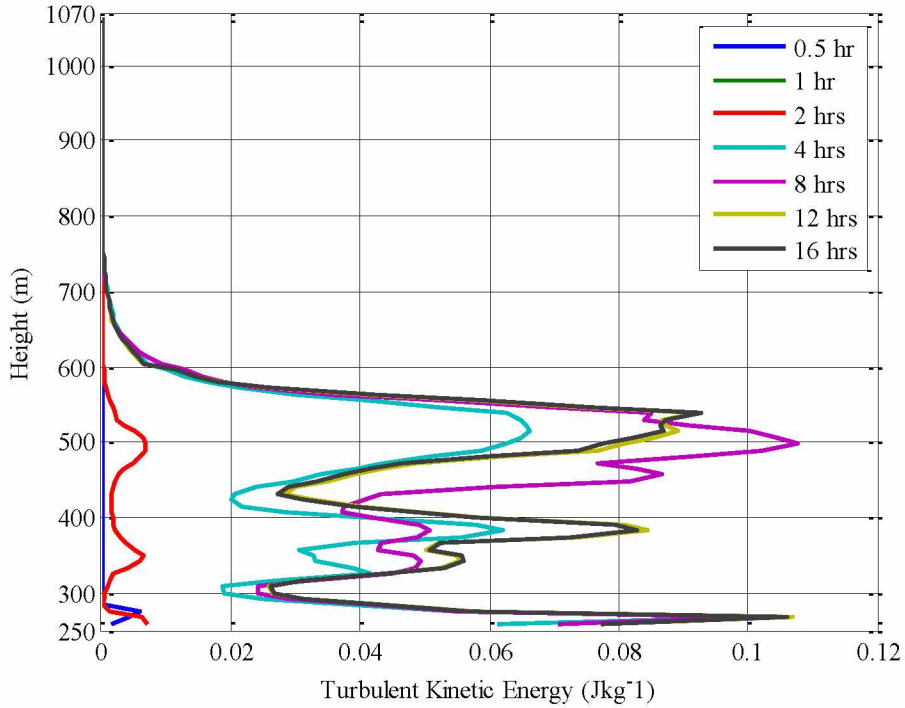

Figure 6.19: Turbulent Kinetic Energy (J/kg) along Line 1 at Various Time Intervals.

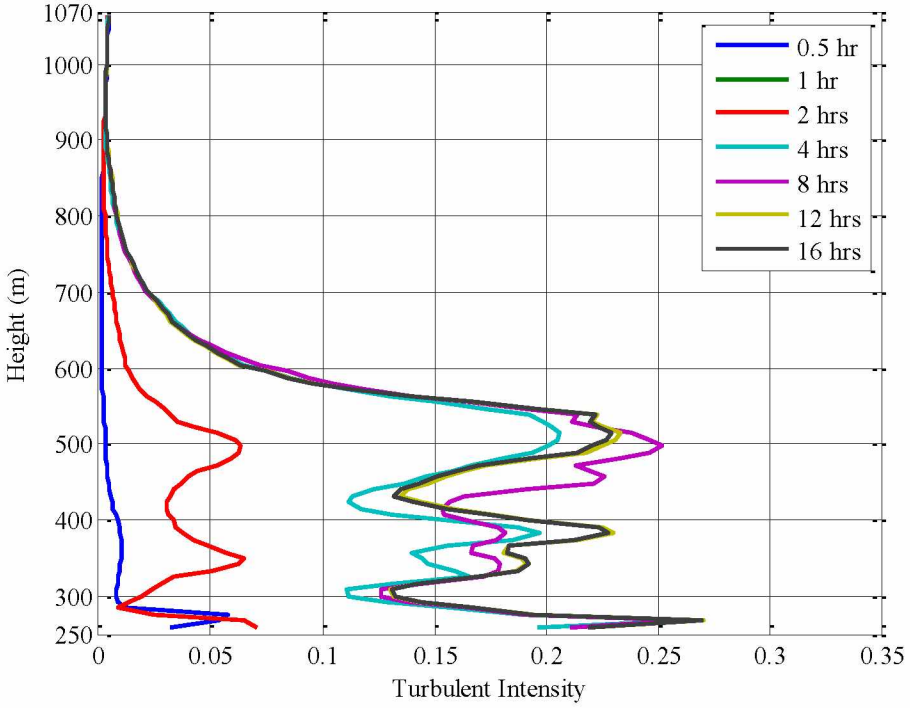

Figure 6.20: Turbulent Intersity along Line 1 at Various Time Intervals.

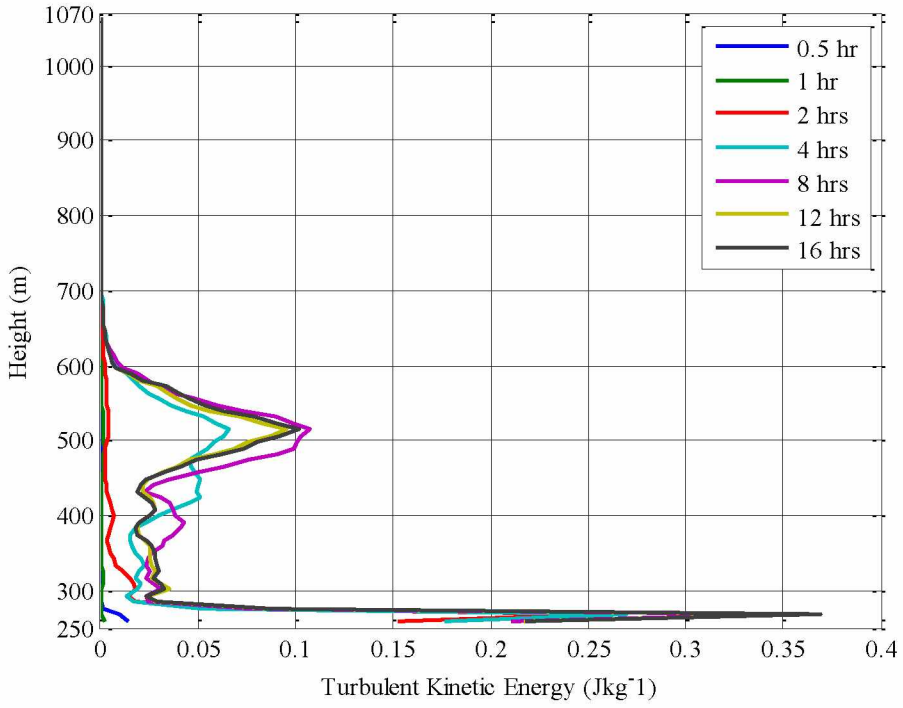

Figure 6.21: Turbulent Kinetic Energy (J/kg) along Line 5 at Various Time Intervals.

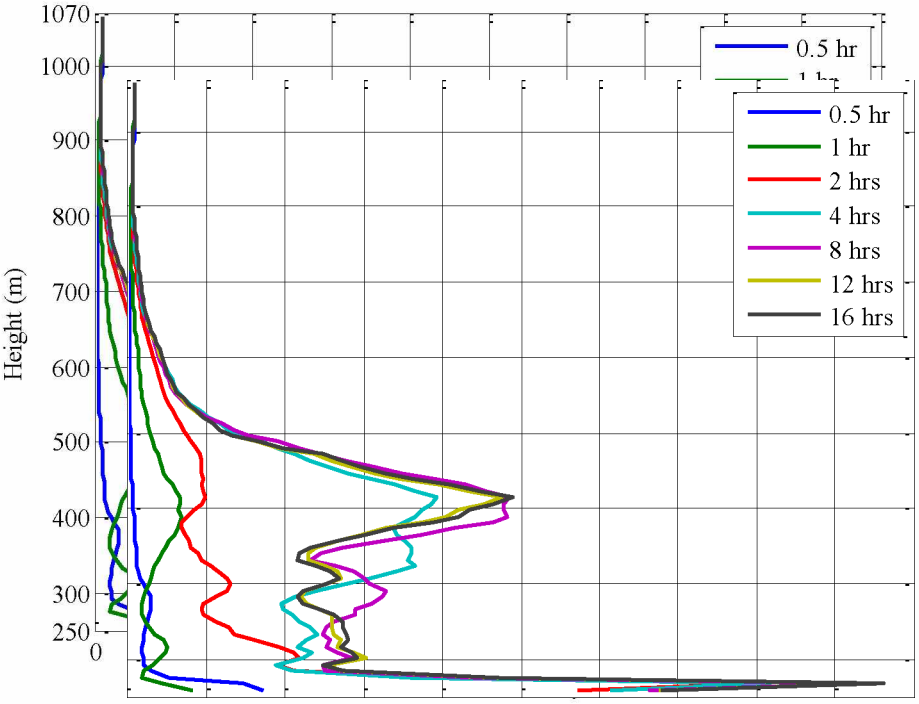

Figure 6.22: Turbulent Intensity along Line 5 at Various Time Intervals.

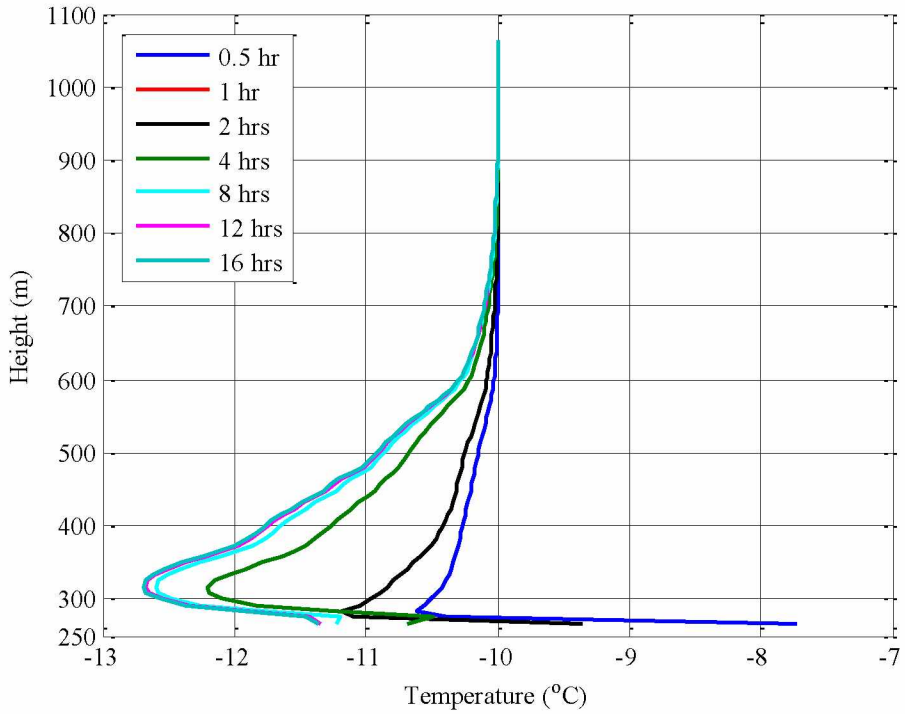

Figure 6.23: Temperature Profiles along Line 1 at Various Time Intervals.

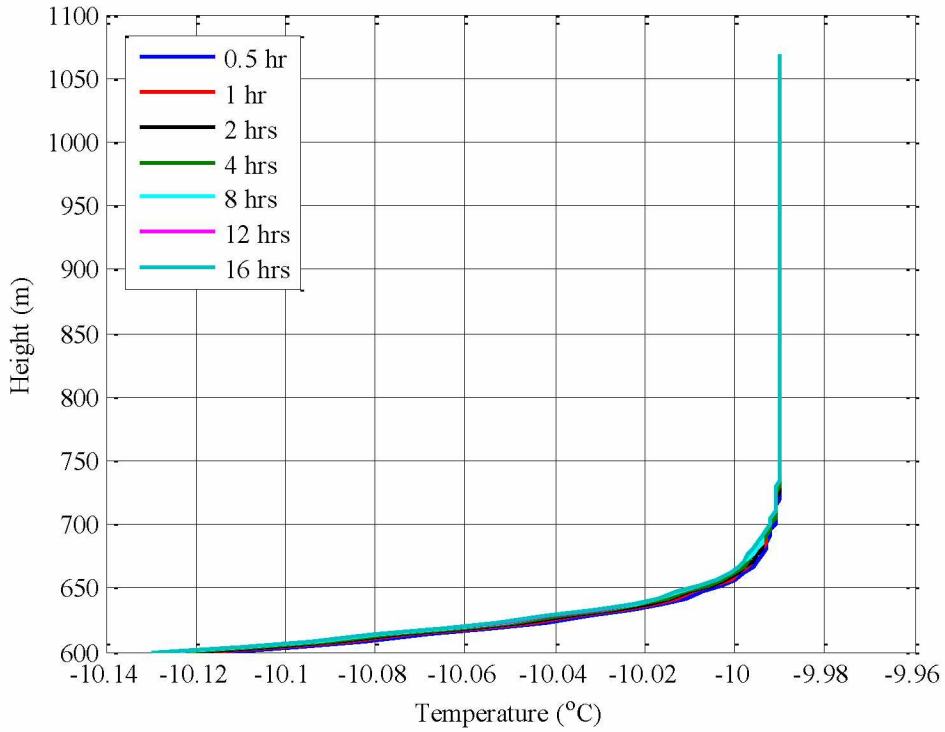

Figure 6.24: Temperature Profiles along Line 6 at Various Time Intervals.

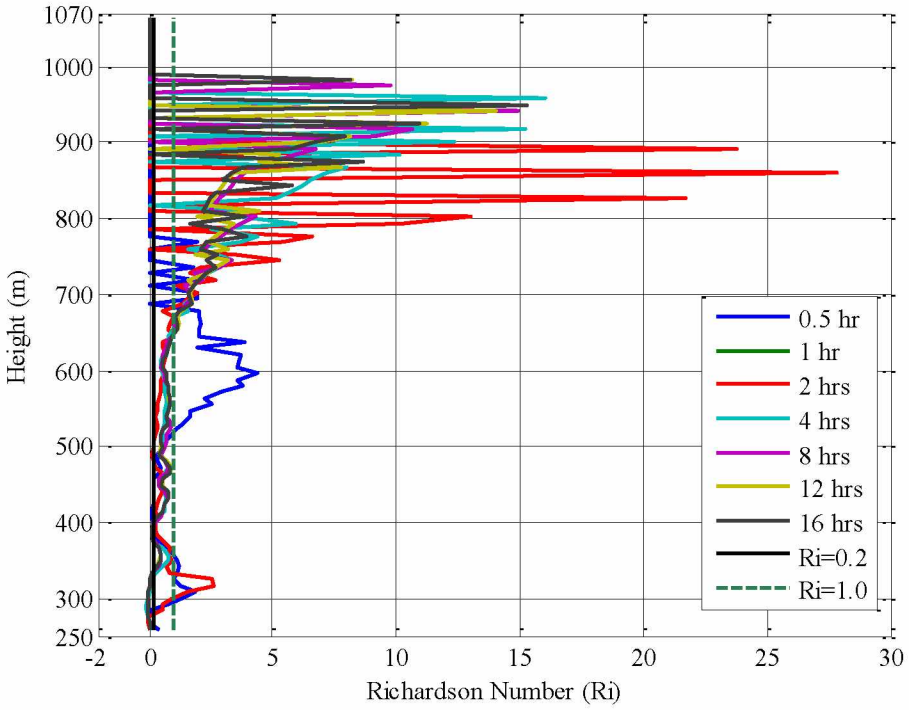

Figure 6.25: Richardson Number Profiles along Line 1 at Various Time Intervals.

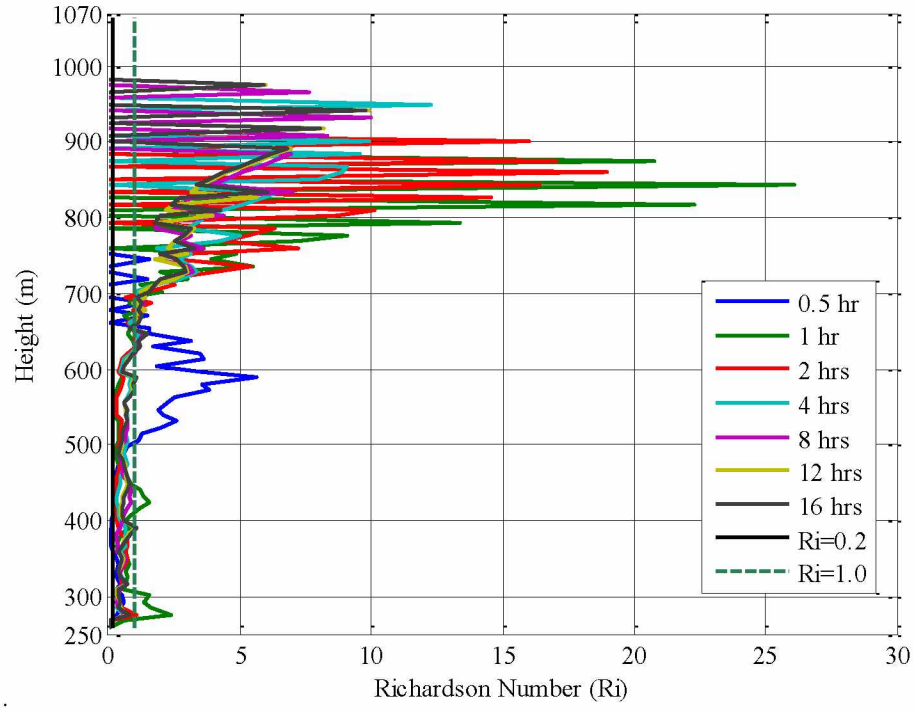

Figure 6.26: Richardson Number Profiles along Line 5 at Various Time Intervals.

From Figure 6.25, it can be seen that at the beginning ($t \approx 0.5$ hr.), the atmospheric conditions are neutral and a low TKE is observed along all the selected lines located in the pit. It appears that the inlet flow entering the pit expands and moves out of the pit. A small change in the TKE can be observed due to the wind shear/wall shear near the surface (pit wall). At an approximate elevation of 352 m (1157 ft.) and 483 m (1585 ft.) elevation levels, there is perhaps, recirculatory movement of air and /or the vorticity caused by the gaseous emission from the equipment, thus, resulting in some turbulence. The corresponding Richardson number plot shows that flow is turbulent at the pit bottom and with increasing altitude, the flow is in the intermittent zone which is characterized by a Richardson number between 0.2-1 (represented by the two vertical lines, red and black). The turbulence intensity plot for the same line (Line 1) shows that near the pit bottom, there is a high TI and with increasing height, however, its magnitude decreases.

At around four hours of simulation run, the pit is under inversion and stable boundary layer is in place. Near the surface, (pit bottom), stratified turbulence with its characteristic low frequency shear, the air velocity in Z-direction is suppressed, and flow field (as well as pollutant concentrations) disperse in X-Y direction, i.e., horizontally. The quasi-horizontal flows are examples of complex horizontal and vertical SBL structures. Such behavior is characteristic of forced two-dimensional turbulence due to density stratification (Riley and Lelong 2000). There is an increased TKE (Figure 6.17) near the pit bottom, due to the influence of constant cooling of air mass (above the pit surface) and the increased air mass density. Due to the gravity, the air flows in downward direction, resulting in increased TKE just above the surface. The vectors in Figure 6.27 show the downward direction of flow close to the pit surface. It is also important to note that the downward flow near the pit walls is due to gravity.

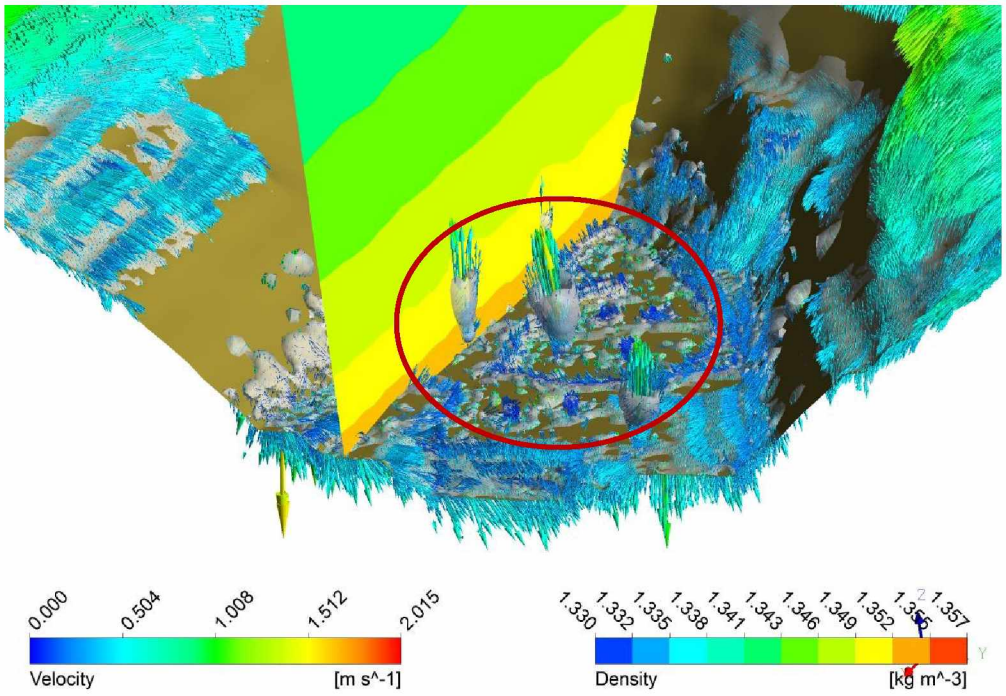

Figure 6.27**:** A Composite Plot of Density Profile, Velocity Vector and Vorticity Core Region at 4 hrs. for κ-ε Model.

However, at 352 m (1157 ft.) level, the change in the TKE level is primarily due to the buoyancy created by the operating shovels/drill located close to the vertical line (Line 1). The dynamics are strongly influenced by the presence of a stable vertical density gradient. The plumes emanating of the equipment (shown as red circle in Figure 6.27) are also a constant source of turbulence. These plumes out of equipment are forced plumes as it has both buoyancy and momentum from the exhaust (Turner 1979). Under a strong inversion, the plumes are trapped due to the air mass not possessing enough buoyant force to penetrate the stable stratified layer. Over time, however, the plumes may gain enough buoyant force to penetrate the inversion layer, it moves out of inversion layer in form of thermals. A cone shape structure can be seen in Figure 6.27 due to the formation of vortex ring. This is a result of continuous emission of pollutants into a comparatively small volume of air that is characterized by limited horizontal and vertical dispersion. The horizontal pancake-like vortex structure (Figure 6.27) of the flow can be expected to enhance the horizontal mixing of the momentum and scalars even when the vertical mixing is largely suppressed (Davidson 2004).

Line 5 is located near Line 1 but is at a considerable distance away from any equipment, starting at 260 m (850 ft.) level. Similar observations as that of Line 1 can be noted after half an hour of the simulation. The TKE and TI are very small, almost following the Y-axis at zero and increase slightly at the bottom of the pit. Around four hours of simulation, the pit is under inversion and a stable boundary layer within the pit is in place. A stable stratification of the boundary layer starts to develop just before the sunset, when the radiative cooling of the surface layer close to the pit bottom results in the development of a thermally stable layer. The vertical movement of air is suppressed and the flow fields are active mainly in the horizontal direction. Increased TKE value can be observed near the pit wall due to the gravity flow of denser air mass (Figure 6.19) which corresponds with the gradient Richardson number (Figure 6.25). The negative buoyancy as experienced by the eddy under stable stratification and the actual level of turbulence is thus mainly as a result of buoyancy production. Consequently, turbulence does not necessarily occur continuously but may have an intermittent character. The Richardson number is between 0.2 and 1 at higher elevation below 600 m (1950 ft.) which is very close to the pit rim. When unstable thermal stratification enhances above the pit rim (increased Richardson number) the mean streamline velocity profile becomes more uniform. It is mainly due to enhanced turbulent mixing, which can be observed from higher Richardson number above the pit rim. Since, the Ri is used to define turbulent regimes within SBL, Ri above the SBL is not very useful. In general, the level of turbulence is weak under SBL, other effects such as the radiative cooling influence the structure of the ABL. When turbulence is generated in the presence of stable density stratification, it often occurs locally.

Between the 475-548 m (1500-1800 ft.) levels, the fluctuation in TKE is mainly due to the wind-shear. This layer (475-548 m) is relatively close to the pit rim. The inlet air collides with the dense air mass, and due to the wind shear, turbulence is generated. During the night time, in a stable boundary layer, the source of TKE is due to mechanical wind shear production by the nocturnal jet (Banta et al. 2003). In an open pit mine, similar phenomenon of nocturnal jet and shear production can be observed at a higher elevation level of the pit, where the inlet air velocity and the temperature are constant. Thus, a large TKE can result between 475-548 m levels. However, from Figure 6.26, it could be seen that the turbulence is mostly intermittent. This intermittency could also be due to the vertical plumes from the equipment.

Similar observations can be made from other simulated time periods, only the magnitudes of TKE vary to a small extent. At the higher elevation (bench level), however, the flow is mostly in the laminar regime. Thus, it can be said that in the selected open pit under inversion, the layer close to the pit bottom is turbulent; the middle section is large scale intermittency. Whereas, the top portion of the pit is again turbulent due to shear.

An interesting observation that can also be made by analyzing the magnitudes of the turbulent kinetic energy for all the selected lines, except for Line 6 which is located at the pit rim, and outside the inversion layer. A high turbulent intensity can be observed at a height around 530 m (1750 ft.) level. This rise in turbulent intensity also corresponds with the higher turbulent kinetic energy near the pit wall/surface and tends to decrease initially and then increases again with increasing altitude. A clearly visible brown haze can be seen in the pit (Figure 6.28). The visible brown haze is due to the emissions from the diesel engines operating during the time of inversion (Waggoner et al. 1983; Senaratne and Shooter 2004). The heights where the turbulent intensity and kinetic energy are the highest, it correspond to the same brown haze height. Since, the magnitude of the TKE is unknown; a sudden increase in the turbulent intensity and the turbulent kinetic energy is attributed to the turbulence generated due to the thermal buoyancy at the pit bottom.

In general, a somewhat decaying total amount of turbulent kinetic energy is expected since the initial velocity distribution is subjected to a non-zero viscosity, and lacking additional energy input. The pit bottom surface is colder due to the negative radiation balance. As a result, the air mass above the pit bottom is denser, and settles downward, resulting in a weak turbulence. The perturbation of these turbulences, however, does not reach enough height due to weak turbulence intensity leading to its dissipation.

Figure 6.29-Figure 6.35 are composite plots of density profile, velocity vector and vorticity core regions at various times. The plane representing the density profile contains equipment in and nearby. These figures show how the density changes over time and effect of density stratification on dynamic flow fields.

Figure 6.28: Pit under Inversion with Brown Haze.

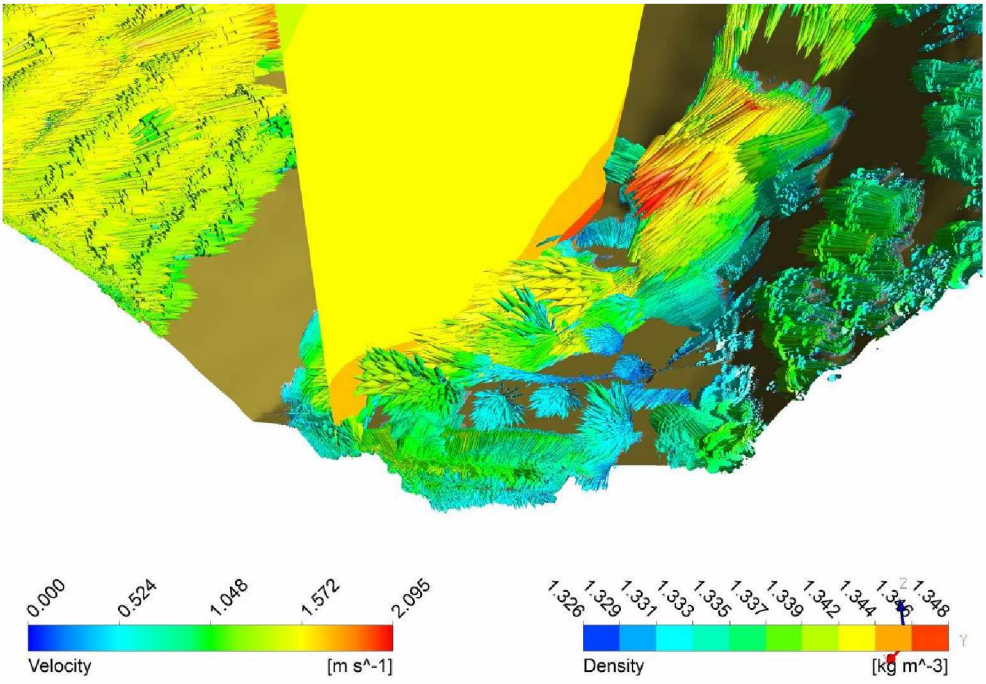

Figure 6.29: A Composite Plot of Density Profile, Velocity Vector and Vorticity Core Region at 0.5 hr. for κ-ε Model.

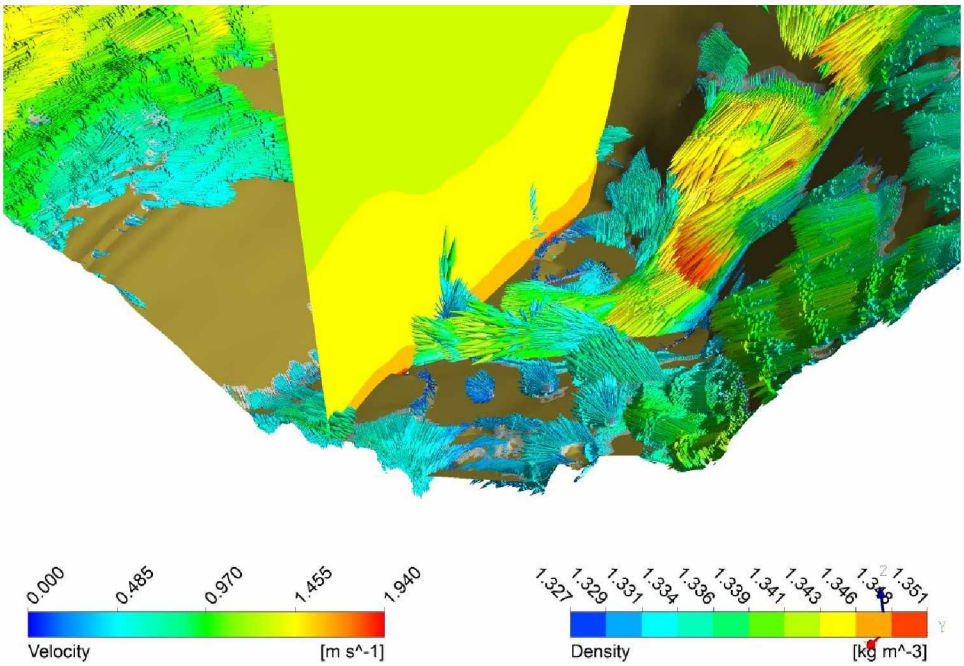

Figure 6.30: A Composite Plot of Density Profile, Velocity Vector and Vorticity Core Region at 1 hr. for κ-ε Model.

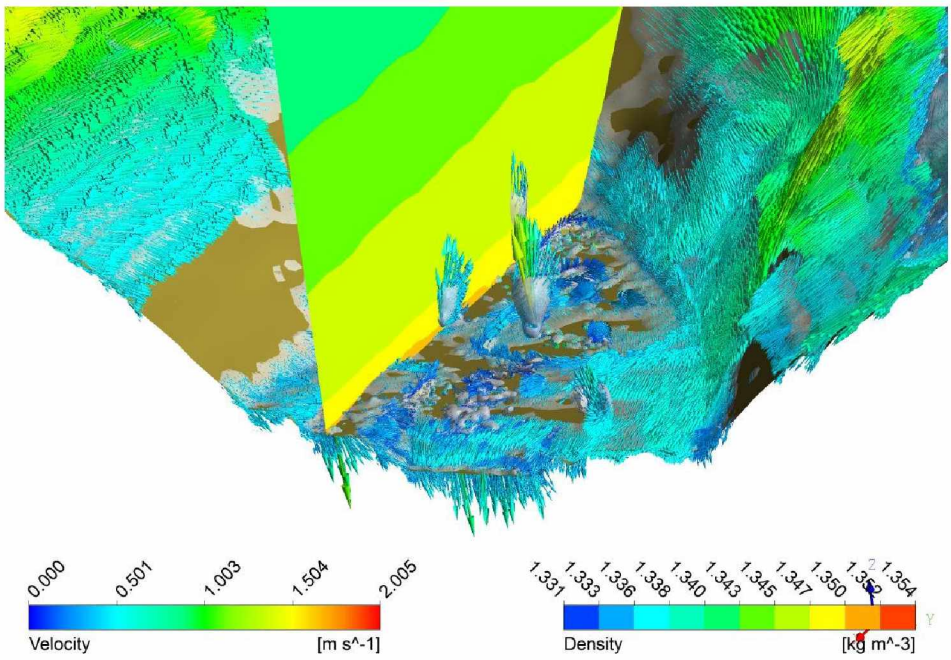

Figure 6.31: A Composite Plot of Density Profile, Velocity Vector and Vorticity Core Region at 2 hrs. for κ-ε Model.

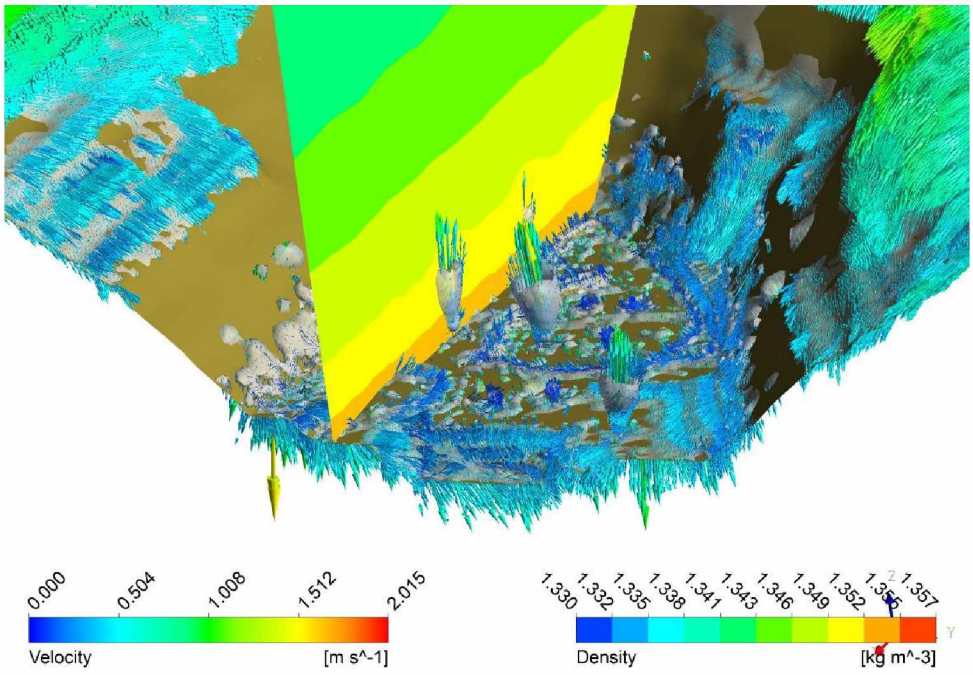

Figure 6.32: A Composite Plot of Density Profile, Velocity Vector and Vorticity Core Region at 4 hrs. for κ-ε Model.

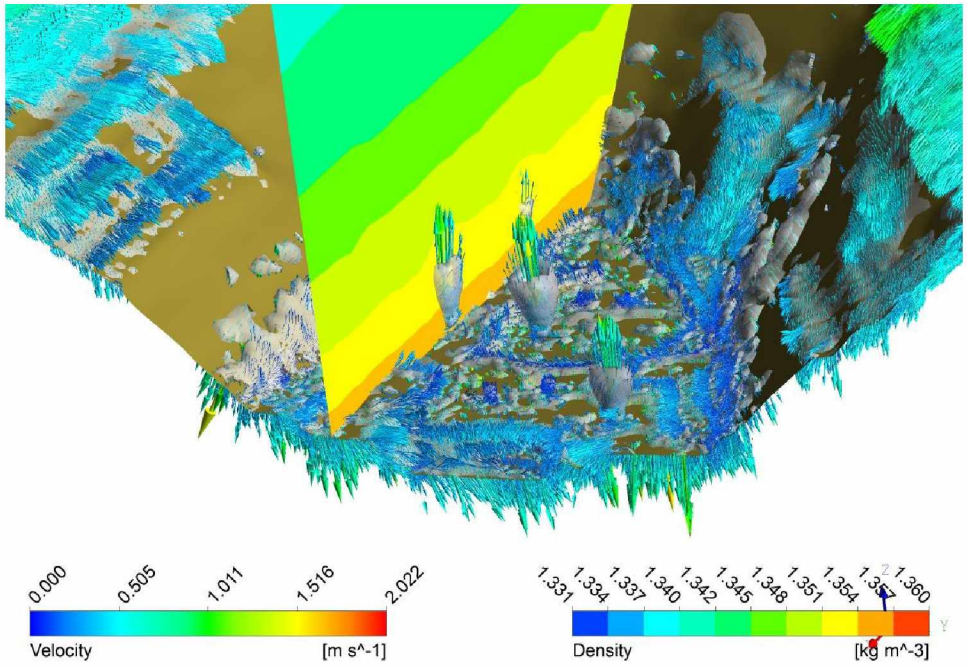

Figure 6.33: A Composite Plot of Density Profile, Velocity Vector and Vorticity Core Region at 8 hrs. for κ-ε Model.

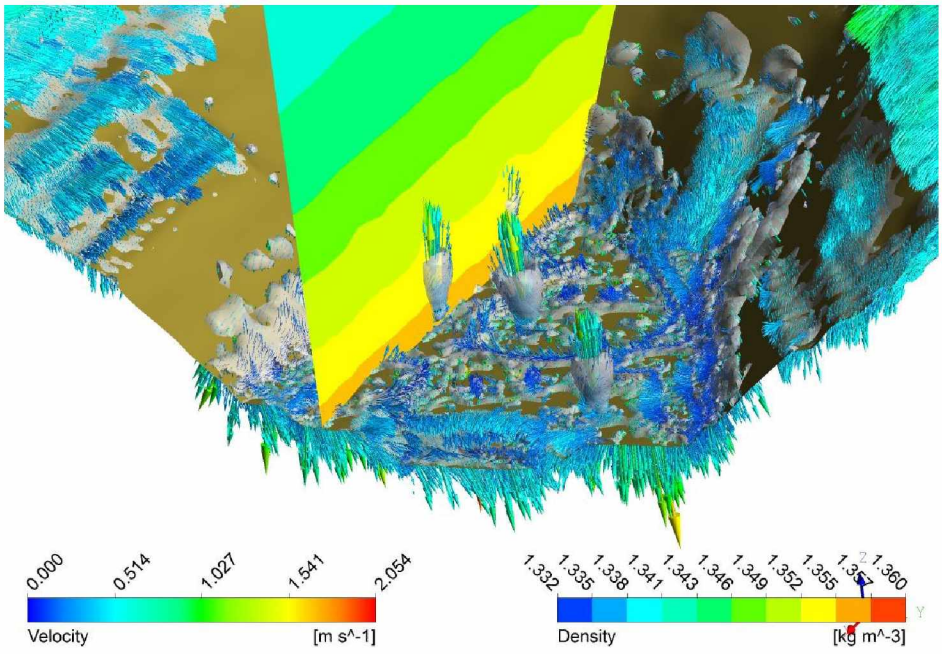

Figure 6.34: A Composite Plot of Density Profile, Velocity Vector and Vorticity Core Region at 12 hrs. for κ-ε Model.

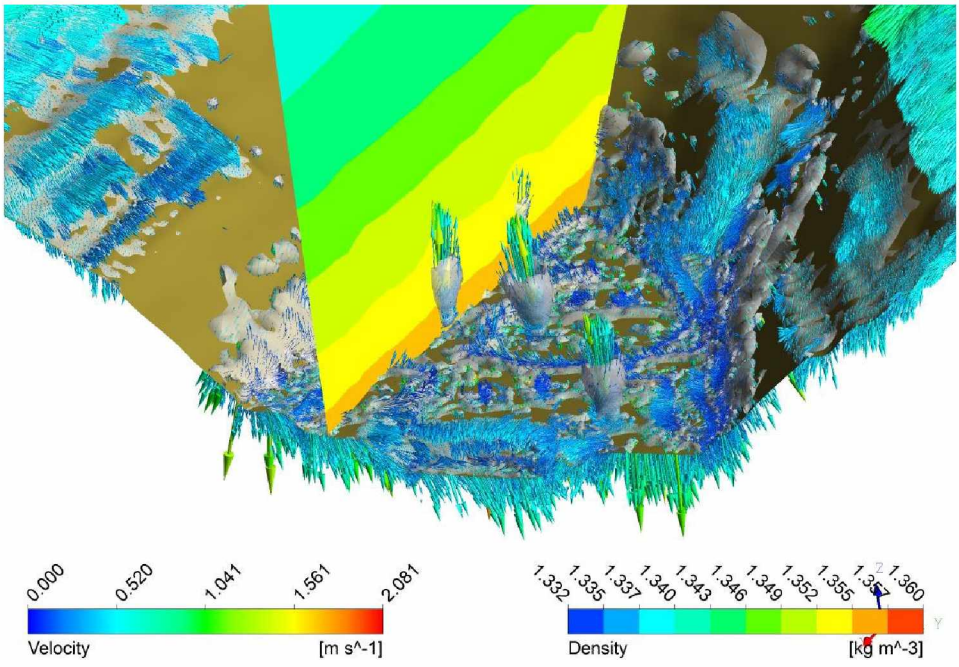

Figure 6.35: A Composite Plot of Density Profile, Velocity Vector and Vorticity Core Region at 16 hrs. for κ-ε Model.

6.6 Modeling of Contaminant Transport under SBL using LES

The air flow models of large open pit mines often features numerous complex nonlinear terms that are designed to resolve a specific problem in the problem domain. The side effects of such terms in complex flows are often not sufficiently understood.

It is important to note that ANSYS-FLUENT is a commercial CFD package. These programs are generally calibrated based on certain benchmarks and problems involving small-scale flows such as pipe flow and flow around wing bodies. Thus, the model settings are intended to aid the convergence of these types of flow phenomena. The results are therefore limited to the methods implemented in ANSYS-FLUENT, Version 13-14.

6.6.1 Meshing

The mesh created for the RANS model is used for LES modeling of air flow. Exactly same mesh is used to assess the differences in the results.

6.6.2 Time Stepping

The LES model in ANSYS-FLUENT only allows for the fixed time-stepping method. Notably, for model to converge at each time-step and to occur during initial simulation run, the time-steps must be small. Once the model convergence is achieved in subsequent time-steps, the time interval can be increased. At the initial stage of the simulation, the selected time-steps are extremely small (0.001 second) to ensure model convergence. With the progression of the simulation run, the time-step is increased to a maximum of 10 seconds. The time-steps, however, are decreased to 5 seconds for convergence of model. As in the κ-ε model, the LES model is run for 16 hours to include the diurnal cycle of the short day span and the longer night time in the Arctic. Initial simulation clock resembles 4:00 PM of the day and ends at 8:00 AM in the following day.

6.6.3 Simulation Results

Results are taken from the same vertical section plan (Figure 6.5) in East-West direction and various lines (Figure 6.7) for the LES model. Figure 6.36 through Figure 6.49 presents temperature, velocity and NO_2 concentration profiles. NO and CO concentration profiles are presented in Appendix II

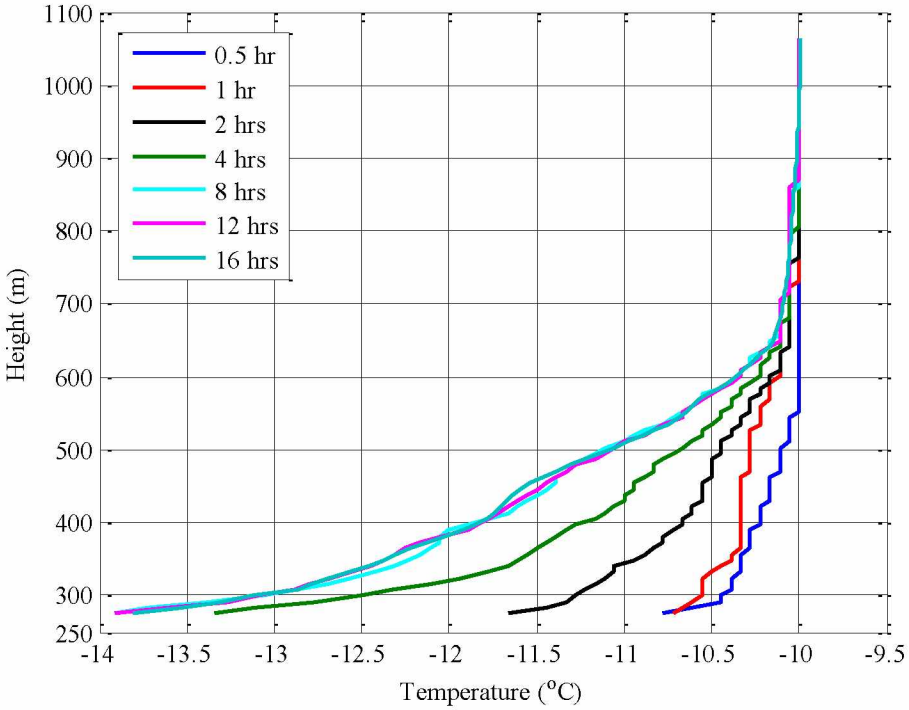

Figure 6.36: Temperature Profiles along Line 5 at Various Time Intervals.

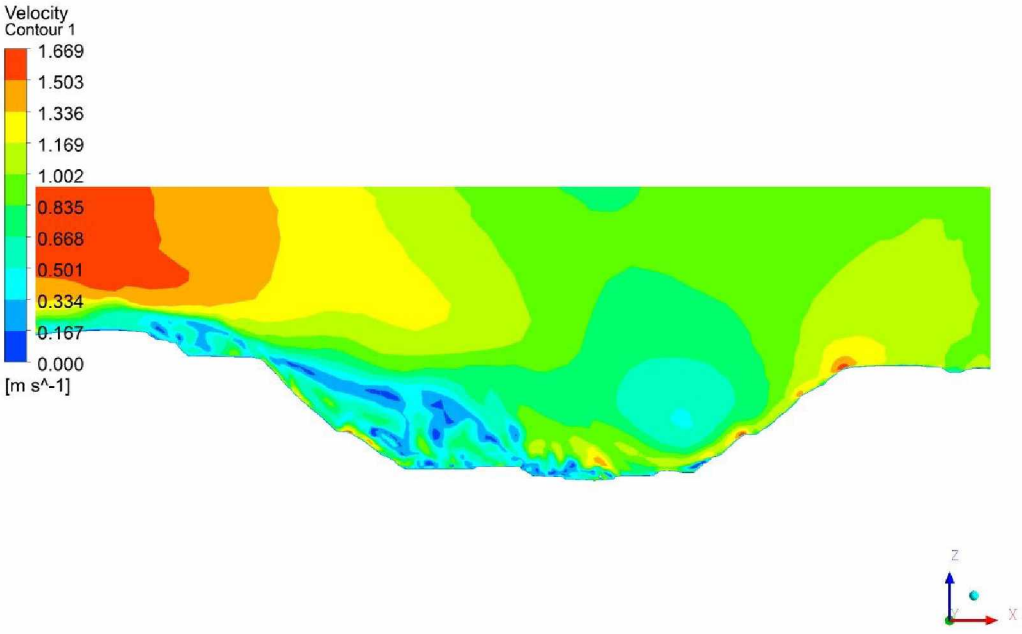

Figure 6.37: Velocity Profile at Time-Step (t ≈ 0.5 hr.).

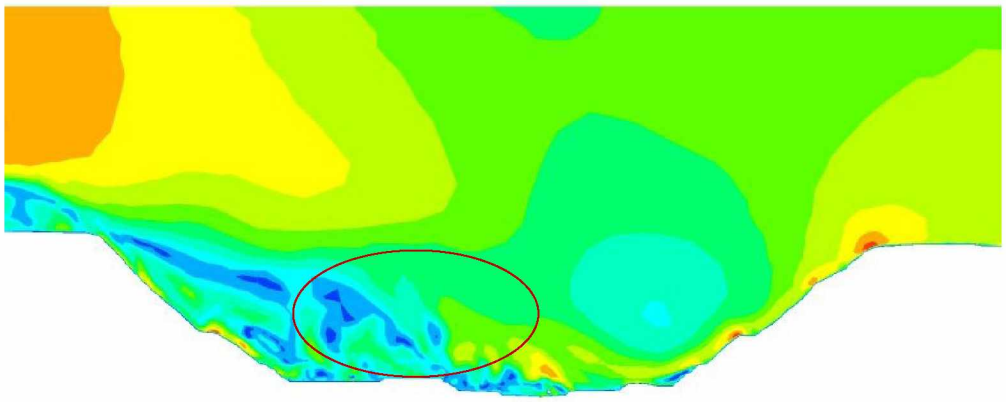

Figure 6.38: Recirculation Zone in Velocity Profile at Time-Step (t ≈ 0.5 hr.).

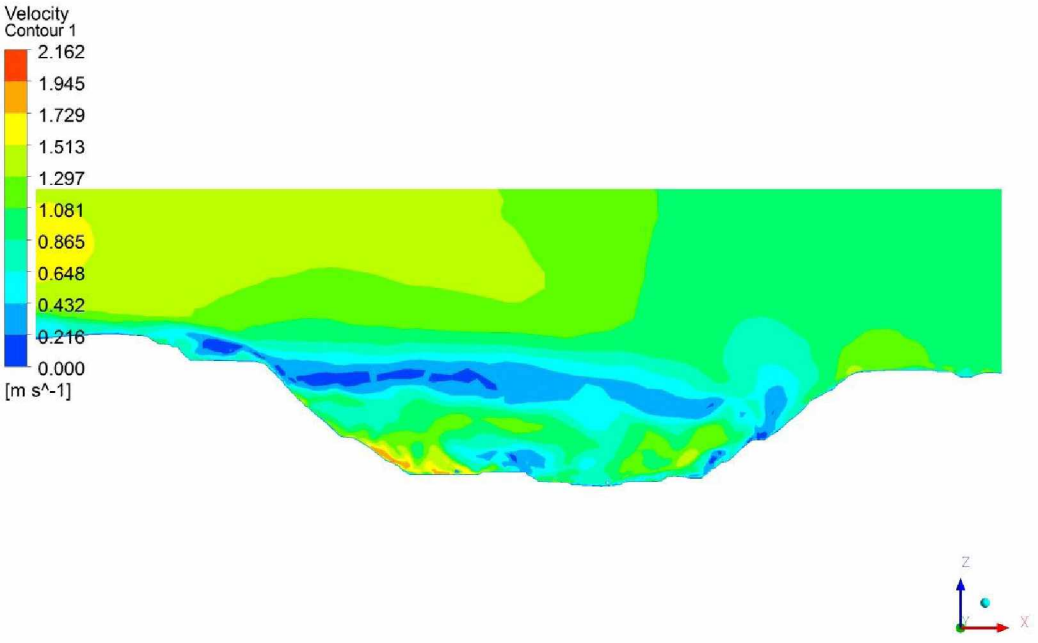

Figure 6.39: Velocity Profile at Time-Step (t ≈ 1 hr.).

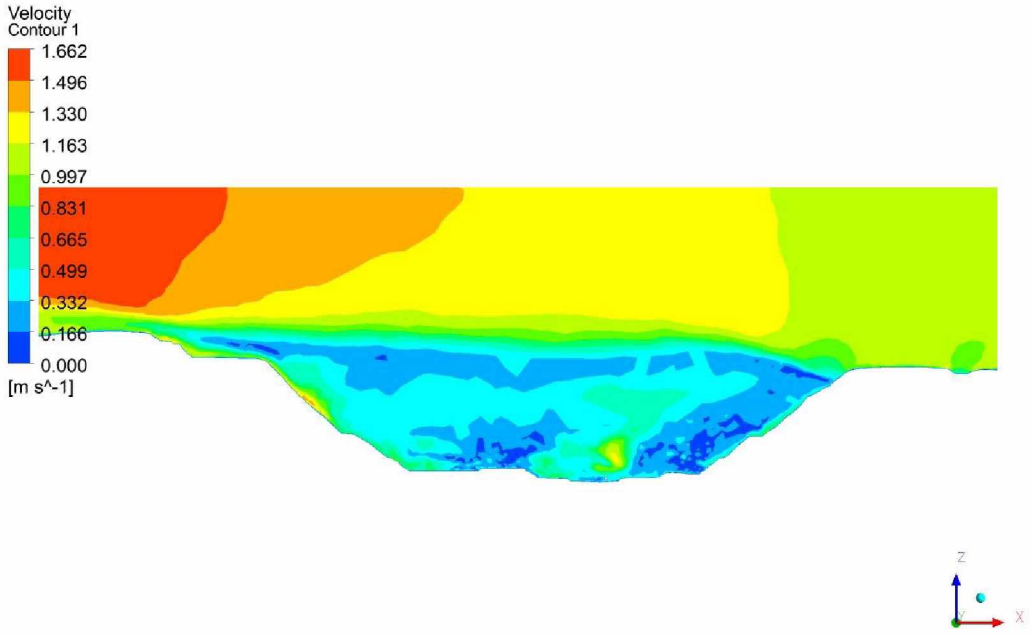

Figure 6.40: Velocity Profile at Time-Step (t ≈ 2 hrs.).

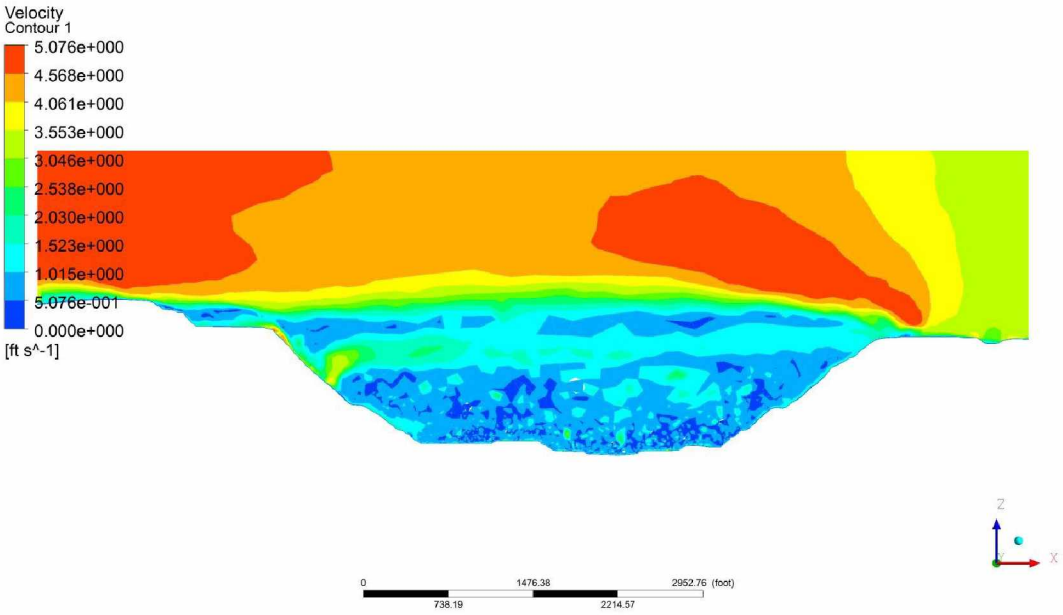

Figure 6.41: Velocity Profile at Time-Step (t ≈ 4 hrs.).

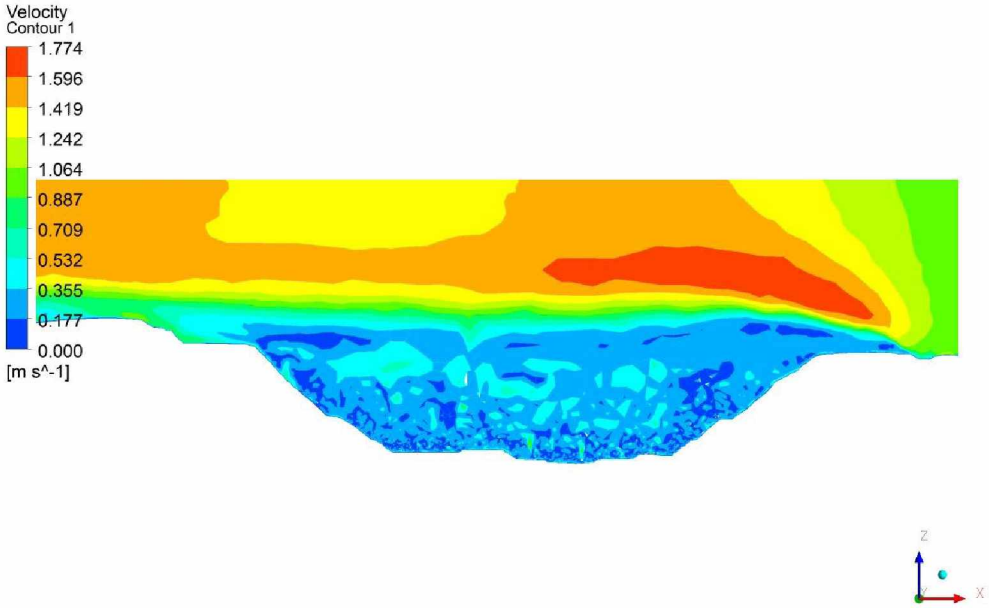

Figure 6.42: Velocity Profile at Time-Step (t ≈ 8 hrs.).

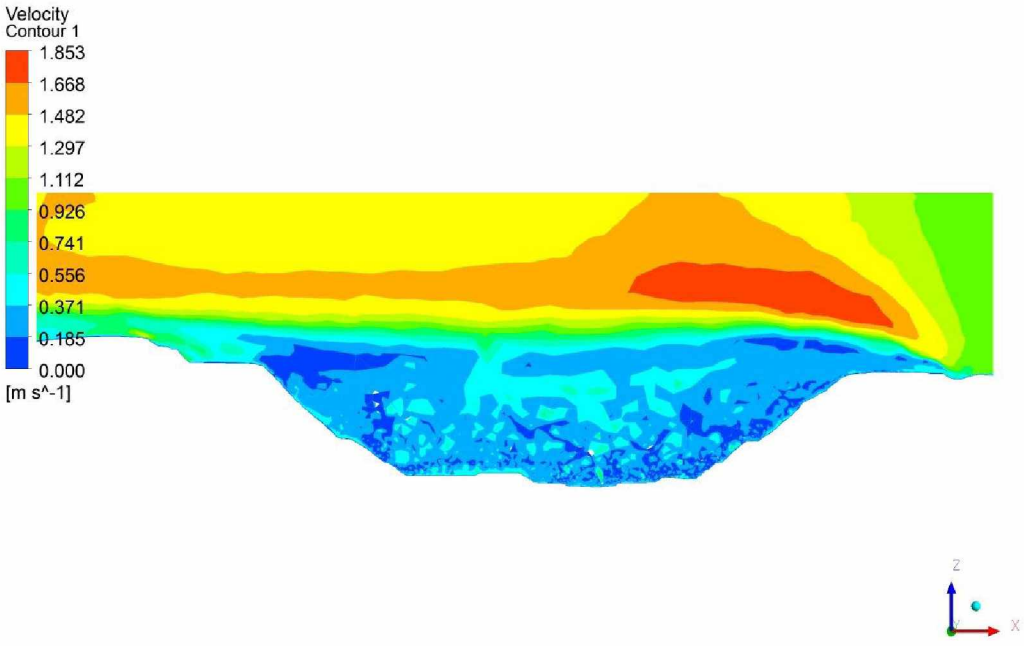

Figure 6.43: Velocity Profile at Time-Step (t ≈ 16 hrs.).

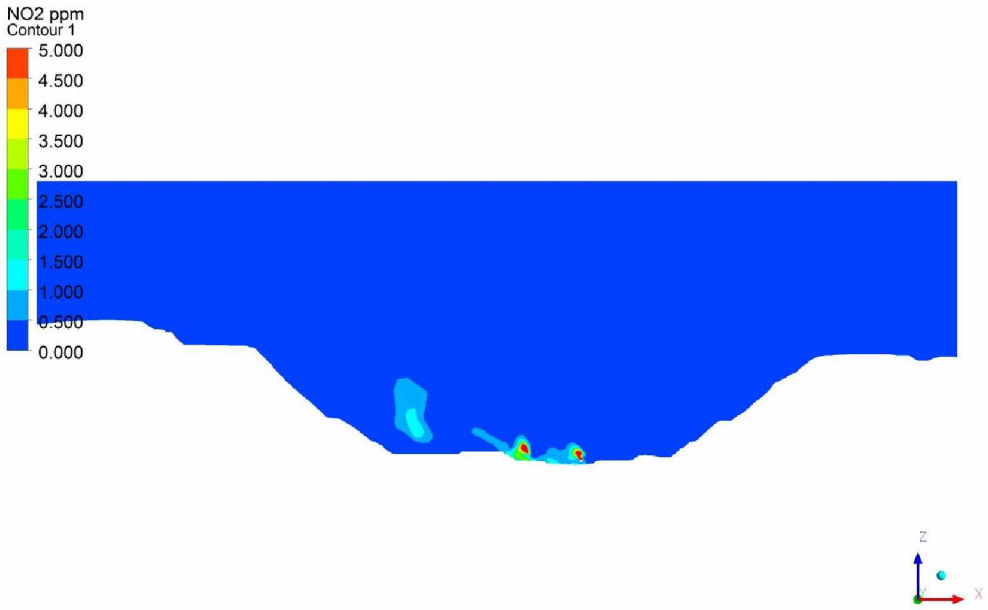

Figure 6.44: Concentration of NO_2 (in ppm) at Time-Step ($t \approx 0.5$ hr.).

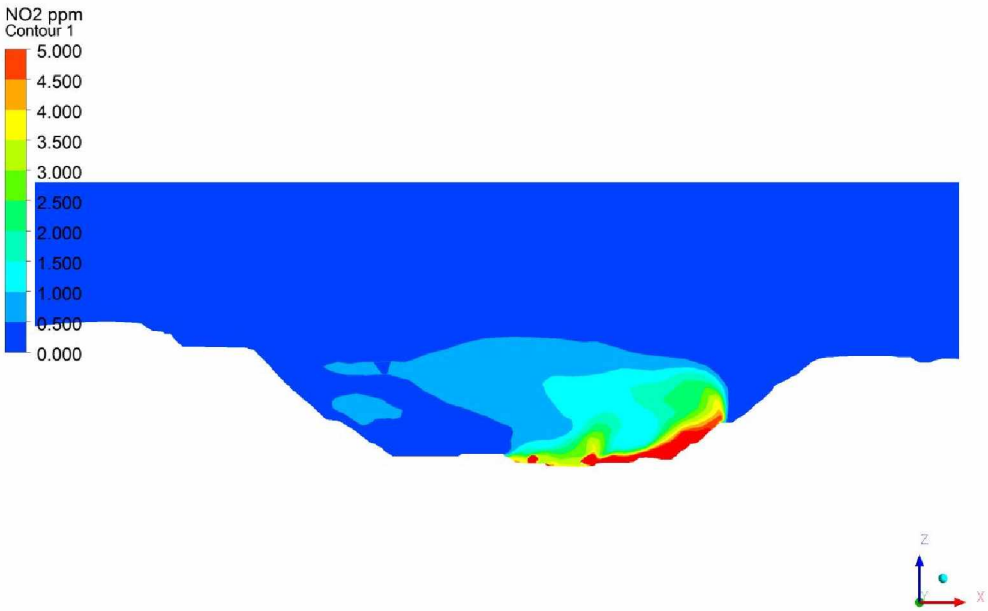

Figure 6.45: Concentration of NO_2 (in ppm) at Time-Step ($t \approx 1$ hr.).

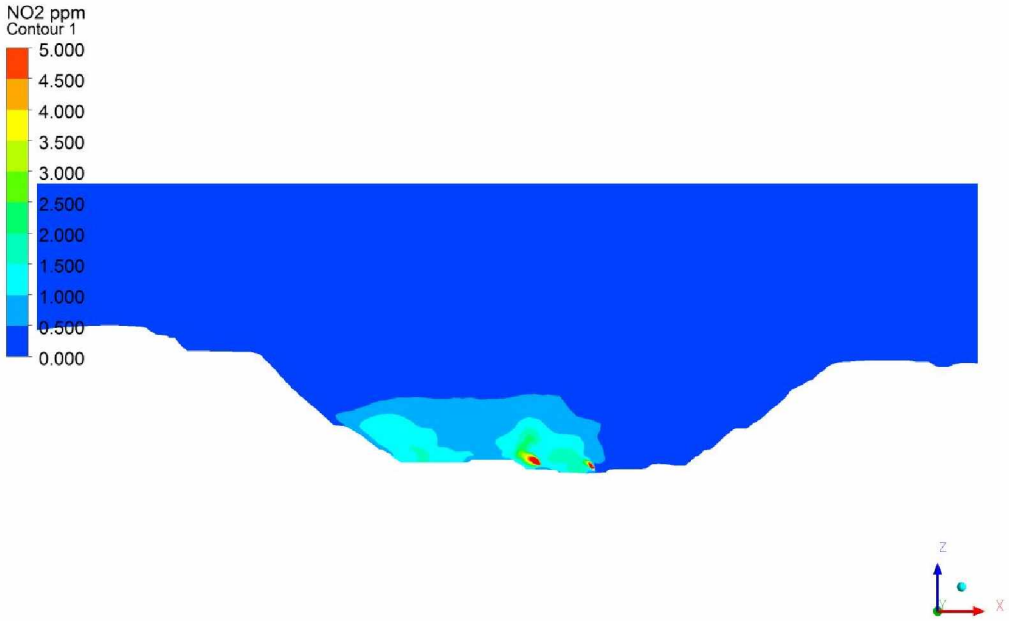

Figure 6.46: Concentration of NO_2 (in ppm) at Time-Step (t ≈ 2 hrs.).

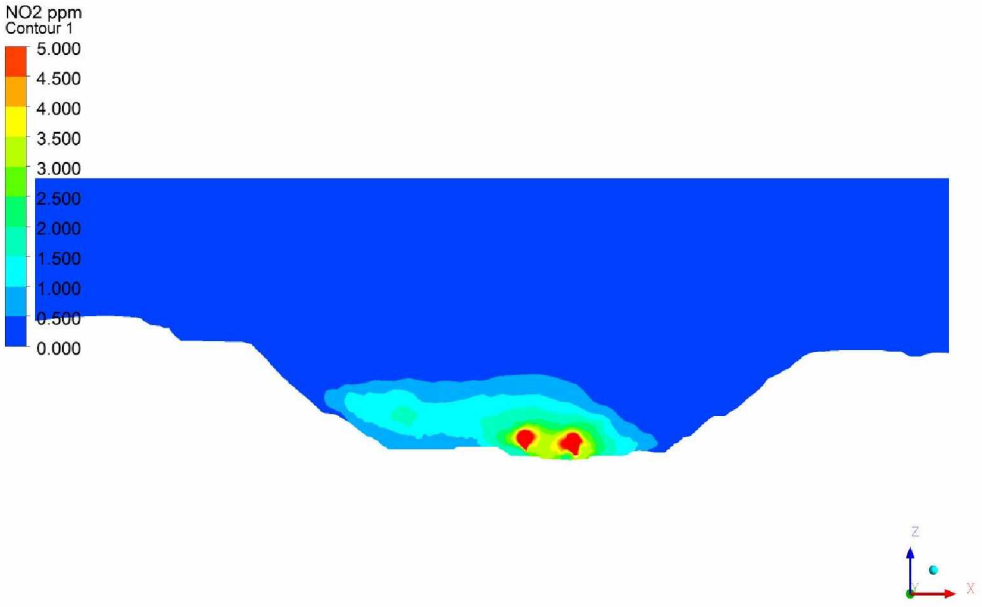

Figure 6.47: Concentration of NO_2 (in ppm) at Time-Step (t ≈ 4 hrs.).

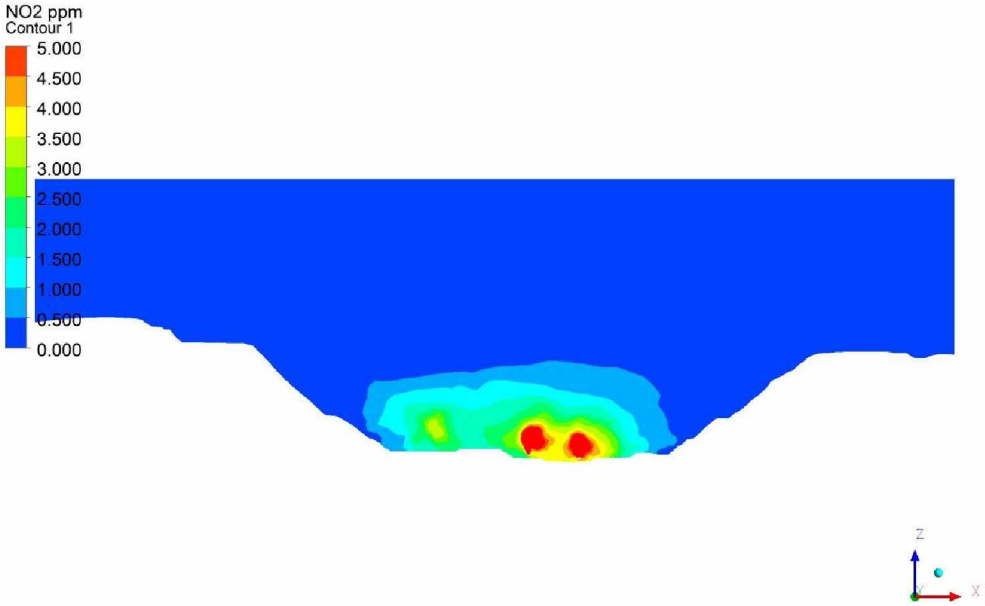

Figure 6.48: Concentration of NO_2 (in ppm) at Time-Step (t ≈ 8 hrs.).

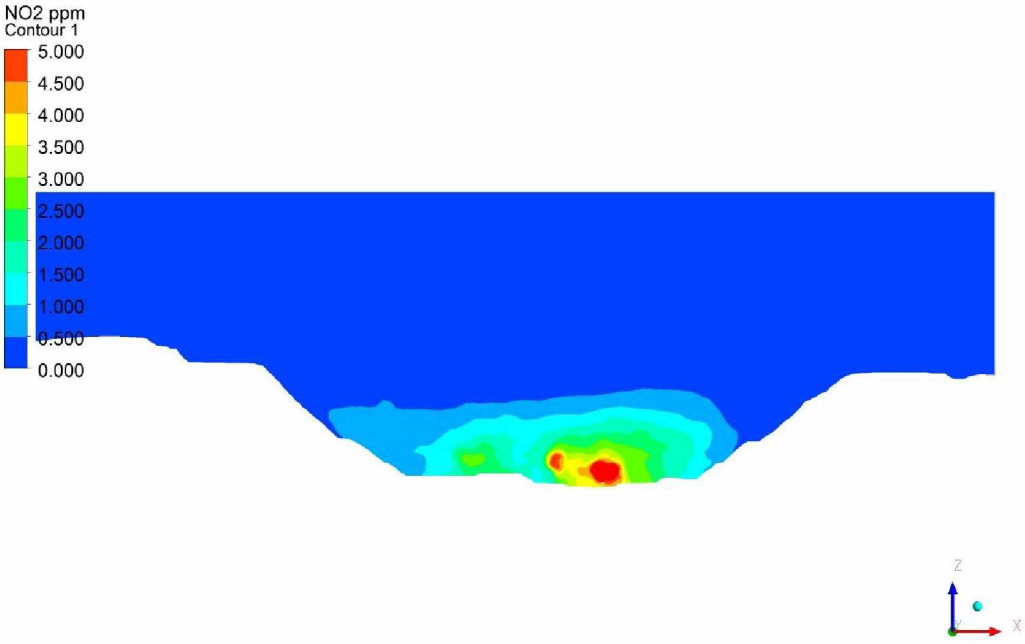

Figure 6.49: Concentration of NO2 (in ppm) at Time-Step (t ≈ 16 hrs.).

Figure 6.36 demonstrate the temperature profiles within the pit at various time intervals. A gradual increase in the strength of inversion over time is seen in Figure 6.36. It is also interesting to observe the step-like structure of the temperature profiles. This is the result of the LES simulation outcomes. The LES produces instantaneous value of the variables modeled making the structure step-like. On the other hand, temperature profiles (Figure 6.8) of the κ-ε model are smooth as κ-ε based on RANS produces time-averaged simulation results. The velocity profiles of wind are presented in Figure 6.37 to Figure 6.43 and demonstrate that the air velocity within the pit gradually decreases as the dense air starts settling at the bottom of the pit with increasing inversion strength. The pollutant concentration distributions (NO_2) are presented in Figure 6.44 to Figure 6.49. With growing inversion intensity within the open pit, the pollutant concentration continues to increase.

The initial and boundary conditions are similar to those of the realizable κ-ε model. Figure 6.36 demonstrates the temperature profile at approximately 30 minutes from the start of the simulation run. The change in the thermal regime at the bottom of the pit is observed; however, the effect of change is insignificant in the retention of any contaminants (Figure 6.44) in the pit bottom. At this juncture, the velocity profile (Figure 6.37) indicates the presence of several, although small, recirculation zones in the pit.

An enlarged version of Figure 6.37 is presented in Figure 6.38 to clearly demonstrate the presence of various sizes of eddies in the recirculatory zones within the pit. Since, there is no inversion yet developed, the air mass coming from the East boundary of the pit (inlet boundary) reaches the leading edge of the pit, where it fully expands. At this point, the flow separates into two parts: one goes over the pit and the other goes into the pit. The air mass flowing within the pit has a lower energy, and further loses energy when it comes in contact with the pit wall, so the velocity lowers within the pit.

After approximately one hour of simulation, changes in the temperature profile (Figure 6.36) near the East side of the pit wall are apparent; however, at this point, the air velocity has a role in distributing the temperature within the pit. From the velocity profile (Figure 6.39), the presence of some recirculatory zones in the pit is observed; however, a shift in the position and the size of these eddies is also apparent. Thus, it is suggested that the change in the thermal regime in the pit affects the characteristics of the eddies within the pit. From the velocity profile, the variation in

the velocity contours within the pit can also be observed. In the West portion of the pit, (leeward side) there is a zone with a high velocity and, in contrast to the middle portion of the pit which is a zone with a low velocity. When the thermal regimes are compared in both zones, the effect of temperature change on the velocity and vice versa can be observed. The corresponding concentration profile (Figure 6.45) of NO_2 indicates some visible accumulation in the region where the thermal regime changed with a low air velocity.

The temperature profile (Figure 6.36) after two hours of simulation displays a significant change in the thermal regime within the pit, and the presence of inversion layers is evident. Figure 6.36 demonstrates that the change in the thermal regime covered more than half of the pit depth. This change prevails due to the negative heat flux at the pit wall. The ground surface is losing heat due to rapid cooling of the air masses just above the surface compared to the air masses above it. Corresponding to the temperature change, the density of the air mass also changes according to the incompressible ideal gas law, where density is only the function of temperature assuming constant pressure. The change in density is directly reflected on the velocity profile (Figure 6.40), where there is a noticeable change in the velocity profile within the pit. As the lighter air mass from the inlet boundary comes in contact with the slightly denser air mass, the air velocity changes at the point of contact. There is still a flow separation region in the pit, but this time, the occurrence of flow separation is not as prominent. This is because the air coming from the inlet is less dense, and when it comes in contact with the air of high density over the pit, it acts as the large flat plate with flat plate surface density slightly higher than the air mass. Therefore, the thin flow of varying velocity over the denser air masses becomes apparent. Additionally, due to the wind shear, the air velocity of the denser air mass changes little. Figure 6.40 demonstrates two distinct zones of flow velocities: one just above the dense air mass and one within the dense air mass in the pit. A high velocity zone also exists within the pit due to the temperature change. There are two pieces of equipment near the section plan from where the results are taken. Heat emitted from the equipment surfaces and the exhaust changes the velocity profile in that near-region.

The concentration profile of NO_2 is now visible in the pit. Figure 6.46 illustrates that the West portion within the pit is covered by NO_2; however, the concentration is still below the NO_2 threshold value.

Similarly, with increasing time, the inversion strength increases, and the air mass within the pit becomes much denser and heavier. The change in the temperature and density directly impacts the flow regime within the pit. The air mass within the pit has an extremely low velocities (ranging from 0 to 0.55 m/s) compared with the less dense air out of the open-pit with velocities ranging from 0.55 to 1.85 m/s, and there is negligible impact on the air mass within the pit due to the inlet air velocity. These observations cause pollutants to accumulate within the pit. However, the NO_2 concentration within the pit does not exceed the threshold value of 5 ppm during the entire simulation run. This might be due to the value of time-stepping used in the simulation. LES needs a much finer grid and a small time-stepping for a good quality results. It is extremely likely that a high value of time-steps (between 1 to 10 seconds) affects the pollutant concentration. The turbulence scale within the pit varies in size, and the turbulence scale from the equipment is extremely small in comparison to the overall scale of the model. The smaller time-step tends to capture small scale turbulence. Thus, it is important to use an extremely small time-step in the simulation run.

6.6.4 Turbulence Results from the Simulation

In order to analyze the turbulence with the SBL developed using the LES, similar to the realizable κ-ε, Richardson number (Ri) is calculated along the selected lines (1 and 5). Presented here are the temperature profiles (Figure 6.50 and Figure 6.51) along Line 1 and Line 6 for explanations. Figure 6.52 and Figure 6.53 show the Richardson number plot along Line 1 and 5 at different time intervals.

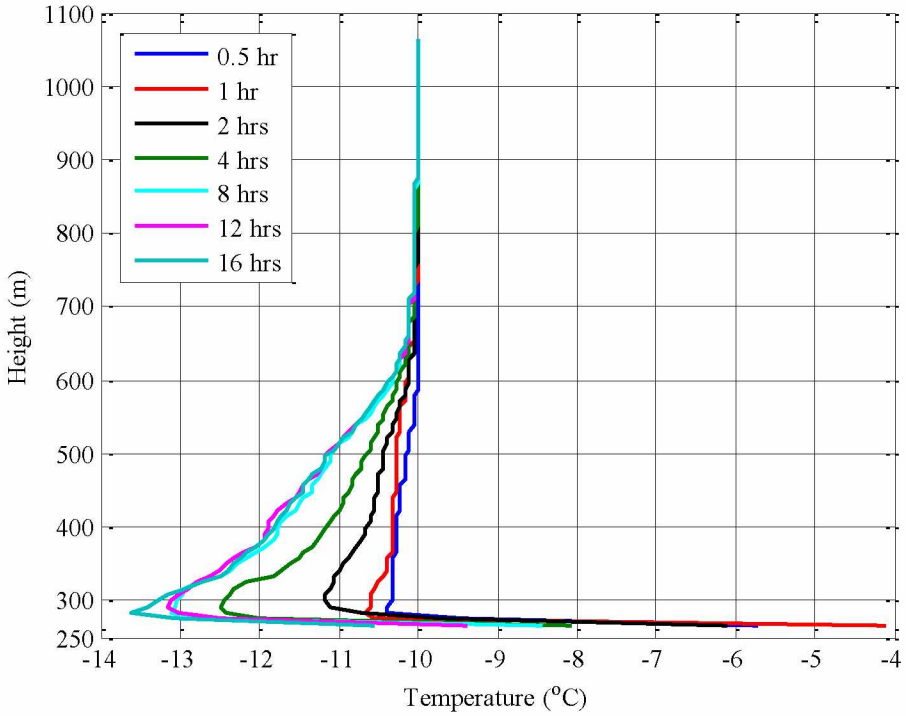

Figure 6.50: Temperature Profiles along Line 1 at Various Time Intervals.

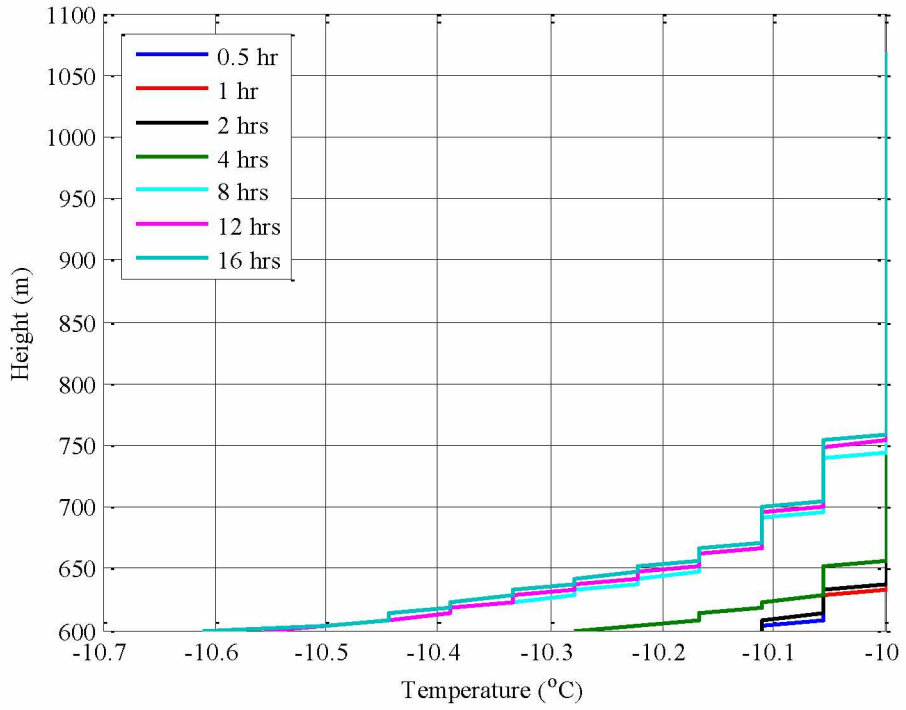

Figure 6.51: Temperature Profiles along Line 6 at Various Time Intervals.

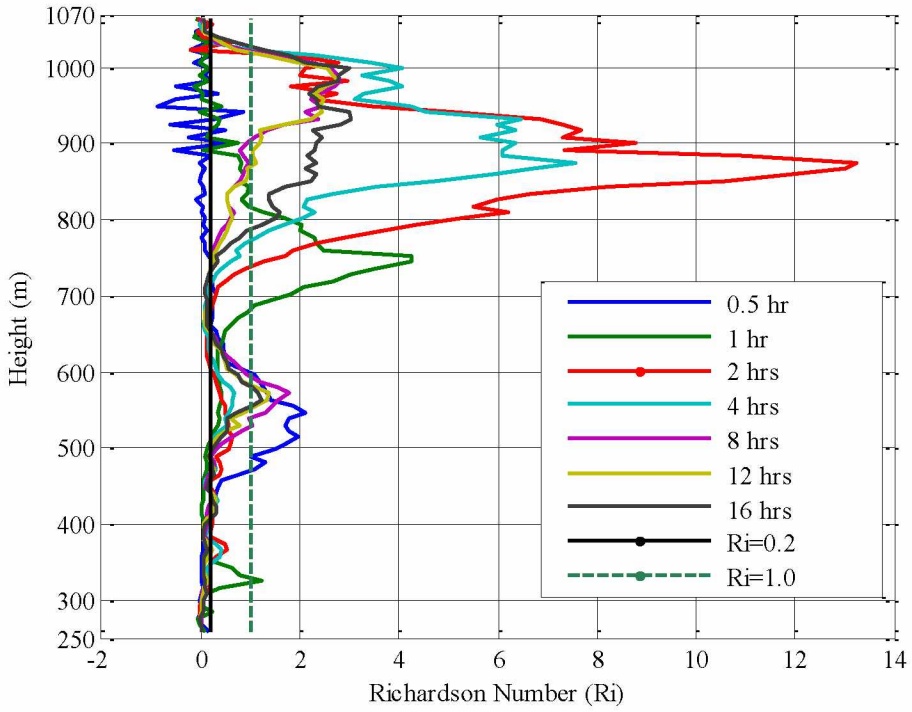

Figure 6.52: Richardson Number Profiles along Line 1 at Various Time Intervals.

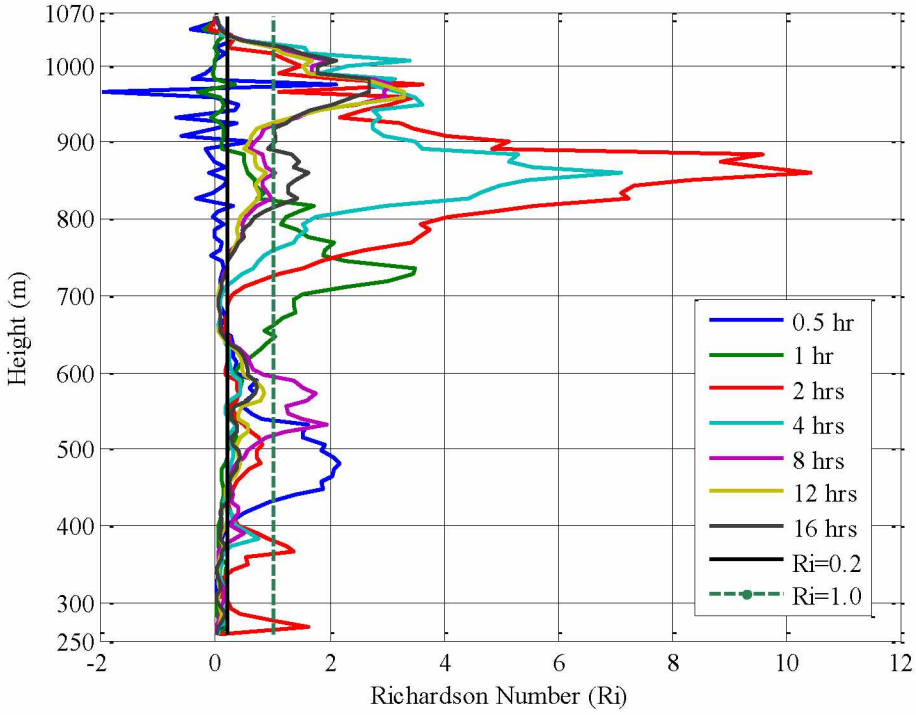

Figure 6.53: Richardson Number Profiles along Line 5 at Various Time Intervals.

From Figure 6.50, it can be seen that the temperature at the bottom of the pit is decreasing with time, however, there is a sudden jump or rise in temperature. It is because the line is very close to

an equipment. At higher elevation, the temperature should decrease with time. The behavior is clearly exhibited in the temperature profile along line 1.

As stated, Line 6 is located at the pit rim and the temperature profile is in contrast with Line 1. The development of SBL is affected by both inlet air temperature and the inlet air velocity. At the pit rim, turbulent mixing is on-going and development of SBL is rather small. At around four hours, the pit is under the stable boundary layer. From the velocity profile (Figure 6.41) at four hours, a flow separation can be observed. This indicates that the strength of inversion is still weak and there is a movement of pollutants towards the leeward side of the pit.

At around sixteen hours, existence of turbulence could be observed, which is primarily due to thermal buoyancy. Referring to velocity profile (Figure 6.43), one could observe the suppression of upward buoyancy due to strong inversion (SBL), the vortex of the pollutants expends in the X-Y dimensions, indicating horizontal mixing (Figure 6.60). The circulation has reversing, low velocity and capping structure due to SBL. Between elevation levels of 500-600 m, the turbulent is intermittent, and between 650 to 750 m, the flow is again turbulent due to the presence of wind shear, an effect of the inlet wind velocity. At elevation between 750 to 800 m, the flow seems to be intermittent, and at the elevation beyond 800 m elevation, the flow can be characterized as laminar. At the bottom of the pit (250-300 m elevation level), the flow is turbulent ($R_i < 0.2$). The air is relatively denser. Above 350 m elevation level, the turbulent is generally intermittent. At higher elevation of 800 m and above, the flow becomes laminar (as indicated by the Richardson number).

Along Line 5 (Figure 6.36), a decrease in temperature is exhibited with time, due to radiative cooling of the pit surfaces. At higher elevation, the temperature attains a value of -10°C (14°F), due to the imposed boundary condition. In all of these figures, the development of SBL can be observed, and the SBL moves upward direction over time (around half an hour to 480 m; around 2 hour to 600 m; at 8 hour to 700 m, which is the height of the inversion layer or SBL. An intermittent layer formation can be seen around 600 m; however, it changes over time.

Richardson number (Ri) is most commonly used to explain flow under SBL. The Richardson number plot along Line 1 (Figure 6.52) indicates that between at around 0.30 hours, at elevation between 250 to 400 m, the Richardson number for this region is between 0.0 to 0.2, i.e., $0 < Ri < 0.2$, the flow is turbulent. The boundary layer is however not yet stable. The line 1 is located very

close to equipment; there is some upward thermal buoyancy. This buoyancy gets dissipated at around 400 m level, primarily due to wind shear. The zone between the 450-475 m elevation level, the value of the Ri is between 0.2 and 1.0 ($0.2 < Ri < 1.0$), the flow can be characterized as intermittent. Elevation above 475 m level, the Richardson number is greater than one ($Ri > 1.0$), the flow at this level can be classified as laminar flow. Near the pit rim (elevation 550-650 m levels), the flow is intermittent. Above an elevation of 650 m, unstable turbulent flow is dominant. The vertical profiles of the Richardson number at 8.0, 12 and 16 hours, have the similar trend.

Line 5 is not located near any equipment. During the first 30 minutes of simulation, there is no inversion at elevation levels between 250-400 m. Flow separation can be observed at the pit rim (Figure 6.37). The air in the pit moves towards the leeward side. Small eddied can be seen in the pit. The flow is mostly in the horizontal direction and there is less turbulence as can be seen from the composite plot (Figure 6.54). The Richardson number is less than 0.2 ($0.0 < R_i < 0.2$), these values are very similar to line 1, and mostly affected due to the initial simulation bias.

At around four hours, at elevation levels between 250-375 m levels, the flow is turbulent because of dense air mass settling due to negative buoyancy (Figure 6.57). This zone being close to the pit bottom, there is a constant rate of cooling, thus, creates a downward flow. Between 375-650 m levels, turbulence is intermittent. Any turbulence created is due to wind shear at higher elevation. After 600 m level, the velocity increases due to shear resulting from the inlet air. Beyond the 750 m level, the flow is laminar and consistent with observations along Line 1.

After 8 hours of simulation, there is not much change in the system dynamics. High velocity (Figure 6.58) results at the pit bottom (250 m elevation) primarily due to negative buoyancy. An increased magnitude of velocity can be noted at the 600-800 m elevation level due to inlet velocity. The magnitude of the velocity is, however, more than the inlet velocity magnitude. The entire pit surface cools down due to the net negative radiation balance. The inlet velocity is at higher temperature (-10°C) tries to mix with the cold air in the model domain (open pit) results in creating turbulence in the windward side (leading edge) of the pit. Near the windward side, flow separation also takes place, creating higher velocity zone.

Figure 6.54 through Figure 6.60 are composite plots of density profile, velocity vector and Vorticity core regions. The plane representing density profile contains equipment in and nearby.

These figures show how the density changes over time and effect of density stratification on dynamic flow fields.

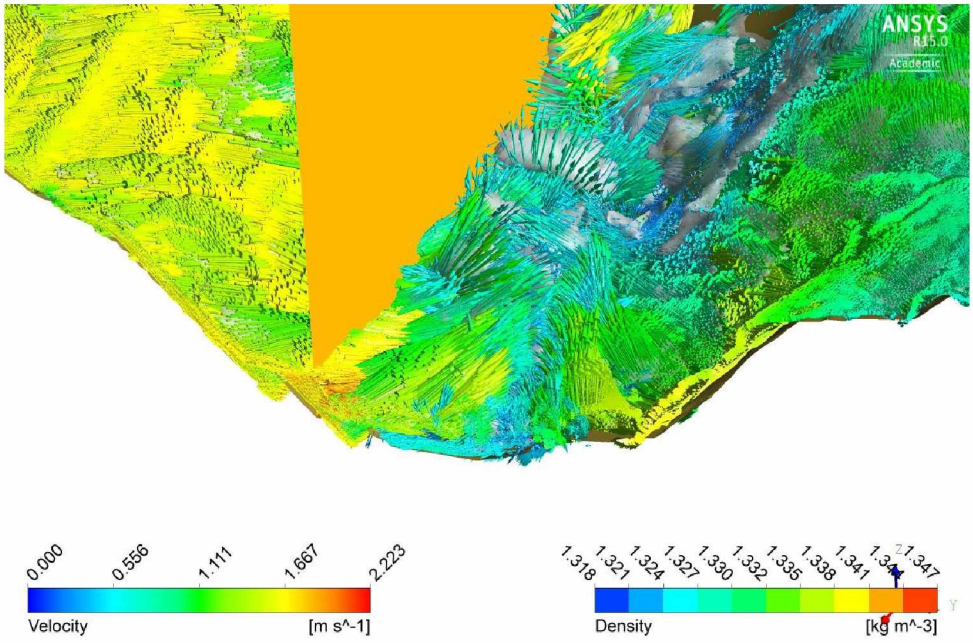

Figure 6.54: A Composite Plot of Density Profile, Velocity Vector and Vorticity Core Region at 0.5 hr. for LES Model.

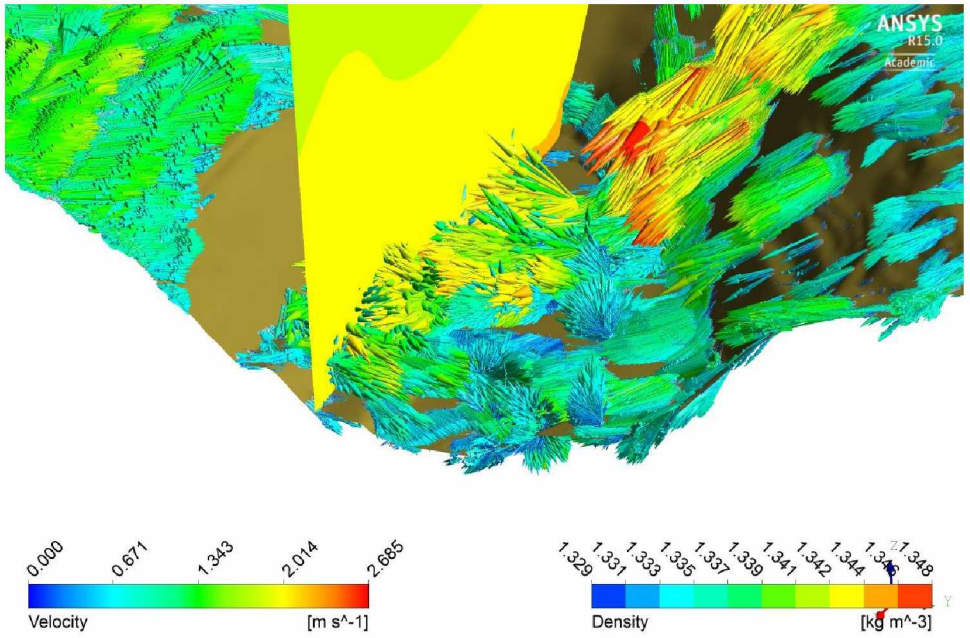

Figure 6.55: A Composite Plot of Density Profile, Velocity Vector and Vorticity Core Region at 1 hr. for LES Model.

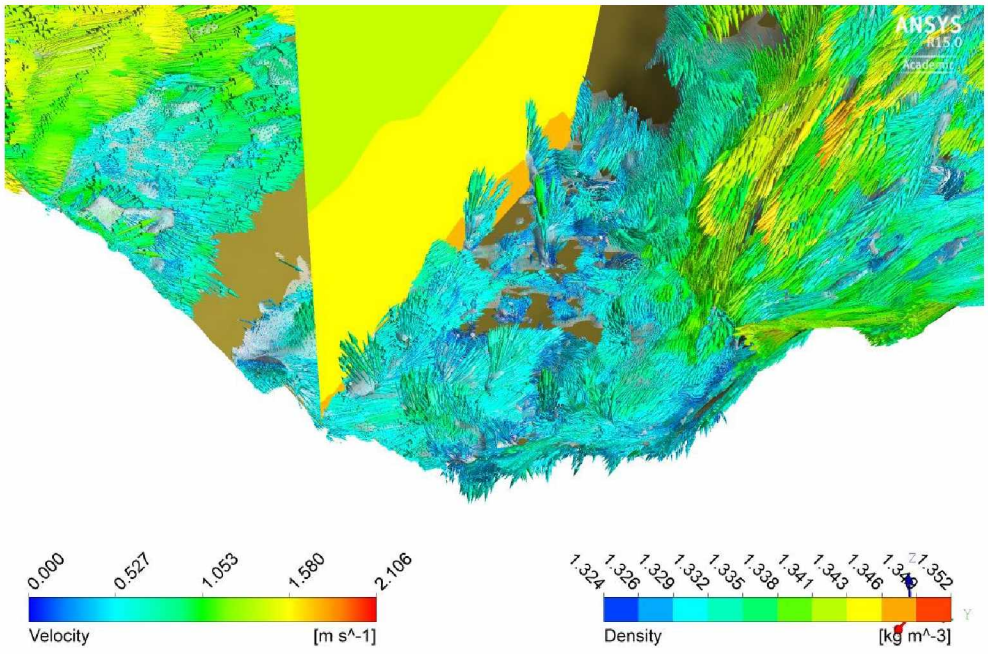

Figure 6.56: A Composite Plot of Density Profile, Velocity Vector and Vorticity Core Region at 2 hrs. for LES Model.

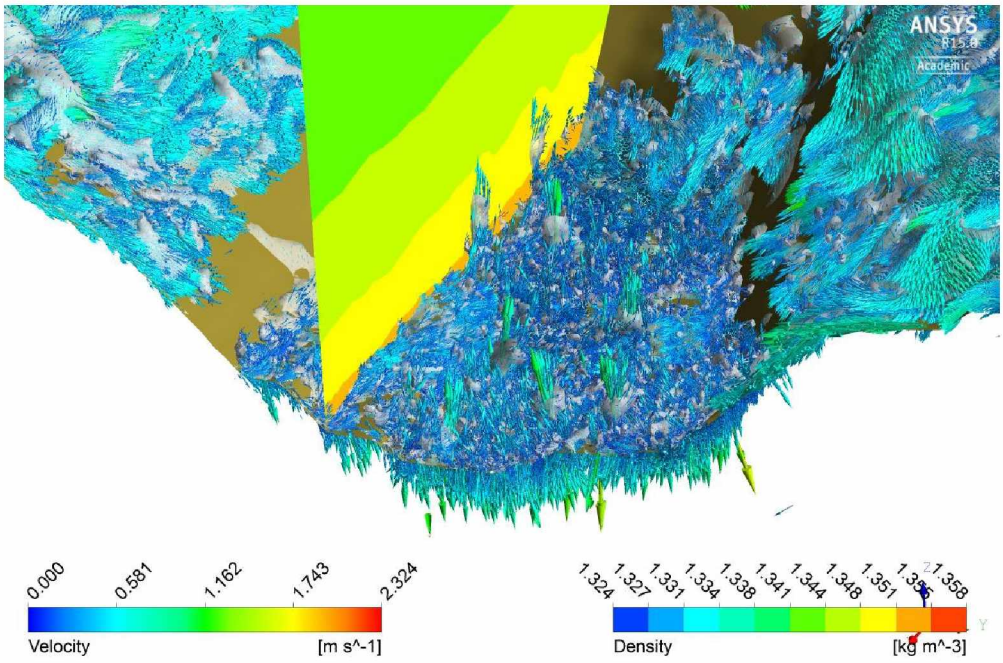

Figure 6.57: A Composite Plot of Density Profile, Velocity Vector and Vorticity Core Region at 4 hrs. for LES Model.

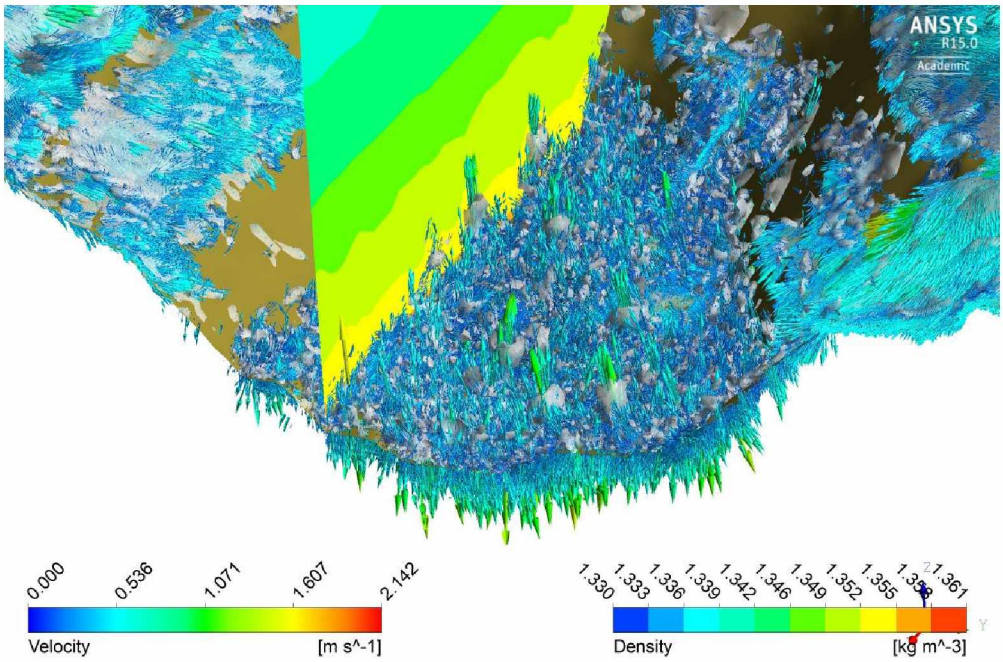

Figure 6.58: A Composite Plot of Density Profile, Velocity Vector and Vorticity Core Region at 8 hrs. for LES Model.

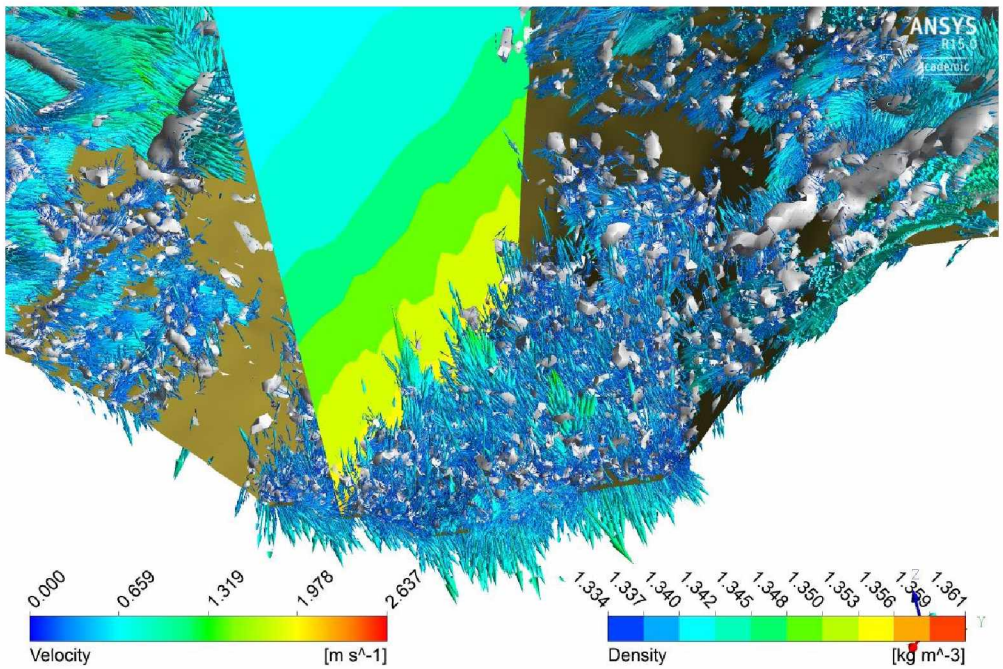

Figure 6.59: A Composite Plot of Density Profile, Velocity Vector and Vorticity Core Region at 12 hrs. for LES Model.

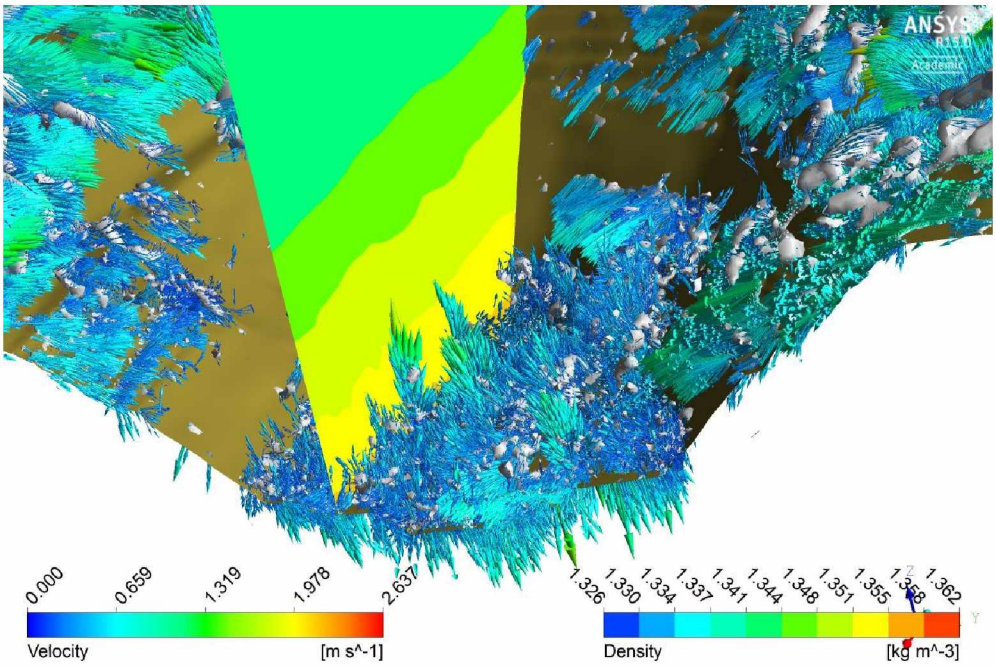

Figure 6.60: A Composite Plot of Density Profile, Velocity Vector and Vorticity Core Region at 16 hrs. for LES Model.

6.7 Comparison of Turbulent Models

A number of simulation runs have been performed either using a realizable κ-ε model or a LES model. To overcome the difficulties found with the RANS simulation, more sophisticated and challenging methodologies of turbulent treatment are analyzed. A second approach to the turbulence modeling which is gaining more and more applications is the Large Eddy Simulation, which is based on the space filtered Navier-Stokes equations. The finite volume technique is equivalent to applying a space filter to the Navier-Stokes equations; in this fashion only the big eddies whose dimensions are larger than the filter width, which is connected to the cells dimensions, are computed directly. The non-resolvable eddies or sub-filter eddies are modeled with specific turbulent models named sub grid scale (SGS) turbulence models. Due to the fact that the biggest eddies have to be calculated directly, a LES simulation can only be three dimensional and unsteady. The LES have multiple sub-grid scale models such as the Smagorinsky-Lilly model, the Wall-Adapting Local Eddy-Viscosity (Monti et al. 2002) model, the Algebraic Wall-Modeled LES (WMLES), and the dynamic kinetic energy model. In the present study, the WMLES sub-grid scale model is used.

Open pit air flow simulation and pollution transport are often highly sensitive to the type of flow model employed. As such, in this section, the effects of both a RANS model and a LES model on the flow field simulation and pollution transport are investigated. The models differ in resolving the turbulence and it is required to compare these models in terms of the simulation outcome for the particular case of open pit ventilation.

The geometry and mesh remains identical to those described in Chapter 5. The objective is mainly to test turbulence models using the same input conditions, model constants, and similar geometry. The results from WMLES sub-grid scale model of LES are compared with the results from the realizable κ-ε models. In the previous sections, contours of vertical temperature, velocity, density, and contaminants profiles in East-West direction are presented for different turbulent models, however, in order to compare the results vertical profiles of different variables such as temperature, velocity, velocity ratios, eddy viscosity and NO_2 concentration, are plotted around the same time frame. Results are presented along a vertical line taken at the deepest part of the pit to the top of the model domain (Figure 6.61). In these plots, the horizontal axis represents the various variables and elevations are represented by the vertical axis.

Figure 6.62 presents a plot of temperatures along the vertical line at different times for both the realizable κ-ε and WMLES models. It can be seen from the temperature plot, around 30 minutes of the simulation time, the change in the temperature at the lower level. However, the change is very small and development of inversion has started at the pit bottom. For both the models there is no significant difference in the temperature profile. After two hours, it is seen that there is some change in the temperature at the bottom of the pit for both the models. The realizable κ-ε model shows much steeper change in temperature than the WMLES model. However, a much steeper decrease in the temperature at the lower level of the pit is observed in the case of LES. At higher elevations, both the models follow similar trend and able to produce temperature of same magnitude.

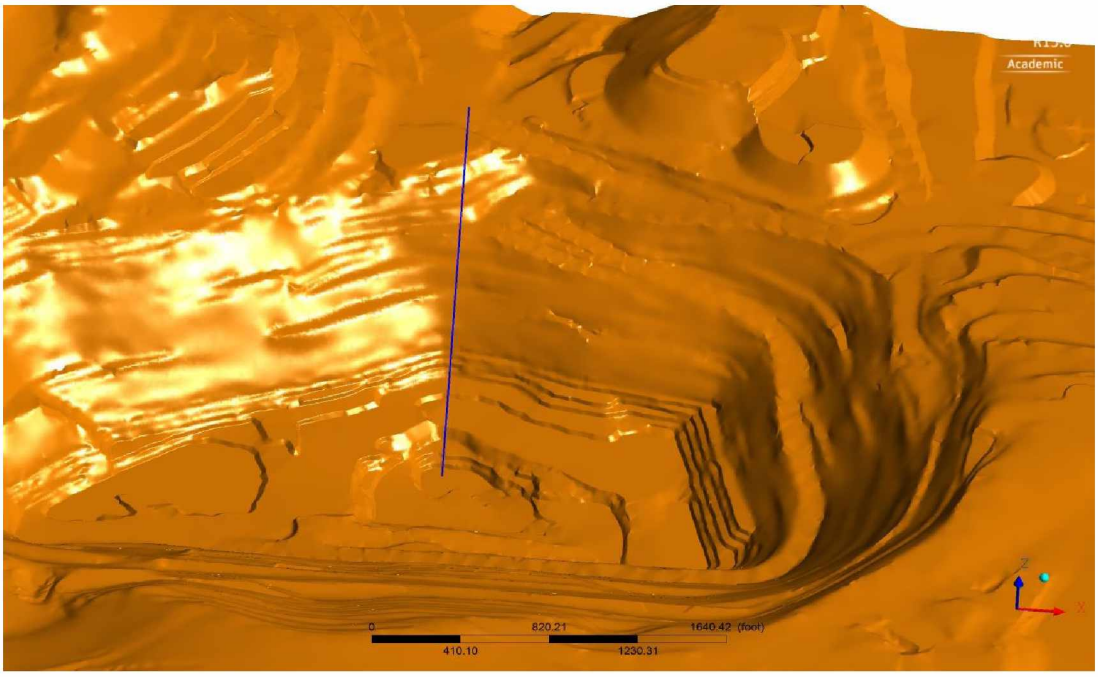

Figure 6.61: Vertical Line for Plotting Various Turbulence Variables.

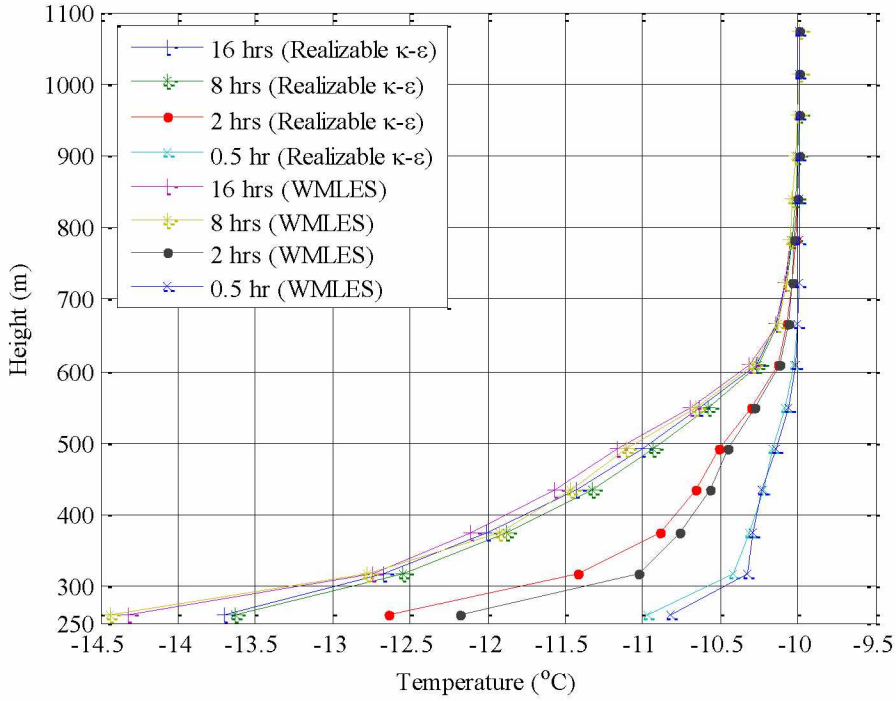

Figure 6.62: Temperature Profile along Vertical Lines at Different Times.

Comparison of the velocity magnitudes is presented in Figure 6.63-Figure 6.69. It is not expected that both the models would show the same velocity at same time. It is, however,

interesting to look at the pattern of the velocity along the selected line. Figure 6.63 shows the velocity magnitude around 30 minutes of the simulation time. After half an hour, inversion started to build up at the bottom of the pit but it is not significant, therefore, the magnitude of velocity is different. Figure 6.64 shows the velocity magnitude along the vertical line and there is some resemblance in both the models output except around elevation 376 m (1234 ft.). However, the velocity patterns after two hours of simulation are very similar. As the strength of the inversion develops, the magnitude of velocity in the pit starts to decrease considerably. The high velocity at the bottom of the pit is, however, due to the settling of the air mass towards the pit surface. This can be further explained by examining the different (x, y, and z) components of the velocity. However, instead of plotting the components of the velocity, the ratio of component of velocity to the velocity magnitude are presented. Figure 6.70 through Figure 6.76 show the ratio of the x-component of the velocity (V_u) to the air velocity. Since the incoming air velocity is from East side of the pit, the ratio is below zero (negative) for most of the time. During the initial time period (30 minutes) the plots are smooth curves with V_u increasing with height and at the lower level the ratio is positive representing a recirculation of air at the pit bottom. For the WMLES model, the recirculation zone seems to be smaller as transition from positive to negative velocity happens at a smaller time interval but for the realizable κ-ε model the transition length is larger. After one hour of simulation, the WMLES model results show the recirculation pattern with low V_u magnitude compared to the velocity and follows the prescribed direction of velocity at higher elevations. On the other hand, the realizable κ-ε model shows multiple recirculation pattern as the ratio fluctuates around zero. When the ratio is close to zero means that the velocity component is also close to zero and recirculations are evident with the changing directions. It can be seen from the figures that with advance of the simulation the ratio is getting close to zero indicating that the V_u is also close to zero and, thus small eddies are formed. The ratios of y-component of the velocity to the velocity magnitude are presented in Figure 6.77 through Figure 6.83. However, there is no y-component of the inlet velocity in the model domain but the change in the ratio presented in the plots are mainly at the lower levels where the air mass coming from the East side descends the pit benches and strikes the side walls resulting in the y-component of the velocity within the pit. From Figure 6.77 is can be inferred that at lower levels due to the interaction of the pit wall there is some horizontal movement of air and formation of recirculation zones. This ratio

shows the effects of the pit wall on the horizontal velocity. From the figures, it can be said that the y-component of horizontal velocity is more prominent within the pit.

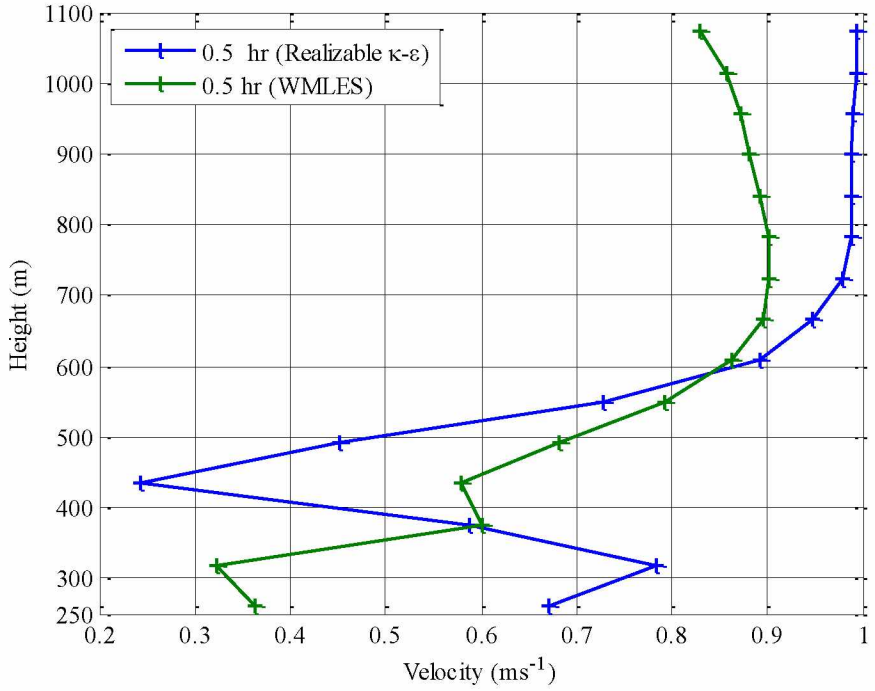

Figure 6.63: Velocity Change around 0.5 hr. for the Two Turbulent Models.

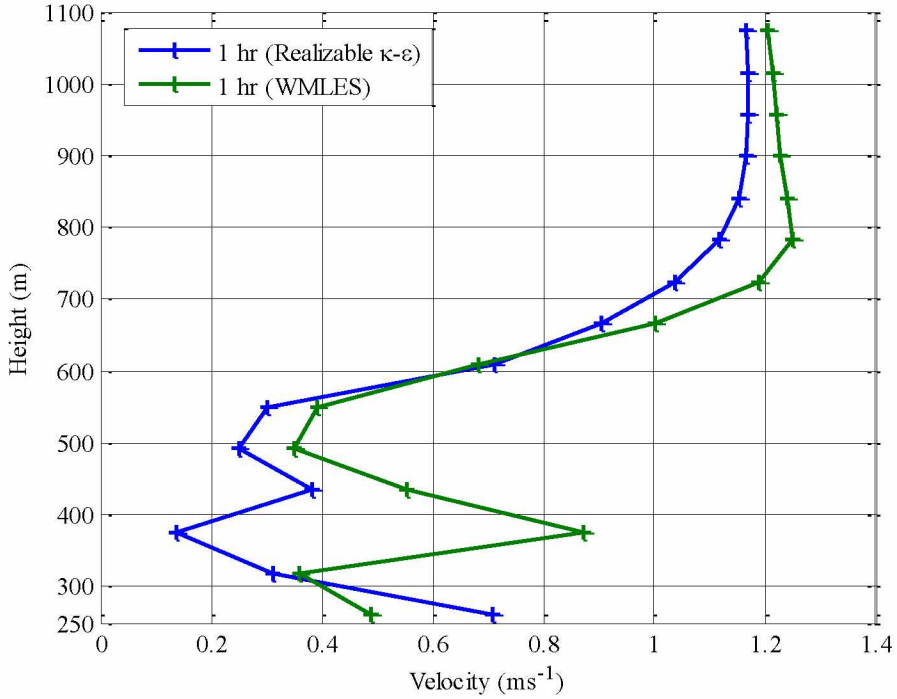

Figure 6.64: Velocity Change around 1 hr. for the Two Turbulent Models.

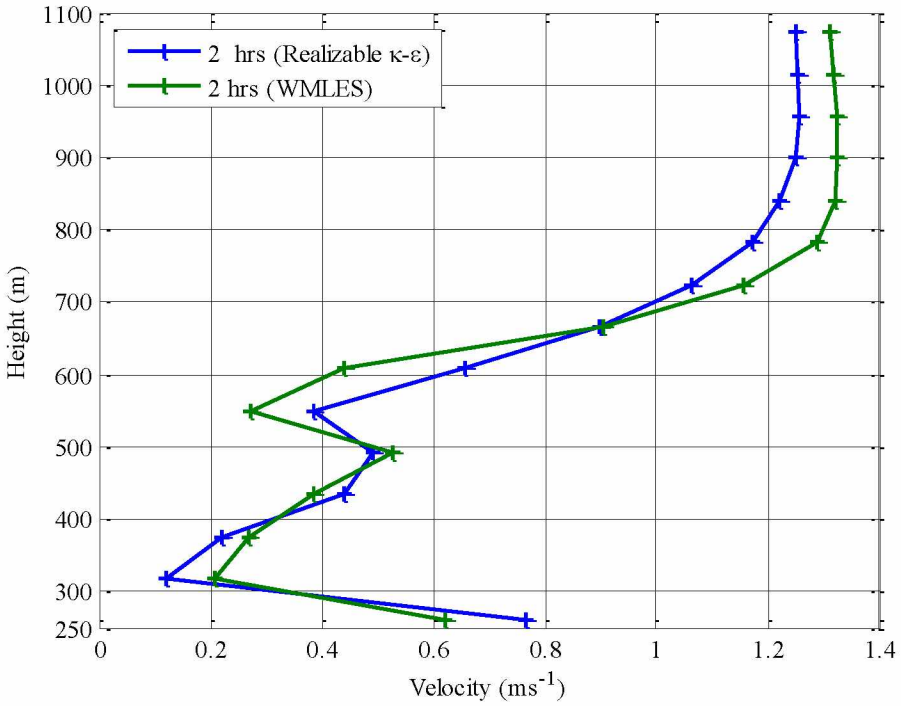

Figure 6.65: Velocity Change around 2 hs for the Two Turbulent Models.

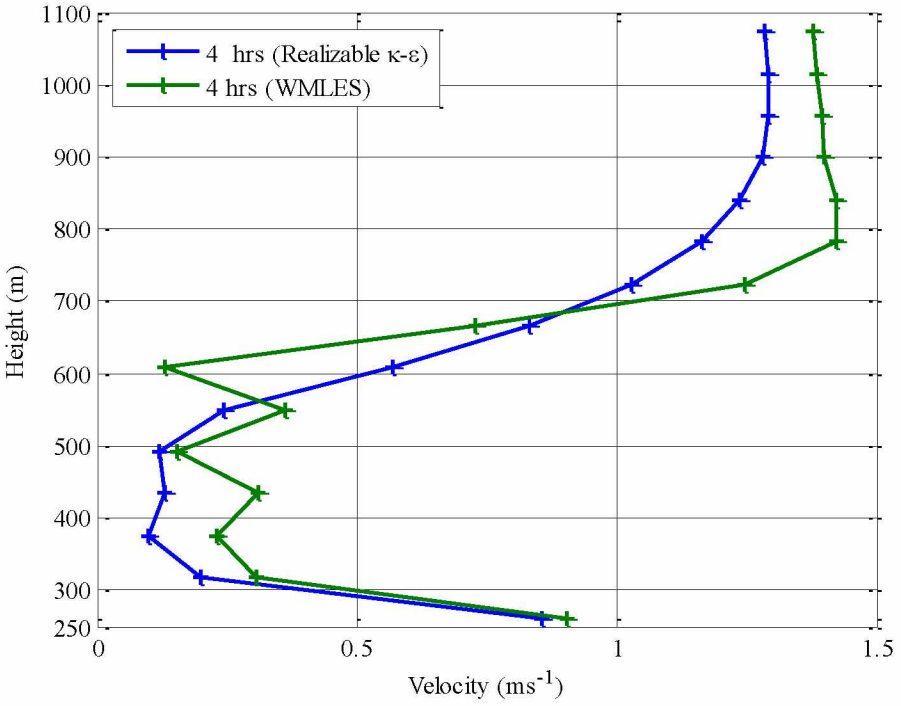

Figure 6.66: Velocity Change around 4 hrs. for the Two Turbulent Models.

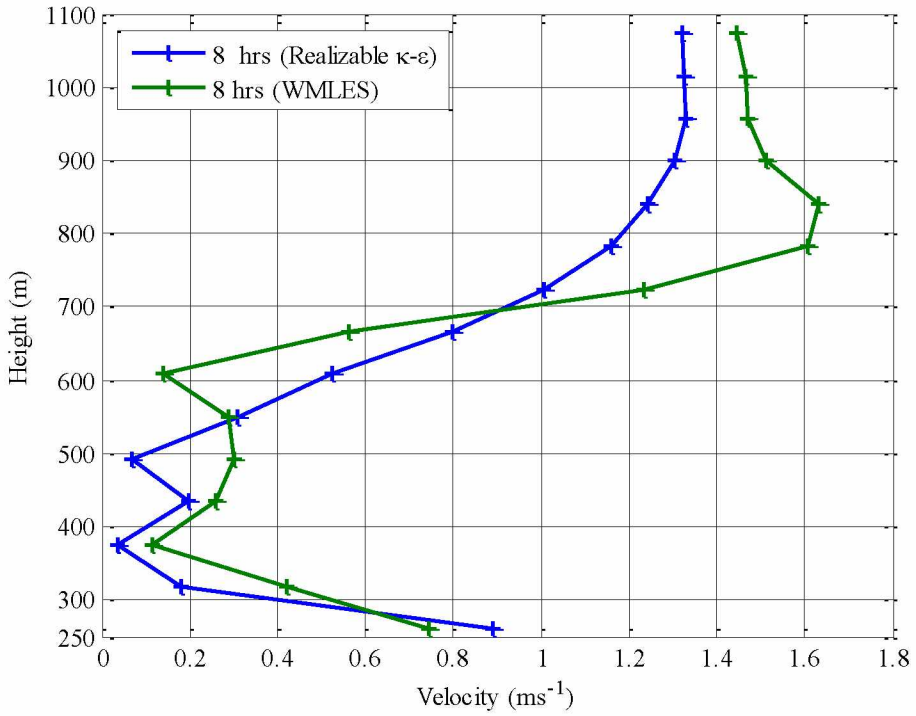

Figure 6.67: Velocity Change around 8 hrs. for the Two Turbulent Models.

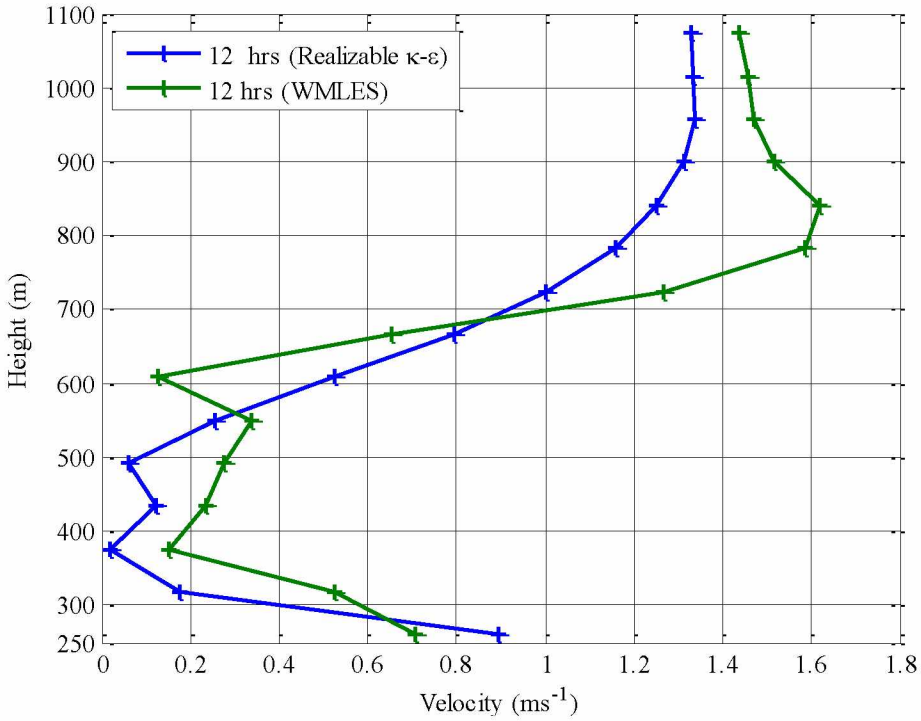

Figure 6.68: Velocity Change around 12 hrs. for the Two Turbulent Models.

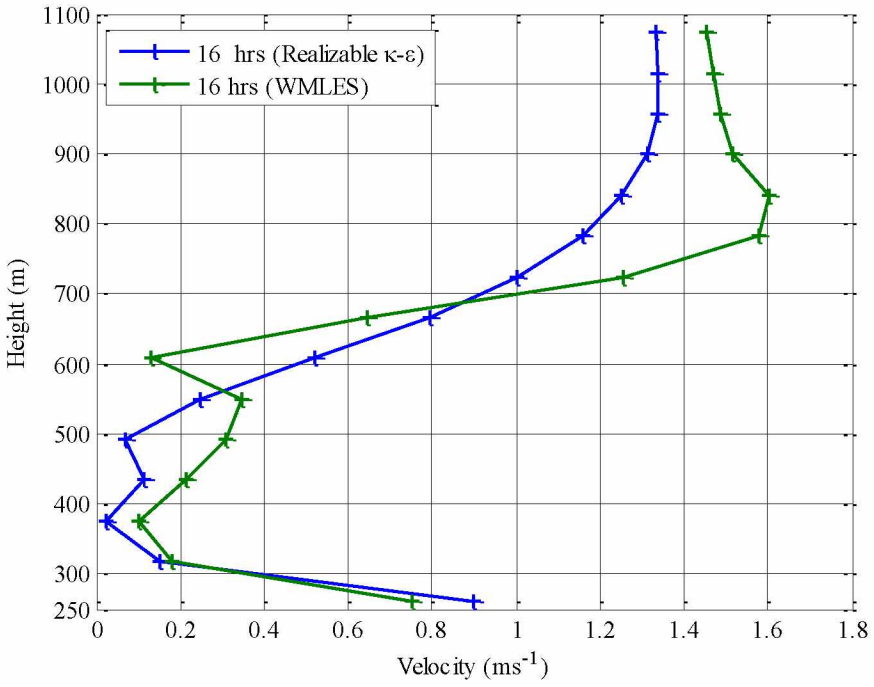

Figure 6.69: Velocity Change around 16 hrs. for the Two Turbulent Models.

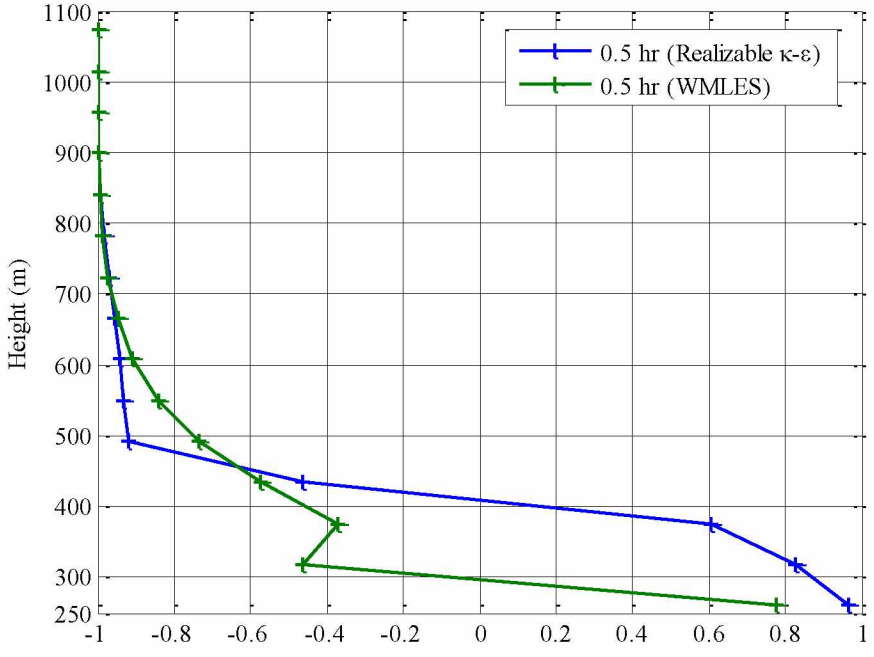

Figure 6.70: V_u/V Change around 0.5 hr. for the Two Turbulent Models.

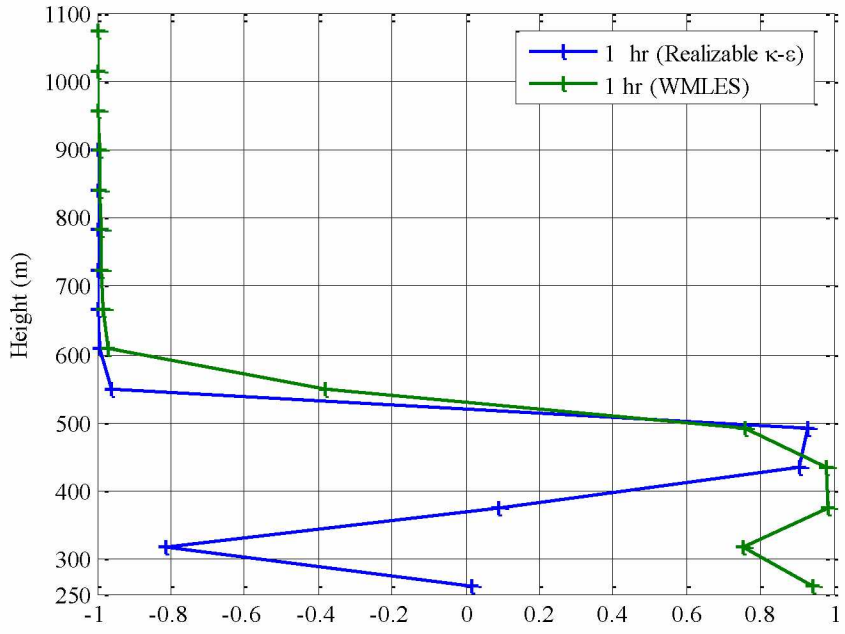

Figure 6.71: V_u/V Change around 1 hr. for the Two Turbulent Models.

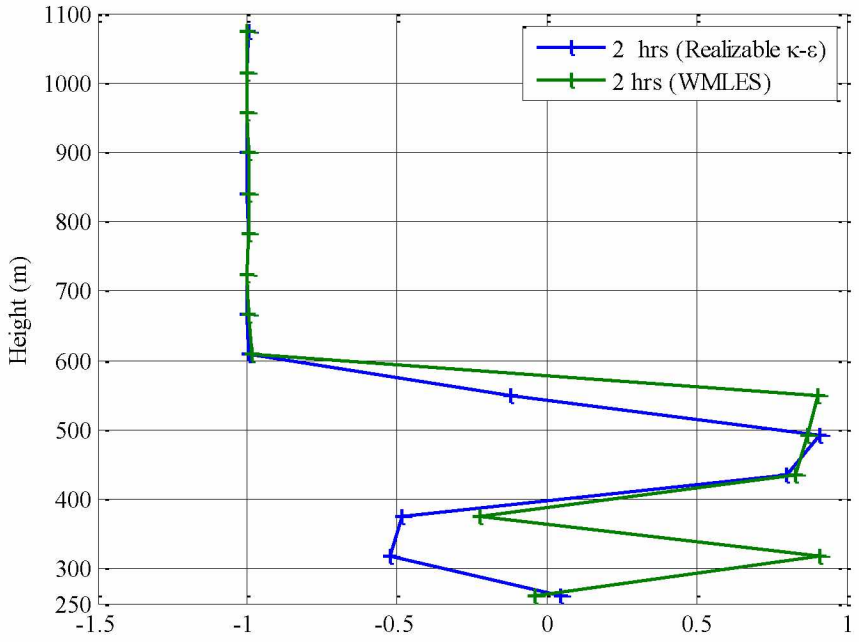

Figure 6.72: V_u/V Change around 2 hrs. for the Two Turbulent Models.

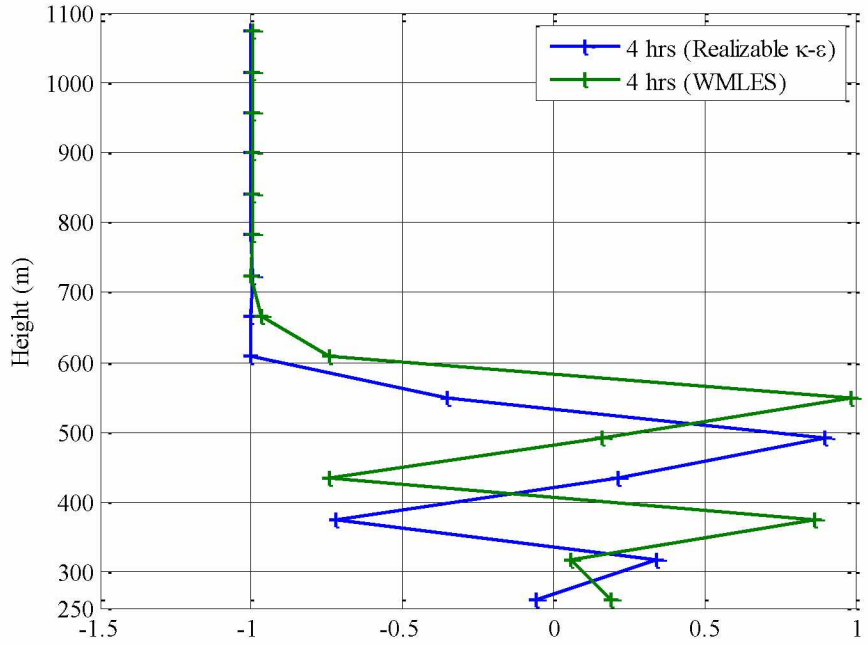

Figure 6.73: V_u/V Change around 4 hrs. for the Two Turbulent Models.

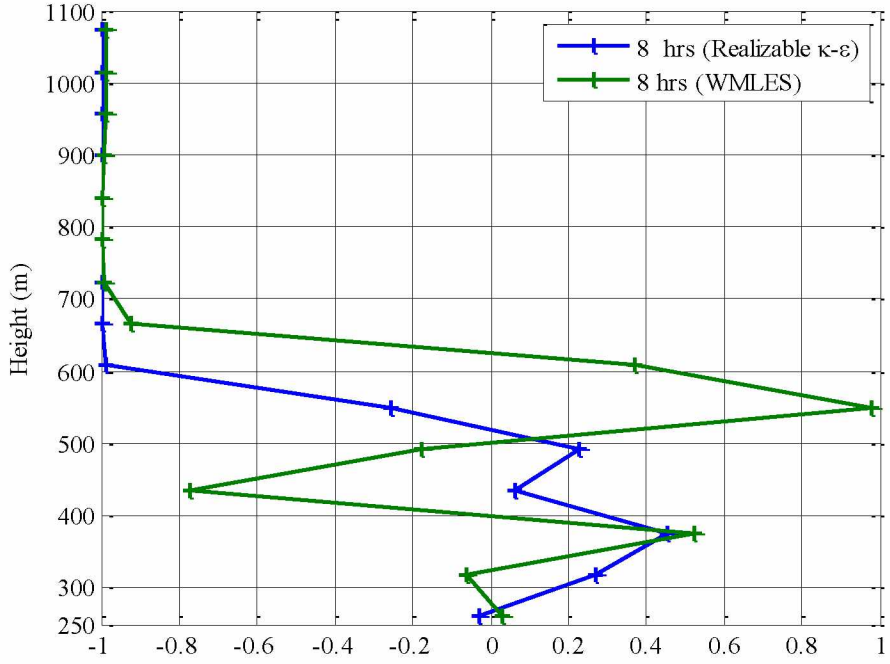

Figure 6.74: V_u/V Change around 8 hrs. for the Two Turbulent Models.

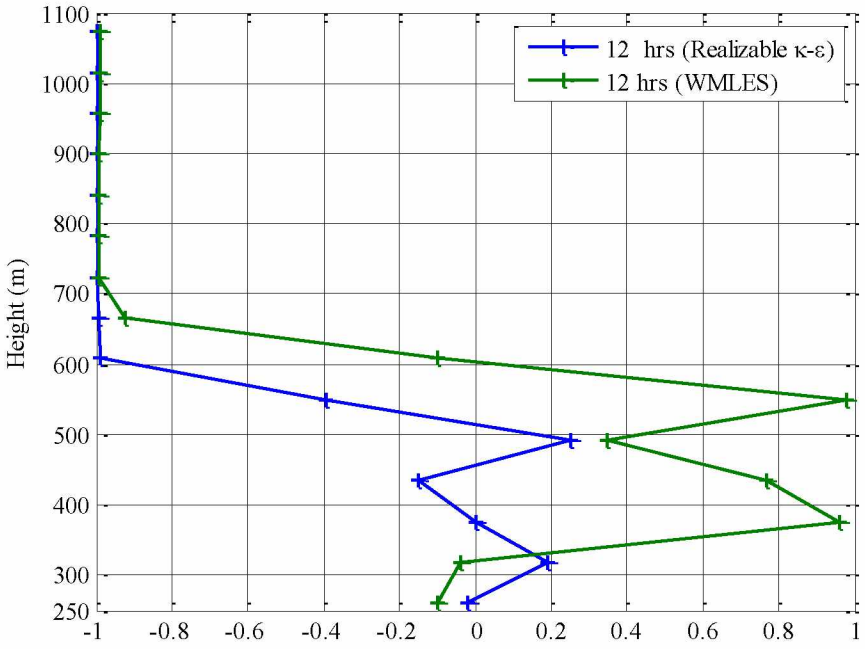

Figure 6.75: V_u/V Change around 12 hrs. for the Two Turbulent Models.

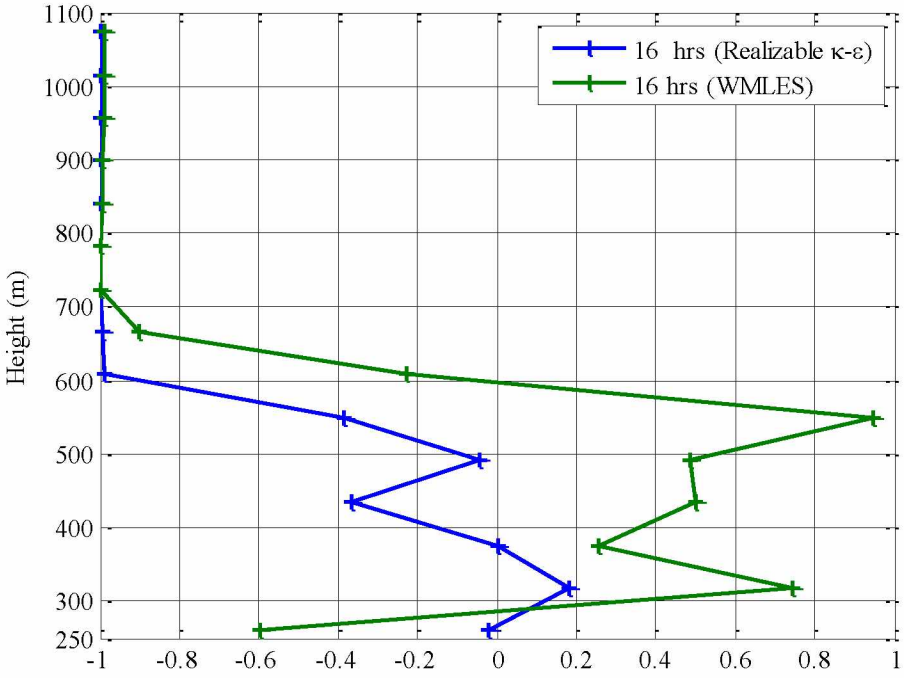

Figure 6.76: V_u/V Change around 16 hrs. for the Two Turbulent Models.

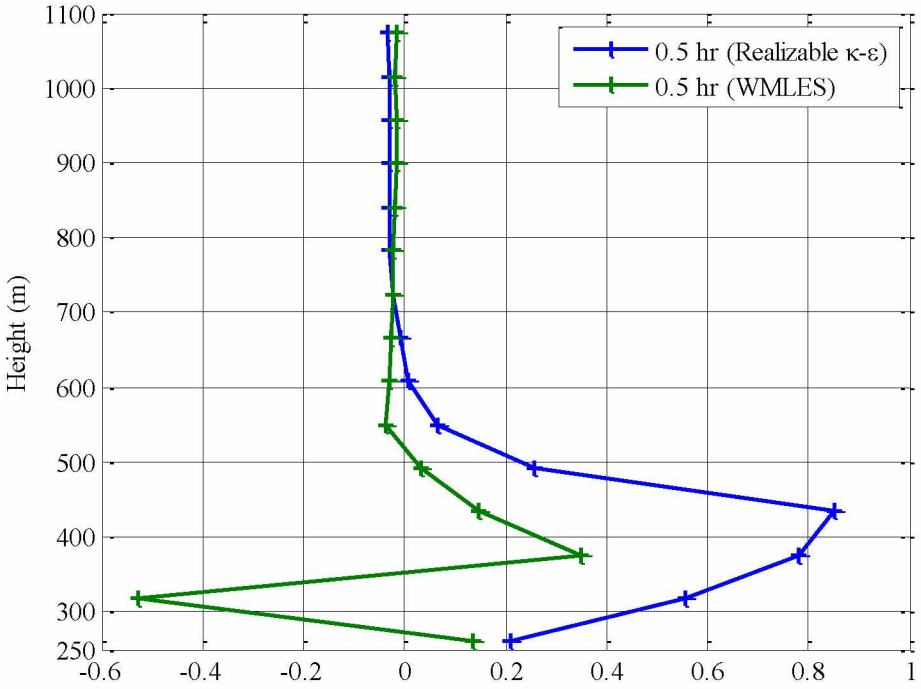

Figure 6.77: V_v/V Change around 0.5 hr. for the Two Turbulent Models.

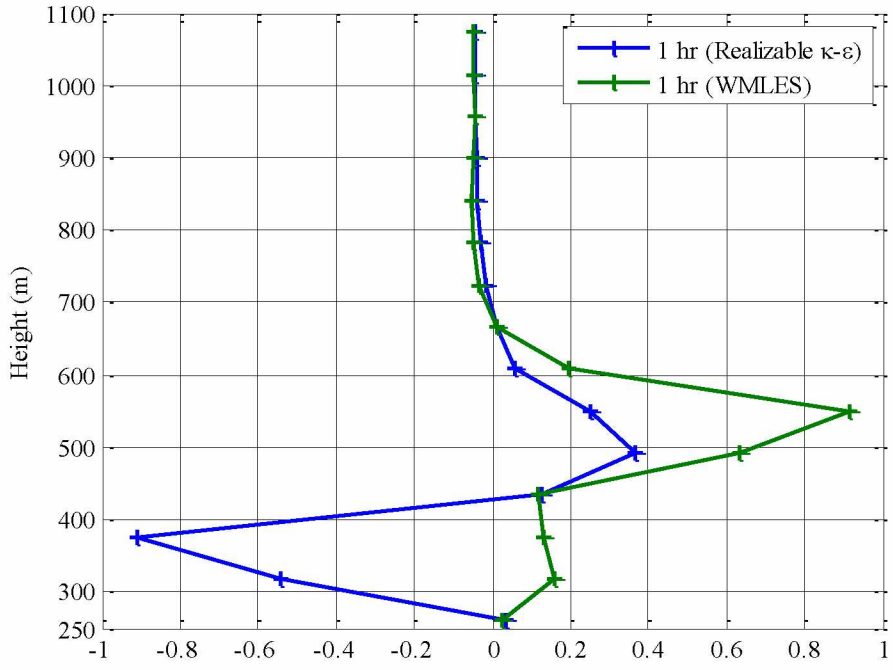

Figure 6.78: V_v/V Change around 1 hr. for the Two Turbulent Models.

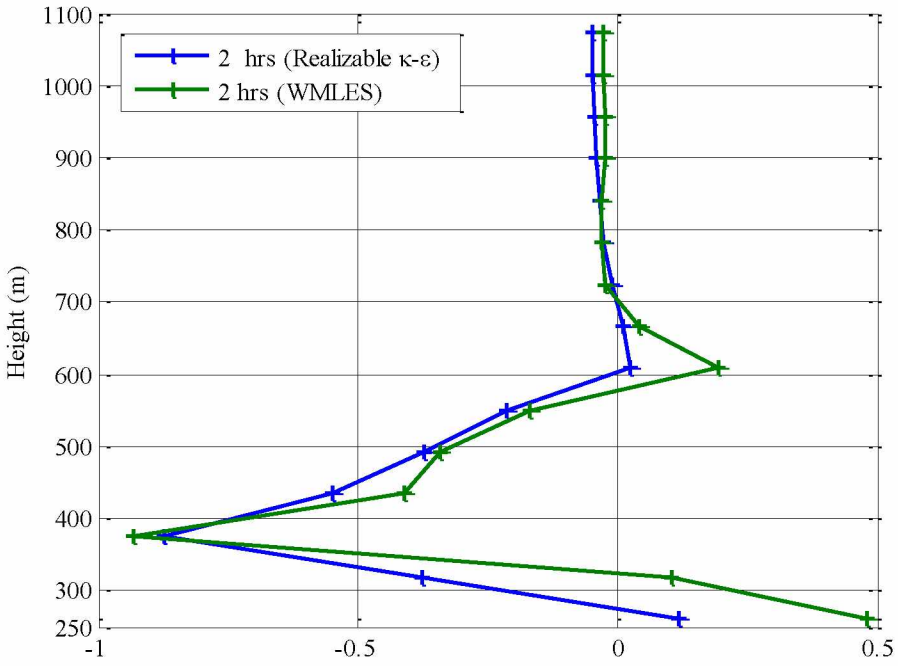

Figure 6.79: V_v/V Change around 2 hrs. for the Two Turbulent Models.

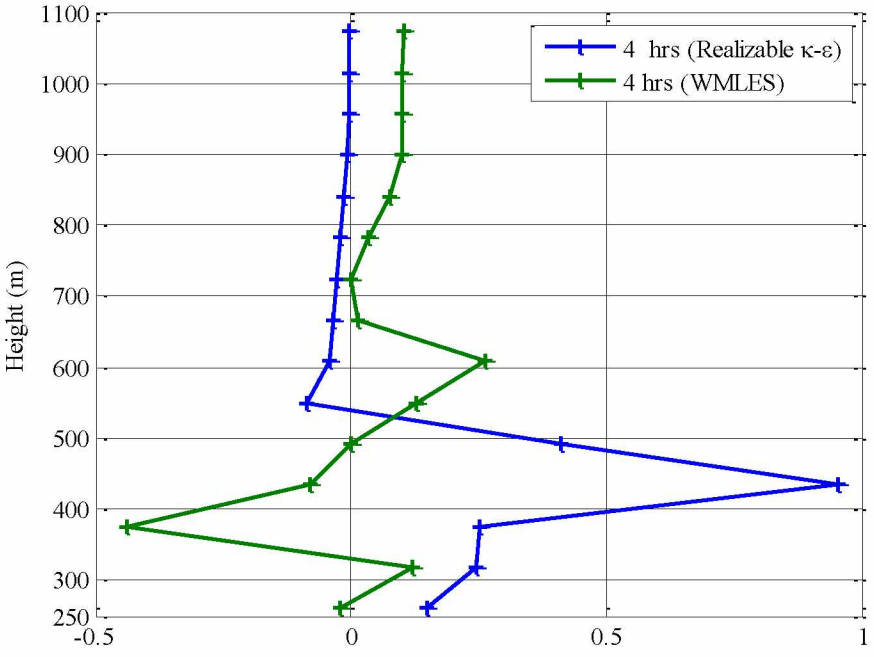

Figure 6.80: V_v/V Change around 4 hrs. for the Two Turbulent Models.

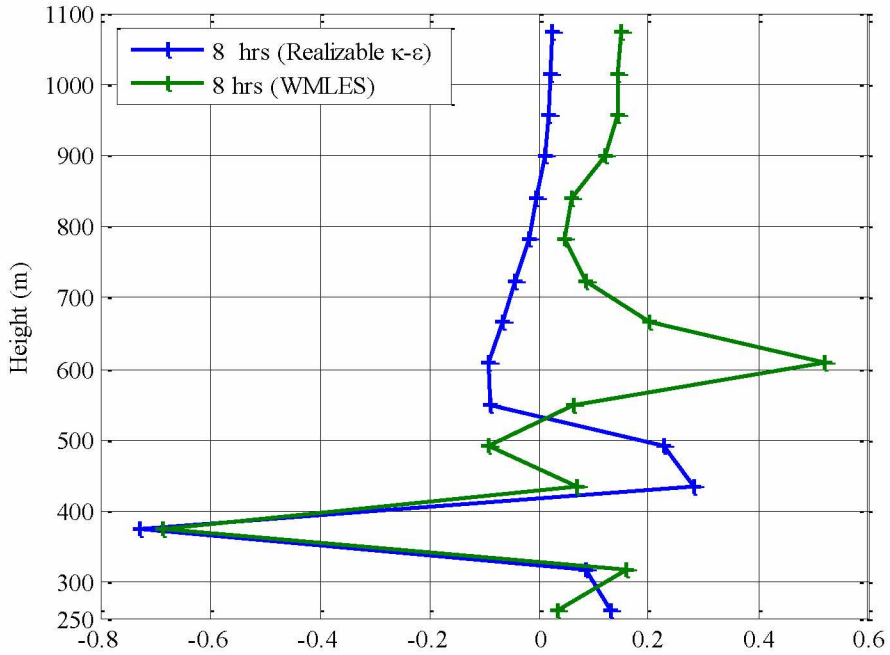

Figure 6.81: V_v/V Change around 8 hrs. for the Two Turbulent Models.

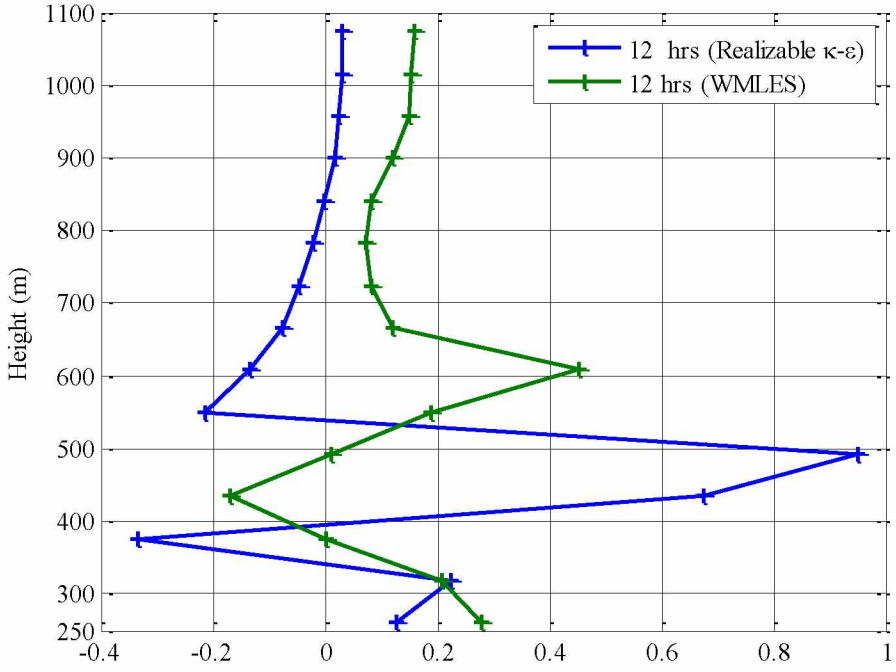

Figure 6.82: V_v/V Change around 12 hrs. for the Two Turbulent Models.

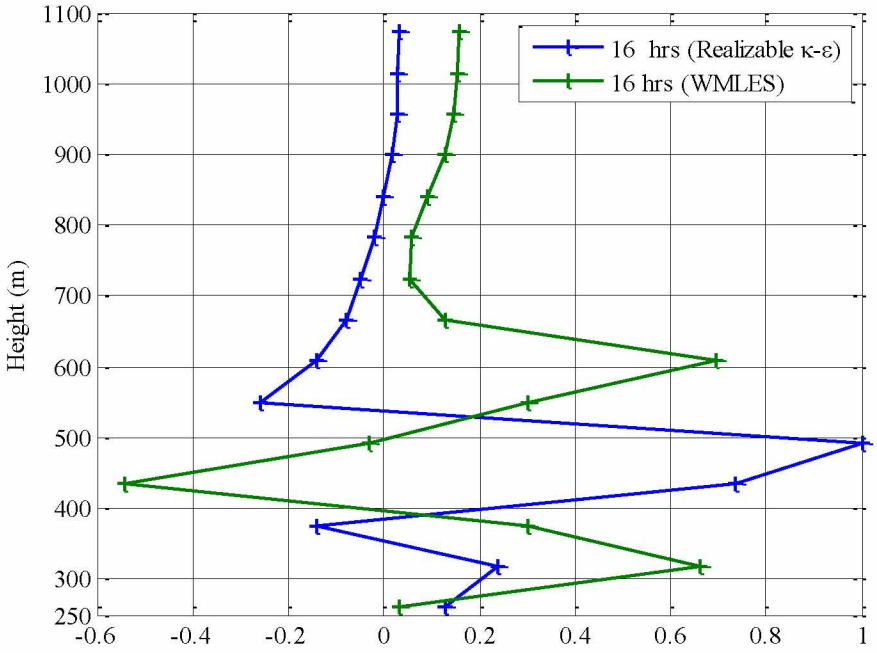

Figure 6.83: V_v/V Change around 16 hrs. for the Two Turbulent Models.

The horizontal velocity component of the sinking airflow (downward movement shown in Figure 6.29 to Figure 6.35 and Figure 6.54 to Figure 6.60) gradually increases on the top of the windward side and finally turns to flow straight. The circulation is larger and deeper. The strong rising and sinking airflow accelerates the changes of the physical flow variables (temperature, pollutant concentrations, etc.) within the pit.

The major characteristic of the SBL structure over the selected open pit is the existence of recirculatory zones. This circulation has reversing low velocity structure. The ratio of the vertical velocity to the air velocity is important as the strength of the velocity in the vertical direction determines the dispersion of pollutants from the pit. Figure 6.84 through Figure 6.90 present the ratio of the vertical velocity to the air velocity. Figure 6.84 shows the ratio at around half an hour into the simulation where the ratio is negative at the bottom of the pit, and the ratio becomes positive with increasing altitude. During the early stages of simulation, the negative ratio can be a result of the downward movement of air or the formation of a recirculation zone at the bottom of the pit. However from Figure 6.70, it can be observe that the ratio of the x-component of the velocity to the air velocity fluctuates indicating that there is a greater chance of forming a recirculation zone at the bottom. After one hour of simulation (Figure 6.85), the trend of the ratio for both the models is similar. For the realizable κ-ε model, however, the frequency of fluctuation

around zero is more than the WMLES model. Thus, it can be inferred that there are multiple recirculation zones formed in the realizable κ-ε model domain. As the inversion develops within the open pit, at the lower level or close to the surface, the air tends to sink because of the gravitational pull. Near the pit surface the air cools rapidly and its density increases with a decrease in temperature. As a result, the vertical velocity near the pit surface tends to be negative.

The NO_2 concentration along the horizontal line recorded in an East-West direction at an elevation of 300 m (1000 ft.) level and, the Y-axis is at 3166 m (10388 ft.) are presented in Figure 6.91 through Figure 6.97. This horizontal line is located on the vertical plane on which the results have been presented earlier. Figure 6.91 shows the NO_2 concentration approximately 30 minutes after the start of the simulation. Both the models show a high value of NO_2 concentration in some section of the pit which could be caused by the presence of the sampling location close to the equipment. However, for the realizable κ-ε model the concentration value is rather high. Higher concentration of NO_2 is in a small portion of the pit and is advected by the incoming flow of air in the pit. The NO_2 concentration is lower in other parts of the pit away from an equipment. The NO_2 concentration increases with the increasing strength of the inversion for both models. The concentration in the realizable κ-ε model is much higher and increases rapidly in the pit. Whereas, for the WMLES model the pollutant concentration increases slowly.

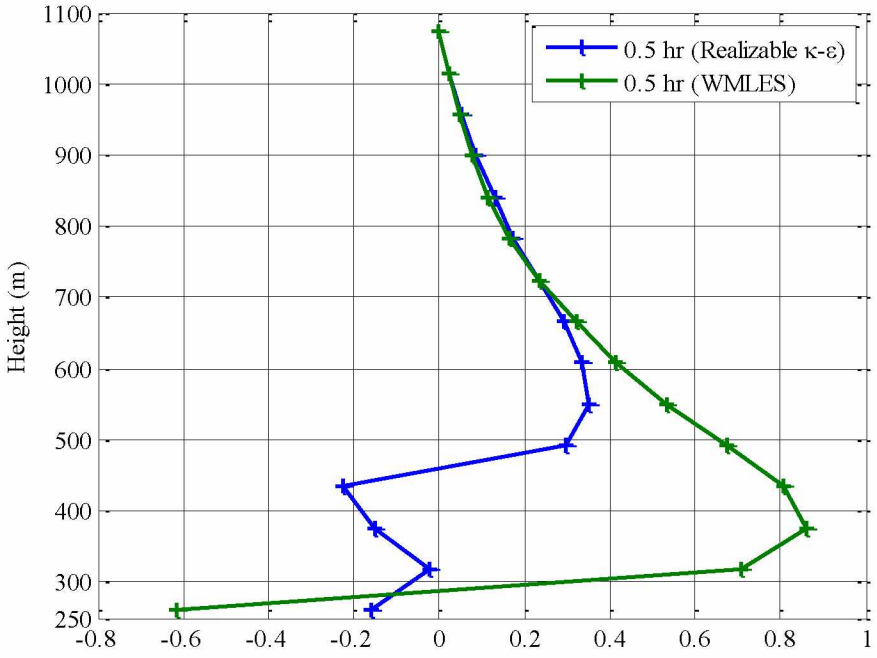

Figure 6.84: V_z/V Change around 0.5 hr. for the Two Turbulent Models.

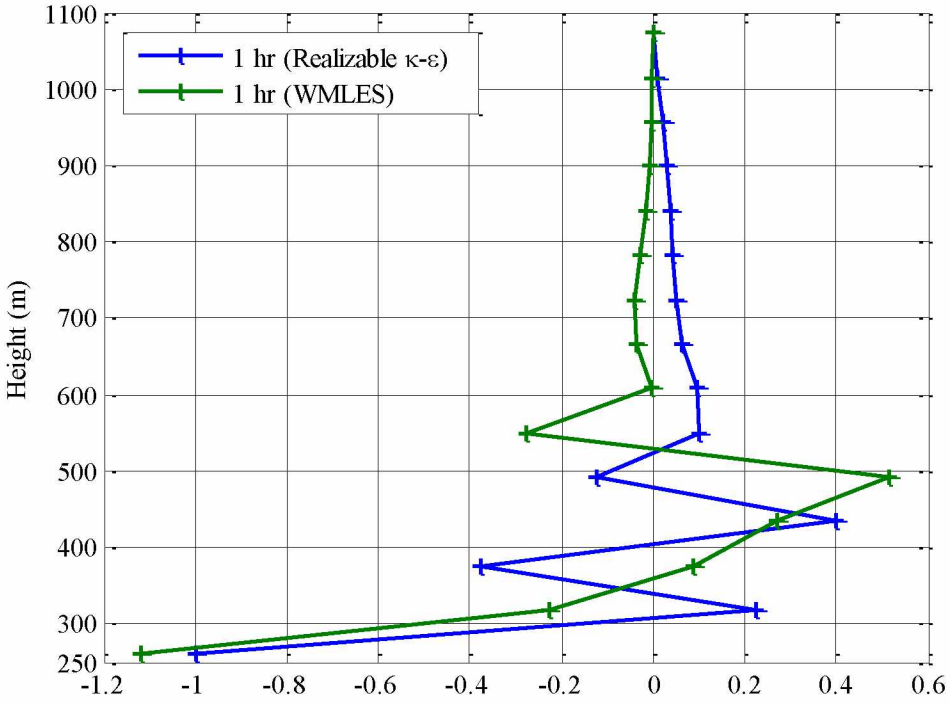

Figure 6.85: V_z/V Change around 1 hr. for the Two Turbulent Models.

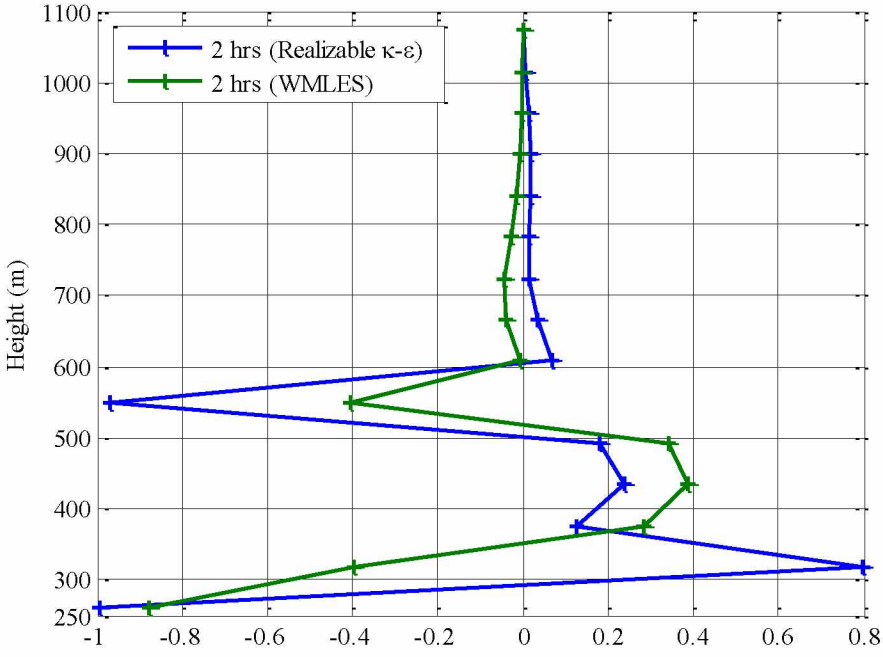

Figure 6.86: V_z/V Change around 2 hrs. for the Two Turbulent Models.

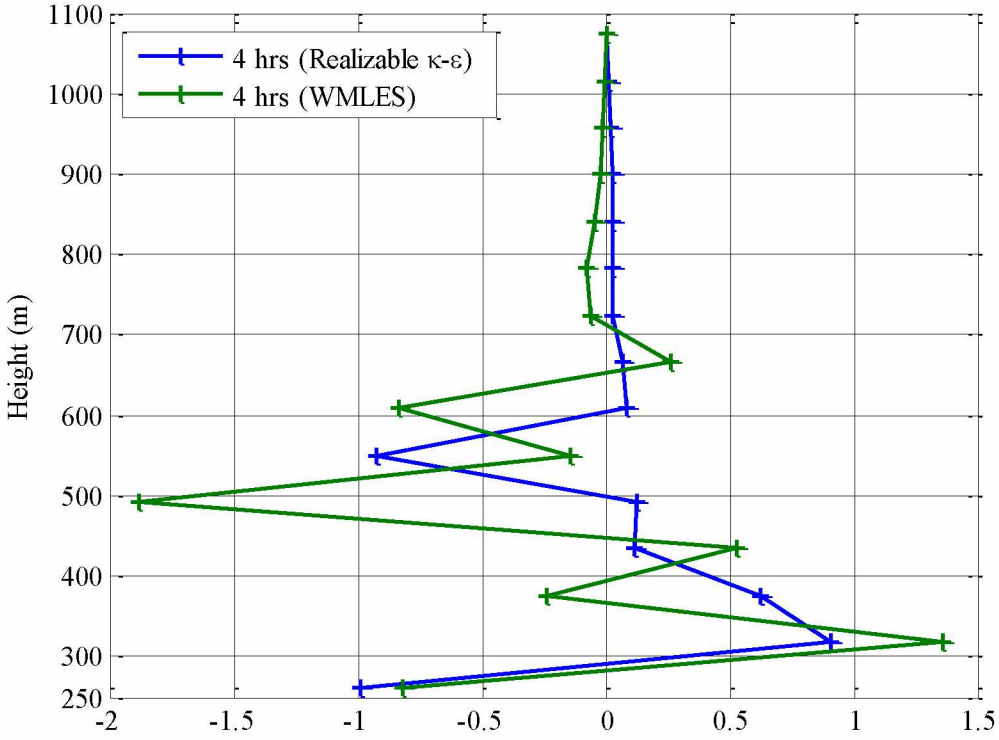

Figure 6.87: V_z/V Change around 4 hrs. for the Two Turbulent Models.

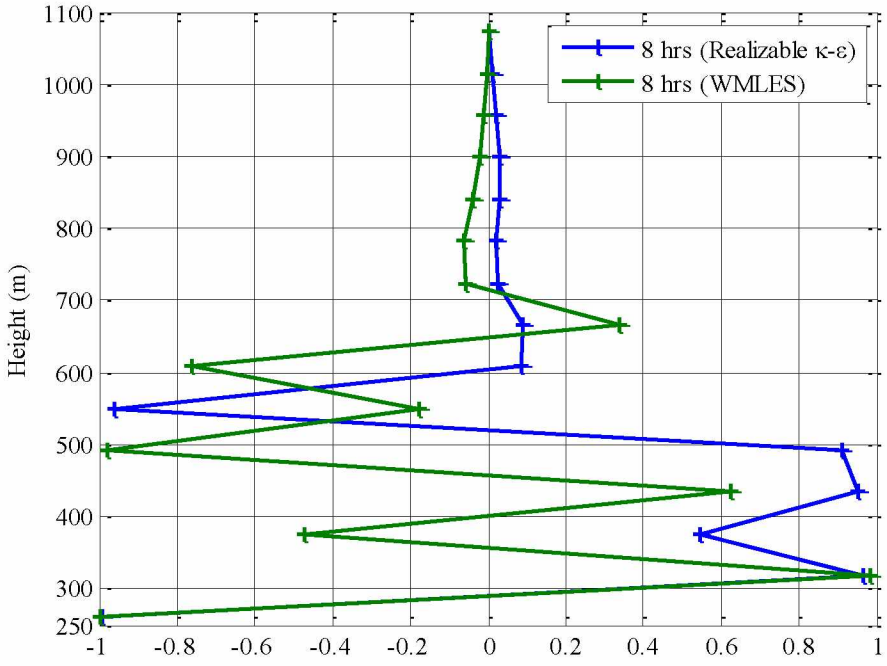

Figure 6.88: V_z/V Change around 8 hrs. for the Two Turbulent Models.

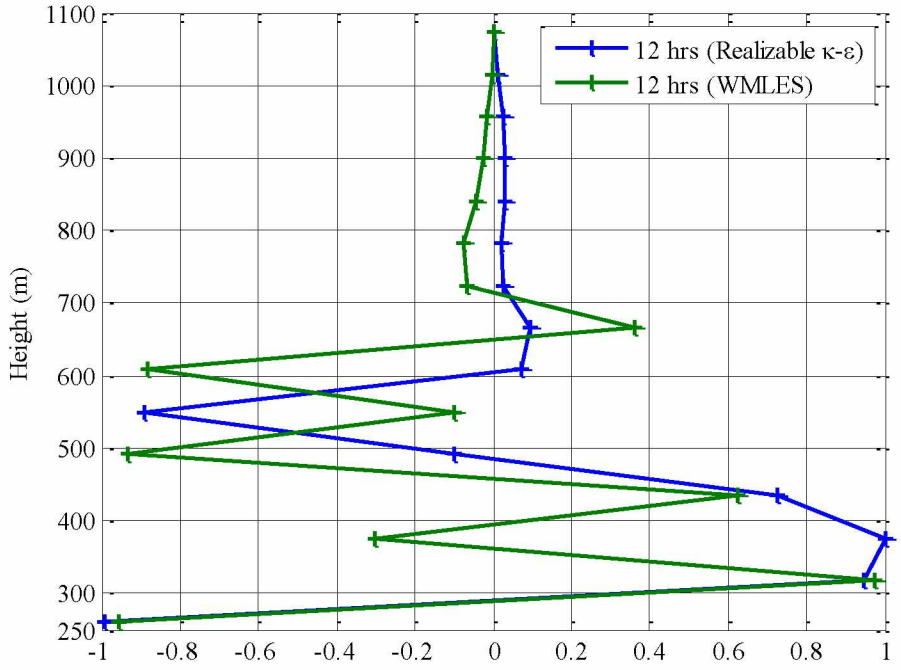

Figure 6.89: V_z/V Change around 12 hrs. for the Two Turbulent Models.

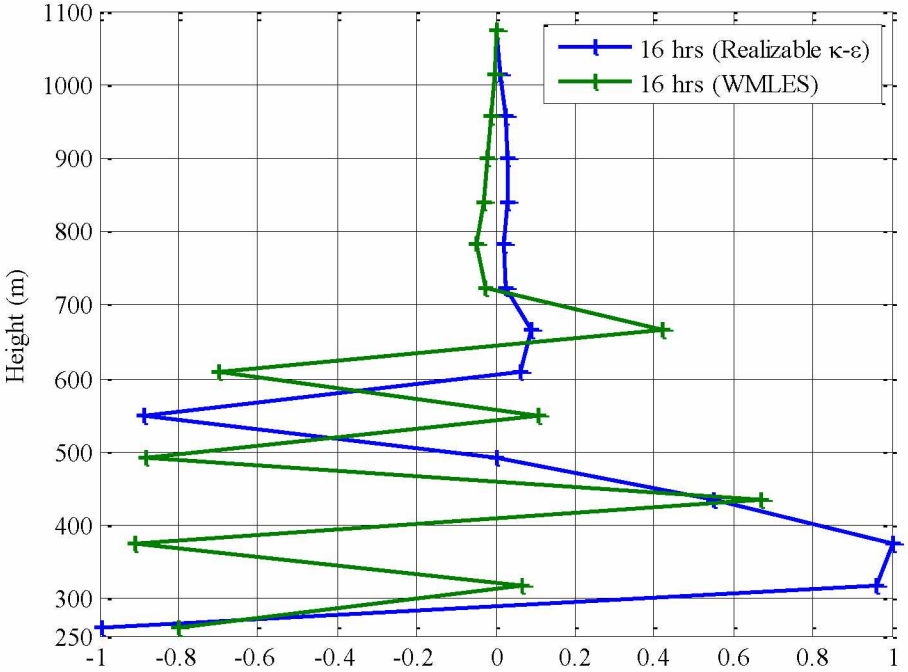

Figure 6.90: V_z/V Change around 16 hrs. for the Two Turbulent Models.

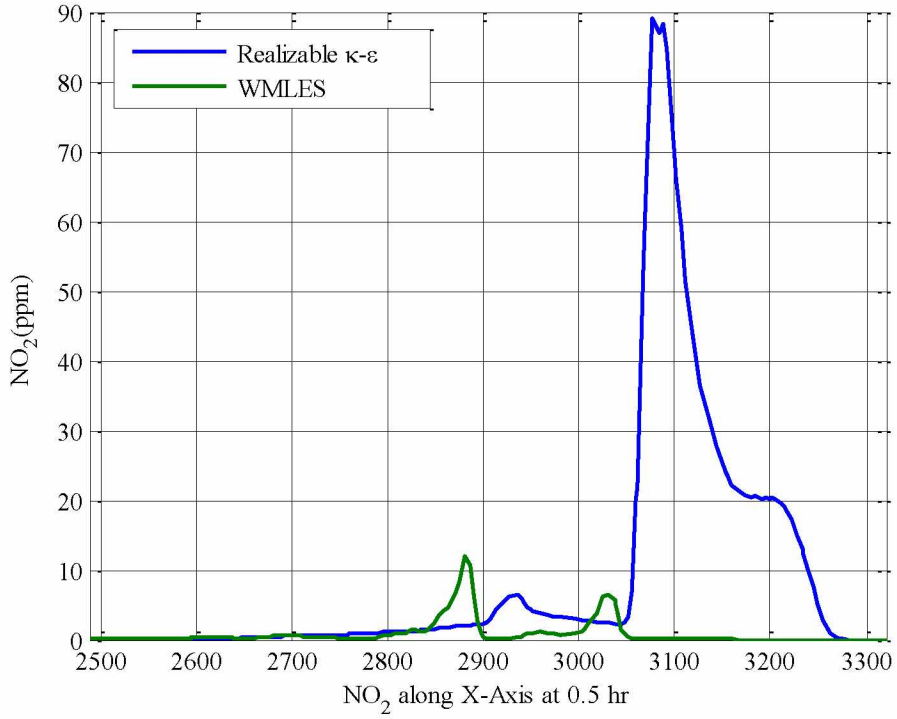

Figure 6.91: NO_2 Concentration around 0.5 hr. for the Two Turbulent Models.

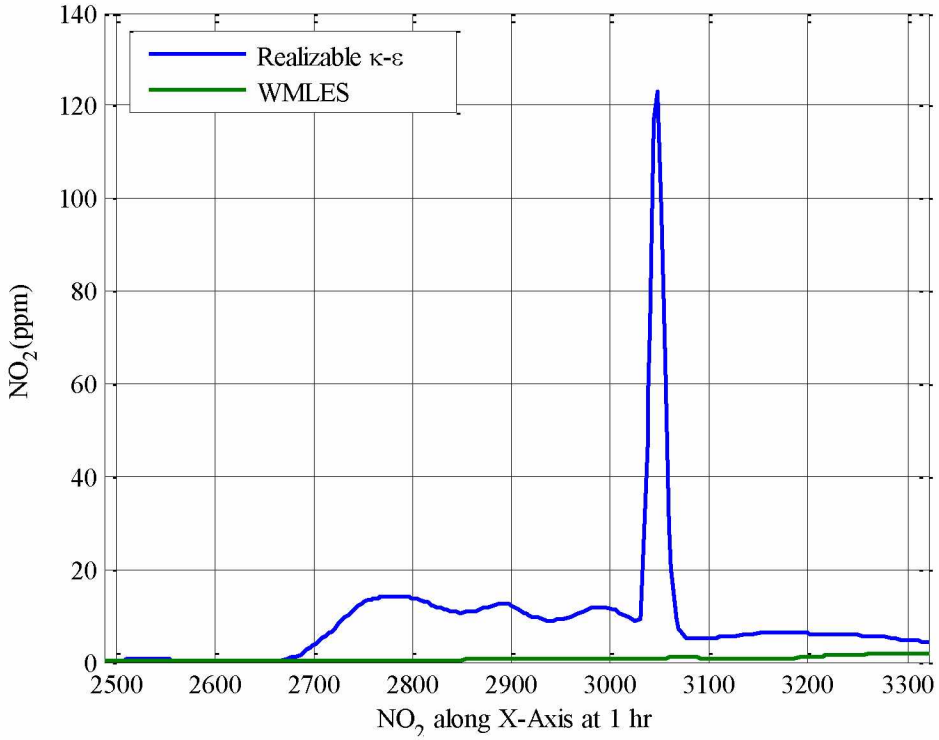

Figure 6.92: NO_2 Concentration around 1 hr. for the Two Turbulent Models.

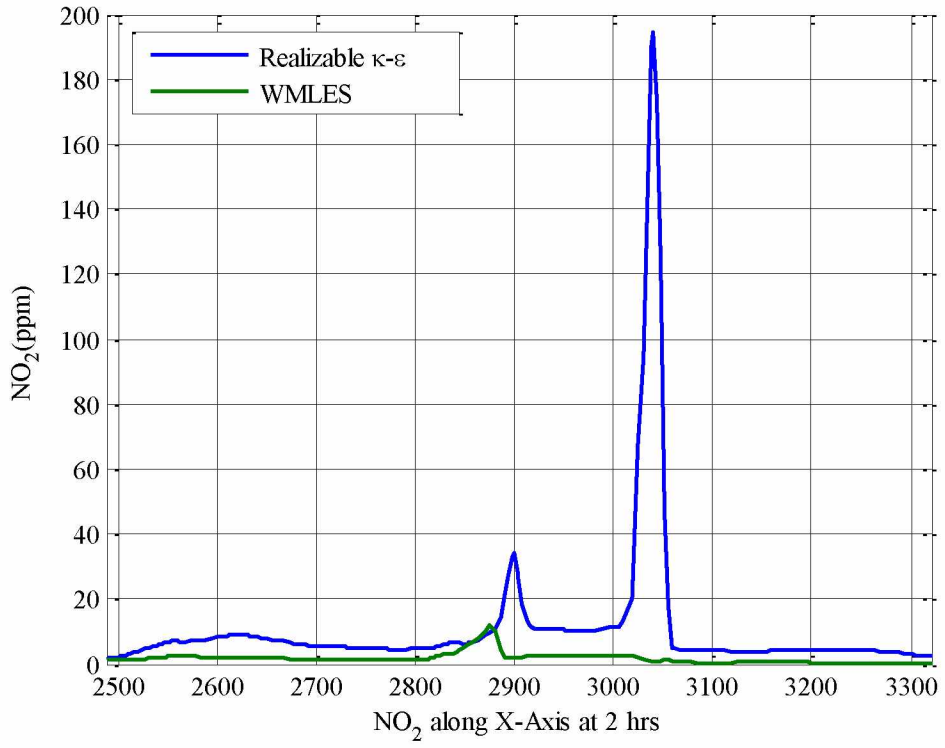

Figure 6.93: NO_2 Concentration around 2 hrs. for the Two Turbulent Models.

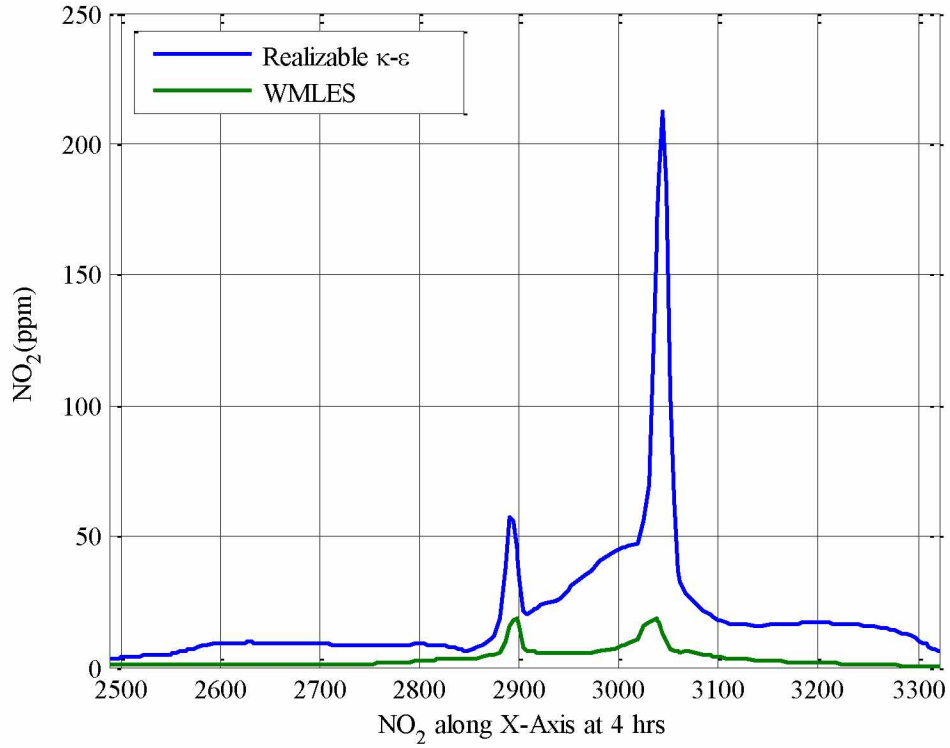

Figure 6.94: NO_2 Concentration around 4 hrs. for the Two Turbulent Models.

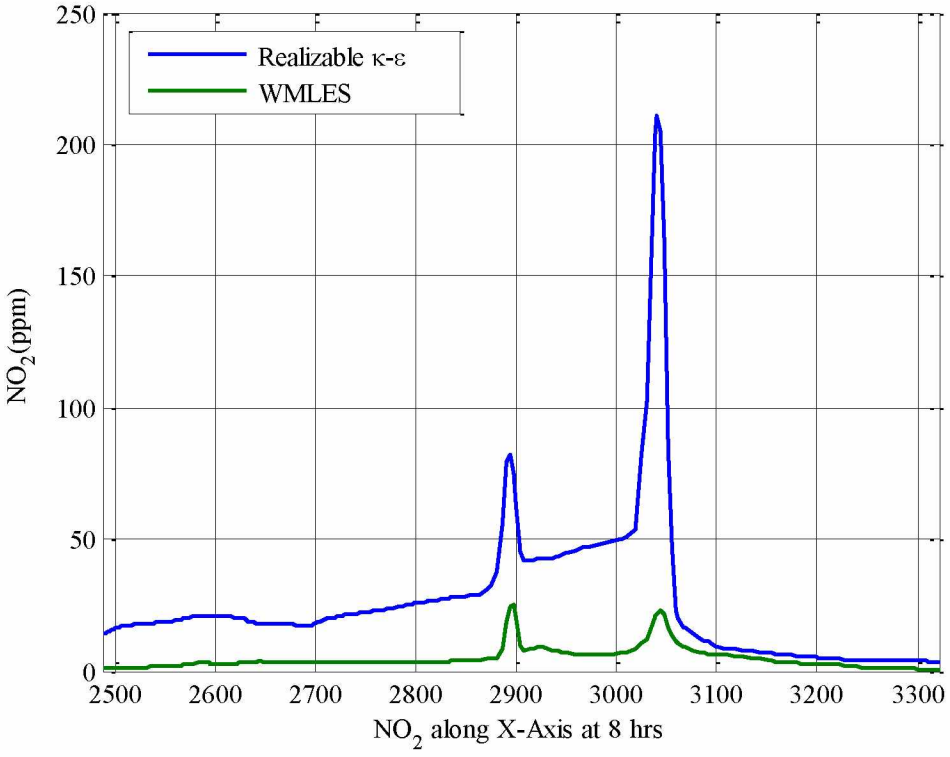

Figure 6.95: NO_2 Concentration around 8 hrs. for the Two Turbulent Models.

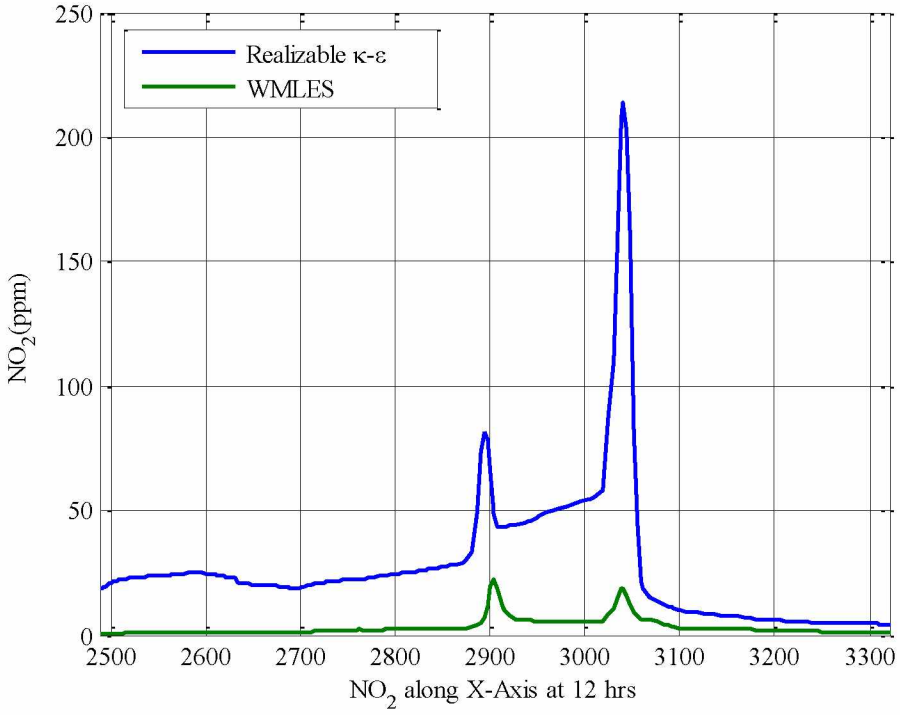

Figure 6.96: NO_2 Concentration around 12 hrs. for the Two Turbulent Models.

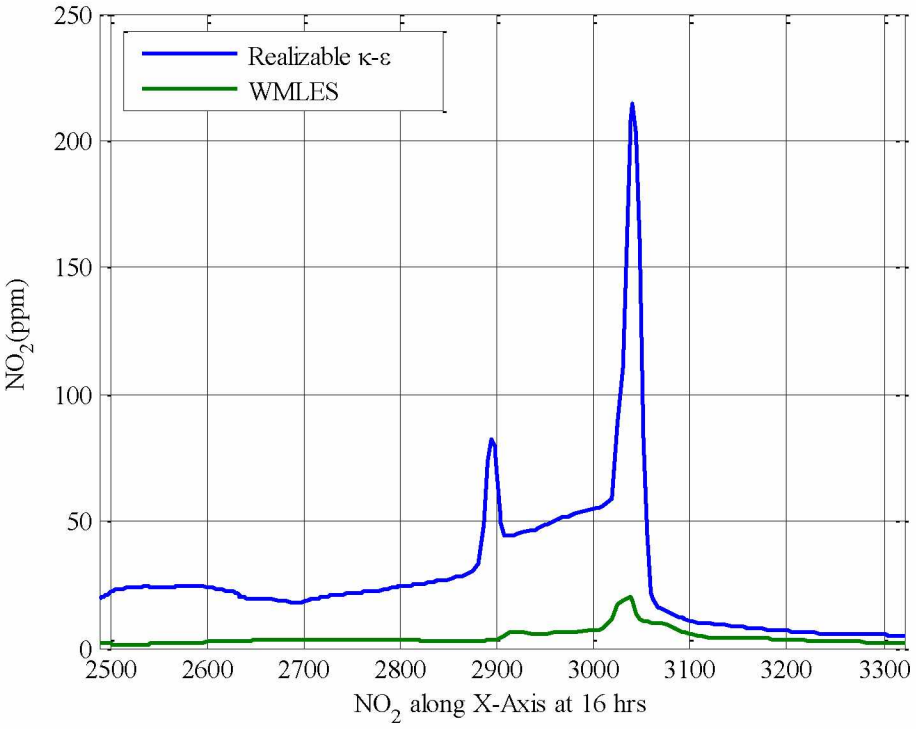

Figure 6.97: NO_2 Concentration around 16 hrs. for the Two Turbulent Models.

Apart from the graphical results presented above, a side by side comparison between the realizable κ-ε and WMLES model with respect to the actual measured data is given in Table 6.2. Four sampling location, specifically, Bench 940E, Bench 970W, Lift Station 1 (LS1) and DW223 are selected for which the measured data was available.

The models are not expected to reproduce a one to one match of the measured data due to the uncontrolled experimentation and other sampling error. It can be seen from Table 6.2 that the predicted values are largely different. However, the realizable κ-ε model is able to predict the concentration closely. It can be concluded that the models are consistently in good agreement in determining the direction of the dispersion. The high uncertainty in the concentration values may be as a result of the largely turbulent treatment of the models. The results indicate that both turbulent models can simulate the stable boundary layer problems over complex terrain such as an open pit mine.

The vertical profiles of the temperature and the wind velocity are consistent with the observations of other researcher (Wendler and Jayaweera 1972) which shows a small vertical gradient in the mixed layer below the capping inversion. This is because of the large amount

turbulence, particularly in vertical direction. The simulated turbulence structure shows the dominance of vertical velocity variance within the mixed/intermittent layer (Figure 6.90), whereas, the horizontal velocity variances are dominant in the SBL (Figure 6.76).

Table 6.2 : A Comparison of 2010 Realizable κ-ε and WMLES Simulations Result.

Location	Concentration (NO_2)		
	Measured	κ-ε model	LES
Time = 4 hrs.			
Bench 940E	3.8	10.110	0.498
Bench 970W	3.8	5.047	1.296
LS 1	3.6	2.619	0.301
DDW 223	4	1.240	0.529
Time = 8 hrs.			
Bench 940E	4.3	3.762	0.863
Bench 970W	--	18.750	1.814
LS 1	4.3	2.995	0.372
DDW 223	4.7	4.777	0.740
Time = 12 hrs.			
Bench 940E	4.7	4.629	1.083
Bench 970W	--	24.130	0.888
LS 1	4.2	4.017	0.645
DDW 223	4.6	5.713	0.772
Time = 16 hrs.			
Bench 940E	4.8	5.373	1.522
Bench 970W	--	24.850	1.475
LS 1	4.3	4.477	0.382
DDW 223	4.8	6.558	1.147

Both models are able to capture the general trend of the recirculation zones, velocity and pollutant concentrations. The WMLES performed better in regions of strong wall effects and recirculation found along the pit bottom and pit walls. In these regions of complex flow phenomenon, a more accurate turbulence solver is required. In terms of concentration, the results

from realizable κ-ε model are more consistent with the observed data from the mine compared to the WMLES model.

During the initial time period, the deviation between the actual data and the simulation result is high. With increasing simulation time, the deviations between the actual data and the simulation results are much smaller for the realizable κ-ε model. The simulated results from the WMLES model are much smaller than the actual data as well as that of the realizable κ-ε model. The WMLES only resolves large eddies which are in the minority in the SBL. Consequently, the WMLES model may not work satisfactorily in a stable boundary layer due to the discontinuity introduced by the capping inversion.

The κ-ε turbulence model, in its RNG version, provided a better estimation of the concentration profiles compared to the LES model. The RANS based CFD simulation, however, under-predicts the velocity field, therefore, leads to over-prediction of the pollution concentrations. Simulation results underscores that the RANS based realizable κ-ε model largely over-estimated the pollution concentration, whereas, the WMLES model under-estimated the pollution concentrations.

A stable boundary layer is shallower and characterized by small scale eddies. A higher accuracy in predicting the pollutant distribution can be obtained if these eddy are modeled based on their length scales. LES requires a much finer grid size to capture the small scale eddies. It is likely that the grid resolution used in the WMLES simulation model is not adequate in resolving the small eddies within the SBL. Therefore, the WMLES model under predicted the pollutants concentrations.

The model predicted pollution concentration values in selected locations exhibited large differences, but remained within the same order of magnitude in most cases. Uncertainty between models is probably caused the difference in turbulent treatment. For the RANS based model, the turbulence is modeled as isotropic, whereas the LES resolves the anisotropy of the turbulence. Due to the high computational cost of the LES model, however, it is helpful to consider the circumstances under which a more simplistic RANS model is sufficiently accurate.

Chapter 7 Model Validation

The purpose of this chapter is to develop a comparison of the model predicted pollutant concentration and actual measured pollutant concentrations at the mine. The validation of a developed model is important in assessing the quality and accuracy of the simulation predicted results. In general, experiments are done in control environment numerous times to assess the validity of the collected data. Control experiments with real time meteorological data is not feasible.

There are two types of assessments used in CFD simulations, verification and validation. Model verification is all about checking the accuracy of the computer codes during the implementation phase of a real world problem within specific limits of accuracy. Model validation, on the other hand, is secondary to the model verification related to the computer codes to reproduce a reasonable output within the model domain (Oberkampf and Trucano 2002). Since, the pollution transport model developed in this research used a commercial CFD package, such as the ANSYS-FLUENT, verification is not needed as many of the commercial CFD programs have been tested and verified numerous times.

Most research work on pollution transport is focused on the convective boundary layer, whereas more frequently the stable boundary layer occurring in the Arctic imposes the most sever conditions. Even without a complex topography, strong wind shears and inversions the prediction of pollutant concentration can be challenging.

The structure of an atmospheric boundary layer (ABL) in a model is based on mean meteorological variables (temperature, wind, etc.) or on turbulent parameters (fluxes, TKE, structure parameters, etc.). In addition, several turbulent and non-turbulent processes (heating and cooling, convection and subsidence, radiation processes, etc.) interact with each other within the ABL. It is often difficult, if not impossible, to separate the various contributions of the physical variables to the modeled structure of the ABL. Under certain conditions, pollutants trapped within a SBL can cause a systematic over-estimation.

Therefore, the questions of model validation and of the uncertainties of its results within the model domain should be addressed appropriately in each dispersion analysis, also in relation to the wind field simulation. Most validation tests have found that the κ-ε model often over predicts the

length of the leeward side recirculation zone and under-predicts the length of the windward side recirculation zones (Salim et al. 2011a; Salim et al. 2011b).

As discussed in Chapter 2, a stable stratification of the boundary layer develops, when there is a radiative cooling of the surface layers at the pit bottom or an advection of warm air over the open pit. This results in the development of a stable boundary layer (SBL). While surface measurement of pollutants have limitations (from a 3-D perspective) even for the case fully developed turbulence, it becomes very difficult in case of SBL to make inference from surface data about the nature and characteristics of the process.

For model validation, the realizable κ-ε model is selected. The selection of realizable κ-ε model is based on the site specific data such as the wind velocity and the temperature. For model validation, the 2013 pit geometry is selected. The pit domain is extremely large and discretization of such an extended domain to meet the resolution requirement for LES model would need extensive computational resources as well as time. Moreover, under SBL, eddies are of smaller scales and to resolve these smaller scale eddies a much finer grid size is needed. Thus, for the application of a LES model is prohibitive given the computational resources available for this research.

7.1 Data for Model Validation

It is not possible to monitor pollutant concentrations at several locations for the verification and validation of the model, because of the cost and time involved. It is decided, therefore, to monitor pollutant concentrations at three locations in the open pit, and then compare them with model predicted concentrations. The extent of agreement between the two sets of data will form the basis for model validation. From a consideration of toxicity of various gaseous pollutants in the open pit, nitrogen dioxide (NO_2) is selected for monitoring. The simulation runs in previous chapter (Chapter 6) are based on the 2010 pit geometry and corresponding to 2010 pit data collected from the mine. For validation purpose, additional pollution concentration data, equipment locations, and extended geometry of the 2013 pit are collected. An extended 2013 pit is used for modeling (Figure 7.1). The reasons for selecting the 2013 pit geometry and associated data are (1) to examine the effect of aspect ratios on the pollutant transport and parameterization of the turbulence variables and (2) to reduce the influence of the boundary effects on the simulation results. One of the major purposes of the extended pit in the model is to understand the various physical phenomena occurring within the pit, thus, it is necessary to have the domain boundaries far away from the open pit. It is important to

note that, during 2012-13 there were no production activities in the pit, therefore the geometry of the pit and aspect ratios are the same that of the 2011 pit configuration. Due to the lack of production activities in the pit during the 2012-2013 no pollution data are available.

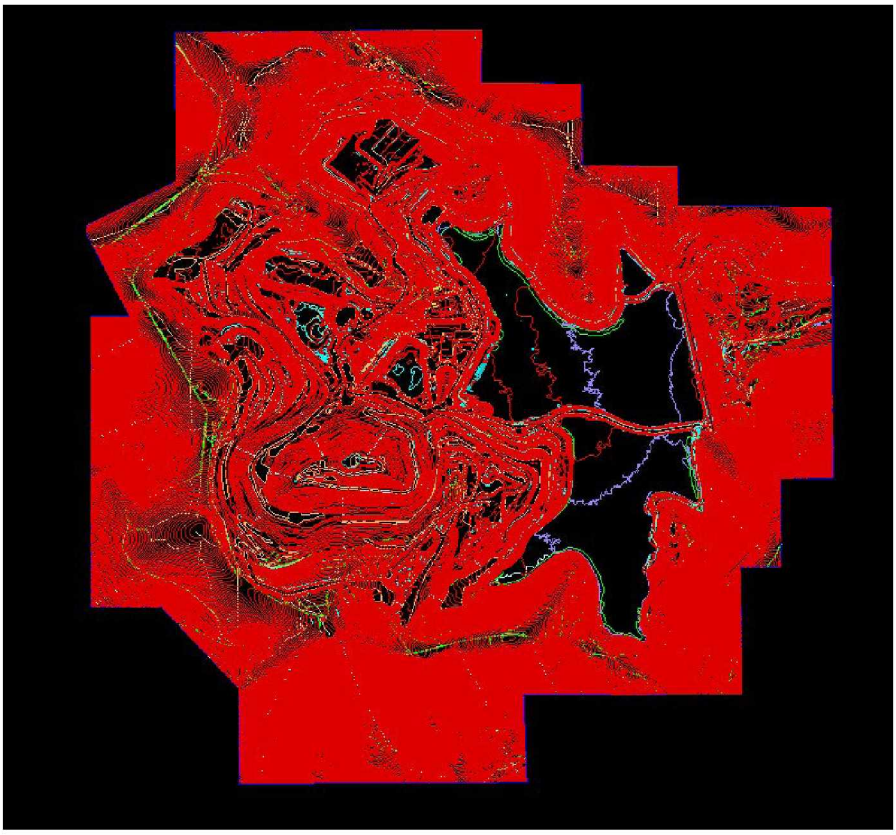

Figure 7.1: Contour Data Collected from the Partner Mine.

7.1.1 Sampling Procedures for Pollution Data

The selected mine has collected data during various times of inversion, which includes the measurement locations, pollutants concentrations, temperature at the pit rim and at the pit bottom at various times. However, the sample collection process at the mine is not very systematic, since pollution data are not collected at regular intervals. Often, other relevant information (such as temperature and the location of temperature measurement) is not recorded. The collected data includes NO_2, NO and CO concentrations at all the locations, in addition to the temperature at the pit bottom and at the pit rim. During the time of inversion, if there is any visible sign of brown haze (Figure 7.2) in the pit, the mine management starts to take measurement of the pollutants concentrations and temperature at the selected sampling points (Figure 7.3). The deepest point of observation is the 213 m (700 ft.) Bench, which is one of the production benches; other sampling

locations are the 286 m (940 ft.) Bench, and the Lift Station which is located on the ramp. With the first visible sign of brown haze in the pit, which is generally observed at the selected mine to be approximately one parts per million (ppm)(Waggoner et al. 1983), measurements are taken at the bottom most part of the pit (213 m Bench). As the concentration rises to four ppm, the trucks are pulled out of the pit. The shovel and drill machine are, however, keep idling. If the concentration at the 213 m Bench level reaches to five ppm no further measurements are taken at the 213 m Bench but samples are taken at Bench 286 m, which is located at a higher elevation. Similarly, if the measurements at any locations are found around five ppm, further measurements are taken only at higher bench elevations.

Figure 7.2**:** Pit under Inversion with Brown Haze.

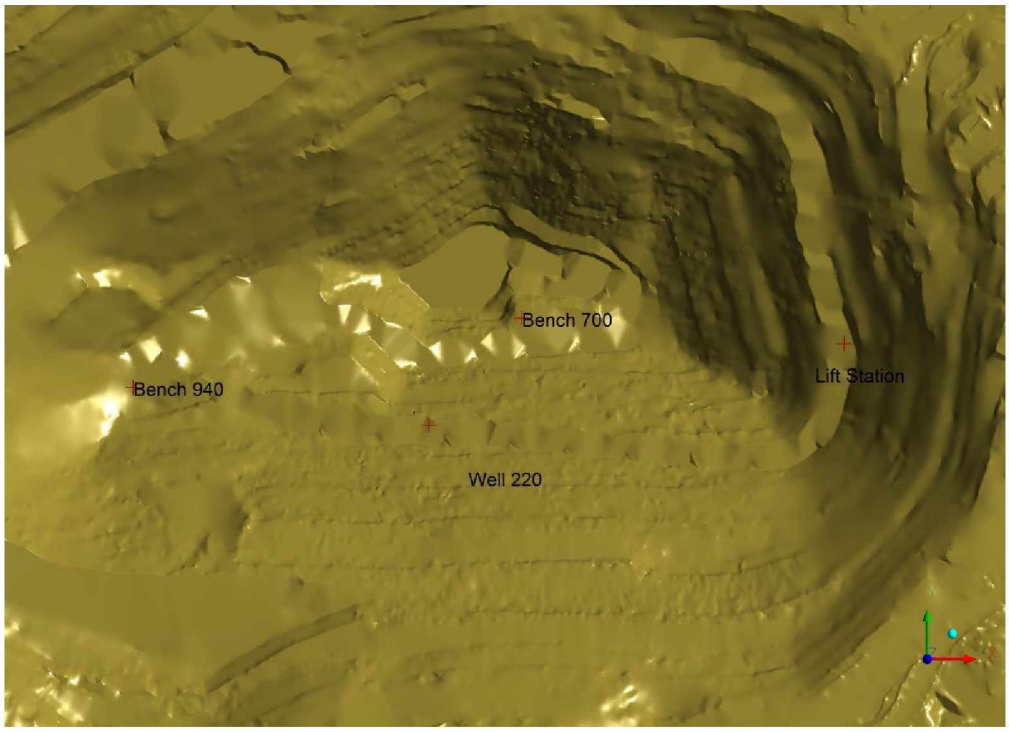

Figure 7.3: Sampling Locations for Collecting Data during Inversion.

For model validation, measured pollution concentration data collected on January 3rd 2011 are used. On January 3rd, 2011, inversion is observed in the pit, and subsequently, the pollution concentration data are collected following the established procedure. The data collected from the mine on the selected date is provided in Table 7.1. The pollution concentration data are available from 7:45 AM onwards, on January 3rd, 2011. The data collected at 7:45 AM is not included in Table 7.1. It is not used in validation model, since this initial point of the simulation run would be affected by initial bias. There is no sequence in the collected data in terms of time, i.e. data are not collected at any regular intervals. From Table 7.1, it is evident that around 7:45 PM, the pollutant concentration level at 213 m Bench is around 5 ppm or above, therefore, no data is collected at that location at 7:57 PM and beyond. The time referred in the text is Alaska Standard Time (AKST).

The management of the selected mine has provided the 2013 pit geometry (Figure 7.1), as well as an access to the dispatch system for identifying precise locations of the pollutant sources such as the trucks, the shovels and the drill-machines, which provided a realistic data for the simulation run. The exact sampling locations, contaminant concentration values at those locations, and the coordinate values of those locations are significant in validating the simulation model.

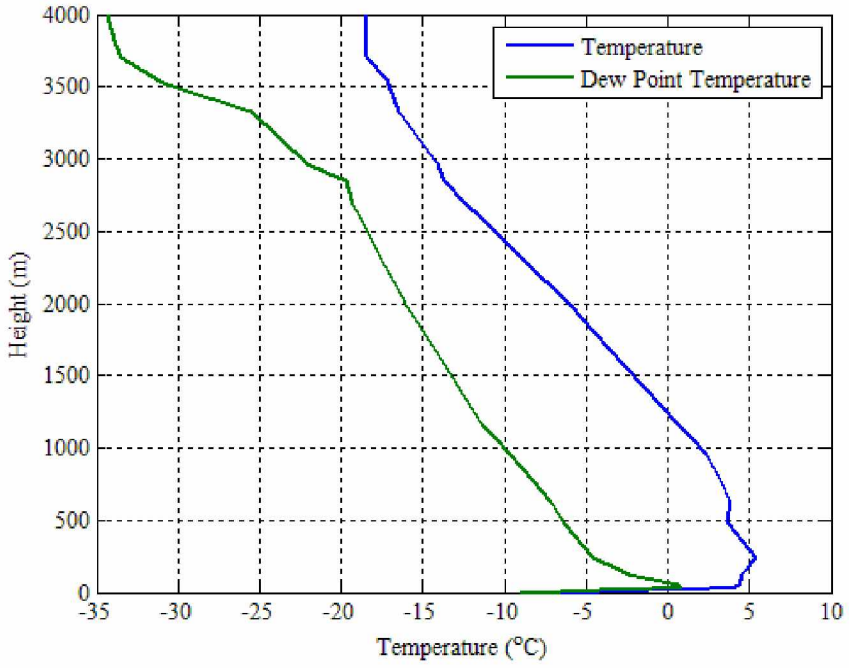

Figure 7.4: Temperature and Dew Point Variation with Altitude at 3:00 AM January 3rd 2011.

Figure 7.4 is the plot of temperature and the dew point, which indicates the absence of cloud over the Fairbanks area at the time of measurements.

Apart from the above information from the selected mine, it is equally important to have realistic boundary conditions regarding the inlet velocity and the inlet temperature, which varies with altitude and time. Since, the model is an atmospheric model developed using the CFD tool, one of the major challenges is its reproducibility. Validation of the data collected from such experiments is also challenging due to various phenomena occurring at different time and spatial resolutions.

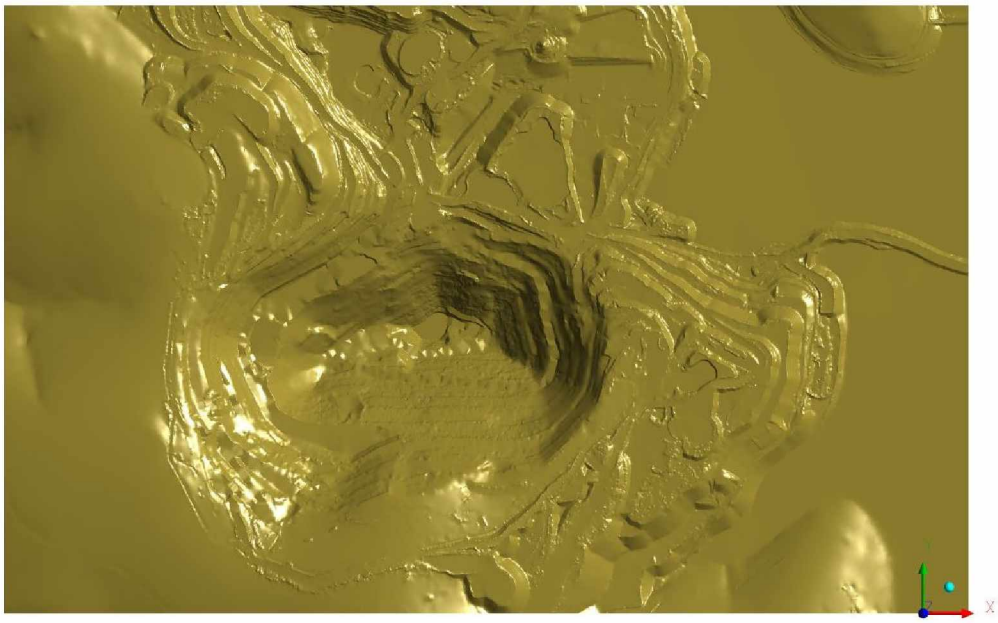

Figure 7.5: Pit Extent used for Modeling.

Table 7.1: Pollutant Concentration Data Collected from the Mine during Inversions.

Date	Time of the day (AKST)	Bench 700	bench 940	Lift Station
January 3rd 2011	10:15 AM	3.50		2.80
January 3rd 2011	1:20 PM	3.60		2.50
January 3rd 2011	3:30 PM	4.00		0.00
January 3rd 2011	4:30 PM	4.30		
January 3rd 2011	7:45 PM		4.80	4.10
January 3rd 2011	9:40 PM		4.90	1.50
January 3rd 2011	11:00 PM			2.50
January 4th 2011	0:05 AM			2.60
January 4th 2011	1:20 AM		4.90	0.90
January 4th 2011	2:43 AM	4.5	4.50	0.20
January 4th 2011	3:50 AM		4.90	0.20
January 4th 2011	4:55 AM		5.00	0.20
January 4th 2011	5:05 AM		4.90	0.70
January 4th 2011	6:00 AM	4.7	4.20	0.00

7.2 Incorporating Variable Boundary Conditions in the Model

As discussed in previous section, the wind velocity and air temperature are both space and time dependent. It is important to incorporate such variability in the model domain, via appropriate boundary conditions. The velocity and temperature at the velocity-inlet boundary are functions of height, more precisely, within the first hundred meters of the atmospheric boundary layer (ABL). According to Stull (1988), the wind velocity follows a logarithmic wind profile under neutral conditions (Equation 7.1). More information, however, is required, such as the friction (shear) velocity (u_*) and the aerodynamic roughness length (z_0) to define the inlet velocity. The constant κ in equation (7.1) is the von Kármán constant with a value of 0.41 and z is the reference height which is generally known. The aerodynamic roughness length for various terrain types are also available in the literature (Stull 1988). The friction velocity, however, is difficult to obtain as it requires some experimental data for velocity at the site. Due to the non-availability of the wind velocity data at the mine site, the friction velocity is calculated using a power low wind profile (Equation 7. 2).

$$u_z = \left(\frac{u_*}{K}\right) \ln\left(\frac{z}{z_0}\right) \tag{7.1}$$

$$u_z = u_r \left(\frac{z}{z_r}\right)^{\alpha} \tag{7.2}$$

The power low wind profile generally provides a good estimate of the wind velocity within the boundary layer. In equation 7.2, the variable, u_r is the reference velocity at a reference height, z_r, and the exponent, α, which depends on the stability of the atmosphere. The value of the exponent (α) is taken as 1/7, assuming a neutral stable atmospheric condition. Since the wind velocity at the mine is unknown, an approximation is, therefore, made using data from a weather station located close to the mine. The collected wind velocity data and the temperature data from the weather station are assumed to be representative of the mine air velocity and temperature fields for the (inlet) boundary conditions. The velocity at the reference height, u_r, is obtained from the same weather station; the elevation of the weather station is taken as the reference height, z_r. The reference height used in the model is 690.67 m (2266 ft.). Equation 7.3 is used to develop the vertical temperature profile at the inlet boundary:

$$T = T_O + L.z \tag{7.3}$$

Where, T is the temperature at height, z, L is the lapse rate and T_0 is the reference temperature. A lapse rate of -6.5°C per kilometer is considered for the simulation. Varying temperature and velocity profiles are incorporated in the ANSYS-FLUENT simulation model by introducing two user defined functions (UDFs). The input vertical temperature and velocity profiles are presented in Figure 7.6 and Figure 7.7. The initial elevation is 457 m (1500 ft.) above sea level located at the east wall boundary of the model domain.

It is important to recognize that the wind and temperature profiles not only vary with height but also with respect to time. Thus incorporation of the temporal variability into the boundary conditions makes the simulation model to behave closer to the real system. For this purpose, a time varying temperature and velocity distribution is adopted at the velocity-inlet boundary, where both the temperature and the velocity are the function of height, i.e. temperature and velocity varies with height.

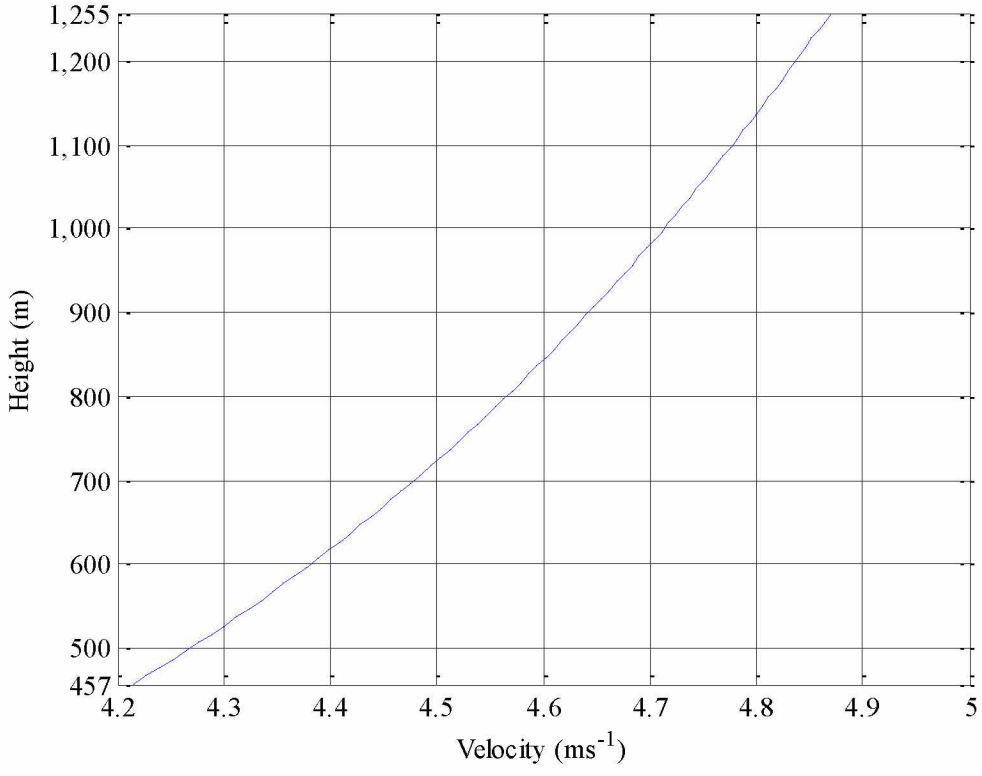

Figure 7.6: Vertical Velocity Profile at the Inlet Boundary.

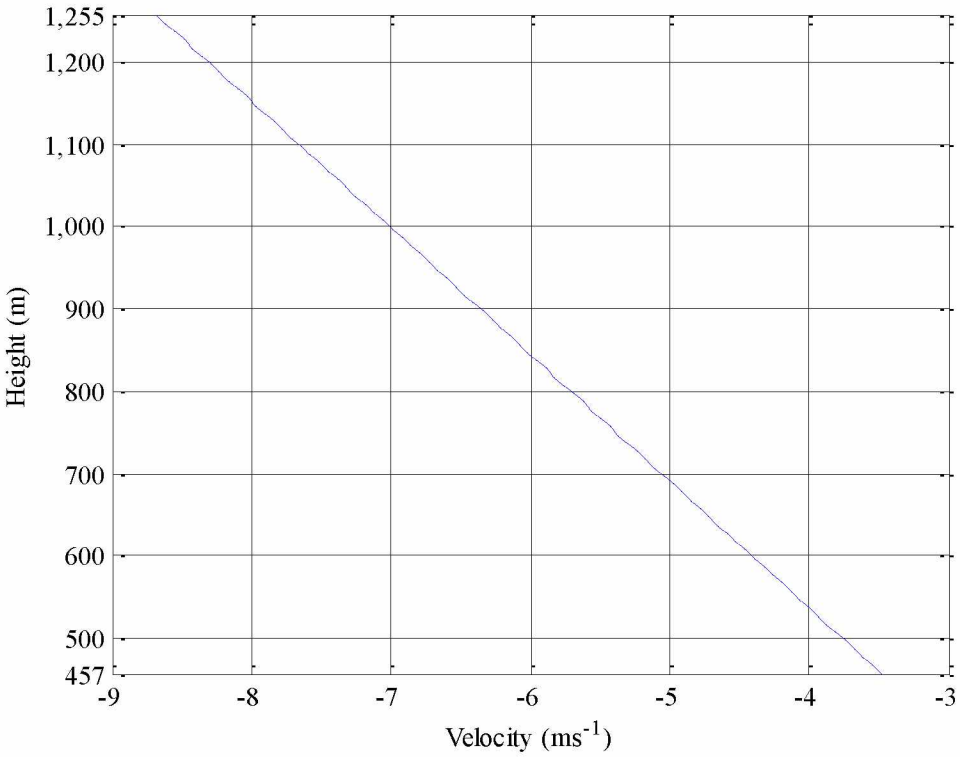

Figure 7.7: Vertical Temperature Profile at the Inlet Boundary.

7.3 Equipment Locations and Dispatch

From the dispatch data collected from the mine, there are five shovels and two drill machines operating in the pit on January 3rd, 2011. The numbers of trucks, however, varied, and are deployed according to production need. There is a shovel and a drill machine located at the pit bottom, near the 213 m Bench. These are the major sources of pollution at the pit bottom along with deployed trucks. Other shovels are operating near 609.6 m (2000 ft.) elevation level, as well as a number of trucks. In the model, equipment are placed according to the collected location data, as well as the location of trucks serving the shovels, the time interval at which the contaminant are released and its magnitude and duration. Various contaminant sources present in the pit are shown in Figure 7. 6. Figure 7.7 shows the three locations where the pollutant samples are collected.

Apart from adapting, the time varying boundary conditions in the simulation model, additional information regarding the location of the pollutant sources in the pit are also obtained from the selected open pit mine. The actual coordinate locations of shovels and drill machines are used for the simulation. The movements of the trucks are also incorporated by creating another set of UDFs with an on and off switch for the trucks at intervals of 4, 8 and 12 minutes. From the dispatch, it

is found that the inter arrival time of trucks as well as the loading time of trucks at the shovel station are approximately 4 minutes. The average queuing time of a truck is approximately 12 minutes. There are five trucks included in the model simulation. There is a shovel, drill machine and five trucks operating at 700 Bench. Locations of other equipment are above the inversion level and did not contribute to the pollution load. Therefore, the equipment are not included in the validation model.

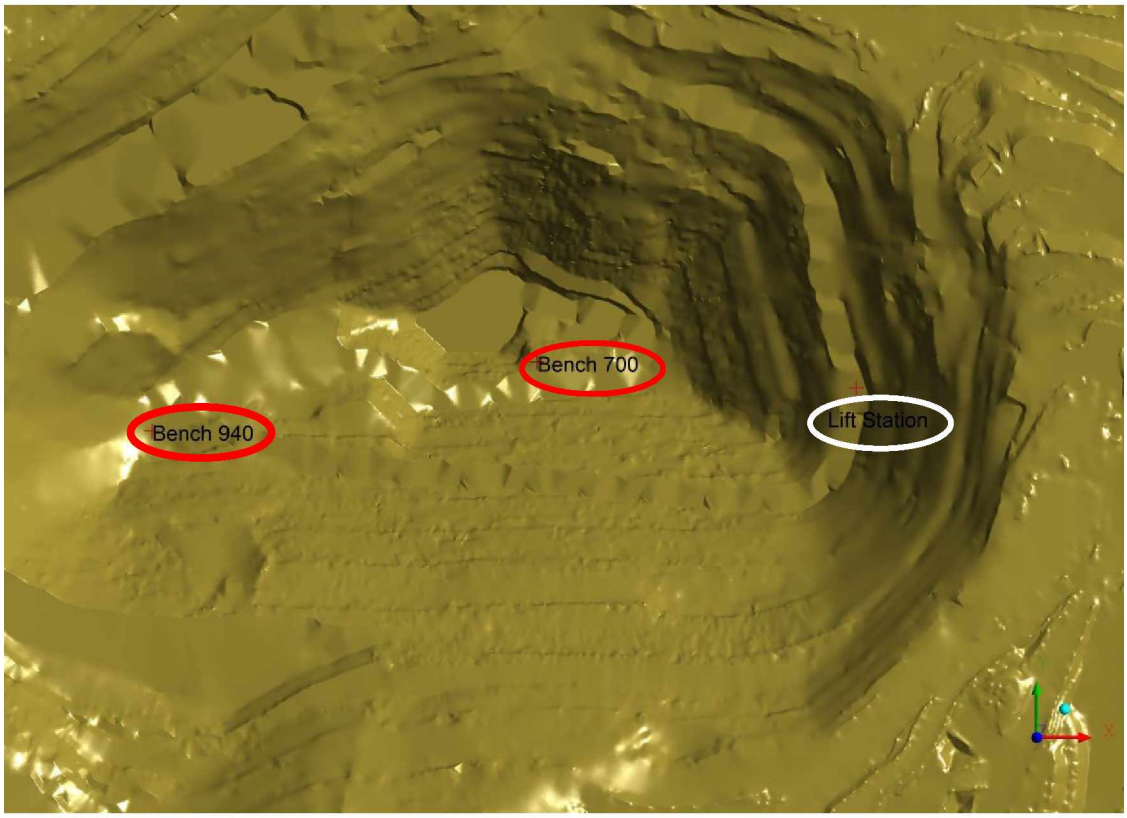

Figure 7.8: Sampling Locations during Inversion at the Open Pit.

7.4 Simulation using Realizable κ-ε Model

The simulation run is performed for a period of twenty four hours, starting 7:45 AM on January 3rd 2011, along with its time varying boundary conditions. The results presented in the following section are from the realizable κ-ε model simulation. Many of the parameters are kept the same as in the simulation performed in the previous chapter (Chapter 6). Time steps are manually adjusted during the simulation. Initial time steps are kept to a low value (0.001 second) to ensure model convergence. Once the convergence is achieved time step is increased gradually. The maximum time step is fixed to five seconds where model convergence is reached.

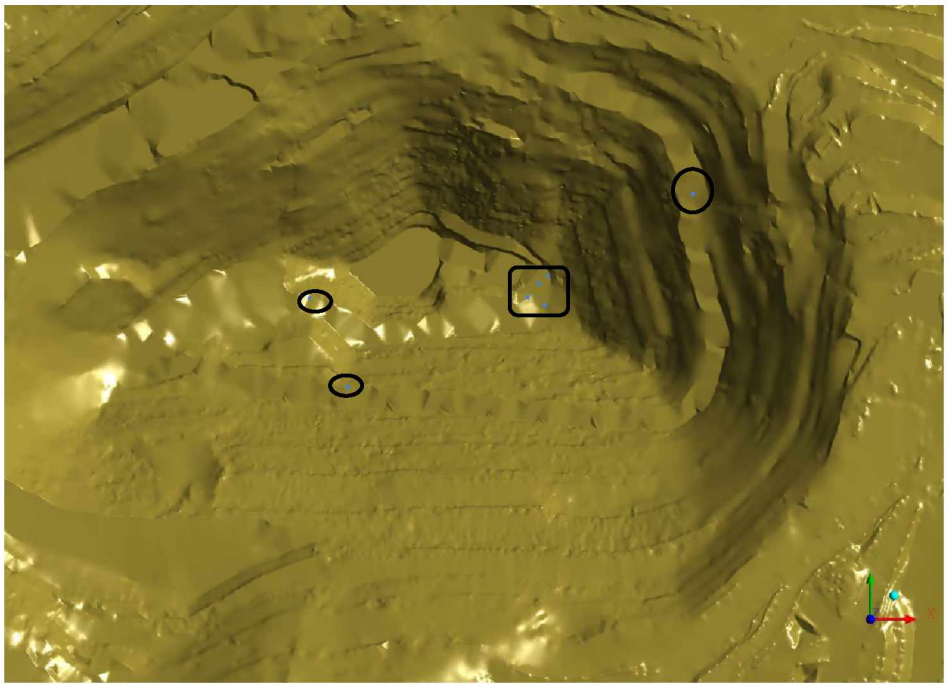

Figure 7.9: Pollutant sources placed at different Location in the pit.

7.4.1 Simulation Results

Figure 7.10 shows five lines located in the open pit domain. Line 5 is on the pit rim and rests of the lines are within the pit. Line 2 is near some equipment running all the time, whereas, Line 1 is from bottom most part of the pit to the top of the model domain. Along the lines, temperature, turbulent kinetic energy, turbulent intensity and other variables are plots at different time intervals.

Vertical profiles of temperature and wind velocity for the simulated SBL agree well with observations by other researchers (Hartmann and Wendler 2005) which shows small vertical gradient below the capping inversion. This is due to the large amount of turbulence, especially in the vertical direction. The simulated turbulence structure shows the dominance of the vertical velocity variance within mixed layer, while the horizontal variances dominate within the SBL. The SBL after several hours of cooling shows a strong, surface-based temperature inversion (Figure 7.11).

Line 2 is located near the operating equipment and heat released from the equipment is captured in the temperature profile (Figure 7.13). A sudden jump in the magnitude of the temperature during the initial time period is observed at the lower level of the pit surface. However, settling of the inversion layer at the pit bottom the sudden jumps in temperature are not

visible. After 16 hours, trucks were switched off, thus, less amount of heat is released at the bottom of the pit.

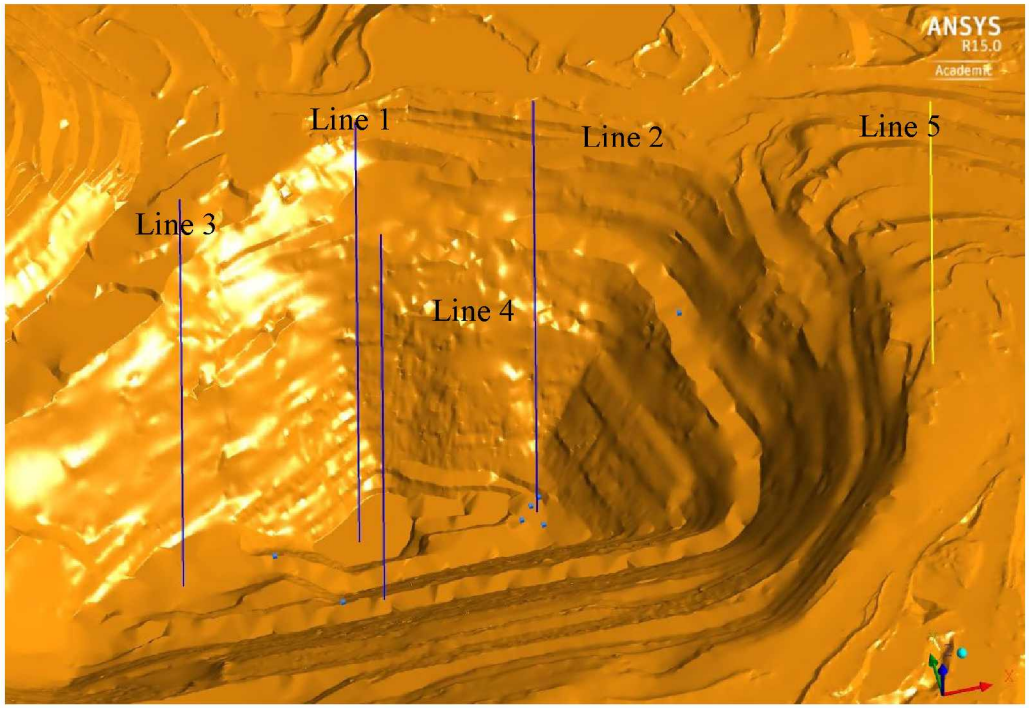

Figure 7.10: Different Lines for Sampling Simulated Data.

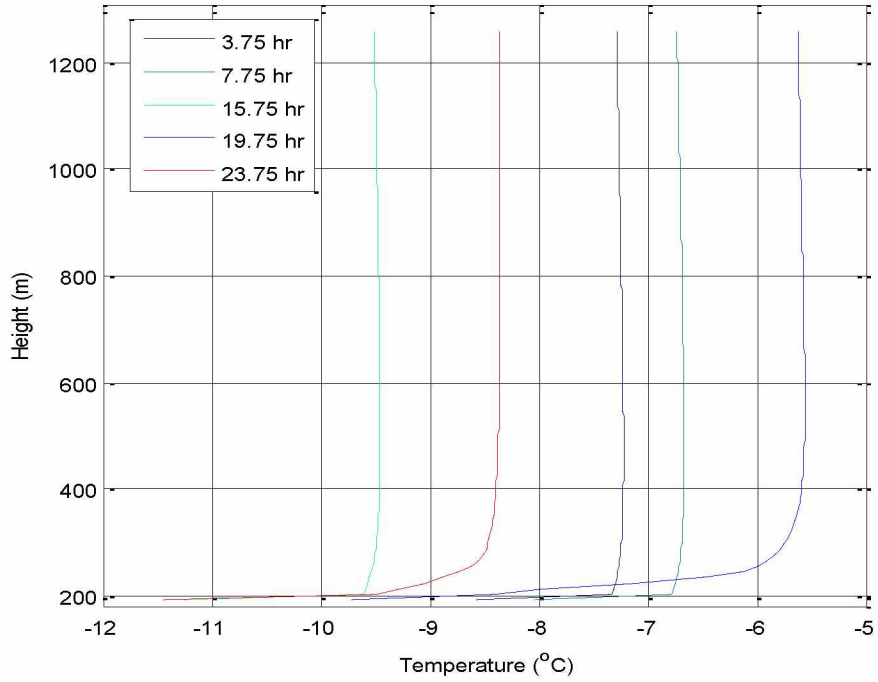

Figure 7.11: Temperature Profile along Line 1 at Various Time Intervals.

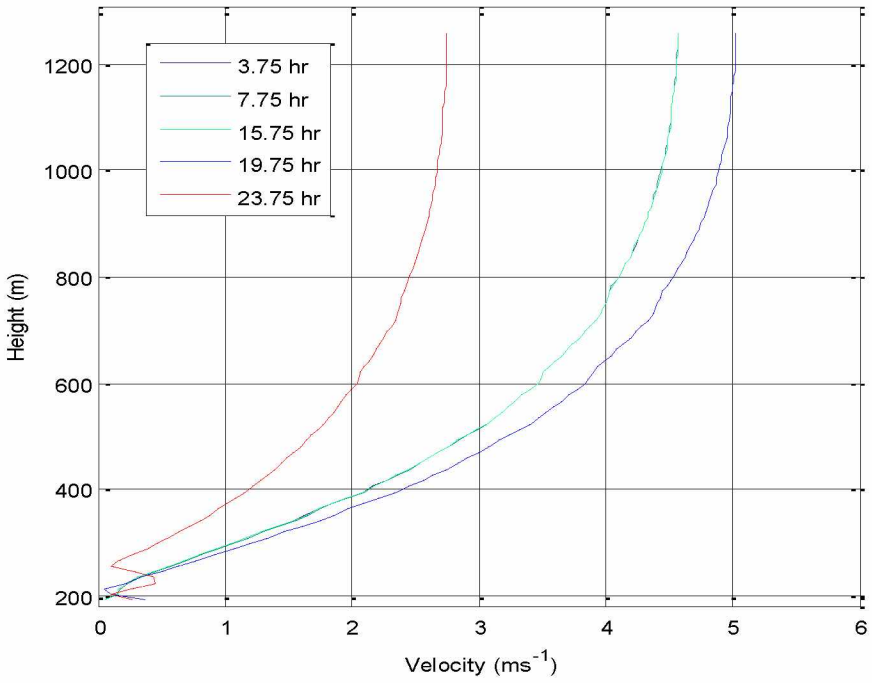

Figure 7.12: Velocity Profile along Line 1 at Various Time Intervals.

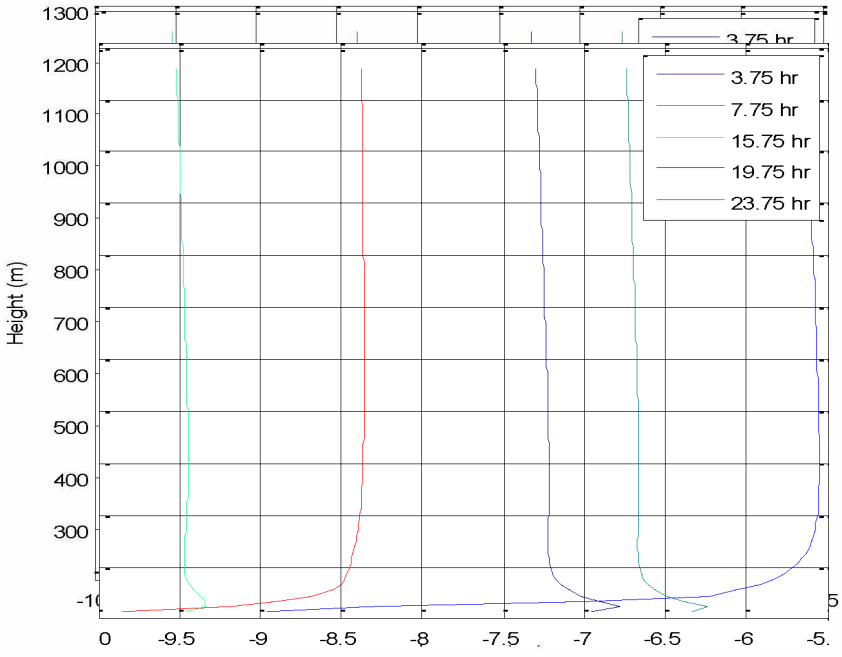

Figure 7.13: Temperature Profile along Line 2 at Various Time Intervals.

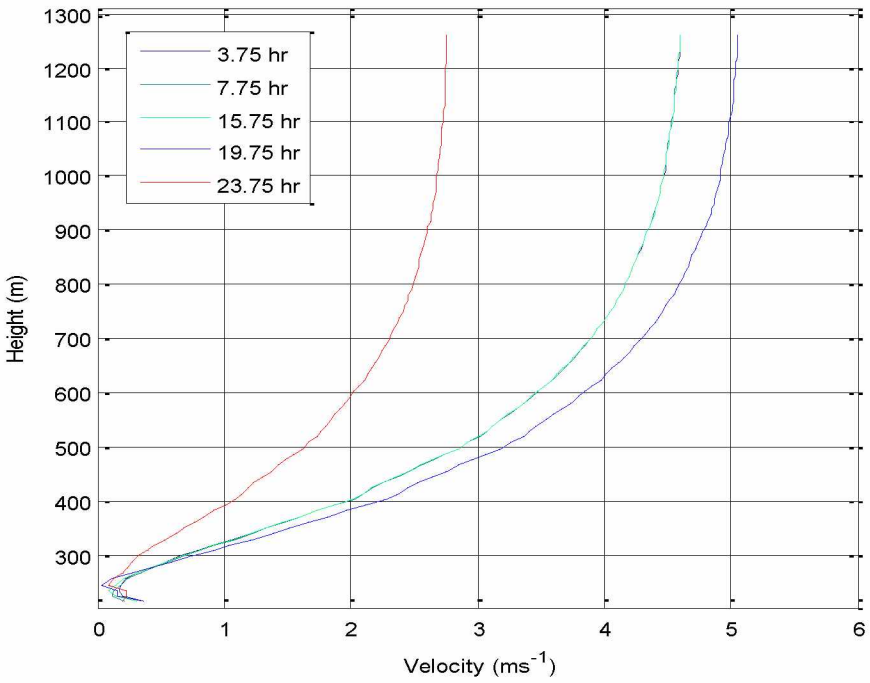

Figure 7.14: Velocity Profile along Line 2 at Various Time Intervals.

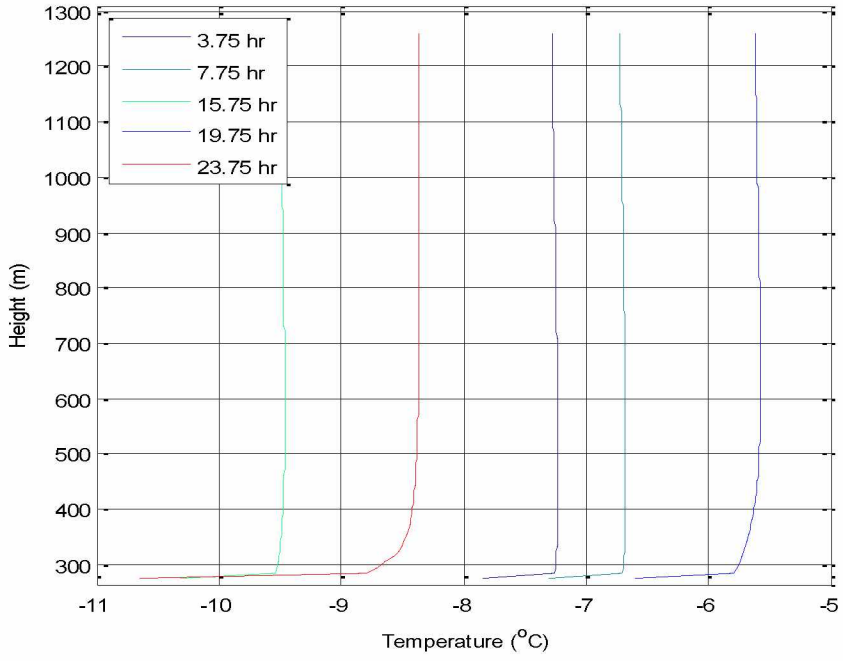

Figure 7.15: Temperature Profile along Line 3 at Various Time Intervals.

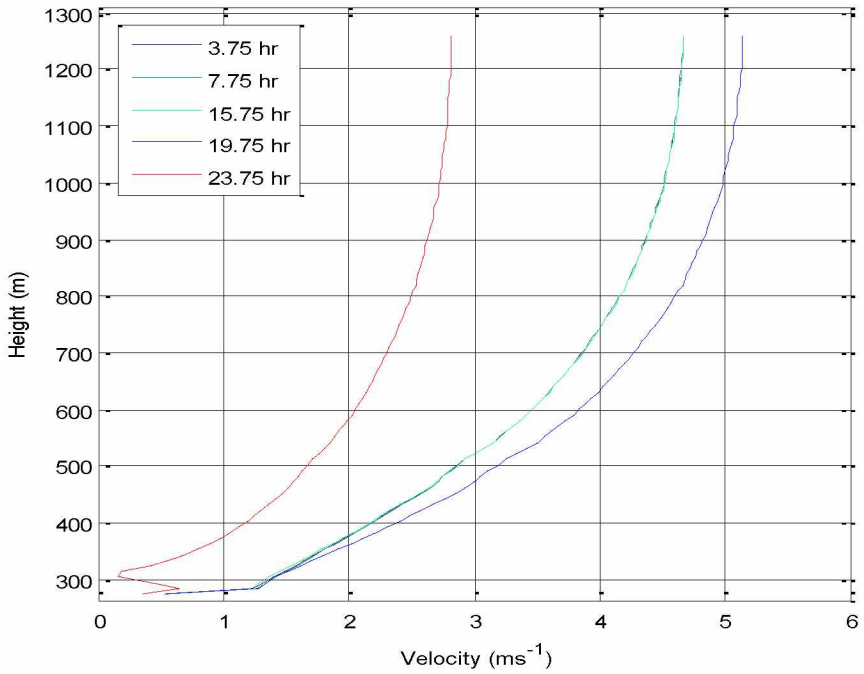

Figure 7.16: Velocity Profile along Line 3 at Various Time Intervals.

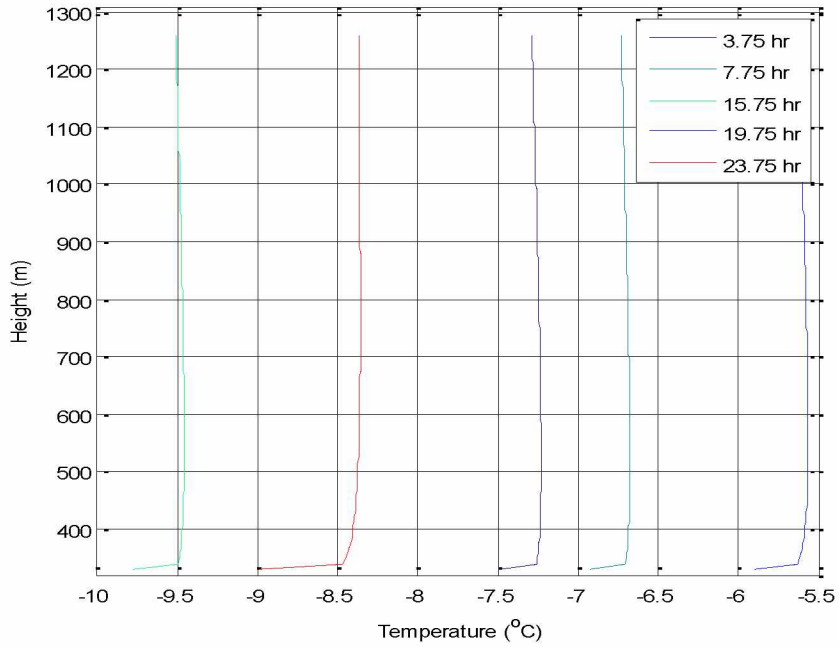

Figure 7.17: Temperature Profile along Line 4 at Various Time Intervals.

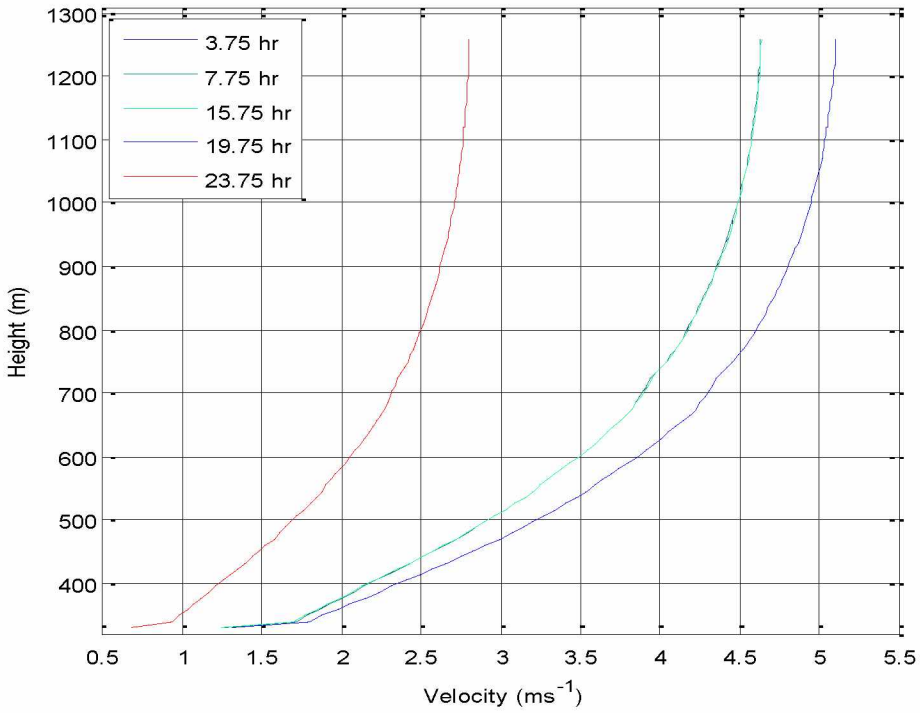

Figure 7.18: TKE Profile along Line 4 at Various Time Intervals.

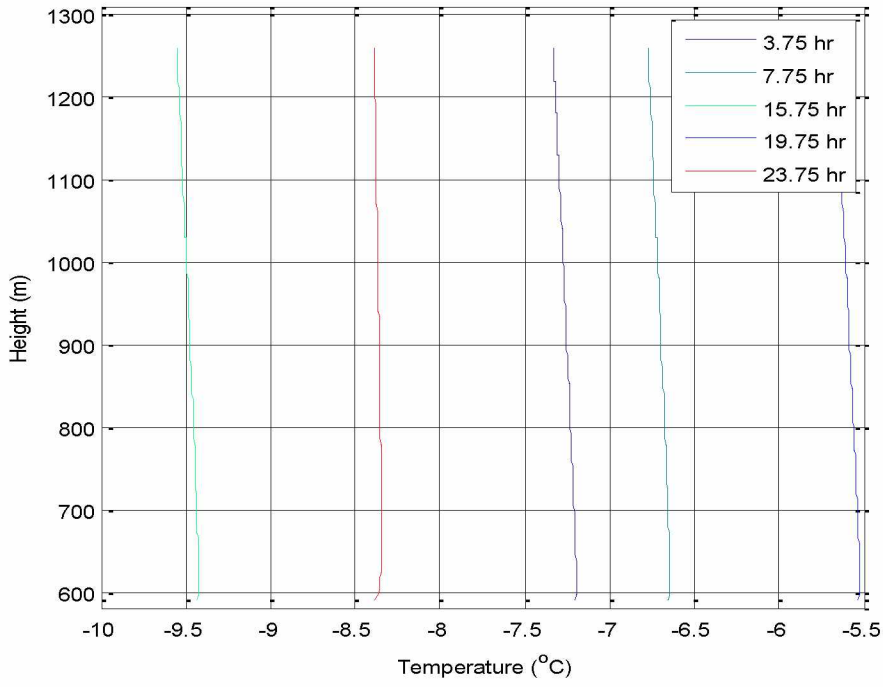

Figure 7.19: Temperature Profile along Line 5 at Various Time Intervals.

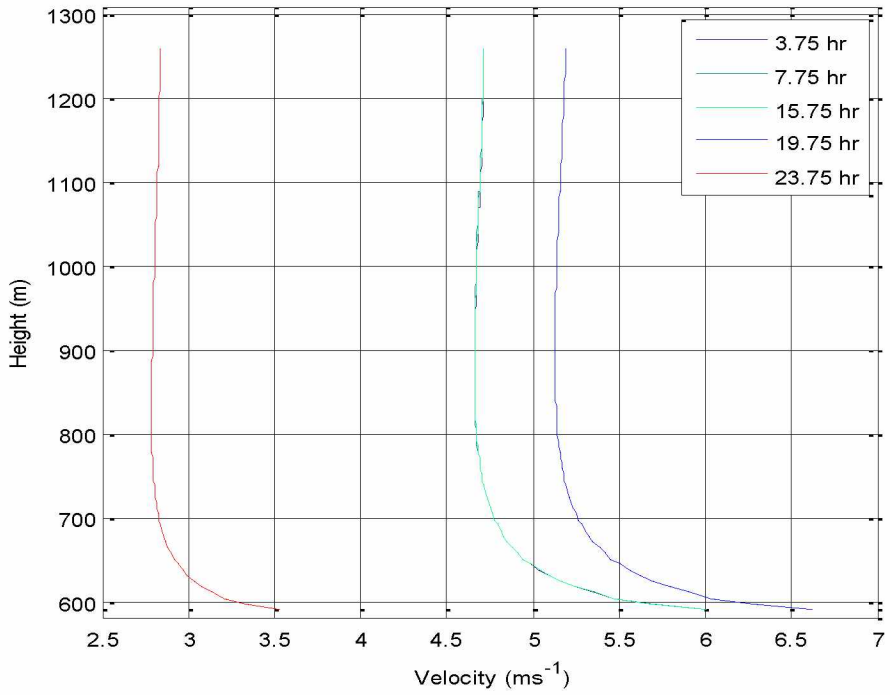

Figure 7.20: Velocity Profile along Line 5 at Various Time Intervals.

7.4.2 Parameterization of Simulated Turbulent Variables

The model developed can be used to understand the ABL/SBL structures over an open pit mine and to characterize the nature of turbulence which could explain recirculatory nature of the airflow in the pit. The turbulent kinetic energy (TKE) in boundary layer is an important determination of turbulent mixing and dispersion. The increase in wind shear and TKE leads to enhanced dispersion. It is also important to have several turbulence variables/quantities from the simulation; however, there is no data available on measured turbulence values at the selected mine. Apart from the TI and TKE, Richardson number (Ri) is calculated and plotted at different time intervals along the vertical lines at these seven locations.

After 3 hours of simulation, the TKE plot (Figure 7.21) along line 1 which is located at the deepest part of the 2013 pit, Figure 7.21 shows that the TKE is very low (0.5 Jkg^{-1} > TKE). With increasing time from 3.75 hours till 15.75 hours, the TKE fluctuates between 190-250 m elevation levels, and a re-circulatory velocity pattern (Figure 7.12) can be observed. Furthermore, the Richardson number (Figure 7.22) is always greater than unity (R_i > 1.0). There is very little turbulence. The Richardson number at the bottom of the pit (Figure 7.22), however, indicates a laminar flow.

At 19.75 hour of simulation along Line 1, an increased TKE at the bottom most part of the pit (190–200 m) can be observed (Figure 7.21), due to the buoyancy driven turbulence. The flow seems to be turbulent between 200–300 m elevation levels, as indicated by the Richardson number (Figure 7.25). Above that level (300 m – 375 m), turbulence seems to be intermittent. Beyond 375 m, the flow can be characterized as laminar. At around 600 m elevation, the flow can be characterized as unsteady (turbulent) flow.

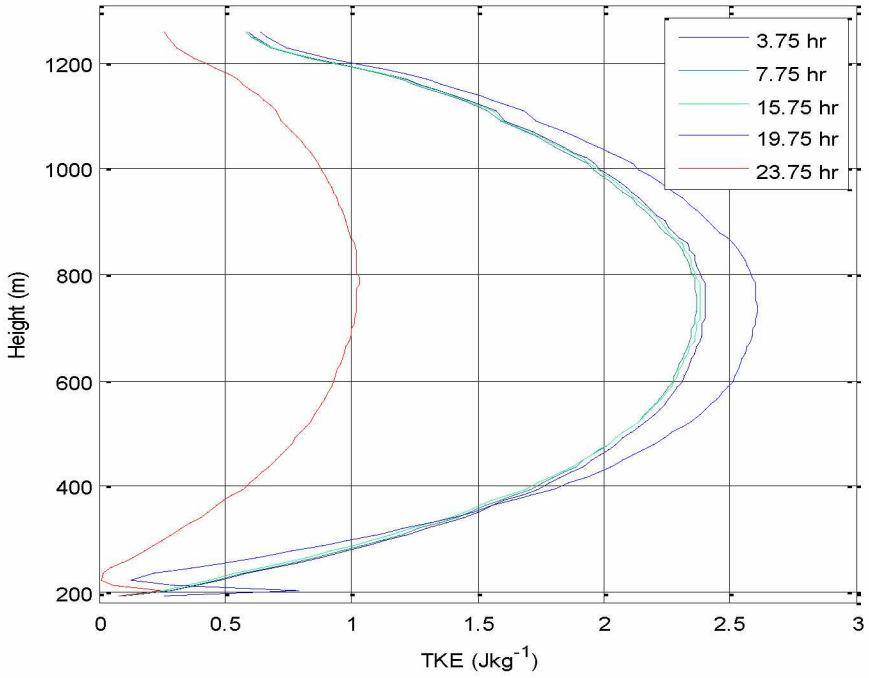

Figure 7.21: Turbulent Kinetic Energy Profile along Line 1 at Various Time Intervals.

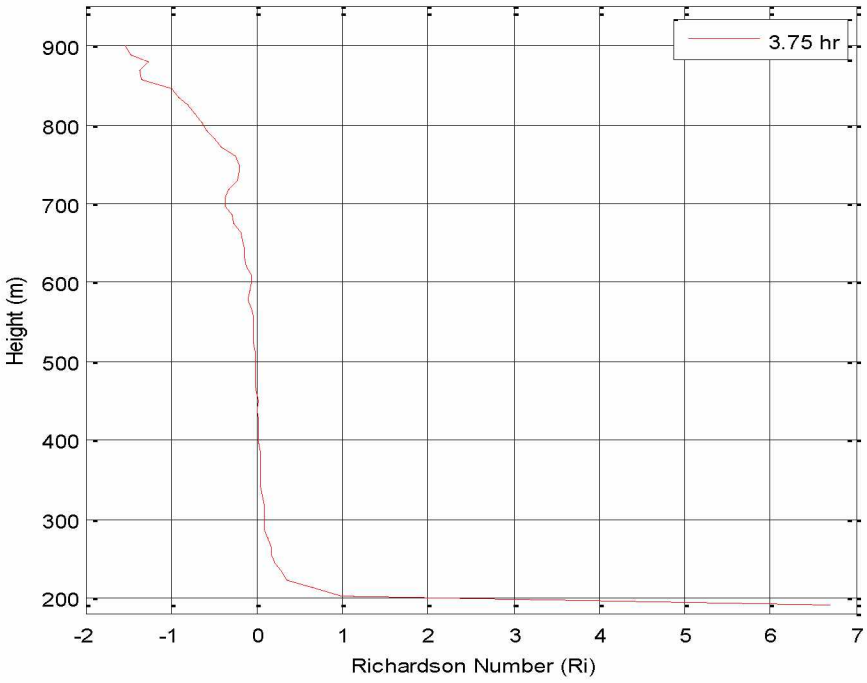

Figure 7.22: Richardson Number Profile along Line 1 at 3.75 hrs.

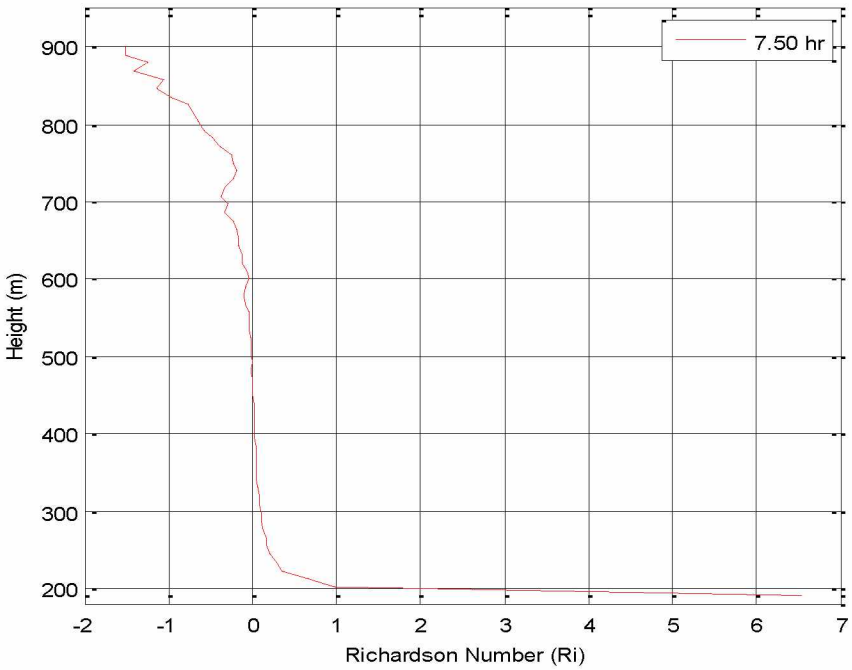

Figure 7.23: Richardson Number Profile along Line 1 at 7.50 hrs.

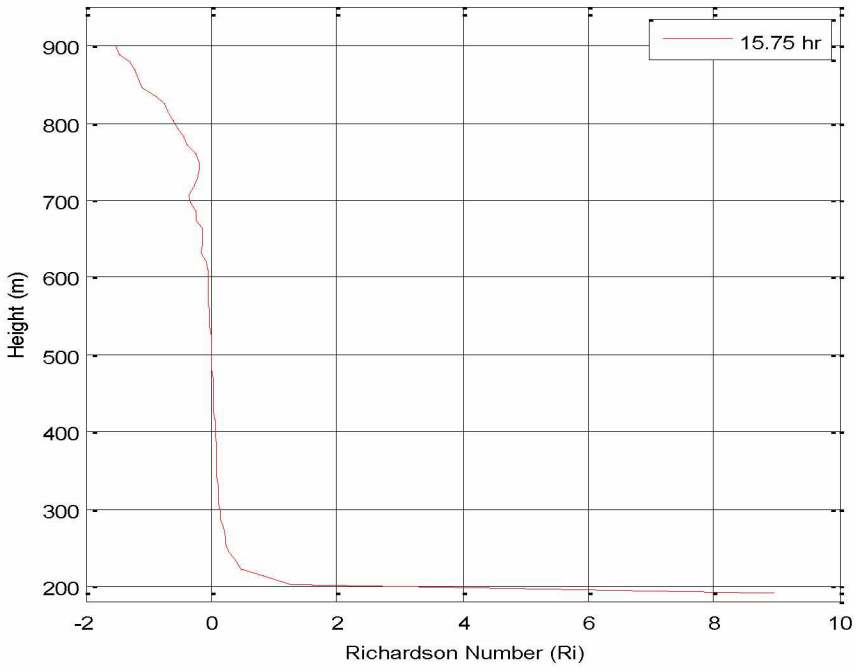

Figure 7.24: Richardson Number Profile along Line 1 at 15.75 hrs.

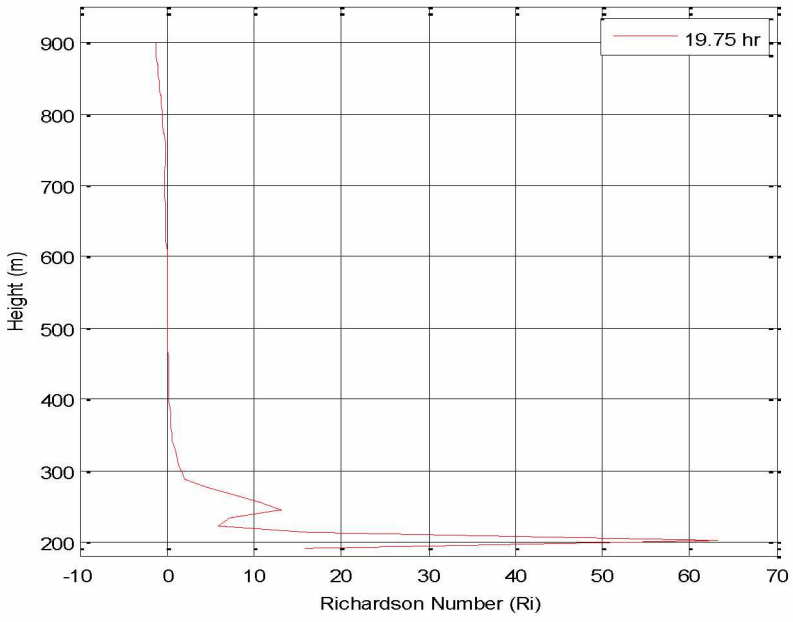

Figure 7.25: Richardson Number Profile along Line 1 at 19.75 hrs.

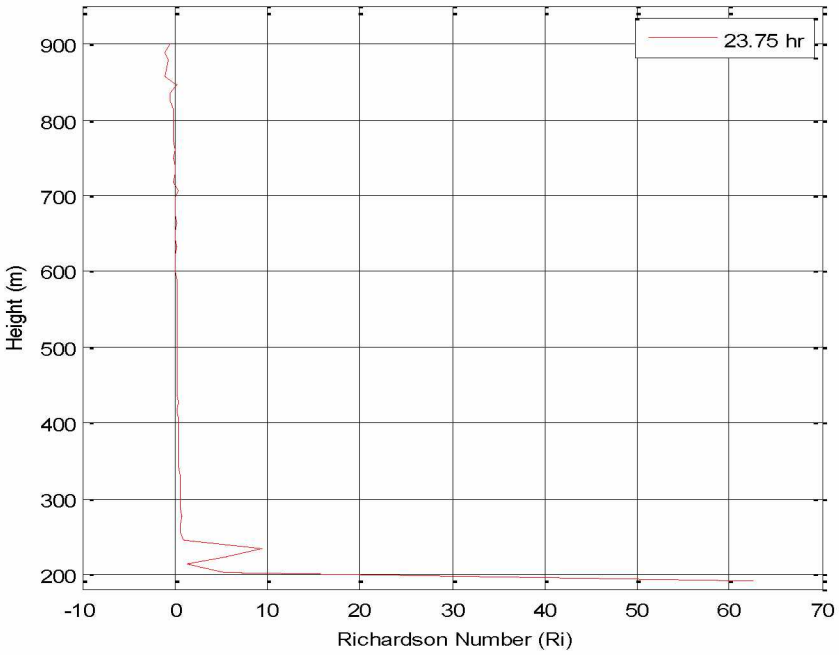

Figure 7.26: Richardson Number Profile along Line 1 at 23.75 hrs.

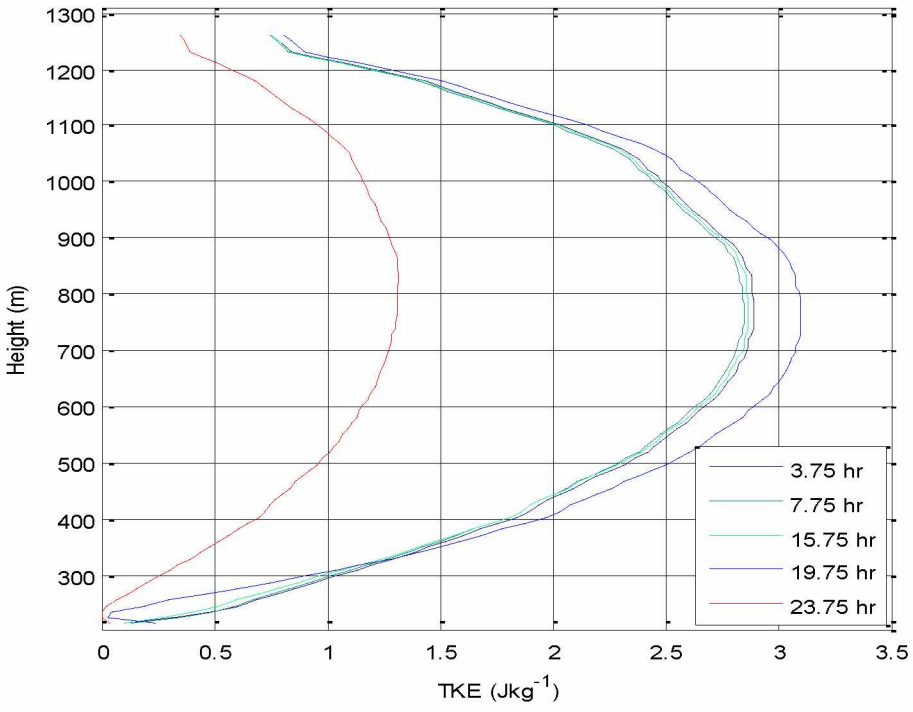

Figure 7.27: Turbulent Kinetic Energy Profile along Line 2 at Various Time Intervals.

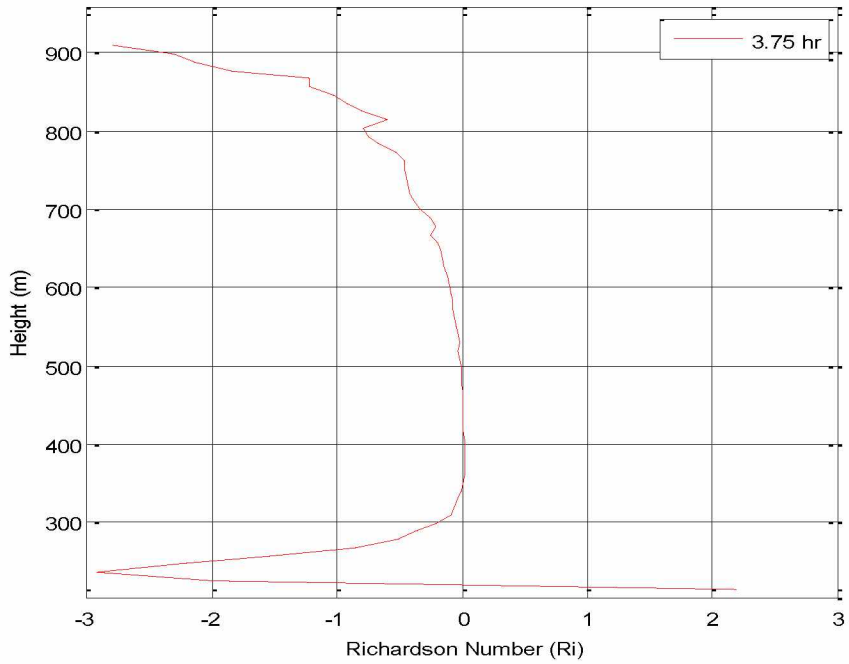

Figure 7.28: Richardson Number Profile along Line 2 at 3.75 hrs.

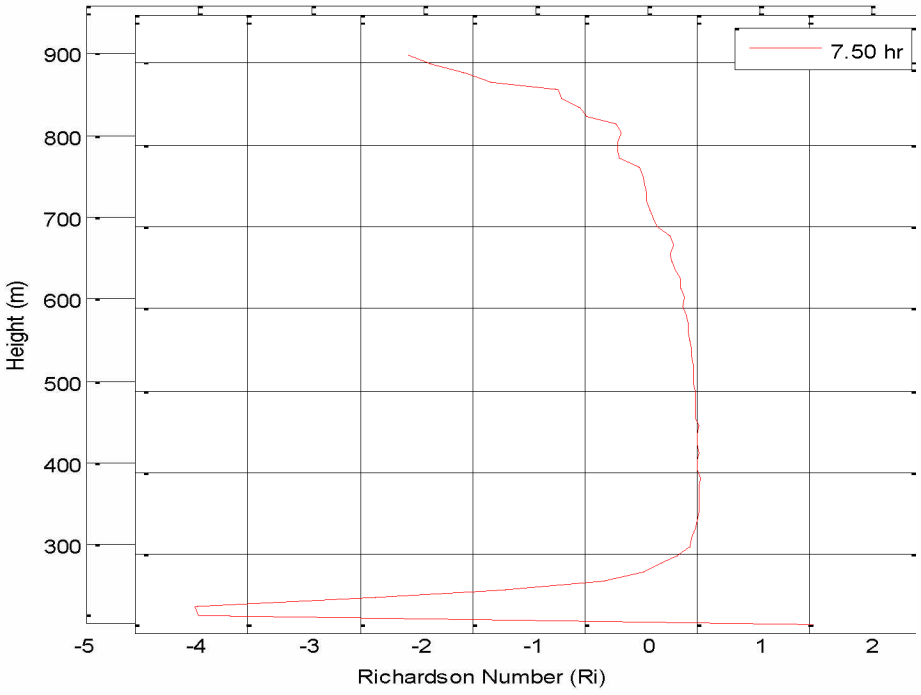

Figure 7.29: Richardson Number Profile along Line 2 at 7.50 hrs.

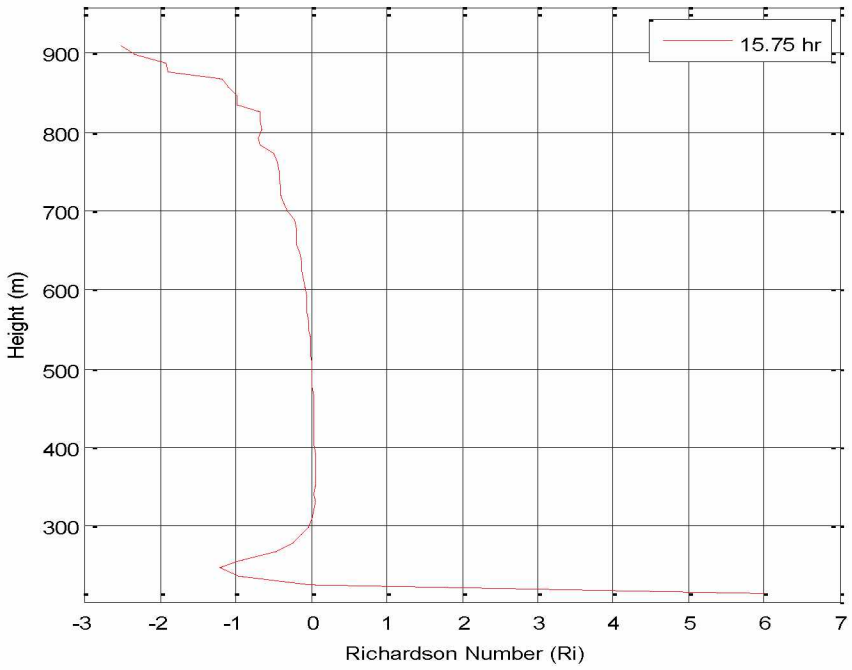

Figure 7.30: Richardson Number Profile along Line 2 at 15.75 hrs.

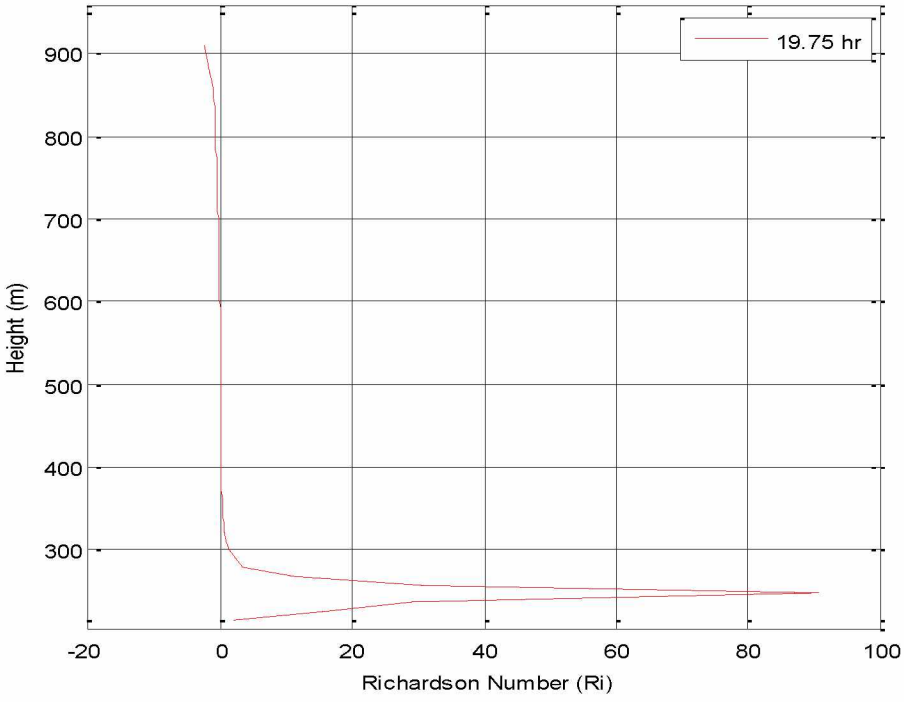

Figure 7.31: Richardson Number Profile along Line 2 at 19.75 hrs.

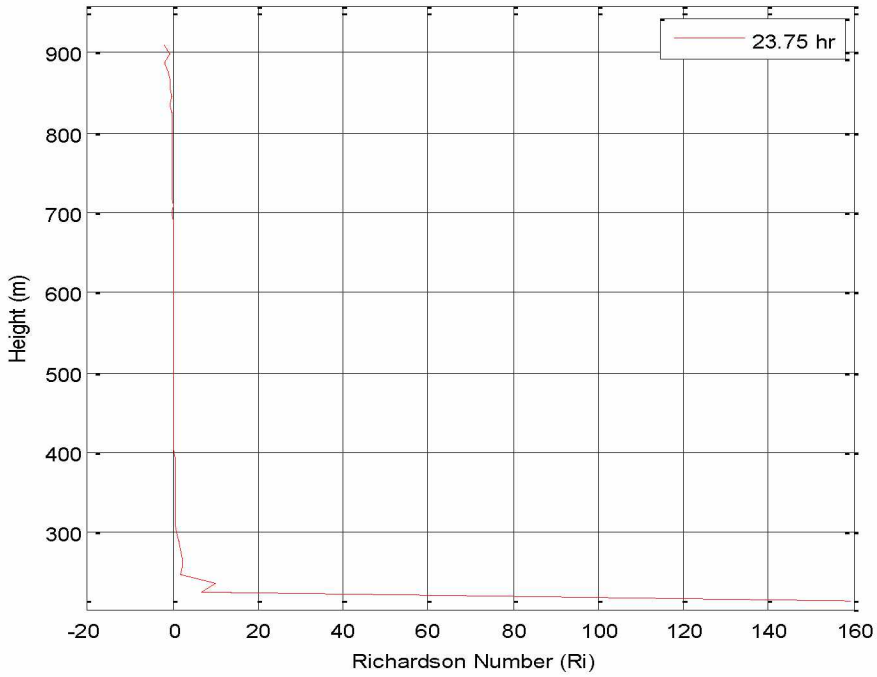

Figure 7.32: Richardson Number Profile along Line 2 at 23.75 hrs.

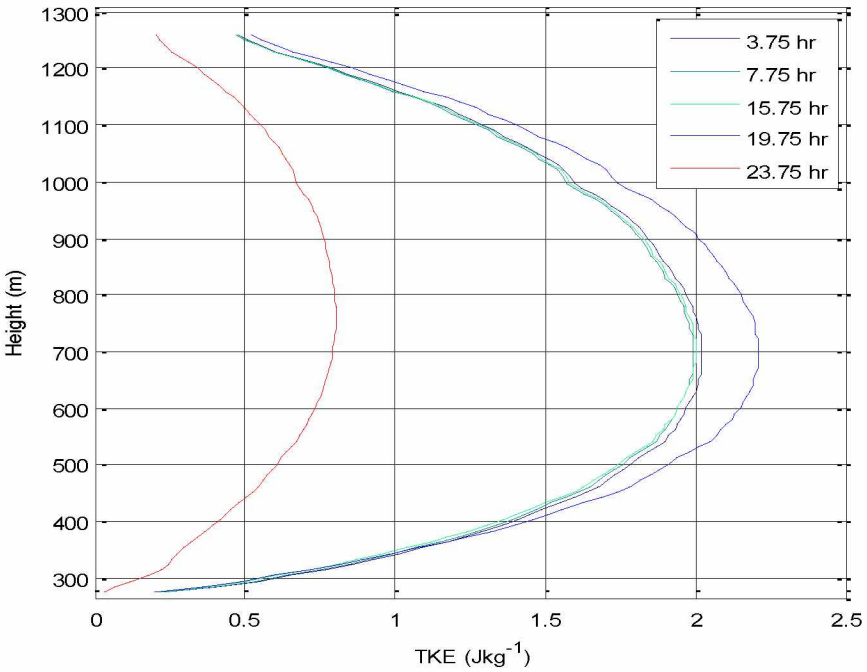

Figure 7.33: Turbulent Kinetic Energy Profile along Line 3 at Various Time Intervals.

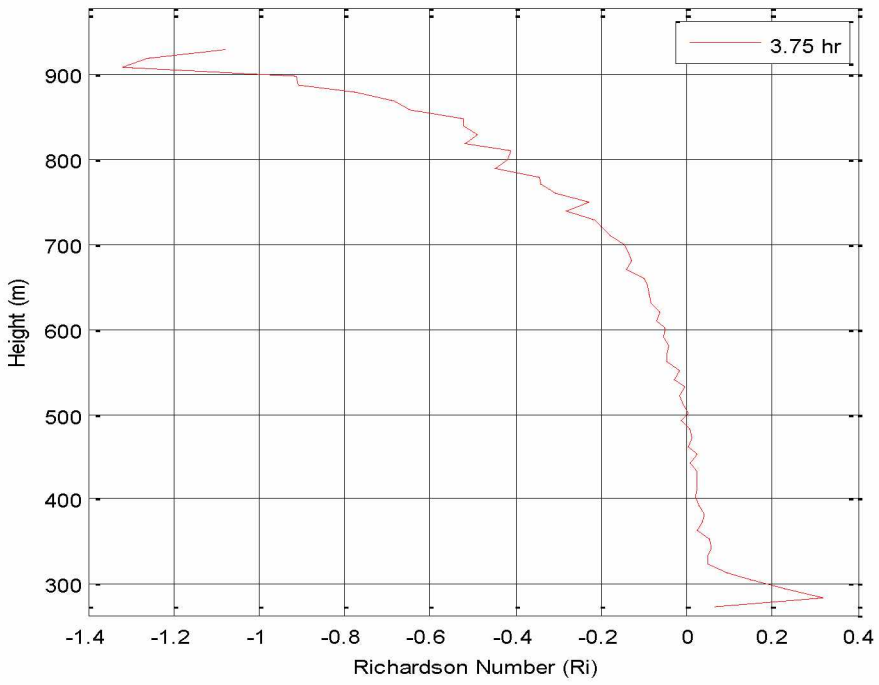

Figure 7.34: Richardson Number Profile along Line 3 at 3.75 hrs.

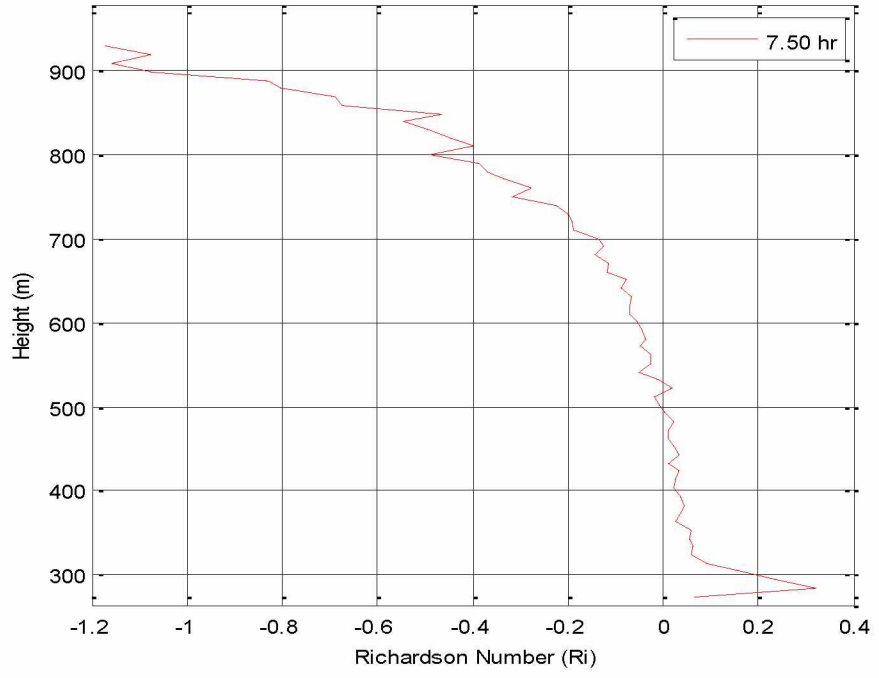

Figure 7.35: Richardson Number Profile along Line 3 at 7.50 hrs.

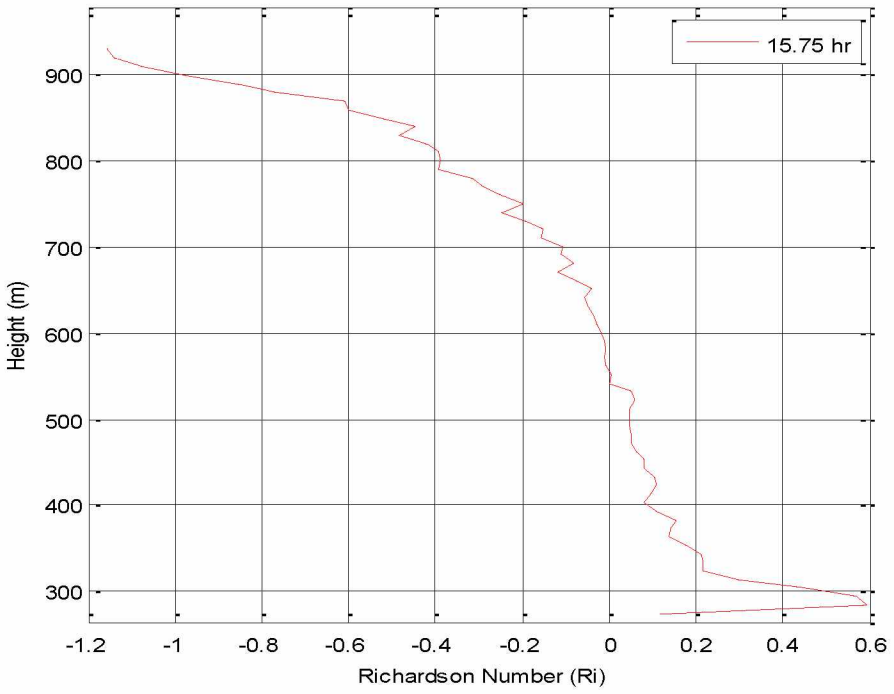

Figure 7.36: Richardson Number Profile along Line 3 at 15.75 hrs.

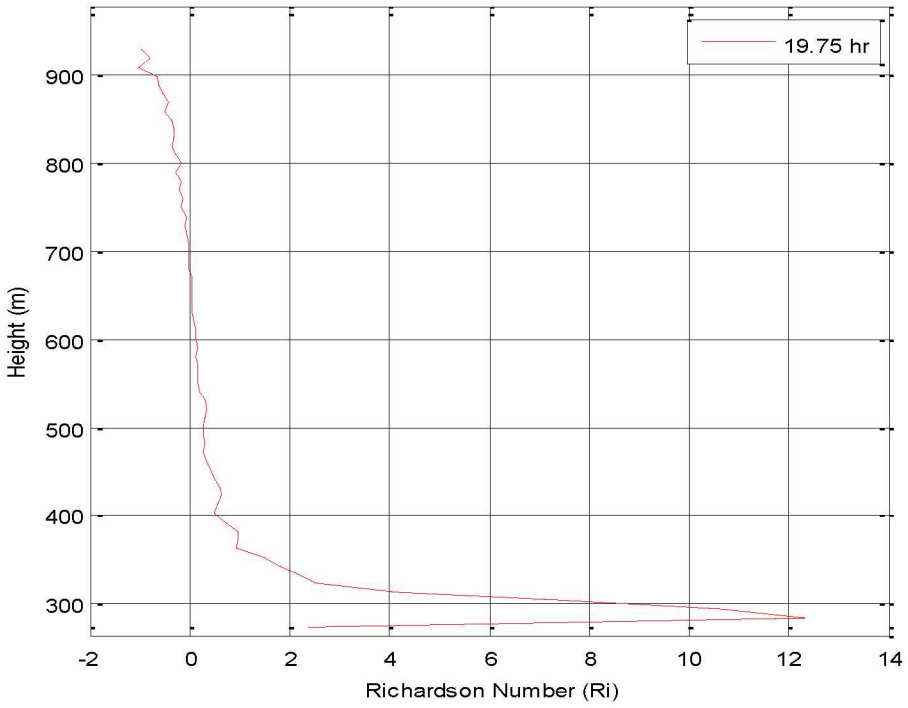

Figure 7.37: Richardson Number Profile along Line 3 at 19.75 hrs.

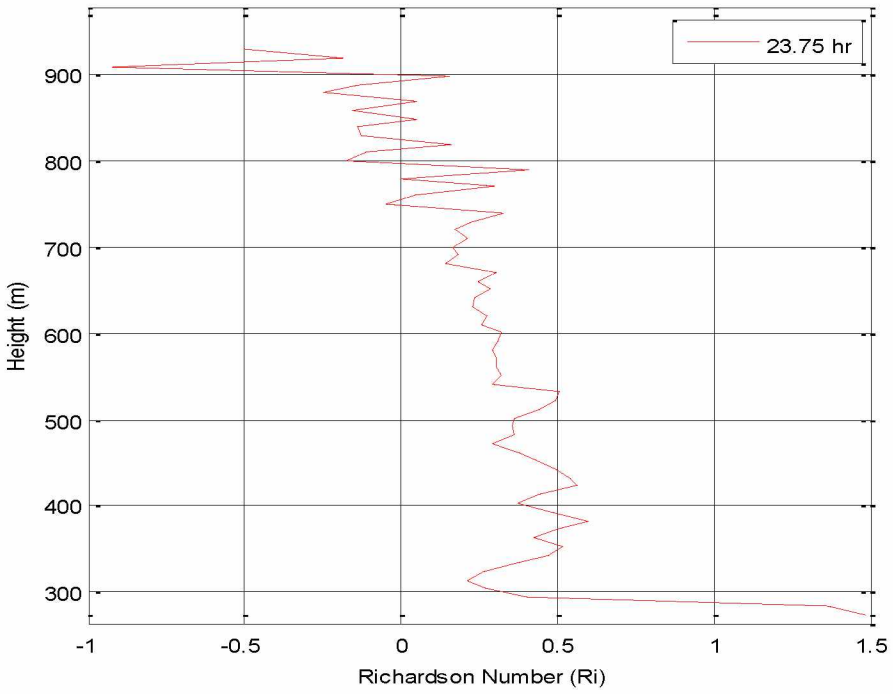

Figure 7.38: Richardson Number Profile along Line 3 at 23.75 hrs.

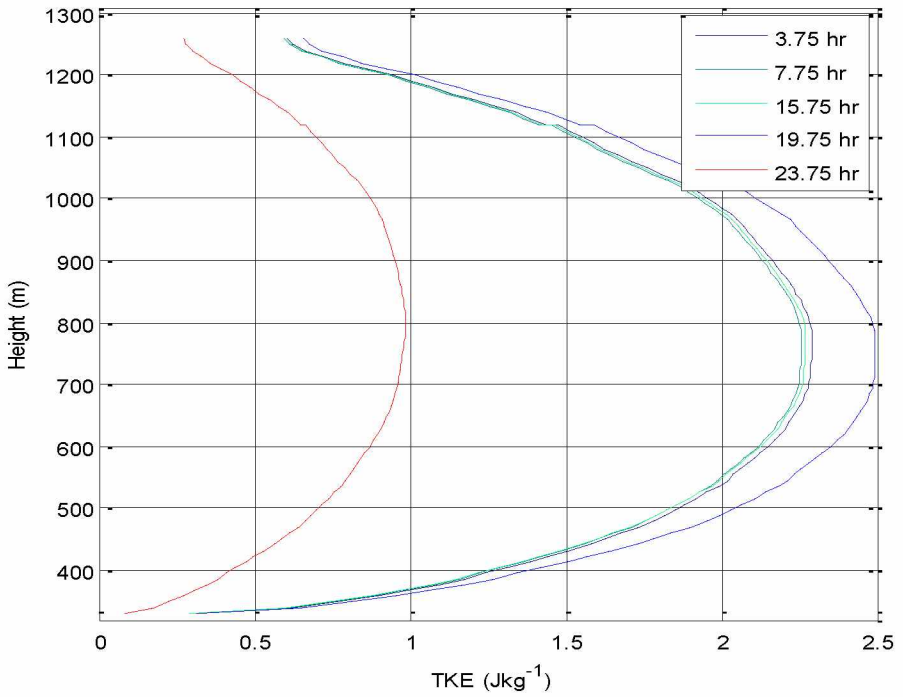

Figure 7.39: Turbulent Kinetic Energy Profile along Line 4 at Various Time Intervals.

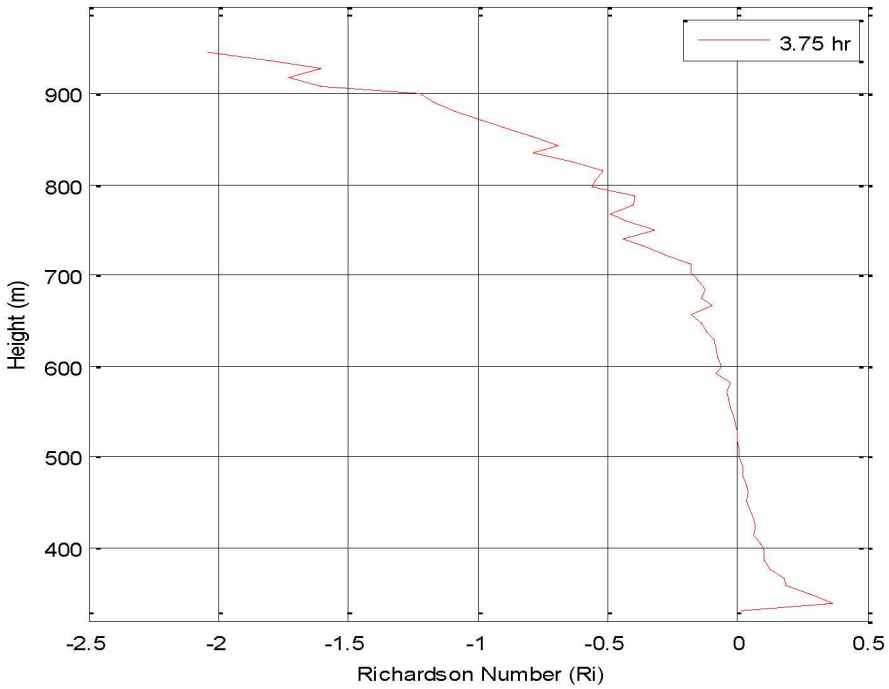

Figure 7.40: Richardson Number Profile along Line 4 at 3.75 hrs.

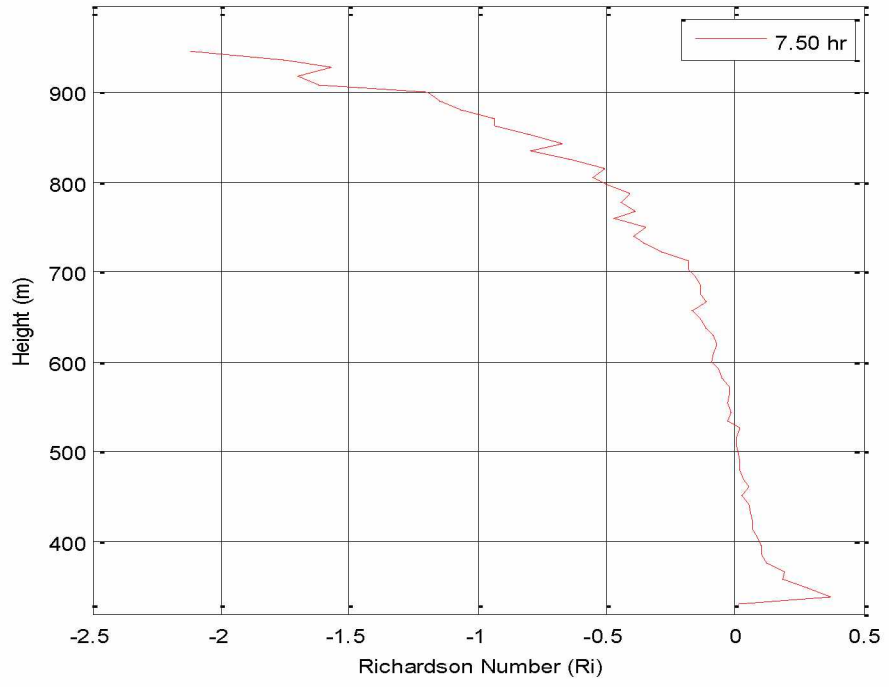

Figure 7.41: Richardson Number Profile along Line 4 at 7.50 hrs.

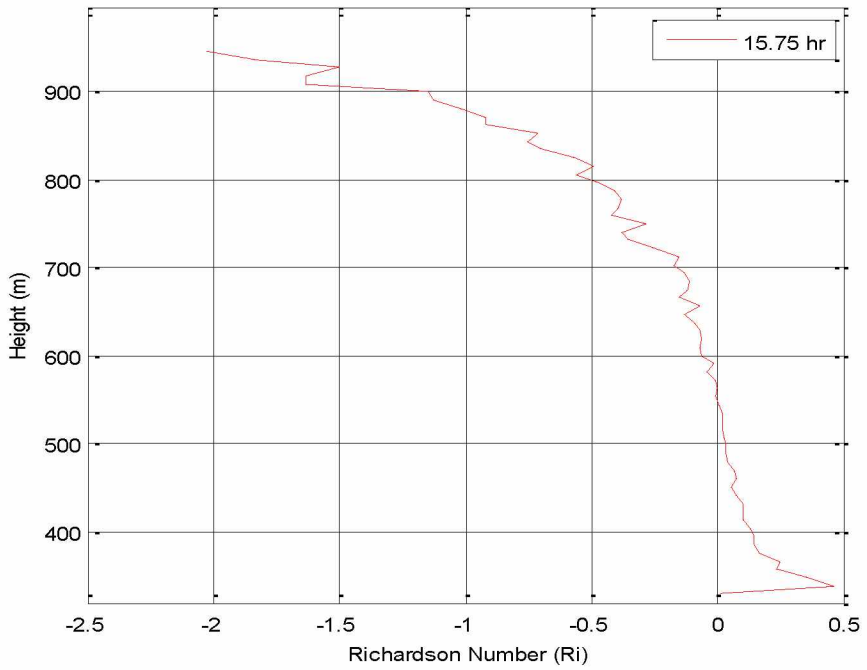

Figure 7.42: Richardson Number Profile along Line 4 at 15.75 hrs.

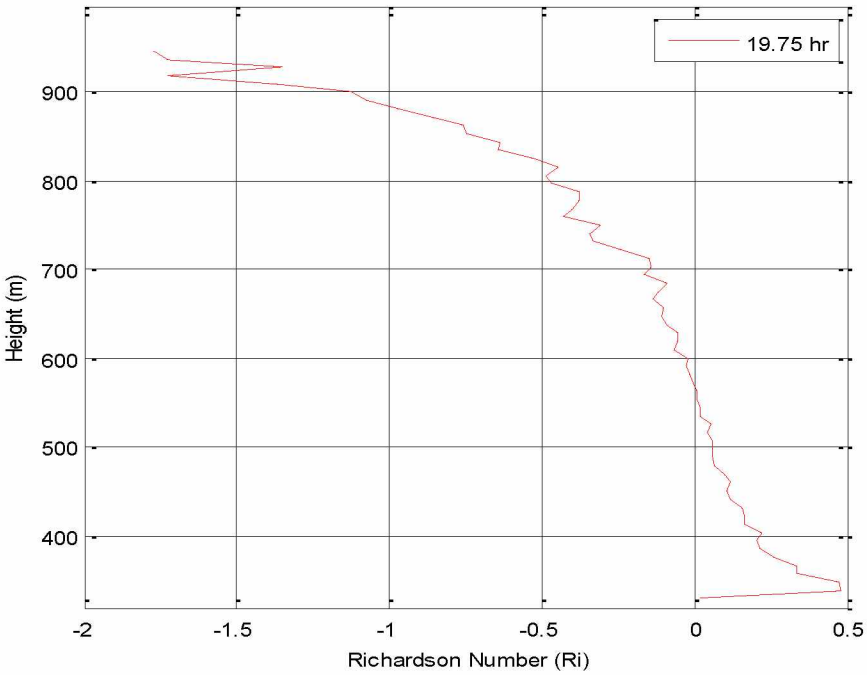

Figure 7.43: Richardson Number Profile along Line 4 at19.75 hrs.

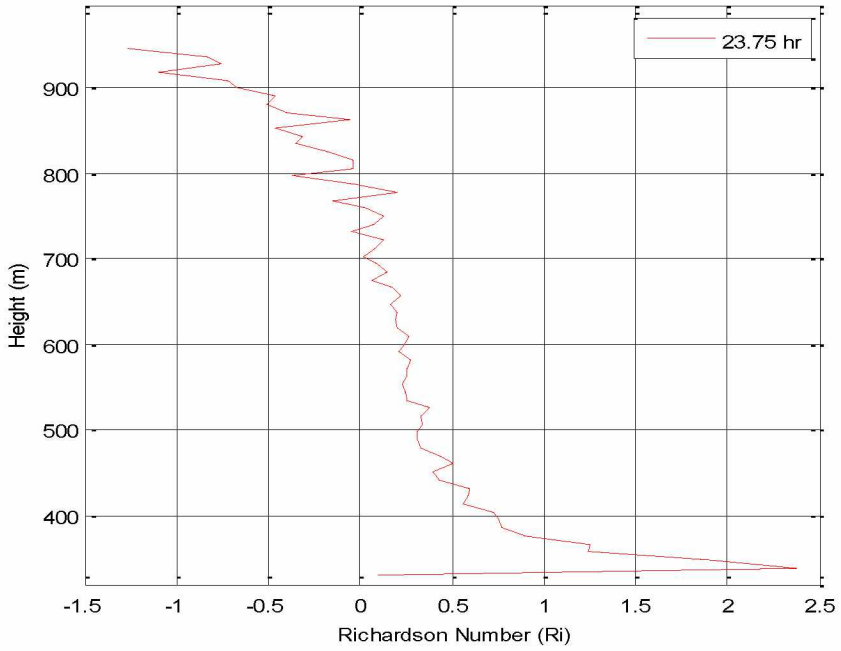

Figure 7.44: Richardson Number Profile along Line 4 at 23.75 hrs.

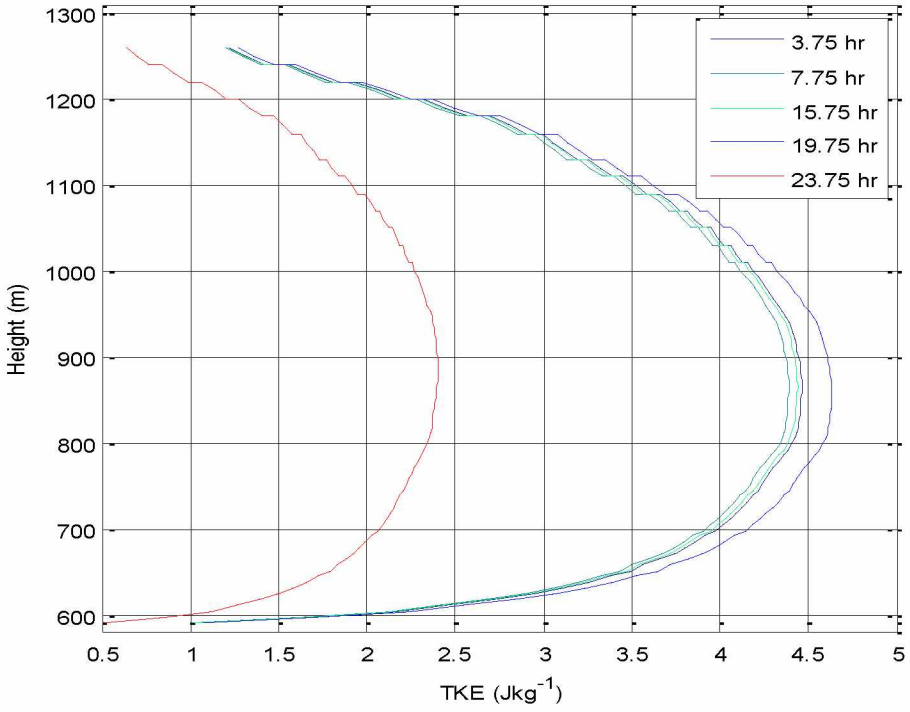

Figure 7.45: Turbulent Kinetic Energy Profile along Line 5 at Various Time Intervals.

Line 5 which is on the pit rim, various profiles are not similar to that of the profiles within the pit. In order to characterize the nature of turbulence near pit rim, Richardson number is plotted at different time intervals. In the first 30-40 m, turbulent flow is prevalent due to the mechanical wind shear as well as the effect of radiative cooling. Above that height normal atmospheric lapse rate prevails.

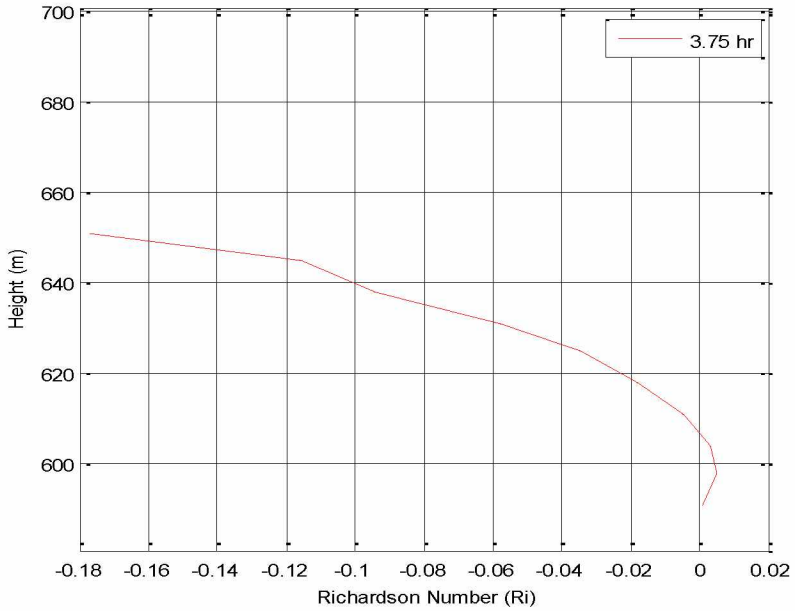

Figure 7.46: Richardson Number Profile along Line 5 at 3.75 hrs.

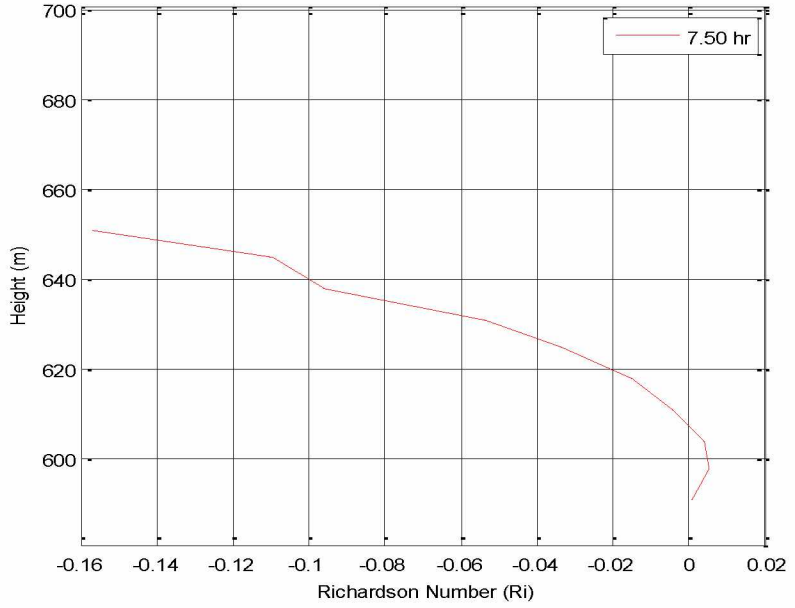

Figure 7.47: Richardson Number Profile along Line 5 at 7.50 hrs.

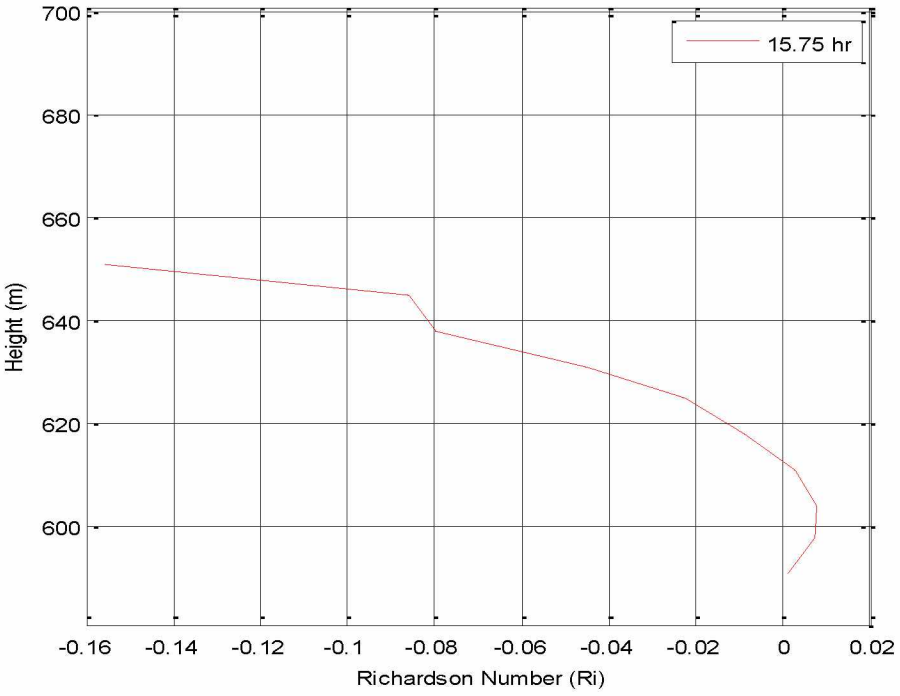

Figure 7.48: Richardson Number Profile along Line 5 at 15.75 hrs.

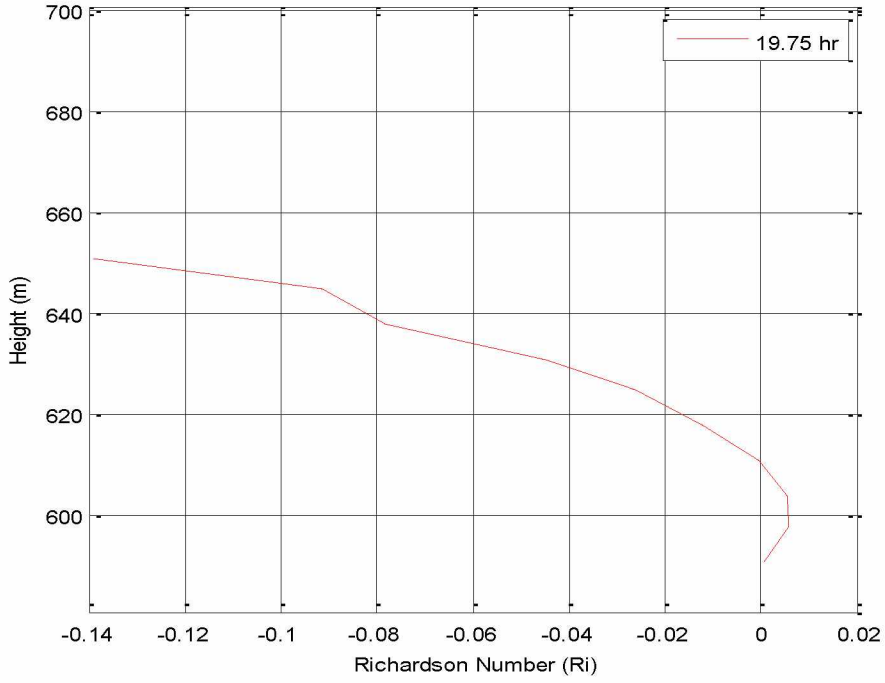

Figure 7.49: Richardson Number Profile along Line 5 at 19.75 hrs.

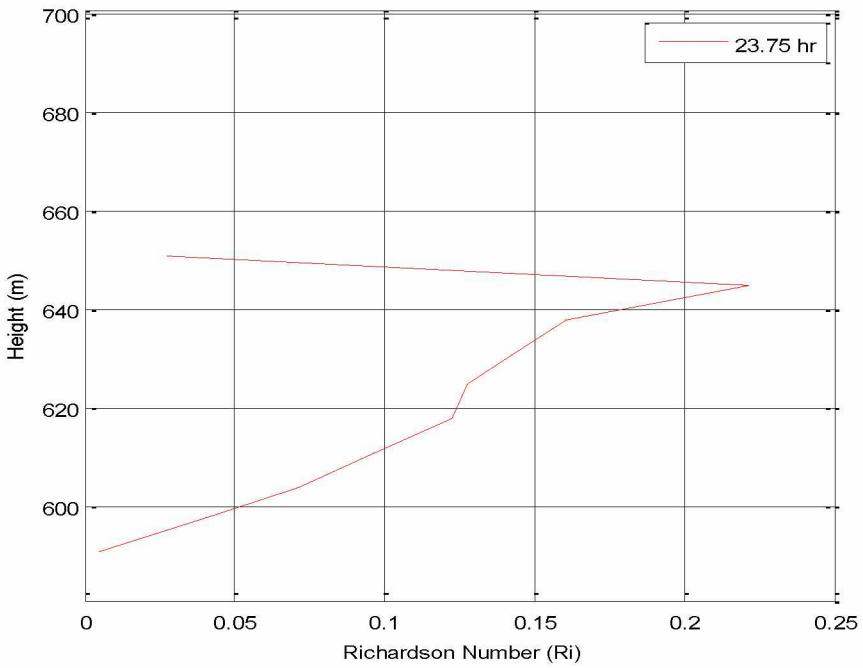

Figure 7.50: Richardson Number Profile along Line 5 at 23.75 hrs.

7.5 Comparison with Measured Data

Simulated results for a volume cell in a computational domain are for the Reynolds Averaged value and cannot be readily compared with the measured data (a point in time) or evaluated without further time averaging. However, it is not obvious what time period should be used for time averaging.

The threshold limit value (TLV) of pollutants in mining environment is time-averaged on an eight hour shift basis. For comparison, the data are divided into a group of eight hour period for averaging. Each averaged data value over the time is compared with the simulated data averaged over the same time frame and a percentage difference is obtained. The measured data are provided in Table 7.1, averaged over a period of eight hours.

Table 7.2 presents a comparative assessment of the actual data and the simulated data averaged over a similar time period of eight hours. The data shown are only for NO_2, values since the concentration of NO_2 is the limiting factor for the mine operation during an inversion.

From Table 7.2, it can be seen that for Bench 700 location for the first eight hour time period the model over predicts by approximately twenty two percent. For the Lift Station, the model over

predicts by three percent only. The RANS models under-predicts the flow fields, and thus, the CFD profiles are confirmed to over-predict the pollutant concentrations.

In the second eight hour time period, the concentration data from Bench 700 are not collected, as it is assumed that the NO_2 concentration is higher than five ppm. Simulated averaged value at Bench 940 under-estimates the pollution concentration by approximately ten percent. Whereas, at the Lift Station, the concentration value is under-predicted by 600 percent. The low simulated value of NO_2 at the Lift Station can be due to mixing of pollutants by the air mass at the leading edge of the pit rim. In the final eight hours of simulation time period, the pollutant concentration data from the Lift Station is only available for comparison which is around 41 percent below the actual value.

Table 7.2: Comparison of Measured Data and Simulation Model Predicted Data.

	Bench 700			Bench 940			Lift Station		
	Actual Time Averaged Value	Simulated Time Averaged Value	Percentage difference (%)	Actual Time Averaged Value	Simulated Time Averaged Value	Percentage difference (%)	Actual Time Averaged Value	Simulated Time Averaged Value	Percentage difference (%)
First 8 hour average	3.85	4.93	21.89				1.77	1.82	2.85
Second 8 hour average				4.85	4.39	-10.48	2.68	0.38	-607.59
Third 8 hour average							0.44	0.31	-41.39

The variation in transport and dispersion of pollutants in SBL depends strongly on height, due to the strong wind shear and the variation in strength of turbulence. The height dependence of wind velocity and direction of transport is clearly evident. There is no strong variation in

dispersion with height, however, within the middle portion of the SBL near the Lift Station there is much greater dispersion due to higher wind velocity (velocity at Line 2). The temperature profile (temperature plot of Line 2) indicates that the inversion is very weak and there is probably higher wind shear. This leads to significantly reduced pollutant concentration at that location.

During a mine visit for data collection, a 180 degree turn of the wind direction was observed, as the dominant East-West wind turning into West-East direction for a few hours. Despite such complex synoptic situations, the different meteorological input data and the fast changing conditions, the simulation results are in good agreement regarding the dispersion of pollutant and other turbulent variables. Pollutant concentration values in the selected locations showed differences, but remained within the same order of magnitude in most cases.

To understand the reasons for the differences in the model predicted values and the measured concentrations, additional parametric runs are made. These results indicated that the predicted flow fields in the open pit are sensitive to the localized heat sources. The difference in the model predicted values and the measured concentrations may be partly due to the fact that although initial conditions are consistent with Arctic observations (measured data in the pit), the surface cooling rate is more an idealized value.

For the first eight hour time frame, trucks are passing by the Lift Station, thus, releasing pollutants and additional heat in the open pit. The pollutants released from incoming and outgoing trucks are reflected in the measured data at the lift station. Whereas, in the model domain the trucks are placed on the ramp at fixed locations. In effect, the pollutants and heat released by the trucks are dispersed in the model domain. Once the concentration reaches to five ppm in the pit trucks are withdrawn which is accomplished in the model by turning it off.

Slight changes in the operating conditions, especially the heat release rate, can disrupt idealized thermal balance and can lead to very different flow fields. Furthermore, dispersion of pollutants in the presence of temperature inversion depends on the wind that has a constant mean velocity in the x-direction, and eddy diffusivities in the x, y, and z directions, respectively, and the height of inversion. Representative data for eddy diffusivities is not available, and had to be estimated.

In some way, the RANS turbulent models are all problem dependent and this is one big drawback of the RANS model. Some of the differences between the model-predicted value and measured concentration are probably due to the possibility that important unsteady phenomena are

present in the flow over the selected open pit mine, such as intermittent flow separation in the windward side of the pit. This results in unsteady turbulence which could not be modeled with a high degree of certainty by RANS simulations.

This model is a good candidate for prediction of pollutant transport under neutral conditions, and for extension to stable boundary layer. The effect of boundary conditions noticeably influences the model results of the computational domain. The enlargement of the computational domain has the disadvantage of increasing the grid point number and therefore requiring longer computation time.

Comparison of model results with observed data over complex topography is very rare, especially as far as turbulent variables are concerned. Therefore, the effectiveness of the turbulent parameterization for complex terrain application is rather uncertain. The success of the simulation performed is dependent on correctly specifying the initial state of the atmosphere in the open pit and its time variation along the lateral boundaries of the model domain. Initial and boundary conditions permit information on the synoptic scale flow and its time evolution to be introduced in the simulation.

7.6 Limitations of the Model

Mathematical modeling is a scientific exercise with the objective of developing simplified mathematical statements that relate to one another in the same way as the process that is being modeled. The utility value of a model is dependent on the ability of the model to closely approximate prototype behavior. However, for a model to be acceptable for application, its operating characteristics or data generated from it should, within reasonable accuracy, duplicate the prototype performances. The validity and accuracy of a model depends on the mathematical constraints presupposed in the model formulation. The final model must be tested for mathematical validity and closeness of representation of the prototype.

The experiments performed by (Skobunov 1970) provide an interesting commentary on modeling and the problems and limitation of any attempt to emulate physical systems by mathematical models. His laboratory experiments with aniline dye dispersal permitted control and quantification of model input parameters. On the other hand, his experiments with oxides of nitrogen are conducted in a blind mine haulage drift where it is not possible to control and quantify

all input variables. The magnitude of disparities between the model-predicted and observed contaminant concentrations in these two experimental setups all together is high and can be attributed to the variability and control of the physical conditions at the time of monitoring. The limitations of the model validation procedures are related to the degree of desired or required correspondence between model predictions and reality and the additional costs required to achieve incremental improvements in validation exercise. Better initialization schemes for the atmospheric conditions and improved turbulence closure models will improve the model performance.

Chapter 8 Mitigation of Pollutants in Deep Open Pit Mines under Arctic Air Inversion

A detailed description of atmospheric boundary layer (ABL) and formation of stable boundary layer (SBL) over an open pit in the Arctic region is presented in Chapter 2. Air inversion is a natural meteorological phenomenon. Mitigation of pollutants in deep open pit mines in the Arctic is a challenging task. Release of pollutants below the inversion height in an open pit mine during periods of weak winds and consequently weak vertical mixing may result in very high levels of concentrations of primary and secondary pollutants, causing serious consequences for human health. The mine operations ceases if the concentration of oxides of nitrogen (NO_x) or carbon monoxide (CO) exceeds the threshold limit value (TLV) of the pollutants. Sustained cessation of a mine operation has serious economic consequences. For continued mining operation, the levels of the pollutants must be below the TLVs.

During an inversion, if no significant synoptic meteorological situations changes then a warm air mass sits over the cold air mass within the open pit. Artificial ventilation is required to dilute the pollutants to an extent that mine workers can safely resume work. Some of the early approaches in artificially ventilating open pits were attempted in the former Soviet Union (USSR). Most of the studies by the Soviet researchers suggested the use of turbo-jets and turbo-propeller engines, airscrews, axial pit fans, and meteotrons (Parakhonskii and Severin 1976; Vershinin 1976). However, majority of these studies are only theoretical in nature with no evidence of an approach that really worked in practice.

Depending on the pit dimension, Vershinin (1976) proposed two schemes; (i) upward scheme and downward scheme for ventilating an open pit. In the upward scheme, the purpose of the descending fresh air current is to clear the contaminant zone. Whereas, in the downward scheme, the fresh air is introduced in the pit to increase the volume of the contaminant zone, thus, reducing the resultant pollutant concentrations. The preference of using either of the schemes is based on a numerical study. No unique solution to this problem, however, is suggested. Parakhonskii and Severin (1976) suggested the use of high efficiency mechanical ventilators for artificially ventilating deep open pits. Their study provided a theoretical background of various mechanical ventilators that might result in the dispersion of pollutants. It is suggested that the use of meteotrons might break

the atmospheric inversion in deep open pit mines. None of the proposed methods, however, was tested in field.

Control of the boundary layer to ventilate open pit mines is also suggested by Belousov (1989), by allowing the laminar zone to increase and reducing the recirculation zone. He proposed to install flat wings at the windward side of a pit to control the air flow entering the pit. It is assumed that a free air stream enters the open pit at an opening angle, $\alpha \approx 15°$ (Figure 8.1). By changing the slope angle of the flat wing, which is based on the opening angle (α), the air entering the pit can be controlled. This would allow the wind to penetrate deep into the pit, which in turn will reduce the recirculation zones, thus, resulting in low pollutant concentrations.

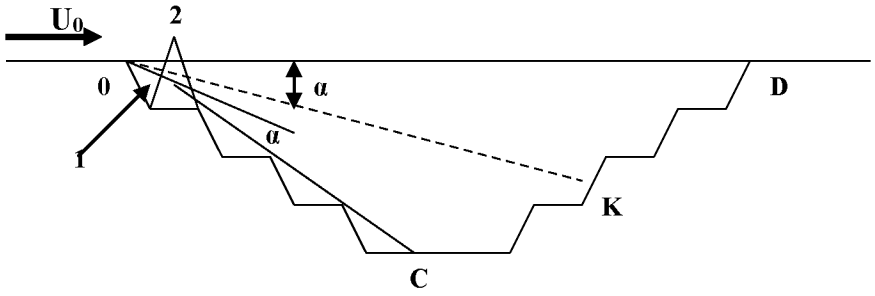

Figure 8.1: The Angle of Expansion of an Air Jet in an Open-pit Mine (Belousov 1989).

Baklanov and Rigina (1993) presented a numerical study for analyzing the effectiveness of cascade ventilation systems in open pit mines. Five different scenarios are modeled to test the effectiveness of the cascade ventilation systems. Contrary to the expectation that cascade ventilation system will help reducing the contaminants in deep open pits, it is found that cascade ventilation system are not effective, although, an active mixing of the impurity in the local region increased. Furthermore, there is no flow interaction between the ventilators when the wind is very calm which is common under inversion. Belousov (1995) suggested the use of breeze circulation in the pits by artificially creating a thermal gradient of 5-10°C between the air mass over the pit and its surrounding areas at the same elevation. Kosarev et al. (2005) presented a theoretical overview of a jet-suction scheme for ventilation of stagnant zones in deep open pits. Their focus is on the lower part of the pit where air is stagnant, and most of the mining activities are performed. They proposed to install a fan in forcing mode, and another fan in an exhaust mode, connected to a ventilation duct out of the pit. The proposed theoretical approach, however, is neither modeled numerically nor tested in practice.

Collingwood et al. (2012) provided a two dimensional CFD model of an actual pit geometry. The CFD modeling approach is first to model the contaminants transport under inversion, and later analyzed the effectiveness of various combinations of fans in exhaust mode to mitigate the pollutants. In their model, a single pollutant source, and an exhaust fan is analyzed. The analysis suggests that the use of mechanical ventilators results in local mixing of air and dilution of pollutant concentrations. It can be seen from the previous sections that several approaches are suggested, but none of the approaches, however, is field tested. Therefore, the efficacy of any of those approaches is questionable at best.

The main stable boundary layer forcings are the pressure gradient force, the Coriolis force, cloud cover, and free flow stability. An increased wind speed, for example, will enhance the turbulent mixing and thus would result in reduced stratification (which can also occur due to incoming clouds). In a very stable regime, a reduced stratification might result in increased surface sensible heat flux. This will alter the surface temperature and therefore the outgoing longwave radiation and so the stratification.

Apart from the large-scale dynamics (i.e., pressure gradient and Coriolis force), the physics that govern the structure of the wind speed and temperature profiles is complex and involves several processes with many positive and negative feedbacks. These physical processes are turbulent mixing, radiative heat transport and heat supply from underlying soil towards the surface.

Studies of the turbulent parameters (Ri Number, TKE, etc.) in chapter 6 suggest that effective ventilation of the pit and removal of the pollutants can be accomplished if a large enough mixing length in the open pit can be created. Turbulent mixing by eddies of different scales in the stable boundary layer (SBL) is produced by wind shear and dissipated by molecular viscosity and buoyancy destruction. The main result of turbulence is mixing of the atmospheric profile and transport of momentum. However, turbulent mixing in the ABL is a highly non-linear process. The turbulent intensity is influenced by wind shear and stratification.

Several approaches can be examined which may create a large mixing length. One of the approaches could be to create local dilution within a working area of the pit such that the levels of pollutant concentrations is well below the TLV, while other areas in the pit could be above the TLV of pollutants. The second approach is to clear the entire pit of any pollutant which is above the TLV. Some of these approaches are modeled and described in the following.

8.1 Field Experiment with a Helicopter

The management of the selected open pit mine in cooperation with the research team conducted a field experiment by flying a helicopter in the open pit during an inversion. The purpose of this field experiment is to increase turbulence mixing length and to ascertain if this would remove the pollutants out of the pit. The helicopter flew all over the open pit in random patterns to facilitate the mixing of the air. The helicopter flying over the pit can be seen in Figure 8.2 . The downward thrust of the rotor-blades increased the mechanical turbulence which resulted in local mixing of the contaminated air with the fresh air. A slight decrease in pollution concentration is observed at the upper bench levels, but very little change in concentration resulted at the lower levels. The turbulent mixing length created by the helicopter, however, is not significant enough for mixing the entire volume of air in the pit.

Figure 8.2: Helicopter over the Brown Haze during Inversion.

8.2 CFD Modeling of the Pollutants Dispersion

In order to examine various mitigation measures that might work, a CFD modeling approach is adopted. For modeling, the fans in forcing and exhaust modes are initially considered. Subsequently, a push-pull ventilation system (similar to a cascade ventilation) is employed. The mitigation models are developed and simulated for the 2010 and the 2013 pit geometries. The

aspect ratios of the 2010 and 2013 pit geometries are not similar and as such dispersion behavior is expected to be different. Contaminant concentrations from previous simulation models are used for analyzing the mitigation approaches.

8.2.1 Mitigation Model of Contaminants for the 2010 Pit Geometry

The realizable κ-ε turbulence model is used to model the contaminant transport for the 2010 pit geometry (Figure 8.3). The simulation results from the 2010 contaminants transport model are used for mitigation modeling. In order to analyze the efficacy of mechanical ventilation, the mitigation model included two fans in running mode, located on the west side of the pit (Figure 8.4). A volumetric flow rate of 142 m^3/s is used in forcing as well as exhaust ventilation mode. The mitigation model included nine pieces equipment as the contaminant sources in the pit. The fan application is tested while all the equipment are in running mode. The pit is under stratified boundary layer due to net outgoing longwave radiation. All other simulation variables are unchanged.

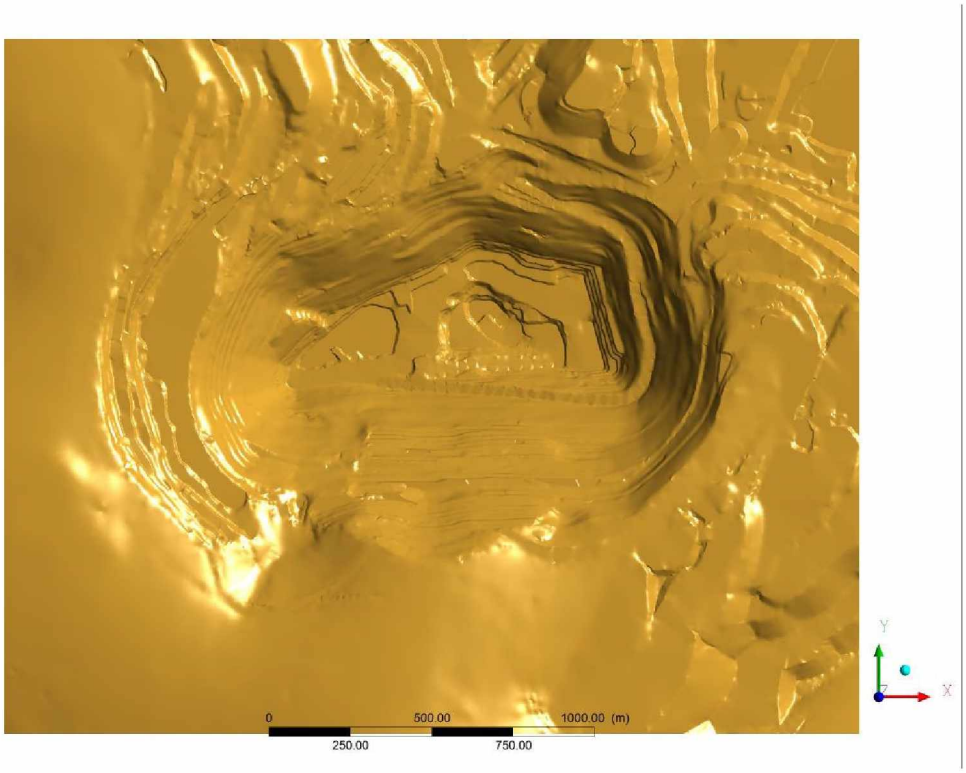

Figure 8.3: The Extent of Model Domain for 2010 Pit Configuration.

8.2.2 Local Dilution of the Pollutants in a Working Area within an Open pit

A safe and healthy working environment for the mine workers can be created by diluting the contaminant to levels below the TLVs. Therefore, it is not be necessary to reduce the contaminant

levels of the entire pit. Dilution of pollutants can be focused in areas where miners are working. In order to simulate conditions where a local dilution might be a solution, it is proposed to place two fans in forcing mode in the west side of the pit (Figure 8.4) providing clean air at temperature higher than ambient temperature in the working areas of the pit. For the purpose of simulation the fans are switched-on after 3 hours of simulation run and then the model is executed for additional 14 hours. The goal is to examine if there is any dilution of pollutants with both the fans operating in forcing mode for a longer time period.

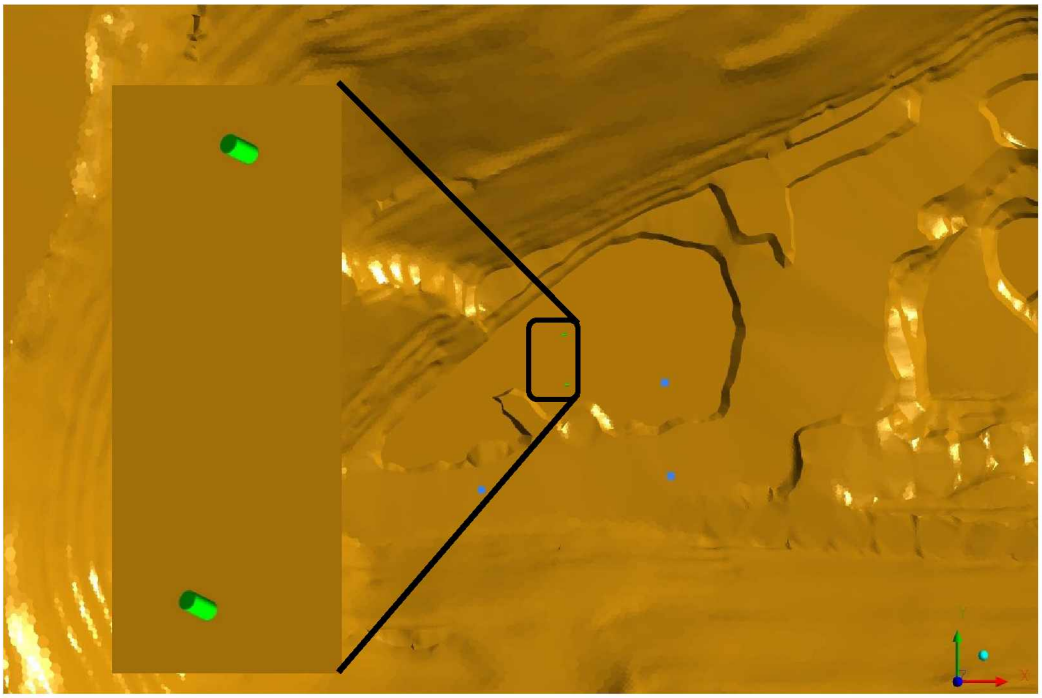

Figure 8.4: Exhaust Fans Located at the West Side of the Pit.

The initial NO_2 concentration profile along the East-West direction prior to turning on the two exhaust fans is presented in Figure 8.5. The concentration profiles for other secondary pollutants such as NO, and CO are not presented in this section, however, these can be found in Appendix III. Figure 8.6 through Figure 8.9 are the NO_2 concentration profiles at various time steps.

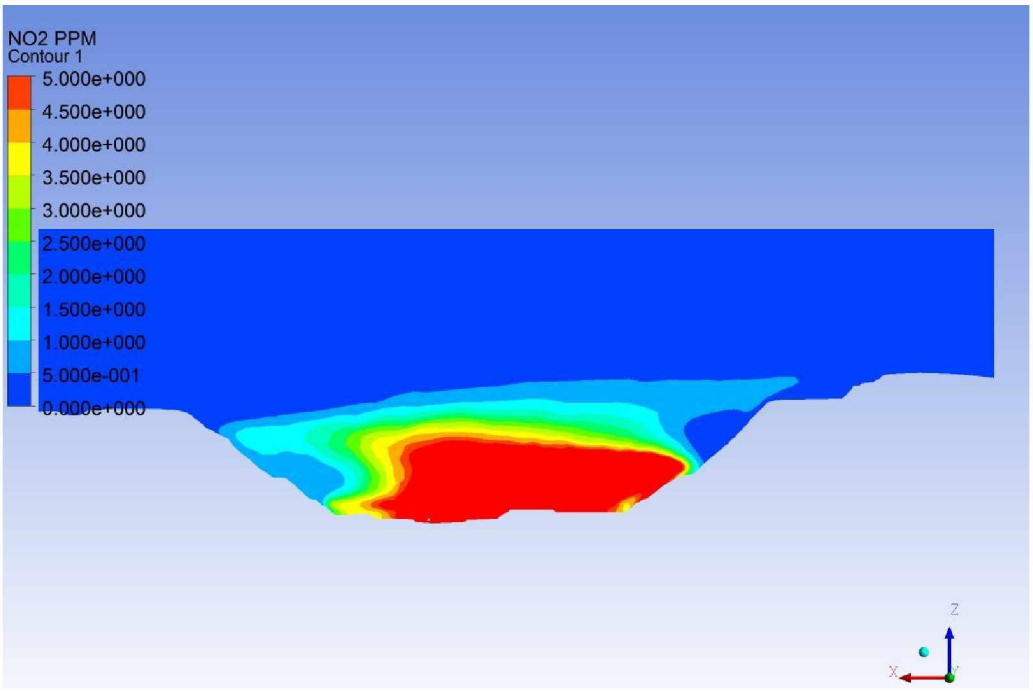

Figure 8.5: Concentration of NO_2 (in ppm) at Time Step ($t \approx 3$ hrs.; Initial State).

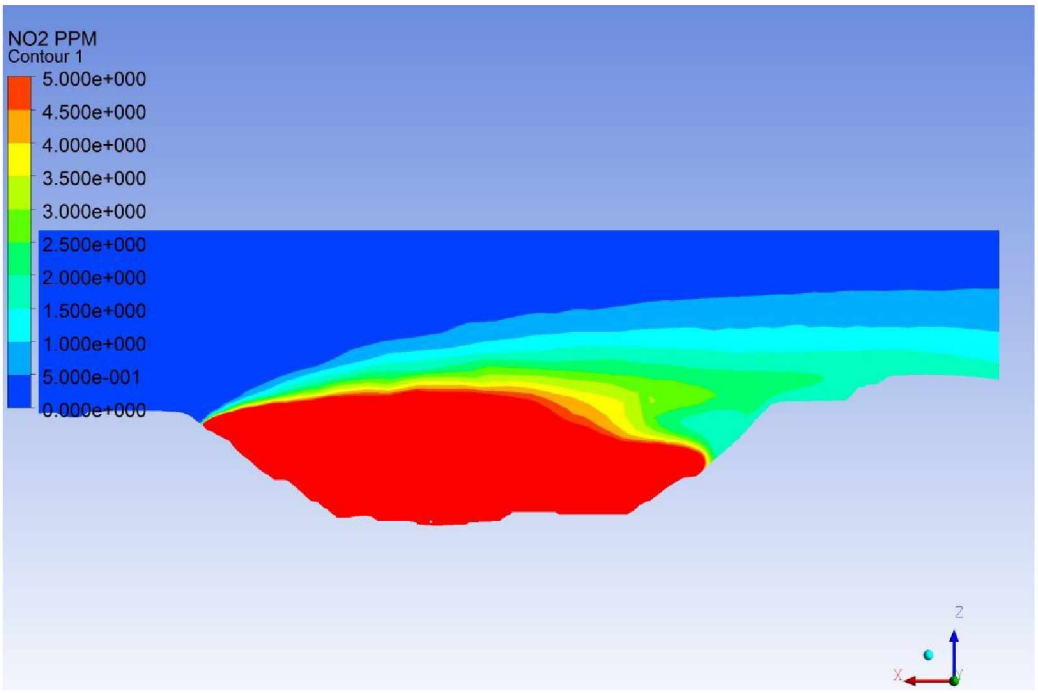

Figure 8.6: Concentration of NO_2 (in ppm) at Time Step ($t \approx 6$ hrs.).

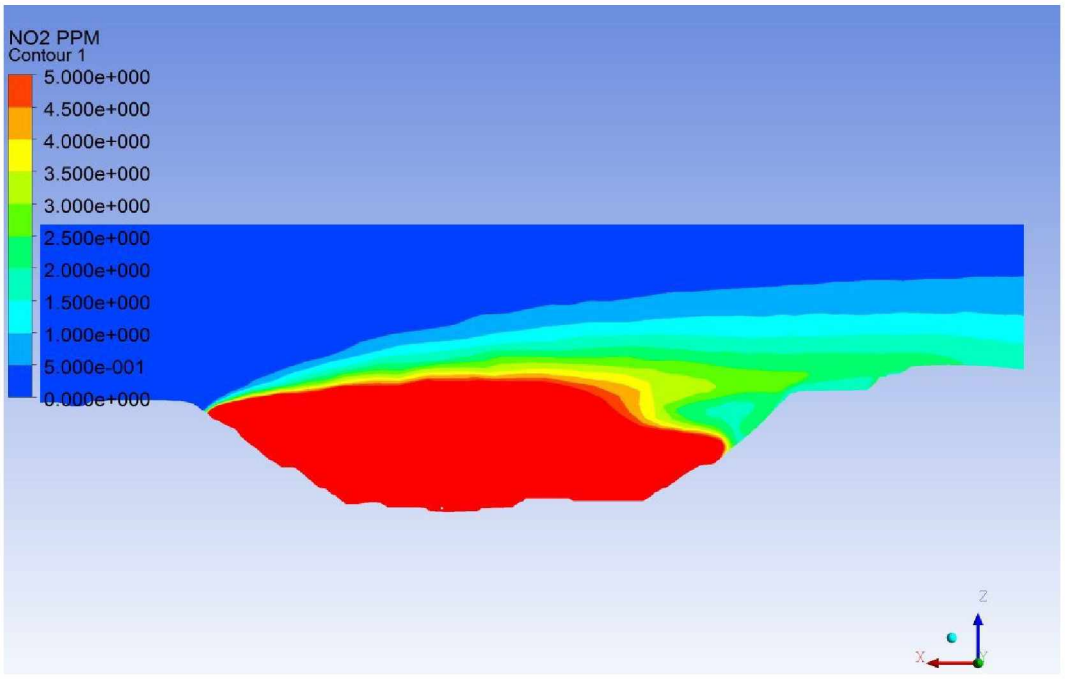

Figure 8.7: Concentration of NO_2 (in ppm) at Time Step ($t \approx 9$ hrs.).

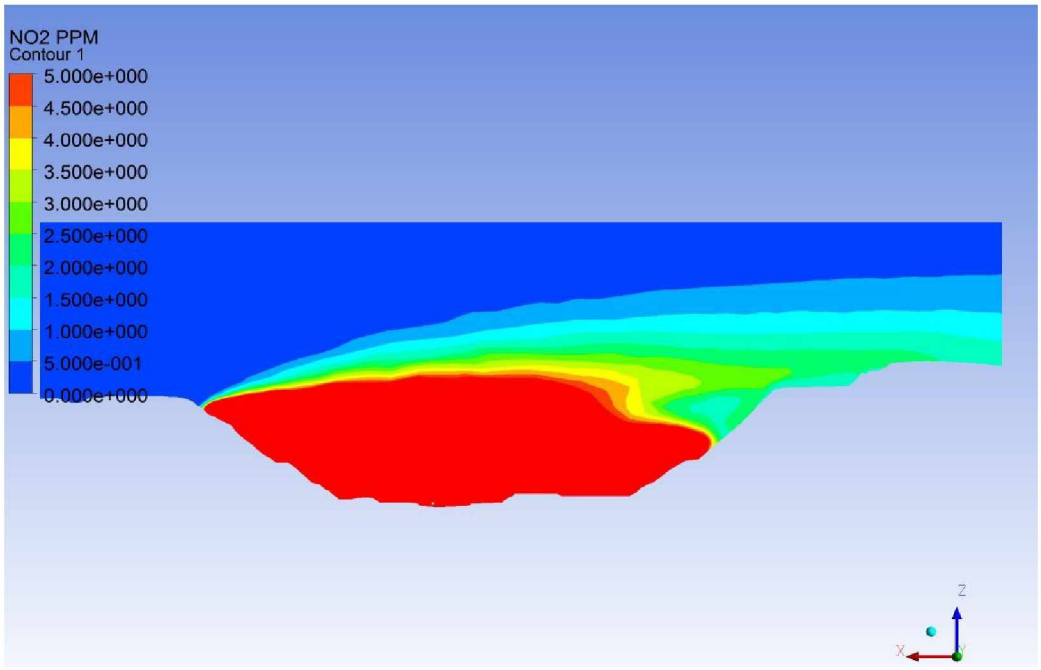

Figure 8.8: Concentration of NO_2 (in ppm) at Time Step ($t \approx 12$ hrs.).

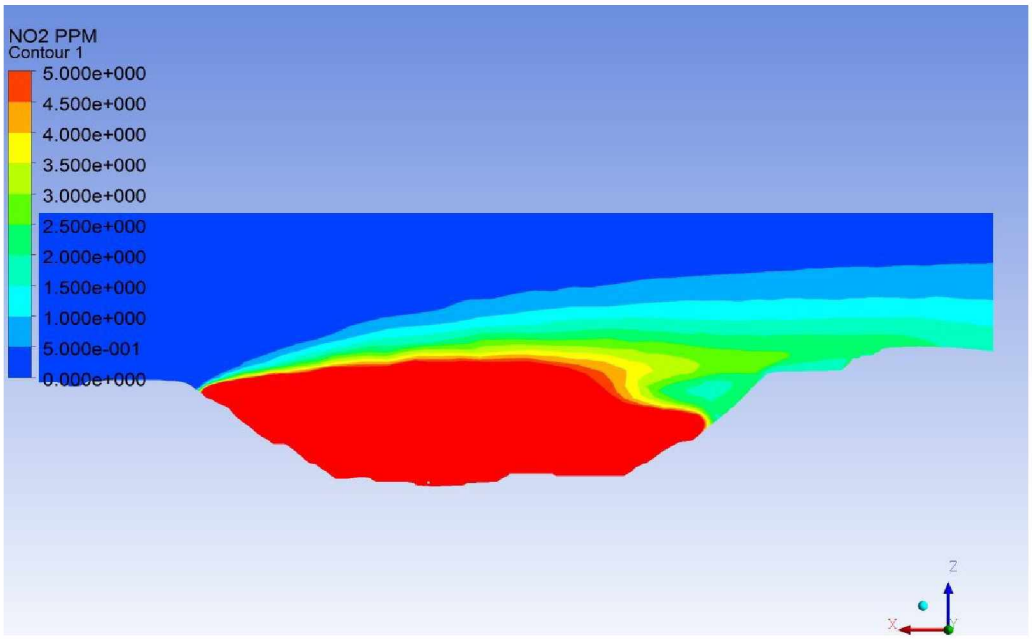

Figure 8.9: Concentration of NO_2 (in ppm) at Time Step (t ≈ 17 hrs.).

From these figures, it can be seen that there is no decrease in the level of pollutant concentration over time. NO_2 concentration in most part of the pit is five ppm or above. The concentration and volume of pollutants is extremely large and addition of a constant stream of clean air did not make any significant change in the concentration level of the pollutants.

8.2.3 Fan in Exhaust Mode

The simulation of the contaminants transport is executed for a sixteen-hour time period. During this interval of time, the strength of inversion in the pit has increased, and the NO_2 concentration level in the entire pit is above the TLV. . Two fans operating in exhaust mode, and made to run for additional four hours.

The initial NO_2 concentration profile along the East-West direction prior to the turning on the two exhaust fans is presented in Figure 8.10. The concentration profiles for other secondary pollutants such as NO, and CO are not presented in this section, however, these can be found in Appendix III.

Figure 8.11 shows the horizontal profile of the NO_2 concentrations in the pit. It can be seen from Figure 8.11 that a large extent of the pit is covered with NO_2 concentration which is well above the TLV.

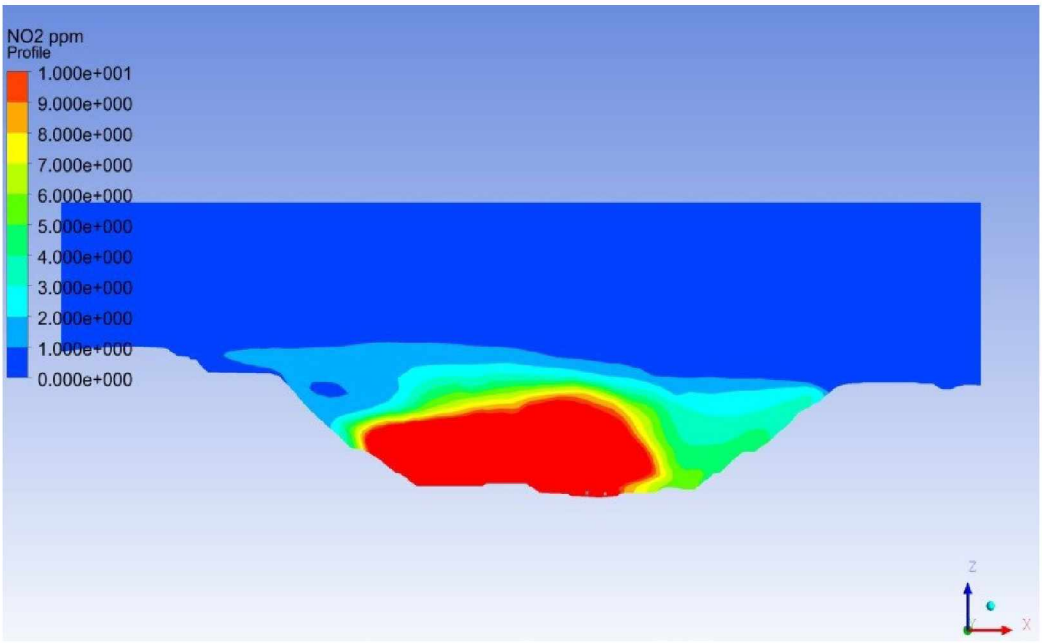

Figure 8.10: Concentration of NO_2 (in ppm) at Time Step ($t \approx 16$ hrs.; Initial State).

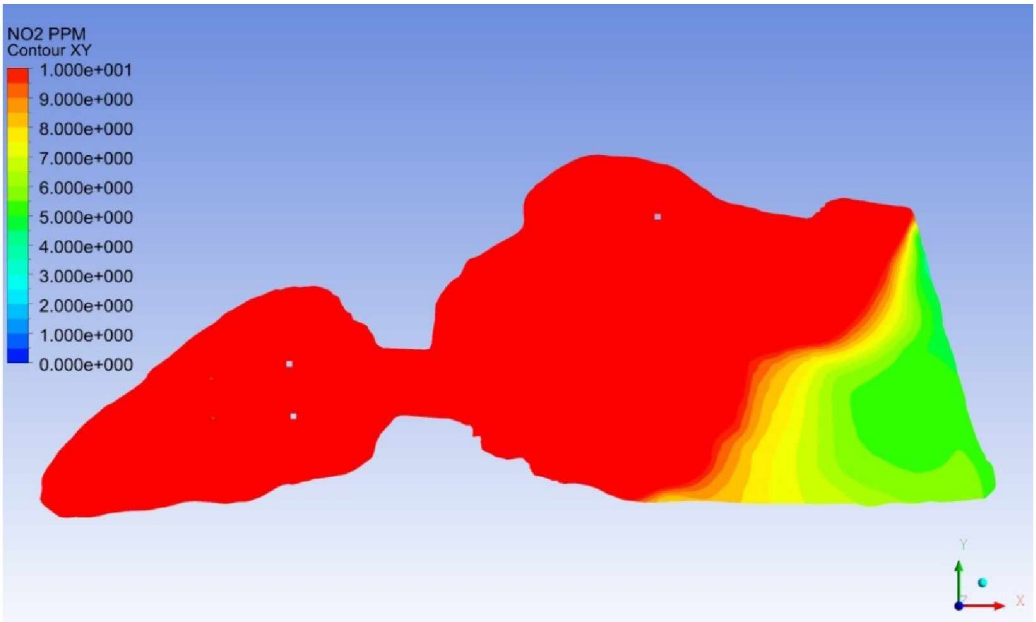

Figure 8.11: Concentration of NO_2 (in ppm) in Horizontal Plane at Time Step ($t \approx 16$ hrs.; Initial State).

The concentration profile of NO_2 after two hours of simulation along the horizontal plane is presented in Figure 8.12. Whereas, the NO_2 concentration profile after four hours along the horizontal plane of simulation is shown in Figure 8.13.

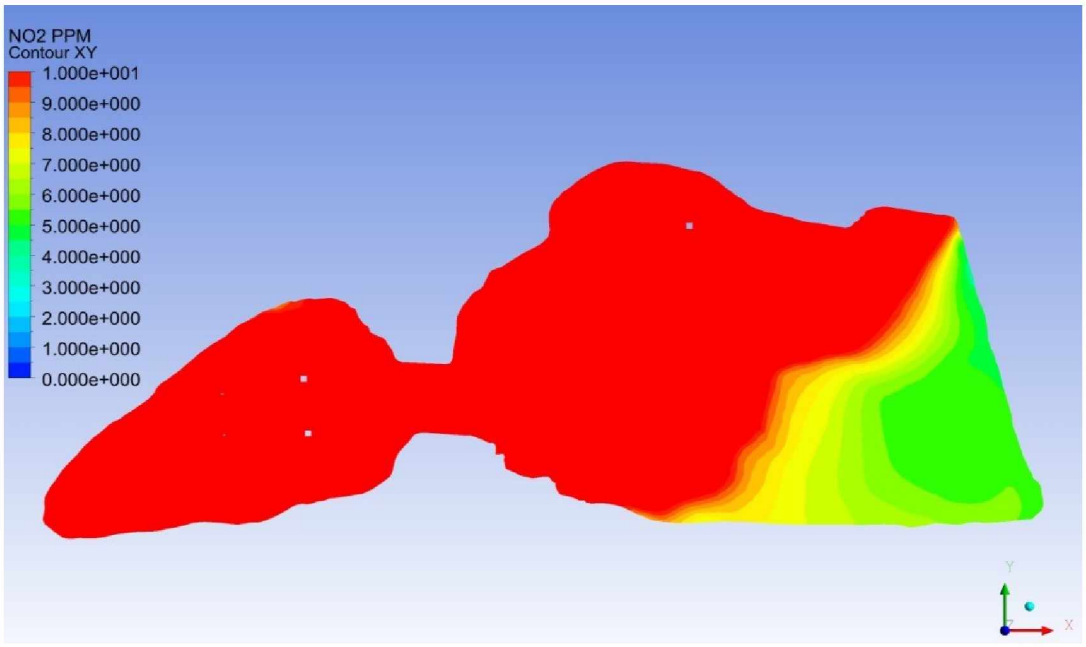

Figure 8.12: Concentration of NO_2 (in ppm) in Horizontal Plane at Time Step ($t \approx 18$ hrs.).

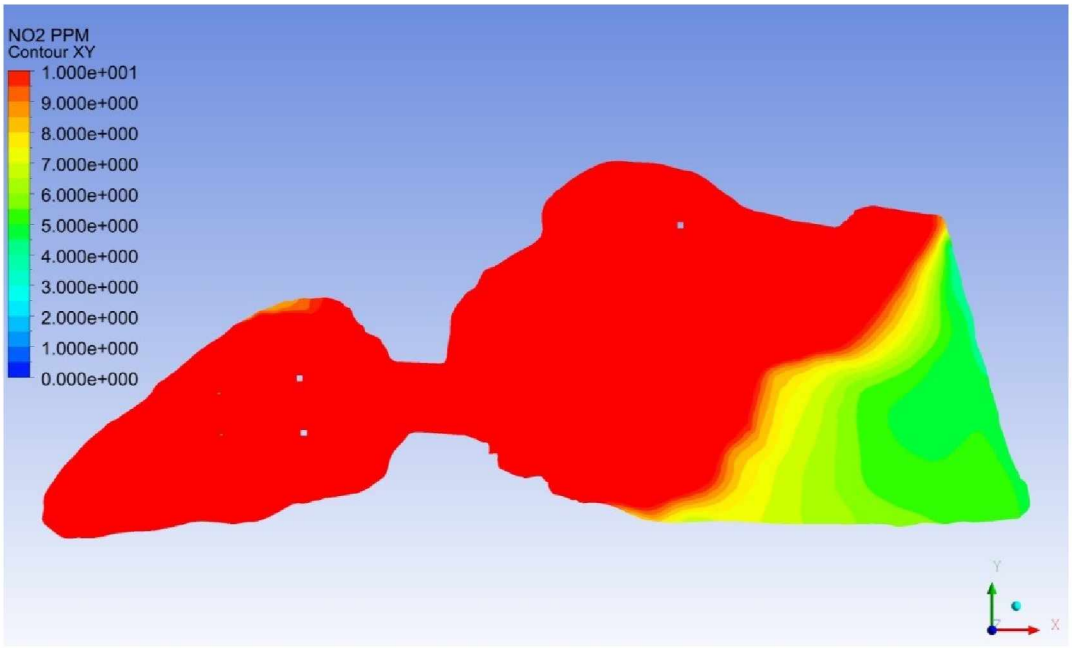

Figure 8.13: Concentration of NO_2 (in ppm) in Horizontal Plane at Time Step ($t \approx 20$ hrs.).

From the above results, the level of pollutant concentration in the pit did not change significantly, even after the fans are in operation for a period of four hours. The contaminant concentration at the pit bottom is still above the TLV for NO_2. The mechanical turbulence created by the fans is not sufficient and strong enough to mix the dense heavy air in the pit, and destabilize the thermal stratification at lower levels of the open pit.

8.2.4 Push-Pull Ventilation Scheme

The model results in the previous section showed that two fans operating in exhaust mode for a period of four hours are not adequate. Therefore, another mechanical ventilation approach is explored. In this mitigation approach, the 2013 pit geometry (Figure 8.14) is used. As before, all other simulation variables are kept unchanged. In this mitigation model two fans in combination, one in forcing mode and the other in exhaust mode are simulated. This fan combination is commonly known as the "push-pull" ventilation. The locations of the five sets of push-pull fan combination are shown in Figure 8.15. An enlarged view of one of the fan combinations is present in Figure 8.16.

In order to simulate this specific mitigation model, the simulation result of the 2013 pit geometry with the resultant pollutant concentration after twelve hour time period is selected as the initial state. The pit is under stratified boundary layer due to net out-going longwave radiation. The realizable κ-ε turbulence model is used for simulating the mitigation of the pollutant. The contaminant concentration in the pit is above the maximum allowable concentration limits. The simulation is run for additional six hours to study the effects of the push-pull ventilation. Figure 8.17 through Figure 8.20 are the vertical profiles of NO_2 concentration at various times. The horizontal profiles of NO_2 concentration are presented in Figure 8.21 through Figure 8.24.

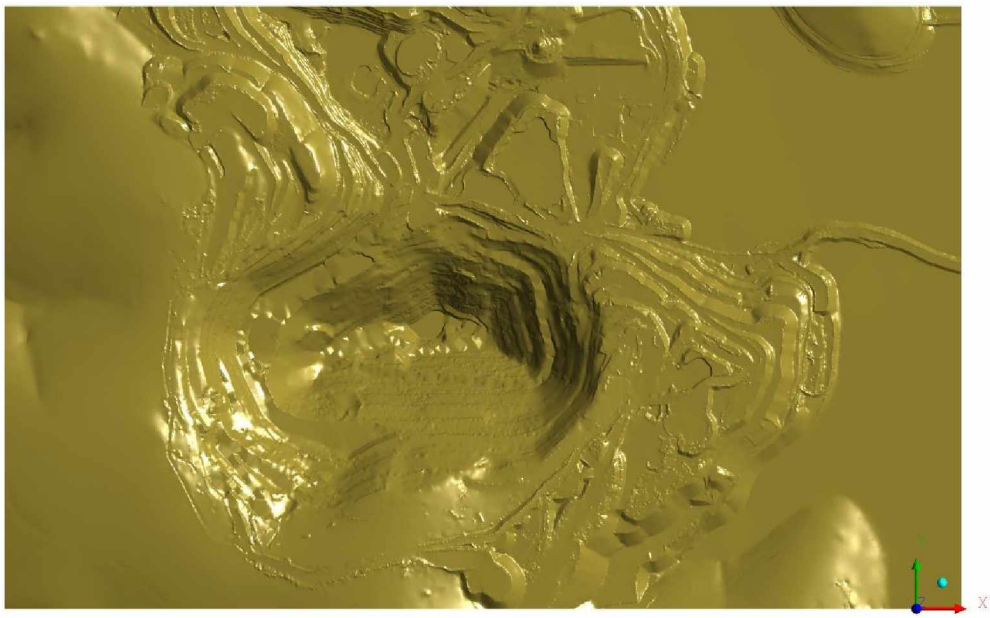

Figure 8.14: The Extent of Model Domain for 2013 Pit Configuration.

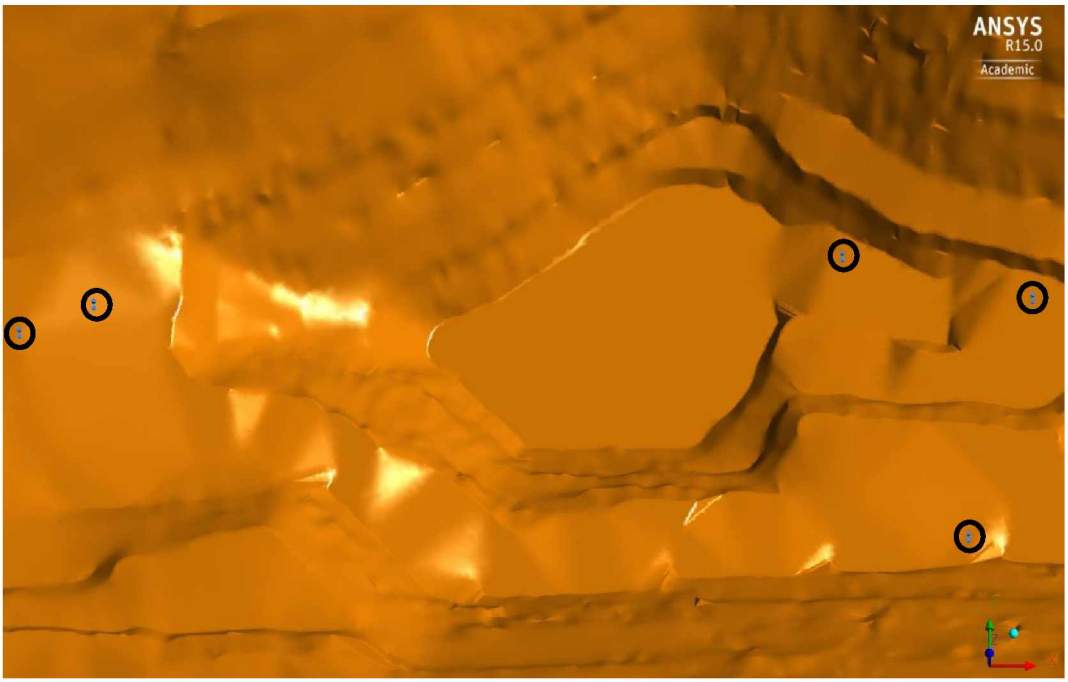

Figure 8.15: Fans located at the Pit Bottom.

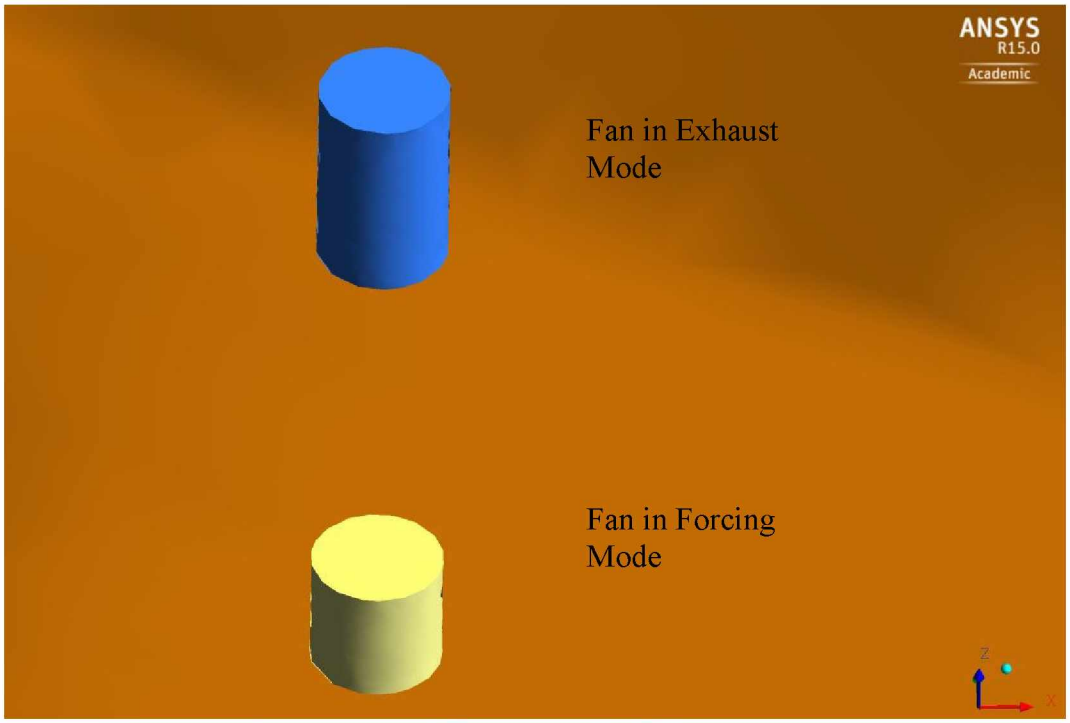

Figure 8.16: Enlarged View of the Fans.

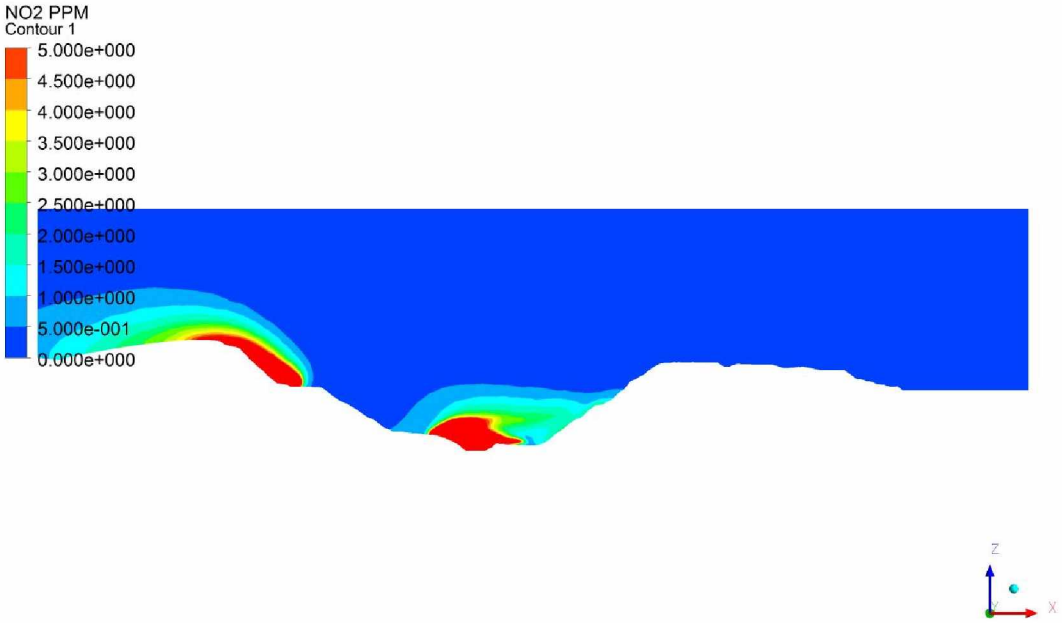

Figure 8.17: Concentration of NO_2 (in ppm) at Time Step ($t \approx 12$ hrs.).

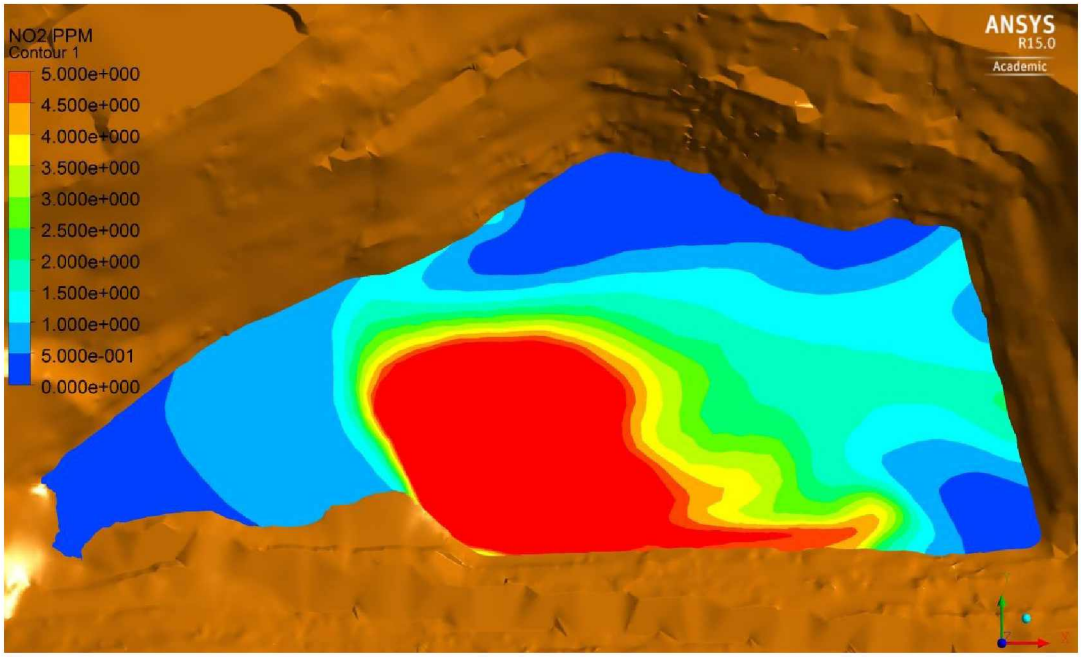

Figure 8.18: Concentration of NO_2 (in ppm) at Time Step ($t \approx 14$ hrs.).

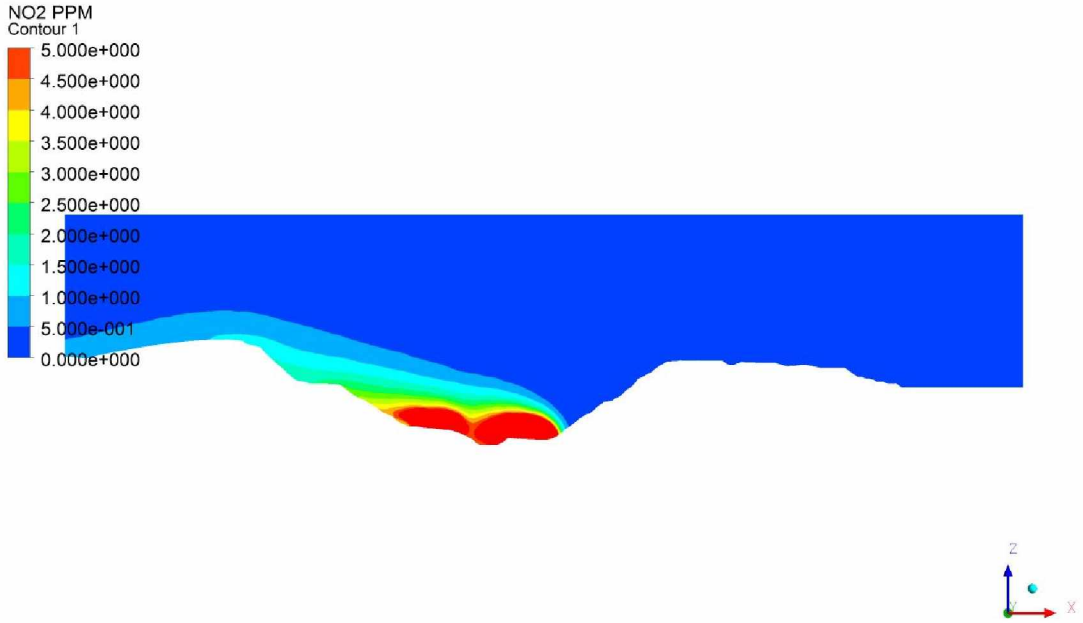

Figure 8.19: Concentration of NO_2 (in ppm) at Time Step ($t \approx 16$ hrs.).

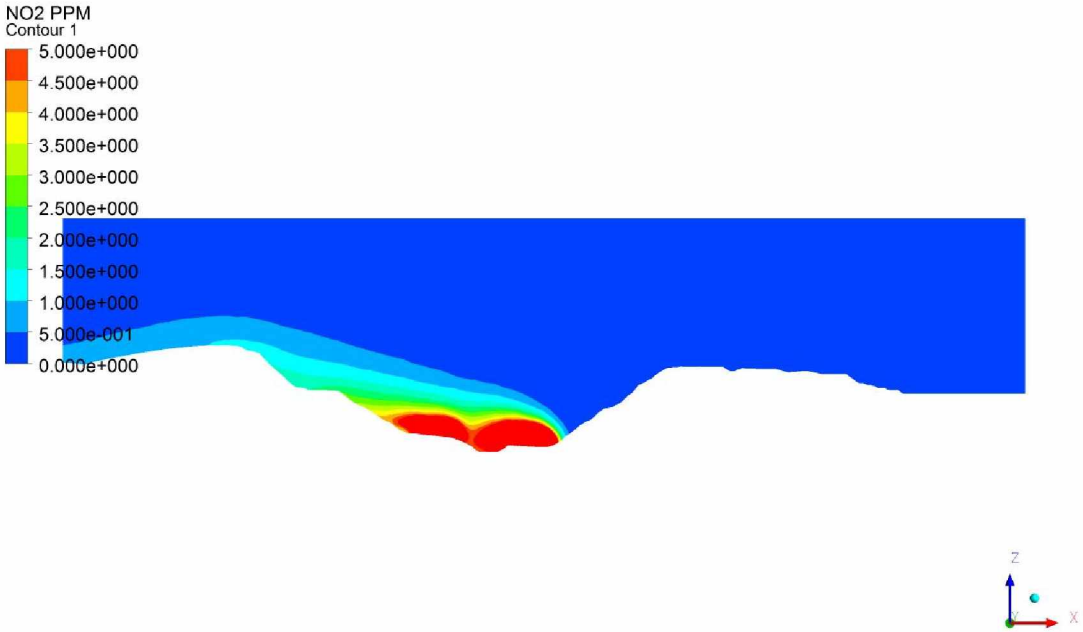

Figure 8.20: Concentration of NO_2 (in ppm) at Time Step ($t \approx 18$ hrs.).

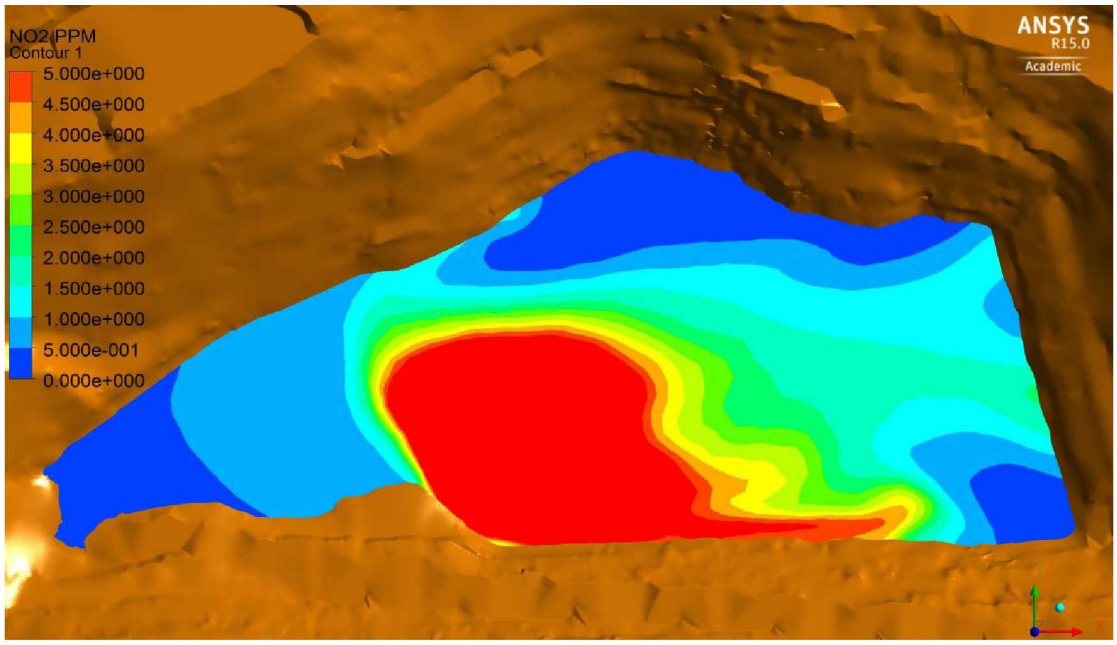

Figure 8.21: Concentration of NO_2 (in ppm) in Horizontal Plane at Time Step ($t \approx 12$ hrs.).

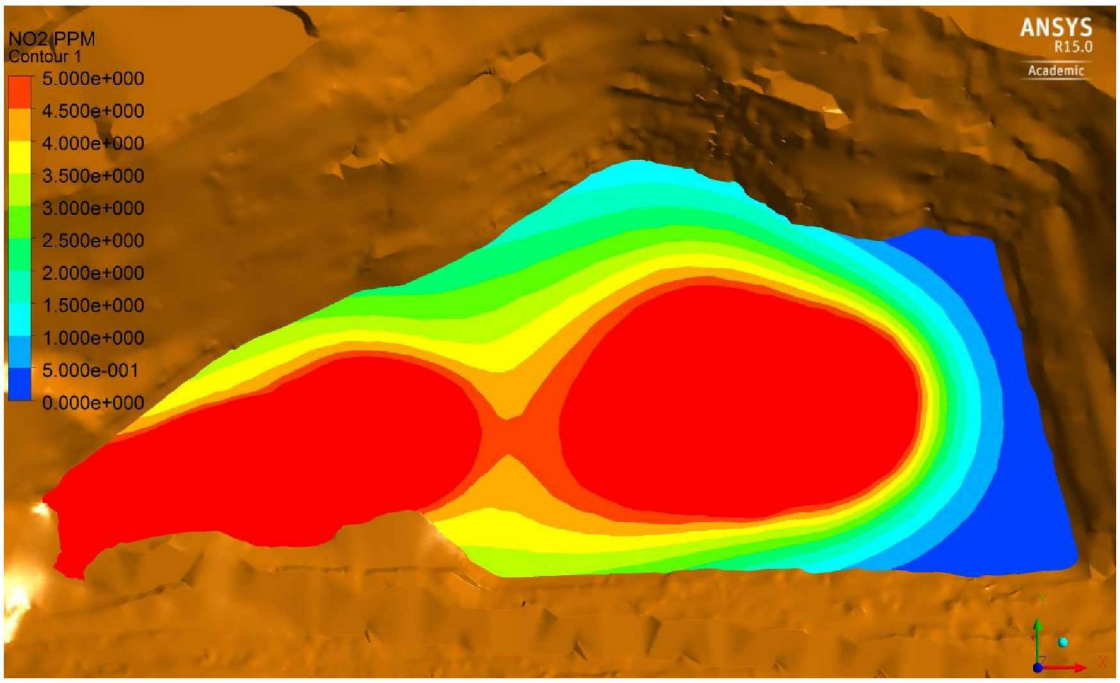

Figure 8.22: Concentration of NO_2 (in ppm) in Horizontal Plane at Time Step ($t \approx 14$ hrs.).

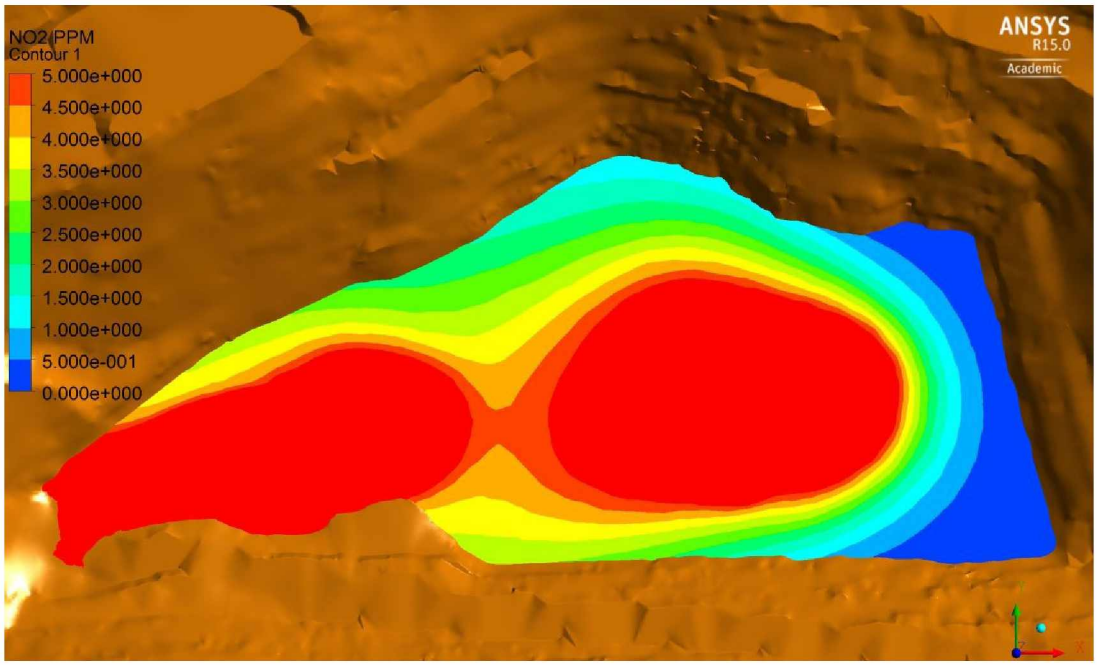

Figure 8.23: Concentration of NO_2 (in ppm) in Horizontal Plane at Time Step ($t \approx 16$ hrs.).

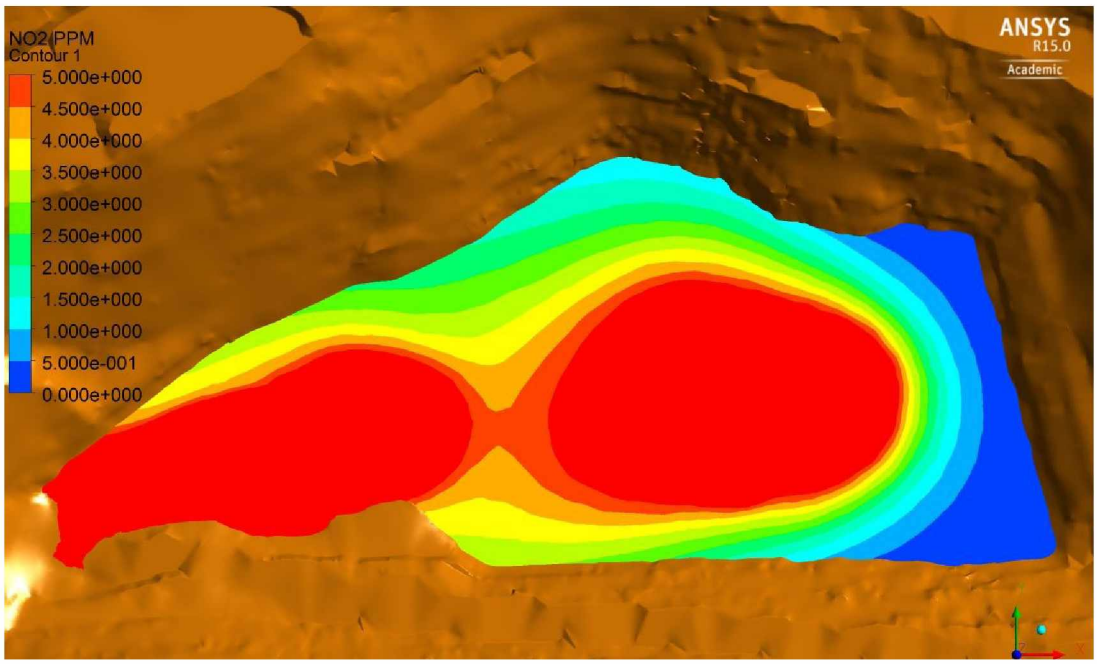

Figure 8.24: Concentration of NO_2 (in ppm) in Horizontal Plane at Time Step ($t \approx 18$ hrs.).

From the above figures, it can be observed that the levels of pollutant concentration did not decrease over time. A large extent of the pit has higher NO_2 concentrations. There is no significant change in the concentration levels due to the push-pull ventilation. The volume of air mass in the pit under consideration is so large that the push-pull ventilation is not efficient. Similar approaches

were also modeled by Baklanov and Rigina (1993) using cascade ventilation which did not successful clear the open pit. This approach, however, might work in other smaller pit configurations.

The simulation results suggest that when the air under inversion is cold and heavy the vertical movement of air is suppressed. The turbulence created by mechanical means is not adequate. The resultant mixing length is small with regards to the inversion height and volume of air in the pit.

Thermal buoyancy could be another approach in creating large mixing lengths. One such approach to create thermal buoyancy is to use the meteotrons (Ingel 2010). Soviet researchers in the sixties developed a machine, meteotron, which could create a huge volume of smoke for modifying weather. The meteotron creates turbulent jets by intense combustion of fuel. The combustion of fuel adds thermal energy whereas exhaust from the turbulent jets creates mechanical instability in the system. Ingel (2010) suggested adding impurity (fine carbon black) to the fuel which is sensitive to shortwave radiation. The carbon particles in the atmosphere would absorb the shortwave radiation and enhance the thermal buoyancy. However, this method is not suitable for open pit in the Arctic region where during deep winters the average day light time is three to four hours. Moreover, the meteotrons has a very low efficiency and high fuel consumption, thus, not viewed as a viable alternative. In addition, the meteotrons contribute to a large volume of smoke and additional pollutions.

8.2.5 Dispersion of Pollutants using Cloud Cover

As described in the previous sections, mitigation measures using mechanical means are not adequate to dilute the contaminants to an extent that mining operations can be resumed. A large amount of thermal energy, however, may be needed for lifting the massive volume of cold and dense air mass. The thermal energy will add buoyancy to the system, thus, create a mixing length large enough to mix and transport the pollutants out of the pit.

It has been observed that, during snow falls in the open pit the inversion lifts, and the pit is cleared of all pollutants. Thus, it is initially hypothesized that the heat released from the snowflakes lifts the inversion. A critical examination of the weather and radiation data suggested that break-up of the inversion layers can happen with or without the snow fall.

On further investigations, it is found that it is not the snow fall but the presence of low level cloud cover lifts the inversion. Presence of low level clouds results in snow fall or rain. These low level cloud covers are also sensible to the infrared radiation. Since all objects (including earth surfaces and cloud covers) emit radiation, properties such as emissivity and reflectivity play a significant role in changing the thermal regime of air between the surface and the clouds. Since, clouds are infrared sensitive they reflect most of the infrared radiation emitted from the ground. Similarly, the snow-covered ground reflects most of the radiation back to the cloud cover (Liou 2002). Clouds, when present are the major contributors to the incoming longwave radiation to the surface. They radiate like blackbodies (Low level clouds are regarded as black body, $\varepsilon \approx 1$) at their respective cloud base temperatures. However, some of the radiation is absorbed by water vapor, CO_2, and other greenhouse gases before reaching the earth's surface (Arya 2001). Due to the temperature and emissivity differences between the air layers as well as the difference in the emitted and absorbed longwave radiation between the layers, results in a net radiative flux.

In the stable boundary layer, the temperature gradient near the surface can be extremely large. Radiative heat transport is a complex process of absorption and emission of thermal radiation (by absorbers) in the atmospheric layers relative to each other, and to and from the surface. The net effect of emission and reflection of radiation results in a state of equilibrium of temperature at the cloud cover as well as at the ground surface. This state of equilibrium leads to the change in the vertical temperature profile of the air. The state of equilibrium of temperature under cloud cover is validated by the infrared sensors data collected at the selected mine. The collected incoming and outgoing infrared radiation data are presented in Figure 8.25-Figure 8.26. It can be seen from Figure 8.25 that the incoming and the outgoing infrared radiation at the pit bottom tend to overlap each other at around 6:00 AM (October 29th, 2013). Whereas, at the pit rim (Figure 8.26), the incoming and the outgoing radiation values are not overlapping with each other although they are very close. The magnitude of the incoming and outgoing radiation are near zero (W/m^2). This is a clear indication that a cloud is passing over the sensors.

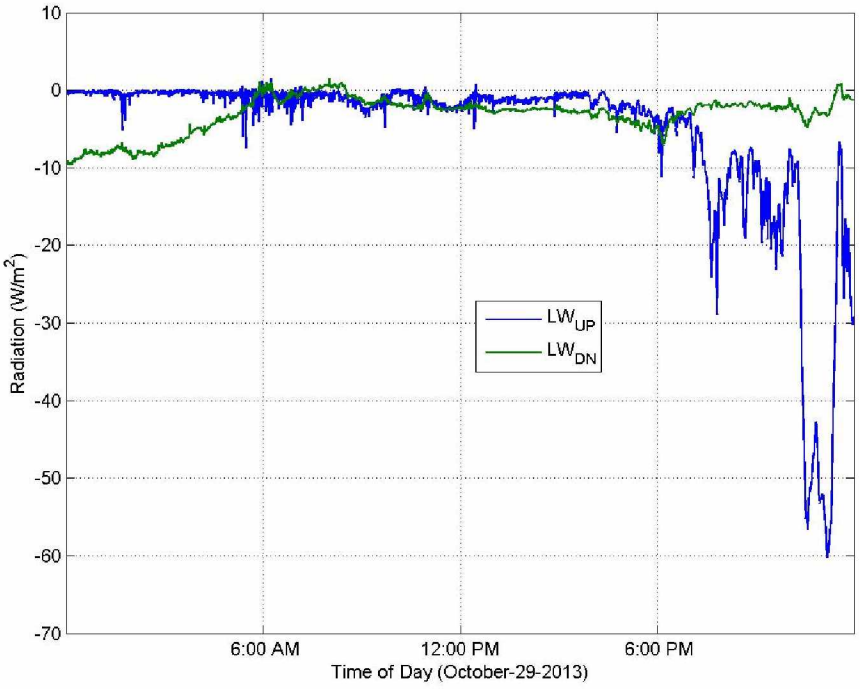

Figure 8.25: Infrared Radiation Measurements at Pit Bottom during Cloud Cover (October 29th 2013).

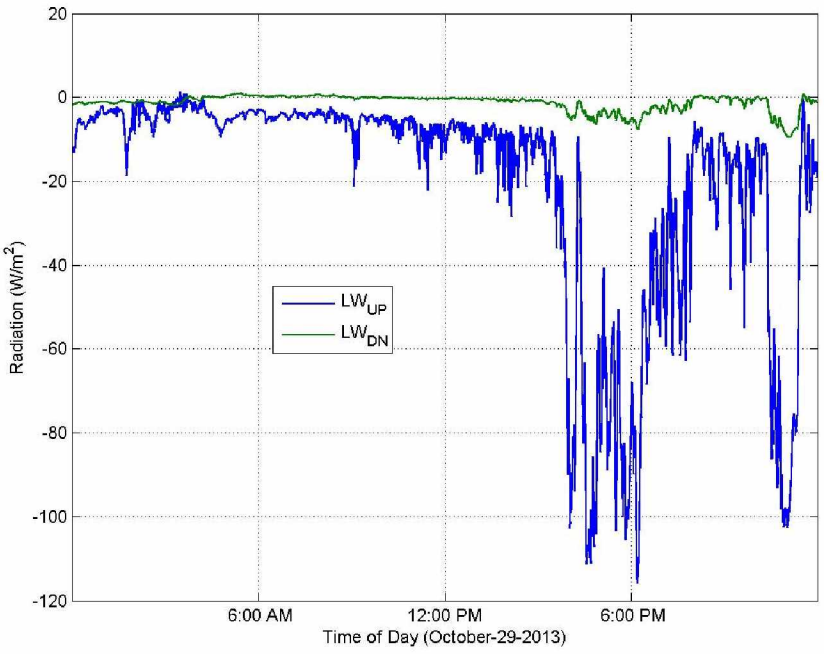

Figure 8.26: Infrared Radiation Measurements at Pit Rim during Cloud Cover (October 29th 2013).

Another clear evidence of a cloud cover over the selected open pit is presented in Figure 8.27, in form of a base reflectivity RADAR data of the same date. The weather RADARs are most

commonly used instrument for detecting the water content in the atmosphere. The area enclosed in the rectangle (Figure 8.27) is the selected mine, and the green shade over it indicates the presence of cloud covers.

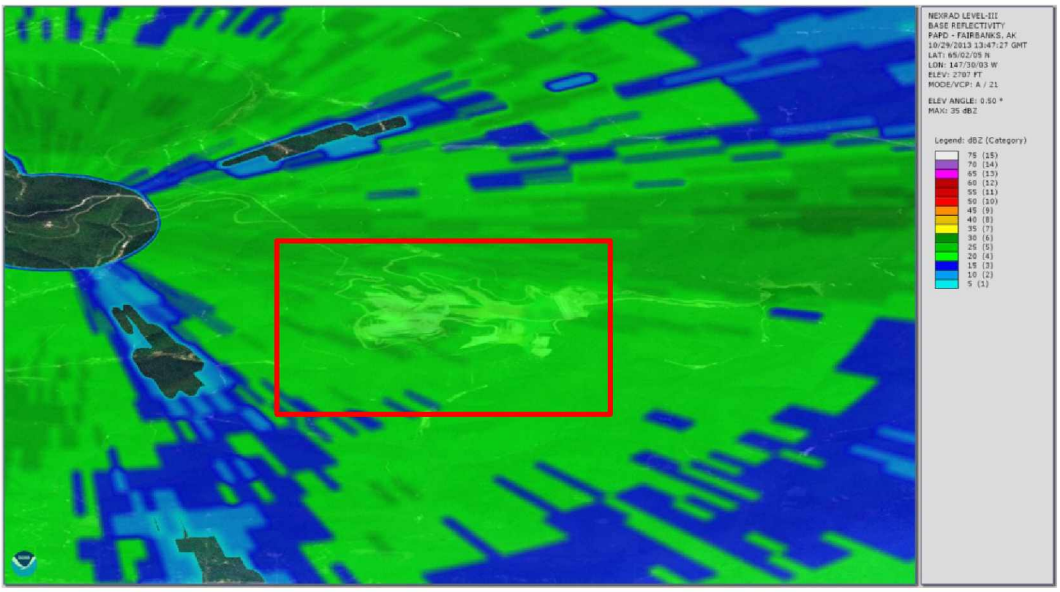

Figure 8.27: RADAR Base Reflectivity Data on October 29th 2013 (http://www.ncdc.noaa.gov/nexradinv/).

Formation of cloud/fog is related to air and dew point temperatures. The dew point temperature is the temperature at which the vapor pressure becomes saturated via isobaric (at a constant pressure) cooling process (Wang 2013). Once the air temperature drops to the dew point temperature, the vapor becomes saturated and the excess water vapor starts to condense. It can be therefore stated that when there is a convergence of air temperature with the dew point temperature, cloud/fog formations occur.

Additional evidences of the cloud cover in the surrounding areas of the selected open pit are presented in Table 8.1 and Table 8.2. Air and dew point temperutures and the relative humidity data presented in Table 8.1 and Table 8.2 are collected from the two weather stations located near the selected open pit. The weather stations are identified as Weather Station 1 (WS 1) and Weather Station 2 (WS 2). The WS 1 has similar elevation (2267 ft./691 m) as that of the west rim of the selected open pit. Whereas, the WS 2 is at a similar elevation (2099 ft./ 640 m) as that of the east side of the pit rim. It can be observed from the WS 1 data presented in Table 8.1 that the water vapor in the atmosphere has reached saturation (the daily average temperature and the dew point temperature are the same and relative humidity as 100%). Whereas, at WS 2, the daily average

temperature and the dew point temperature are very close (difference of 0.55°C) to each other, with a relative humidity level of 96%.

Additional data from various dates are selected to provide support for the discussions presented above (Figure 8.28-Figure 8.33 and Table 8.3-Table 8.6). Analysis of the data indicates that there is a change in the infrared radiation during cloud cover. The presence of cloud cover results in the convergence of the incoming and the outgoing longwave radiation values to zero. Thus, providing a basis for modeling the presence of cloud cover over an open pit. It must be noted that, in practice longwave radiation value cannot be exactly zero. The values presented in Figure 8.25-Figure 8.26 are the longwave radiation values minus the longwave radiation emitted from the sensor.

Table 8.1: Weather Station 1 Data on October 29th 2013 (http://www.wunderground.com/).

	High	Low	Average
Temperature (°C)	1.67	-1.67	-0.67
Dew Point (°C)	1.67	-1.67	0.67
Relative Humidity (%)	100	100	100

Table 8.2: Weather Station 1 Data on October 29th 2013 (http://www.wunderground.com/).

	High	Low	Average
Temperature (°C)	1.11	-2.78	-1.06
Dew Point (°C)	0.56	-3.33	-1.61
Relative Humidity (%)	96	95	96

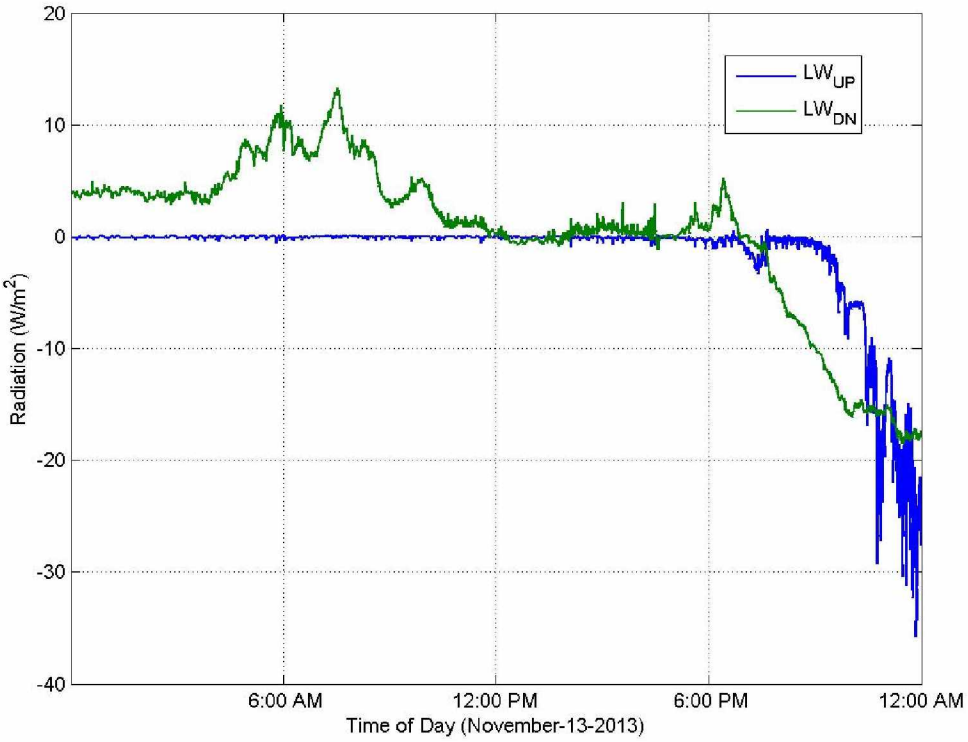

Figure 8.28: Infrared Radiation Measurements at Pit Bottom during Cloud Cover (November 13th 2013).

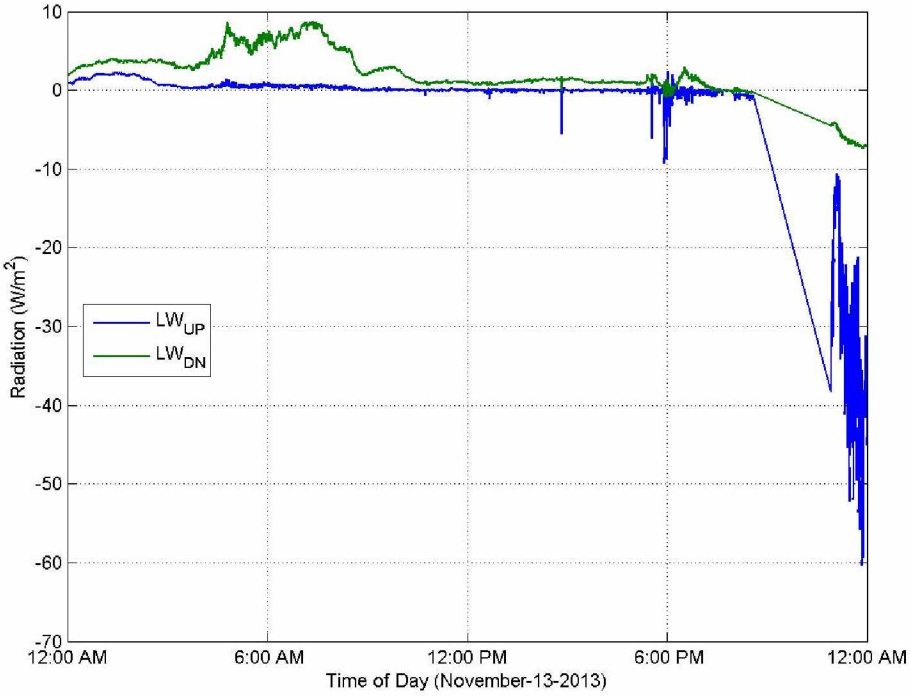

Figure 8.29: Infrared Radiation Measurements at Pit Rim during Cloud Cover (November 13th 2013).

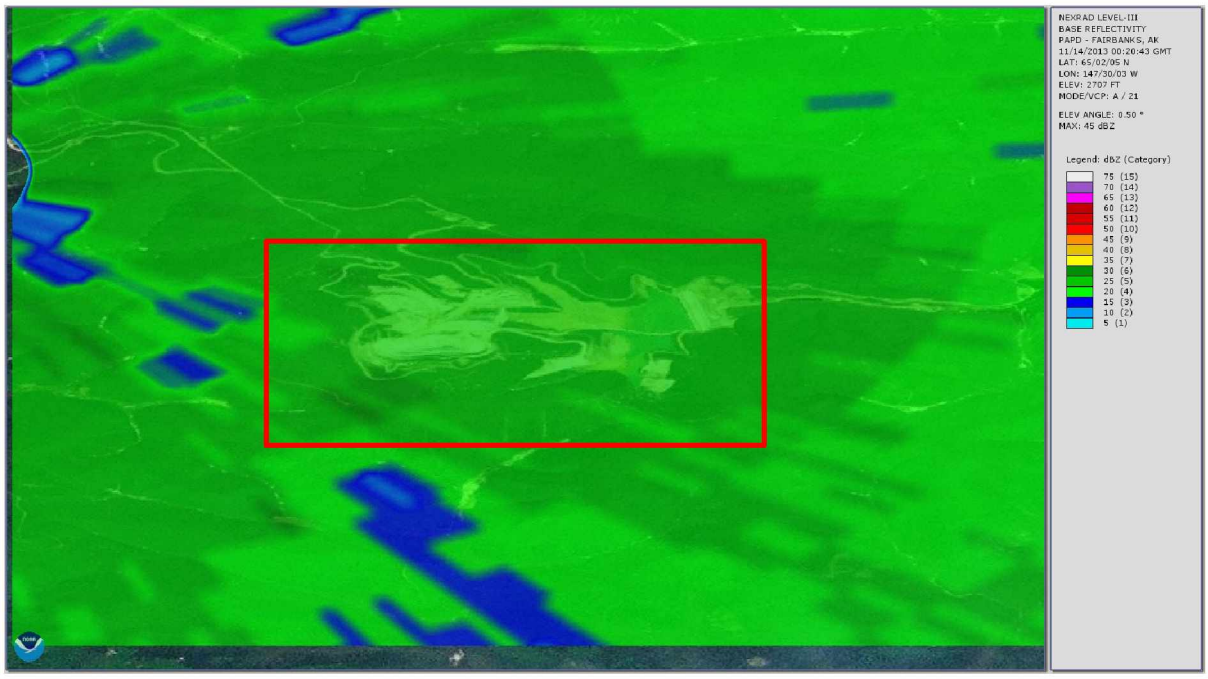

Figure 8.30: RADAR Base Reflectivity Data on November 13th 2013 (http://www.ncdc.noaa.gov/nexradinv/).

Table 8.3: Weather Station 1 Data on November 13th 2013 (http://www.wunderground.com/).

	High	Low	Average
Temperature (°C)	0.0	-13.89	-9.17
Dew Point (°C)	0.0	-15.56	-10.5
Relative Humidity (%)	100	86	90

Table 8.4: Weather Station 2 Data on November 13th 2013 (http://www.wunderground.com/).

	High	Low	Average
Temperature (°C)	1.67	-13.38	-8.67
Dew Point (°C)	1.67	-14.44	-8.83
Relative Humidity (%)	100	92	99

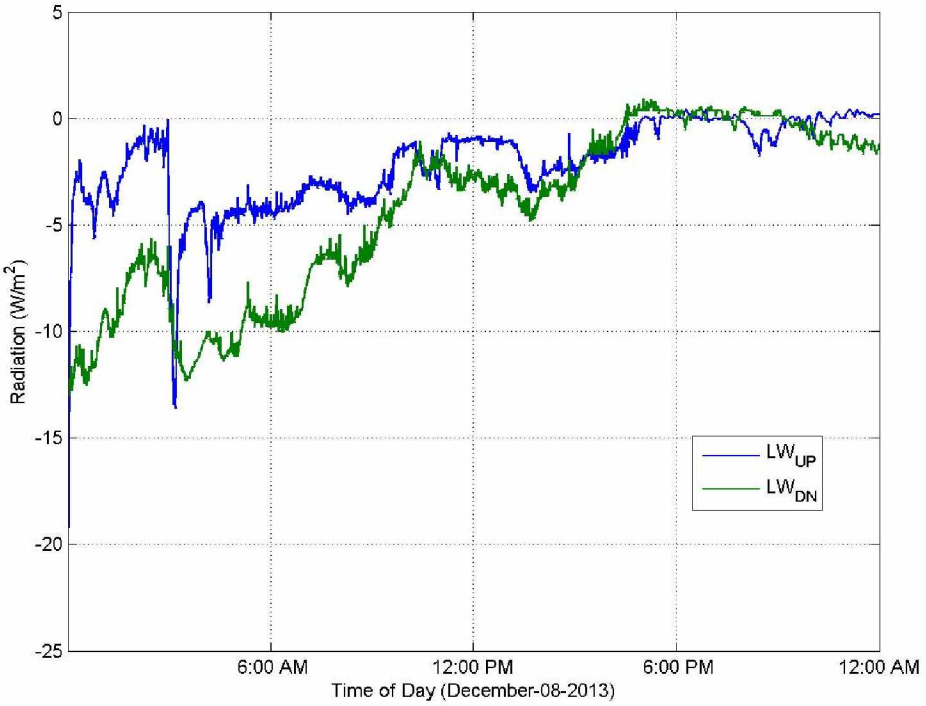

Figure 8.31: Infrared Radiation Measurements at Pit Bottom during Cloud Cover (December 8th 2013).

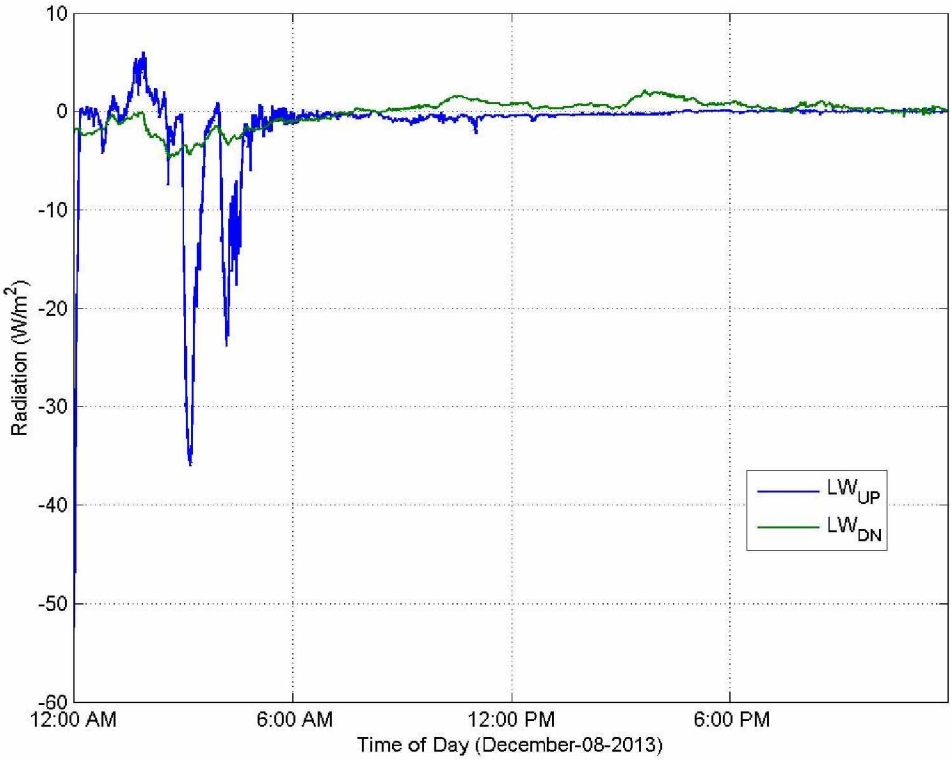

Figure 8.32: Infrared Radiation Measurements at Pit Rim during Cloud Cover (December 8th 2013).

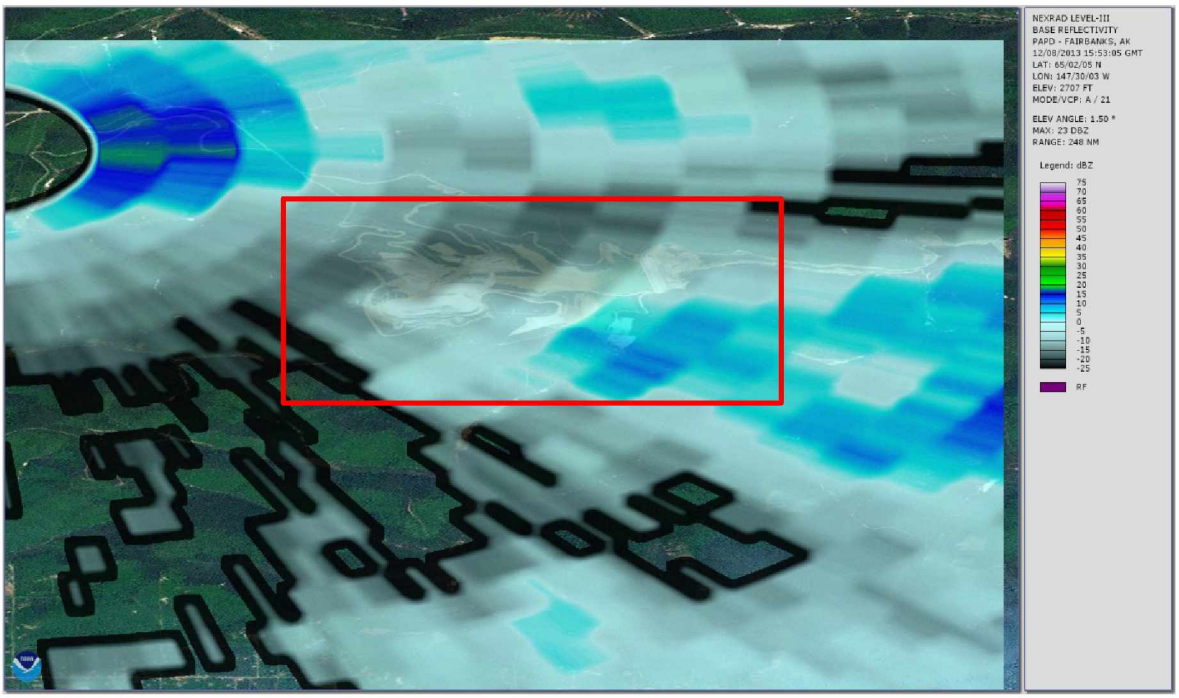

Figure 8.33: RADAR Base Reflectivity Data on December 8th 2013 (http://www.ncdc.noaa.gov/nexradinv/).

Table 8.5: Weather Station 1 Data on December 8th 2013 (http://www.wunderground.com/).

	High	Low	Average
Temperature (°C)	0.56	-1.67	-1.00
Dew Point (°C)	-0.56	-2.78	-1.72
Relative Humidity (%)	96	92	95

Table 8.6: Weather Station 2 Data on December 8th 2013 (http://www.wunderground.com/).

	High	Low	Average
Temperature (°C)	0.0	-1.67	-0.89
Dew Point (°C)	0.0	-1.67	-0.89
Relative Humidity (%)	100	100	100

Contrary to the data presented above, another set of data (November 20th 2013) is presented below when there is an absence of cloud. The relevent data (temperature, radiation, etc.) are different in the absence of a cloud cover. Figure 8.34 shows the infrared radiation data for the pit bottom. Whereas, the pit rim infrared radiation data is presented in Figure 8.35. It can be seen from the infrared radiation data (Figure 8.34 and Figure 8.35) that the incoming and the outgoing infrared radiation are apart from each other. The difference between the incoming and the outgoing radiation, therefore, is non-zero. The absence of cloud over the sensors during that time can be verified from the satellite image (Figure 8.36) of the selected open pit mine on November 20th 2013 which indicates cleary a cloud free day.

An observation of the WS 1 and the WS 2 data on the same date also indicates the absence of any cloud in the surrounding areas of the open pit mine. The data from WS 1 and WS 2 are presented in Table 8.7 and Table 8.8. It is evident from both the tables that the air and the dew point temperatures are different, thus, indicating the absence of cloud cover near the sensors.

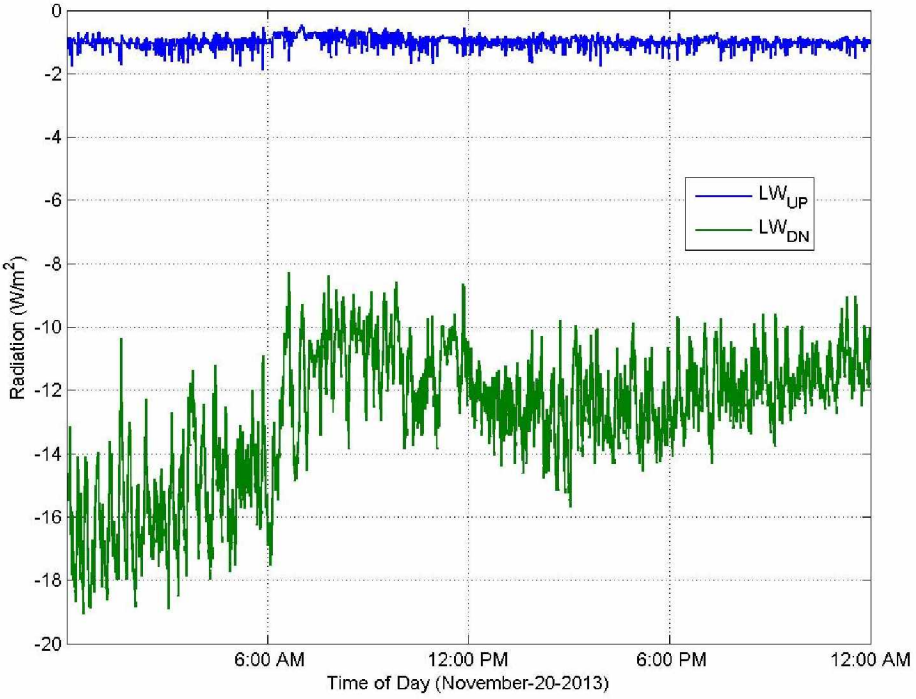

Figure 8.34: Infrared Radiation Measurements at Pit Bottom with No Cloud Cover (November 20th 2013).

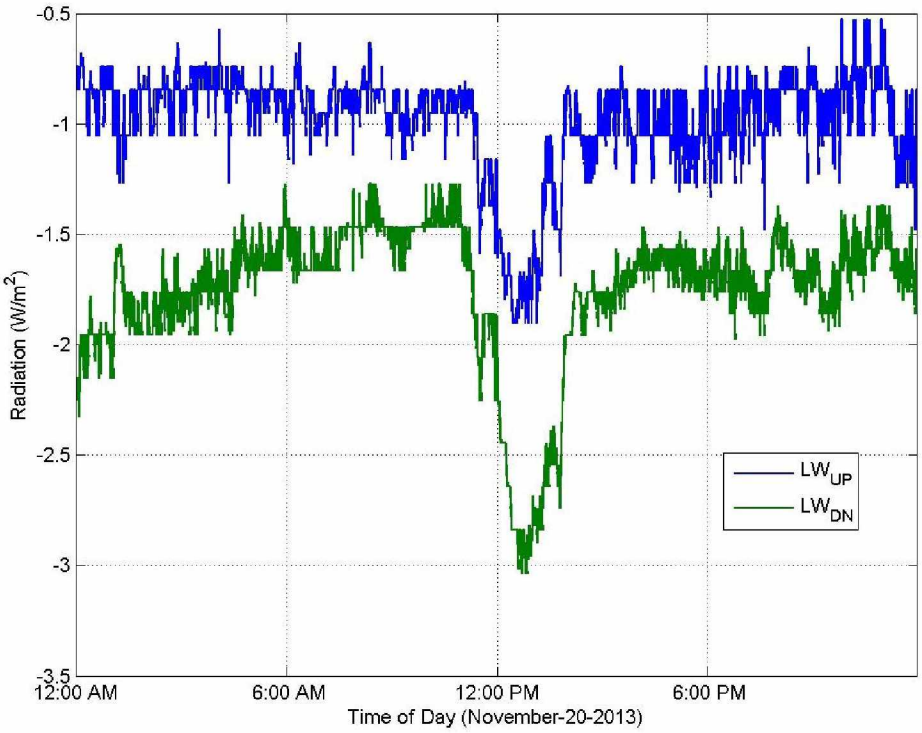

Figure 8.35: Infrared Radiation Measurements at Pit Rim with No Cloud Cover (November 20th 2013).

Figure 8.36: RADAR Base Reflectivity Data on November 20th 2013 (http://www.ncdc.noaa.gov/nexradinv/).

Table 8.7: Weather Station 1 Data on November 20th 2013 (http://www.wunderground.com/).

	High	Low	Average
Temperature (°C)	-20.00	-25.56	-22.94
Dew Point (°C)	-22.78	-27.78	-25.50
Relative Humidity (%)	80	75	79

Table 8.8: Weather Station 2 Data on November 20th 2013 (http://www.wunderground.com/).

	High	Low	Average
Temperature (°C)	-20.00	-23.89	-22.22
Dew Point (°C)	-20.56	-25.00	-22.83
Relative Humidity (%)	96	92	94

From above, a conclusion can be made that during an atmospheric inversion advancing clouds or formation of clouds play an important role in changing the vertical temperature profiles. It is hypothesized that introduction of cloud cover over the open pit mine could lift the inversion. It is therefore, the presence of a cloud cover is simulated for mitigation of the contaminants under inversion and the results are analyzed.

8.2.6 Cloud Seeding

Prior to discussing the modeling details, a short description on artificial modification of clouds in the atmosphere is presented in this section. Modification of local weather by artificially generated clouds is generally known as cloud seeding (Wallace and Hobbs 2006). Cloud seeding can be performed by introducing: (i) large hygroscopic particles into warm clouds; (Parakhonskii and Severin) artificial ice nuclei into cold clouds; and (iii) high concentrations of artificial ice nuclei into cold clouds.

Cloud seeding by introducing hygroscopic particles (e.g. NaCl) tends to disperse in the warm clouds and grow by condensation. This method is expensive and not very reliable. Introduction of artificial ice nuclei into cold clouds might increase the ice particles resulting in the formation of dense clouds. In the 1940s, experiments were conducted for cloud modification using dry ice and

silver iodide (Wallace and Hobbs 2006). Now silver iodide is widely used compound for cloud seeding. Formation of cloud can also occur due to the release of large quantities of heat, water vapor, and cloud-active aerosol into atmosphere. These effluents might change the structure of clouds in the surrounding areas.

8.2.7 Introduction of Cloud Cover in the Model Domain

In order to examine the effects of cloud cover, the 2013 pit geometry is selected for the mitigation simulation model. For mitigation modeling with cloud cover, the results after 13 hours of simulation of the 2013 pit geometry is used as the initial condition. The realizable κ-ε turbulent model is used to characterize the transport phenomena.

The data collected from the pit bottom radiation sensor (December 7th 2013) are used in the simulation. The cloud cover is introduced in the model once the inversion sets in.

From the infrared radiation data presented in Figure 8.25, Figure 8.26, Figure 8.28, Figure 8.29, Figure 8.31 and Figure 8.32, it is clear that under cloud cover the incoming and the outgoing infrared radiation values tend to coincide near zero (W/m^2).

As described in Chapter 2, the stable boundary layer in an open pit mine is sensitive to the radiation balance. This boundary layer cools at the surface due to the net negative radiation balance. In the absence of a cloud cover, the clear sky condition give rise to strong radiative cooling. When a cloud arrives, the surface temperature, and the relative humidity increase. The outgoing longwave radiation follows these temperature oscillations.

The introduction of a cloud cover is reflected by setting the heat fluxes in the model domain top wall boundary (the top of the temperature inversion), FA, and the bottom wall boundary, PIT, to zero (W/m^2). The incoming and the outgoing solar (short wave) radiation are assumed to be low and are neglected. In the absence of solar radiation the heat fluxes are only due to the infrared radiation. The sensors at the selected mine collect data every ten seconds. For the stability of the model, the data are averaged over a four-hour time period and used in model to replicate the changing weather conditions. For simulation, the realizable κ-ε turbulence model is used. All other model parameters are kept unchanged. Input of varying temperature, velocity, and radiation/heat fluxes data every four hour changes the boundary conditions in the model. Figure 8.37 through Figure 8.42 show the development of inversion in the open pit mine over a six hour time period. The resulting NO_2

concentration during this six hour time period envelopes the entire open pit. The velocity vector of the initial state (t≈13.69 hrs.) shows that the flow from the east to the west direction of the pit is streamlined. However, the development of the inversion during this time period results in a low air velocity in the high contaminant zones.

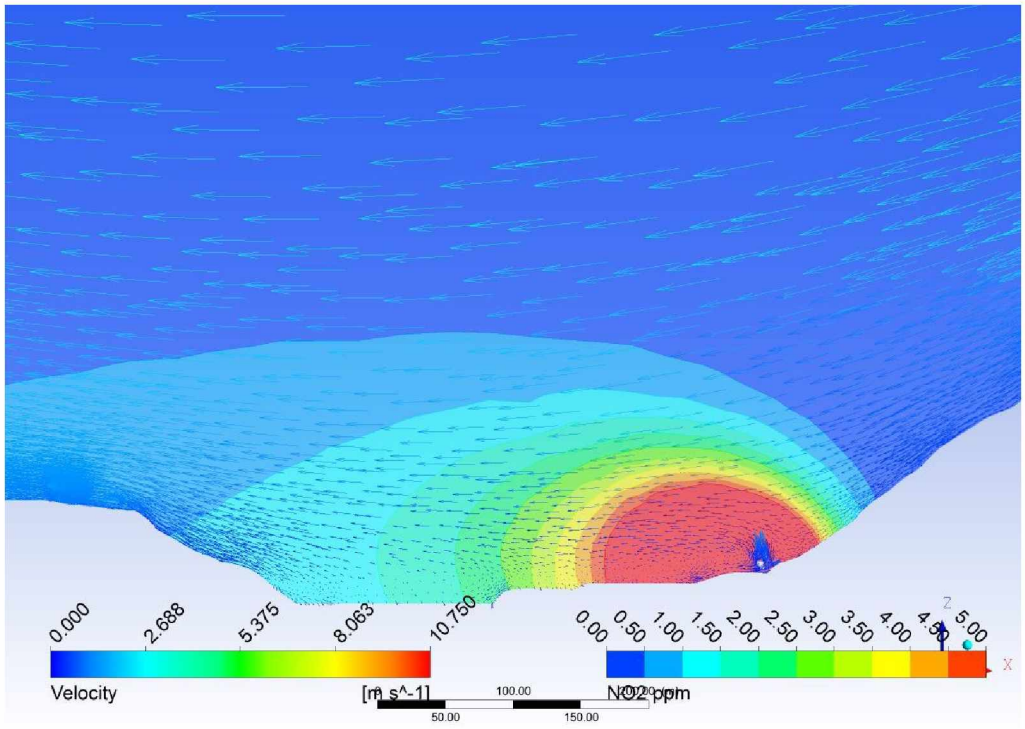

Figure 8.37: Contour of NO_2 Concentration (in ppm) and Velocity Vectors in Vertical Plane along East-West Direction (t ≈ 13.69 hrs.).

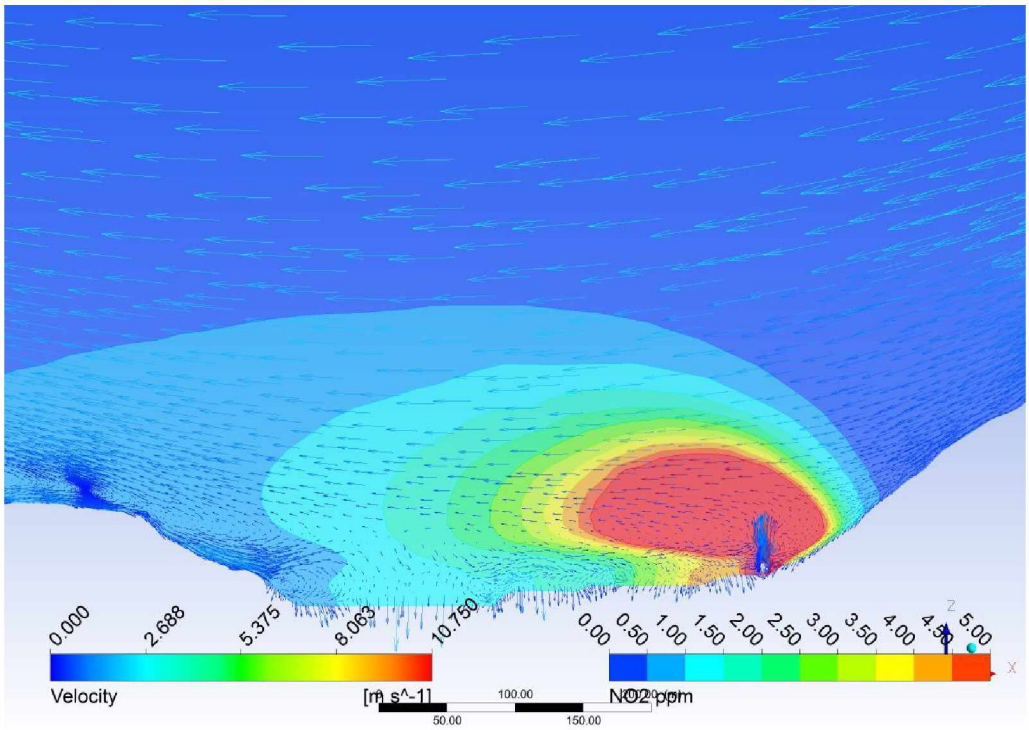

Figure 8.38: Contour of NO_2 Concentration (in ppm) and Velocity Vectors in Vertical Plane along East-West Direction (t ≈ 14.69 hrs.).

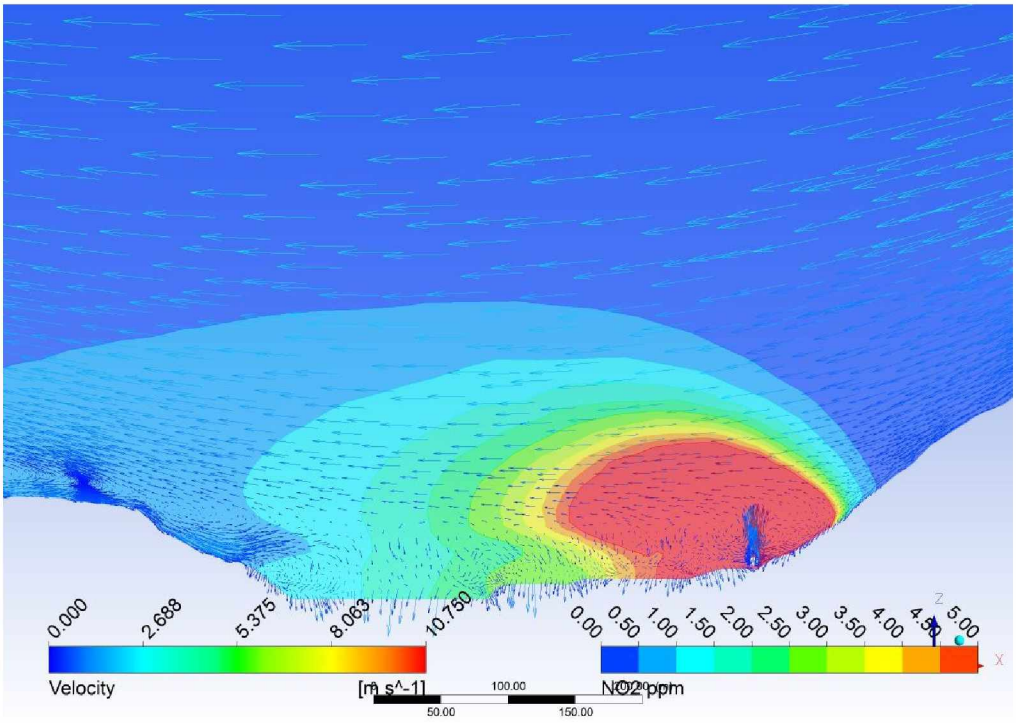

Figure 8.39: Contour of NO_2 Concentration (in ppm) and Velocity Vectors in Vertical Plane along East-West Direction (t ≈ 15.69 hrs.).

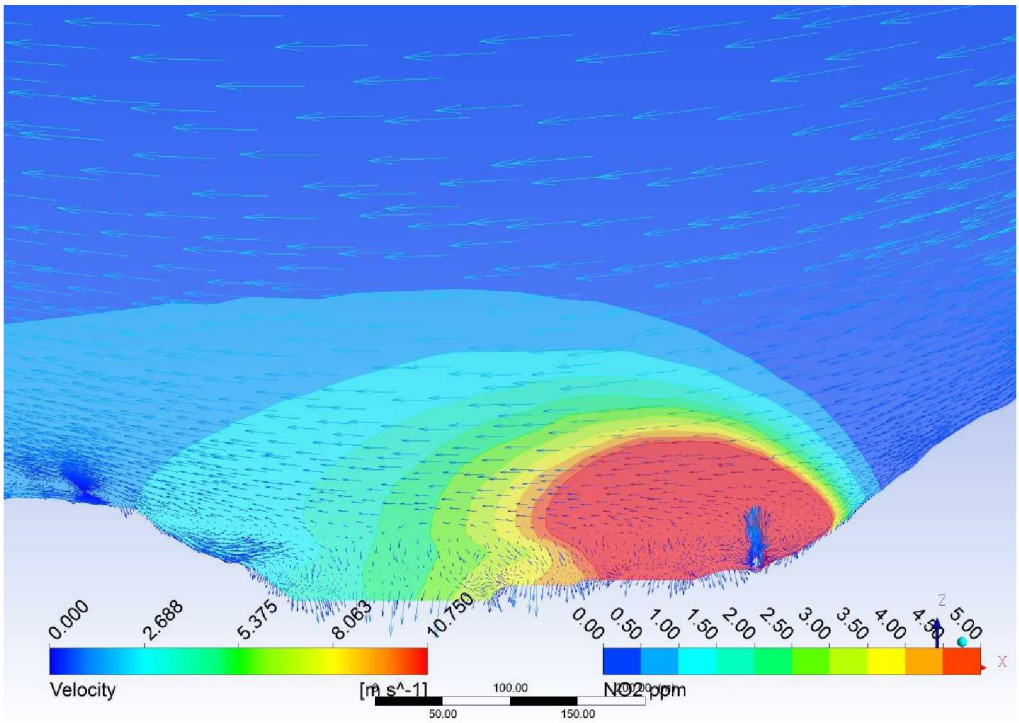

Figure 8.40: Contour of NO_2 Concentration (in ppm) and Velocity Vectors in Vertical Plane along East-West Direction (t ≈ 16.69 hrs.).

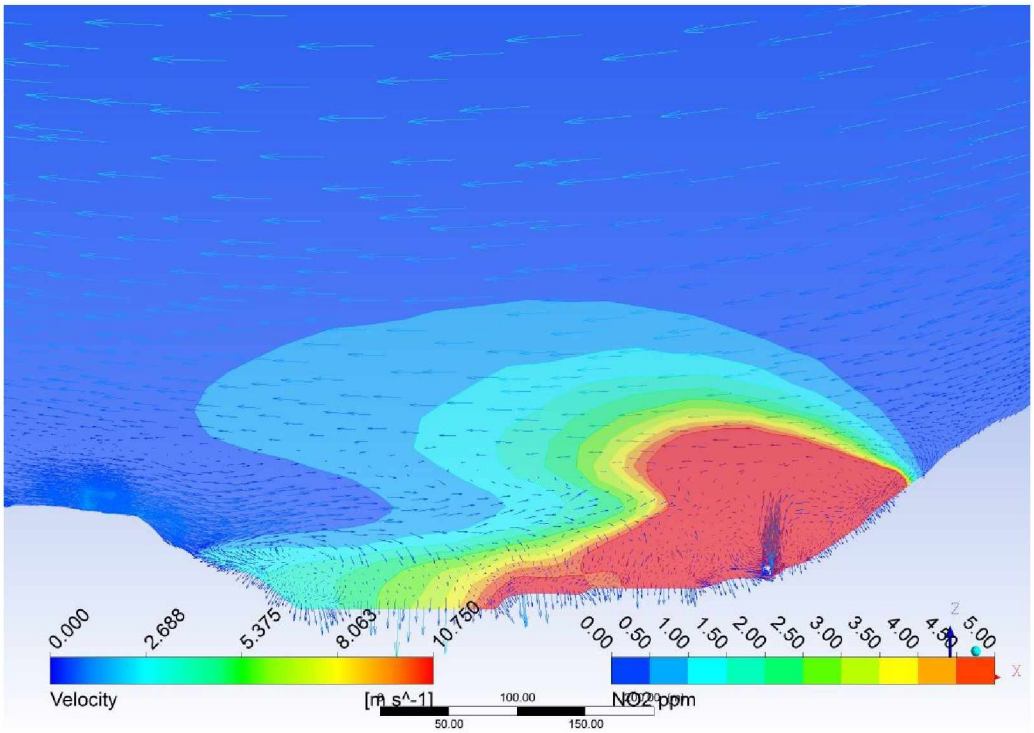

Figure 8.41: Contour of NO_2 Concentration (in ppm) and Velocity Vectors in Vertical Plane along East-West Direction (t ≈ 17.65 hrs.).

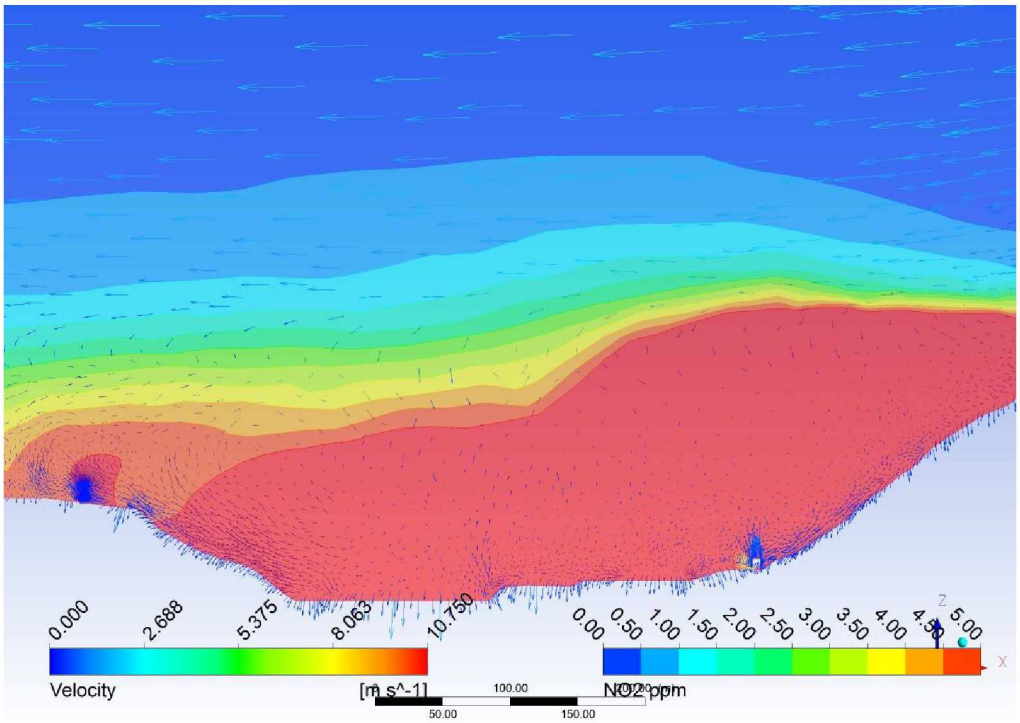

Figure 8.42: Contour of NO_2 Concentration (in ppm) and Velocity Vectors in Vertical Plane along East-West Direction ($t \approx 18.65$ hrs.).

Figure 8.42 shows that the open pit is under strong inversion and a high level of NO_2 concentration (above five ppm) in the entire pit. This pit with high level of NO_2 concentration and with an initially stratified boundary layer is selected for mitigation modeling using a cloud cover.

A cloud cover is introduced in the model domain by changing the heat fluxes at the top and the bottom walls to zero (W/m^2). Figure 8.43 and Figure 8.44 show the changing level of NO_2 concentration after the introduction of a cloud cover in the model domain. It can be seen that within two hours the concentration of NO_2 is three ppm or less which is well below the TLV. The NO_2 concentration, velocity, and temperature profiles are presented along the vertical line from the deepest part of the pit to the top of the model domain.

Figure 8.45 and Figure 8.46 show that the temperature and the NO_2 concentration as a function of time. The changes in the temperature profile are clearly visible from

Figure 8.45 and that following the introduction of cloud cover, the vertical temperature gradient changes from a positive value to a negative value, indicating the break-up of the inversion. From Figure 8.46, it can be seen that the NO_2 concentration increases from two ppm ($t \approx 16.69$ hrs.) to nine ppm ($t \approx 18.65$ hrs.). With the introduction of the cloud cover, however, it decreases

to around three ppm (t ≈ 20.31 hrs.). Thus, it can be stated that introduction of a cloud cover over the open pit changes the vertical temperature profile resulting in the break-up of stable boundary layer and the dilution of pollutants below the TLV.

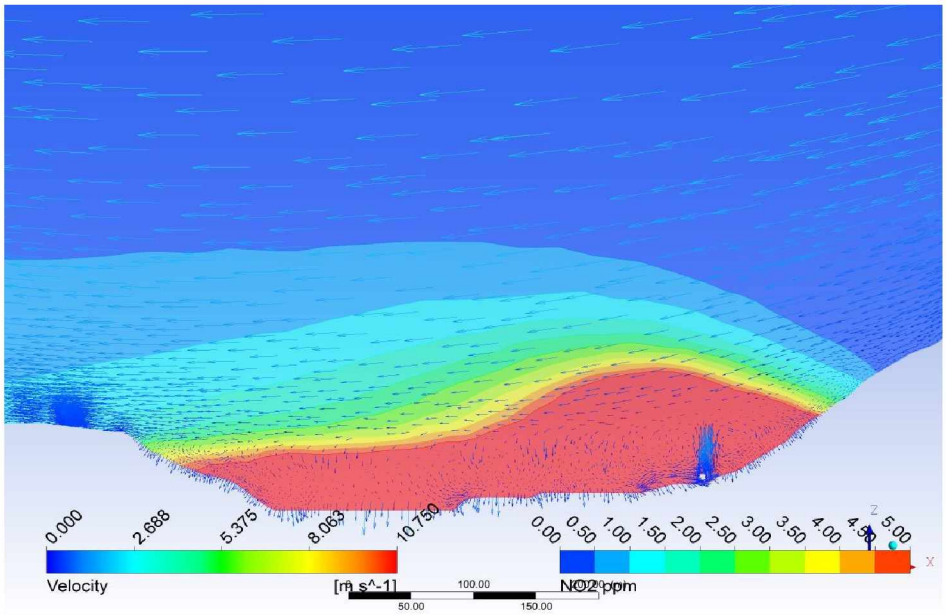

Figure 8.43: Concentration of NO_2 (in ppm) and Velocity Vectors in Vertical Plane along East-West Direction (t ≈ 19.65hrs).

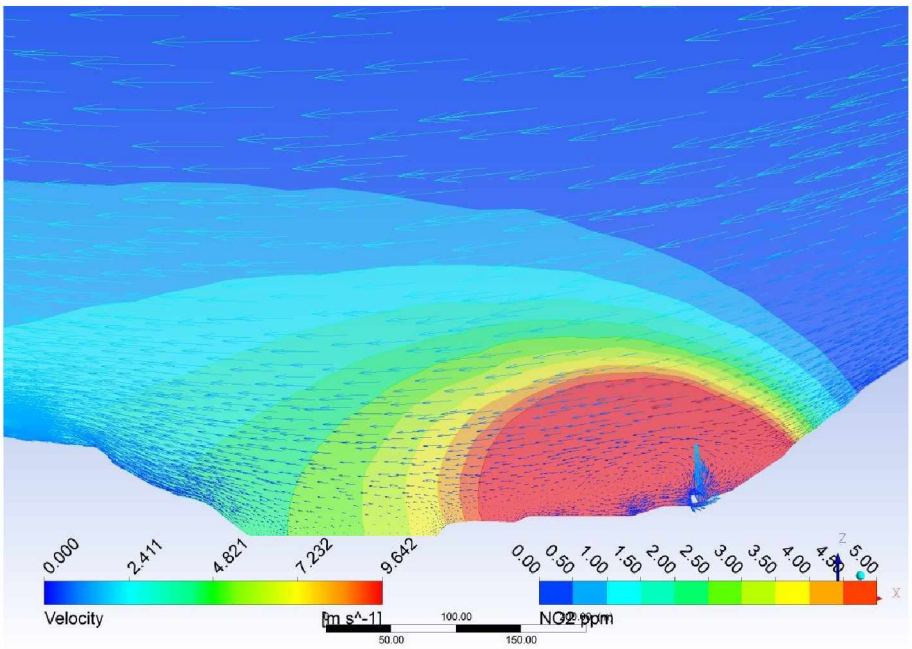

Figure 8.44: Concentration of NO_2 (in ppm) and Velocity Vectors in Vertical Plane along East-West Direction (t ≈ 20.31hrs).

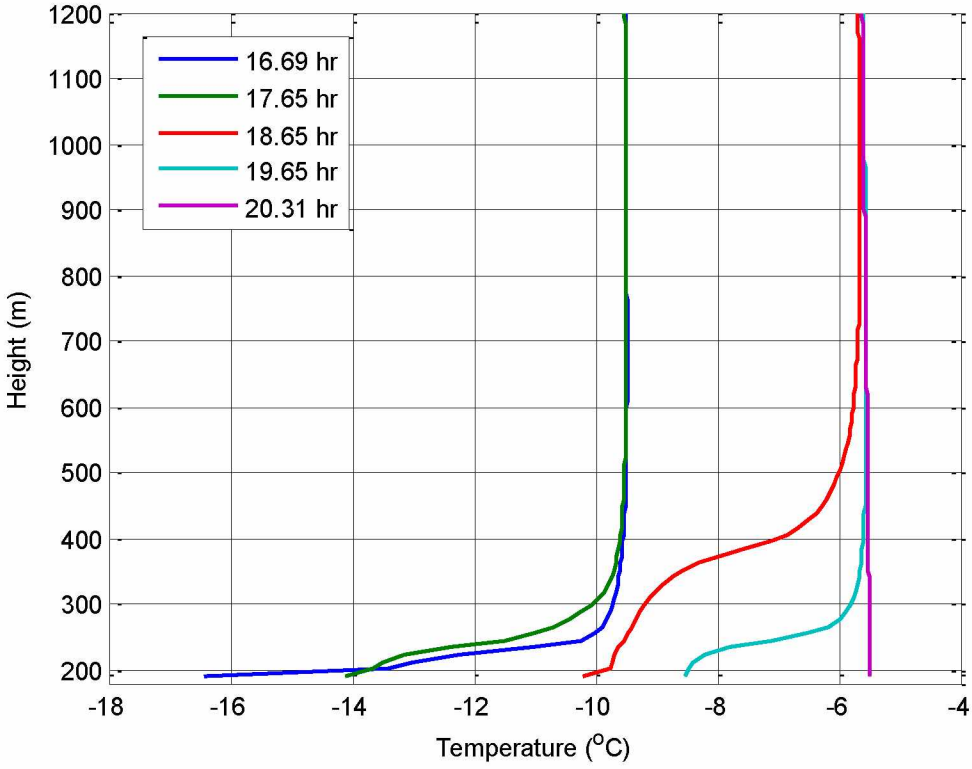

Figure 8.45: Temperature profiles along the Vertical Line.

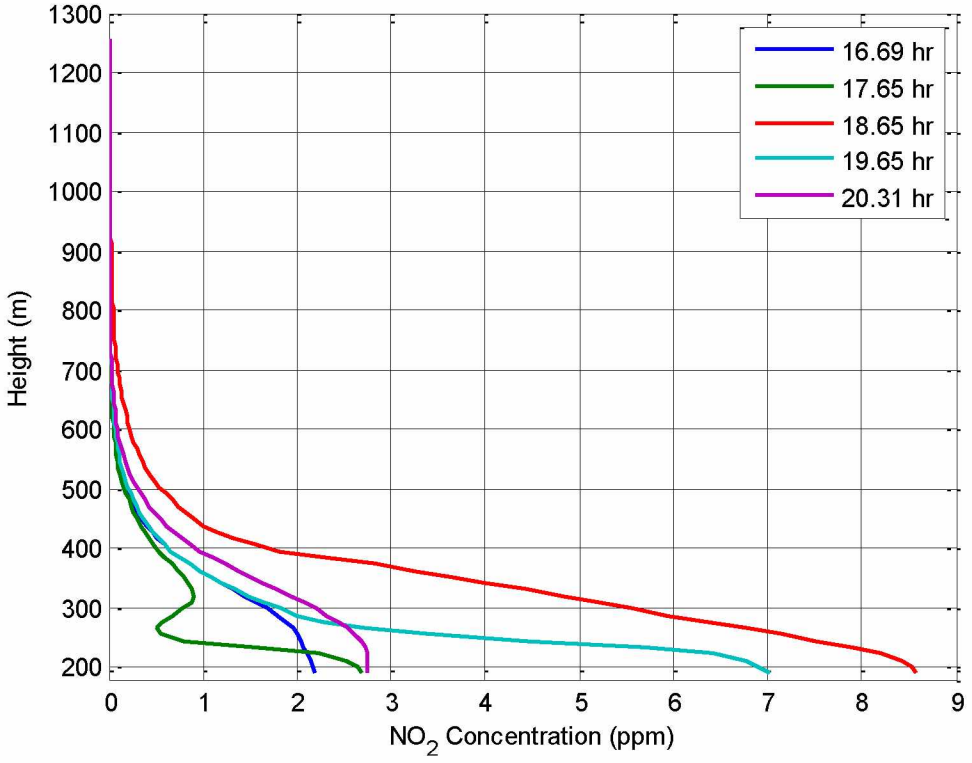

Figure 8.46: Concentration of NO_2 (in ppm) along the Vertical Line.

The simulated model results show that the cloud cover over the open pit mine changes the vertical temperature profiles. The results presented above show that within a couple of hours the pit is cleared of the high NO_2 concentrations. There are other factors, however, such as the elevation, extent of cloud cover over the area, and thickness of cloud cover over the pit, may influence the amount of time needed for break-up of the inversion and removal of pollutants out of the pit.

In the scope of the current research, the simulation results of the 2010 pit geometry are also used to assess the effectiveness of cloud cover and the influence of the aspect ratio of the model geometry. The model domain 2010 pit is smaller than the 2013 pit configuration. Thus, makes it ideal to test the mitigation model in terms of the extent of the cloud cover over the selected open pit. From both the figures (Figure 8.3 and Figure 8.14) it is clearly visible that the extent of 2013 pit is larger than the 2010 pit geometry. The vertical extent for the 2010 pit model is 1050 m, whereas, for the 2013 pit model configuration the height is 1250 m. Thus, the change in the geometrical configuration of the model domain leads to another set of simulation with cloud cover.

Since, the simulation results for 2010 pit are already available with the realizable κ-ε model and the LES turbulence models, the mitigation modeling is attempted with both the turbulence models. The simulation results from the realizable κ-ε turbulence model for pollution mitigation are presented and analyzed in the following section, followed by the LES simulation results

8.3 Mitigation Model for the 2010 Pit Configuration

8.3.1 Mitigation Results from Realizable κ-ε Model

The final state of the contaminants transport simulation (Chapter 6) executed for a sixteen-hour time period, for a stable stratified boundary layer, is selected as the initial state for the mitigation model. The pit is already full of high levels of contaminants. A magnitude of zero (W/m^2) heat flux is assigned to the top wall and the pit wall boundaries of the model domain which imitates the introduction of the cloud cover. The results of the NO_2 concentration are presented as contour plots (Figure 8.47-Figure 8.55).

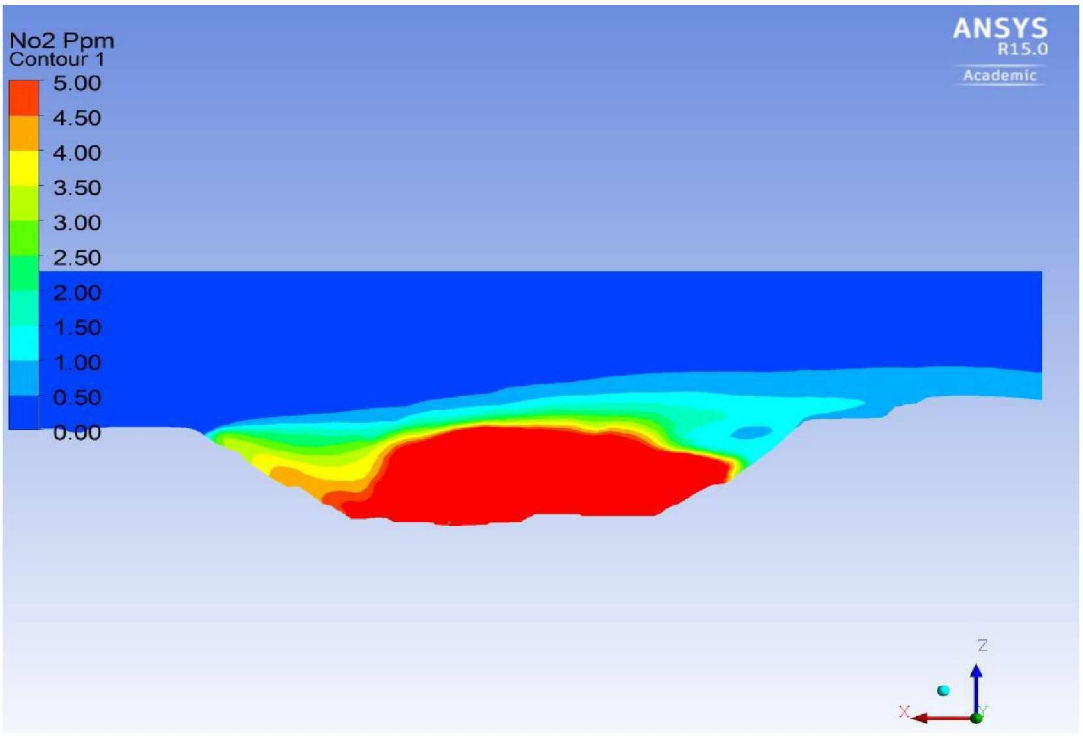

Figure 8.47: Concentration of NO_2 (in ppm) at Time Step ($t \approx 16$ hrs.).

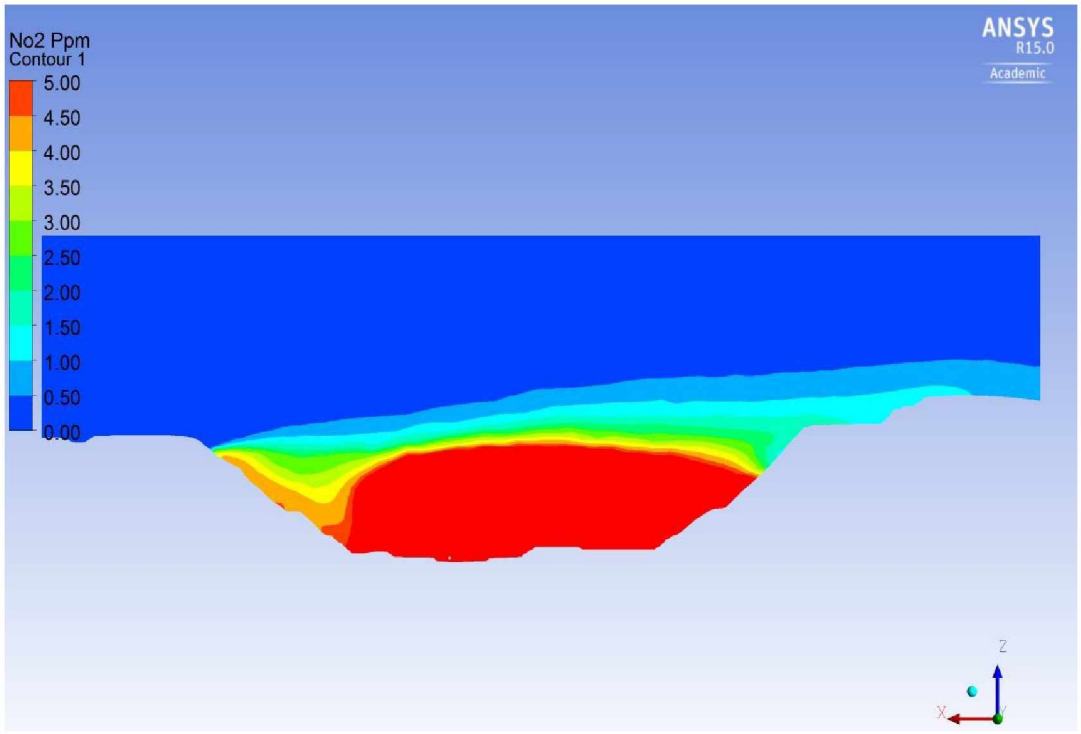

Figure 8.48: Concentration of NO_2 (in ppm) at Time Step ($t \approx 17$ hrs.).

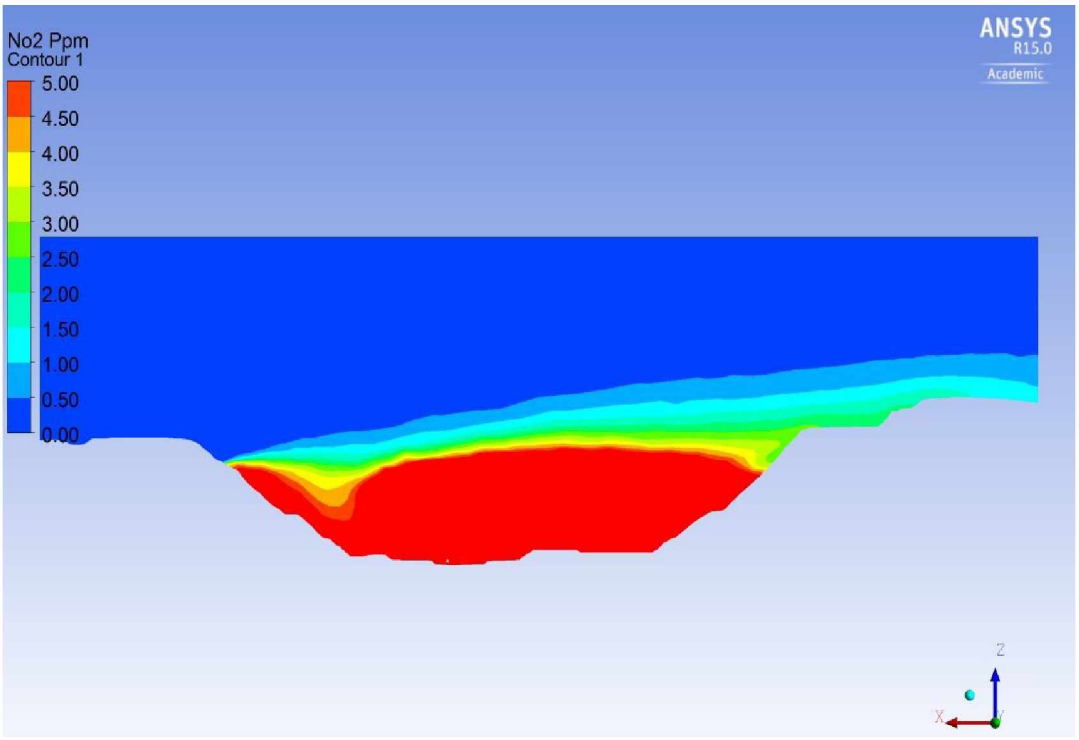

Figure 8.49: Concentration of NO_2 (in ppm) at Time Step ($t \approx 18$ hrs.).

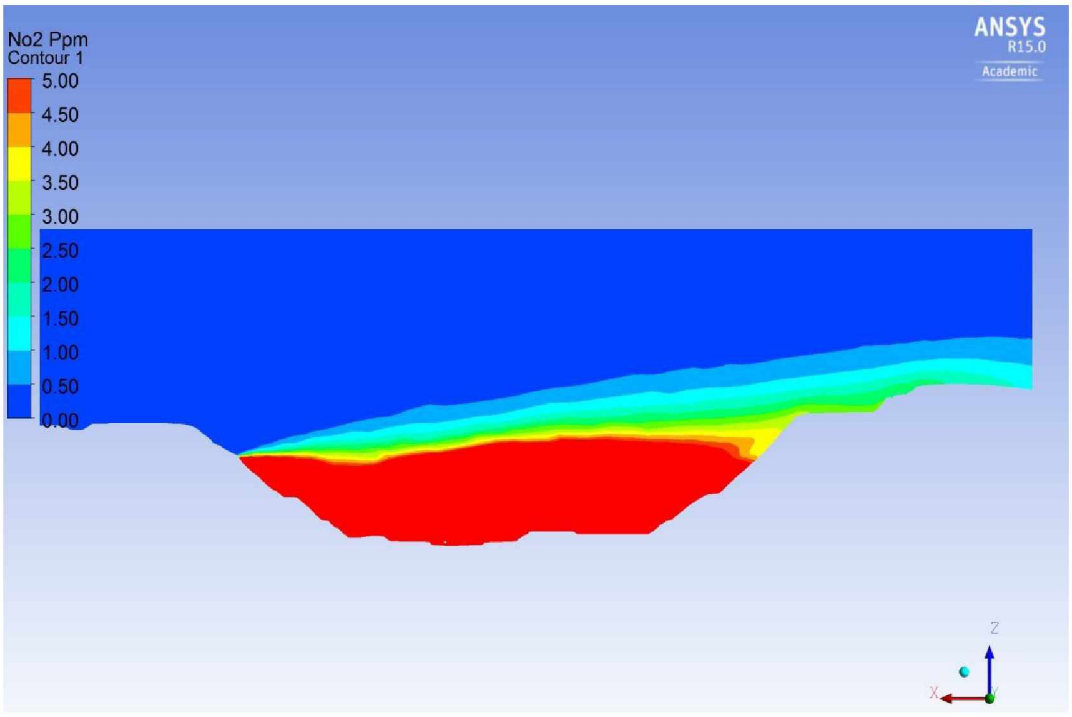

Figure 8.50: Concentration of NO_2 (in ppm) at Time Step ($t \approx 19$ hrs.).

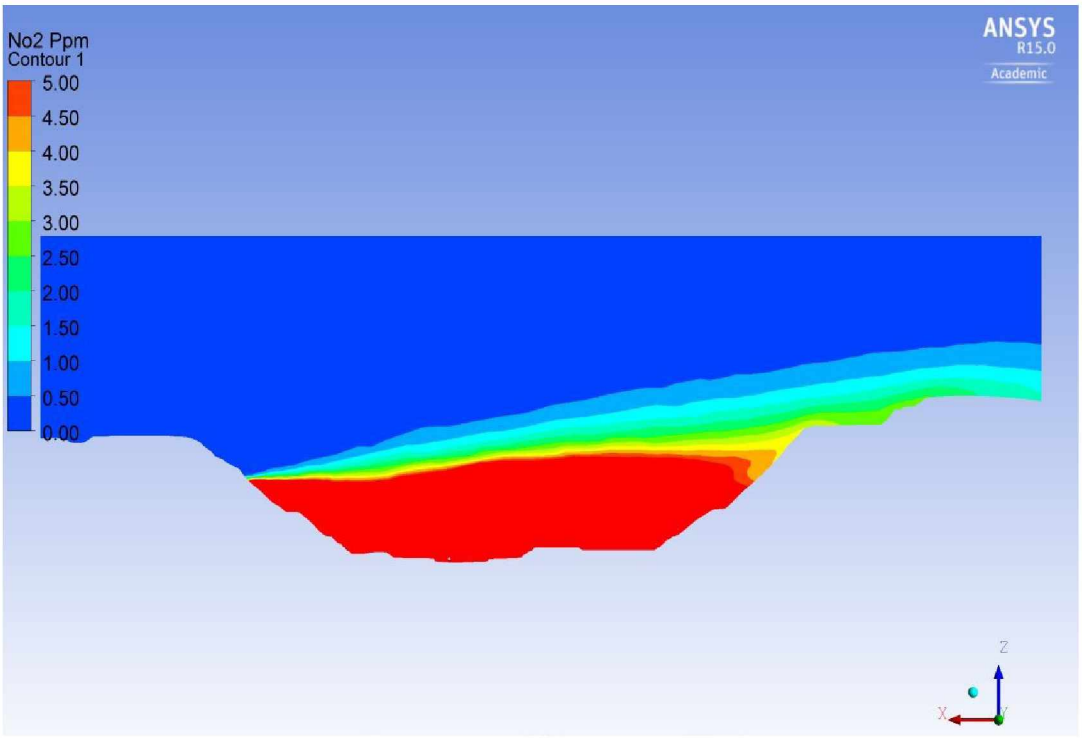

Figure 8.51: Concentration of NO_2 (in ppm) at Time Step ($t \approx 20$ hrs.).

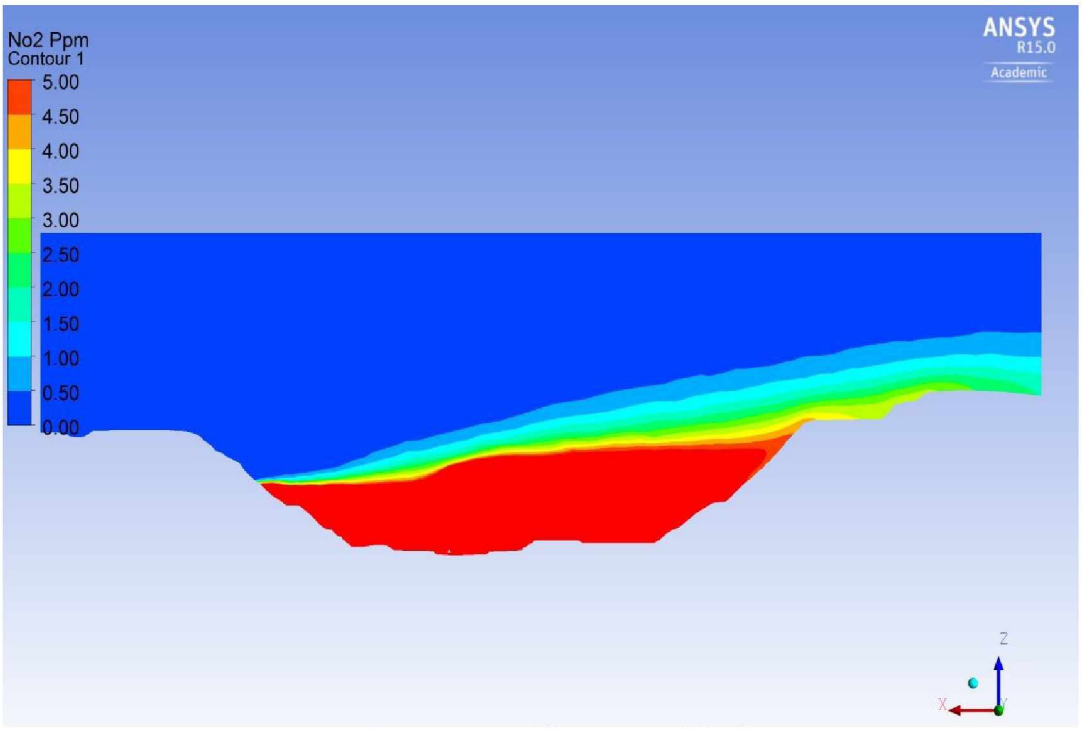

Figure 8.52: Concentration of NO_2 (in ppm) at Time Step ($t \approx 21$ hrs.).

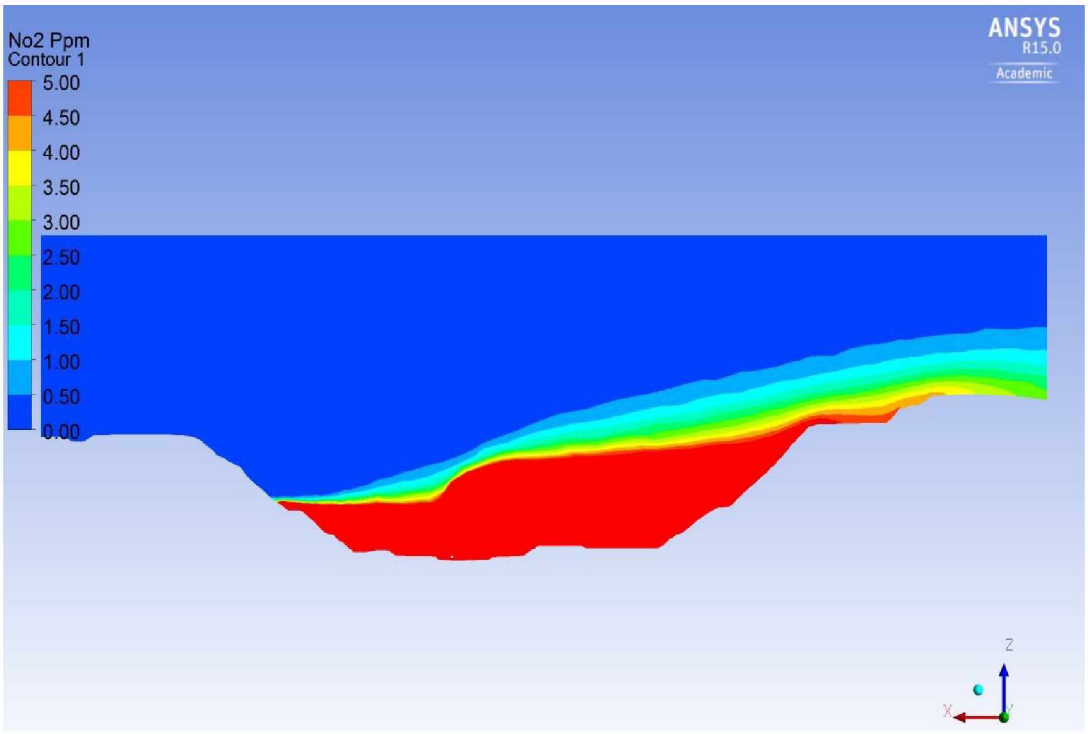

Figure 8.53: Concentration of NO_2 (in ppm) at Time Step ($t \approx 22$ hrs.).

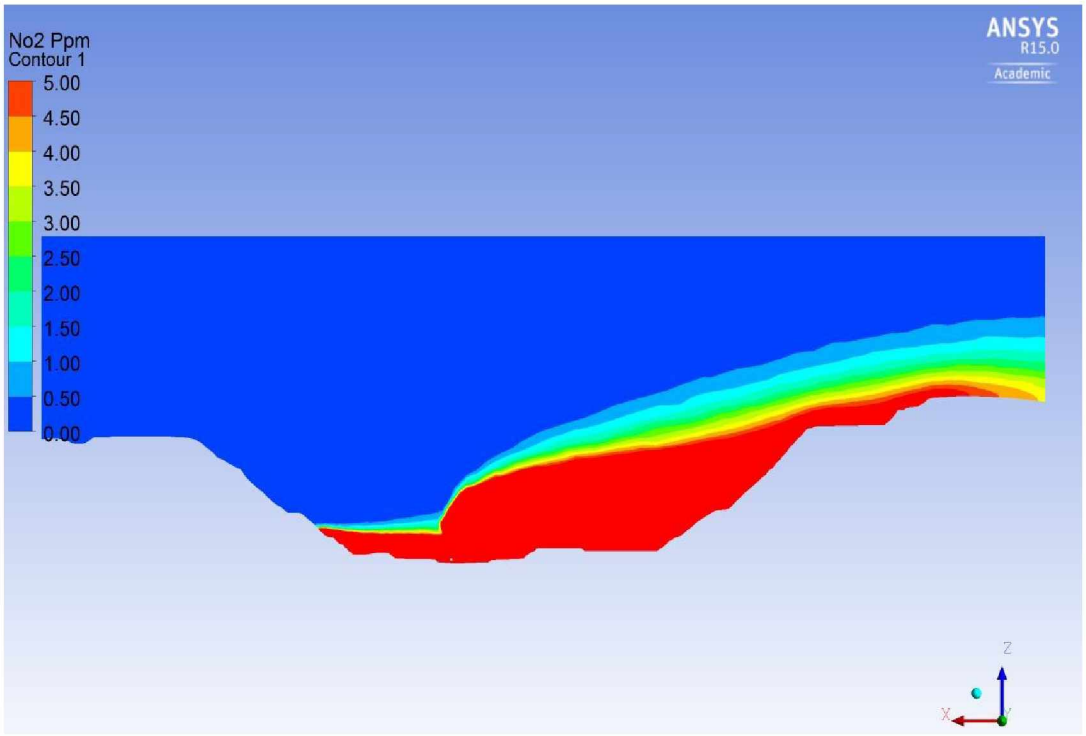

Figure 8.54: Concentration of NO_2 (in ppm) at Time Step ($t \approx 23$ hrs.).

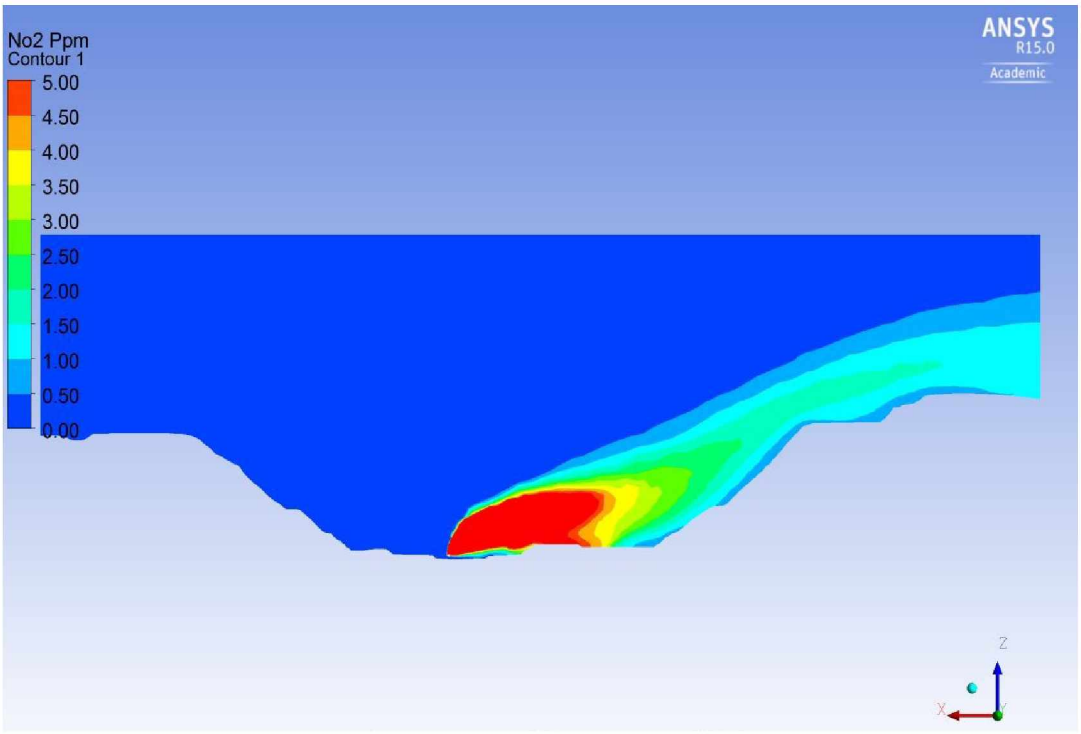

Figure 8.55: Concentration of NO_2 (in ppm) at Time Step ($t \approx 24.8$ hrs.).

A visual inspection of the NO_2 concentration plots indicates that after eight-hours of simulation the pit is cleared of the high level of NO_2 concentration.

8.3.2 Mitigation Results from LES Model

As before, the final state of the prior contaminant transport simulation with a stratified boundary layer is selected as the initial state for the LES model simulation for mitigation of the pollutants. Introduction of the cloud cover is the same as that of the realizable κ-ε model. Figure 8.56-Figure 8.66 show the NO_2 concentration plots for the initial state, as well as for the final state of the simulation.

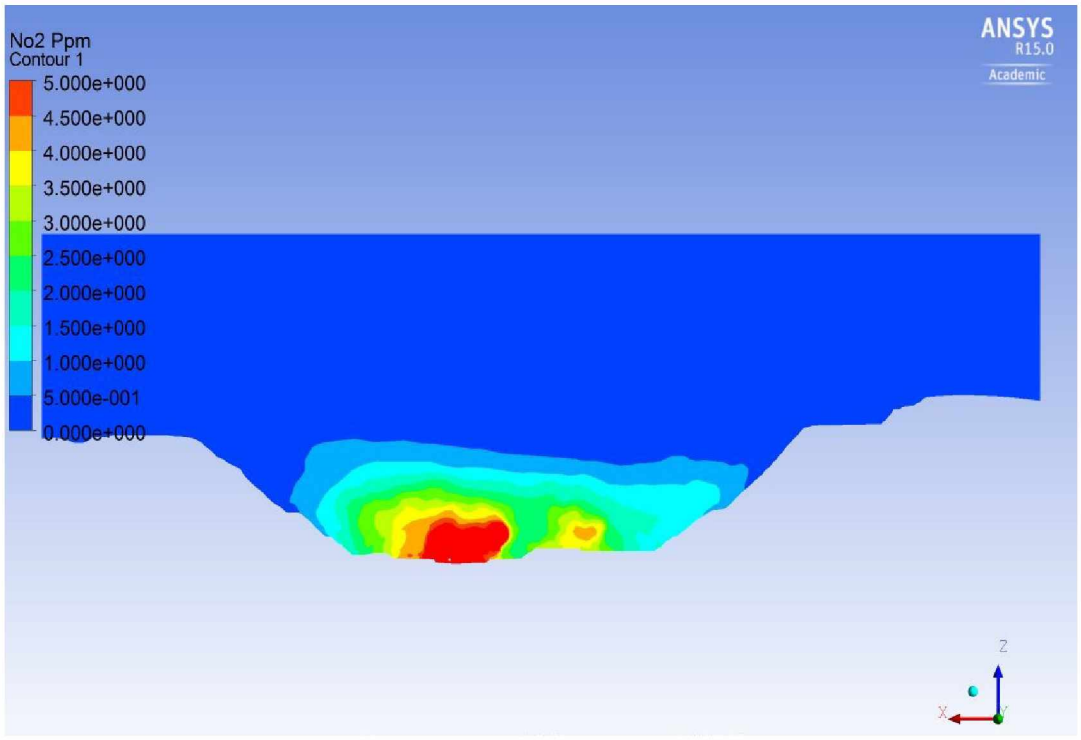

Figure 8.56: Concentration of NO_2 (in ppm) at Time Step ($t \approx 16$ hrs.).

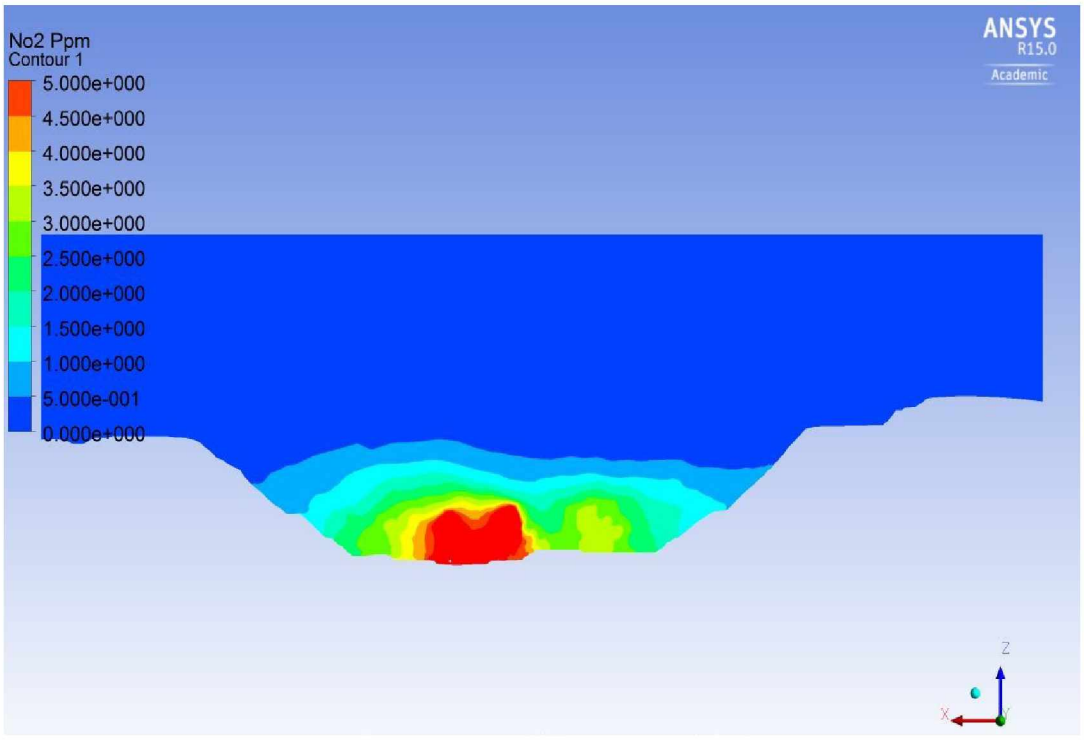

Figure 8.57: Concentration of NO_2 (in ppm) at Time Step ($t \approx 17$ hrs.).

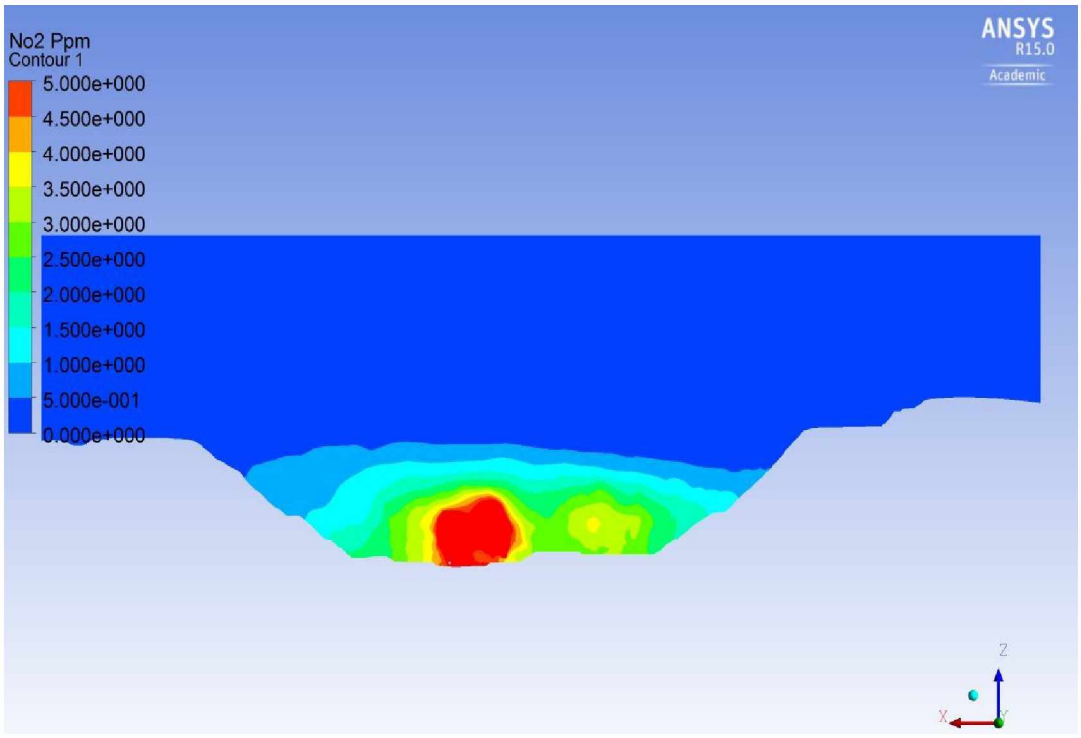

Figure 8.58: Concentration of NO_2 (in ppm) at Time Step ($t \approx 18$ hrs.).

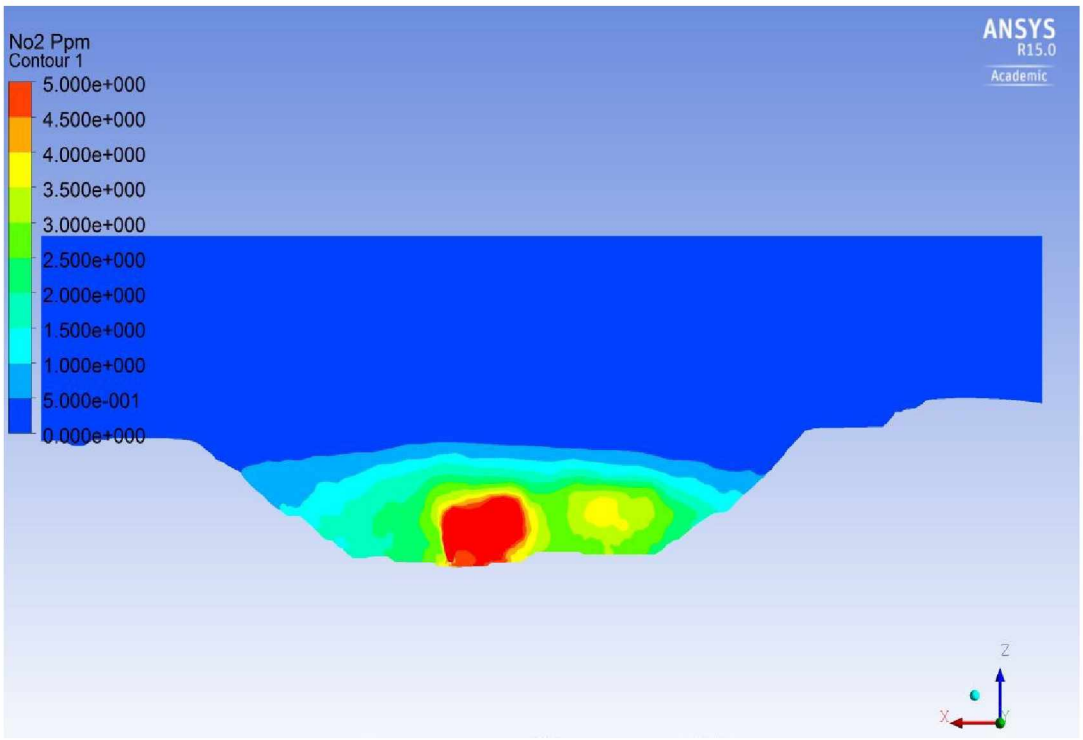

Figure 8.59: Concentration of NO_2 (in ppm) at Time Step ($t \approx 19$ hrs.).

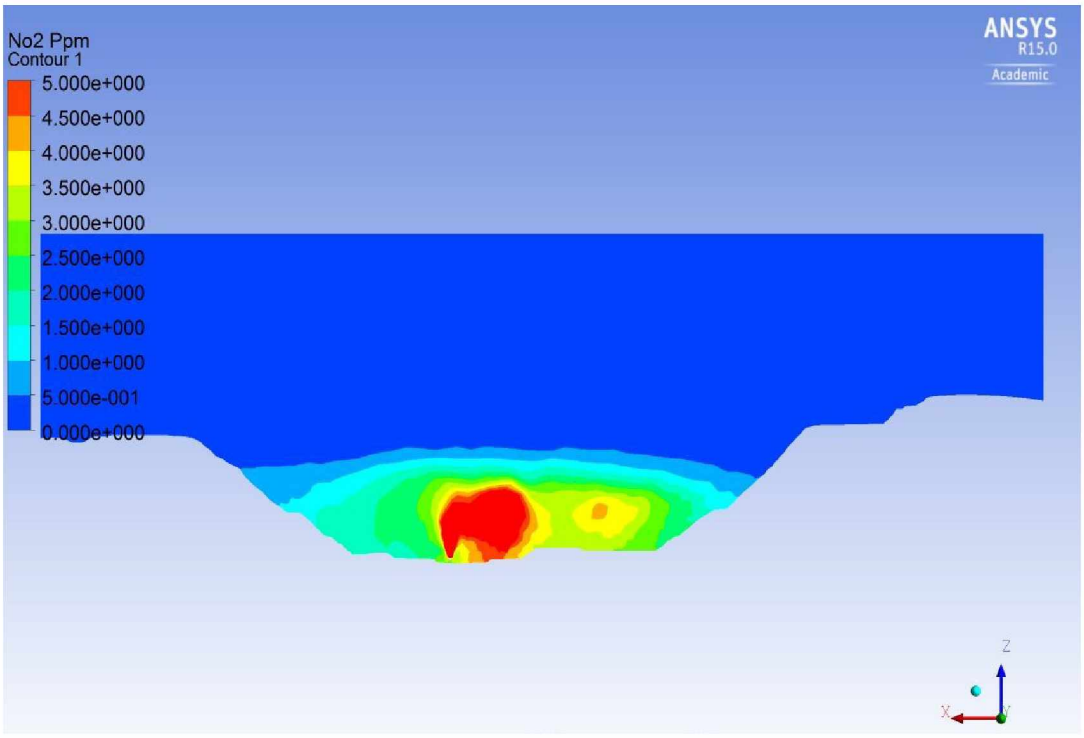

Figure 8.60: Concentration of NO_2 (in ppm) at Time Step ($t \approx 20$ hrs.).

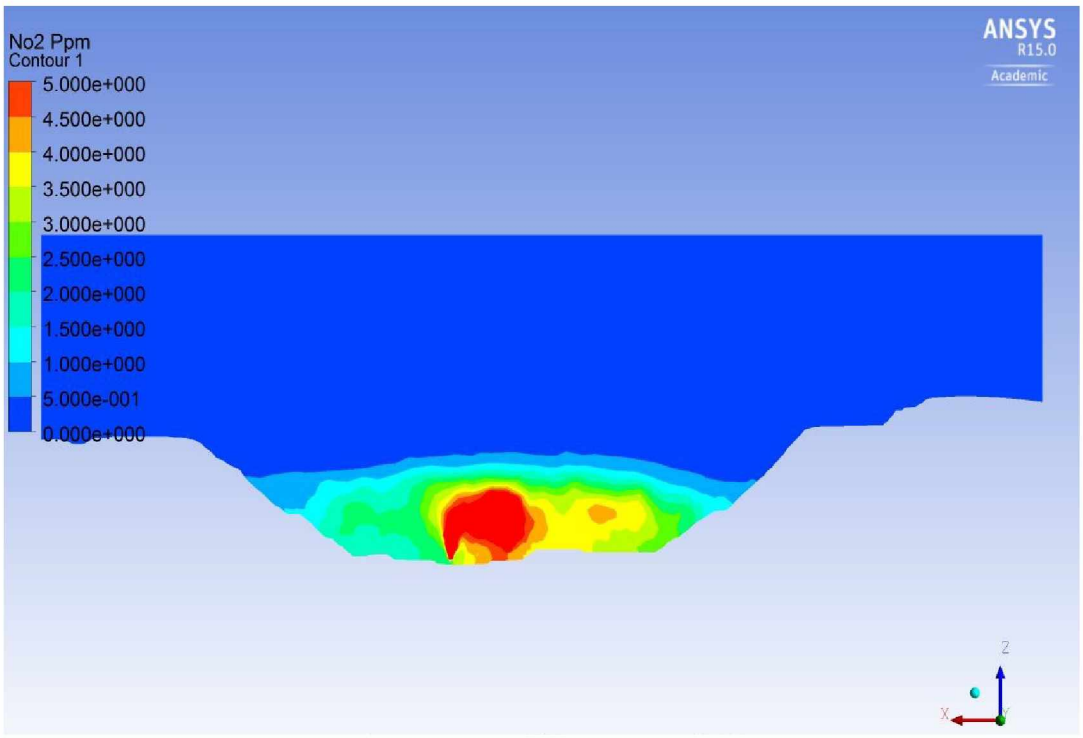

Figure 8.61: Concentration of NO_2 (in ppm) at Time Step ($t \approx 21$ hrs.).

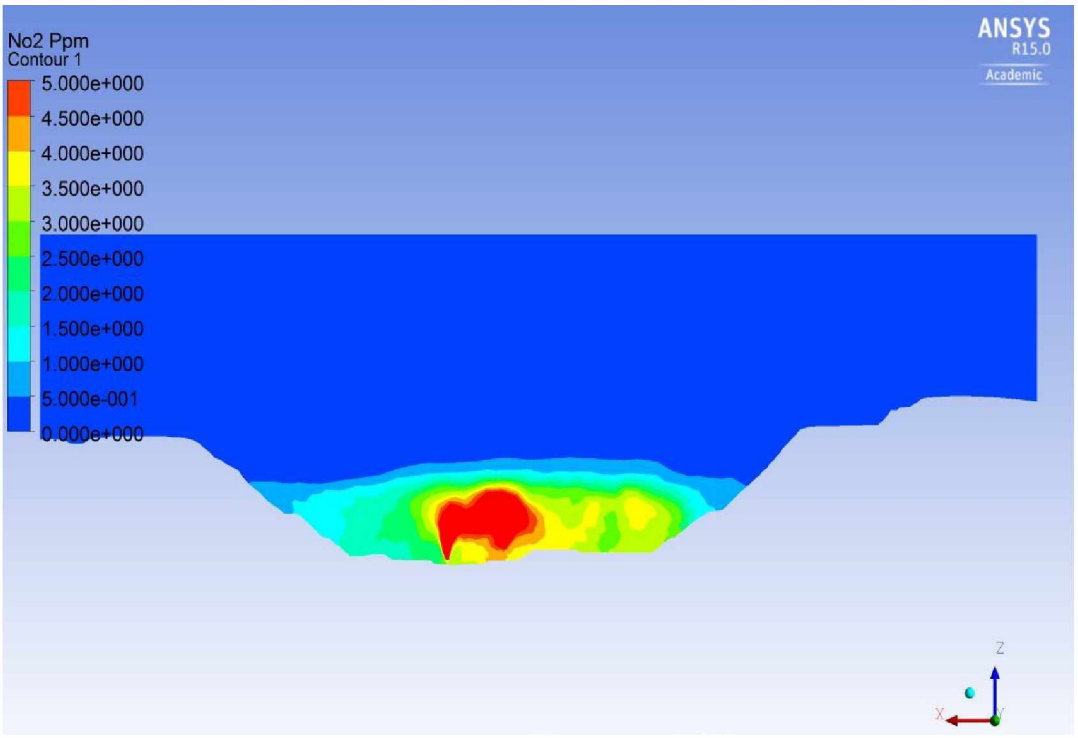

Figure 8.62: Concentration of NO_2 (in ppm) at Time Step ($t \approx 22$ hrs.).

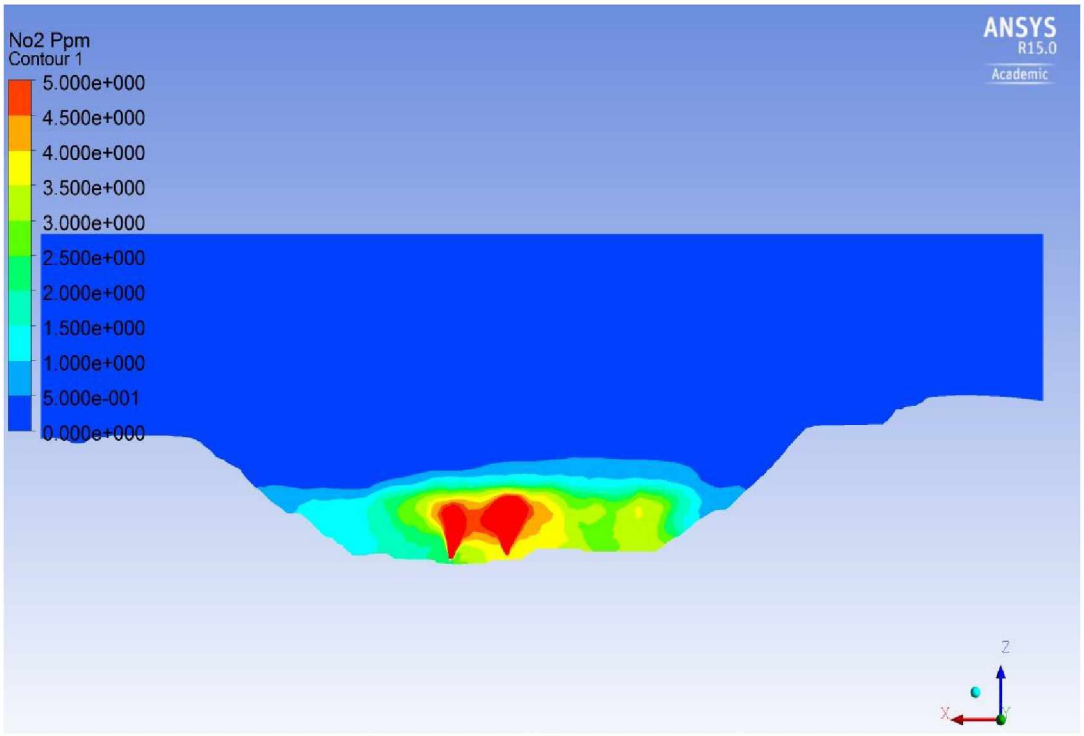

Figure 8.63: Concentration of NO_2 (in ppm) at Time Step ($t \approx 23$ hrs.).

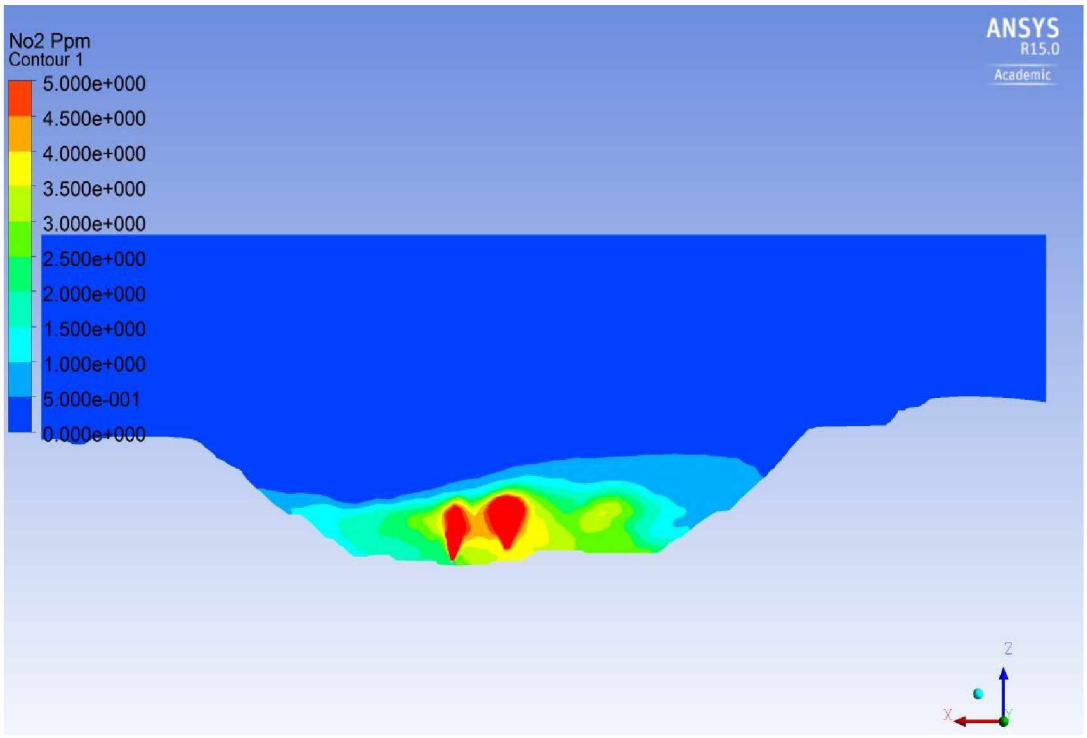

Figure 8.64: Concentration of NO_2 (in ppm) at Time Step ($t \approx 24$ hrs.).

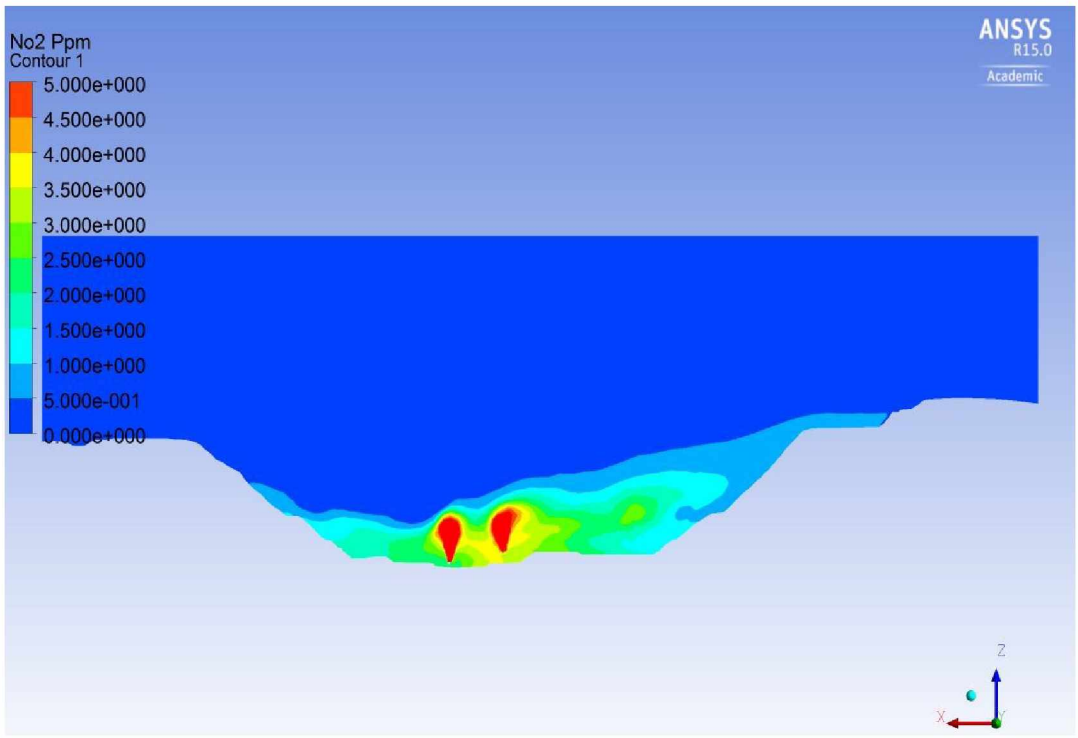

Figure 8.65: Concentration of NO_2 (in ppm) at Time Step ($t \approx 25$ hrs.).

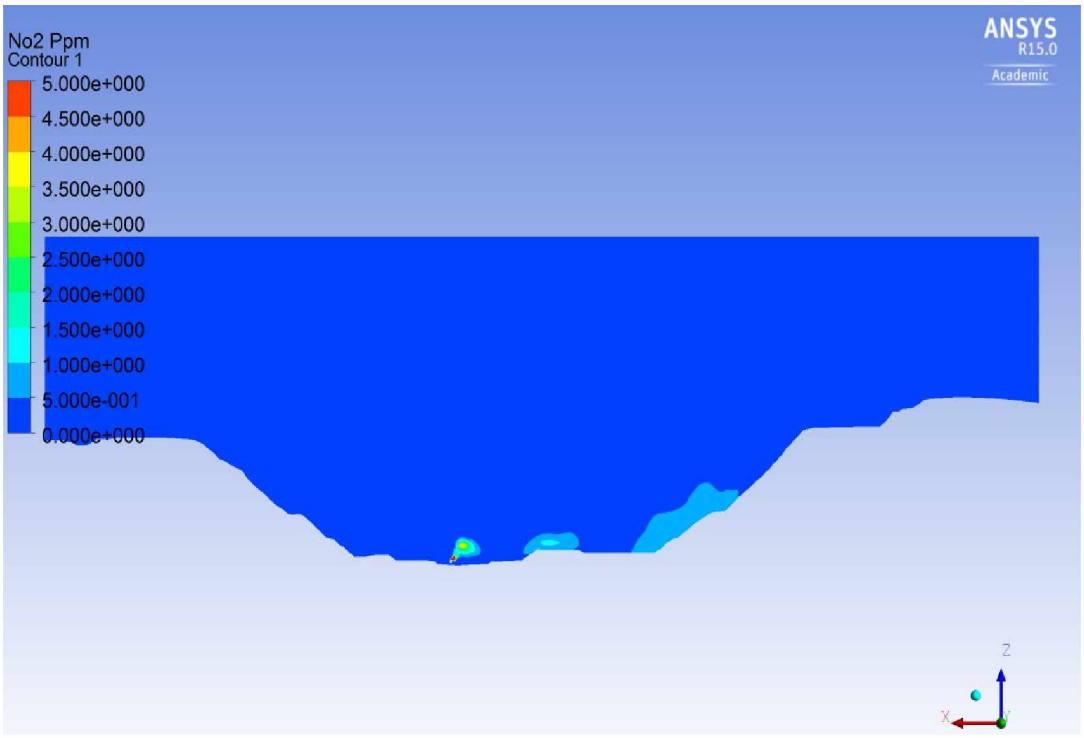

Figure 8.66: Concentration of NO_2 (in ppm) at Time Step ($t \approx 26.6$ hrs.).

The LES mitigation model simulation results show that the pit is cleared of the contaminant concentration after approximately ten hours. The simulation results indicate that the pit starts to clear from the top, and eventually, although slow, reaches the bottom of the pit. This is an indication that with changes in the radiative regime the air mass is able to penetrate deep into the pit and ventilate the contaminants out of the pit. However, compared to the 2013 pit, additional eight to ten hours are required to clear the pit. The extent of cloud cover and the vertical height of the 2010 model domain are less than that of the 2013 model domain. Since the two models use their own internal definition of the boundary layer height, a clear comparison is not possible from direct model output.

Furthermore, some of the boundary condition such as the velocity and the temperature are constant in case of the 2010 mitigation model. Whereas, in case of the 2013 mitigation model the magnitude of the two parameters are made to vary with respect to time and space. The temporal structure of the modeled temperature and the wind speed may have resulted in the additional time needed for clearing the pit. It is known that in very stable conditions, LES results are strongly dependent on the model resolution (Beare and Macvean 2004). Thus, it can be said that the extent

and the height of the cloud cover play a role in determining the time needed to clear the contaminants out of the pit.

Chapter 9 Summary and Conclusions

9.1 Summary

The Arctic region contains vast mineral resources and mining of these resources is a major activity in several countries, including the United States. With the advancement of open pit mining technology, the depth to which minerals can be profitably mined has increased, resulting in deeper pits than ever before. This increase in depth has several inherent challenges for mining operations. One of the challenges for deep open pit mining in a cold climate is atmospheric air inversion. Air inversion, a meteorological phenomenon, occurs mainly due to the negative net radiation balance at the earth's surface. The temperature of the air mass at the pit bottom cools more rapidly than the air mass above it, leading to an increase in air temperature with altitude. By itself, inversion is not hazardous. However, due to the emission of gases and particulates during the mining process, the air within the pit can be severely and sometimes quickly contaminated, leading to serious health and safety problems. To maintain and enhance the health and safety of the mine workers, effective measures are necessary to both minimize pollutant emissions and adequately ventilate the pit to dilute, disperse, and remove toxic pollutants.

Published accounts of open pit mine ventilation, particularly with respect to air inversion, are rare in the English literature. Researchers at the Kola Mining Institute, Murmansk region of Russia, and Yakutsk Mining Institute of the North, Soviet Academy of Sciences, have done some research in open pit mine ventilation. This research includes the only known account of a three-dimensional computational fluid dynamics (CFD) model of pollutant transport in an actual open pit mine under Arctic inversion.

Atmospheric air inversion results from radiative cooling of the earth's surface in the absence of solar radiation. The inversion layer is part of the stable boundary layer of the atmosphere. Analysis of temperature and radiation data indicated that the inversion in the selected open pit mine is due to an elevated inversion, although, most frequently occurring inversions in Fairbanks area are surface based.

Two main types of turbulent transport phenomena are observed in the atmosphere: wind shear driven mechanical turbulence and thermal turbulence due to convection. However, mechanical turbulence is dominated by thermal turbulence during an inversion. As the inversion

layer starts to build up, mechanical turbulence is dissipated due to several thermal layers which act as a cap for the pollutants, impeding their escape into the atmosphere. In deep open pit mines, equipment running continuously during an inversion also enhances the accumulation of pollutants in the pit.

Ventilation design for open pit mines requires the knowledge of the quantity of the pollutants that are liberated into the pit by various operating equipment. The most important items in the total balance of pollutants in open pit mines are the stationary point sources (drilling rigs, excavators, loading machines) and moving sources (such as the trucks). The dispersion of pollutants from these sources in an open pit mine is directly related to the aerodynamics of the airflows in the open pit. Evaluation of the atmospheric conditions in an open pit mine requires a determination of the concentration of pollutants. The problem is complex and any solution approach requires a good understanding of the interaction of the aerodynamic movement of air, the air inversion process, the meteorology, the pollutant sources, and the application of mechanical ventilators in open pit mines. An array of data is required to create and validate open pit mine ventilation CFD models. The meteorological conditions within deep open pit mines are significantly affected by temperature (stability) and roughness conditions, which ultimately generate complex dispersion phenomenon including separation of atmospheric boundary layer and recirculation.

Meteorological data was compiled from a nearby weather station which is located approximately 7.7 kilometers from the selected mine site. Operational data was collected from the selected open pit mine. Operational data includes the numbers of stationary equipment in place (shovels, generators, drills, etc.), the numbers of moving equipment (dozers, graders, trucks, etc.), the locations of the equipment, and the status of operation (ready hours, delay hours, and standby hours). Data was also collected on moving sources (such as trucks) from shift reports and status reports to develop the duty cycles of the trucks so that reasonable pollution loading information could be developed for model application. To have a significant model outcome, actual radiation data from the selected open pit mine were collected. Two sets of instruments containing one four-component radiometer (NR01) and three 109-L temperature probes were installed in the pit and one four-component radiometer (NR01) along two 109-L temperature probes were installed at the pit rim. The radiometers provided the shortwave and longwave radiation data for the pit bottom and the pit rim. Three temperature probes at heights of 1.5, 4.5 and 10.6 m were also installed at

the pit bottom to obtain temperature profile in the vertical direction. Similarly, two temperature probes at the height of 1.5 and 4.5 m were installed at the pit rim. The radiative flux data and the shortwave and longwave radiation, provided the effect of radiative flux on the vertical temperature profile at the pit.

Since the open pit mine is large, computing requirements are also large. There for High performance computing (HPC) was used for simulating the pollutant transport phenomena in the open pit.

To solve the problem of Arctic air inversion in open pit mines, a CFD approach was used, employing the research version of ANSYS-CFD program. In CFD simulation, preprocessing is a critical step in obtaining a good simulation result, and ANSYS-CFD has a number of preprocessing modules. The choice of preprocessing module depends on the input file format. Preprocessing of the open pit model geometry was done by using the preprocessing module, ANSYS ICEM-CFD. Pit configurations from various years were used in the study. Once the preprocessing of the model domain was accomplished, the solver, ANSYS-FLUENT, was used to simulate the phenomenon of air inversion and contaminant transport. Finally, the post-processing of the simulation results was completed. Simulations were performed for contaminant transport, validation, and pollutant mitigation.

Because an exact flow situation in open pit mines is not known a priori, it is necessary to investigate various turbulent models to identify a model that would simulate the flow phenomena with reasonable accuracy and predict the contaminant distributions within the pit. Dispersion models differ in their assumptions and structures as well as in the algorithm used and, as a result, predictions vary from model to model. Furthermore, it is also important to investigate the behavior of a CFD model when simulating complex phenomena such as the transport and distribution of contaminants in an open pit mine under an Arctic air inversion. The simulation of an enhanced period of turbulence in SBL is of particular interest because traditional air pollution dispersion models cannot explicitly treat intermittent turbulence events, and yet the SBL is often the worst-case scenario in open pit pollution transport.

Open pit air flow simulation and pollution transport are often highly sensitive to the type of flow model employed. An important issue when using CFD is the type of turbulent model selected, where a range of turbulent models are available with varying complexity and accuracy. Thus, it

is important to select appropriate turbulence models for CFD analysis to get a better understanding of air flow patterns and turbulence characteristics in open pit mines, particularly under SBL.

Reynolds Averaging Navier-Stokes (RANS) based realizable κ-ε model and Scale-Resolving Simulation (SRS) based Large Eddy Simulation (Lesieur et al.) model were used to study the pollution transport problem. A realizable κ-ε model and an LES were performed on the 2010 pit configuration of the selected open pit mine for analyzing the contaminant transport, but only the realizable κ-ε model was used for validation of the model. The predicted values were largely different, but remained within the same order of magnitude for all three the locations where measured pollutant data were available. Thus it can be concluded that the models are consistent in determining the direction of the dispersion. The high uncertainty in the concentration values may be a result of the largely turbulent treatment of the models. The results indicate that both turbulent models can simulate stable boundary layer problems over complex terrain such as an open pit mine.

The model simulation results were analyzed using various graphic techniques such as contour plots of pollutants in vertical and horizontal planes, and profiles along vertical lines of temperature, velocity, Richardson number, turbulent kinetic energy and turbulent intensity.

Because mine-specific data were available, the 2013 pit was used for validation purposes. The exact sampling locations, contaminant concentration values at those locations, and coordinate values of those locations were significant in validating of the simulation model. The selection of the extended 2013 pit for validation of the simulation model was to reduce the influence of the boundary effects. One of the major purposes of the extended pit in the model was to understand the various physical phenomena occurring within the pit, so it was necessary to have the domain boundaries far away from the open pit. Apart from having the above information from the selected open pit mine, it was equally important to have realistic boundary conditions regarding the inlet velocity and inlet temperature, which in reality vary with space and time. Since the model is an atmospheric model developed using CFD, one of the major challenges is reproducibility. The major challenge in modeling atmospheric phenomena is that the actual measurements can only be made once, so there is only one set of data available for validation.

Despite the complex synoptic situation, different meteorological input data, and the fast changing conditions, the simulation results from the validation model are in good agreement

regarding the dispersion of pollutants and other turbulent variables. Pollutant concentration values in the selected locations showed differences, but remained within the same order of magnitude in most cases.

One of the goals of the present study was to remove the pollutants accumulated in the pit during an inversion. The mitigation models were developed for both the 2010 and the 2013 pit configurations. Removal of the harmful pollutants from the pit is significantly important for the health and safety of the mine workers, and could also be economically attractive. Conventional and novel approaches were modeled for mitigating the pollutants.

9.2 Conclusions

9.2.1 Atmospheric Boundary Layer

Air inversions in Fairbanks are mostly surface based inversions (SBI). In contrast, the occurrence of air inversions at the selected open pit mine are mainly due to the elevated inversion. The location, topography, and altitude of the open pit mine affect the nature of the inversions. Because the selected open pit mine is located at a higher elevation than the nearby valley, the mine experiences elevated inversions.

9.2.2 Computational Resource

An assessment of computational resources requirement is important before conducting a CFD simulation of a deep open pit. It is advisable to have a computational resource that can handle fine grid size. Thus, the use of high performance computing (HPC) is needed in CFD simulation of deep open pit mines.

9.2.3 Preprocessing of the Model

A good-quality and appropriately sized mesh is required to obtain good results from a CFD simulation. Any strategy for CFD modeling starts with the geometry. If the geometry is simple, then meshing usually is not a problem. In the case of a highly unstructured and irregular geometry, as described in this study, a considerable amount of time and a significant effort are required to generate a good-quality mesh. Instead of depending on automatic meshing processes, it is preferable to manually edit the mesh to achieve the desired quality. Converting the mesh type from tetrahedron to polyhedron can significantly reduce simulation run time without compromising the mesh quality.

9.2.4 Modeling Results using κ-ε Model and LES

Most commercially available CFD packages have a variety of turbulence models. The choice of a turbulence model should be based on the physics of the flow. Appropriate boundary conditions should be set to obtain realistic results. However, a good-quality mesh alone does not ensure model convergence. Air flow models often feature many complex, nonlinear terms that are designed to resolve a very specific problem in the problem domain. The side effects of such terms in complex flows are often not sufficiently considered. To ensure that the model runs and produces meaningful output, several model settings, such as the pressure–velocity coupling method, the under-relaxation factor, and the solution limits should be monitored because many of these settings are meant for small-scale flow such as that in pipe flow or wing bodies. One such setting that helped in achieving convergence in this open-pit mine analysis was increasing the maximum turbulence viscosity ratio from 10^5 to 10^{10}.

Time stepping is critical for model convergence. Various phenomena occur at various time scales and to capture these phenomena, setting of appropriate time step is a must. A smaller time stepping at the initial phase of the simulation promotes quicker model convergence. Once model convergence is achieved during the initial phase of the simulation the time step can be increased to a value at which the model converges.

The model results show that both models are capable of capturing the temperature and flow fields reasonably well. This is not the case for pollutant concentrations. The realizable κ-ε model over-predicts the pollutants concentrations, while the LES model under-predicts contaminant concentrations below the TLVs of the selected pollutants. The reason that the LES model under-predicts the contaminants concentrations could be the course grid size in the model domain.

The difference in the model predicted values and the measured concentrations may be partly due to the fact that although initial conditions are consistent with Arctic observations (measured data in the pit), the surface cooling rate is more idealized. This behavior is not surprising because air velocity is close to the critical velocity, as evidenced by the small back layering during the quasi-steady-state period, and the in-mine conditions represent a balance between buoyancy forces and flow inertia. Slight changes in the operating conditions, especially the heat release rate of the trucks, can disrupt this balance and can lead to very different flow fields. Furthermore, dispersion of pollutants in the presence of an inversion depends on the wind that has a constant mean velocity

in the x-direction, and eddy diffusivities in the x, y, and z directions, respectively, and the height of inversion. Representative data for eddy diffusivities was not available, and had to be estimated.

Turbulence near the pit rim in the open pit under temperature inversion is mostly due to the effects of wind shear. However, any generated turbulence at the bottom of the pit is due to the negative buoyancy. Turbulence due to mechanical shear is dominant at around 530 m level (1750-ft.) while the thermal turbulence is clearly evident near the pit wall.

The results indicate that the predicted flow field and the pollutant concentration in the pit are sensitive to the heat release profile. With increasing time, the inversion strength increases and the air mass within the pit becomes much denser and heavier. The changes in the temperature and density directly influence the flow regime within the pit. The air mass within the pit has an extremely low velocity. This behavior is not surprising because the air velocity at the pit bottom is close to the critical velocity, as evidenced by the small eddies. The pit bottom conditions represent a balance between buoyancy forces and flow inertia. Slight changes in the operating conditions, especially in the heat release rate, can disrupt this balance and can lead to strikingly different flow fields.

The accuracy of CFD simulations for pollutant transport and dispersion can be severely compromised by using different turbulent models, the boundary conditions, and time-stepping. Time-stepping can be a critical factor in determining the accuracy of the simulations due to the occurrence of various processes at various time-steps. Additionally, to capture the phenomena occurring in quick successions, the time-stepping applied during simulation must represent that particular phenomenon.

Both the κ-ε and LES models are able to capture the temperature inversion reasonably well; however, there is a discrepancy in predicting the pollutants concentrations. The LES under-predicts the NO_2 concentration, while the κ-ε model predicts it reasonably well.

9.2.5 Validation of the Model

Stable boundary layers over open pit mines is characterized by small scale eddies. A higher accuracy in predicting the pollutant distribution can be obtained if the eddies are modeled based on their length scales.

The realizable κ-ε model was used for validation of the model. Three locations in the selected open pit were used to compare the actual and simulated data. Simulation results were averaged over an eight hour time period. The validation model shows that the output data and the actual data from the open pit are reasonably close except for a point at the leading edge of the open pit rim.

Despite the complex synoptic situations, different meteorological data, and the fast changing conditions, the simulation results are in good agreement regarding the dispersion of pollutants. Pollutant concentration values at selected locations showed differences, but remained within the same order of magnitude in most of the cases.

In general, the simulation outcomes agree with the measured values. It is well known that RANS turbulence models are characterized by a few constants that have to be tuned to best simulate the flow problem. Thus, the RANS turbulent models are problem dependent and this is one big drawback of the RANS model.

Simulated results for a cell provide an instantaneous solution and cannot readily be compared to the measured data or evaluated without further time averaging. However, it is not obvious what time period should be used for the time averaging. In this comparison, a time averaging of eight hours was selected.

The effect of boundary conditions noticeably influences the model results. The enlargement of the computational domain has the disadvantage of increasing the grid point number and therefore requiring longer computation time.

Comparison of model results with observed data over complex topography is very rare, especially as far as turbulent variables are concerned. Therefore, the effectiveness of the turbulent parameterization for complex terrain applications is rather uncertain. The success of the simulation performed here was dependent on correctly specifying the initial state of the atmosphere in the open pit and its time variation along the lateral boundaries of the model domain. Initial and boundary conditions permit information on the synoptic scale flow and its time evolution to be introduced in the simulation.

9.2.6 Mitigation of Pollutants

A number of mitigation approaches were modeled for the 2010 and 2013 pit configurations. Mitigation by creating mechanical turbulence using large fans in forcing and exhaust modes was not effective for dilution of the pollutants in the pit to a safe level. A push-pull ventilation system was similarly ineffective.

A novel approach using a cloud cover to disrupt the inversion was modeled. This approach is based on the infrared data collected at the selected open pit mine. Introduction of cloud cover led to the lifting of or disruption of the inversion and consequently the removal of the pollutants out of the pit. The 2013 pit configuration results indicated that the pit would be cleared of all pollutants in approximately two hours. For the 2010 pit configuration, the mitigation times were approximately eight and ten hours for the realizable κ-ε and WMLES models, respectively. The difference in the mitigation times is due to the extent of the model domains. The model domain of the 2013 pit is larger and deeper than the 2010 pit model domain.

Cloud seeding is routinely applied in various weather modification applications, and thus might be used in open pit mines to break or lift the inversion and remove the pollutants.

9.3 Limitations of the Study

During modeling the pollutant transport phenomena several limitations were identified:

(i) Very few studies on ventilation of deep open pit mines, especially in the Arctic, have been conducted.

(ii) There was a lack of weather data (velocity, turbulence parameters) at the mine.

(iii) The model domain of an open pit mine is extremely large, and requires extensive computational resources.

(iv) There was a lack of continuously monitored data of pollutants concentrations at various locations in the pit.

9.4 Future Research

Based on the research presented here, it is suggested that further studies should be conducted in several areas:

(i) The results from the mitigation model suggest that induced formation of a cloud cover may be a viable approach to removing the pollutants from an open pit. There are however various aspects of induced cloud cover formation that need further investigation. A study of the minimum extent and the height of a cloud cover over an open pit required to clear the pollutants is needed.

(ii) Continuous monitoring data of pollution concentrations and wind velocity from the open pit mine is needed for accurate model validation.

(iii) Air inversions affecting mining operations at various open pit mines in the Arctic, and other regions should be further explored to provide a better understanding of the problem.

(iv) Implementation of cloud seeding at the selected mine during an inversion should be further analyzed for its usefulness in practice.

References

Allwine, K. J., X. Bian, C. D. Whiteman, and H. W. Thistle (1997). "VALDRIFT—A Valley Atmospheric Dispersion Model." *Journal of Applied Meteorology* no. 36 (8):1076-1087.

Aloyan, A. E., A. A. Baklanov, and V. V. Penenko (1982). "Fictitious Regions in Numerical Simulation of Quarry Ventilation." *Soviet Meteorology & Hydrology* no. 7:32-37.

Andrén, A. (1995). "The structure of stably stratified atmospheric boundary layers: A large-eddy simulation study." *Quarterly Journal of the Royal Meteorological Society* no. 121 (525):961-985.

ANSYS (2011a). ANSYS FLUENT Theory Guide 14.0, ANSYS Inc., Canonsburg, PA.

ANSYS (2011f). ANSYS FLUENT User's Guide 14.0, ANSYS Inc., Canonsburg, PA.

Arya, P. S. (2001). *Introduction to Micrometeorology*. Vol. 79: Academic press.

Baklanov, A. A. (1984). "Determining the Propagation of Impurity in the Atmosphere of a Pit on the Basis of Mathematical Modeling." *Soviet Mining* no. 20 (5):402-407.

Baklanov, A. A. (1986). "A method for evaluating the energy characteristics of the air in an open pit mine." *Soviet Mining* no. 22 (1):66-70.

Baklanov, A. A., and O. Y. Rigina (1993). "Effectiveness of Cascade Ventilation Systems for Open-Pit Mines." *Journal of Mining Science* no. 29 (2):152-157.

Bandopadhyay, S., and V. Y. Izaxon (2005). Health and Safety Problems in Mining in the Arctic. In *Proceedings of the 8th International Symposium on Mining in the Arctic*, edited by N. N. Melnikov and S. P. Reshetnyak, June 20-23, at Mining Institute of the Kola Science Center, Apatity, Murmansk region, Russia, 139-156. St. Petersburg: JSC "Ivan Fyodorov Printing House".

Bandopadhyay, S., and R. V. Ramani (1983). "Computer-Aided Analysis of Diesel Exhaust Dispersions in Underground Airways." *CIM Magazine* no. 76 (858):69-74.

Bandopadhyay, S., and R. V. Ramani (1984). Convection-Diffusion Equations in Mine Ventilation Planning. In *Proceedings 3rd International Mine Ventilation Congress*, edited by M. J. Howes and M. J. Jones, June 13-19, at Harrogate, England, 397-404. London: Institution of Mining and Metallurgy.

Bandopadhyay, S., and R. V. Ramani (1985). Mine Planning with Diesel Powered Equipment - Ventilation Considerations. In *Proceedings of the 2nd U.S. Mine Ventilation Symposium*, edited by P. Mousset-Jones, September 23-25 at Reno, Nevada, 627-636. Accord, MA: A A Belkema.

Bandopadhyay, S., and R. V. Ramani (1988). Mass Transfer Problems in Mine Ventilation: Some Solution Strategies. In *Proceedings 4th International Mine Ventilation Congress*, edited by A. D. S. Gillies, July 3-6, at Queensland, Australia, 73-83. Melbourne, Australia: AusIMM.

Banta, R. M., Y. L. Pichugina, and R. K. Newsom (2003). "Relationship between Low-Level Jet Properties and Turbulence Kinetic Energy in the Nocturnal Stable Boundary Layer." *Journal of the Atmospheric Sciences* no. 60 (20):2549-2555.

Bardina, J. E., P. G. Huang, and T. J. Coakley (1997). "Turbulence Modeling Validation, Testing, and Development." *NASA Technical Memorandum* no. 110446.

Basu, S., and F. Porté-Agel (2006). "Large-Eddy Simulation of Stably Stratified Atmospheric Boundary Layer Turbulence: A Scale-Dependent Dynamic Modeling Approach." *Journal of the Atmospheric Sciences* no. 63 (8):2074-2091.

Beare, R. J., and M. K. Macvean (2004). "Resolution Sensitivity and Scaling of Large-Eddy Simulations of the Stable Boundary Layer." *Boundary-Layer Meteorology* no. 112 (2):257-281.

Belousov, V. I. (1985). "Natural Dynamic Ventilation of Open Mines." *Journal of Mining Science* no. 21 (3):264-267.

Belousov, V. I. (1989). "Ventilation of Open-Pit Mines by Controlling the Boundary Layer of the Wind Stream." *Soviet Mining* no. 25 (3):267-270.

Belousov, V. I. (1995). "Breeze Circulation in Open-Pit Mines." *Journal of Mining Science* no. 31 (3):216-220.

Blocken, B., T. Stathopoulos, and J. Carmeliet (2007). "CFD Simulation of the Atmospheric Boundary Layer: Wall Function Problems." *Atmospheric Environment* no. 41 (2):238-252.

Bowling, S. A. (1986). "Climatology of High Latitude Air Pollution as Illustrated by Fairbanks and Anchorage, Alaska." *Journal of Climate and Applied Meteorology* no. 25 (1):22-34.

Bowling, S. A., T. Ohtake, and C. S. Benson (1968). "Winter Pressure Systems and Ice Fog in Fairbanks, Alaska." *Journal of Applied Meteorology* no. 7 (6):961-968.

Bradley, R. S., F. T. Keimig, and H. F. Diaz (1992). "Climatology of surface-based inversions in the North American Arctic." *Journal of Geophysical Research: Atmospheres* no. 97 (D14):15699-15712.

Carlson, M. A., and R. B. Stull (1986). "Subsidence in the Nocturnal Boundary Layer." *Journal of Climate and Applied Meteorology* no. 25 (8):1088-1099.

Chang, P. K. (1970). *Separation of Flow*. Vol. 3: Elsevier.

Collingwood, W., K. V. Raj, and S. Bandopadhyay (2012). CFD Modeling of Pollution Transport in Open Pit Mines under Arctic Air Inversion. In *Proceedings of the 14th U. S. /North American Mine Ventilation Symposium*, edited by F. Calizaya and M. Nelson, June 17-20, at Salt Lake City, Utah, 151-160. Accord, MA: University of Utah.

Davidson, P. A. (2004). *Turbulence: An Introduction for Scientists and Engineers*. Oxford: Oxford University Press.

Fochesatto, G. J., P. Drobinski, C. Flamant, D. Guedalia, C. Sarrat, P. H. Flamant, and J. Pelon (2001a). "Evidence of Dynamical Coupling between the Residual Layer and the Developing Convective Boundary Layer." *Boundary-Bayer Meteorology* no. 99 (3):451-464.

Fochesatto, G. J., P. Drobinski, C. Flamant, D. Guedalia, C. Sarrat, P. H. Flamant, and J. Pelon (2001b). Observational and Modeling of the Atmospheric Boundary Layer Nocturnal-Diurnal Transition during the ESQUIF Experiment. In *Advances in Laser Remote Sensing*, edited by A. Dabas, C. Loth and J. Pelon, at Paris, France, 439-442.

Fochesatto, G. J., J. A. Mayfield, D. P. Starkenburg, M. A. Gruber, and J. Conner (2013). "Occurrence of Shallow Cold Flows in the Winter Atmospheric Boundary Layer of Interior of Alaska." *Meteorology and Atmospheric Physics*:1-14.

Fomin, A. A. (1996). "Modeling of Natural Convection in an Open Pit." *Fluid Dynamics* no. 31 (4):490-496.

Garratt, J. R. (1994). *The Atmospheric Boundary Layer*: Cambridge university press.

Garratt, J. R., and R. A. Brost (1981). "Radiative Cooling Effects within and above the Nocturnal Boundary Layer." *Journal of the Atmospheric Sciences* no. 38 (12):2730-2746.

Hartmann, B., and G. Wendler (2005). Climatology of the winter Surface Temperature Inversion in Fairbanks, Alaska. In *8th Conference on Polar Meteorology and Oceanography*, edited by V. Alexeev, at San Diego, CA, 1-7: American Meteorological Society.

Ingel, L. K. (2010). "Radiation Amplification of the Meteotron Effect." *Journal of Engineering Physics and Thermophysics* no. 83 (1):122-129.

Kosarev, N. P., S. A. Timukhin, Y. V. Popov, A. S. Potapova, and N. E. Kamysheva (2005). "Aerodynimcs of Jet-Suction Scheme for Ventilation of Deep Open-Pit Stagnant Zones." *Izvestiya Vysshikh Uchebnykh Zavedenii, Gornyi Zhurnal [in Russian]* (6):16-19.

Kosović, B., and J. A. Curry (2000). "A Large Eddy Simulation Study of a Quasi-Steady, Stably Stratified Atmospheric Boundary Layer." *Journal of the Atmospheric Sciences* no. 57 (8):1052-1068.

Kotin, P., and H. L. Falk (1955). "Air Pollution and its Effect on Health." *California medicine* no. 82 (1):19-24.

Launder, B. E., and D. B. Spalding (1974). "The Numerical Computation of Turbulent Flows." *Computer methods in applied mechanics and engineering* no. 3 (2):269-289.

Lesieur, M., O. Métais, and P. Comte (2005). *Large-Eddy Simulations of Turbulence*. Cambridge; New York: Cambridge University Press.

Mahrt, L. (1998). "Nocturnal Boundary-Layer Regimes." *Boundary-Layer Meteorology* no. 88 (2):255-278.

Malingowski, J., D. Atkinson, J. Fochesatto, J. Cherry, and E. Stevens (2014). "An observational study of radiation temperature inversions in Fairbanks, Alaska." *Polar Science* no. 8 (1):24-39.

Mason, P. J., and S. H. Derbyshire (1990). "Large-Eddy Simulation of the Stably-Stratified Atmospheric Boundary Layer." *Boundary-Layer Meteorology* no. 53 (1-2):117-162.

Mason, P. J., and D. J. Thomson (1987). "Large-Eddy Simulations of the Neutral-Static-Stability Planetary Boundary Layer." *Quarterly Journal of the Royal Meteorological Society* no. 113 (476):413-443.

Mayfield, J. A., and G. J. Fochesatto (2012). "The Layered Structure of the Winter Atmospheric Boundary Layer in the Interior of Alaska." *Journal of Applied Meteorology and Climatology* no. 52 (4):953-973.

Menter, F. R. (2010). Turbulence Modeling for Engineering Flows. ANSYS INC.

Menter, F. R. (2012). Best Practice: Scale-Resolving Simulations in ANSYS CFD.

Menter, F. R., R. Langtry, and S. Völker (2006). "Transition Modelling for General Purpose CFD Codes." *Flow, Turbulence and Combustion* no. 77 (1-4):277-303.

Moeng, C. H. (1984). "A Large-Eddy-Simulation Model for the Study of Planetary Boundary-Layer Turbulence." *Journal of the Atmospheric Sciences* no. 41 (13):2052-2062.

Monin, A. S., and A. M. *,*I*,*Aglom (1971). *Statistical fluid mechanics; mechanics of turbulence*. English ed. 2 vols. Cambridge, Mass.,: MIT Press.

Monti, P., H. J. S. Fernando, M. Princevac, W. C. Chan, T. A. Kowalewski, and E. R. Pardyjak (2002). "Observations of Flow and Turbulence in the Nocturnal Boundary Layer over a Slope." *Journal of the Atmospheric Sciences* no. 59 (17):2513-2534.

Nicoud, F., and F. Ducros (1999). "Subgrid-Scale Stress Modelling Based on the Square of the Velocity Gradient Tensor." *Flow, Turbulence and Combustion* no. 62 (3):183-200.

Oberkampf, W. L., and T. G. Trucano (2002). "Verification and validation in computational fluid dynamics." *Progress in Aerospace Sciences* no. 38 (3):209-272.

Orszag, S. A., V. Yakhot, W. S. Flannery, F. Boysan, D. Choudhury, J. Maruzewski, and B. Patel (1993). Renormalization Group Modeling and Turbulence Simulations. In *Proceedings of the International Conference on Near-Wall Turbulent Flows*, edited by R. M. C. So, C. G. Speziale and B. E. Launder, March 15-17, at Tempe, 1031-1046: Elsevier Science Limited.

Parakhonskii, É. V., and L. P. Severin (1976). "High-efficiency ventilator plants for artificial ventilation of deep open-cut mines." *Soviet Mining* no. 12 (6):665-670.

Peng, X., and G. R. Lu (1995). "Physical Modeling of Natural Wind and its Guide in Large Open Pit Mine." *Journal of Wind Engineering and Industrial Aerodynamics* no. 54–55 (0):473-481.

Plank, V. G., A. A. Spatola, and J. R. Hicks (1971). "Summary Results of the Lewisburg Fog Clearing Program." *Journal of Applied Meteorology* no. 10 (4):763-779.

Prandtl, L. (1904). Ueber Flussigkeitbewegung bei sehr kleiner Reibung (On Fluid Motion with Very Small Friction). In *Verhandlungen des dritten internationalen Mathematiker-Kongresses*, at Heidelberg, Germany (in German) [English translation in NACA Technical Memo. 452].

Raj, K. V., and S. Bandopadhyay (2014). A Large Eddy Simulation of Air Flow and Pollutant Transport in a Deep Open Pit Mine under Arctic Inversion. In *SME Annual Meeting*, February 23-26, at Salt Lake City, UT, Preprint# 14-017: Society for Mining, Metallurgy and Exploration.

Richards, P. J., and R. P. Hoxey (1993). "Appropriate Boundary Conditions for Computational Wind Engineering Models using the k-ε Turbulence Model." In *Computational Wind Engineering 1*, edited by S. Murakami, 145-153. Oxford: Elsevier.

Riley, J. J., and M. P. Lelong (2000). "Fluid Motions in the Presence of Strong Stable Stratification." *Annual review of fluid mechanics* no. 32 (1):613-657.

Saiki, E. M., C. H. Moeng, and P. P. Sullivan (2000). "Large-Eddy Simulation Of The Stably Stratified Planetary Boundary Layer." *Boundary-Layer Meteorology* no. 95 (1):1-30.

Salim, S. M., R. Buccolieri, A. Chan, and S. Di Sabatino (2011a). "Numerical Simulation of Atmospheric Pollutant Dispersion in an Urban Street Canyon: Comparison between RANS and LES." *Journal of Wind Engineering and Industrial Aerodynamics* no. 99 (2–3):103-113.

Salim, S. M., K. C. Ong, and S. C. Cheah (2011b). Comparison of RANS, URANS and LES in the Prediction of Airflow and Pollutant Dispersion. In Proceedings of the World Congress on Engineering and Computer Science.

Senaratne, I., and D. Shooter (2004). "Elemental Composition in Source Identification of Brown Haze in Auckland, New Zealand." *Atmospheric Environment* no. 38 (19):3049-3059.

Sharan, M., and M. Modani (2006). "A Two-Dimensional Analytical Model for the Dispersion of Air Pollutants in the Atmosphere with a Capping Inversion." *Atmospheric environment* no. 40 (19):3479-3489.

Shi, Y., X. S. Feng, F. S. Wei, and W. Jiang (2000). "Three-Dimensional Nonhydrostatic Numerical Simulation for the PBL of an Open-Pit Mine." *Boundary-Layer Meteorology* no. 94 (2):197-224.

Shih, T. H., W. W. Liou, A. Shabbir, Z. Yang, and J. Zhu (1995). "A New k-ϵ Eddy Viscosity Model for High Reynolds Number Turbulent Flows." *Computers & Fluids* no. 24 (3):227-238.

Shur, M. L., P. R. Spalart, M. K. Strelets, and A. K. Travin (2008). "A Hybrid RANS-LES Approach with Delayed-DES and Wall-Modelled LES Capabilities." *International Journal of Heat and Fluid Flow* no. 29 (6):1638-1649.

Skobunov, V. V. (1970). "Turbulent Diffusion of Exhaust Gases in a Transportation Working." *Soviet Mining* no. 6 (4):404-411.

Sorbjan, Z. (1989). *Structure of the Atmospheric Boundary Layer*. New Jersey: Prentice Hall.

Stull, R. B. (1988). *An Introduction to Boundary Layer Meteorology*. Netherlands: Kluwer Academic Publishers.

Turner, J. S. (1979). *Buoyancy Effects in Fluids*. Cambridge: Cambridge University Press.

Vershinin, A. A. (1976). "Comparative assessment of schemes for artificial ventilation of quarries." *Soviet Mining* no. 12 (6):627-630.

Versteeg, H. K., and W. Malalasekera (1995). *An Introduction to Computational Fluid Dynamics: The Finite Volume Method*: Longman Scientific & Technical, England.

Waggoner, A., R. Weiss, and N. Ahlquist (1983). "The Color of Denver Haze." *Atmospheric Environment (1967)* no. 17 (10):2081-2086.

Wallace, J. M., and P. V. Hobbs (2006). *Atmospheric Science: An Introductory Survey*. Vol. 92: Academic press.

Wang, P. K. (2013). *Physics and dynamics of clouds and precipitation*: Cambridge University Press.

Wendler, G. (1969). "Heat Balance Studies During an Ice-Fog Period in Fairbanks, Alaska." *Monthly Weather Review* no. 97 (7):512-520.

Wendler, G., and K. O. L. F. Jayaweera (1972). "Some Measurements of the Development of the Surface Inversion in Central Alaska During Winter." *Pure and Applied Geophysics* no. 99 (1):209-221.

Wendler, G., and P. Nicpon (1975). "Low-Level Temperature Inversions in Fairbanks, Central Alaska." *Monthly Weather Review* no. 103 (1):34-44.

Whiteman, C. D. (1980). *Breakup of Temperature Inversions in Colorado Mountain Valleys*, Department of Atmospheric Science, Colorado State University, Fort Collins, CO.

Whiteman, C. D. (1982). "Breakup of Temperature Inversions in Deep Mountain Valleys: Part I. Observations." *Journal of Applied Meteorology* no. 21 (3):270-289.

Whiteman, C. D., and S. W. Hoch (2014). Bingham Mine Cold-Air Pool Structure and Evolution. Salt Lake City, Utah: Department of Atmospheric Sciences, University of Utah.

Wilkins, E. T. (1954). "Air Pollution Aspects of the London Fog of December 1952." *Quarterly Journal of the Royal Meteorological Society* no. 80 (344):267-271.

Yakhot, V., S. A. Orszag, S. Thangam, T. B. Gatski, and C. G. Speziale (1992). "Development of Turbulence Models for Shear Flows by a Double Expansion Technique." *Physics of Fluids A* no. 4 (7):1510-1520.

Appendix A

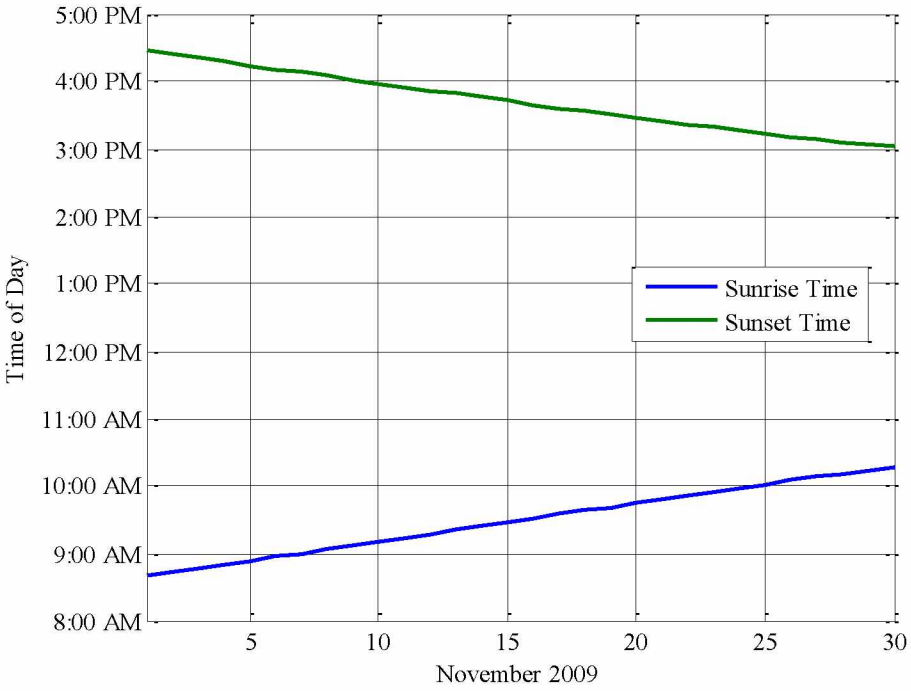

Figure A-1: Sunrise and Sunset Times (November 2009).

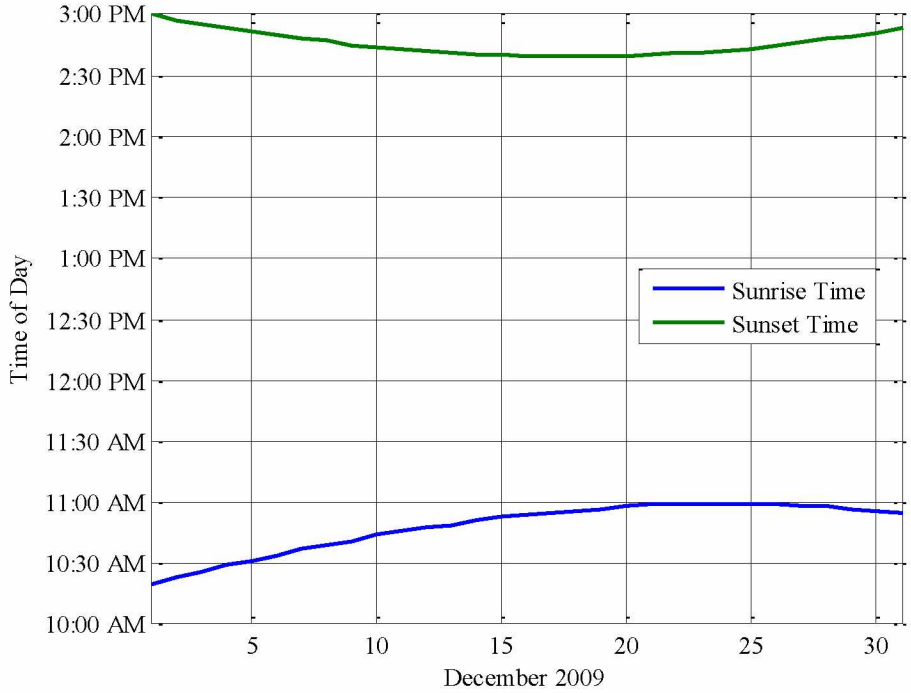

Figure A-2: Sunrise and Sunset Times (December 2009).

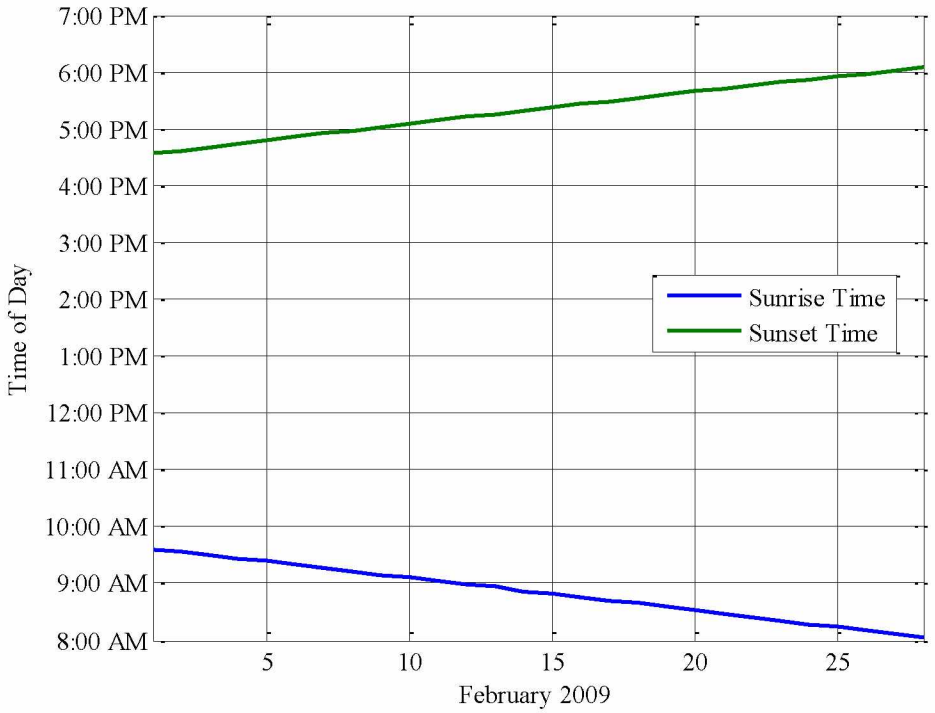

Figure A-3: Sunrise and Sunset Times (February 2010).

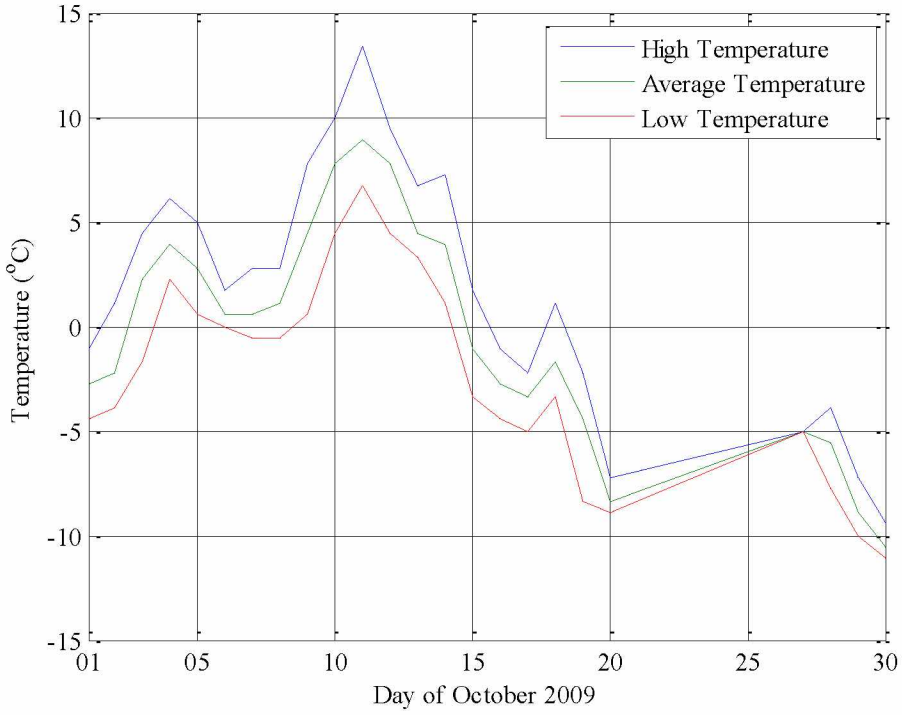

Figure A-4: Daily High, Average and Low Temperature at the Weather Station near the Open Pit for October 2009.

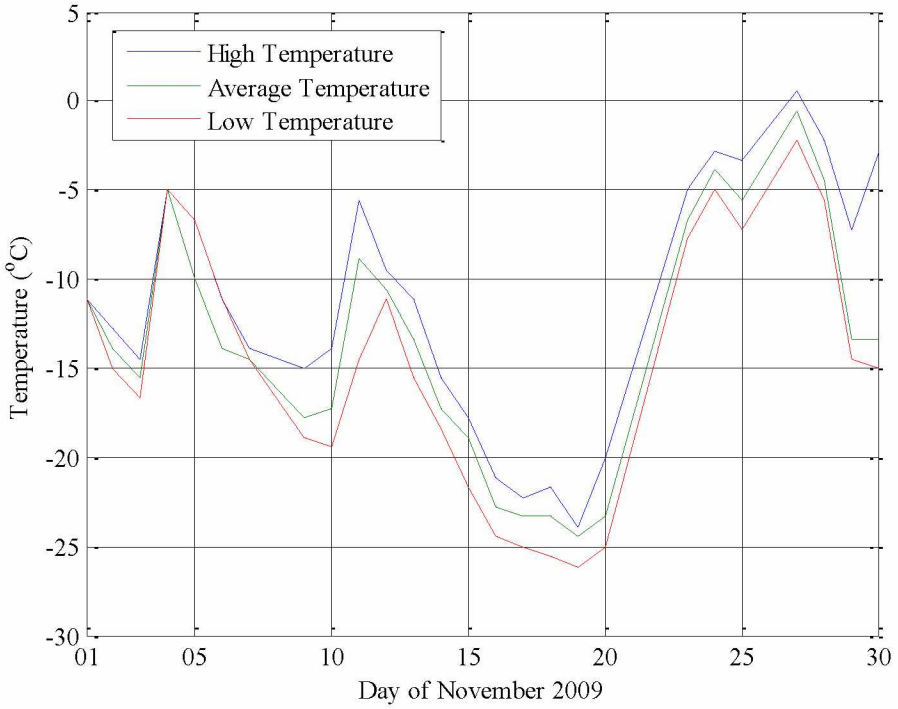

Figure A-5: Daily High, Average and Low Temperature at the Weather Station near the Open Pit for November 2009.

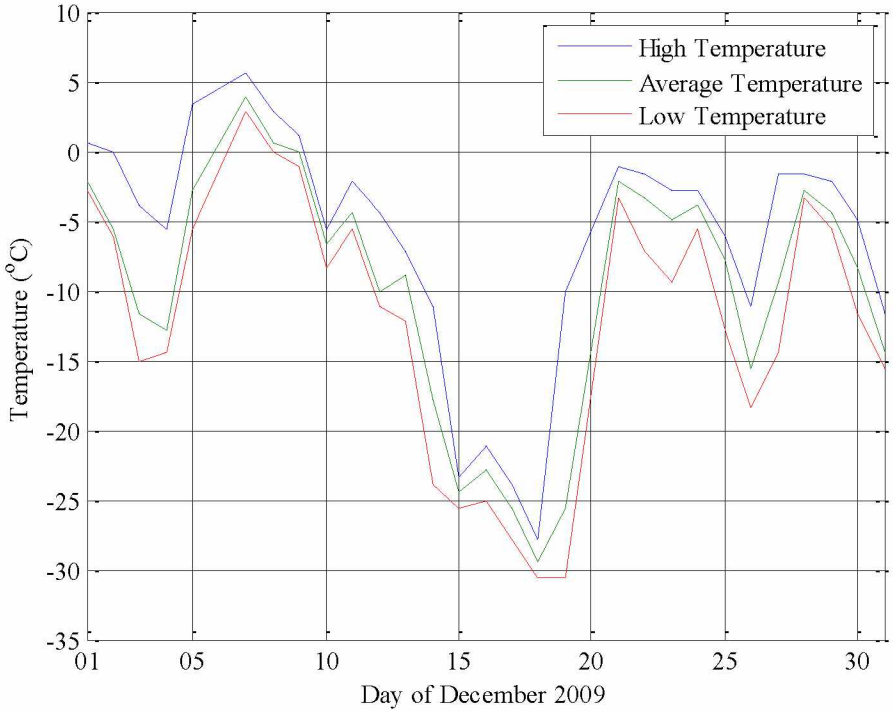

Figure A-6: Daily High, Average and Low Temperature at the Weather Station near the Open Pit for December 2009.

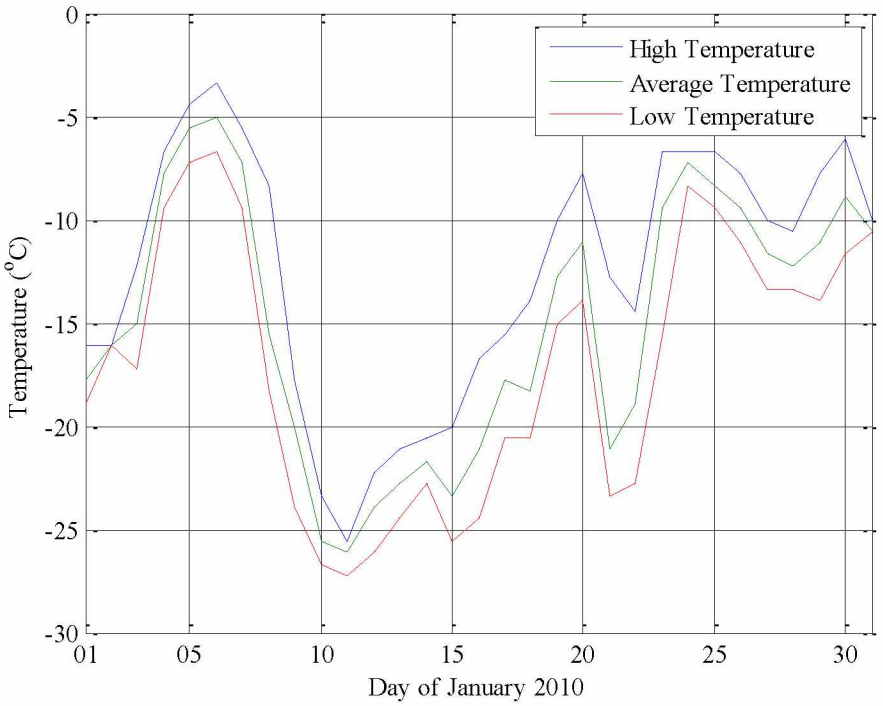

Figure A-7: Daily High, Average and Low Temperature at the Weather Station near the Open Pit for January 2010.

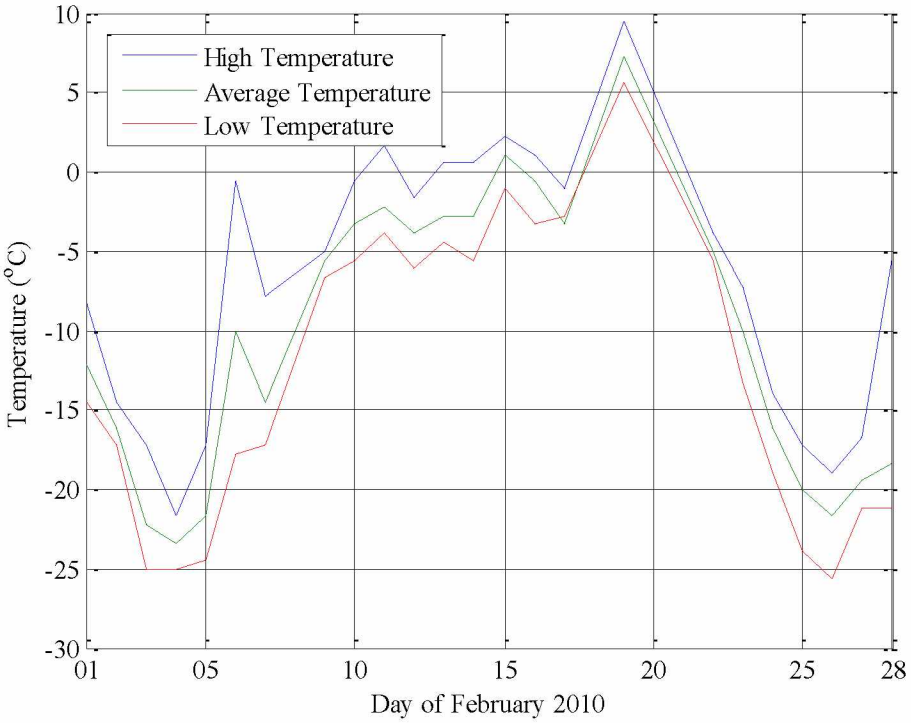

Figure A-8: Daily High, Average and Low Temperature at the Weather Station near the Open Pit for February 2010.

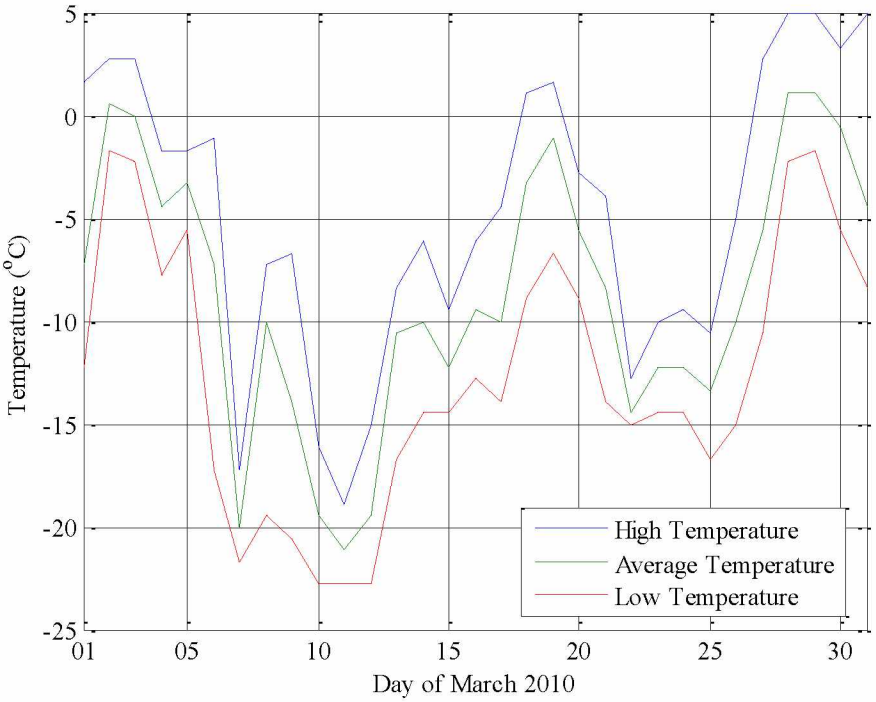

Figure A-9: Daily High, Average and Low Temperature at the Weather Station near the Open Pit for March 2010.

Table A-1: Types of Diesel Engines used and Fuel Consumption Rate at the Mine.

Engine Make	Engine Model	Total in Fleet	Full Load Fuel, lit/hr.
Cummins	QSK19	6	111.20
	QSK50	1	271.37
	QSK60	2	486.08
Caterpillar	3512: 121-5785	9	271.37
	3512: 100-8085	9	271.37
	3512: 175-5285	9	271.37
	3516: 100-8089	9	271.37
	3516 :175-5289	9	271.37
	3516: 235-0300	7	271.37
	3516: 100-8094	1	271.37
	3516: 240-7750	1	271.37

Appendix B

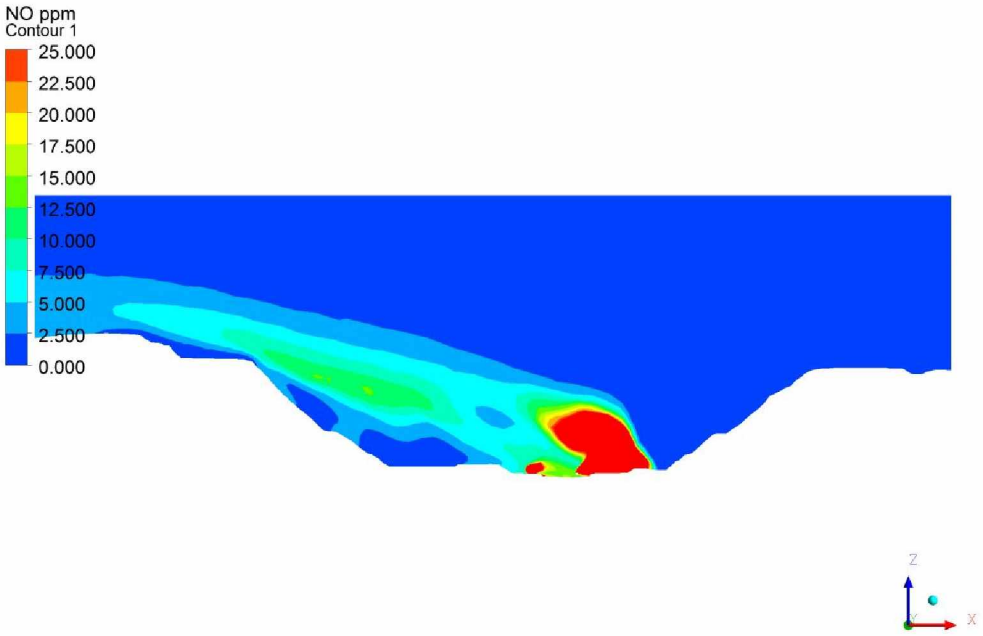

Figure B-1: Concentration of NO (in ppm) at Time Step (t ≈ 0.5 hr.) for κ-ε Model.

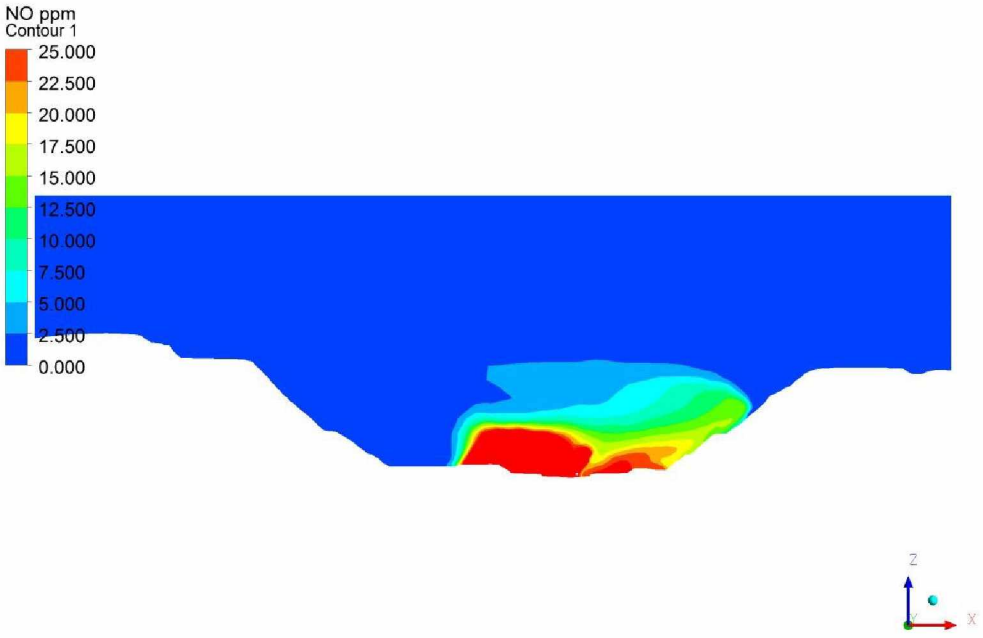

Figure B-2: Concentration of NO (in ppm) at Time Step (t ≈ 1 hr.) for κ-ε Model.

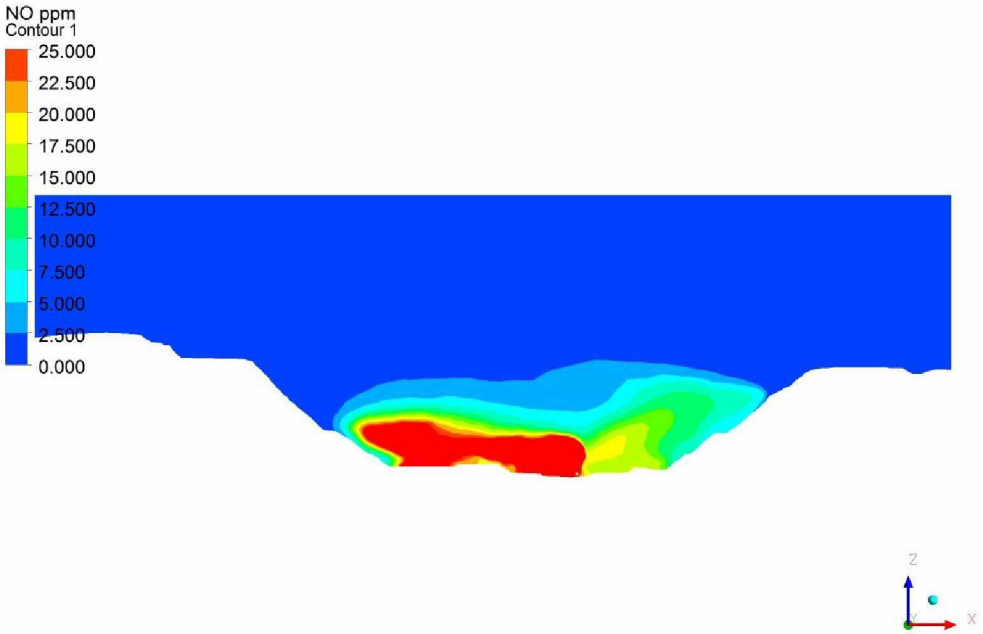

Figure B-3: Concentration of NO (in ppm) at Time Step (t ≈ 2 hrs.) for κ-ε Model.

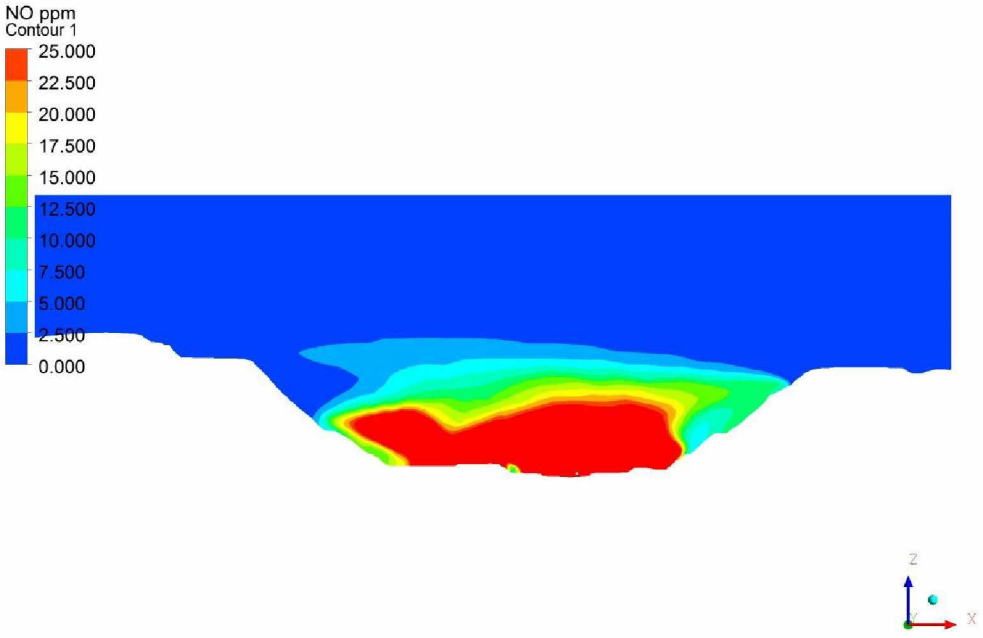

Figure B-4: Concentration of NO (in ppm) at Time Step (t ≈ 4 hrs.) for κ-ε Model.

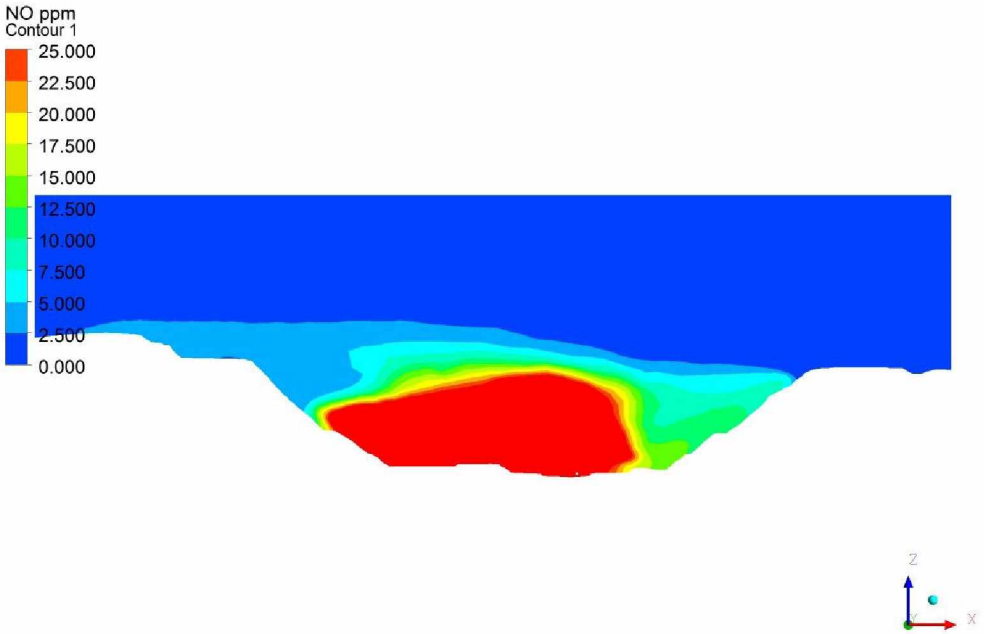

Figure B-5: Concentration of NO (in ppm) at Time Step (t ≈ 8 hrs.) for κ-ε Model.

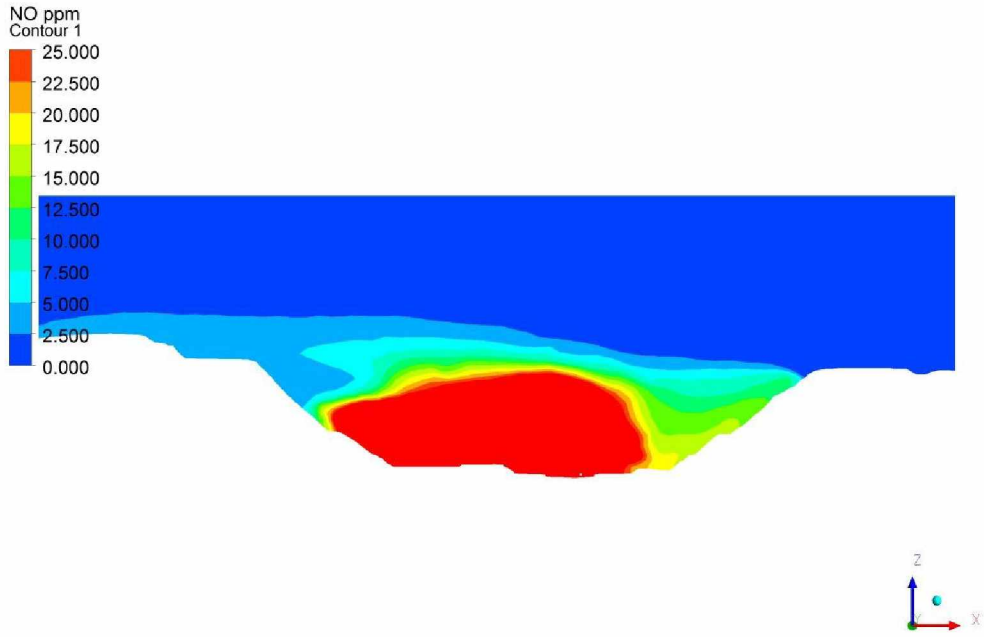

Figure B-6: Concentration of NO (in ppm) at Time Step (t ≈ 12 hrs.) for κ-ε Model.

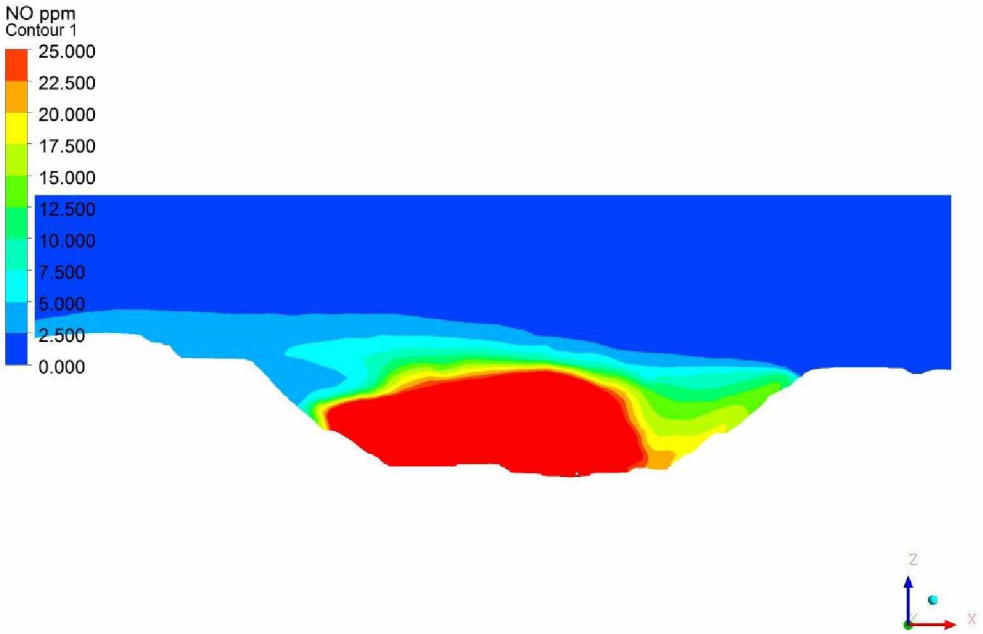

Figure B-7: Concentration of NO (in ppm) at Time Step (t ≈ 16 hrs.) for κ-ε Model.

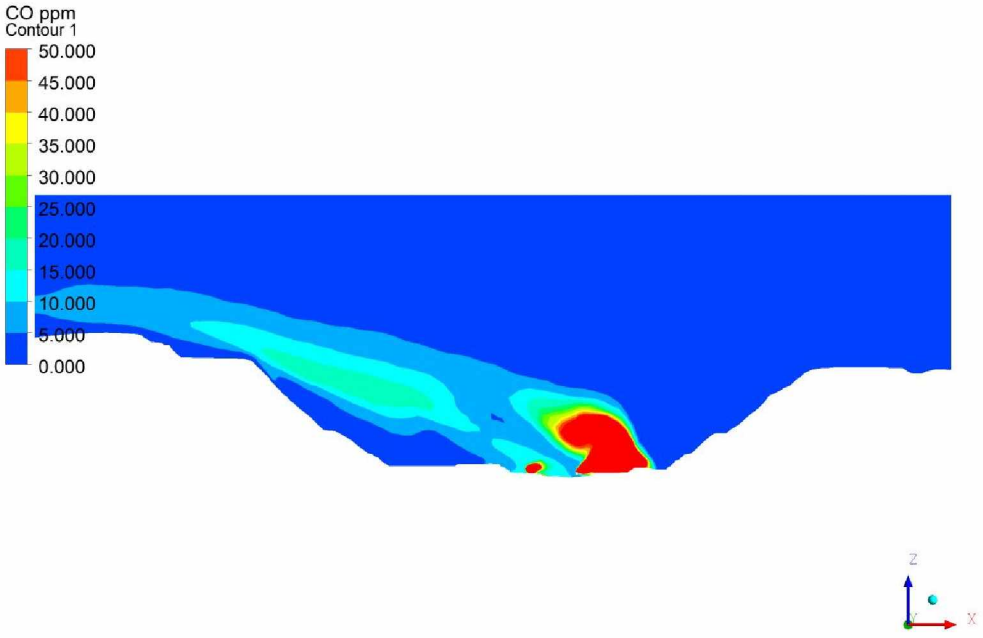

Figure B-8: Concentration of CO (in ppm) at Time Step (t ≈ 0.5 hr.) for κ-ε Model.

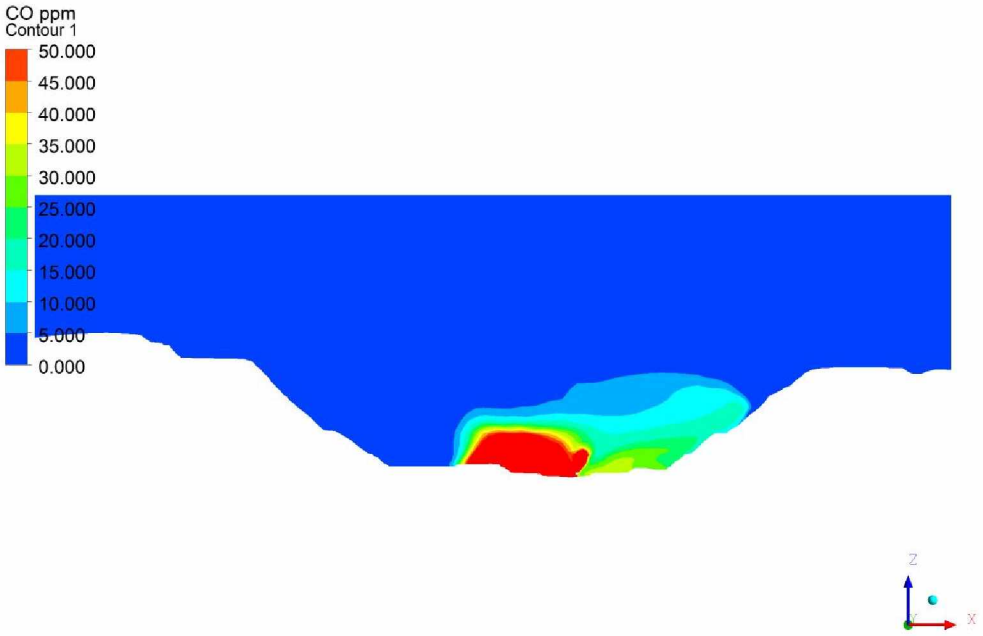

Figure B-9: Concentration of CO (in ppm) at Time Step (t ≈ 1 hr.) for κ-ε Model.

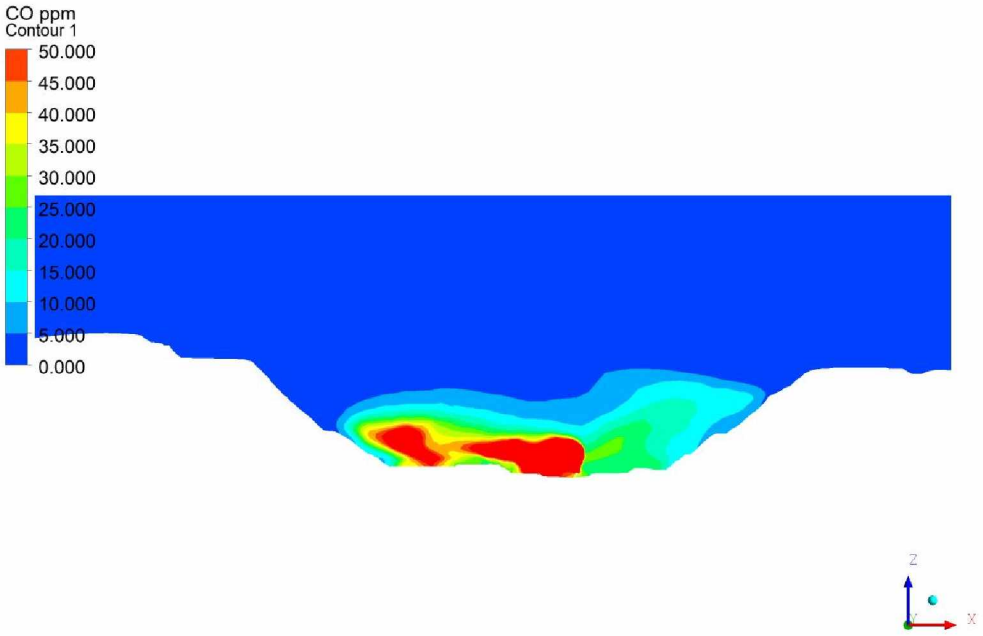

Figure B-10: Concentration of CO (in ppm) at Time Step (t ≈ 2 hrs.) for κ-ε Model.

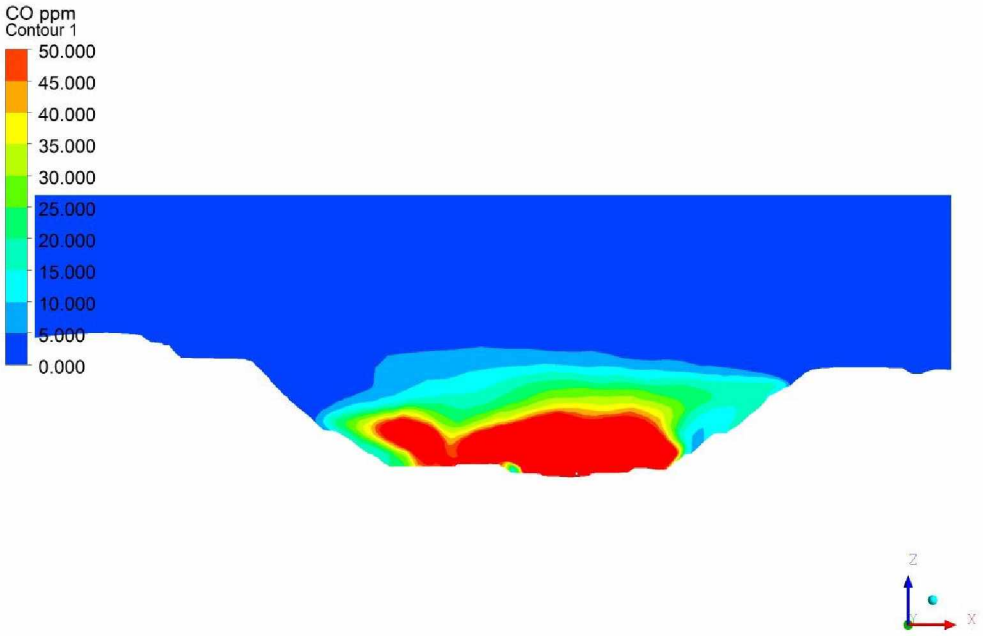

Figure B-11: Concentration of CO (in ppm) at Time Step (t ≈ 4 hrs.) for κ-ε Model.

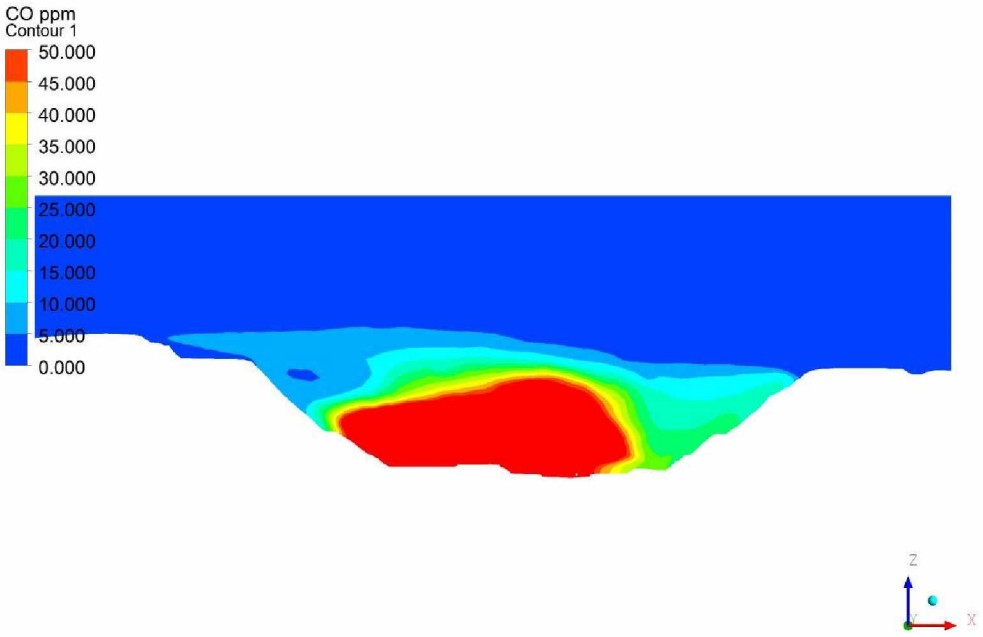

Figure B-12: Concentration of CO (in ppm) at Time Step (t ≈ 8 hrs.) for κ-ε Model.

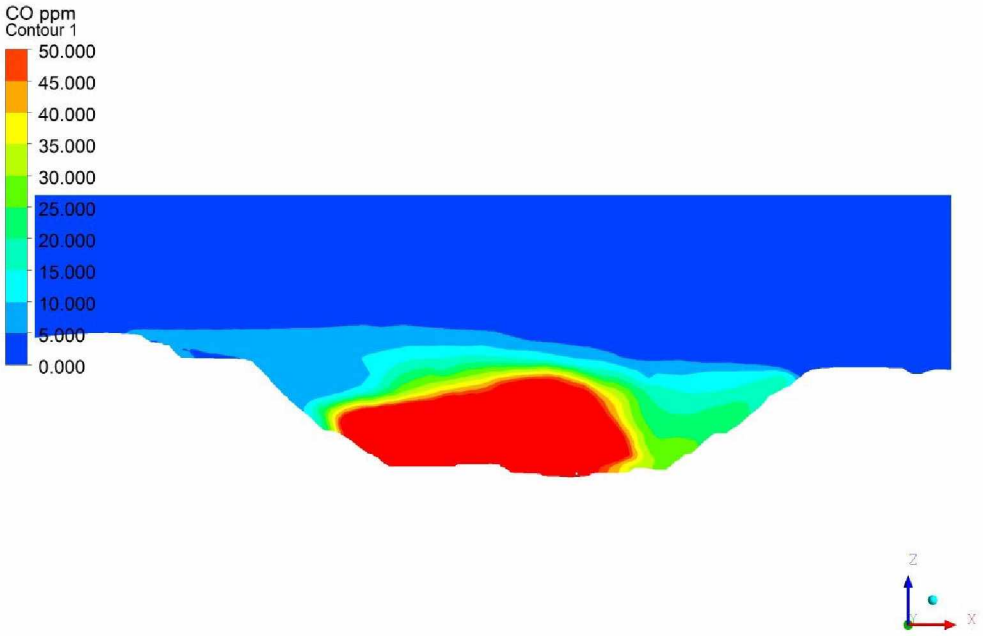

Figure B-13: Concentration of CO (in ppm) at Time Step (t ≈ 12 hrs.) for κ-ε Model.

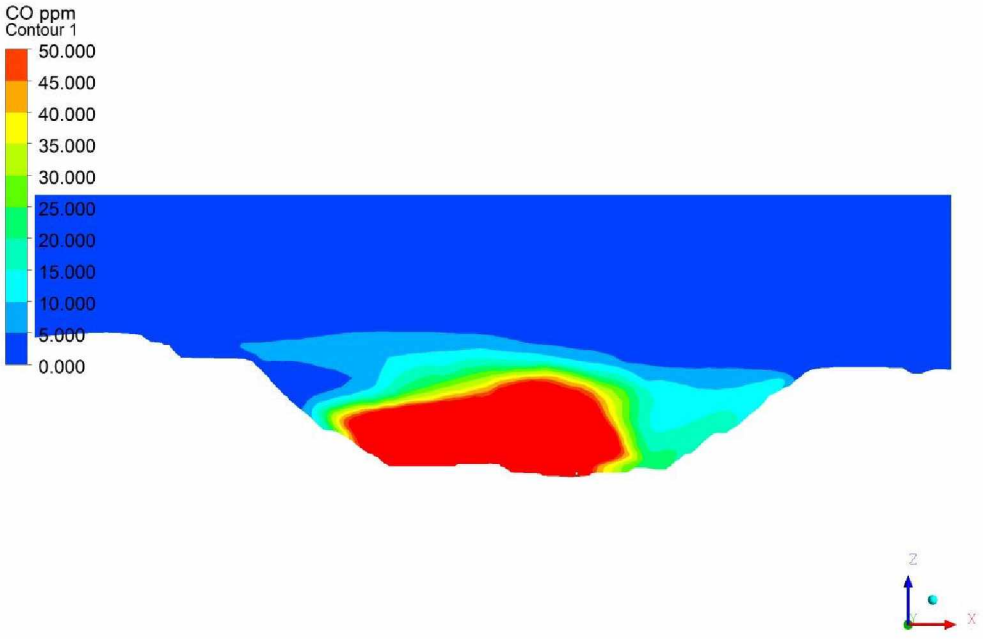

Figure B-14: Concentration of CO (in ppm) at Time Step (t ≈ 16 hrs.) for κ-ε Model.

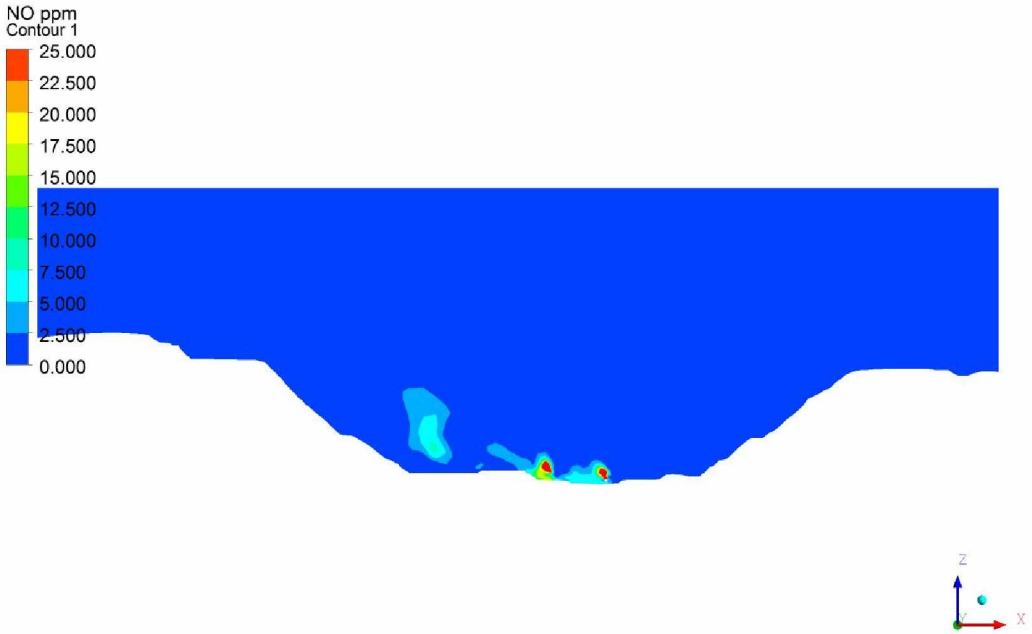

Figure B-15: Concentration of NO (in ppm) at Time Step (t ≈ 0.5 hr.) for LES Model.

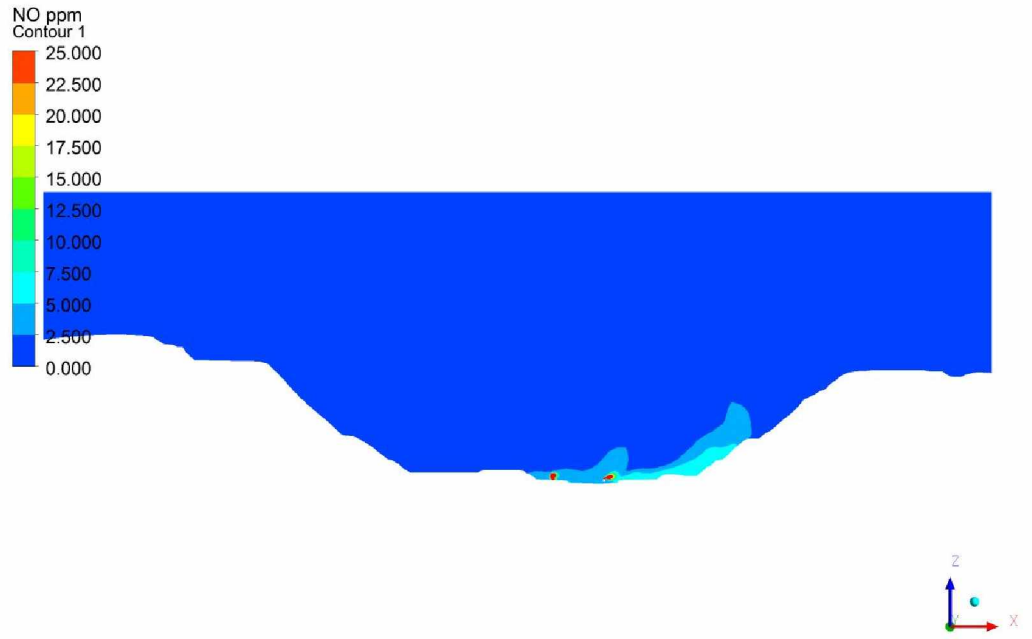

Figure B-16: Concentration of NO (in ppm) at Time Step (t ≈ 1 hr.) for LES Model.

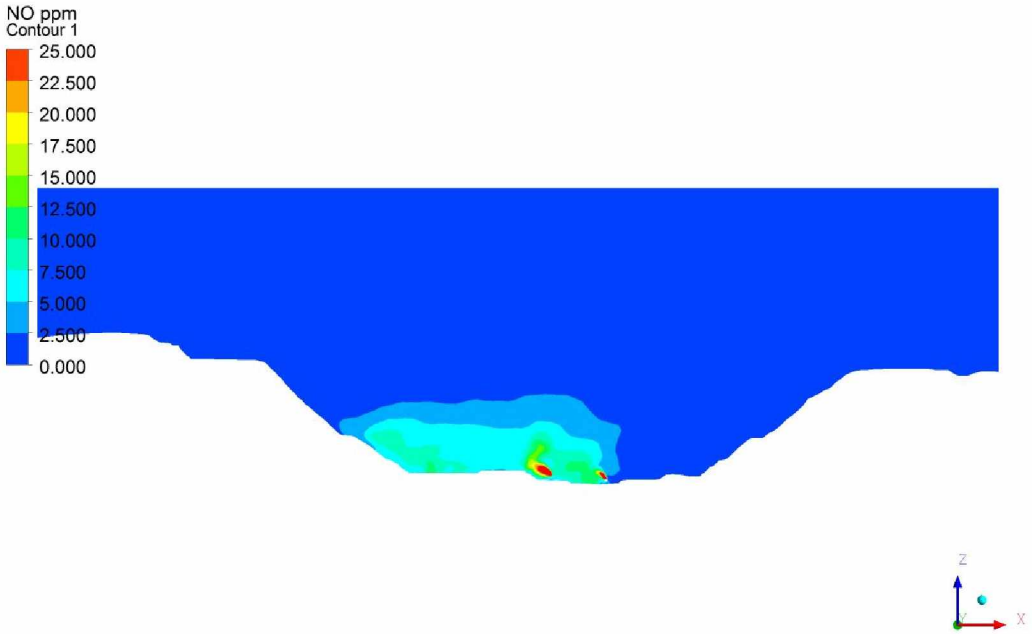

Figure B-17: Concentration of NO (in ppm) at Time Step (t ≈ 2 hrs.) for LES Model.

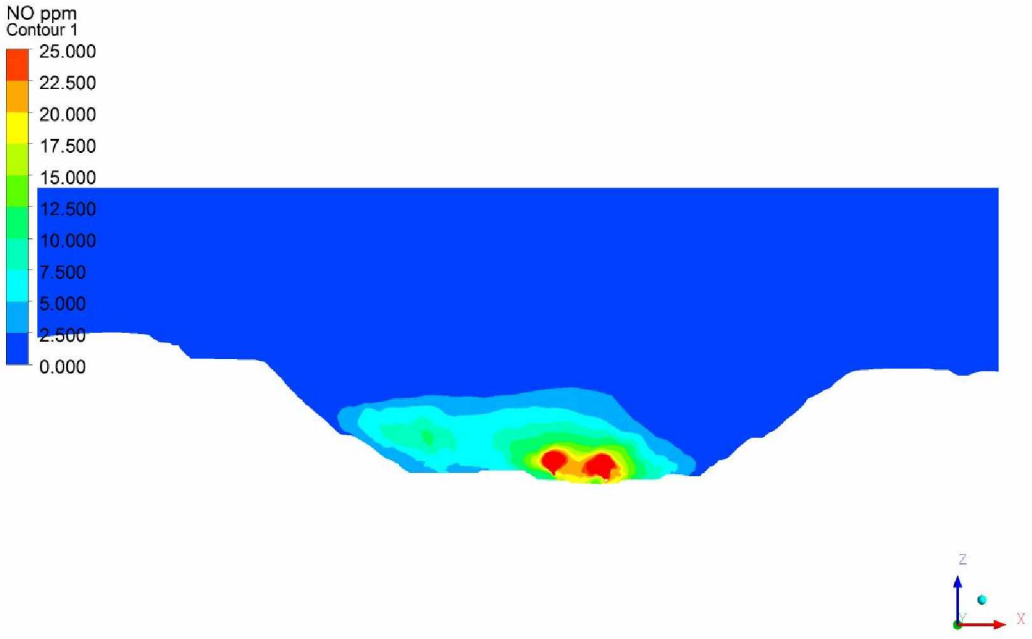

Figure B-18: Concentration of NO (in ppm) at Time Step (t ≈ 4 hrs.) for LES Model.

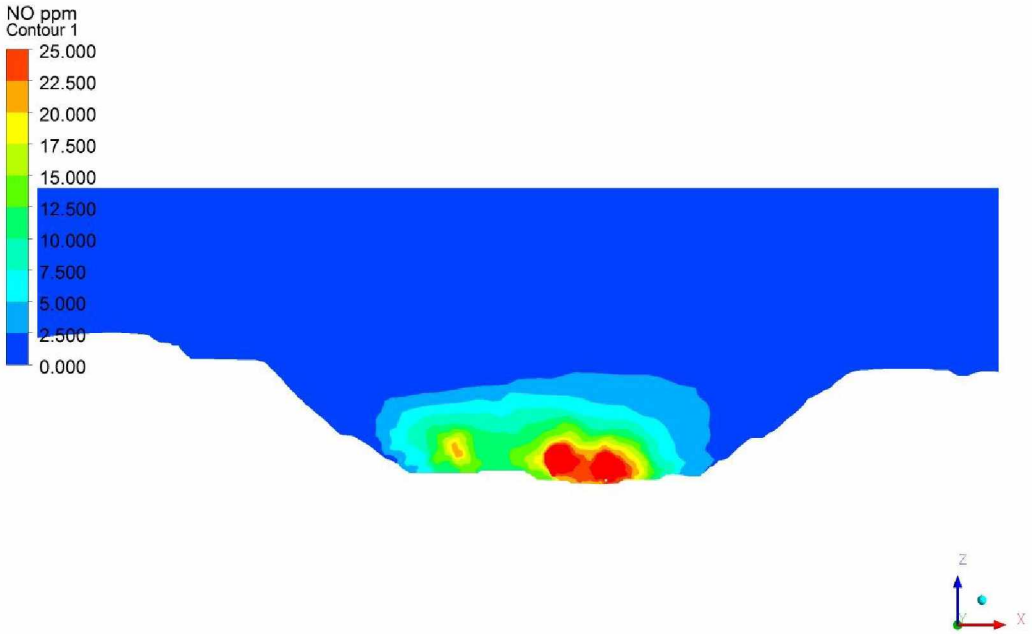

Figure B-19: Concentration of NO (in ppm) at Time Step (t ≈ 8 hrs.) for LES Model.

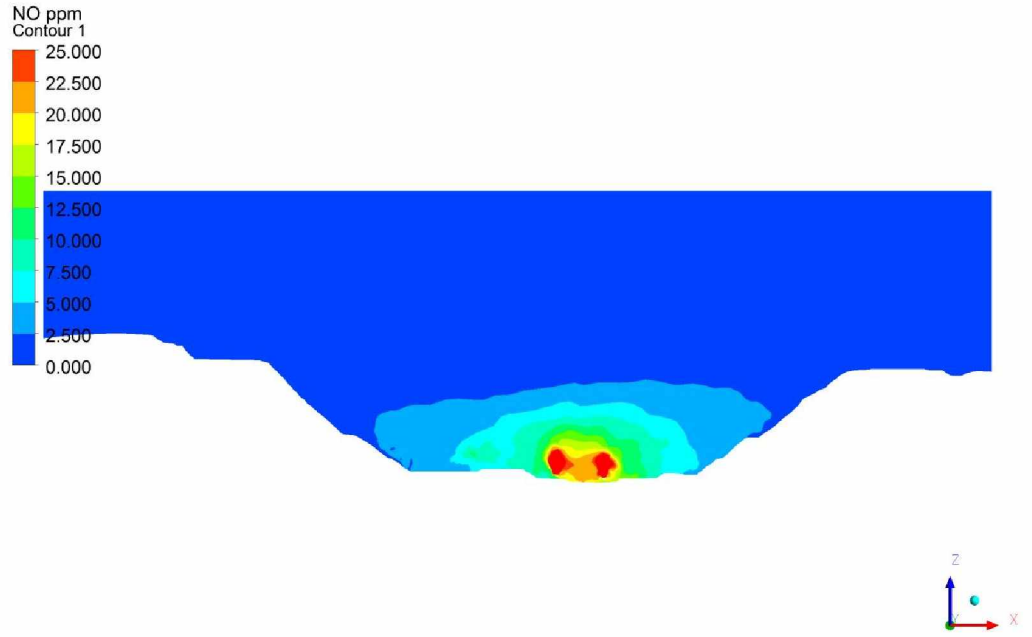

Figure B-20: Concentration of NO (in ppm) at Time Step (t ≈ 12 hrs.) for LES Model.

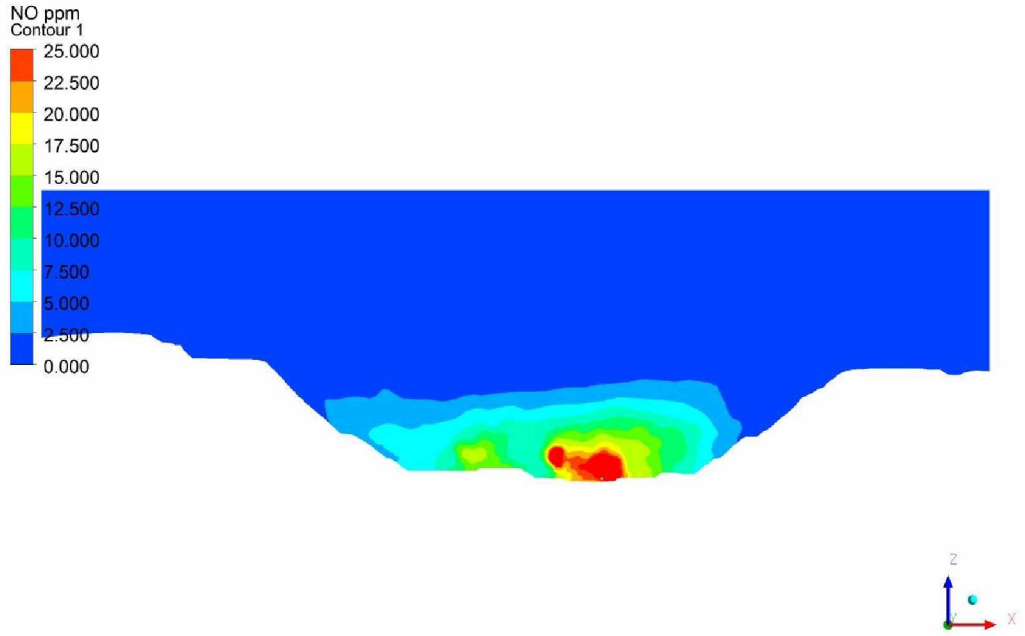

Figure B-21: Concentration of NO (in ppm) at Time Step (t ≈ 16 hrs.) for LES Model.

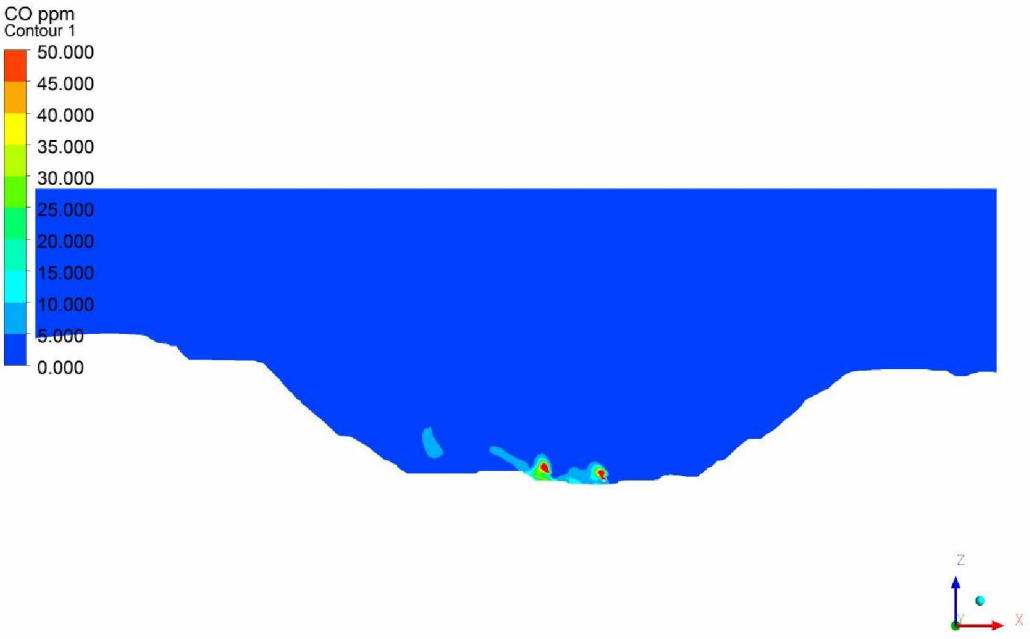

Figure B-22: Concentration of CO (in ppm) at Time Step (t ≈ 0.5 hr.) for LES Model.

Figure B-23: Concentration of CO (in ppm) at Time Step (t ≈ 1 hr.) for LES Model.

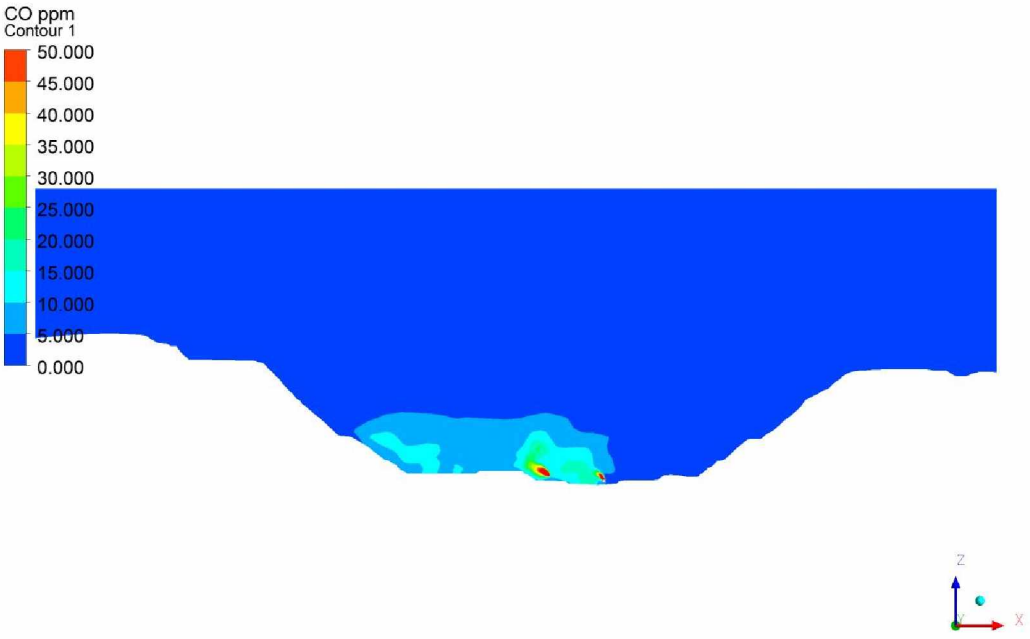

Figure B-24: Concentration of CO (in ppm) at Time Step (t ≈ 2 hrs.) for LES Model.

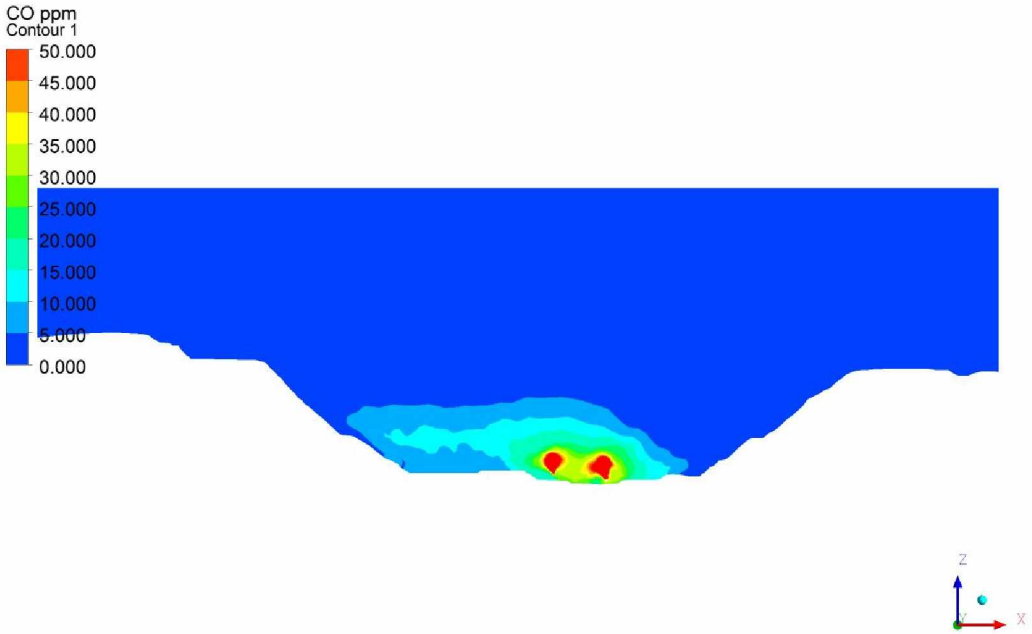

Figure B-25: Concentration of CO (in ppm) at Time Step (t ≈ 4 hrs.) for LES Model.

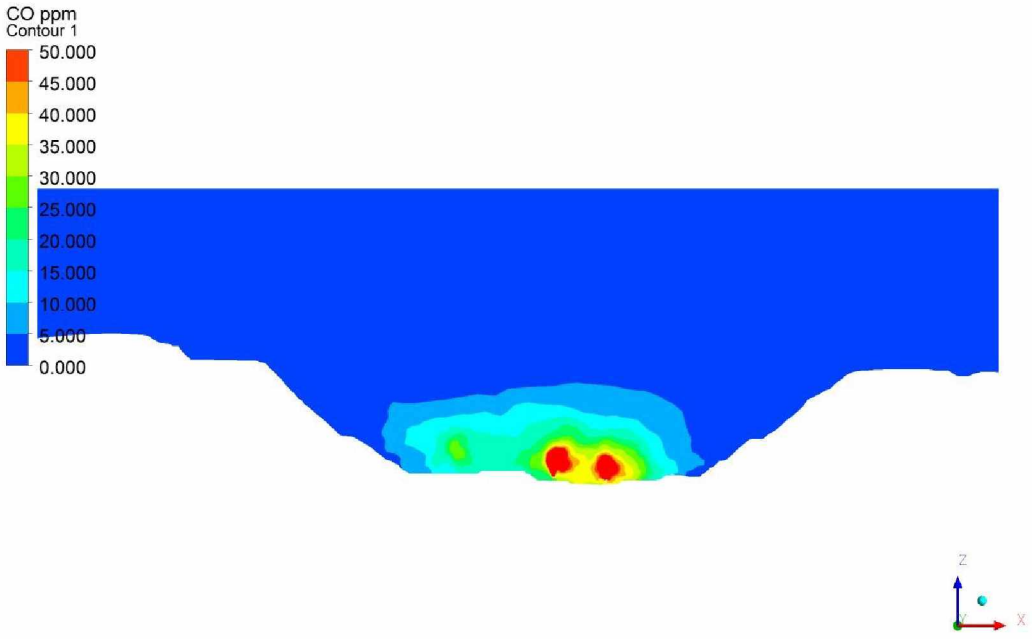

Figure B-26: Concentration of CO (in ppm) at Time Step (t ≈ 8 hrs.) for LES Model.

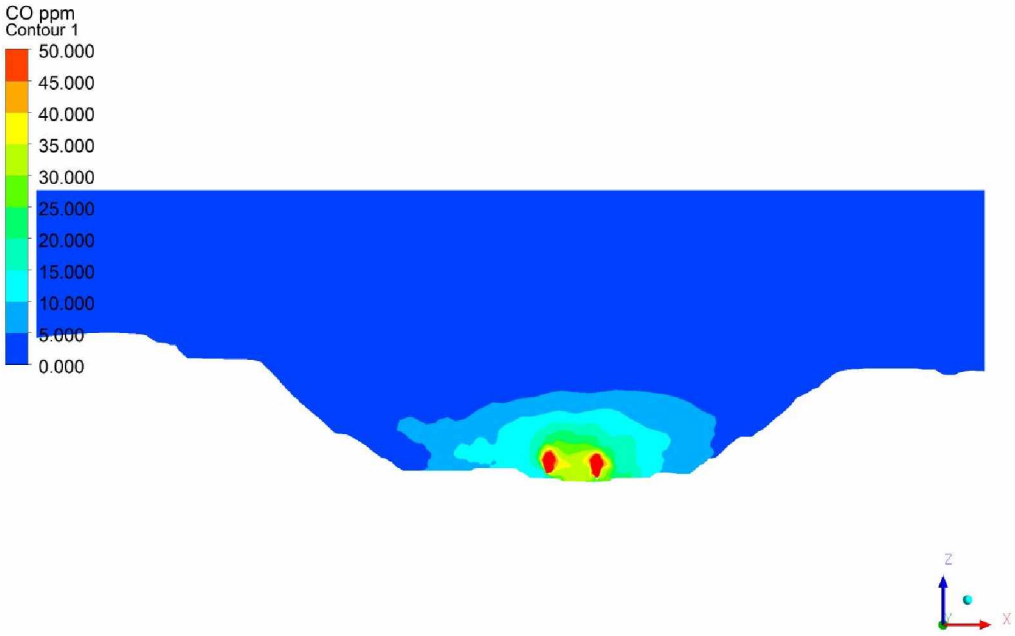

Figure B-27: Concentration of CO (in ppm) at Time Step (t ≈ 12 hrs.) for LES Model.

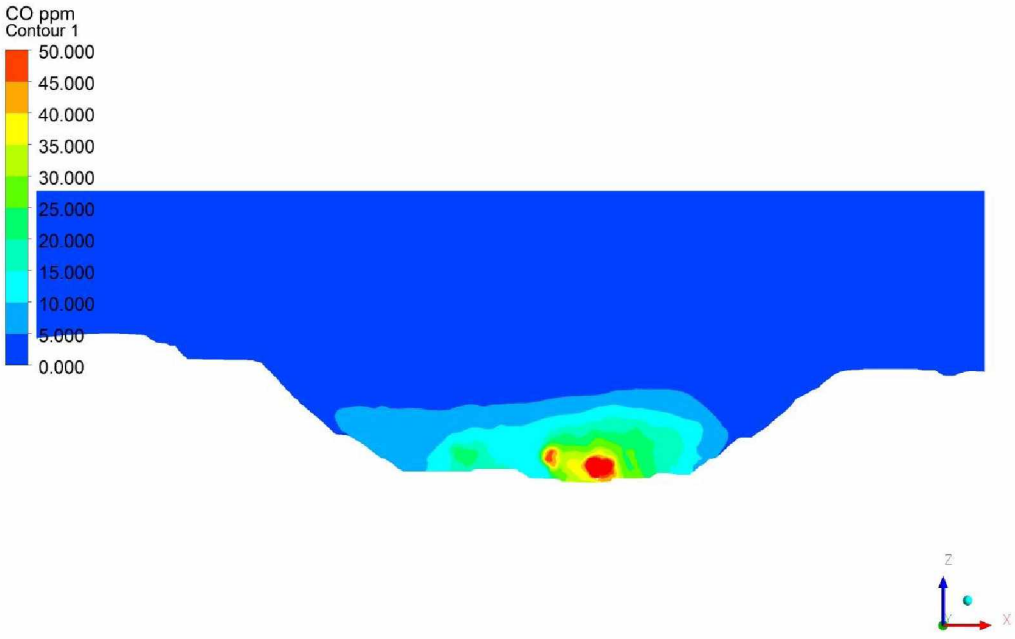

Figure B-28: Concentration of CO (in ppm) at Time Step (t ≈ 16 hrs.) for LES Model.

Appendix C

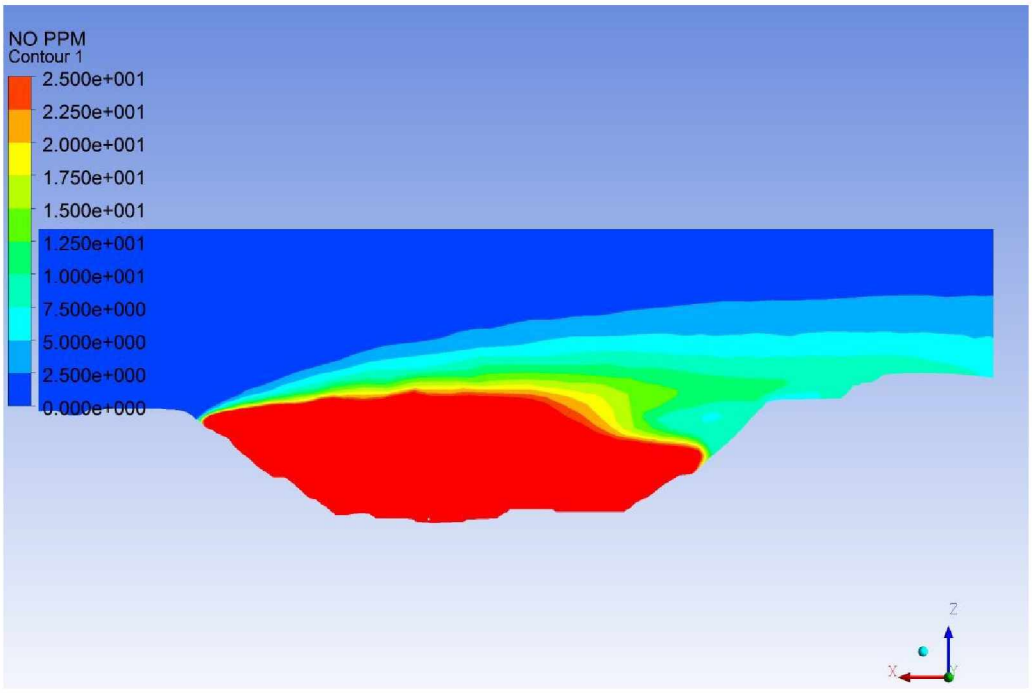

Figure C-1: Concentration of NO (in ppm) at Time Step (t ≈ 3 hrs.) for the Fans in Forcing Mode of 2010 Pit Model.

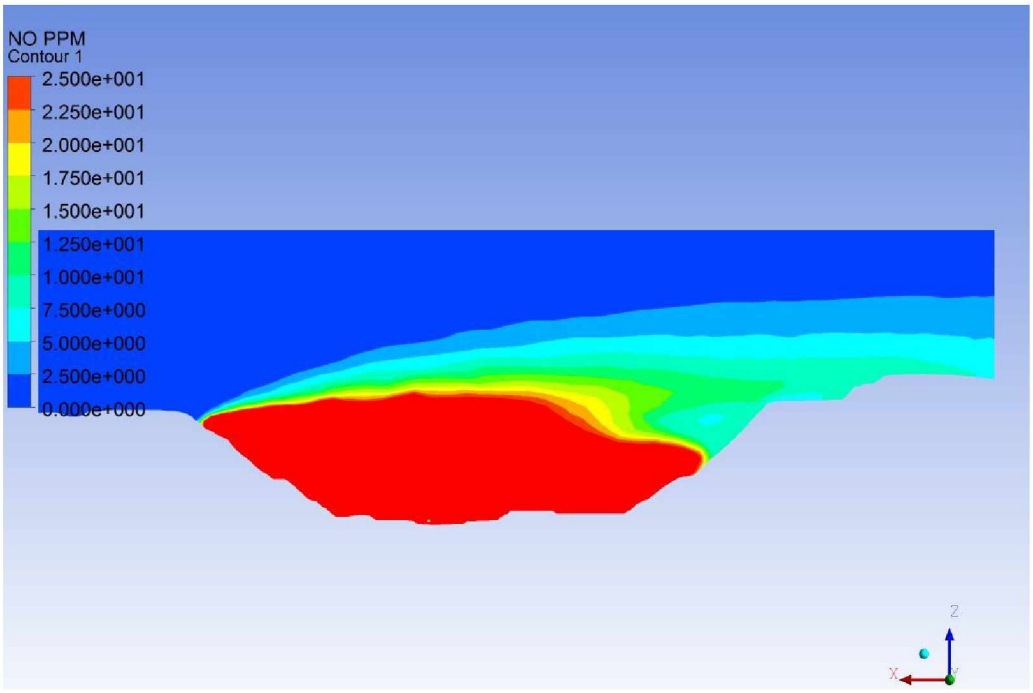

Figure C-2: Concentration of NO (in ppm) at Time Step (t ≈ 6 hrs.) for the Fans in Forcing Mode of 2010 Pit Model.

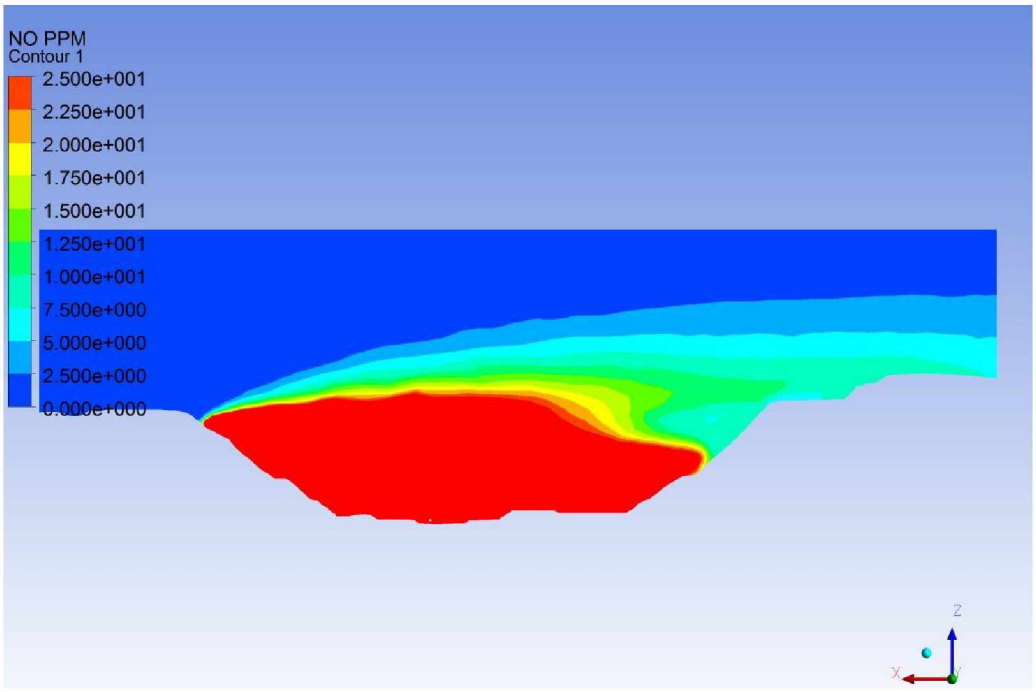

Figure C-3: Concentration of NO (in ppm) at Time Step (t ≈ 9 hrs.) for the Fans in Forcing Mode of 2010 Pit Model.

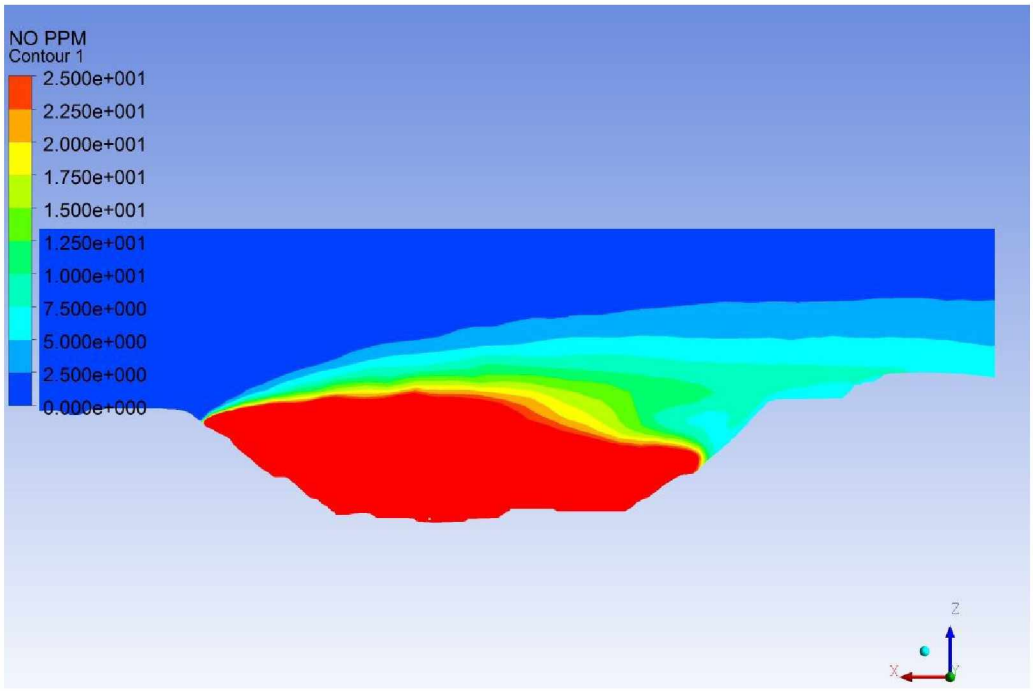

Figure C-4: Concentration of NO (in ppm) at Time Step (t ≈ 12 hrs.) for the Fans in Forcing Mode of 2010 Pit Model.

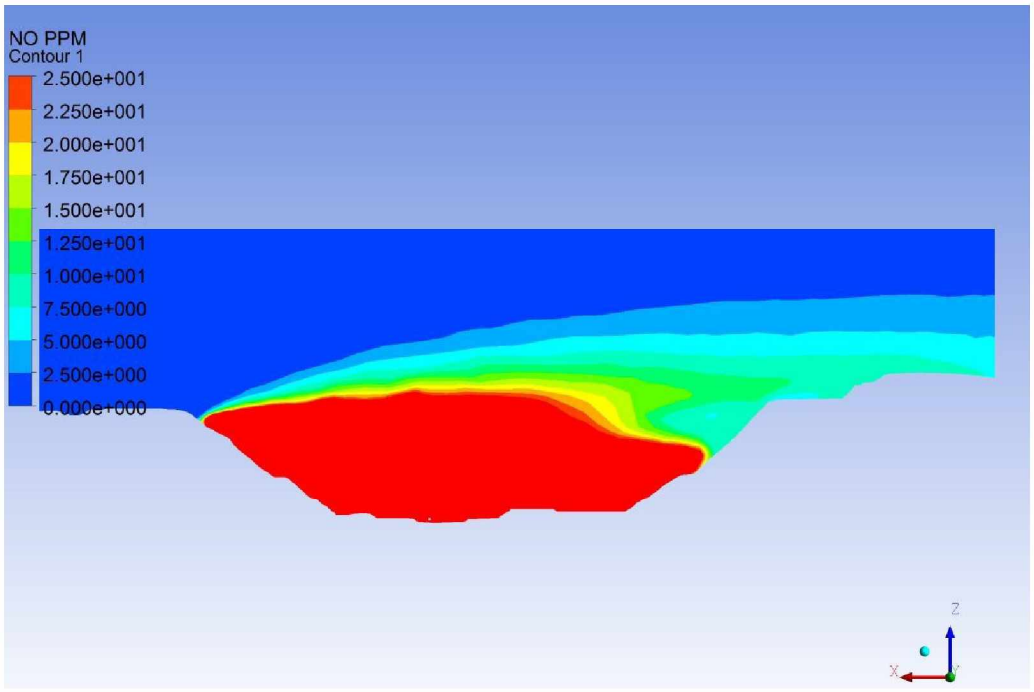

Figure C-5: Concentration of NO (in ppm) at Time Step (t ≈ 17 hrs.) for the Fans in Forcing Mode of 2010 Pit Model.

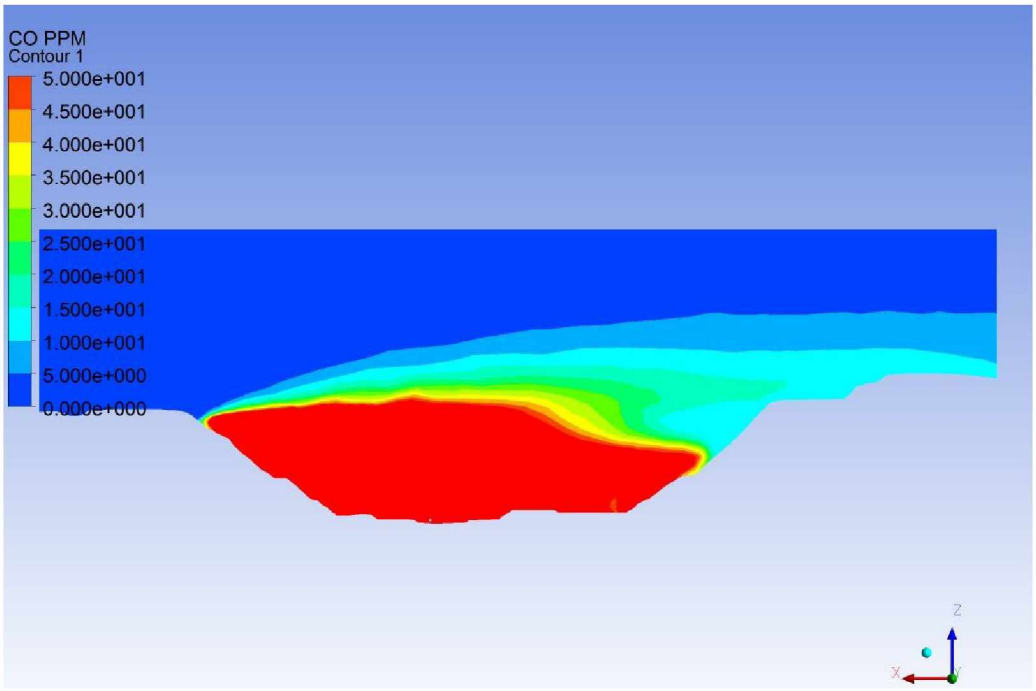

Figure C-6: Concentration of CO (in ppm) at Time Step (t ≈ 3 hrs.) for the Fans in Forcing Mode of 2010 Pit Model.

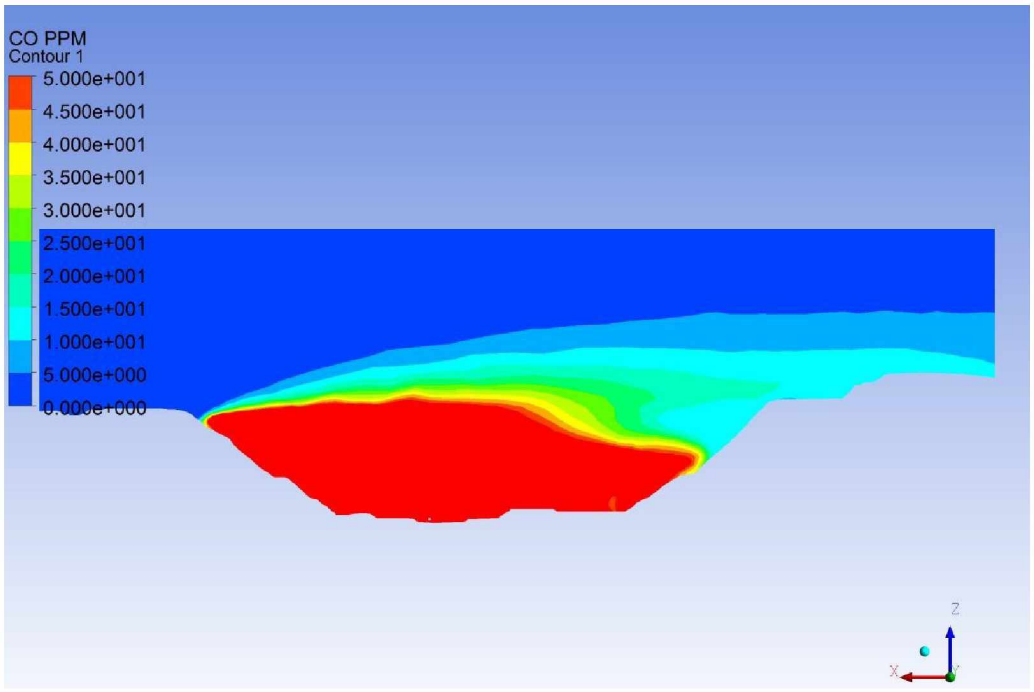

Figure C-7: Concentration of CO (in ppm) at Time Step (t ≈ 6 hrs.) for the Fans in Forcing Mode of 2010 Pit Model.

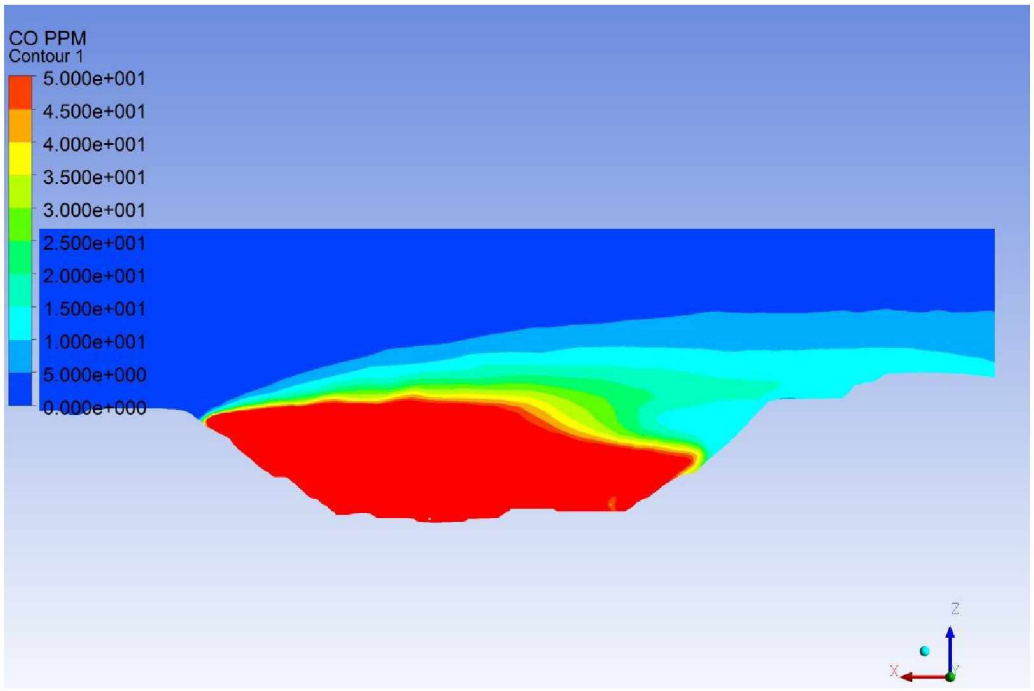

Figure C-8: Concentration of CO (in ppm) at Time Step (t ≈ 9 hrs.) for the Fans in Forcing Mode of 2010 Pit Model.

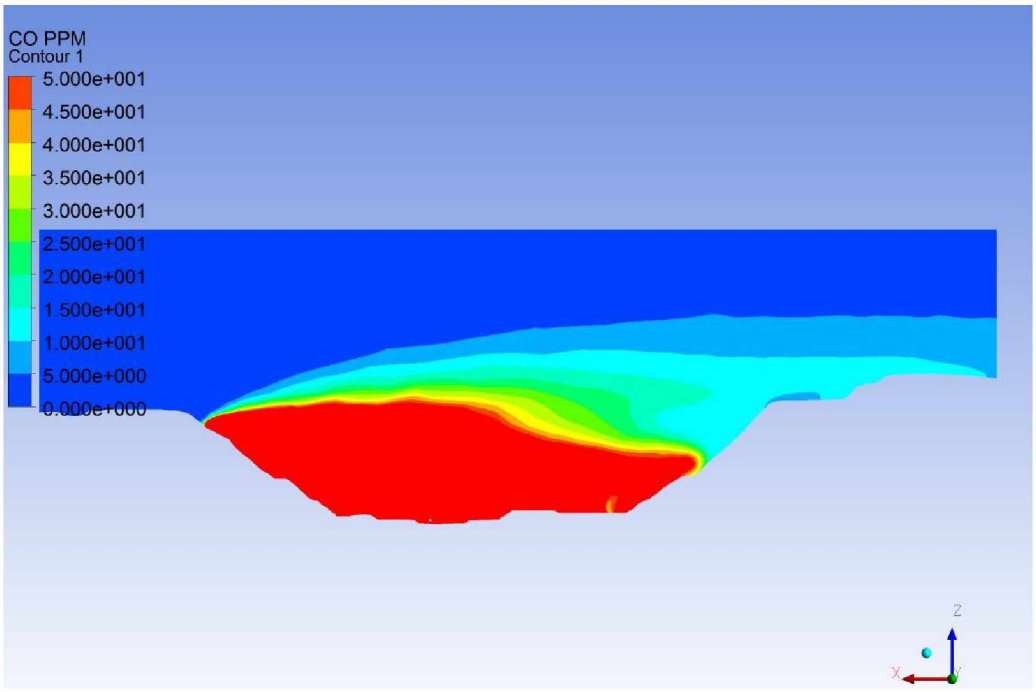

Figure C-9: Concentration of CO (in ppm) at Time Step (t ≈ 12 hrs.) for the Fans in Forcing Mode of 2010 Pit Model.

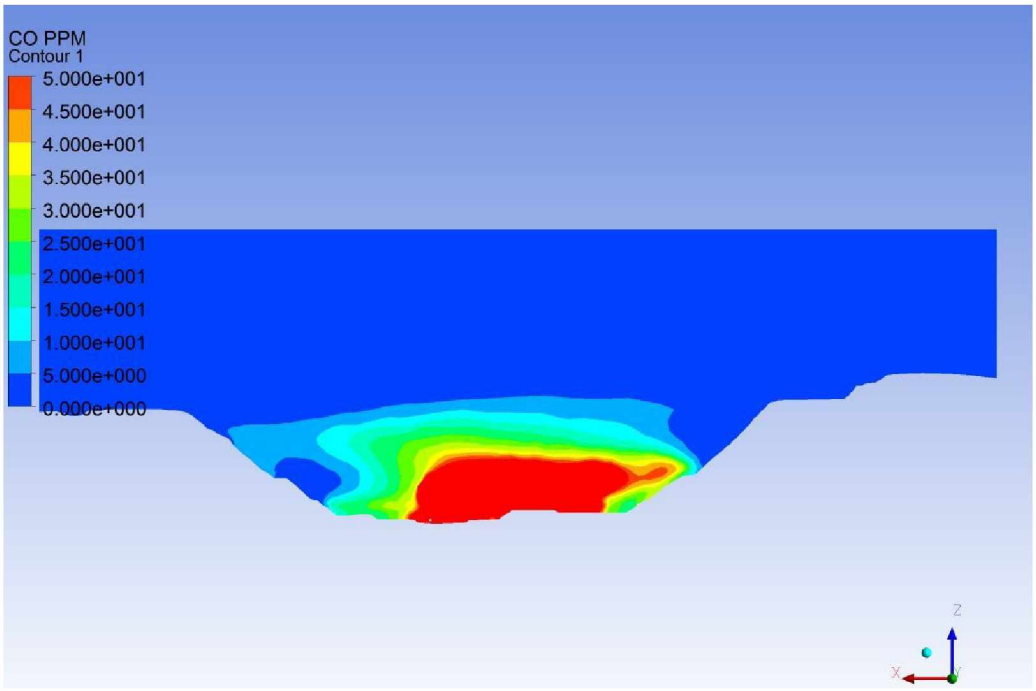

Figure C-10: Concentration of CO (in ppm) at Time Step (t ≈ 17 hrs.) for the Fans in Forcing Mode of 2010 Pit Model.

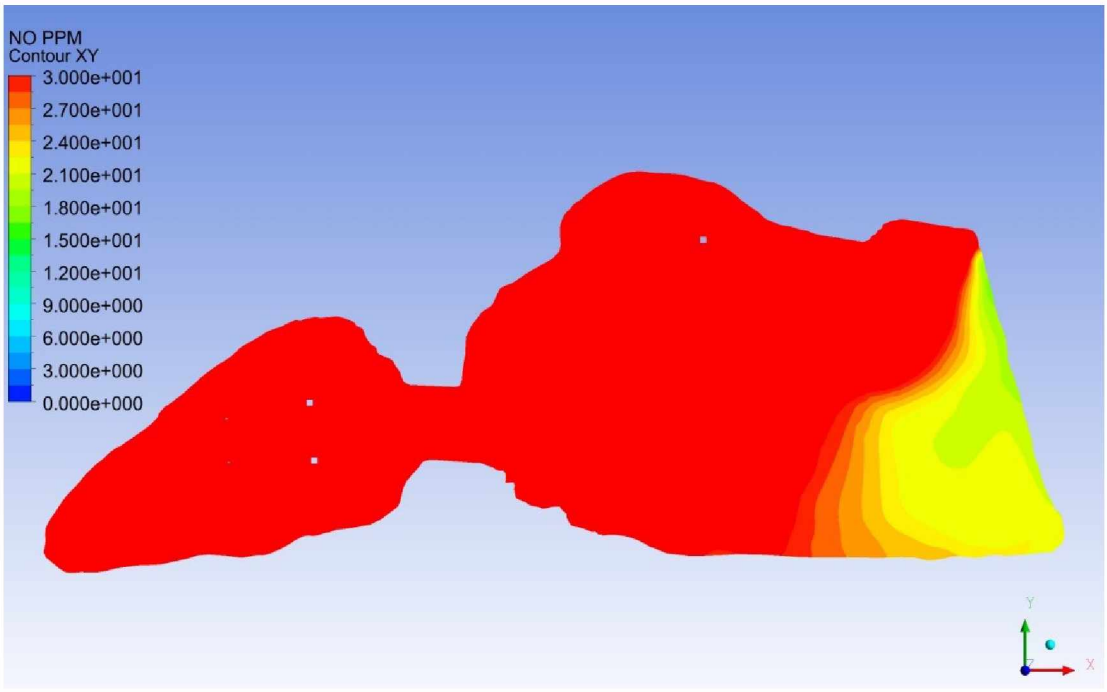

Figure C-11: Concentration of NO (in ppm) in Horizontal Plane at Time Step (t ≈ 16 hrs.; Initial State) for the Fans in Exhaust Mode of 2010 Pit Model.

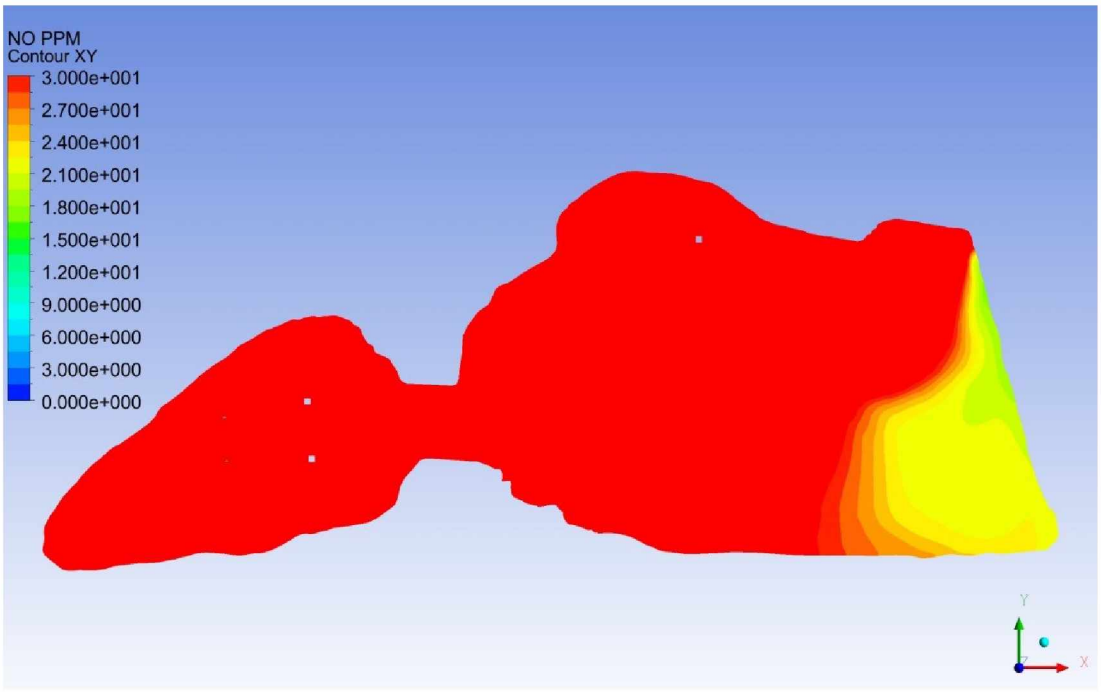

Figure C-12: Concentration of NO (in ppm) in Horizontal Plane at Time Step (t ≈ 18 hrs.) for the Fans in Exhaust Mode of 2010 Pit Model.

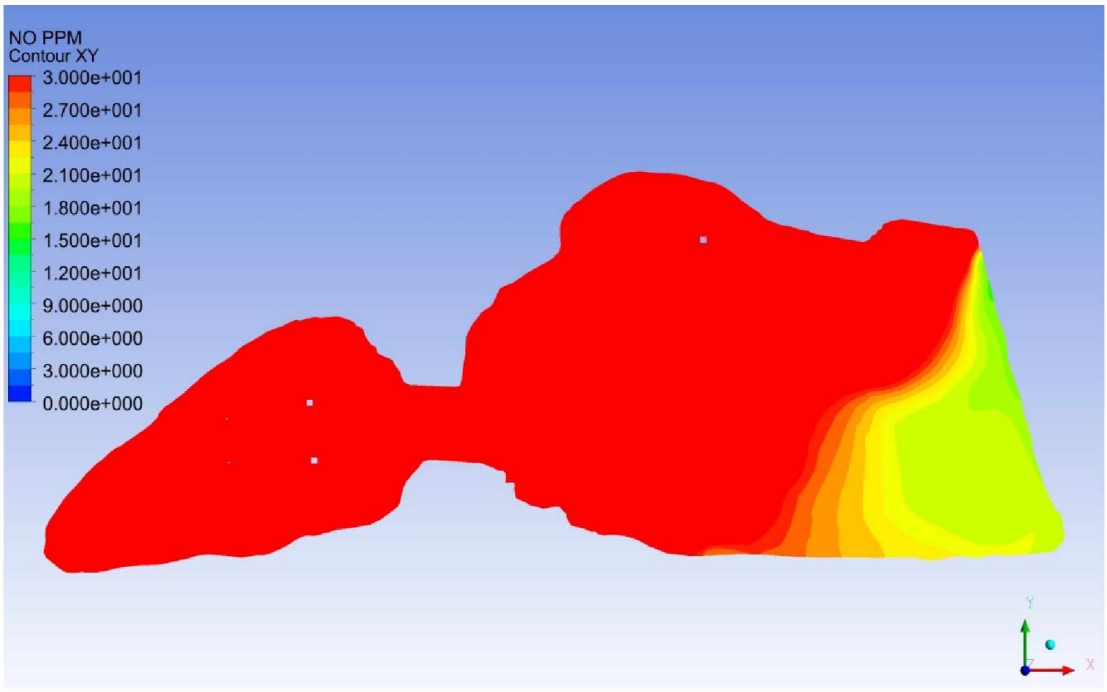

Figure C-13: Concentration of NO (in ppm) in Horizontal Plane at Time Step (t ≈ 20 hrs.) for the Fans in Exhaust Mode of 2010 Pit Model.

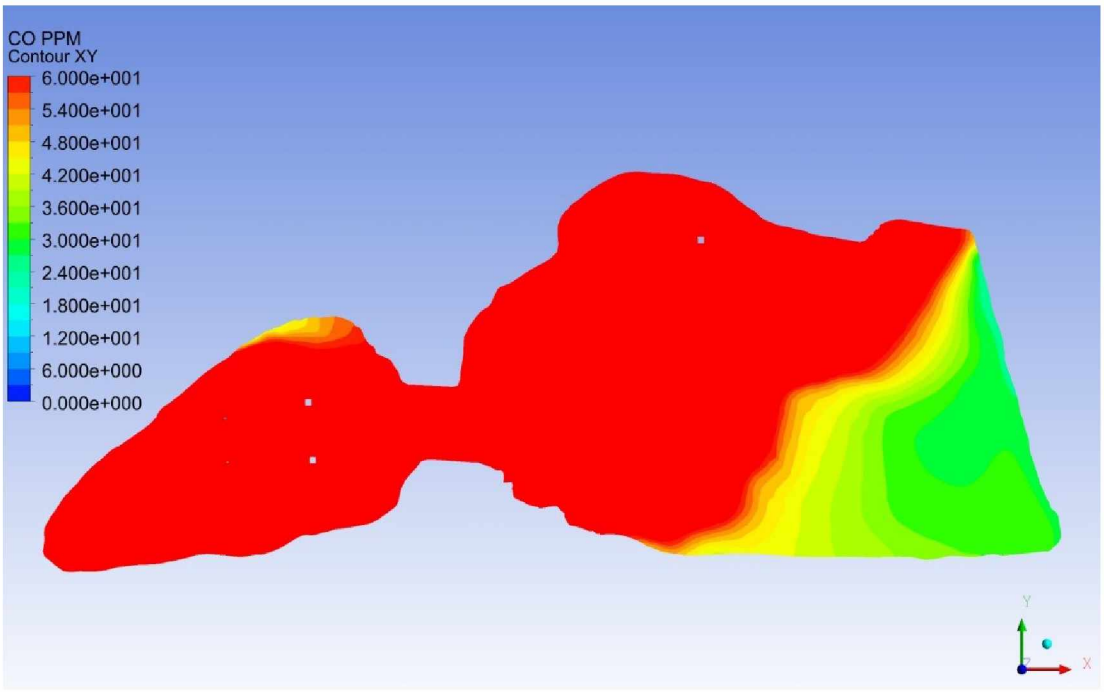

Figure C-14: Concentration of CO (in ppm) in Horizontal Plane at Time Step (t ≈ 16 hrs.; Initial State) for the Fans in Exhaust Mode of 2010 Pit Model.

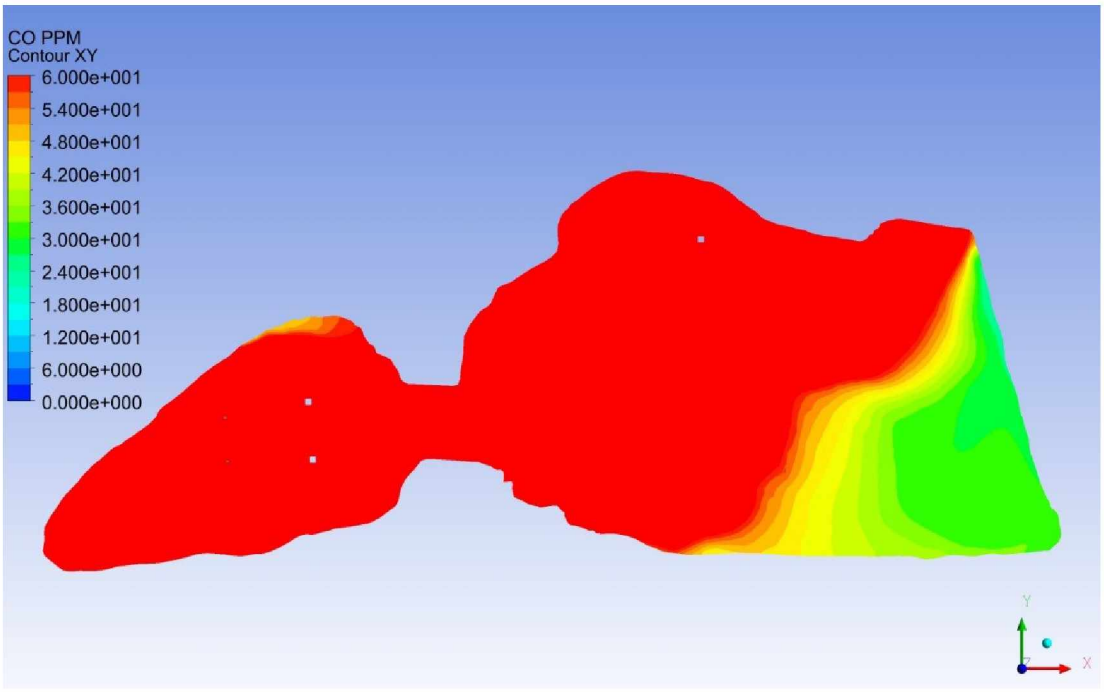

Figure C-15: Concentration of CO (in ppm) in Horizontal Plane at Time Step (t ≈ 18 hrs.) for the Fans in Exhaust Mode of 2010 Pit Model.

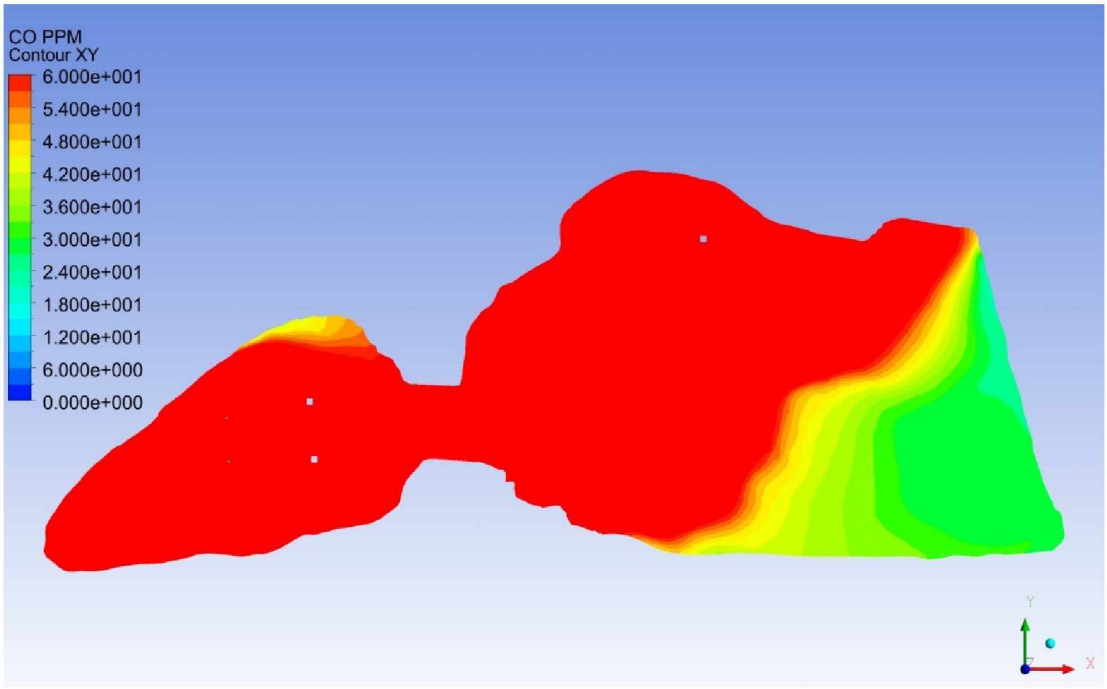

Figure C-16: Concentration of CO (in ppm) in Horizontal Plane at Time Step (t ≈ 20 hrs.) for the Fans in Exhaust Mode of 2010 Pit Model.

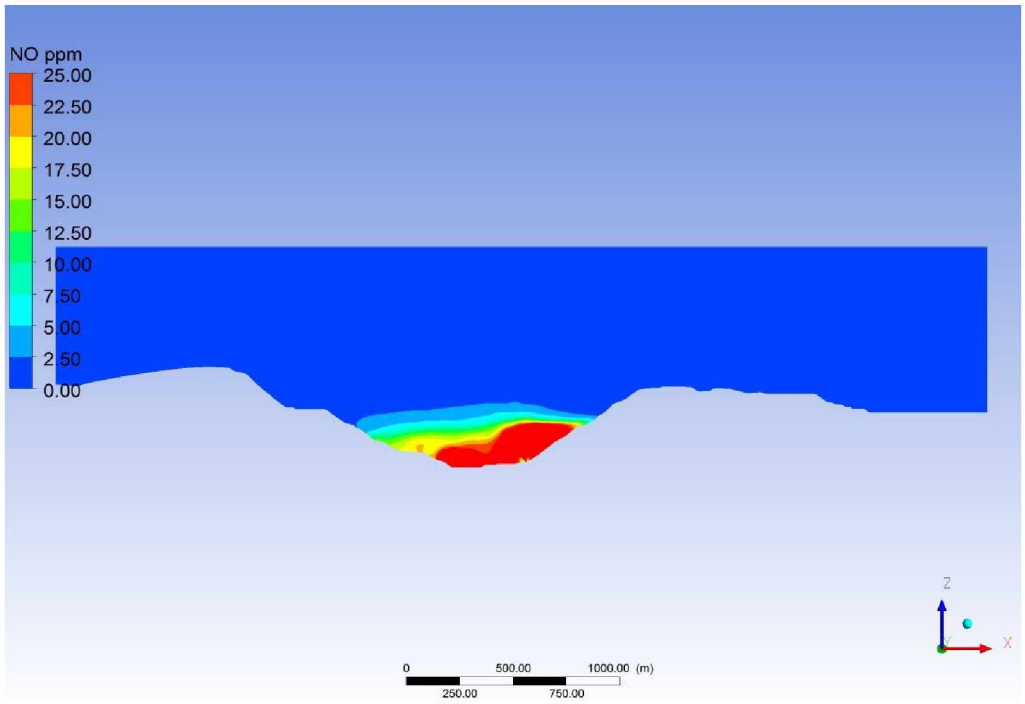

Figure C-17: Concentration of NO (in ppm) at Time Step (t ≈ 18.65 hrs.) for κ-ε Model of 2013 Pit.

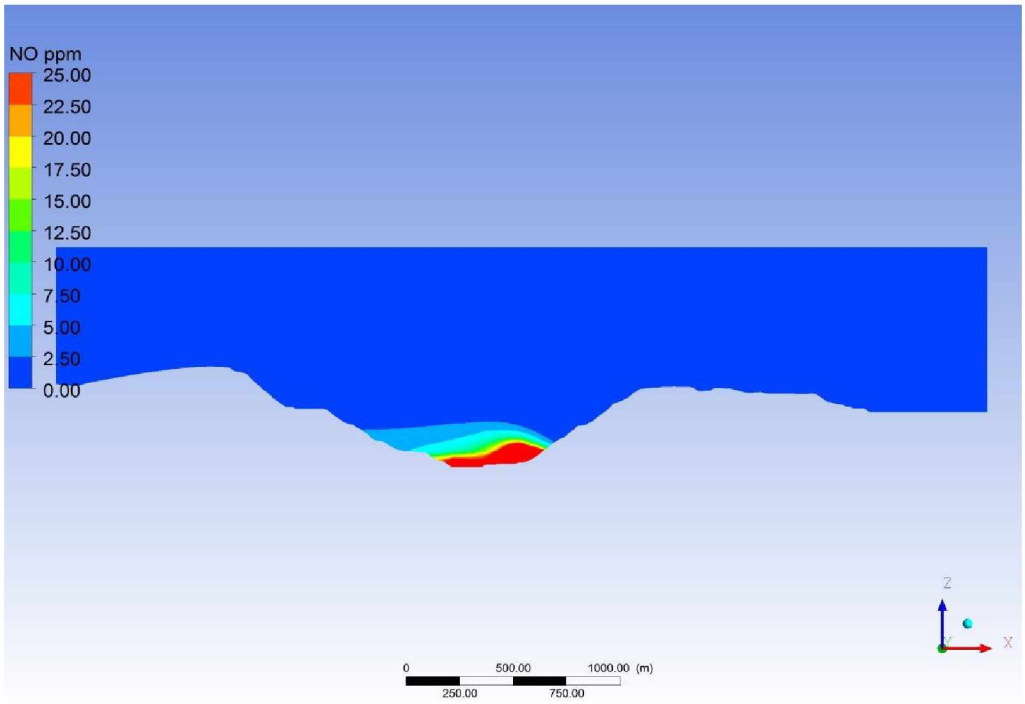

Figure C-18: Concentration of NO (in ppm) at Time Step (t ≈ 19.65 hrs.) for κ-ε Model of 2013 Pit.

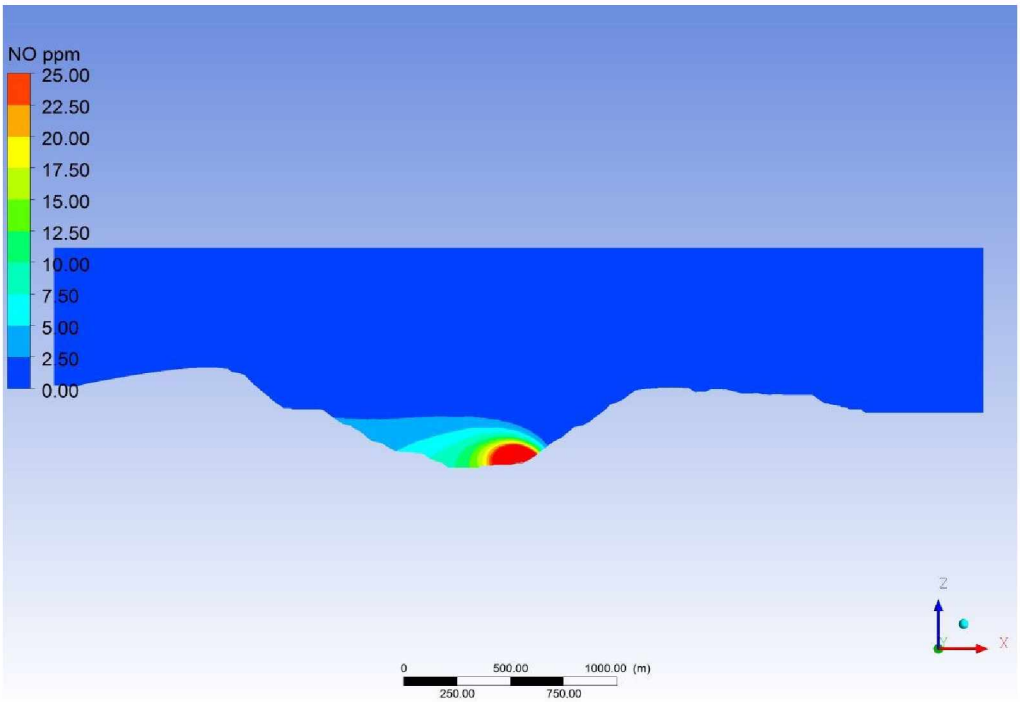

Figure C-19: Concentration of NO (in ppm) at Time Step (t ≈ 20.31 hrs.) for κ-ε Model of 2013 Pit.

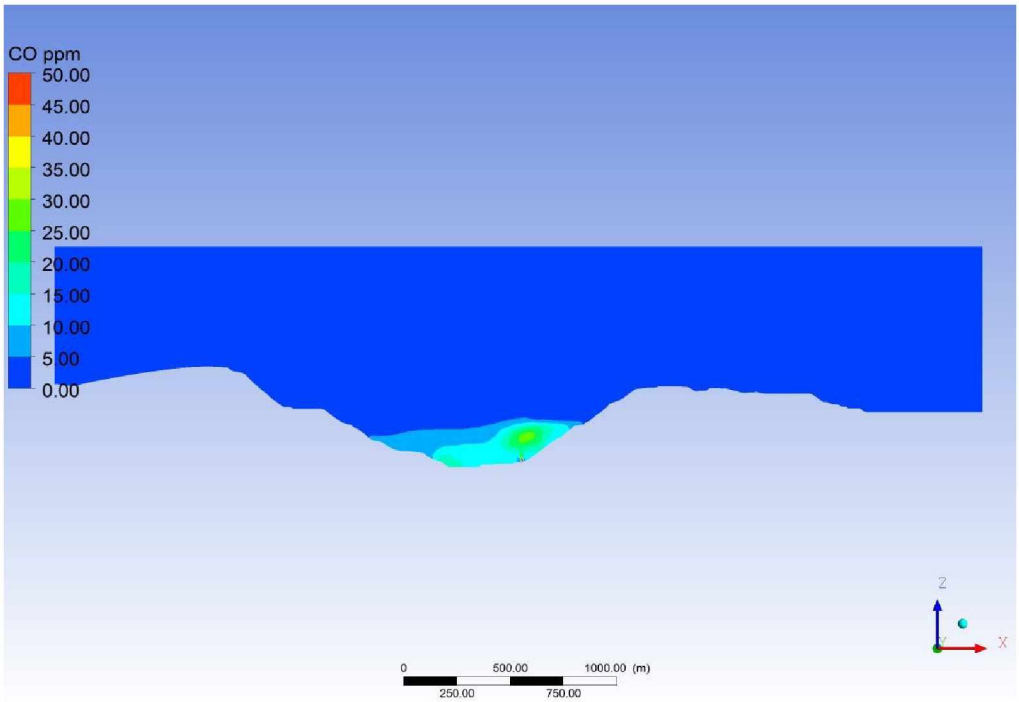

Figure C-20: Concentration of CO (in ppm) at Time Step (t ≈ 18.65 hrs.) for κ-ε Model of 2013 Pit.

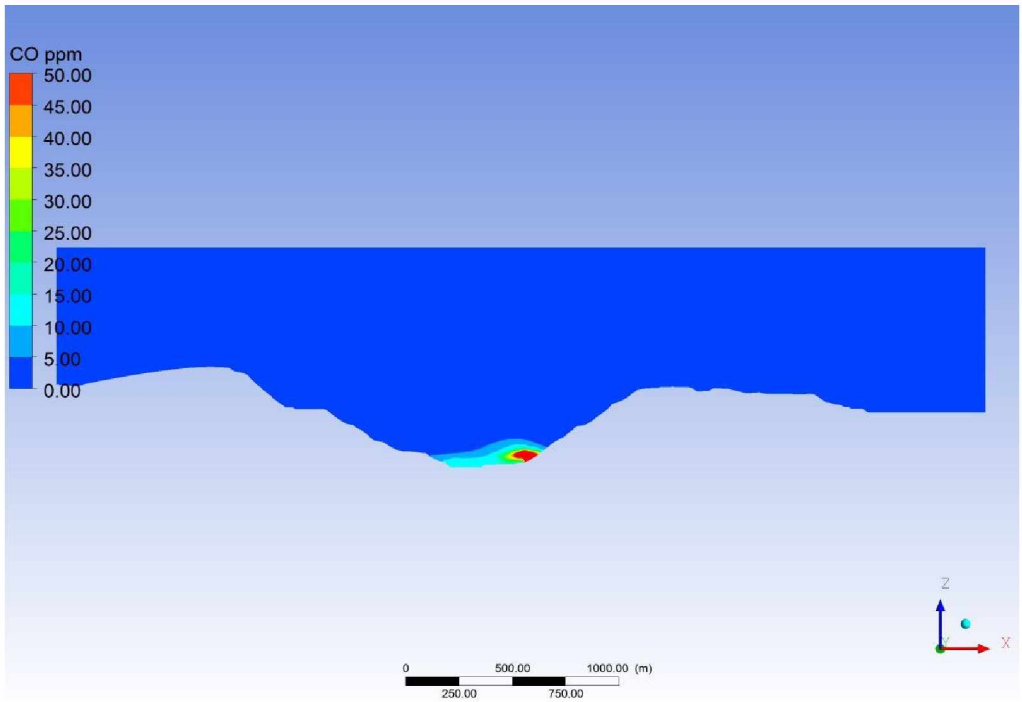

Figure C-21: Concentration of CO (in ppm) at Time Step (t ≈ 19.65 hrs.) for κ-ε Model of 2013 Pit.

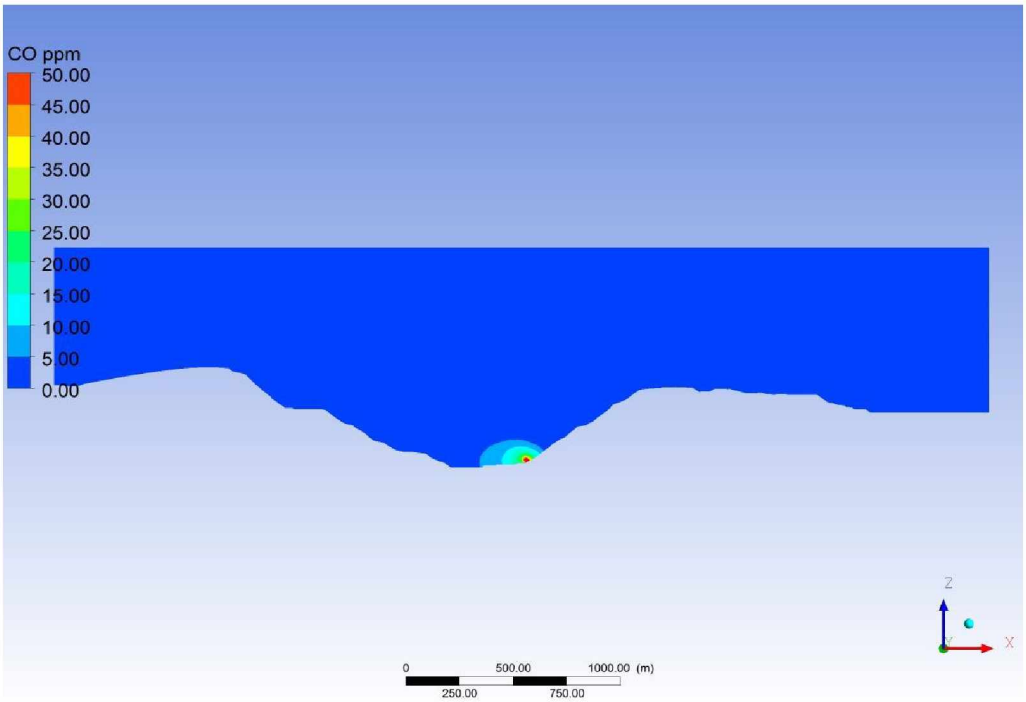

Figure C-22: Concentration of CO (in ppm) at Time Step (t ≈ 20.31 hrs.) for κ-ε Model of 2013 Pit.

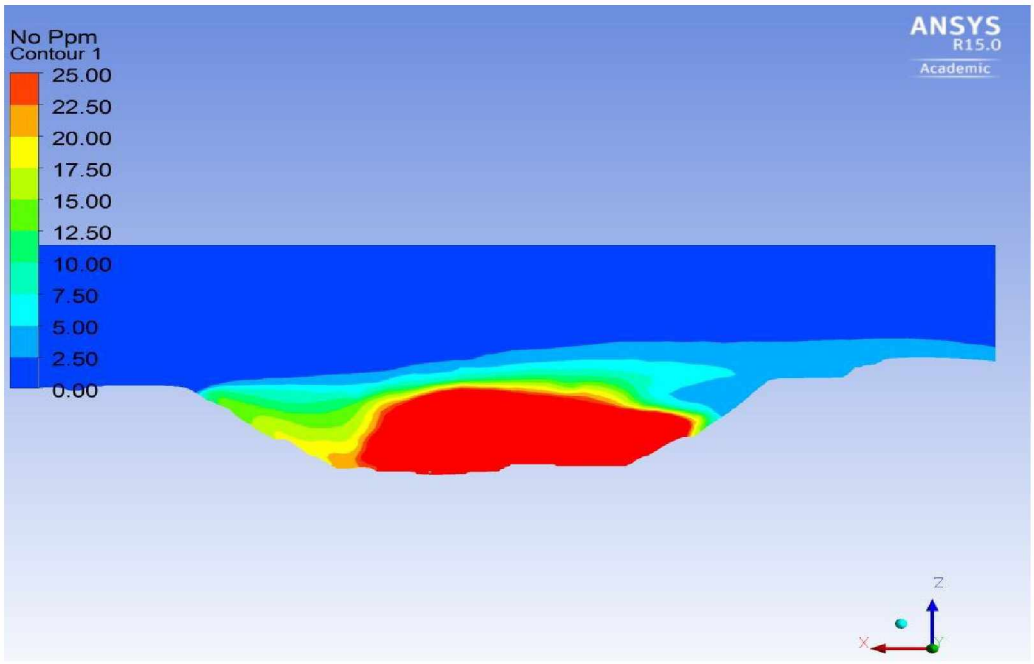

Figure C-23: Concentration of NO (in ppm) at Time Step (t ≈ 16 hrs.) for κ-ε Model of 2010 Pit.

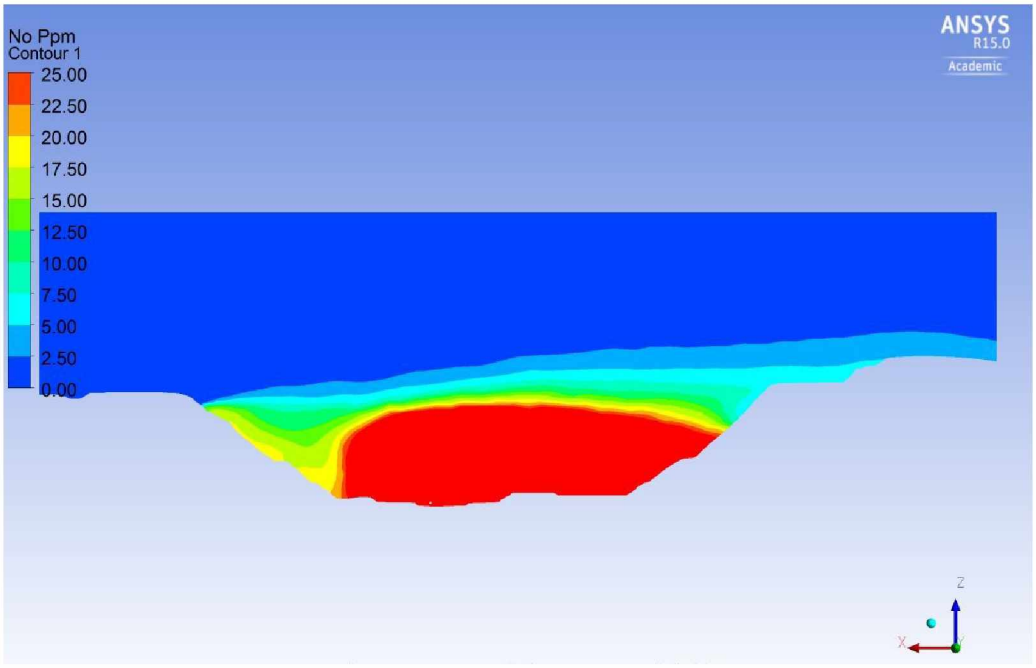

Figure C-24: Concentration of NO (in ppm) at Time Step (t ≈ 17 hrs.) for κ-ε Model of 2010 Pit.

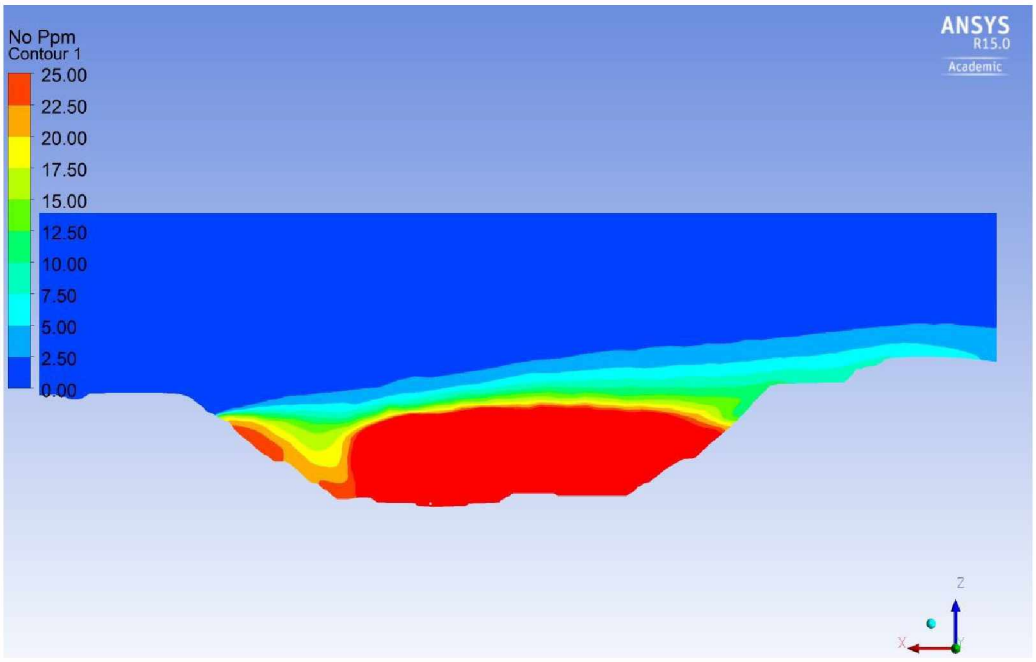

Figure C-25: Concentration of NO (in ppm) at Time Step (t ≈ 18 hrs.) for κ-ε Model of 2010 Pit.

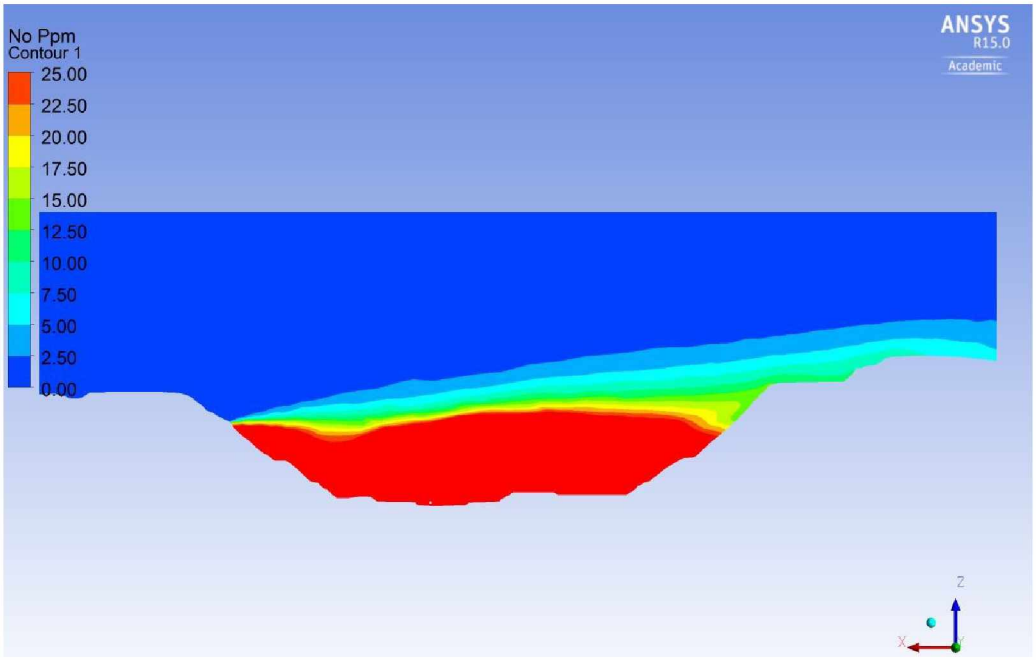

Figure C-26: Concentration of NO (in ppm) at Time Step (t ≈ 19 hrs.) for κ-ε Model of 2010 Pit.

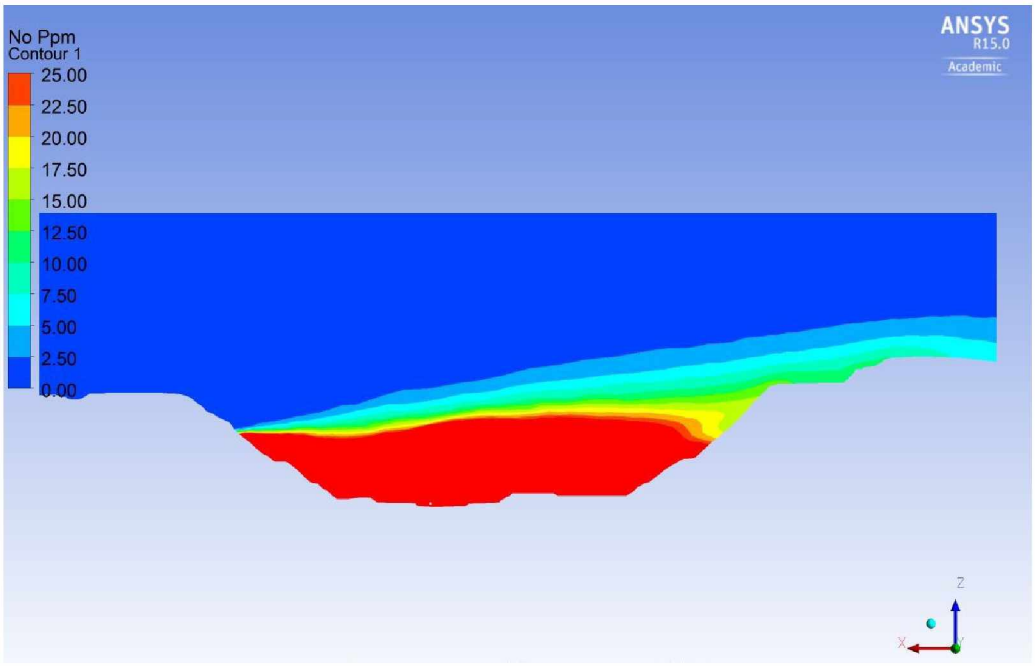

Figure C-27: Concentration of NO (in ppm) at Time Step (t ≈ 20 hrs.) for κ-ε Model of 2010 Pit.

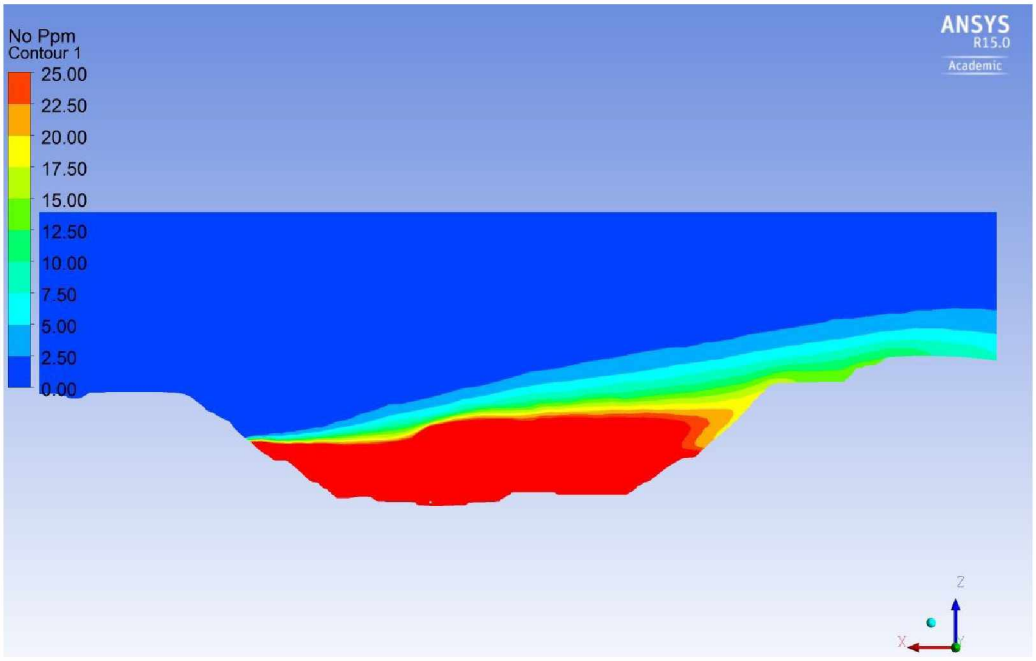

Figure C-28: Concentration of NO (in ppm) at Time Step (t ≈ 21 hrs.) for κ-ε Model of 2010 Pit.

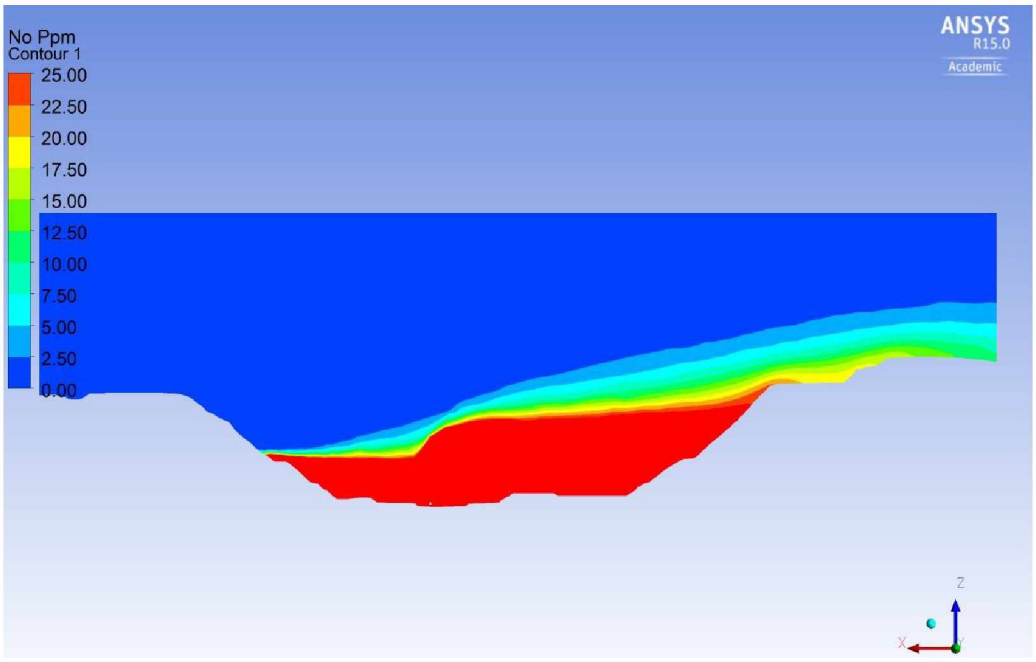

Figure C-29: Concentration of NO (in ppm) at Time Step (t ≈ 22 hrs.) for κ-ε Model of 2010 Pit.

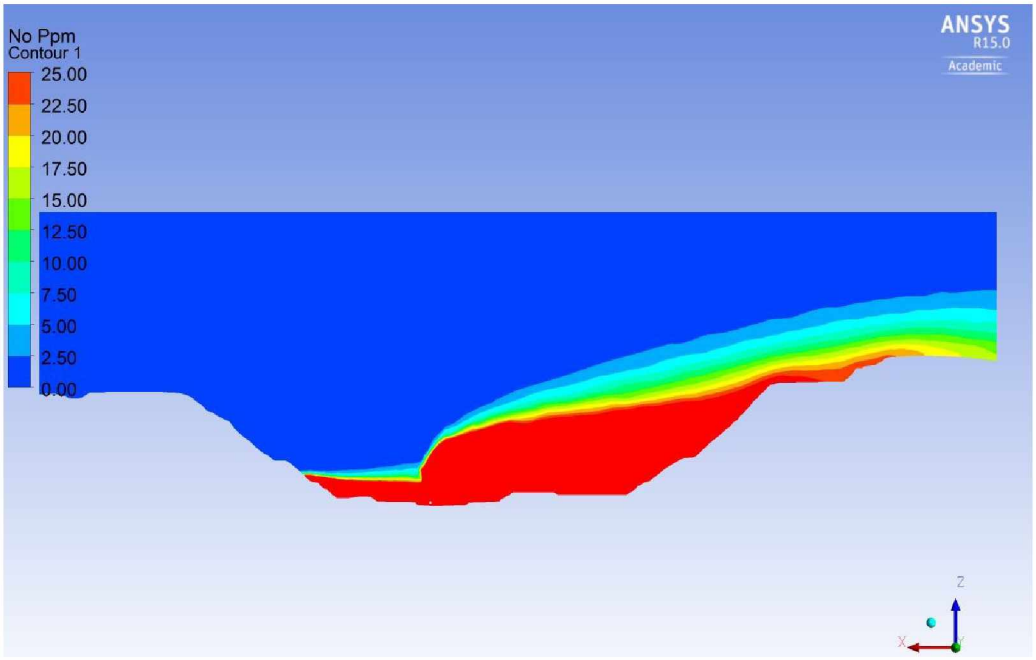

Figure C-30: Concentration of NO (in ppm) at Time Step (t ≈ 23 hrs.) for κ-ε Model of 2010 Pit.

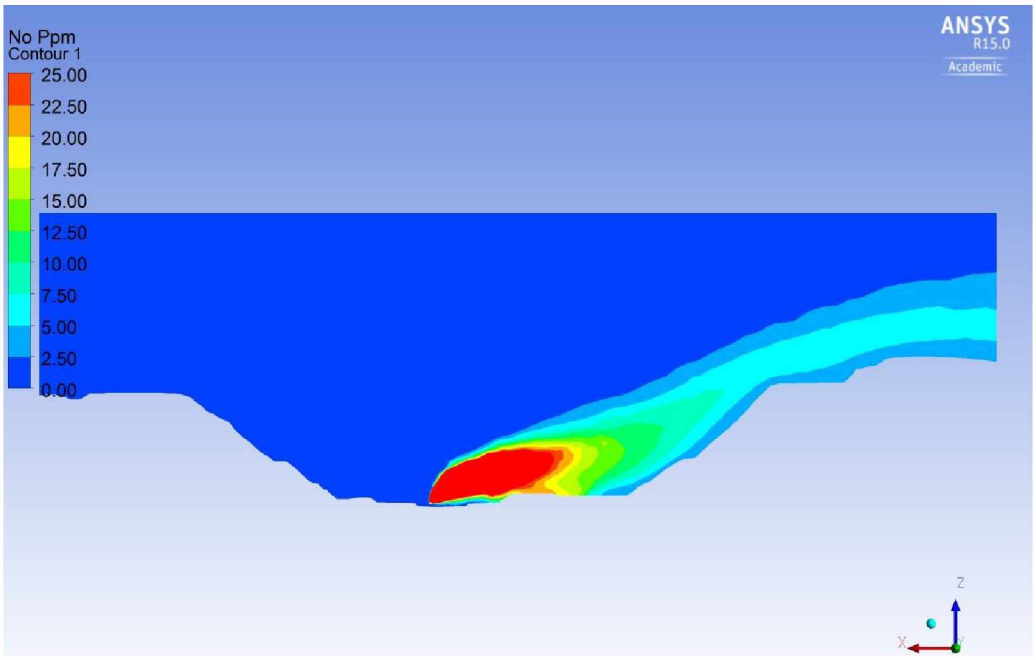

Figure C-31: Concentration of NO (in ppm) at Time Step (t ≈ 24.8 hrs.) for κ-ε Model of 2010 Pit.

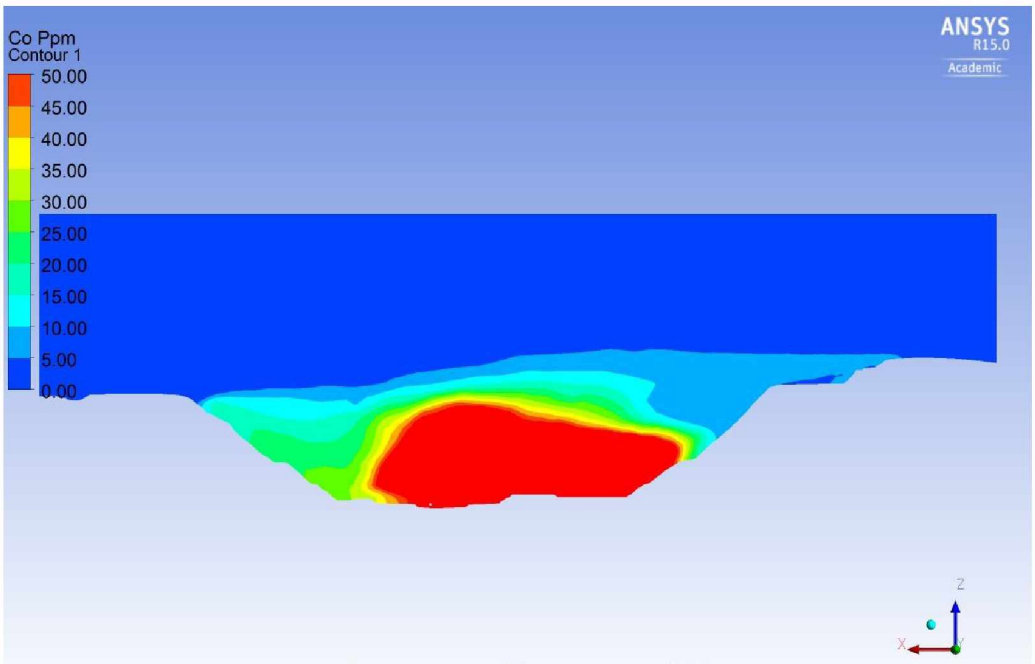

Figure C-32: Concentration of CO (in ppm) at Time Step (t ≈ 16 hrs.) for κ-ε Model of 2010 Pit.

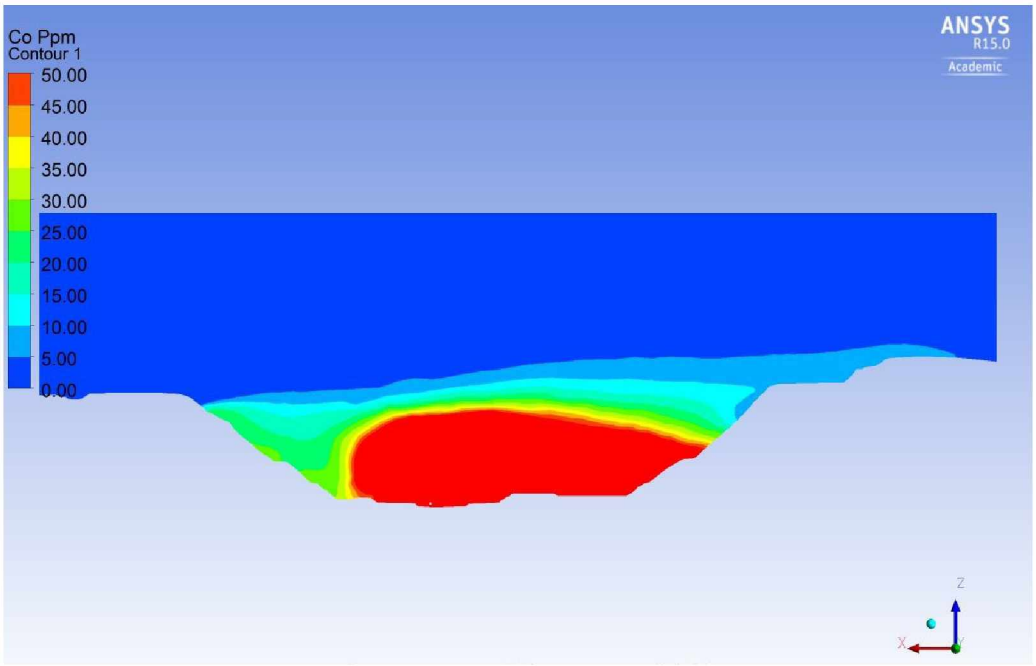

Figure C-33: Concentration of CO (in ppm) at Time Step (t ≈ 17 hrs.) for κ-ε Model of 2010 Pit.

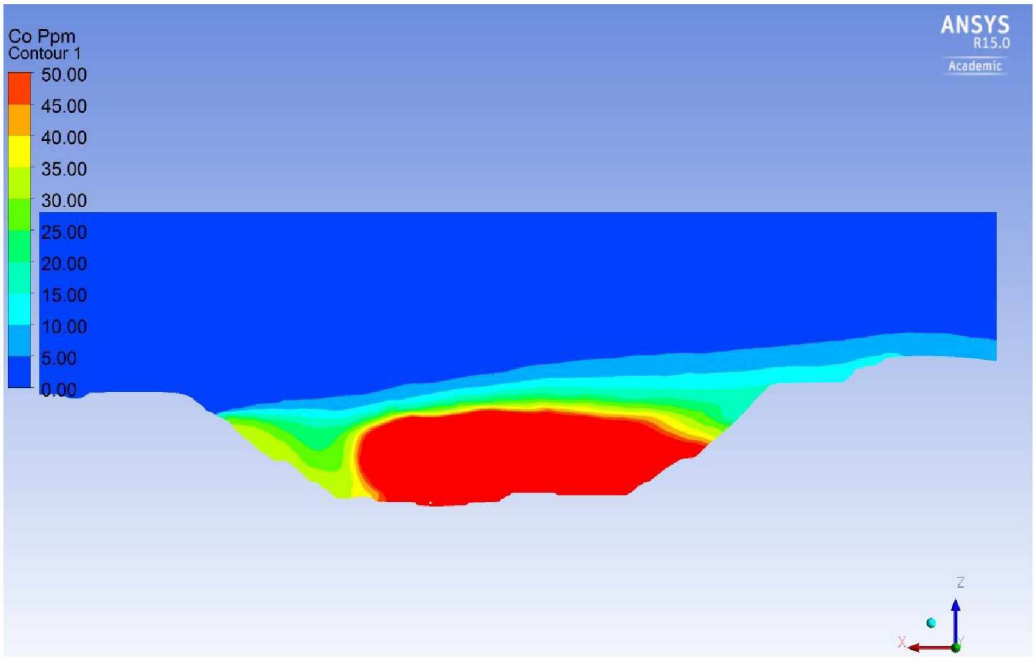

Figure C-34: Concentration of CO (in ppm) at Time Step (t ≈ 18 hrs.) for κ-ε Model of 2010 Pit.

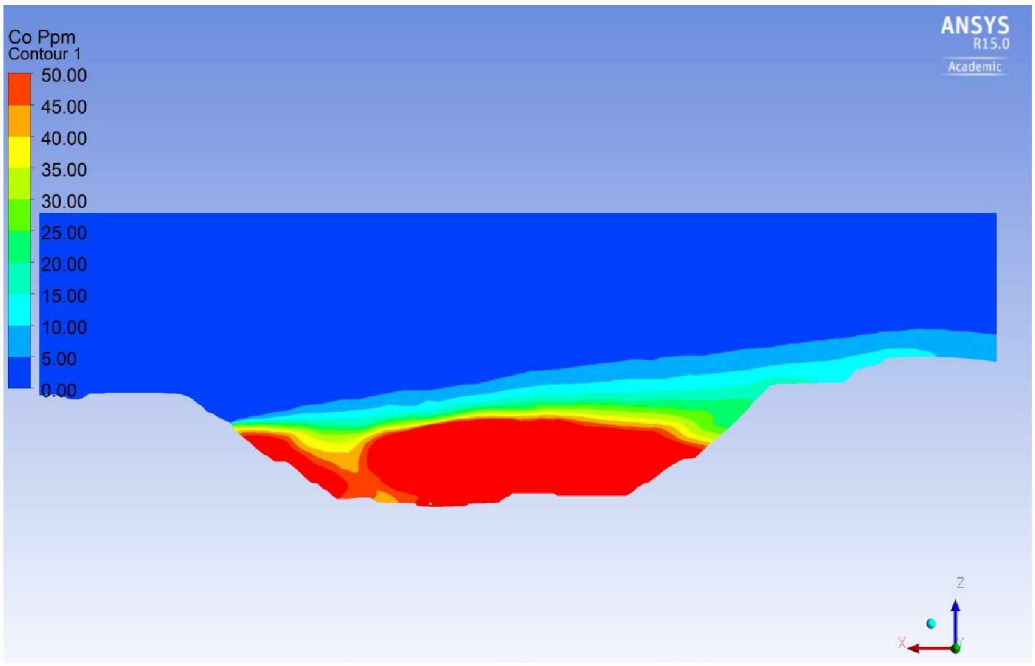

Figure C-35: Concentration of CO (in ppm) at Time Step (t ≈ 19 hrs.) for κ-ε Model of 2010 Pit.

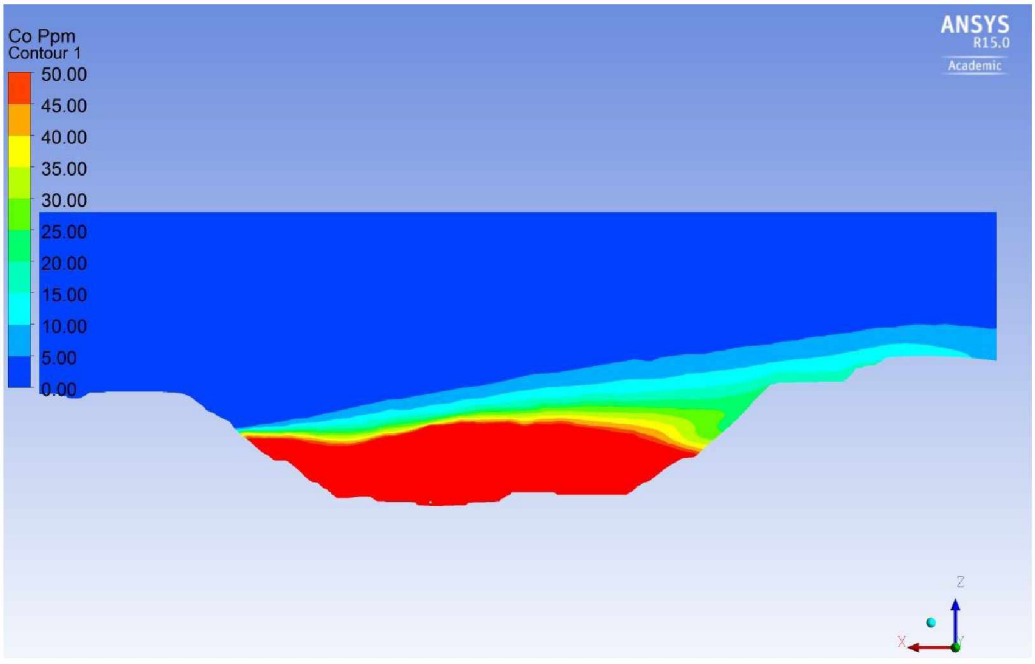

Figure C-36: Concentration of CO (in ppm) at Time Step (t ≈ 20 hrs.) for κ-ε Model of 2010 Pit.

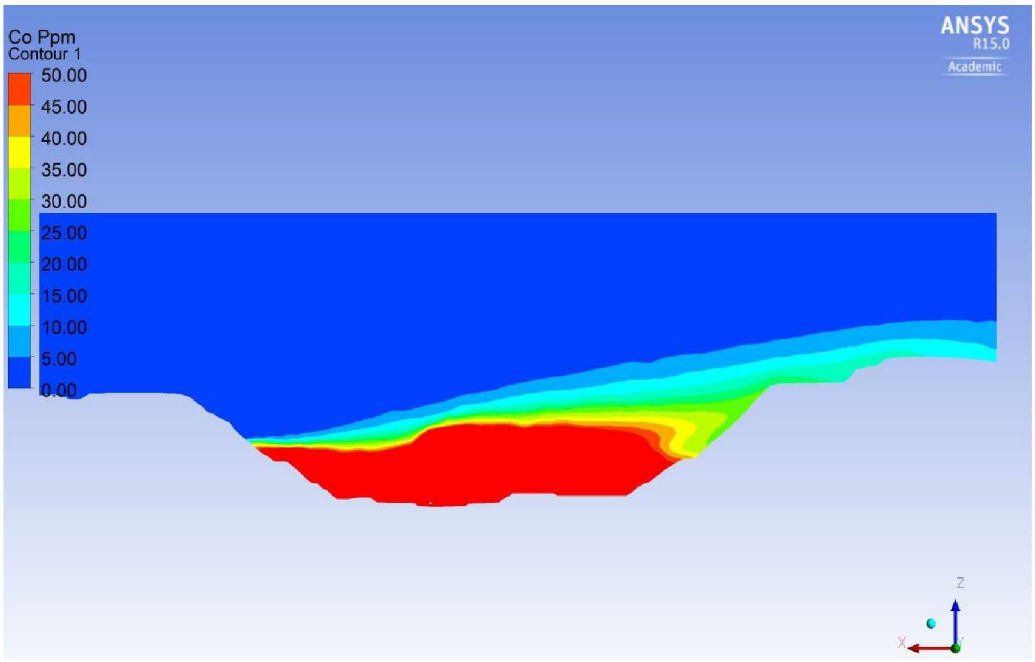

Figure C-37: Concentration of CO (in ppm) at Time Step (t ≈ 21 hrs.) for κ-ε Model of 2010 Pit.

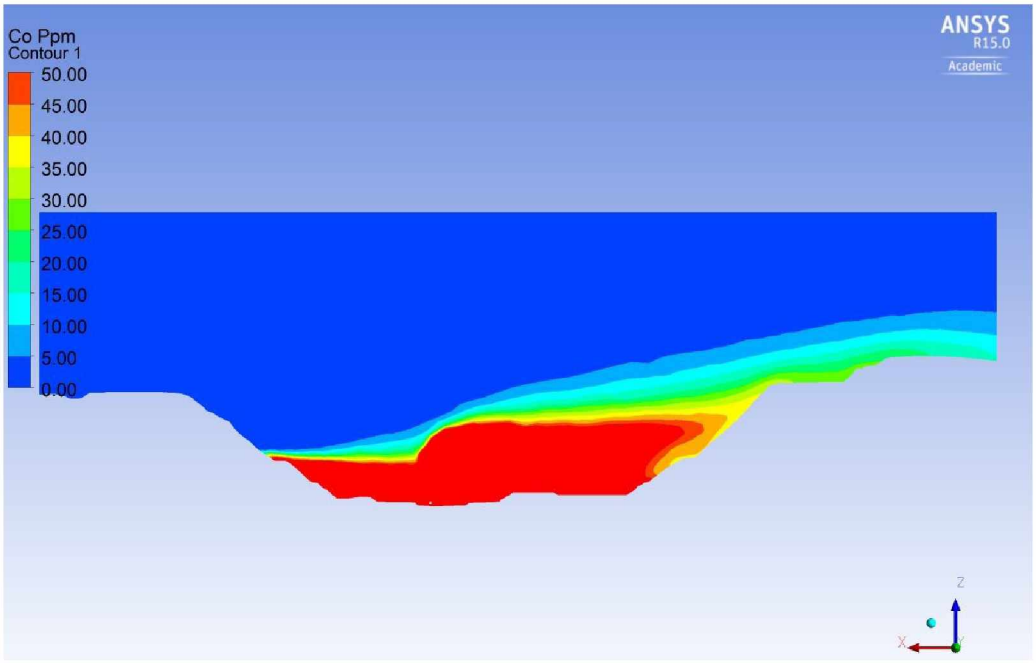

Figure C-38: Concentration of CO (in ppm) at Time Step (t ≈ 22 hrs.) for κ-ε Model of 2010 Pit.

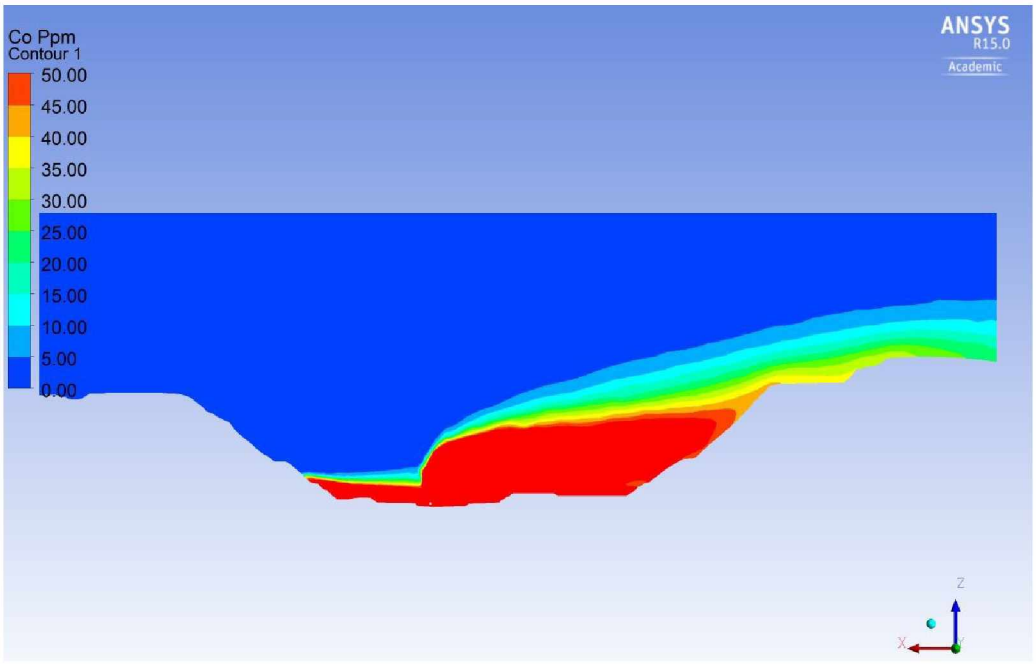

Figure C-39: Concentration of CO (in ppm) at Time Step (t ≈ 23 hrs.) for κ-ε Model of 2010 Pit.

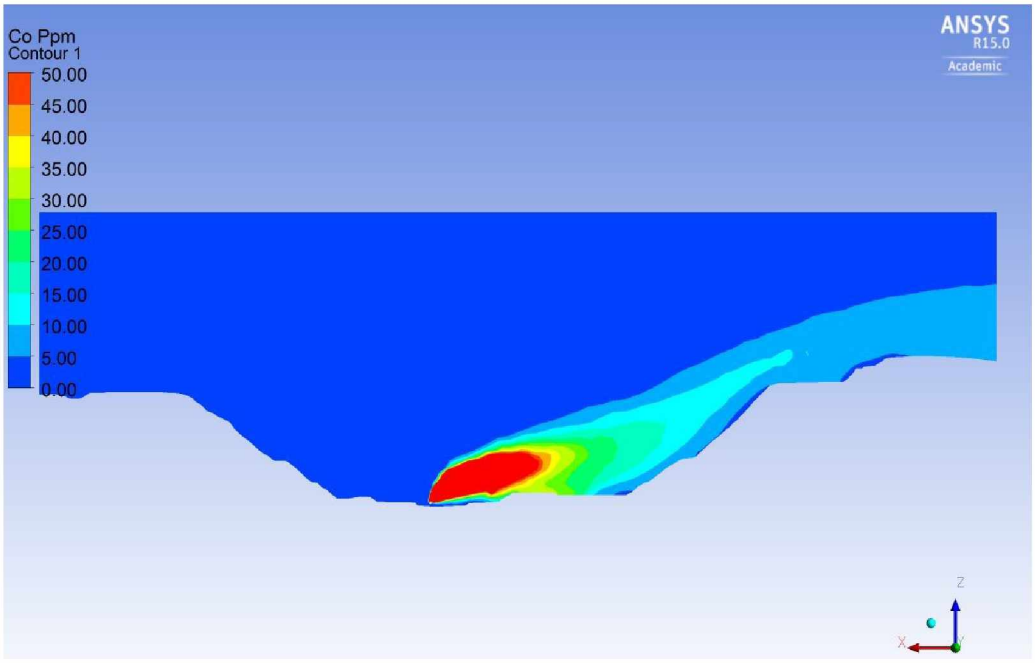

Figure C-40: Concentration of CO (in ppm) at Time Step (t ≈ 24.8 hrs.) for κ-ε Model of 2010 Pit.

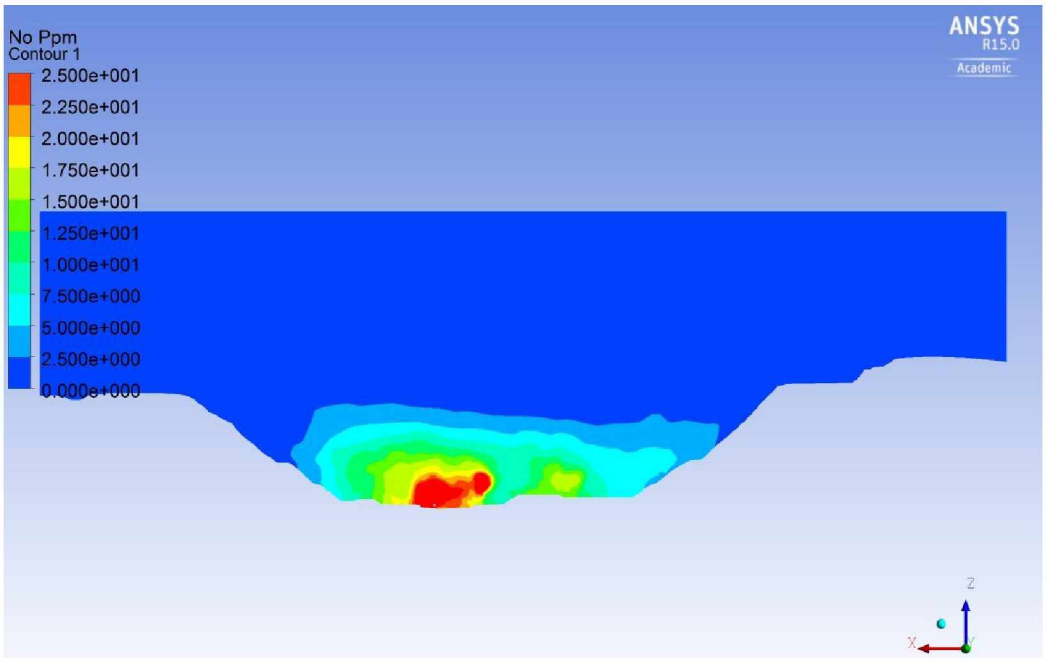

Figure C-41: Concentration of NO (in ppm) at Time Step (t ≈ 16 hrs.) for LES Model of 2010 Pit.

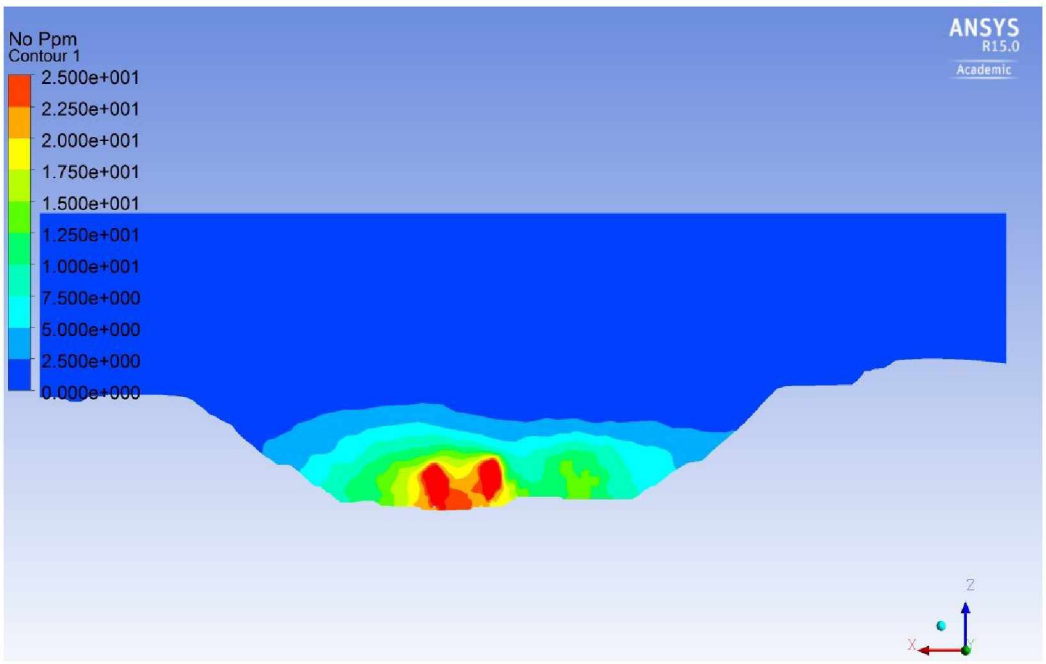

Figure C-42: Concentration of NO (in ppm) at Time Step (t ≈ 17 hrs.) for LES Model of 2010 Pit.

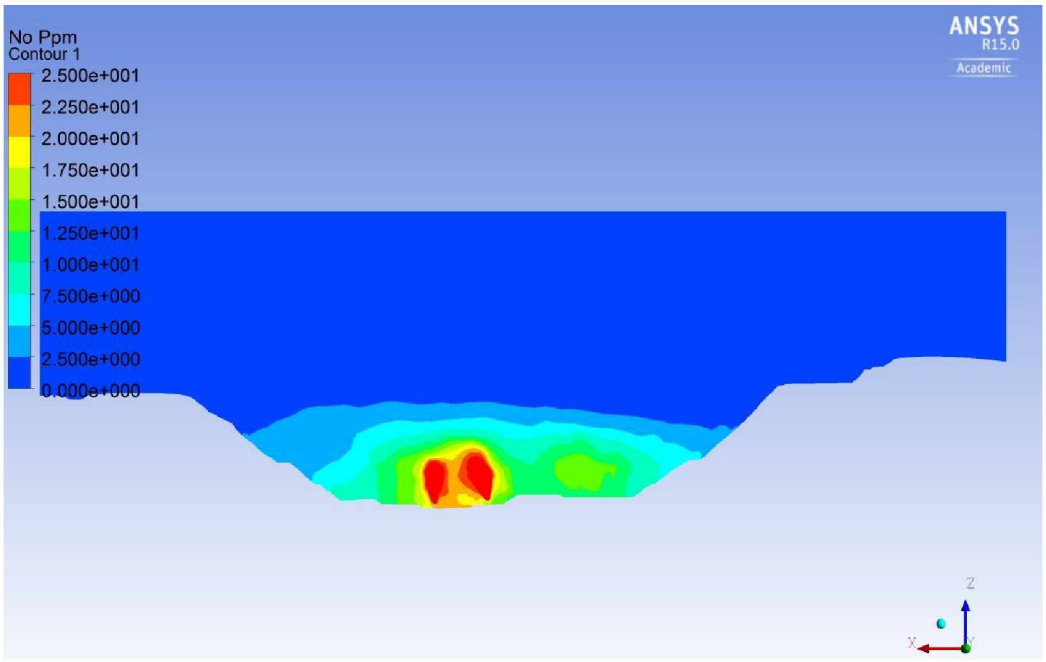

Figure C-43: Concentration of NO (in ppm) at Time Step (t ≈ 18 hrs.) for LES Model of 2010 Pit.

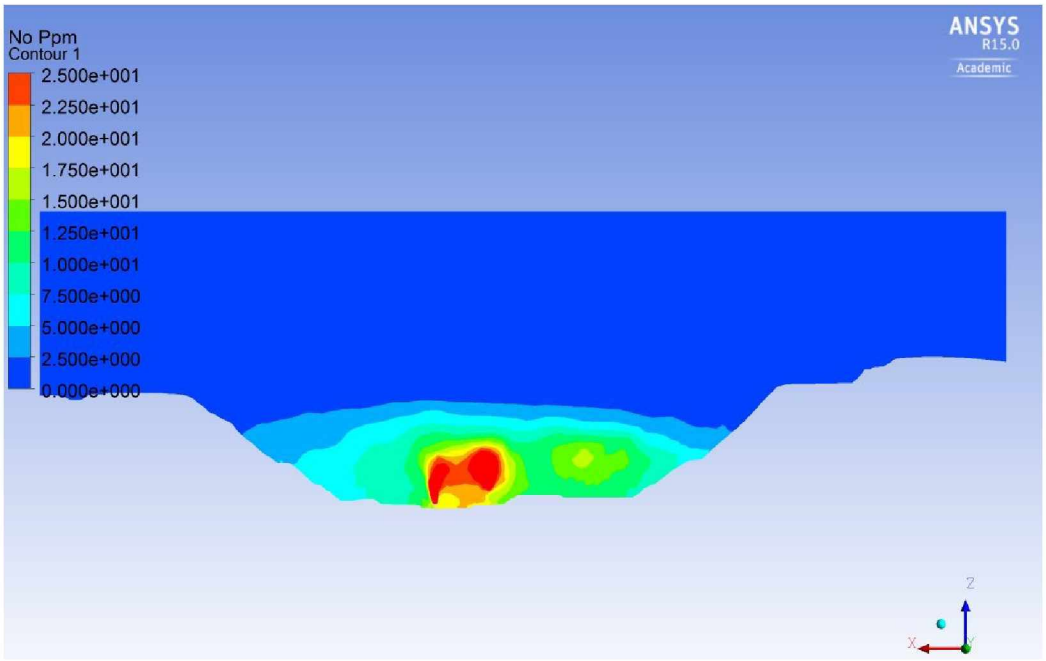

Figure C-44: Concentration of NO (in ppm) at Time Step (t ≈ 19 hrs.) for LES Model of 2010 Pit.

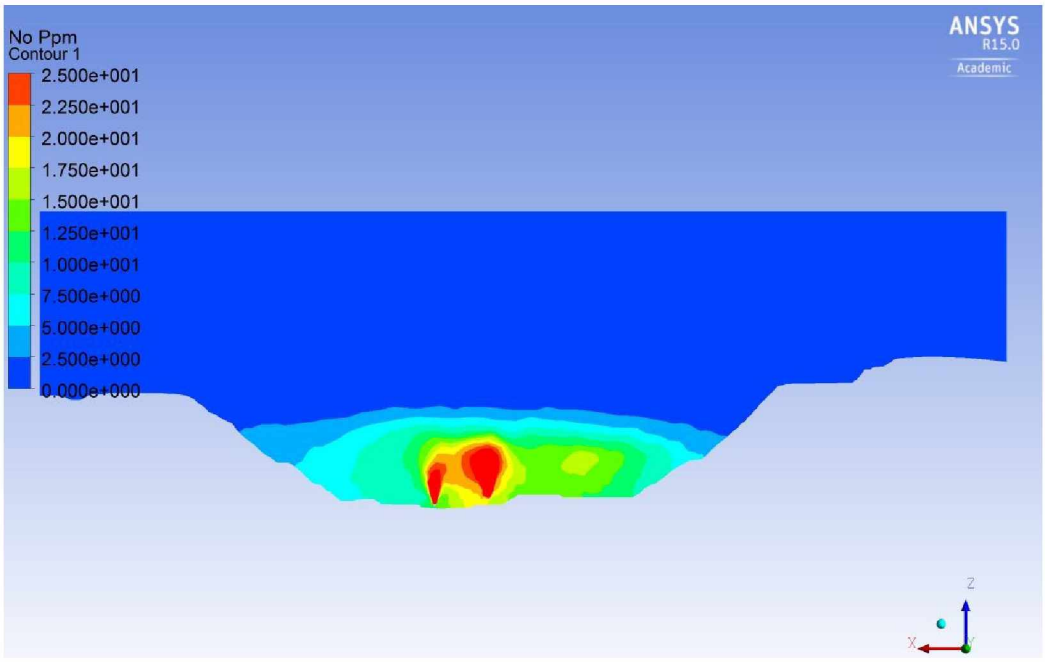

Figure C-45: Concentration of NO (in ppm) at Time Step (t ≈ 20 hrs.) for LES Model of 2010 Pit.

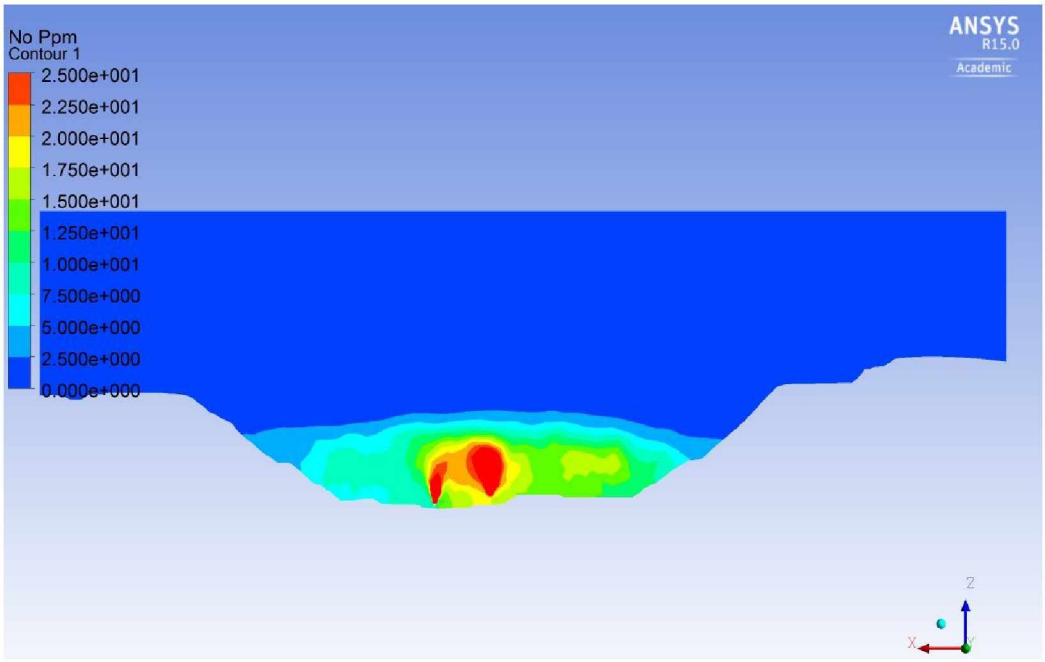

Figure C-46: Concentration of NO (in ppm) at Time Step (t ≈ 21 hrs.) for LES Model of 2010 Pit.

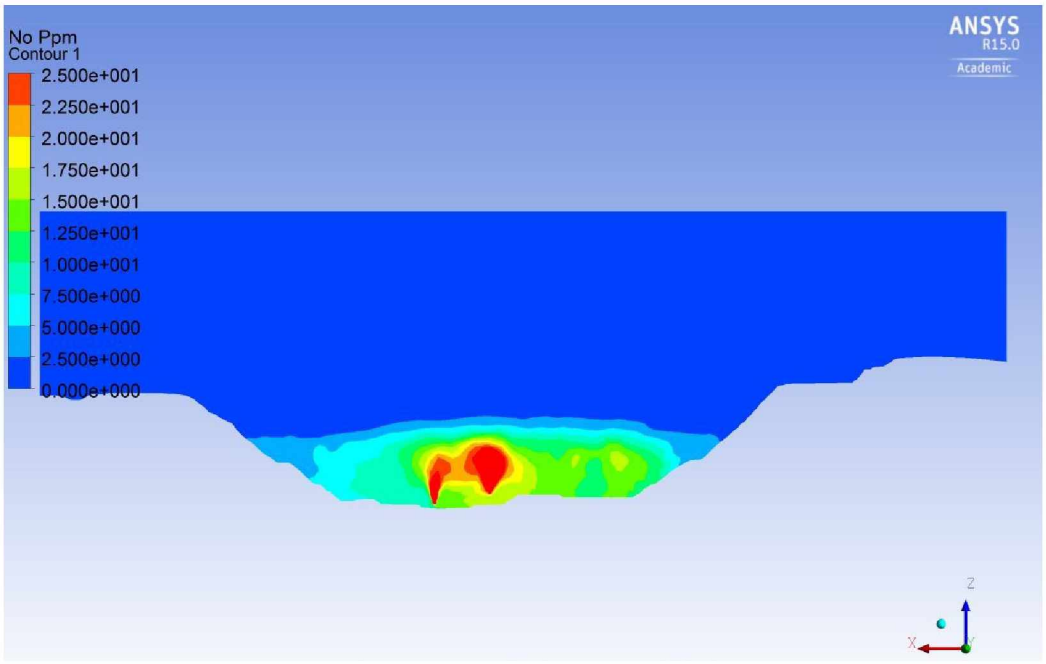

Figure C-47: Concentration of NO (in ppm) at Time Step (t ≈ 22 hrs.) for LES Model of 2010 Pit.

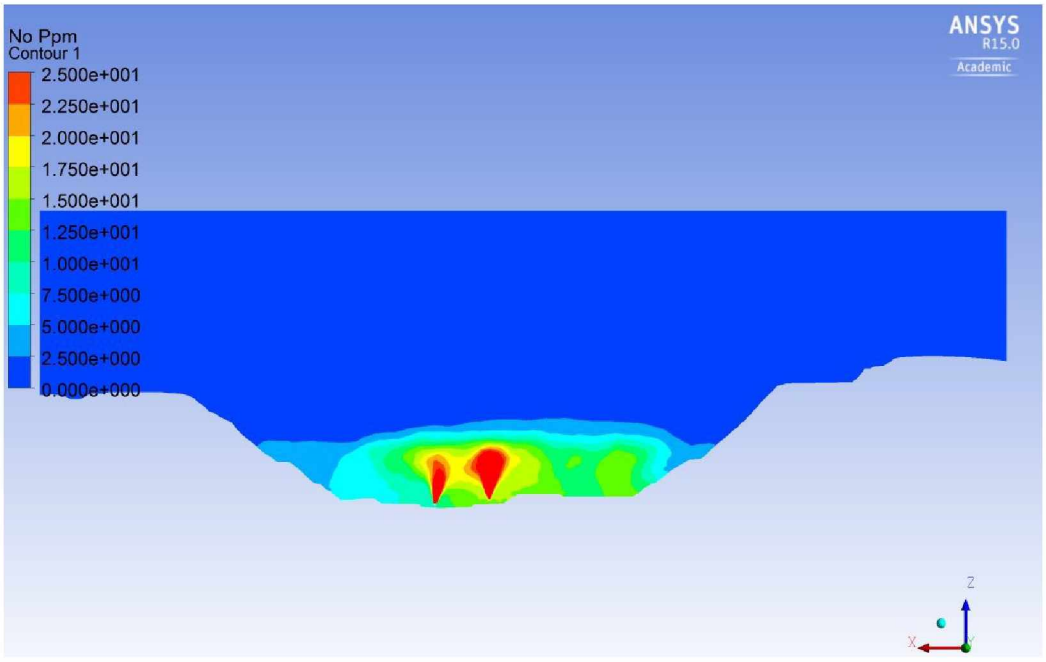

Figure C-48: Concentration of NO (in ppm) at Time Step (t ≈ 23 hrs.) for LES Model of 2010 Pit.

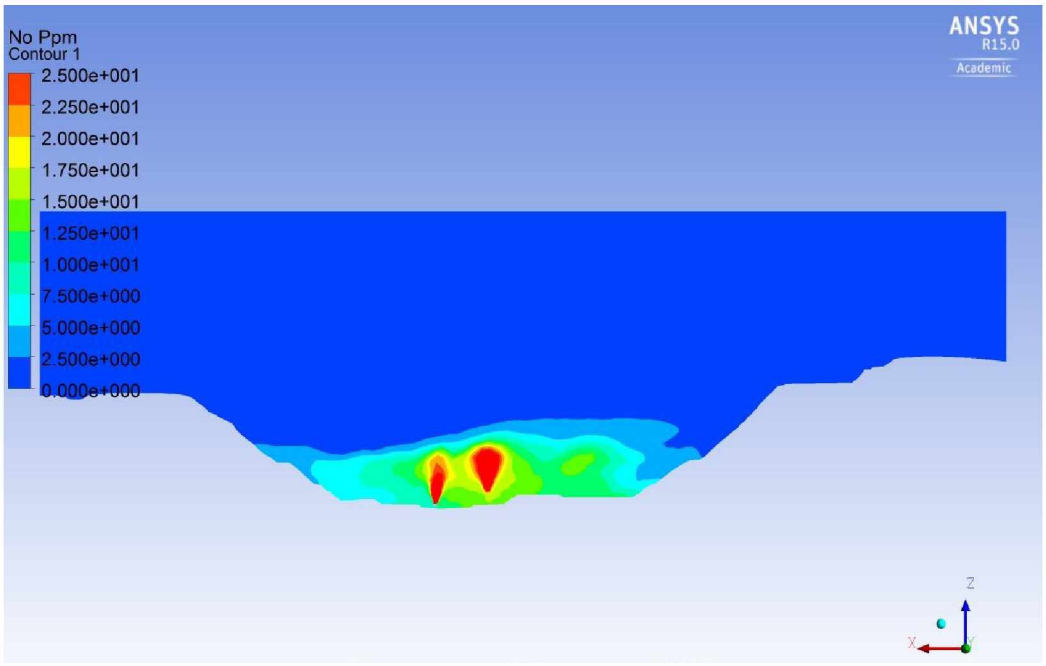

Figure C-49: Concentration of NO (in ppm) at Time Step (t ≈ 24 hrs.) for LES Model of 2010 Pit.

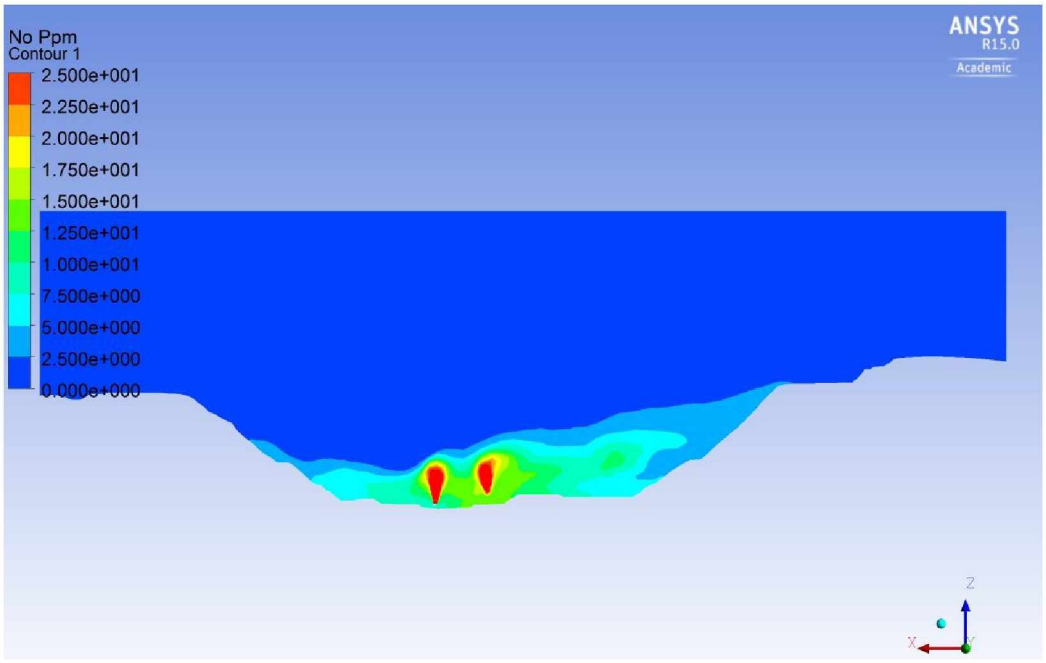

Figure C-50: Concentration of CO (in ppm) at Time Step (t ≈ 25 hrs.) for LES Model of 2010 Pit.

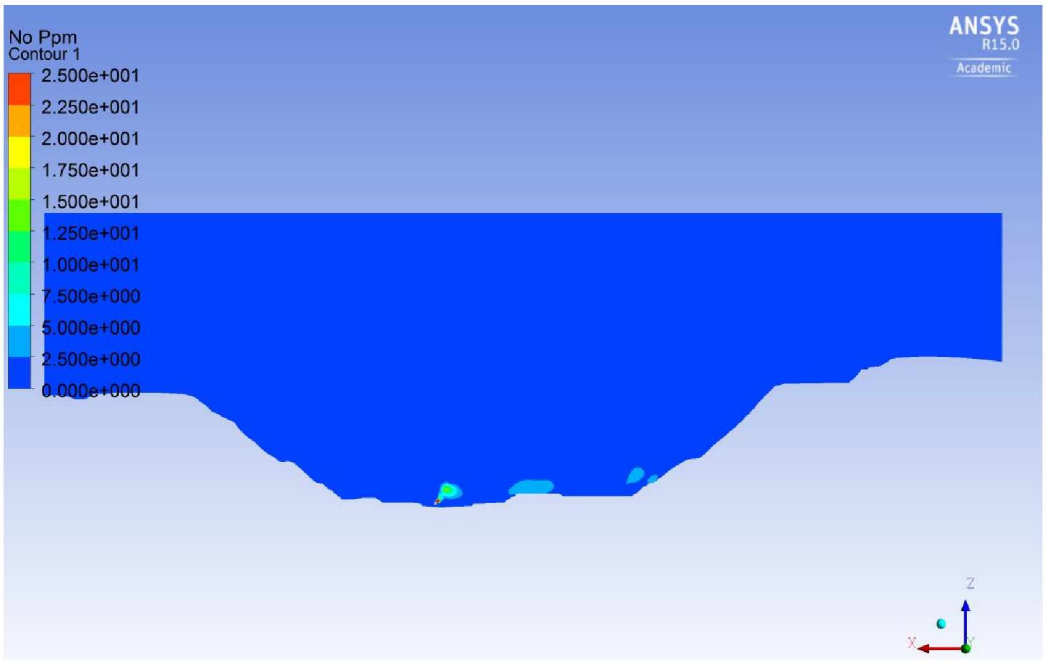

Figure C-51: Concentration of CO (in ppm) at Time Step (t ≈ 26.6 hrs.) for LES Model of 2010 Pit.

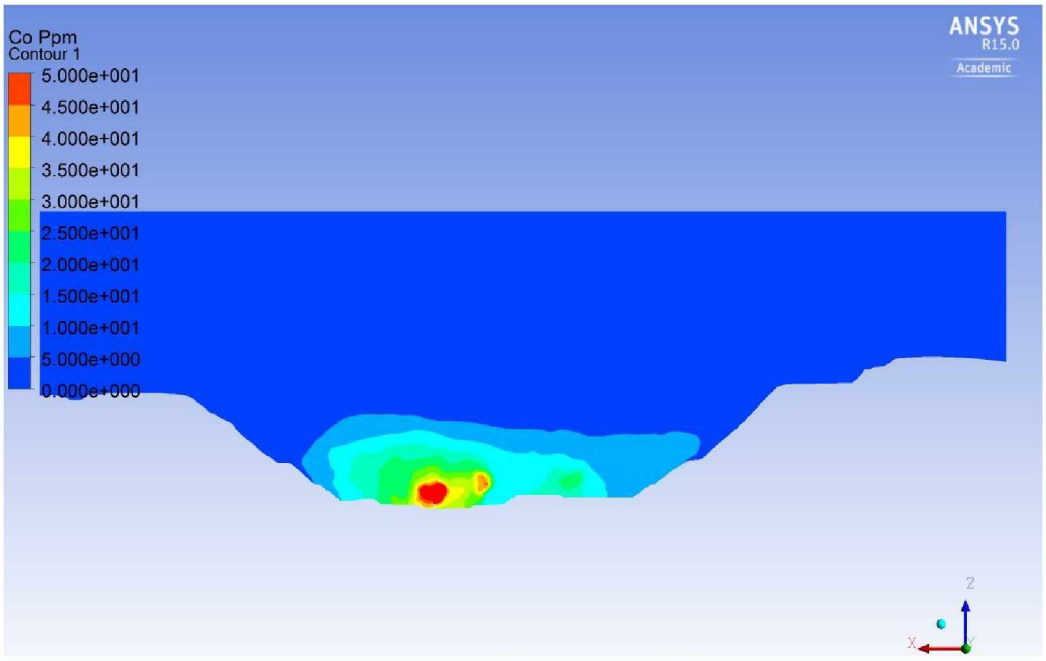

Figure C-52: Concentration of CO (in ppm) at Time Step (t ≈ 16 hrs.) for LES Model of 2010 Pit.

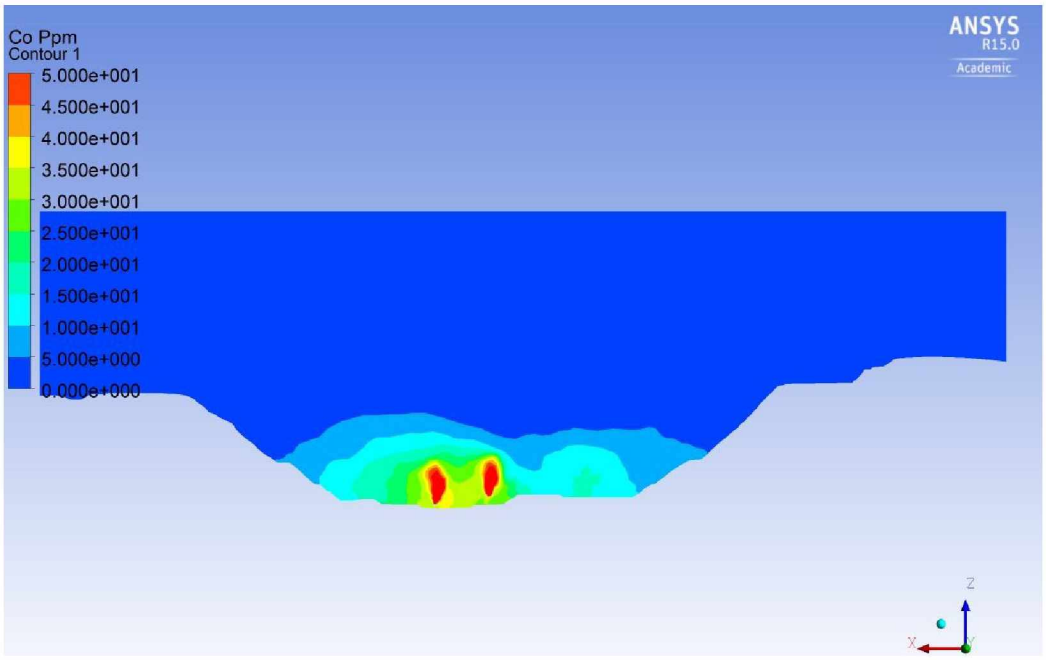

Figure C-53: Concentration of CO (in ppm) at Time Step (t ≈ 17 hrs.) for LES Model of 2010 Pit.

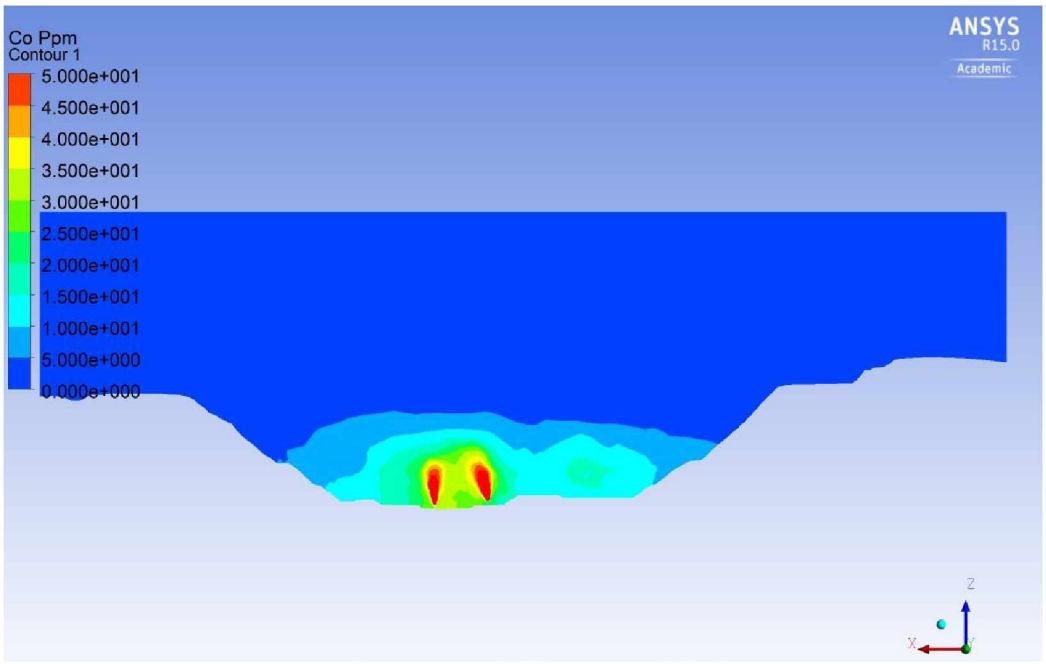

Figure C-54: Concentration of CO (in ppm) at Time Step (t ≈ 18 hrs.) for LES Model of 2010 Pit.

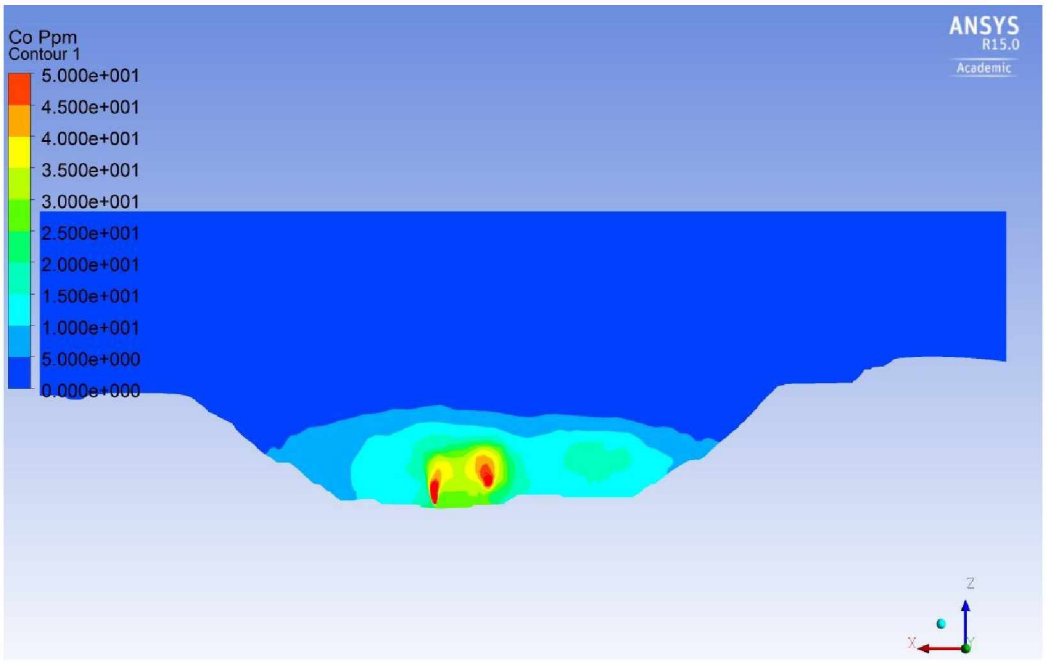

Figure C-55: Concentration of CO (in ppm) at Time Step (t ≈ 19 hrs.) for LES Model of 2010 Pit.

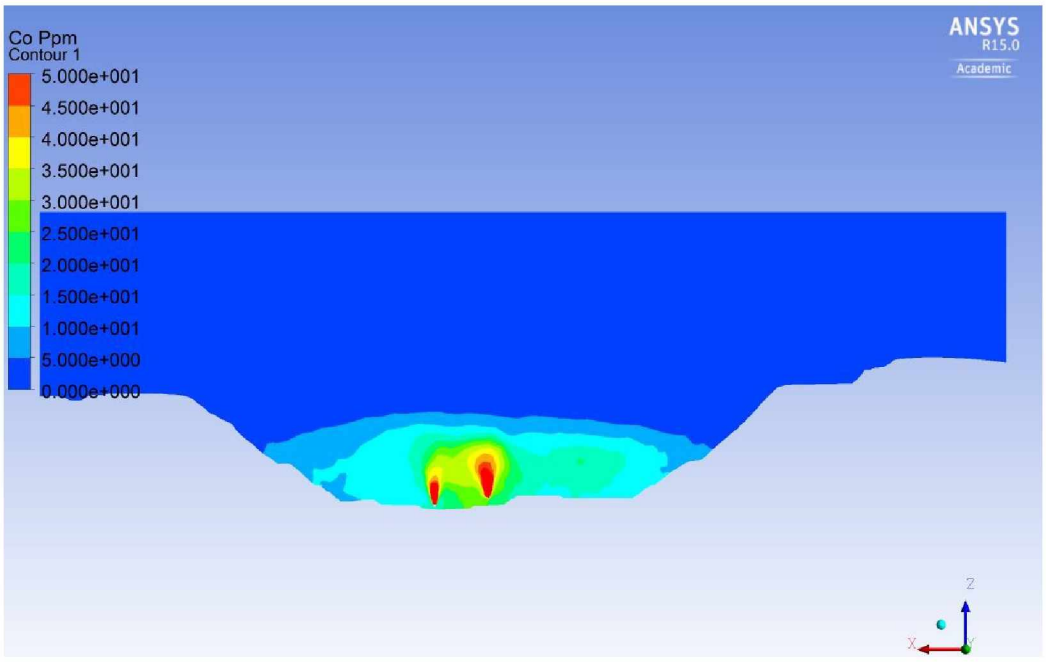

Figure C-56: Concentration of CO (in ppm) at Time Step (t ≈ 20 hrs.) for LES Model of 2010 Pit.

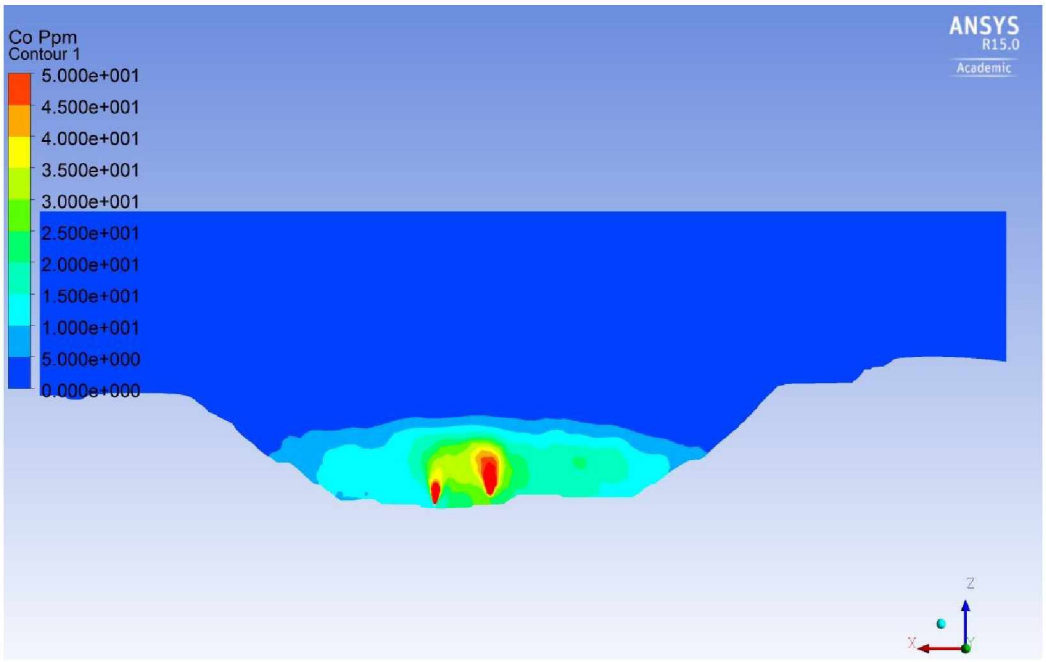

Figure C-57: Concentration of CO (in ppm) at Time Step (t ≈ 21 hrs.) for LES Model of 2010 Pit.

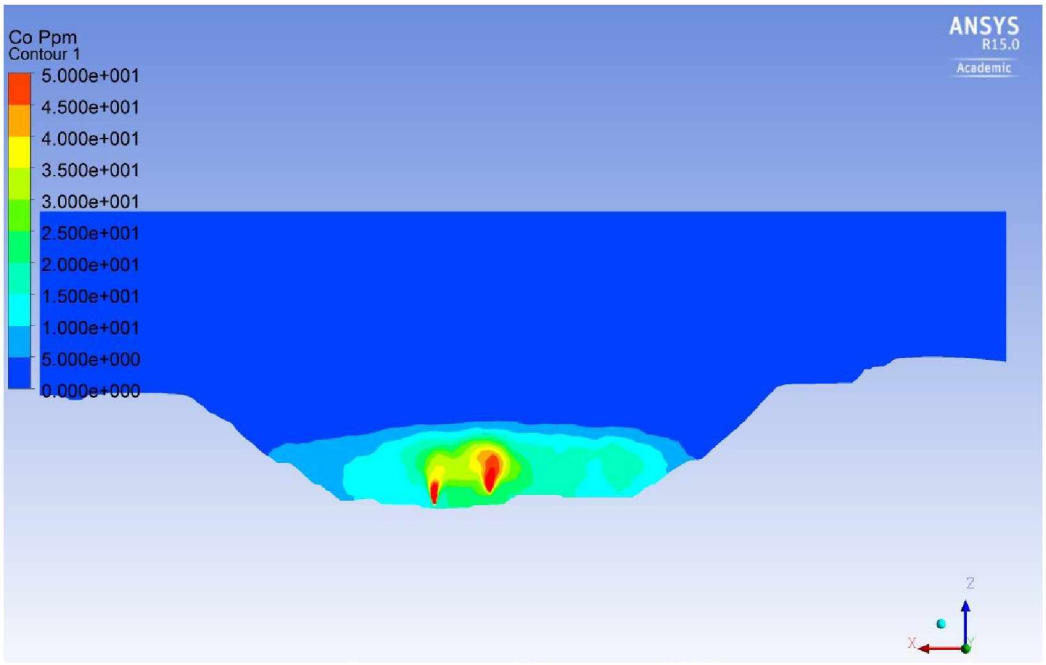

Figure C-58: Concentration of CO (in ppm) at Time Step (t ≈ 22 hrs.) for LES Model of 2010 Pit.

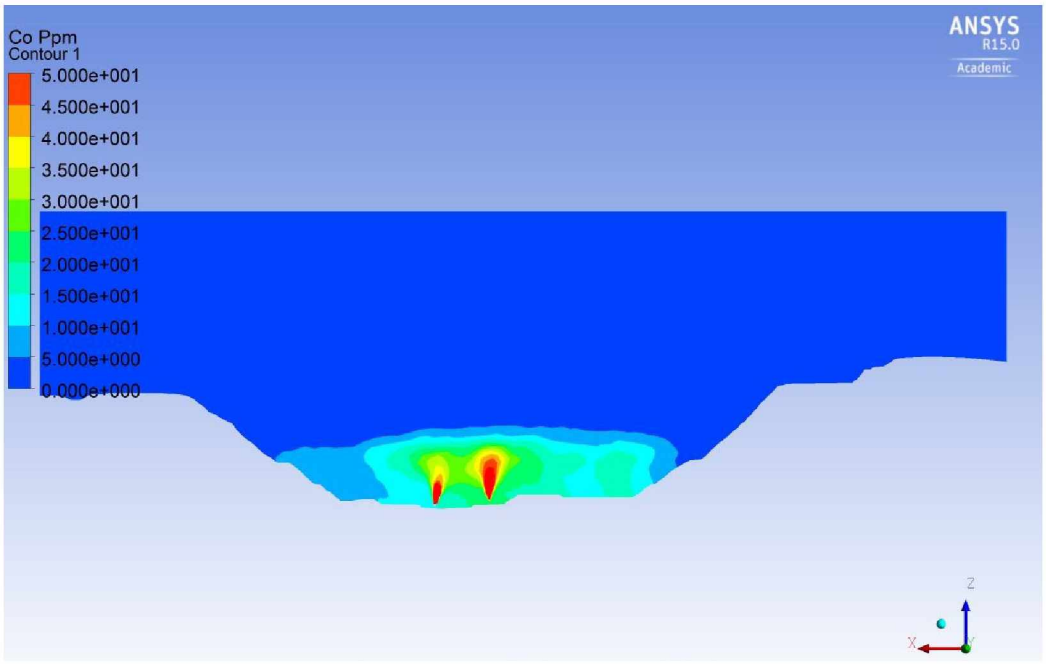

Figure C-59: Concentration of CO (in ppm) at Time Step (t ≈ 23 hrs.) for LES Model of 2010 Pit.

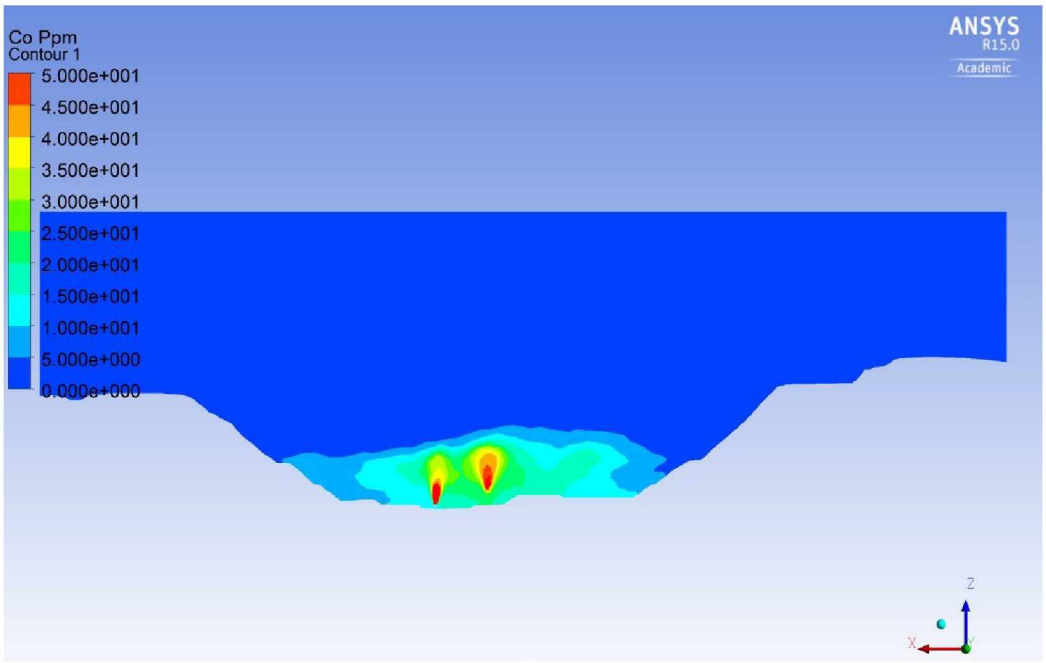

Figure C-60: Concentration of CO (in ppm) at Time Step (t ≈ 24 hrs.) for LES Model of 2010 Pit.

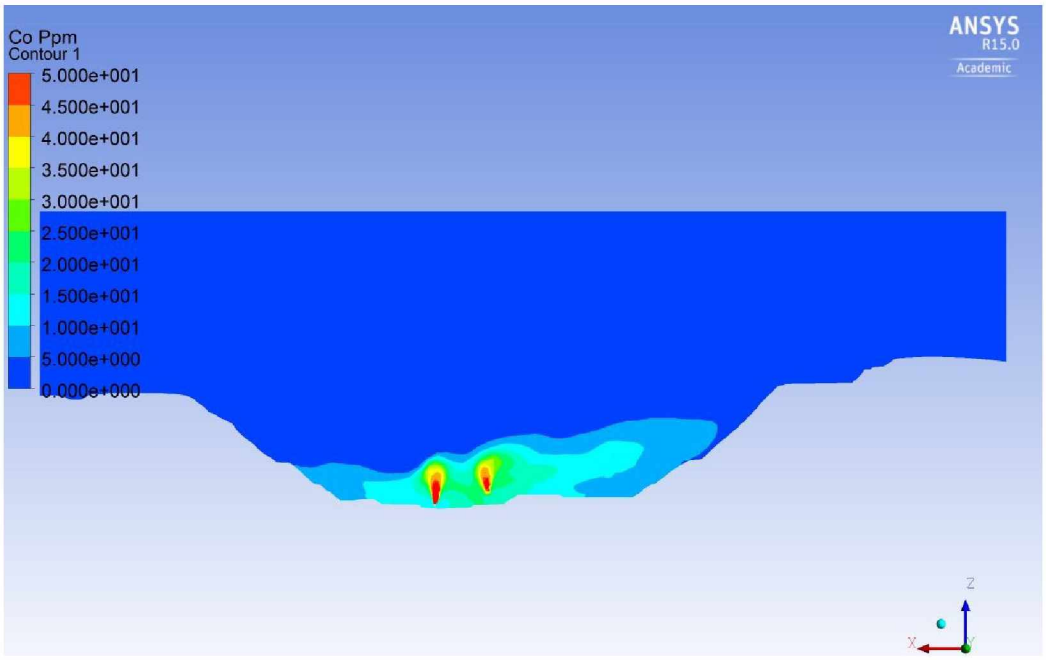

Figure C-61: Concentration of CO (in ppm) at Time Step (t ≈ 25 hrs.) for LES Model of 2010 Pit.

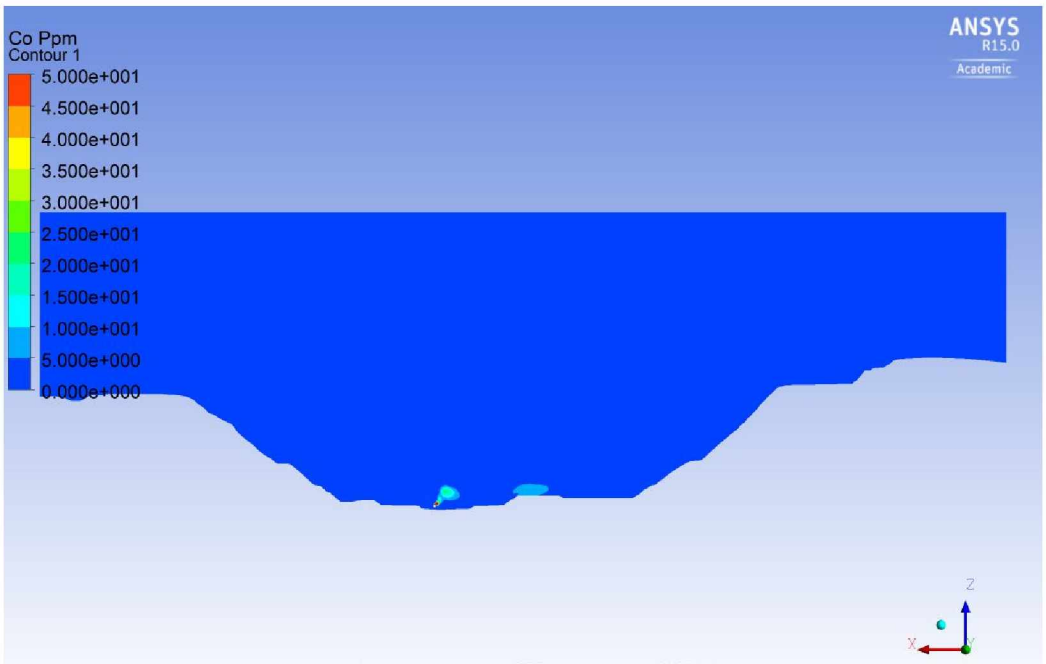

Figure C-62: Concentration of CO (in ppm) at Time Step (t ≈ 26.6 hrs.) for LES Model of 2010 Pit.